STUDIES ON CHEMISTRY OF SOME POLYDENTATE LIGANDS AND THEIR METAL COMPLEXES

Ph. D. THESIS

by

VARUN MOHAN

DEPARTMENT OF CHEMISTRY
INDIAN INSTITUTE OF TECHNOLOGY ROORKEE
ROORKEE - 247 667 (INDIA)
MARCH, 2014

STUDIES ON CHEMISTRY OF SOME POLYDENTATE LIGANDS AND THEIR METAL COMPLEXES

A THESIS

Submitted in partial fulfilment of the requirements for the award of the degree

of

DOCTOR OF PHILOSOPHY

in

CHEMISTRY

by

VARUN MOHAN

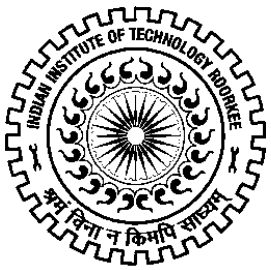

DEPARTMENT OF CHEMISTRY
INDIAN INSTITUTE OF TECHNOLOGY ROORKEE
ROORKEE-247 667 (INDIA)
MARCH, 2014

INDIAN INSTITUTE OF TECHNOLOGY ROORKEE
ROORKEE

CANDIDATE'S DECLARATION

I hereby certify that the work which is being presented in the thesis entitled **"STUDIES ON CHEMISTRY OF SOME POLYDENTATE LIGANDS AND THEIR METAL COMPLEXES"** in partial fulfilment of the requirements for the award of the Degree of Doctor of Philosophy and submitted in the Department of **Chemistry** of the Indian Institute of Technology Roorkee, Roorkee is an authentic record of my own work carried out during a period from **January, 2008** to **March, 2014** under the supervision of **Dr. Kaushik Ghosh, Associate Professor, Department of Chemistry, Indian Institute of Technology Roorkee, Roorkee**.

The matter presented in the thesis has not been submitted by me for the award of any other degree of this or any other Institute.

(VARUN MOHAN)

This is to certify that the above statement made by the candidate is correct to the best of my knowledge.

(Kaushik Ghosh)
Supervisor

Date: March, 2014

The Ph.D. Viva-Voce examination of **Mr. Varun Mohan**, Research Scholar, has been held on …… .

Signature of Supervisor Chairman, SRC Signature of External Examiner

Head of the Deptt./Chairman, ODC

ACKNOWLEDGEMENT

Foremost, I humbly and politely bow my head to thyness, the *Lord Shiv*a and *Goddess Saraswati* "*The Goddess of Wisdom*"who bestowed upon me an opportunity to do this work and gave me ample vision and strength to accomplish this task successfully. I thank the almighty *God* whose gracious blessings and spiritual support always help me to withstand and overcome the difficulties in my life.

I would like to convey my deepest gratitude and reverence to my supervisor **Dr. Kaushik Ghosh** for his helpful counsel, management, professionalism and continued hopefulness, which make him an outstanding advisor. I am highly thankful for his time, attempt and editing skills. His constant support, the trust he placed in my abilities, encouragement and judicious interventions made this thesis to come into picture. I humbly acknowledge a life time's gratitude to him. No words articulate to acknowledge the didactic guidance rendered by him.

I am thankful to Prof. Anil Kumar, Prof. V. K. Gupta and Prof. Kamaluddin, the present and the former Heads, Department of Chemistry, IIT Roorkee, for providing me all the instrumental and necessary facilities and support to carry out these investigations.

The financial support from Ministry of Human Resource Development (MHRD) and University Grants Commission (UGC), New Delhi to complete the present investigations is highly acknowledged.

My thanks are due for the Institute Instrumentation Centre, IIT Roorkee. I am thankful to Prof. U. P. Singh, Dr. Sujata Singh, Dr. Nidhi Goel, Dr. Sandeep Singh, Dr. Kapil Tomar and Shikha Narang for the help in XRD analysis and Prof. Ritu Barthwal, Pradeep, Asif and Amit for the NMR facility. I am also thankful to Dr. Partha Roy, Swati Shrivastava and Pradeep for their help in biological experiments and Dr. Shankar Rath for EPR analysis.

I wish to thank all the faculty members and non-teaching staff of the Department of Chemistry, IIT Roorkee. I would also like to thank Mr. V. P. Saxena, Mr. Abdul Haq and Mr. Madan Pal for all the technical assistance in the Department of Chemistry and Mr. Saini for his kind cooperation in the Department of Biotechnology.

In my lab, I express my special thanks to Dr. Pramod Kumar for all the scientific discussions and his invaluable help to make my work more precious. Without his help it was not possible to produce so many results. My sincere appreciation goes to Ms. Sweety Rathi for her timely help during the execution of this work and moral support. Her valuable suggestions were always helpful for improving the quality of the work.

I wish to thank my other lab members Dr. Nidhi Tyagi, Dr. Sushil Kumar, Hemant, Isha, Archita, Rajan, Ashish, Ovender, Anand, Manju, Kiran and Kapil for their support in their own way.

I express my special thanks to my lovely friend Harish who always stayed with me during all the ups and downs of my life. His amusing company with positive attitude has always been inspiring me to achieve best in the life. My sincere appreciation goes to my friends Raman Maurya, Manohar Lal, Triloki pant, Rahul Tyagi, Prasad, Deep and Kranti. I always feel lucky to have friends like them. I gratefully acknowledge the help from Rajesh, Anjaneyulu, Abhishek and Syantan.

Finally, I express my heartfelt gratitude to my highly respectable and adorable father, Sh. Vinod Kumar and mother Smt. Suman Lata for their unconditional love, encouragement and blessings. I also wish to express my feelings for my brothers Tarun and Akshaya from the bottom of my heart for which my mere expression of thanks will not suffice. My little, adorable sister Gudiya, is always a very important and invaluable constituent of my life. I want to thank her for each and every moment I share with her. I am also obliged to Sheena and Ritu for their affectionate behaviour.

At last, I am extremely grateful to the people whose names have been unknowingly left. I apologize and believe that their wishes will always be with me as they were during the times of need.

Varun Mohan

ABSTRACT

The coordination chemistry deals with the chemistry of ligands and metal ions and the ligands play an indispensible role in determining the coordination geometry, redox chemistry and spectroscopic properties of the metal complexes. In general, ligands serve as electron donors acting as Lewis base and metals as electron acceptors acting as Lewis acid. According to Pearson's "Hard and Soft Acids and Bases" (HSAB) concept, stable bonds may exist only between hard acids and hard bases or soft acids and soft bases. A little modification in the ligand architecture may lead to significant improvements in the reactivities exhibited by complexes. According to Jorgenson, the ligands may be innocent or non-innocent depending on the assignment of oxidation states. Non-innocent ligands give rise to the metal complexes with intriguing redox and electronic properties. A number of non-innocent ligands are present in the biosystem and galactose oxidase enzyme is one of the best examples of such systems. Nitric oxide, porphyrinic ligands, catecholate ligands and phenolato ligands also represent this family and give rise to complexes with exciting properties. Complexes derived from such ligands receive special significance due to their resemblance with biosystems as well as due to their ability to serve as electron reservoirs.

Being inspired from biology, several biomimmetic complexes have been developed which can catalyze various chemical reactions of potential biological interest like water oxidation, dinitrogen activation and amide hydrolysis at reasonable rates and under ambient conditions. A number of metal complexes have been prepared using planar ligands like bipy, o-phen, dpq, dppz and terpy which can interact with nucleic acids and such complexes are of medicinal values. Such compounds find their application in developing the foot-printing agents, conformational probes and chemotherapeutic agents. Hence, judicial design of the ligand frame is the essential step to finely tune the properties and reactivities exhibited by the metal complexes.

In the present study, few ligands were designed, synthesized and characterized by several spectroscopic studies. Cobalt, nickel, copper and zinc complexes were synthesized and characterized by spectroscopic and electrochemical studies. Molecular structures of representative metal complexes were determined by single crystal X-ray diffraction. Various type of biological activities were examined for these complexes including DNA interaction

studies, nuclease activity, superoxide dismutase activity, phenoxyl radical generation, catecholase activity, protein interaction studies, protein cleavage activity and anticancer activity. The effect of donor atoms and ligand structure on reactivity studies was investigated in this thesis. The thesis is divided into following chapters.

The **First chapter** presents an introduction to coordination chemistry of various types of ligands as well as to the general properties of few first row transition metals. Role of ligand to determine the chemical properties and biological activities of various coordination complexes is thoroughly discussed. A number of ligands were described which were used for the structural/functional mimicking of the active sites of various metalloenzymes. Various physical methods and spectroscopic techniques used were comprehensively summarized in this chapter.

Chapter two presents the synthesis and characterization of mononuclear cobalt complexes namely $[Co(Pyimpy)Cl_2]$ (**1a**), $[Co(Pyimpy)_2](ClO_4)_2$ (**1b**), $[Co(Pamp)Cl_2]$ (**2a**) and $[Co(Pamp)_2](ClO_4)$ (**2b**) (where Pyimpy = 1–phenyl–1–(pyridin–2–yl)–2–(pyridin–2–ylmethylene)hydrazine; PampH = N'–phenyl–N'–(pyridin–2–yl)picolinohydrazide and H stands for the dissociable proton). The molecular structure of complex **1a** was authenticated using X–ray diffraction study. Redox behavior of the metal complexes was investigated through electrochemical methods. DNA interaction and nuclease activity studies over all the complexes were performed and the mechanism of DNA cleavage was established using various types of scavengers. Superoxide dismutase (SOD) activity of the complexes was assayed by xanthine/xanthine oxidase/nitroblue tetrazolium assay and a correlation was developed with the DNA cleavage activity.

Chapter three describes the synthesis and characterization of a tridentate ligand N_3L (where N_3L=2–((1–phenyl–2–(1–(pyridin–2–yl)ethylidene)hydrazinyl)methyl)pyridine) and its mononuclear metal complexes of copper, zinc, cobalt and nickel namely $[Cu(N_3L)Cl_2]$ (**3a**), $[Cu(N_3L)_2](ClO_4)_2$ (**3b**), $[Zn(N_3L)Cl_2]$ (**4a**), $[Zn(N_3L)_2](ClO_4)_2$ (**4b**), $[Co(N_3L)Cl_2]$ (**5a**), $[Co(N_3L)_2](ClO_4)_2$ (**5b**), $[Ni(N_3L)Cl_2]$ (**6a**) and $[Ni(N_3L)_2](ClO_4)_2$ (**6b**) respectively. The structures of complexes **3a** and **5a** were established by X-ray diffraction methods. Cyclic voltammetric experiments were performed to examine the redox properties of the metal complexes. All the complexes were found to be stable in the buffer solutions at

physiological pH and subjected to DNA interaction studies by absorption spectroscopy, emission spectroscopy and circular dichroism spectroscopy. The complexes represent the rare kind of complexes which bind covalently with nucleic acids and the mechanism has been established by titration with potential small ligands using absorption spectral technique. The DNA cleavage activities of the complexes were investigated and the mechanisms were determined using inhibition experiments involving radical scavengers. Binding of these complexes with bovine serum albumin (BSA) was also investigated. The mechanism of binding with protein was explored by the titration of these complexes with amino acids using electronic absorption spectroscopy and a covalent attachment of metal complexes with the amino acids side chains was observed. The family represents novel examples of complexes which are still less explored and highly desirable for *in vivo* applications.

In **chapter four**, two mononuclear cobalt(III) complexes namely $[Co(Phimp)_2](ClO_4)\cdot CH_3CN$ (**7**$\cdot CH_3CN$) and $[Co(^tBuPhimp)_2](ClO_4)$ (**8**) derived from tridentate ligands PhimpH and ^{t}BuPhimpH (PhimpH = 2–((2–phenyl–2–(pyridin–2–yl)hydrazono)methyl)phenol and ^{t}BuPhimpH = 2,4–di–*tert*–butyl–6–((2–phenyl–2–(pyridin–2–yl)hydrazono)methyl)phenol where H stands for the dissociable proton) were synthesized and characterized by various physical and spectroscopic techniques. X–ray crystallographic studies were performed to determine the molecular structure of the representative complex **7**$\cdot CH_3CN$. These complexes gave rise to the phenoxyl radical species in solution on chemical oxidation due to the non–innocent character of the ligands. Such species are very much significant to understand the mechanism of galactose oxidase enzyme. Generation of phenoxyl radical species was confirmed by UV–visible and EPR spectroscopy. The complexes were subjected to DNA cleavage activity and the complex **8** was found to be very efficient for DNA cleavage leading to extensive DNA degradation. Protein interaction studies of these complexes were performed by tryptophan fluorescence quenching assay using BSA as a protein model. Protease activity of both complexes was scrutinized and complex **8** was found to be efficient in protein cleavage also. The anticancer activities of these complexes were also studied against various cell lines and promising results were obtained for complex **8**.

In **chapter five**, the synthesis and characterization of nickel complexes $[Ni(Phimp)_2]\cdot 3H_2O\cdot CH_3OH$ (**9a**$\cdot 3H_2O\cdot CH_3OH$), [Ni(Phimp)Cl] (**9b**), $[Ni(Phimp)(Pyimpy)](ClO_4)\cdot H_2O$ (**9c**$\cdot H_2O$), $[Ni(^tBuPhimp)_2]$ (**10a**), [Ni(^{t}BuPhimp)Cl] (**10b**), and [Ni(^{t}BuPhimp)(Pyimpy)](ClO_4) (**10c**) was described. The molecular structures of the complexes **9a**$\cdot 3H_2O\cdot CH_3OH$ and **9c**$\cdot H_2O$ were determined using X–ray diffraction methods. The redox behavior of these complexes was investigated using cyclic voltammetry. The ability of the complexes to generate phenoxyl radical species in solution by chemical oxidation was investigated and supported by DFT calculations. DNA and protein interaction studies of these complexes were accomplished in this chapter. Nuclease activities of these complexes and their mechanisms were also investigated.

In **chapter six**, the fluorescence properties of two ligands Gimpy and Timpy (where Gimpy = 1,2–bis(2–phenyl–2–(pyridin–2–yl)hydrozono)ethane and Timpy = 1,2–bis((2–phenyl–2–(pyridin–2–yl)hydrozono)methyl)benzene) were examined in presence of various transition metal ions in solution and enhancement in fluorescence was observed in presence of Ni^{2+}. To confirm the binding mode of these ligands, nickel complexes of these ligands namely $[(Ni(Gimpy)(\mu\text{–}Cl))_2](ClO_4)_2$ (**11**) and $[(Ni(Timpy)(\mu\text{–}Cl))_2](ClO_4)_2\cdot 2(CH_3)_2CO$ (**12**$\cdot 2(CH_3)_2CO$) were synthesized and characterized. Cyclic voltammetric experiments were performed to investigate the redox behavior of these complexes. Molecular structures of Gimpy and **12**$\cdot 2(CH_3)_2CO$ were determined using X–ray crystallography.

Chapter seven deals with the synthesis and characterization of dinuclear copper(II) and cobalt(II) complexes namely $[\{Cu(Simpy)(\mu\text{–}Cl)Cl\}_2]\cdot 4H_2O$ (**13a**$\cdot 4H_2O$), $[\{Co(Simpy)(\mu\text{–}Cl)Cl\}_2]$ (**13b**), $[\{Cu(Impy)(\mu\text{–}Cl)Cl\}_2]$ (**14a**) and $[\{Co(Impy)(\mu\text{–}Cl)Cl\}_2]$ (**14b**) derived from two bindentate ligands Simpy and Impy (Simpy = 2–(1–phenyl–2–(1–(thiophen–2–yl)ethylidene)hydrazinyl)pyridine and Impy = 2–(2–benzylidene–1–phenylhydrazinyl)pyridine). Molecular structures of complexes **13**$\cdot 4H_2O$ and **14** were authenticated using X–ray diffraction studies. The complexes were examined for the catecholase activity as well as DNA cleavage activity. Complex **13a**$\cdot 4H_2O$ exhibited moderate catecholase activity and excellent self-activated nuclease activity.

LIST OF PUBLICATIONS

Journal Publications

1. Kaushik Ghosh, Pramod Kumar, **Varun Mohan**, Udai P. Singh, Sahba Kasiri, Subhrangsu S. Mandal "Nuclease activity via self-activation and anticancer activity of a mononuclear copper(II) complex: Novel role of the tertiary butyl group in the ligand frame" *Inorg. Chem.* **2012**, *51*, 3343-3345.

2. Kaushik Ghosh, Pramod Kumar, **Varun Mohan**, Udai P. Singh "Self-activated DNA cleavage and nitric oxide reactivity studies on mononuclear copper complexes derived from tetradentate ligands" *Inorg. Chem. Commun.* **2012**, *15*, 55-60.

3. Kaushik Ghosh, **Varun Mohan**, Pramod Kumar, Udai P. Singh "DNA binding, nuclease and superoxide scavenging activity studies on mononuclear cobalt complexes derived from tridentate ligands" *Polyhedron* **2013**, *49*, 167-176.

4. Kaushik Ghosh, **Varun Mohan**, Pramod Kumar, S. W. Ng, E. R. T. Tiekink "Selective fluorescence sensing of Ni^{2+} by tetradentate ligands: Synthesis of nickel complexes and crystal structures" *Inorg. Chim. Acta* **2014**, (ASAP article).

5. Kaushik Ghosh, **Varun Mohan**, Udai P. Singh, Swati Shrivastava, Partha Roy "Synthesis, and characterization of biomimetic cobalt(III) complexes derived from ligands containing NNO donors: Generation of phenoxyl radical complex, DNA interaction and protein interaction studies" (Manuscript under preparation).

6. Kaushik Ghosh, **Varun Mohan**, Udai P. Singh "Mononuclear nickel(II) complexes and their phenoxyl radical analogues: DFT calculation, DNA and protein interaction studies" (Manuscript under preparation).

7. Kaushik Ghosh, **Varun Mohan**, Udai P. Singh "Dinuclear copper(II) and cobalt(II) complexes of potential biological interest derived from bidentate ligands: DNA cleavage via self-activation" (Manuscript under preparation).

8. Kaushik Ghosh, **Varun Mohan**, Udai P. Singh "A new family of Cu(II), Zn(II), Co(II) and Ni(II) complexes: Covalent binding with DNA and proteins and self-activated DNA cleavage" (Manuscript under preparation).

Contribution in conferences/workshops

1. Kaushik Ghosh, Sushil Kumar, **Varun Mohan**, Akash Mittal, Ramakant Sahu, Pramod Kumar, Nidhi Tyagi "Synthesis and characterization of cycloruthenated complexes and their photolability studies" 4th Asian biological Inorganic Chemistry Conference; November 10-13, 2008; Jeju, Korea (Article published).

2. International workshop on chemical evolution and origin of life; March 5-7, 2010; Indian Institute of Technology, Roorkee.

3. **Varun Mohan**, Pramod Kumar, Nidhi Goel and Kaushik Ghosh "Synthesis and characterization of mononuclear cobalt complexes derived from tridentate ligands" 4th Conference on Recent Trends in Instrumental Methods of Analysis; February 18-20, 2010; Indian Institute of Technology, Roorkee (Oral presentation).

4. Kaushik Ghosh, **Varun Mohan**, Pramod Kumar, U. P. Singh "Interaction of DNA with Cu(II), Zn(II) and Co(II) complexes: Generation of new species and role of redox active centers in nuclease activity" 3rd Asian Conference on Coordination Chemistry (ACCC–3, 2011); October 17-20, 2011; India Habitat Center, New Delhi.

5. Kaushik Ghosh, **Varun Mohan**, Pramod Kumar, U. P. Singh "Cobalt complexes derived from tridentate ligands: Generation of phenoxyl radical and nuclease activity" Diamond Jubilee Symposium on Recent Trends in Chemistry (DJSRTC)–2011; October 21-23, 2011; Department of chemistry; Indian Institute of Technology, Kharagpur (Poster presentation) .

6. Kaushik Ghosh, **Varun Mohan**, Pramod Kumar, U. P. Singh "Synthesis and characterization of cobalt and copper complexes: Role of tertiary butyl group in nuclease activity" Symposium on Modern Trends In Inorganic Chemistry (MTIC)–XIV; December 10-13, 2011; School of Chemistry, University of Hyderabad, Hyderabad (Poster presentation as well as oral presentation).

7. Kaushik Ghosh, **Varun Mohan**, Pramod Kumar, U. P. Singh, Partha Roy "Copper(II) and zinc(II) complexes derived from ligands containing phenolato donor(s): Generation of phenoxyl radical, nuclease and protease activity studies" International Conference on Biological Inorganic Chemistry (ICBIC)-2013; February 20-22, 2013; Department of chemistry, Periyar university, Salem, Tamilnadu.

TABLE OF CONTENTS

		Candidate's Declaration	*i*
		Acknowledgement	*ii*
		Abstract	*iv*
		List of Publications	*viii*
		Table of contents	*x*
		List of Figures	*xvi*
		List of Tables	*xxxvi*
		List of Schemes	*xxxviii*
S. No.		**Chapter**	**P. No.**
Chapter 1		**General Introduction and Salient Features of Various Ligands and Systems Derived from Copper, Zinc, Cobalt and Nickel**	**1–101**
1.1.		Introduction	1
	1.1.1.	Ligand	1
		Classification of ligands	3
		Special types of ligands	5
	1.1.2.	Metals	6
		Cobalt	*16*
		General comments	16
		Role in biosystems	17
		Applications of cobalt	18
		Nickel	*24*
		General comments	24
		Role in biosystems	25
		Applications of nickel	25
		Copper	*28*
		General comments	28
		Role in biosystems	29
		Applications of copper	31
		Zinc	*34*
		General comments	34
		Role in biosystems	35
		Applications of zinc	36
	1.1.3.	Relevance among Co, Ni, Cu and Zn	37
1.2.		Metalloenzymes	37
	1.2.1.	Galactose oxidase and glyoxal oxidase	38

1.2.2. Superoxide dismutase 40
1.2.3. Catechol oxidase 42
1.3. Metal complexes as enzyme models 45
1.3.1. *Cobalt complexes* *46*
Galactose oxidase models 46
Superoxide dismutase models 47
Catecholase models 47
Nitrile hydratase models 48
Liver alcohol dehydrogenase models 50
1.3.2. *Nickel complexes* *50*
Galactose oxidase models 50
Superoxide dismutase models 52
Catecholase models 54
1.3.3. *Copper complexes* *55*
Galactose oxidase models 55
Superoxide dismutase models 57
Catecholase models 58
1.3.4. *Zinc complexes* *60*
Galactose oxidase models 60
Catecholase models 61
Liver alcohol dehydrogenase models 62
1.4. DNA, DNA binding and DNA cleavage 63
1.4.1. Structure of DNA 63
1.4.2. DNA binding 63
Covalent binding 64
Non–covalent binding 65
1.4.3. DNA cleavage or nuclease 67
1.5. Metal complexes as artificial metallonucleases 70
1.5.1. Cobalt complexes 70
1.5.2. Nickel complexes 71
1.5.3. Copper complexes 72
1.5.4. Zinc complexes 74
1.6. Protein models, protein binding and protein cleavage 75
1.6.1. Structure of albumin and binding sites 75
1.6.2. Protein cleavage or protease 77
1.7. Metal complexes as artificial metalloproteases 79
1.7.1. Cobalt complexes 80
1.7.2. Copper complexes 81
1.8. Present investigation 83
1.8.1. Synthesis of ligands and metal complexes 83

	1.8.2.	Description of activity studies	84
		Generation of phenoxyl radical complexes	84
		Superoxide dismutase activity	84
		DNA interaction studies	86
		Nuclease activity	88
		Cell viability assay	89
		Protein interaction studies	90
		Protease activity	92
		Catecholase activity	93
	1.8.3.	Summary of present investigation	93
1.9.		Measurements	98
Chapter 2		**Synthesis and Reactivity Studies on Mononuclear Cobalt Complexes derived from tridentate ligands: SOD activity, DNA binding and DNA cleavage**	**102–143**
2.1.		Introduction	102
2.2.		Results and discussion	104
	2.2.1.	Synthesis and characterization of the ligands	104
	2.2.2.	Synthesis and characterization of cobalt complexes	105
	2.2.3.	Description of molecular structure	113
	2.2.4.	Electrochemistry	117
	2.2.5.	Superoxide dismutase activity studies	120
	2.2.6.	DNA binding studies	125
	2.2.7.	Nuclease activity	132
2.3.		Conclusions	136
2.4.		Experimental section	137
	2.4.1.	Reagents and materials	137
	2.4.2.	Synthesis of ligands	138
	2.4.3.	Synthesis of cobalt complexes	138
	2.4.4.	X-ray crystallography	141
	2.4.5.	Superoxide dismutase assay	142
	2.4.6.	DNA binding and cleavage experiments	143
Chapter 3		**Mononuclear Copper(II), Zinc(II), Cobalt(II) and Nickel(II) Complexes Derived from Tridentate Ligand: Covalent Binding with DNA and Protein and Self–activated DNA Cleavage**	**144–228**
3.1.		Introduction	144
3.2.		Results and discussion	147
	3.2.1.	Synthesis and characterization of the ligand	147
	3.2.2.	Synthesis and characterization of metal complexes	153

3.2.3. Description of molecular structures 165
3.2.4. Electrochemistry 175
3.2.5. Superoxide dismutase activity studies 179
3.2.6. DNA interaction studies 180
3.2.7. Nuclease activity 197
3.2.8. Protein interaction studies 206
3.3. Conclusions 216
3.4. Experimental section 217
3.4.1. Reagents and materials 217
3.4.2. Synthesis of ligands 218
3.4.3. Synthesis of metal complexes 219
3.4.4. X-ray crystallography 224
3.4.5. Superoxide dismutase assay 226
3.4.6. DNA binding and cleavage experiments 226
3.4.7. Protein binding experiments 227

Chapter 4 Mononuclear Cobalt(III) Complexes Derived from Tridentate Ligands with NNO Donors: Phenoxyl Radical Generation and Self–activated DNA and Protein Cleavage **229–268**

4.1. Introduction 229
4.2. Results and discussion 230
4.2.1. Synthesis and characterization of the ligands 230
4.2.2. Synthesis and characterization of cobalt complexes 231
4.2.3. Description of molecular structure 238
4.2.4. Electrochemical studies 243
4.2.5. Generation of phenoxyl radical species 245
4.2.6. DNA interaction studies 247
4.2.7. Nuclease activity 250
4.2.8. Protein interaction studies 253
4.2.9. Protein cleavage activity 258
4.2.10. Cytotoxicity studies 260
4.3. Conclusions 261
4.4. Experimental section 262
4.4.1. Reagents and materials 262
4.4.2. Synthesis of ligands 263
4.4.3. Synthesis of cobalt complexes 263
4.4.4. X-ray crystallography 265
4.4.5. DNA binding and cleavage experiments 266
4.4.6. Protein binding and cleavage experiments 267
4.4.7. Cell viability assay 268

Chapter 5 **Synthesis and Characterization of Mononuclear Nickel(II) Complexes: Phenoxyl Radical Generation, DFT Calculation, DNA Interaction and Protein Interaction Studies** **269–324**

5.1. Introduction 269
5.2. Results and discussion 270
5.2.1. Synthesis and characterization of the ligands 270
5.2.2. Synthesis and characterization of nickel complexes 270
5.2.3. Description of molecular structure 278
5.2.4. Electrochemical studies 287
5.2.5. Theoretical calculations 292
5.2.6. Generation of phenoxyl radical species 293
5.2.7. DNA interaction studies 299
5.2.8. Nuclease activity 306
5.2.9. Protein interaction studies 308
5.3. Conclusions 315
5.4. Experimental section 315
5.4.1. Reagents and materials 315
5.4.2. Synthesis of ligands 316
5.4.3. Synthesis of nickel complexes 316
5.4.4. X-ray crystallography 320
5.4.5. Theoretical studies 321
5.4.6. DNA binding and cleavage experiments 322
5.4.7. Protein binding experiments 323

Chapter 6 **Selective Fluorescence Sensing of Nickel(II) by Tetradentate Ligands: Synthesis of Nickel Complexes and Crystal Structures** **325–349**

6.1. Introduction 325
6.2. Results and discussion 327
6.2.1. Synthesis and characterization of the ligands 327
6.2.2. Synthesis and characterization of nickel complexes 328
6.2.3. Description of molecular structure 331
6.2.4. Magnetic properties 337
6.2.5. Photophysical properties 339
6.2.6. Electrochemical properties 343
6.3. Conclusions 345
6.4. Experimental section 346
6.4.1. Reagents and materials 346
6.4.2. Synthesis of ligands 346
6.4.3. Synthesis of nickel complexes 346
6.4.4. X-ray crystallography 348

Chapter 7 **Synthesis and Reactivity Studies on Dinuclear Copper(II) and Cobalt(II) Complexes Derived from Bidentate Ligands: Catecholase Activity and Self-activated Nuclease Activity** **350–375**

7.1. Introduction 350

7.2. Results and discussion 351

7.2.1. Synthesis and characterization of the ligands 351

7.2.2. Synthesis and characterization of metal complexes 355

7.2.3. Description of molecular structure 359

7.2.4. Catecholase activity 367

7.2.5. Nuclease activity 368

7.3. Conclusions 370

7.4. Experimental section 370

7.4.1. Reagents and materials 370

7.4.2. Synthesis of ligands 371

7.4.3. Synthesis of metal complexes 372

7.4.4. X-ray crystallography 374

7.4.5. Catecholase activity 375

7.4.6. DNA cleavage experiments 375

References **376-458**

Summary and Conclusions **459**

LIST OF FIGURES

Fig. 1.1	Active site of galactose oxidase	39
Fig. 1.2	Active site of Cu–Zn SOD enzyme	41
Fig. 1.3	Active site of *I. batatas* catechol oxidase	43
Fig. 1.4	DNA double helix and its structural components	63
Fig. 1.5	Covalent DNA binding by *cis*–platin via intra–strand cross–linking between platinum atom and N7 atoms of adjacent guanines	64
Fig. 1.6	The binding modes of metal complexes with DNA: Groove binding, metallointercalator and metalloinsertor	67
Fig. 1.7	Ribbon representation of the structure of HSA (left) and BSA (right)	76
Fig. 1.8	Conventional drugs vs. peptide–cleaving catalytic drugs	80
Fig. 2.1	UV–visible spectra of complexes **1–2** (50 μM) in methanol	108
Fig. 2.2	^{1}H NMR spectrum of complex **2a** in $CDCl_3$	109
Fig. 2.3	^{13}C NMR spectrum of complex **2a** in $CDCl_3$	109
Fig. 2.4	^{1}H NMR spectrum of complex **2b** in $CDCl_3$	110
Fig. 2.5	^{13}C NMR spectrum of complex **2b** in $CDCl_3$	110
Fig. 2.6	The ESI–MS spectrum of **1a** in acetonitrile	111
Fig. 2.7	The ESI–MS spectrum of **1b** in acetonitrile	112
Fig. 2.8	The ESI–MS spectrum of **2b** in acetonitrile	112
Fig. 2.9	(a) ORTEP representation of the crystal structure of **1a** showing atom numbering scheme and displacement ellipsoid (50% probability level). Hydrogen atoms are omitted for clarity; (b) square pyramidal disposition of donor atoms around metal centre	114
Fig. 2.10	(a) Intermolecular hydrogen bonding network in **1a**; (b) another view (hydrogen atoms are omitted for clarity)	116
Fig. 2.11	Intermolecular hydrogen bonding network and π–stacking interactions in **1a** giving rise to supramolecular polymer–like species	116
Fig. 2.12	Packing diagram in crystal structure of **1a**	117
Fig. 2.13	Cyclic voltammograms of 10^{-3} M solutions of **1–2** in acetonitrile (10^{-3} M) vs. Ag/AgCl in presence of 0.1 M tetrabutylammonium perchlorate as supporting electrolyte; scan rate: 0.1 V/s	118
Fig. 2.14	Cyclic voltammograms of solution of **1a** (10^{-3} M) in acetonitrile exhibiting individual redox couples obtained by scanning within the potential ranges (a) +0.300 V and +0.650 V, (b) -0.700 V and -0.500 V, and (c) -1.100 V and -0.650 V respectively; 0.1 M TBAP was used as a supporting electrolyte, glassy–carbon as a working electrode and Ag/AgCl as reference electrode; scan rate 0.1 V/s	120
Fig. 2.15	SOD activity of complexes **1a** and **2a** by xanthine/xanthine oxidase–nitro	121

blue tetrazolium assay with an incubation time of 10 min

Fig. 2.16 Absorption spectral changes exhibiting the uric acid formation in presence of complexes **1a** and **1b** in phosphate buffer (pH 7.8) containing 1% dimethylformamide (DMF). Equal concentration of complexes was maintained in both (sample and reference) cuvettes. [xanthine] = 200 μM, [xanthine oxidase] = 2.1 mU/mL, [Complex] = 100 μM. Incubation time was varied from 0 min to 20 min 122

Fig. 2.17 Electronic absorption spectrum exhibiting negligible change in the absorption profile of NBT (50 μM) due to incubation or presence of complex 124

(a) No change in absorption profile of NBT after incubation in absence of any complex

(b) – (e) No change in absorption profile of NBT after incubation with **1a**, **1b**, **2a** and **2b** (all 50 μM) respectively
(f) – (i) No change in absorption profile of **1a**, **1b**, **2a** and **2b** (50 μM) respectively after incubation

Fig. 2.18 Absorption spectra of cobalt complexes in the presence of increasing amounts of DNA in 0.1 M phosphate buffer (pH 7.2) (a) [**1a**] = 50 μM, [DNA] = 0–116.5 μM and (b) [**1b**] = 40 μM, [DNA] = 0–93 μM. Dotted line represents the spectrum in the absence of DNA 125

Fig. 2.19 Electronic absorption spectrum of complexes (a) **1a**, (b) **1b**, (c) **2a** and (d) **2b** in phosphate buffer (pH 7.2) and water exhibiting no spectral shift 127

Fig. 2.20 Reverse titration experiment of CT–DNA with complex **1a** in 0.1 M phosphate buffer (pH 7.2) showing a shift of 20 nm in UV–vis spectrum. [DNA] = 120 μM and [**1a**] = 0–64 μM respectively 128

Fig. 2.21 Absorption spectra of cobalt complexes in the presence of increasing amounts of DNA in 0.1 M phosphate buffer (pH 7.2) (a) [**2a**] = 100 μM, [DNA] = 0–123 μM, (b) [**2b**] = 80 μM, [DNA] = 0–80 μM. Dotted line represents the spectrum in the absence of DNA. 129

Fig. 2.22 Fluorescence emission spectra of the EB–DNA in presence of cobalt complexes in 0.1 M phosphate buffer (pH 7.2). λ_{ex} = 250 nm and λ_{em} = 585 nm. [EB] = 5 μM, [DNA] = 25 μM, (a) [**1a**] = 0–45.7 μM, (b) [**1b**] = 0–35.5 μM, (c) [**2a**] = 0–48.7 μM and (d) [**2b**] = 0–35.5 μM. Dotted line represents the spectrum in the absence of complex 130

Fig. 2.23 Stern–Volmer plots for complexes (a) **1a**, (b) **1b**, (c) **2a** and (d) **2b** 131

Fig. 2.24 Circular dichroism spectra in 0.1 M phosphate buffer (pH 7.2) after 10 min incubation at 25 °C. (**a**) CT–DNA and its interaction with complexes **1a** and **1b** (**b**) CT–DNA and its interaction with complexes **2a** and **2b** 132

Fig. 2.25 Gel electrophoresis separations showing the cleavage of supercoiled 134

pBR322 DNA (100 ng) by complexes **1a, 2a, 1b** and **2b** in presence of H_2O_2 (200 μM) and BME (200 μM). Samples were incubated at 37 °C for 2 h. Lane 1, DNA control; lane 2, DNA + H_2O_2; lane 3, DNA + BME; lane 4, DNA + **1a** (50 μM); lane 5, DNA + **1a** (50 μM) + H_2O_2; lane 6, DNA + **1a** (50 μM) + BME; lane 7, DNA + **2a** (50 μM); lane 8, DNA + **2a** (50 μM) + H_2O_2; lane 9, DNA + **2a** (50 μM) + BME; lane 10, DNA + **1b** (50 μM); lane 11, DNA + **1b** (50 μM) + H_2O_2; lane 12, DNA + **1b** (50 μM) + BME; lane 13, DNA + **2b** (50 μM); lane 14, DNA + **2b** (50 μM) + H_2O_2; lane 15, DNA + **2b** (50 μM) + BME

Fig. 2.26 Gel electrophoresis separation showing the cleavage of supercoiled pBR 322 DNA (100 ng) by complexes **1a** and **1b** (100 μM). The samples were incubated at 37 ˚C for 2 h except wherever mentioned. Lane 1, DNA; lane 2, DNA + H_2O_2 (200 μM); lane 3, DNA + BME (200 μM); lanes 4–6, DNA + **1a +** H_2O_2 (200 μM) (incubation time 15 min, 60 min and 90 min respectively); lanes 7–9, DNA + **1a +** BME (200 μM) (incubation time 15 min, 60 min and 90 min respectively); lane 10, DNA + **1b**; lane 11, DNA + **1b** + H_2O_2 (200 μM); lane 12, DNA + **1b** + BME (200 μM); lane 13, DNA + **1a** + H_2O_2 (25 μM); lane 14, DNA + **1a** + H_2O_2 (50 μM); lane 15, DNA + **1a** + H_2O_2 (100 μM) 135

Fig. 2.27 Gel electrophoresis separations showing the cleavage of supercoiled pBR322 DNA (100 ng) by complex **1a** (50 μM) in presence of H_2O_2 (200 μM) and BME (200 μM). Samples were incubated at 37 °C for 2 h. Lane 1, DNA; lane 2, DNA + **1a** + H_2O_2; lanes 3-8, DNA + **1a** + H_2O_2 + DMSO, ethanol, NaN_3, D_2O, L- histidine (20 mM) and catalase (10 U) respectively; lane 9, DNA + **1a** + BME; lanes 10-15, DNA + **1a** + BME + DMSO, ethanol, NaN_3, D_2O, L–histidine (20 mM) and catalase (10 U) respectively 136

Fig. 3.1 ^{1}H NMR spectrum of ligand N_3L in $CDCl_3$ 150

Fig. 3.2 ^{13}C NMR spectrum of ligand N_3L in $CDCl_3$ 151

Fig. 3.3 DEPT-135 NMR spectrum of ligand N_3L in $CDCl_3$ 151

Fig. 3.4 DEPT–90 NMR spectrum of ligand N_3L in $CDCl_3$ 152

Fig. 3.5 DEPT–45 NMR spectrum of ligand N_3L in $CDCl_3$ 152

Fig. 3.6 The ESI–MS spectrum of ligand N_3L in acetonitrile 153

Fig. 3.7 Quantitative UV–visible spectra of ligand and complexes (50 μM) in methanolic solution (a) **3a–b** and **4a**–**b**; (b) **5a–b** and **6a**–**b** 156

Fig. 3.8 ^{1}H NMR spectrum of **4a** in $CDCl_3$ 157

Fig. 3.9 ^{13}C NMR spectrum of **4a** in $CDCl_3$ 157

Fig. 3.10 DEPT–135 NMR spectrum of **4a** in $CDCl_3$ 158

Fig. 3.11 ^{1}H NMR spectrum of **4b** in CD_3CN 158

Fig. 3.12 ^{13}C NMR spectrum of **4b** in CD_3CN 159

Fig. 3.13 DEPT−135 NMR spectrum of **4b** in CD_3CN 159
Fig. 3.14 The ESI–mass spectrum of **3a** in acetonitrile 160
Fig. 3.15 The ESI–mass spectrum of **3b** in acetonitrile 161
Fig. 3.16 The ESI–mass spectrum of **4a** in acetonitrile 161
Fig. 3.17 The ESI–mass spectrum of **4b** in acetonitrile 162
Fig. 3.18 The ESI–mass spectrum of **5a** in acetonitrile 162
Fig. 3.19 The ESI–mass spectrum of **5b** in acetonitrile 163
Fig. 3.20 The ESI–mass spectrum of **6a** in acetonitrile 163
Fig. 3.21 The ESI–mass spectrum of **6b** in acetonitrile 164
Fig. 3.22 (a) ORTEP representation of the crystal structure of $[Cu(N_3L)Cl_2]$ (**3a**) showing atom numbering scheme and displacement ellipsoid (50% probability level). Hydrogen atoms are omitted for clarity; (b) trigonal bipyramidal disposition of donor atoms showing the bond distances from the metal centre 166
Fig. 3.23 (a) ORTEP representation of the crystal structure of $[Co(N_3L)Cl_2]$ (**5a**) showing atom numbering scheme and displacement ellipsoid (50% probability level). Hydrogen atoms are omitted for clarity; (b) trigonal bipyramidal disposition of donor atoms showing the bond distances from the metal centre 166
Fig. 3.24 Three dimensional network in **3a** exhibiting hydrogen bonding, π–π interactions and C–H···π interactions 169
Fig. 3.25 Three dimensional hydrogen bonding network in the crystal structure of **3a** 169
Fig. 3.26 Intermolecular hydrogen bonding network in **3a** 171
Fig. 3.27 Packing diagram in crystal structure of **3a** 171
Fig. 3.28 Three dimensional network in **5a** exhibiting hydrogen bonding, π–π interactions and C–H···π interactions 173
Fig. 3.29 Three dimensional hydrogen bonding network in the crystal structure of **5a** 173
Fig. 3.30 Intermolecular hydrogen bonding network in the crystal structure of **5a** 175
Fig. 3.31 Packing diagram in crystal structure of **5a** 175
Fig. 3.32 Cyclic voltammograms of 10^{-3} M solutions of (a) $[Cu(N_3L)Cl_2]$ (**3a**) in dichloromethane and (b) $[Cu(N_3L)_2](ClO_4)_2$ (**3b**) in acetonitrile, respectively, in presence of 0.1 M TBAP as a supporting electrolyte, glassy-carbon as a working electrode and Ag/AgCl as reference electrode; scan rate 0.1 V/s 177
Fig. 3.33 Cyclic voltammograms of 10^{-3} M solutions of $[Co(N_3L)Cl_2]$ (**5a**) and $[Co(N_3L)_2](ClO_4)_2$ (**5b**) in (a) dichloromethane (b) acetonitrile in presence of 0.1 M TBAP as a supporting electrolyte, glassy-carbon as a working electrode and Ag/AgCl as reference electrode; scan rate 0.1 V/s 178
Fig. 3.34 Cyclic voltammograms of a 10^{-3} M solution of (a) $[Ni(N_3L)Cl_2]$ (**6a**) in 179

acetonitrile and (b) $[Ni(N_3L)_2](ClO_4)_2$ (**6b**) in dichloromethane, respectively, in presence of 0.1 M TBAP as a supporting electrolyte, glassy-carbon as a working electrode and Ag/AgCl as reference electrode; scan rate 0.1 V/s

Fig. 3.35 SOD activity of complex (a) **3a** and (b) **3b** by xanthine/xanthine oxidase–nitro blue tetrazolium assay with an incubation time of 10 min 180

Fig. 3.36 Absorption spectra of (a) **3a** (100 μM) and (b) **3b** (100 μM) in phosphate buffer (pH 7.2) containing 10% DMF exhibiting no shift in wavelength over 48 h 181

Fig. 3.37 Absorption spectra of (a) **4a** (100 μM) (b) **4b** (100 μM) in phosphate buffer (pH 7.2) containing 10% DMF exhibiting no shift in wavelength over 48 h 181

Fig. 3.38 Absorption spectra of (a) **5a** (100 μM) and (b) **5b** (100 μM) in phosphate buffer (pH 7.2) containing 10% DMF exhibiting no shift in wavelength over 6 h 182

Fig. 3.39 Absorption spectra of (a) **6a** (100 μM) and (b) **6b** (100 μM) in phosphate buffer (pH 7.2) containing 10% DMF exhibiting no shift in wavelength over 48 h 182

Fig. 3.40 Absorption spectral changes of complex (a) **3a** (70 μM) in 0.1 M phosphate buffer (pH 7.2) in the presence of increasing amounts of DNA (0 – 447 μM) (b) hypsochromic shift with DNA between the initial and final spectra. Dotted line represents the spectrum in the absence of DNA 183

Fig. 3.41 Absorption spectral changes of complex (a) **3b** (70 μM) in 0.1 M phosphate buffer (pH 7.2) in the presence of increasing amounts of DNA (0 – 500 μM) (b) hypsochromic shift with DNA between the initial and final spectra. Dotted line represents the spectrum in the absence of DNA 184

Fig. 3.42 Absorption spectral changes of complex (a) **4a** (70 μM) in 0.1 M phosphate buffer (pH 7.2) in the presence of increasing amounts of DNA (0 – 698 μM) (b) hypsochromic shift with DNA between the initial and final spectra. Dotted line represents the spectrum in the absence of DNA 184

Fig. 3.43 Absorption spectral changes of complex (a) **4b** (70 μM) in 0.1 M phosphate buffer (pH 7.2) in the presence of increasing amounts of DNA (0 – 385 μM) (b) hypsochromic shift with DNA between the initial and final spectra. Dotted line represents the spectrum in the absence of DNA 185

Fig. 3.44 Absorption spectral changes of complex (a) **5a** (100 μM) in 0.1 M phosphate buffer (pH 7.2) in the presence of increasing amounts of DNA (0 – 316 μM) (b) hypsochromic shift with DNA between the initial and final spectra. Dotted line represents the spectrum in the absence of DNA 185

Fig. 3.45 Absorption spectral changes of complex (a) **5b** (100 μM) in 0.1 M phosphate buffer (pH 7.2) in the presence of increasing amounts of DNA (0 – 501 μM) (b) hypsochromic shift with DNA between the initial and 186

final spectra. Dotted line represents the spectrum in the absence of DNA

Fig. 3.46 Absorption spectral changes of complex (a) **6a** (100 μM) in 0.1 M phosphate buffer (pH 7.2) in the presence of increasing amounts of DNA (0 – 546 μM) (b) hypsochromic shift with DNA between the initial and final spectra. Dotted line represents the spectrum in the absence of DNA 186

Fig. 3.47 Absorption spectral changes of complex (a) **6b** (70 μM) in 0.1 M phosphate buffer (pH 7.2) in the presence of increasing amounts of DNA (0 – 348 μM) (b) hypsochromic shift with DNA between the initial and final spectra. Dotted line represents the spectrum in the absence of DNA 187

Fig. 3.48 Absorption spectral changes exhibiting (a) a hypsochromic shift of ~11 nm after incremental addition of AMP (470 μM) and (b) no shift in wavelength after incremental addition of GMP (4760 μM) to the complex **4a** (100 μM) in 0.1 M phosphate buffer (pH 7.2) containing 10% DMF. The dotted line represents the spectrum of the complex in absence of nucleotide. AMP (500 μM) did not show any absorption within the experimental wavelength range. Each successive addition was followed by 3 min incubation 190

Fig. 3.49 (a) Fluorescence emission spectra of CT–DNA in presence of complex **3a** in 0.1 M phosphate buffer (pH 7.2) containing 2% DMF. [DNA] = 38.12 – 36.94 μM, [**3a**] = 0 – 31.01 μM, λ_{ex} = 250 nm and λ_{em} = 600 nm. Dotted line represents the spectrum in the absence of **3a** (b) Stern–Volmer plot for complex **3a** 192

Fig. 3.50 (a) Fluorescence emission spectra of CT–DNA in presence of complex **3b** in 0.1 M phosphate buffer (pH 7.2) containing 2% DMF. [**3b**] = 25.87 – 25.42 μM, [**3b**] = 0 – 17.29 μM, λ_{ex} = 250 nm and λ_{em} = 600 nm. Dotted line represents the spectrum in the absence of complex (b) Stern–Volmer plot for complex **3b** 192

Fig. 3.51 (a) Fluorescence emission spectra of CT–DNA in presence of complex **4a** in 0.1 M phosphate buffer (pH 7.2) containing 2% DMF. [DNA] = 25.87 – 25.07 μM, [**4a**] = 0 – 31.01 μM, λ_{ex} = 250 nm and λ_{em} = 600 nm. Dotted line represents the spectrum in the absence of complex **4a** (b) Stern–Volmer plot for complex **4a** 193

Fig. 3.52 (a) Fluorescence emission spectra of CT–DNA in presence of complex **4b** in 0.1 M phosphate buffer (pH 7.2) containing 2% DMF. [DNA] = 25.87 – 25.07 μM, [**4b**] = 0 – 31.01 μM, λ_{ex} = 250 nm and λ_{em} = 600 nm. Dotted line represents the spectrum in the absence of complex **4b**; (b) Stern–Volmer plot for complex **4b** 193

Fig. 3.53 (a) Fluorescence emission spectra of CT–DNA in presence of complex **5a** in 0.1 M phosphate buffer (pH 7.2) containing 2% DMF. [DNA] = 25.87 – 25.03 μM, [**5a**] = 0 – 31.01 μM, λ_{ex} = 250 nm and λ_{em} = 600 nm. Dotted 194

line represents the spectrum in the absence of complex **5a**; (b) Stern–Volmer plot for **5a**

Fig. 3.54 (a) Fluorescence emission spectra of CT–DNA in presence of complex **5b** in 0.1 M phosphate buffer (pH 7.2) containing 2% DMF. [DNA] = 25.87 – 25.07 μM, [**5b**] = 0 – 31.01 μM, λ_{ex} = 250 nm and λ_{em} = 600 nm. Dotted line represents the spectrum in the absence of complex **5b**; (b) Stern–Volmer plot for **5b** 194

Fig. 3.55 (a) Fluorescence emission spectra of CT–DNA in presence of complex **6a** in 0.1 M phosphate buffer (pH 7.2) containing 2% DMF. [DNA] = 38.12 – 36.93 μM, [**6a**] = 0 – 31.01 μM, λ_{ex} = 250 nm and λ_{em} = 600 nm. Dotted line represents the spectrum in the absence of complex **6a**; (b) Stern–Volmer plot for **6a** 195

Fig. 3.56 (a) Fluorescence emission spectra of CT–DNA in presence of complex **6b** in 0.1 M phosphate buffer (pH 7.2) containing 2% DMF. [DNA] = 38.12 – 36.94 μM, [**6b**] = 0 – 31.01 μM, λ_{ex} = 250 nm and λ_{em} = 600 nm. Dotted line represents the spectrum in the absence of complex **6b**; (b) Stern–Volmer plot for **6b** 195

Fig. 3.57 Circular dichroism spectra of CT–DNA and its interaction with complexes (a) **3a** and **3b**, (b) **4a** and **4b**, (c) **5a** and **5b** and (d) **6a** and **6b** in 0.1 M phosphate buffer (pH 7.2) after 15 min incubation at 298 K 196

Fig. 3.58 Gel electrophoresis separations showing cleavage of supercoiled pBR322 DNA (70 ng) by complex **3a** (a) in absence and presence of H_2O_2 (200 μM) and BME (200 μM). Lane 1, DNA control; lane 2, DNA + H_2O_2; lane 3, DNA + BME; lanes 4-7, DNA + **3a** (50, 100, 200 and 500 μM respectively); lanes 8, 10, 12, 14, DNA + H_2O_2 + **3a** (50, 100, 200 and 500 μM respectively); lanes 9, 11, 13, 15, DNA + BME + **3a** (50, 100, 200 and 500 μM respectively); (b) in presence of H_2O_2. Lane 1, DNA control; lane 2─8, DNA + **3a** (50 μM) + H_2O_2 (20 μM, 50 μM, 100 μM, 250 μM, 500 μM, 1 mM and 2 mM respectively). Samples were incubated at 37 °C for 2.5 h in 0.1 M phosphate buffer containing 10% DMF 198

Fig. 3.59 Gel electrophoresis separations showing cleavage of supercoiled pBR322 DNA (70 ng) by complex **3b** (a) in absence and presence of H_2O_2 (200 μM) and BME (200 μM). Samples were incubated at 37 °C for 2.5 h in 0.1 M phosphate buffer containing 10% DMF. Lane 1, DNA control; lane 2, DNA + H_2O_2; lane 3, DNA + BME; lanes 4-7, DNA + **3b** (50, 100, 200 and 500 μM respectively); lanes 8, 10, 12, 14, DNA + H_2O_2 + **3b** (50, 100, 200 and 500 μM respectively); lanes 9, 11, 13, 15, DNA + BME + **3b** (50, 100, 200 and 500 μM respectively); (b) in presence of H_2O_2 (200 μM). Samples were incubated at 37 °C for varying intervals in 0.1 M phosphate 199

buffer containing 10% DMF. Lane 1, DNA control; lane 2–8, DNA + **3b** (50 μM) + H_2O_2 with incubation time 5 min, 15 min, 30 min, 60 min, 90 min, 120 min and 150 min respectively

Fig. 3.60 Gel electrophoresis separations showing the cleavage of supercoiled pBR322 DNA (70 ng) by complexes **4a** and **4b**. Samples were incubated at 37 °C for 24 h in 0.1 M phosphate buffer containing 10% DMF. Lane 1, DNA control; lanes 2-7, DNA + **4a** (50 μM, 100 μM, 250 μM, 500 μM, 1 mM and 2 mM respectively); lanes 8-13, DNA + **4b** (50 μM, 100 μM, 250 μM, 500 μM, 1 mM and 2 mM respectively), lane14, DNA + ligand [N_3L] (2 mM); lane 15, DNA + $ZnCl_2$ (2 mM) 199

Fig. 3.61 Gel electrophoresis separations showing the cleavage of supercoiled pBR322 DNA (70 ng) by complex **5a** (a) in absence and presence of H_2O_2 (200 μM) and BME (200 μM). Lane 1, DNA control; lane 2, DNA + H_2O_2; lane 3, DNA + BME; lanes 4-7, DNA + **5a** (50, 100, 200 and 500 μM respectively); lanes 8, 10, 12, 14, DNA + H_2O_2 + **5a** (50, 100, 200 and 500 μM respectively); lanes 9, 11, 13, 15, DNA + BME + **5a** (50, 100, 200 and 500 μM respectively); (b) in presence of varying amount of H_2O_2. Lane 1, DNA control; lane 2–8, DNA + **5a** (50 μM) + H_2O_2 (20 μM, 50 μM, 100 μM, 250 μM, 500 μM, 1 mM and 2 mM respectively). Samples were incubated at 37 °C for 2.5 h in 0.1 M phosphate buffer containing 10% DMF 200

Fig. 3.62 Gel electrophoresis separations showing the cleavage of supercoiled pBR322 DNA (70 ng) by complex **5b** in absence and presence of H_2O_2 (200 μM) and BME (200 μM). Samples were incubated at 37 °C for 2.5 h in 0.1 M phosphate buffer containing 10% DMF. Lane 1, DNA control; lane 2, DNA + H_2O_2; lane 3, DNA + BME; lanes 4-7, DNA + **5b** (50, 100, 200 and 500 μM respectively); lanes 8, 10, 12, 14, DNA + H_2O_2 + **5b** (50, 100, 200 and 500 μM respectively); lanes 9, 11, 13, 15, DNA + BME + **5b** (50, 100, 200 and 500 μM respectively) 201

Fig. 3.63 Gel electrophoresis separations showing negligible cleavage of supercoiled pBR322 DNA (70 ng) in absence and presence of H_2O_2 (200 μM) and BME (200 μM) by complexes (a) **6a** and (b) **6b**; Lane 1, DNA control; lane 2, DNA + H_2O_2; lane 3, DNA + BME; lanes 4-7, DNA + complex (50, 100, 200 and 500 μM respectively); lanes 8, 10, 12, 14, DNA + H_2O_2 + complex (50, 100, 200 and 500 μM respectively); lanes 9, 11, 13, 15, DNA + BME + complex (50, 100, 200 and 500 μM respectively). Samples were incubated at 37 °C for 2.5 h in 0.1 M phosphate buffer containing 10% DMF 201

Fig. 3.64 Gel electrophoresis separations showing the cleavage of supercoiled pBR322 DNA (70 ng) by complex **3a** in presence of H_2O_2 (200 μM). 203

Samples were incubated at 37 °C for 2.5 h in 0.1 M phosphate buffer containing 10% DMF. Lane 1, DNA control; lane 2, DNA + ligand [N_3L] (50 μM); lane 3, DNA + ligand [N_3L] (50 μM) + H_2O_2; lanes 4, DNA + **3a** (50 μM) + H_2O_2; lanes 5-9, DNA + **3a** (50 μM) + H_2O_2 + DMSO, ethanol, urea, sodium azide and L-histidine (20 mM each) respectively; lane 10, DNA + **3a** (50 μM) + D_2O (10%); lane 11, DNA + **3a** (50 μM) + catalase (10 U); lanes 12-13; DNA + **3a** (50 μM) + neocuproine and sodium chloride respectively (400 μM each)

Fig. 3.65 Gel electrophoresis separations showing the cleavage of supercoiled pBR322 DNA (70 ng) by complex **3a** in absence of H_2O_2 and BME. Samples were incubated at 37 °C for 2.5 h in 0.1 M phosphate buffer containing 10% DMF. Lane 1, DNA control; lane 2, DNA + DMF (10 %); lane 3, DNA + ligand [N_3L] (200 μM); lanes 4, DNA + **3a** (200 μM); lanes 5-9, DNA + **3a** (200 μM) + DMSO, ethanol, urea, sodium azide and L-histidine (20 mM each) respectively; lane 10, DNA + **3a** (200 μM) + D_2O (10 %); lane 11, DNA + **3a** (200 μM) + catalase (10 U); lanes 12-13; DNA + **3a** (200 μM) + neocuproine and sodium chloride respectively (400 μM each) 204

Fig. 3.66 Gel electrophoresis separations showing the cleavage of supercoiled pBR322 DNA (70 ng) by complex **4a**. Samples were incubated at 37 °C for 18 h in 0.1 M phosphate buffer containing 10% DMF. Lane 1, DNA control; lanes 2-5, DNA + **4a** (1 mM) + DMSO, ethanol, urea and sodium azide (20 mM each) respectively; lane 6, DNA + **4a** (1mM) + D_2O (10%); lane 7, DNA + **4a** (1 mM) + L-histidine (20 mM); lane 8, DNA + **4a** (1 mM) + catalase (10 U); lane 9, DNA + **4a** (1 mM) + sodium chloride (400 μM); lanes 10-11, DNA + **4a** (1 mM); lanes 12-13, DNA + **4a** (2 mM); lanes 14-15, DNA + **4a** (5 mM); lanes 11, 13 and 15 represent cleavage in exclusion of air *(anaerobic conditions)* 204

Fig. 3.67 Gel electrophoresis separations showing the cleavage of supercoiled pBR322 DNA (70 ng) by complex **5a** (200 μM) in presence of H_2O_2 (200 μM). Samples were incubated at 37 °C for 2.5 h in 0.1 M phosphate buffer containing 10% DMF. Lane 1, DNA control; lane 2, DNA + **5a** + H_2O_2; lanes 3-7, DNA + **5a** + H_2O_2 + DMSO, ethanol, urea, sodium azide and L-histidine (20 mM each) respectively; lane 8, DNA + **5a** + H_2O_2 + D_2O (10%); lane 9, DNA + **5a** + H_2O_2 + catalase (10 U); lane 10, DNA + **5a** + H_2O_2 + sodium chloride (400 μM), lane 11, DNA + ligand [N_3L] (200 μM) + H_2O_2 206

Fig. 3.68 Difference absorption spectral changes between BSA (100 μM) containing **6a** (100 μM) and BSA solution (100 μM) exhibiting a hypsochromic shift of 3 nm (350 nm to 347 nm) after an incubation for 50 min in 0.1 M 207

phosphate buffer (pH 7.2) containing 10% DMF

Fig. 3.69 (a) Absorption spectral changes exhibiting a hypsochromic shift of ~12 nm after incremental addition of L-histidine to the complex **4a** (100 μM) in 0.1 M phosphate buffer (pH 7.2) containing 10% DMF. The dotted line represents the spectrum of the complex in absence of L-histidine; (b) Spectral shift encountered in the absorption profile of complex **4a** (100 μM) after addition of excess of L-histidine (10 mM) and on incubation for 3 h 208

Fig. 3.70 (a) Absorption spectral changes exhibiting a hypsochromic shift of ~5 nm along with the formation of isosbestic point near 379 nm after incremental addition of L–histidine to the complex **6a** (100 μM) in 0.1 M phosphate buffer (pH 7.2) containing 10% DMF. The dotted line represents the spectrum of the complex in absence of L–histidine; (b) Spectral shift encountered in the absorption profile of complex **6a** (100 μM) after addition of excess of L–histidine (10 mM) 209

Fig. 3.71 (a) Fluorescence emission spectra of BSA in presence of complex **3a** in 0.1 M phosphate buffer (pH 7.2) containing 2% DMF. [BSA] = 2 μM, [**3a**] = 0–25.34 μM, λ_{ex} = 295 nm and λ_{em} = 344 nm. Dotted line represents the spectrum in the absence of complex; inset: Stern–Volmer plot of complex **3a**; (b) Plot of log (F_0-F)/F vs. log [Q] for complex **3a** 210

Fig. 3.72 (a) Fluorescence emission spectra of BSA in presence of complex **3b** in 0.1 M phosphate buffer (pH 7.2) containing 2% DMF. [BSA] = 2 μM, [**3b**] = 0–23.43 μM, λ_{ex} = 295 nm and λ_{em} = 344 nm. Dotted line represents the spectrum in the absence of complex; inset: Stern–Volmer plot of complex **3b**; (b) Plot of log (F_0-F)/F vs. log [Q] for **3b** 211

Fig. 3.73 (a) Fluorescence emission spectra of BSA in presence of complex **4a** in 0.1 M phosphate buffer (pH 7.2) containing 2% DMF. [BSA] = 2 μM, [complex] = 0–25.34 μM, λ_{ex} = 295 nm and λ_{em} = 344 nm. Dotted line represents the spectrum in the absence of complex; inset: Stern–Volmer plot of complex **4a**; (b) Plot of log (F_0-F)/F vs. log [Q] for **4a** 211

Fig. 3.74 (a) Fluorescence emission spectra of BSA in presence of complex **4b** in 0.1 M phosphate buffer (pH 7.2) containing 2% DMF. [BSA] = 2 μM, [**4b**] = 0–25.34 μM, λ_{ex} = 295 nm and λ_{em} = 344 nm. Dotted line represents the spectrum in the absence of complex inset: Stern–Volmer plot of complex **4b**; (b) Plot of log (F_0-F)/F vs. log [Q] for **4b** 212

Fig. 3.75 (a) Fluorescence emission spectra of BSA in presence of complex **5a** in 0.1 M phosphate buffer (pH 7.2) containing 2% DMF. [BSA] = 2 μM, [**5a**] = 0–25.34 μM, λ_{ex} = 295 nm and λ_{em} = 344 nm. Dotted line represents the spectrum in the absence of complex inset: Stern–Volmer plot of complex 212

5a; (b) Plot of log (F_0-F)/F vs. log [Q] for **5a**

Fig. 3.76 (a) Fluorescence emission spectra of BSA in presence of complex **5b** in 0.1 M phosphate buffer (pH 7.2) containing 2% DMF. [BSA] = 2 μM, [**5b**] = 0–25.34 μM, λ_{ex} = 295 nm and λ_{em} = 344 nm. Dotted line represents the spectrum in the absence of complex; inset: Stern–Volmer plot of complex **5b**; (b) Plot of log (F_0-F)/F vs. log [Q] for **5b** 213

Fig. 3.77 (a) Fluorescence emission spectra of BSA in presence of complex **6a** in 0.1 M phosphate buffer (pH 7.2) containing 2% DMF. [BSA] = 2 μM, [**6a**] = 0–25.34 μM, λ_{ex} = 295 nm and λ_{em} = 344 nm. Dotted line represents the spectrum in the absence of complex inset: Stern–Volmer plot of complex **6a**; (b) Plot of log (F_0-F)/F vs. log [Q] for **6a** 213

Fig. 3.78 (a) Fluorescence emission spectra of BSA in presence of complex **6b** in 0.1 M phosphate buffer (pH 7.2) containing 2% DMF. [BSA] = 2 μM, [**6b**] = 0–25.34 μM, λ_{ex} = 295 nm and λ_{em} = 344 nm. Dotted line represents the spectrum in the absence of complex **6b**; inset: Stern–Volmer plot of complex **6b**; (b) Plot of log (F_0-F)/F vs. log [Q] for **6b** 214

Fig. 3.79 Circular dichroism spectra of BSA and its interaction with complexes (a) **3a** and **3b**, (b) **4a** and **4b**, (c) **5a** and **5b** and (d) **6a** and **6b** in 0.1 M phosphate buffer (pH 7.2) after 15 min incubation at 25 °C 216

Fig. 4.1 UV–visible spectra of ligands (PhimpH and ^{t}BuPhimpH) and their complexes **7**·CH_3CN and **8** (50 μM) in acetonitrile 233

Fig. 4.2 ^{1}H NMR spectra of **7**·CH_3CN in CD_3CN 234

Fig. 4.3 ^{13}C NMR Spectrum of **7**·CH_3CN in $(CD_3)_2SO$ 234

Fig. 4.4 ^{1}H NMR spectra of **8** in CD_3CN 235

Fig. 4.5 ^{13}C NMR Spectrum of **8** in $CDCl_3$ 235

Fig. 4.6 DEPT–45 NMR Spectrum of **8** in $CDCl_3$ 236

Fig. 4.7 ESI–mass spectrum of **7**·CH_3CN in acetonitrile 237

Fig. 4.8 ESI–mass spectrum of **8** in acetonitrile 237

Fig. 4.9 (a) ORTEP representation of the crystal structure of $[Co(Phimp)_2]ClO_4$·CH_3CN (**7**·CH_3CN) showing atom numbering scheme and displacement ellipsoid (50% probability level). Hydrogen atoms, perchlorate anion and the solvent molecule are omitted for clarity; (b) octahedral disposition of donor atoms showing the bond distances from metal centre 238

Fig. 4.10 Hydrogen–bonding interaction network between aryl hydrogens and perchlorate anions in the crystal structure of **7**·CH_3CN 241

Fig. 4.11 Extensive C–H···π interactions in the crystal structure of **7**·CH_3CN 242

Fig. 4.12 Three–dimensional packing diagram of **7**·CH_3CN 242

Fig. 4.13 (a) Cyclic voltammogram of **7**·CH_3CN and **8** in acetonitrile (10^{-3} M) vs. 244

Ag/AgCl at 298 K in presence of 0.1 M tetrabutylammonium perchlorate as supporting electrolyte; scan rate 0.1 V/s. (b) Cyclic voltammograms of **8** at different scan rates i.e. 0.05, 0.1, 0.2, 0.3, 0.4 and 0.5 V/s respectively

Fig. 4.14 (a) Absorption spectral changes upon oxidation of complex **8** (5×10^{-5} M) with CAN upto six equivalents in CH_3CN at 298 K; (b) time course of decomposition of $[\mathbf{8}]^{\bullet+}$ monitored at 562 nm 246

Fig. 4.15 X–band EPR spectra of phenoxyl radical complexes derived from frozen solutions of (a) **7**·CH_3CN and (b) **8** in CH_3CN at 120 K 247

Fig. 4.16 Emission spectral changes of EB–DNA in the absence (dotted line) and presence of cobalt complexes (solid lines) in 0.1 M phosphate buffer (pH 7.2) containing 2% DMF. λ_{ex} = 250 nm; λ_{em} = 585 nm. [EB] = 5 μM, [DNA] = 25 μM, (a) [**7**] = 0–10.97 μM, (c) [**8**] = 0–11.07 μM; (b) and (d) Stern–Volmer plots for complexes **7**·CH_3CN and **8** respectively 248

Fig. 4.17 Circular dichroism spectra of CT–DNA in presence of complexes **7**·CH_3CN and **8** in 0.1 M phosphate buffer (pH 7.2) after 10 min incubation at 298 K 250

Fig. 4.18 Gel electrophoretogram of DNA incubated with **7**·CH_3CN at 37 °C for 1.5 h. DMF (5%) was used for the better solubility of the complex. Keys: Lane 1, DNA control; lane 2, DNA + H_2O_2 (200 μM); lane 3, DNA + BME (200 μM); lane 4–5, DNA + **7**·CH_3CN (50 and 100 μM respectively); Lane 6, DNA + **7**·CH_3CN (100 μM) + H_2O_2 (200 μM); Lane 7, DNA + **7**·CH_3CN (100 μM) + BME (200 μM) 251

Fig. 4.19 Gel electrophoresis separation showing the cleavage of pBR322 DNA by complex **8**. All lanes except lane 1 and 5 contain 5% DMF. Keys: (a) Incubation was done at 37°C for 1.5 h (Lanes 1–7). Lane 1, DNA control; lane 2, DNA + DMF (5%); lane 3, DNA + PhimpH (50 μM); lane 4, DNA + ^{t}BuPhimpH (50 μM); lane 5, DNA + $CoCl_2 \cdot 6H_2O$ (25 μM); lane 6, DNA + **7**·CH_3CN (25 μM); lane 7, DNA + **8** (25 μM); (b) Lane 8, DNA control; lanes 9–15, DNA + **8** (25 μM). Samples were incubated at 37°C for 5, 10, 20, 30, 45, 60, 90 min respectively (lanes 9–15) 252

Fig. 4.20 Gel electrophoresis separation showing the cleavage of pBR322 DNA by complex **8**. All lanes except lane 1 contain 5% DMF. Samples were incubated at 37°C for 1.5 h. Keys: (a) Lane 1, DNA control; lanes 2–7, DNA + **8** (5, 10, 20, 30, 40 and 50 μM respectively). (b) Lane 8, DNA control; lane 9, DNA + **8** (25 μM); lanes 10–15, DNA + **8** (25 μM) + DMSO, ethanol, urea, NaN_3, L–histidine (20 mM each) and catalase (10 U) respectively 252

Fig. 4.21 Emission spectra of BSA in the absence (dotted lines) and presence of complexes **7**·CH_3CN and **8** (solid lines) respectively, in 0.1 M phosphate 254

buffer containing 2% DMF; (a) [BSA] = 2 μM, [**7**] = 0–40 μM; (b) [BSA] = 2 μM, [**8**] = 0–22 μM. Arrows show the intensity changes with increasing concentration of metal complexes

Fig. 4.22 Stern–Volmer plots exhibiting the interaction of complexes **7**·CH_3CN and **8** with BSA 255

Fig. 4.23 Scatchard plots for the interaction of complexes (a) **7**·CH_3CN and (b) **8** with BSA 255

Fig. 4.24 Fluorescence emission spectra of (a) warfarin (80 μM) and BSA (40 μM) equilibrated for 1 h in phoshphate buffer (pH 7.2) containing 10% DMF in (i) absence or (ii–iv) presence of complex **7**·CH_3CN (ii) 40 μM, (iii) 80 μM and (iv) 160 μM respectively; λ_{ex} = 335 nm, λ_{em} = 378 nm. (b) BSA (2 μM) treated with the site marker ibuprofen (2 μM) in 0.1 M phoshphate buffer (pH 7.2) containing 2% DMF in absence (dotted line) and presence of complex 7. [**7**] = 0 – 11.928 μM; λ_{ex} = 295 nm, λ_{em} = 344 nm; incubation time = 2 min. Ibuprofen (2 μM) and complex **7**·CH_3CN (100 μM) exhibited negligible emission intensity under similar experimental conditions, inset: Stern–Volmer plot for complex **7**·CH_3CN 257

Fig. 4.25 Fluorescence emission spectra of (a) warfarin (80 μM) and BSA (40 μM) equilibrated for 1 h in phoshphate buffer (pH 7.2) containing 10% DMF in (i) absence or (ii–iv) presence of complex **8** (ii) 40 μM, (iii) 80 μM and (iv) 160 μM respectively; λ_{ex} = 335 nm, λ_{em} = 378 nm, (b) BSA (2 μM) treated with the site marker ibuprofen (2 μM) in phoshphate buffer (pH 7.2) containing 2% DMF in absence (dotted line) and presence of complex **8**. [**8**] = 0 – 11.928 μM; λ_{ex} = 295 nm, λ_{em} = 344 nm; incubation time = 2 min. Ibuprofen (2 μM) and complex **7** (100 μM) exhibited negligible emission intensity under similar experimental conditions, inset: Stern–Volmer plot for complex **8** 257

Fig. 4.26 Modified Stern–Volmer plots of complexes (a) **7**·CH_3CN and (b) **8** in the absence and presence of ibuprofen respectively 258

Fig. 4.27 SDS–PAGE separation showing the cleavage of bovine serum albumin (BSA) by complex **8** in HEPES buffer (10 mM, pH 7.3). Incubation was done at 50°C for 20 h. Keys: (a) Lane 1, BSA (15 μM) control; lanes 2–4, BSA (15 μM) + **7** (10, 25 and 50 μM respectively); lanes 5–7, BSA (15 μM) + **8** (10, 25 and 50 μM respectively); lane 8, BSA + Phimph (50 μM); lane 9, BSA + ^{t}BuPhimph (50 μM) and lane 10, BSA + $CoCl_2 \cdot 6H_2O$ (50 μM); (b) Lane 1, BSA (15 μM) control; lane 2, BSA (15 μM) + **8** (100 μM); lanes 3–6, BSA (15 μM) + **8** (100 μM) + DMSO (20%), glycerol (20%), NaN_3 (20 mM) and catalase (10 U) respectively 259

Fig. 4.28 Histogram of relative toxicities of complexes **7**·CH_3CN and **8**, $CoCl_2 \cdot 6H_2O$ 261

and 5–fluorouracil against various cell lines.

Fig. 5.1 UV–visible spectra of complexes **9-10** (50 μM) in methanol 273

Fig. 5.2 The ESI–mass spectrum of **9a** in acetonitrile 274

Fig. 5.3 The ESI–mass spectrum of **9b** in acetonitrile 275

Fig. 5.4 The ESI–mass spectrum of **9c** in acetonitrile 275

Fig. 5.5 The ESI–mass spectrum of **10a** in acetonitrile 276

Fig. 5.6 The ESI–mass spectrum of **10b** in acetonitrile 277

Fig. 5.7 The ESI–mass spectrum of **10c** in acetonitrile 277

Fig. 5.8 (a) ORTEP representation of the crystal structure of **9a**·$3H_2O$·CH_3OH showing atom numbering scheme and displacement ellipsoid (50% probability level). Hydrogen atoms and solvent molecules are omitted for clarity; (b) octahedral disposition of donor atoms around metal center 280

Fig. 5.9 Hydrogen–bonding network in crystals of **9a**·$3H_2O$·CH_3OH 281

Fig. 5.10 Diagrammatic representation of extensive C–H···π interactions in crystals of **9a**·$3H_2O$·CH_3OH forming a loop like structure within star-shaped geometry 282

Fig. 5.11 A view of packing in projection down the '*c*'–axis in the unit cells of **9c**·H_2O 283

Fig. 5.12 (a) ORTEP representation of crystal structure of **9c**·H_2O showing atom numbering scheme and displacement ellipsoid (50% probability level). Hydrogen atoms, perchlorate counter anion and solvent molecule are omitted for clarity; (b) octahedral disposition of donor atoms around metal center 284

Fig. 5.13 Diagrammatic representation of hydrogen bonding network between aryl hydrogens and perchlorate oxygens in the unit cells of **9c**·H_2O 285

Fig. 5.14 Hydrogen bonding network and π–stacking interactions in the crystal structure of **9c**·H_2O 286

Fig. 5.15 A view of packing in projection down the '*a*'–axis in the unit cells of **9c**·H_2O 286

Fig. 5.16 Cyclic voltammograms of 10^{-3} M solutions of (a) **9a**·$3H_2O$·CH_3OH and (b) **10a** in acetonitrile at 298 K under nitrogen atmosphere in presence of 0.1 M TBAP as a supporting electrolyte, glassy-carbon was used as working electrode, Ag/AgCl as reference electrode and platinum wire as auxiliary electrode; scan rate 0.1 V/s 288

Fig. 5.17 Cyclic voltammograms of 10^{-3} M solutions of (a) **9b** in dimethylformamide and (b) **10b** in acetonitrile at 298 K under nitrogen atmosphere in presence of 0.1 M TBAP as supporting electrolyte, glassy-carbon was used as working electrode, Ag/AgCl as reference electrode and platinum wire as auxiliary electrode; scan rate 0.1 V/s 290

Fig. 5.18 Cyclic voltammograms of 10^{-3} M solutions of (a) **9c**·H_2O and (b) **10c** in acetonitrile at 298 K under nitrogen atmosphere in presence of 0.1 M TBAP as a supporting electrolyte, glassy-carbon was used as working electrode, Ag/AgCl as reference electrode and platinum wire as auxiliary electrode; scan rate 0.1 V/s 291

Fig. 5.19 Contour plots of (a) HOMO and (b) LUMO in **9c**·H_2O 292

Fig. 5.20 Absorption spectral changes upon oxidation of (a) **9a**; (c) **9b**; and (e) **9c** (50 μM each) with varying equivalents of CAN in CH_3CN at 298 K; (b) time course of decomposition of phenoxyl radical analogues derived from (b) **9a**; (d) **9b**; and (f) **9c** monitored at 719, 964 and 709 nm respectively 294

Fig. 5.21 Repetitive scans exhibiting absorption spectral changes of phenoxyl complex derived from **9b** (50 μM) in acetonitrile at 298 K 295

Fig. 5.22 Absorption spectral changes upon oxidation of (a) **10a** (50 μM); (c) **10b** (100 μM); and (e) **10c** (50 μM) with varying equivalents of CAN in CH_3CN at 298 K; (b) time course of decomposition of phenoxyl radical analogues derived from (b) **10a**; (d) **10b**; and (f) **10c** monitored at 527, 529 and 529 nm respectively 296

Fig. 5.23 X–band EPR spectra of phenoxyl radical complexes derived from frozen solutions of (a) **10a** and (b) **10b** in CH_3CN at 110 K 298

Fig. 5.24 Absorption spectral changes of complex (a) **9a**·$3H_2O$·CH_3OH, (b) **9b** and (c) **9c**·H_2O in 0.1 M phosphate buffer (pH 7.2) containing 10% DMF in presence of increasing amounts of CT–DNA (0 – 385 μM for (a) and (c); 0 – 176 μM for (b) respectively). Dotted line represents the spectrum in absence of CT–DNA 300

Fig. 5.25 (a) Fluorescence emission spectra of the EB–DNA in presence of **9a**·$3H_2O$·CH_3OH in 0.1 M phosphate buffer (pH 7.2) containing 5% DMF. λ_{ex} = 250 nm and λ_{em} = 585 nm. [EB] = 5 μM, [DNA] = 25 μM, [**9a**] = 0–14.29 μM. Dotted line represents the spectrum in the absence of complex; (b) Stern–Volmer plot for interaction of **9a**·$3H_2O$·CH_3OH with CT–DNA 301

Fig. 5.26 (a) Fluorescence emission spectra of the EB–DNA in presence of **9b** in 0.1 M phosphate buffer (pH 7.2) containing 5% DMF. λ_{ex} = 250 nm and λ_{em} = 585 nm. [EB] = 5 μM, [DNA] = 25 μM, [**9b**] = 0–19.01 μM. Dotted line represents the spectrum in the absence of complex; (b) Stern–Volmer plot for interaction of **9b** with CT–DNA 302

Fig. 5.27 (a) Fluorescence emission spectra of the EB–DNA in presence of **9c**·H_2O in 0.1 M phosphate buffer (pH 7.2) containing 5% DMF. λ_{ex} = 250 nm and λ_{em} = 585 nm. [EB] = 5 μM, [DNA] = 25 μM, [**9c**] = 0–14.29 μM. Dotted line represents the spectrum in the absence of complex; (b) Stern–Volmer plot for interaction of **9c** with CT–DNA 302

Fig. 5.28 (a) Fluorescence emission spectra of the EB–DNA in presence of **10a** in 303

0.1 M phosphate buffer (pH 7.2) containing 5% DMF. λ_{ex} = 250 nm and λ_{em} = 585 nm. [EB] = 5 μM, [DNA] = 25 μM, [**10a**] = 0 – 40.75 μM. Dotted line represents the spectrum in the absence of complex; (b) Stern–Volmer plot for interaction of **10a** with CT–DNA

Fig. 5.29 (a) Fluorescence emission spectra of the EB−DNA in presence of **10b** in 0.1 M phosphate buffer (pH 7.2) containing 5% DMF. λ_{ex} = 250 nm and λ_{em} = 585 nm. [EB] = 5 μM, [DNA] = 25 μM, [**10b**] = 0–52.95 μM. Dotted line represents the spectrum in the absence of complex; (b) Stern–Volmer plot for interaction of **10b** with CT–DNA 303

Fig. 5.30 (a) Fluorescence emission spectra of the EB−DNA in presence of **10c** in 0.1 M phosphate buffer (pH 7.2) containing 5% DMF. λ_{ex} = 250 nm and λ_{em} = 585 nm. [EB] = 5 μM, [DNA] = 25 μM, [**10c**] = 0–15.87 μM. Dotted line represents the spectrum in the absence of complex; (b) Stern–Volmer plot for interaction of **10c** with CT–DNA 304

Fig. 5.31 Circular dichroism spectra in 0.1 M phosphate buffer (pH 7.2) containing 10% methanol after 10 min incubation at 25 °C. (a) CT–DNA and its interaction with complexes **9a**·$3H_2O$·CH_3OH, **9b** and **9c**·H_2O; (b) CT–DNA and its interaction with complexes **10a**, **10b** and **10c** 305

Fig. 5.32 Gel electrophoresis separations showing the cleavage of supercoiled pBR322 DNA (100 ng) by complexes **9-10** (50 μM each). Samples were incubated at 37 °C for 2 h in 0.1 M phosphate buffer containing 10% DMF. Lane 1, DNA control; lane 2, DNA + **9a**·$3H_2O$·CH_3OH; lane 3, DNA + **10a**; lane 4, DNA + **9b**; lane 5, DNA + **10b**; lane 6, DNA + **9c**·H_2O; lane 7, DNA + **10c** 306

Fig. 5.33 Gel electrophoresis separations showing the cleavage of supercoiled pBR322 DNA (100 ng) by complexes **10b** (50 μM each). Samples were incubated at 37 °C for 2 h in 0.1 M phosphate buffer containing 10% DMF. Lane 1, DNA control; lane 2, DNA + **10b**; lane 3, DNA + **10b** + D_2O (10%); lane 4–8, DNA + **10b** + NaN_3, L-histidine, DMSO, ethanol, urea respectively (20 mM each); lane 9, DNA + **10b** + catalase (10 U) 307

Fig. 5.34 (a) Fluorescence emission spectra of BSA in presence of complex **9a**·$3H_2O$·CH_3OH in 0.1 M phosphate buffer (pH 7.2) containing 2% DMF. [BSA] = 2 μM, [**9a**] = 0–20.58 μM, λ_{ex} = 295 nm and λ_{em} = 344 nm. Dotted line represents the spectrum in the absence of complex; inset: Stern–Volmer plot of complex **9a**·$3H_2O$·CH_3OH; (b) Plot of log $(F_0\text{-}F)/F$ vs. log [Q] for complex **9a**·$3H_2O$·CH_3OH 309

Fig. 5.35 (a) Fluorescence emission spectra of BSA in presence of complex **9b** in 0.1 M phosphate buffer (pH 7.2) containing 2% DMF. [BSA] = 2 μM, [**9b**] = 0–29.94 μM, λ_{ex} = 295 nm and λ_{em} = 344 nm. Dotted line represents the 309

spectrum in the absence of complex; inset: Stern–Volmer plot of complex **9b**; (b) Plot of log (F_0-F)/F vs. log [Q] for complex **9b**

Fig. 5.36 (a) Fluorescence emission spectra of BSA in presence of complex **9c**·H_2O in 0.1 M phosphate buffer (pH 7.2) containing 2% DMF. [BSA] = 2 μM, [**9c**] = 0–22.15 μM, λ_{ex} = 295 nm and λ_{em} = 344 nm. Dotted line represents the spectrum in the absence of complex; inset: Stern–Volmer plot of complex **9c**·H_2O; (b) Plot of log (F_0-F)/F vs. log [Q] for complex **9c**·H_2O 310

Fig. 5.37 (a) Fluorescence emission spectra of BSA in presence of complex **10a** in 0.1 M phosphate buffer (pH 7.2) containing 2% DMF. [BSA] = 2 μM, [**10a**] = 0–43.81 μM, λ_{ex} = 295 nm and λ_{em} = 344 nm. Dotted line represents the spectrum in the absence of complex; inset: Stern–Volmer plot of complex **10a**; (b) Plot of log (F_0-F)/F vs. log [Q] for complex **10a** 310

Fig. 5.38 (a) Fluorescence emission spectra of BSA in presence of complex **10b** in 0.1 M phosphate buffer (pH 7.2) containing 2% DMF. [BSA] = 2 μM, [**10b**] = 0–22.15 μM, λ_{ex} = 295 nm and λ_{em} = 344 nm. Dotted line represents the spectrum in the absence of complex; inset: Stern–Volmer plot of complex **10b**; (b) Plot of log (F_0-F)/F vs. log [Q] for complex **10b** 311

Fig. 5.39 (a) Fluorescence emission spectra of BSA in presence of complex **10c** in 0.1 M phosphate buffer (pH 7.2) containing 2% DMF. [BSA] = 2 μM, [**10c**] = 0–20.58 μM, λ_{ex} = 295 nm and λ_{em} = 344 nm. Dotted line represents the spectrum in the absence of complex; inset: Stern–Volmer plot of complex **10c**; (b) Plot of log (F_0-F)/F vs. log [Q] for complex **10c** 311

Fig. 5.40 Fluorescence emission spectra of (a) warfarin (80 μM) and BSA (40 μM) equilibrated for 1 h in phosphate buffer (pH 7.2) containing 10% DMF in (i) absence or (ii-v) presence of complex **9a**·$3H_2O$·CH_3OH (ii) 20 μM, (iii) 40 μM, (iv) 80 μM and (v) 160 μM respectively; λ_{ex}=335 nm, λ_{ex}=378 nm. BSA (40 μM) and the complex **9a**·$3H_2O$·CH_3OH (160 μM) ((vi) and (vii) respectively) independently exhibited negligible emission under similar experimental conditions. (b) BSA (2 μM) treated with the site marker ibuprofen (2 μM) in 0.1 M phosphate buffer (pH 7.2) containing 2% DMF in absence (dotted line) and presence of complex **9a**·$3H_2O$·CH_3OH. [**9a**] = 0–10 μM; λ_{ex}=295 nm, λ_{ex}=344 nm. Incubation time = 2 min. Ibuprofen (2 μM) and **9a**·$3H_2O$·CH_3OH (100 μM) exhibited negligible emission intensity under similar experimental conditions, inset: Stern–Volmer plot for complex **9a**·$3H_2O$·CH_3OH 313

Fig. 5.41 Modified Stern–Volmer plot for complex **9a**·$3H_2O$·CH_3OH in the absence and presence of ibuprofen 313

Fig. 5.42 Fluorescence emission spectra of (a) warfarin (80 μM) and BSA (40 μM) equilibrated for 1 h in phosphate buffer (pH 7.2) containing 10% DMF in 314

(i) absence or (ii-v) presence of complex **10a** (ii) 20 μM, (iii) 40 μM, (iv) 80 μM and (v) 160 μM respectively; λ_{ex}=335 nm, λ_{ex}=378 nm. BSA (40 μM) and the complex **10a** (160 μM) ((vi) and (vii) respectively) independently exhibited negligible emission under similar experimental conditions. (b) BSA (2 μM) treated with the site marker ibuprofen (2 μM) in 0.1 M phosphate buffer (pH 7.2) containing 2% DMF in absence (dotted line) and presence of complex **10a**. [**10a**] = 0–16 μM; λ_{ex}=295 nm, λ_{ex}=344 nm. Incubation time = 2 min. Ibuprofen (2 μM) and **10a** (100 μM) exhibited negligible emission intensity under similar experimental conditions, inset: Stern–Volmer plot for complex **10a**

Fig. 5.43 Modified Stern–Volmer plot for complex **10a** in the absence and presence of ibuprofen 314

Fig. 6.1 Electronic absorption spectra of (a) Gimpy and its nickel complex **11**; (b) Timpy and its nickel complex **12**·2$(CH_3)_2CO$ (20 μM each) in methanol at 298 K 329

Fig. 6.2 The ESI–mass spectrum of **11** in acetonitrile 330

Fig. 6.3 The ESI–mass spectrum of **12**·2$(CH_3)_2CO$ in acetonitrile 331

Fig. 6.4 ORTEP representation of the crystal structure of Gimpy showing atom numbering scheme and displacement ellipsoid (50% probability level). Hydrogen atoms are omitted for clarity 332

Fig. 6.5 Supramolecular chain in Gimpy aligned along [1 0 1] and sustained by C–H···π interactions [C2–H2···Cg(C6-C11)^i = 2.87 Å, C2···Cg(C6-C11)^i = 3.6488(15) Å with angle at H2 = 140º for symmetry operation i: 1-x, 2-y, 1-z] shown as red dashed lines 333

Fig. 6.6 A view in projection down the *b*-axis of the assembly of supramolecular chains in the *ab*-plane and the stacking of these along the *c*-axis; no significant intermolecular interactions connect the chains. The C–H···π interactions are shown as red dashed lines 333

Fig. 6.7 (a) ORTEP representation of the crystal structure of **12**·2$(CH_3)_2CO$ showing atom numbering scheme and displacement ellipsoid (50% probability level). Hydrogen atoms are omitted for clarity; (b) octahedral disposition of donors exhibiting the bond distances from metal centers 334

Fig. 6.8 A view in projection down the *a*-axis of the unit cells of **12**.2$(CH_3)_2CO$. The C–H···O interactions are shown as orange dashed lines 336

Fig. 6.9 (a) Molar magnetic susceptibility (χ_m) vs. temperature (T) curve for **11** and (b) plot of χ_mT vs T 338

Fig. 6.10 (a) Molar magnetic susceptibility (χ_m) vs. temperature (T) curve for **12**.2$(CH_3)_2CO$ and (b) plot of χ_mT vs. T 338

Fig. 6.11 Absorption spectral changes of (a) Gimpy (20 μM) and (b) Timpy (20 μM) 339

in presence of equimolar concentrations of different divalent metal ions in methanol at 298 K

Fig. 6.12 (a) Fluorescence emission spectra of Gimpy (50 μM) in presence of different metal ions (50 μM) in methanol at 298 K; (b) bar representation of sensitivity of Gimpy towards different metal ions in methanol at 298 K. Relative intensity is given as the ratio of emission intensity of Gimpy in presence (I) and absence (I_0) of equimolar concentrations of metal ions respectively 340

Fig. 6.13 (a) Fluorescence emission spectra of Timpy (50 μM) in presence of different metal ions (50 μM) in methanol at 298 K; (b) bar representation of sensitivity of Timpy towards different metal ions in methanol at 298 K. Relative intensity is given as the ratio of emission intensity of Gimpy in presence (I) and absence (I_0) of equimolar concentrations of metal ions respectively 341

Fig. 6.14 (a) Emission spectra of Gimpy (50 μM) in absence (dotted line) and presence of Ni^{2+} ions (10, 20, 30, 40 and 50 μM respectively) (solid lines) in methanol at 298 K; (b) Job's plot of Gimpy (50 μM) with varying concentrations of Ni^{2+} ion exhibiting (1:1) stoichiometry where the fluorescent intensity at 447 nm was plotted against the mole fraction of Ni^{2+} 341

Fig. 6.15 (a) Emission spectra of Timpy (50 μM) in absence (dotted line) and presence of Ni^{2+} ions (10, 20, 30, 40 and 50 μM respectively) (solid lines) in methanol at 298 K; (b) Job's plot of Timpy (50 μM) with varying concentrations of Ni^{2+} ion exhibiting (1:1) stoichiometry where the fluorescent intensity at 435 nm was plotted against the mole fraction of Ni^{2+} 342

Fig. 6.16 Electronic absorption spectra of (a) **11** (20 μM) and equimolar mixture of Gimpy and $NiCl_2$ (20 μM each); (b) **12**.2$(CH_3)_2CO$ (20 μM) and equimolar mixture of Timpy and $NiCl_2$ (20 μM each) in methanol at 298 K 343

Fig. 6.17 Absorption spectral changes of (a) Gimpy (20 μM) in presence of increasing concentrations of $NiCl_2$ (5, 10, 20, 100 and 200 μM respectively) and (b) Timpy (20 μM) in presence of increasing concentrations of $NiCl_2$ (20, 100, 200 and 500 μM respectively) in methanol at 298 K 343

Fig. 6.18 Cyclic voltammograms of 10^{-3} M solutions of (a) **11** and (b) **12**.2$(CH_3)_2CO$ in dichloromethane at 298 K under nitrogen atmosphere in presence of 0.1 M TBAP as supporting electrolyte, glassy-carbon is used as working electrode, Ag/AgCl as reference electrode and platinum wire as auxiliary electrode; scan rate 0.1 V/s 345

Fig. 7.1	^{1}H NMR spectrum of ligand Simpy in $CDCl_3$	353
Fig. 7.2	^{13}C NMR spectrum of ligand Simpy in $CDCl_3$	353
Fig. 7.3	The ESI–mass spectrum of Simpy in acetonitrile	354
Fig. 7.4	Mass spectrum of Impy	354
Fig. 7.5	UV–visible spectra of (a) Simpy and its complexes (50 μM each) and (b) Impy and its complexes (50 μM each) in methanol	357
Fig. 7.6	The ESI–mass spectrum of **13a**·4H_2O in acetonitrile	358
Fig. 7.7	The ESI–mass spectrum of **13b** in acetonitrile	358
Fig. 7.8	(a) ORTEP representation of the crystal structure of **13a**·4H_2O showing atom numbering scheme and displacement ellipsoid (50% probability level). Hydrogen atoms are omitted for clarity; (b) distorted square-pyramidal disposition of donor atoms showing the bond distances from the metal centre	359
Fig. 7.9	Intermolecular hydrogen bonding network in **13a**·4H_2O	361
Fig. 7.10	C–H···π interactions in the crystal structure of **13a**·4H_2O	362
Fig. 7.11	Three-dimensional packing of **13a**·4H_2O	363
Fig. 7.12	(a) ORTEP representation of the crystal structure of **13b** showing atom numbering scheme and displacement ellipsoid (50% probability level). Hydrogen atoms are omitted for clarity; (b) trigonal bipyramidal disposition of donor atoms showing the bond distances from the metal centre	363
Fig. 7.13	C–H···π interactions in the crystal structure of **13b**	365
Fig. 7.14	C–H···π interactions and hydrogen bonding interactions in the crystal structure of **13b**	366
Fig. 7.15	Three-dimensional packing diagram of **13b**	366
Fig. 7.16	Time–dependent absorption spectral changes exhibiting oxidation of 3,5–DTBC (3 mM) by complex **13a**·4H_2O (30 μM) in methanol over 2 h at 298 K under aerobic conditions	368
Fig. 7.17	Gel electrophoresis separation showing the cleavage of supercoiled pBR322 DNA (100 ng) by complexes **13a** and **13b** in presence of H_2O_2 (200 μM) and BME (200 μM). The samples were incubated at 37 ˚C for 2.5 h. Lane 1, DNA; lane 2, DNA + H_2O_2; lane 3, DNA + BME; lane 4, DNA + Simpy (200 μM); lanes 5–7, DNA + **13a** (50, 100 and 200 μM respectively); lanes 8–9, DNA + H_2O_2 + **13a** (50 and 100 μM respectively); lanes 10-11, DNA + BME + **13a** (50 and 100 μM respectively); lanes 12-13, DNA + **13b** (100 and 200 μM respectively); lane 14, DNA + H_2O_2 + **13b** (100 μM); lane 15, DNA + BME + **13b** (100 μM)	369

LIST OF TABLES

Table 1.1	Representative examples of some unidenate and polydentate ligands	4
Table 1.2	Protein sources of amino acid radicals	13
Table 1.3	Cobalt–containing proteins and their functions	18
Table 1.4	Nickel containing enzymes and their functions	25
Table 1.5	Copper containing enzymes and their functions	30
Table 1.6	Representative mononuclear [{XYZ}$Zn^{II}(OH_2)$] zinc enzymes with their coordination motifs and functions	35
Table 1.7	Amino acid residues most prone to oxidation and oxidation products	79
Table 2.1	Data for yield, elemental analysis, IR, conductivity and magnetic moment	106
Table 2.2	UV–visible spectral data of complexes **1–2**	107
Table 2.3	Selected bond lengths (Å) and bond angles (˚) for **1a**	114
Table 2.4	Hydrogen–bonding geometries for **1a** (Å)	117
Table 2.5	Redox potentials for complexes **1– 2** at 298 K vs. Ag/AgCl	119
Table 2.6	Binding constants (K_b) and Stern–Volmer constants (K_{SV}) for complexes **1-2**	126
Table 2.7	Summary of the SOD activity and nuclease activity of the complexes.	137
Table 2.8	Crystal data and data collection parameters for **1a**	142
Table 3.1	Data for yield, elemental analysis, IR, conductivity and magnetic moment	154
Table 3.2	UV–visible spectral data of ligand (N_3L) and complexes **3-6**	155
Table 3.3	Selected bond lengths (Å) and angles (˚) for **3a** and **5a**	167
Table 3.4	Hydrogen–bonding geometries for **3a**	170
Table 3.5	Hydrogen–bonding geometries for **5a**	174
Table 3.6	Redox potentials for complexes **3**, **5** and **6** at 298 K vs. Ag/AgCl	176
Table 3.7	SOD activity of complexes **3a** and **3b** as assessed by NBT assay	180
Table 3.8	Summary of the DNA binding events	187
Table 3.9	Binding constants (K_b) and Stern-Volmer (K_{SV}) constants for DNA interaction studies	188
Table 3.10	Summary of DNA cleavage activity studies	202
Table 3.11	Stern–Volmer quenching constants, binding constants and number of binding sites for interactions of complexes **3–6** (**a** and **b**) with BSA	215
Table 3.12	Crystal data and structure refinement details for **3a** and **5a**	225
Table 4.1	Data for yield, elemental analysis, IR and conductivity	232
Table 4.2	UV–visible spectral data of complexes **7**·CH_3CN and **8**	233
Table 4.3	Selected bond lengths [Å] and bond angles [deg] for complex **7**·CH_3CN	239
Table 4.4	Hydrogen bonding geometries for **7**·CH_3CN	240

Table 4.5	Redox potentials for complexes **7**·CH_3CN and **8** at 298 K vs. Ag/AgCl	244
Table 4.6	Stern–Volmer quenching constants of **7**·CH_3CN and **8** with DNA	249
Table 4.7	Stern–Volmer quenching constants, binding constants and number of binding sites for the interaction of **7**·CH_3CN and **8** with BSA	255
Table 4.8	The level of cytotoxicity *in vitro* by complexes **7**·CH_3CN and **8**	260
Table 4.9	Crystal data and structure refinement details for complex $[Co(Phimp)_2]ClO_4 \cdot CH_3CN$ (**7**·CH_3CN)	265
Table 5.1	Data for yield, elemental analysis, IR, conductivity and magnetic moment	272
Table 5.2	UV–visible spectral data of complexes **9–10**	273
Table 5.3	Selected bond lengths (Å) and angles (˚) for **9a**·$3H_2O \cdot CH_3OH$	280
Table 5.4	Hydrogen–bonding interactions for **9a**·$3H_2O \cdot CH_3OH$	282
Table 5.5	Selected bond lengths (Å) and angles (˚) for **9c**·H_2O	284
Table 5.6	Hydrogen–bonding interactions for **9c**·H_2O	287
Table 5.7	Electrochemical data of complexes **9-10** (a, b and c) at 298 K vs. Ag/AgCl	291
Table 5.8	Electronic absorption spectral data of phenoxyl radical complexes	297
Table 5.9	Binding constants and Stern-Volmer quenching constants for DNA interaction of complexes **9-10**	304
Table 5.10	Stern–Volmer quenching constants, binding constants and number of binding sites for interactions of complexes **9–10** (**a**, **b** and **c**) with BSA	312
Table 5.11	Crystal data and structure refinement details for **9a**·$3H_2O \cdot CH_3OH$ and **9c**·H_2O	321
Table 6.1	Data for yield, elemental analysis, IR and conductivity	328
Table 6.2	UV–visible spectral data of complexes **11** and **12.**$2(CH_3)_2CO$	330
Table 6.3	Selected bond lengths (Å) and bond angles (˚) for **12·**$2(CH_3)_2CO$	335
Table 6.4	Geometric parameters for intermolecular interactions in **12**.$2(CH_3)_2CO$	336
Table 6.5	Electrochemical data of complexes **11** and **12**.$2(CH_3)_2CO$ at 298 K vs. Ag/AgCl	344
Table 6.6	Crystallographic parameters and refinement details for Gimpy and complex **12·**$2(CH_3)_2CO$	348
Table 7.1	Data for yield, elemental analysis, IR and conductivity measurements	356
Table 7.2	UV–visible spectral data of Simpy, Impy and their complexes (**13-14**)	356
Table 7.3	Selected bond lengths (Å) and angles (˚) for complex **13a**·$4H_2O$	360
Table 7.4	Geometric parameters for non–covalent interactions of complex **13a**·$4H_2O$	362
Table 7.5	Selected bond lengths (Å) and angles (˚) for complex **13b**	364
Table 7.6	Geometric parameters for non–covalent interactions of complex **13b**	367
Table 7.7	Crystallographic parameters and refinement details for complexes **13a**·$4H_2O$ and **13b**	374

LIST OF SCHEMES

Scheme 1.1	HSAB classification of acids and bases	2
Scheme 1.2	Donor groups commonly employed in pharmaceuticals	3
Scheme 1.3	Ambidentate ligands and their coordination modes	5
Scheme 1.4	Modification sites in pincer ligands and their effects on properties of complexes	7
Scheme 1.5	Schematic representation of a scorpionate ligand and its structural analogy	8
Scheme 1.6	Schematic representation of different types of compartmental ligands	10
Scheme 1.7	Schematic representation of the extent of ligand involvement in charge–transfer interaction with metal center	12
Scheme 1.8	Various amino acid radicals identified in proteins	13
Scheme 1.9	Application of ligand redox–noninnocence in organometallic catalysis	15
Scheme 1.10	Mechanism of cobalt catalyzed hydroformylation of alkenes	21
Scheme 1.11	Alternate dinuclear mechanism of hydroformylation	22
Scheme 1.12	Fluorescent probes used for the detection of NO	31
Scheme 1.13	Function of galactose oxidase (GAO) and glyoxal oxidase (GLO)	38
Scheme 1.14	Catalytic mechanism of galactose oxidase enzyme	40
Scheme 1.15	The two half–reactions catalyzed by superoxide dismutase enzyme	41
Scheme 1.16	Catalytic mechanism of superoxide dismutase enzyme	42
Scheme 1.17	Reaction pathway of the oxygenation and oxidation catalysed by tyrosinase and catechol oxidase	42
Scheme 1.18	Catalytic mechanism involving bidentate coordination of catechol	44
Scheme 1.19	Catalytic mechanism involving monodentate coordination of catechol	45
Scheme 1.20	Schematic representation of (a) active site structure of Co–NHase and (b) structures of ligands PyASH and $PyPepSH_2$	50
Scheme 1.21	Associate mechanism for nucleophilic cleavage of phosphate diester	68
Scheme 1.22	Preferred sites of oxidation in nucleobases by reactive oxygen species	69
Scheme 1.23	Protein oxidation and proteolysis of oxidized proteins	78
Scheme 1.24	Pathways for peptide bond cleavage	78
Scheme 1.25	Ligands used in the present thesis	83
Scheme 1.26	Principle of SOD activity determination by NBT assay	85
Scheme 2.1	Schematic drawing of ligand Pyimpy and PampH	103
Scheme 2.2	Schematic representation of synthesis of ligand Pyimpy	104
Scheme 2.3	Schematic representation of synthesis of ligand PampH	105
Scheme 2.4	Schematic drawing of synthesis of complexes **1–2**	106
Scheme 3.1	Schematic representation of the structure of ligand (N_3L)	147

Scheme 3.2	Schematic representation of synthesis of ligand N_3L by procedure 'A'	148
Scheme 3.3	Schematic representation of synthesis of ligand N_3L by procedure 'B'	149
Scheme 3.4	Schematic representation of the synthesis of complexes **3-6**	154
Scheme 4.1	Schematic drawing of ligand PhimpH and ^{t}BuPhimpH	230
Scheme 4.2	Schematic representation of syntheses of ligands PhimpH and ^{t}BuPhimpH	231
Scheme 4.3	Schematic representation of syntheses of complexes **7**·CH_3CN and **8**	232
Scheme 5.1	Schematic drawing of synthesis of complexes **9** and **10**	271
Scheme 6.1	Schematic drawings of ligands Gimpy and Timpy	326
Scheme 6.2	Schematic representation of syntheses of ligands (i) Gimpy and (ii) Timpy respectively	327
Scheme 6.3	Schematic drawing of synthesis of complexes **11** and **12**·2$(CH_3)_2CO$	328
Scheme 7.1	Schematic drawings of ligands Simpy and Impy	351
Scheme 7.2	Schematic representation of syntheses of ligands (i) Simpy and (ii) Impy respectively	352
Scheme 7.3	Schematic representation of syntheses of complexes **13-14**	355

1.1. Introduction

Coordination chemistry deals with the chemistry of ligands and metal ions where the ligands play an indispensible role in determining the oxidation state, spin state, coordination geometry, redox chemistry and spectroscopic properties of the metal complexes. Rational tailoring of ligand architecture accompanied with the prudent choice of metal ions may gives rise to metal complexes with intriguing chemical and catalytic properties of potential industrial or biological interest.

1.1.1. Ligand

A ligand may be defined as any molecule or ion having at least a pair of electrons which can be donated to the metal ions in order to form the complexes. In general, ligands serve as electron donors acting as Lewis bases and metals as electron acceptors acting as Lewis acids. Fundamentally, any part in a molecule that happens to be more basic than the C-H portions may act as a potential electron donor for the metal atoms and can ligate to the metal behaving as a ligand.[1] Amino acids, peptides, proteins, nucleoproteins, nucleic acids, hormones, carboxylic acids, lipids, simple anions and even the solvent water all contain some electron donor atoms like nitrogen, oxygen, sulphur etc.[1] According to Pearson's "Hard and Soft Acids and Bases" (HSAB) concept, all bonds between heteroatoms may be considered as a combination of an acid and a base part. This theory tells that the stable bonds may exist only between hard acids and hard bases or soft acids and soft bases. The soft acids tend to form complexes with low coordination number and prefer covalency whereas hard acids exhibit high coordination number and ionicity in their complexes.[2] Some representative examples of soft and hard acids and bases are illustrated in Scheme 1.1.

HSAB classification of acids

Hard	**Soft**
H^+, Li^+, Na^+, K^+	Cu^+, Ag^+, Au^+, Tl^+, Hg+
Be^{2+}, Mg^{2+}, Ca^{2+}, Sr^{2+}, Mn^{2+}	Pd^{2+}, Cd^{2+}, Pt^{2+}, Hg^{2+}
	CH_3Hg^+, $Co(CN)_5^{2-}$
	Pt^{4+}, Te^{4+}
Al^{3+}, Sc^{3+}, Ga^{3+}, In^{3+}, La^{3+}	Tl^{3+}, $Tl(CH_3)_3$, BH_3, $Ga(CH_3)_3$
N^{3+}, Cl^{3+}, Gd^{3+}, Lu^{3+}	$GaCl_3$, GaI_3, $InCl_3$
Cr^{3+}, Co^{3+}, Fe^{3+}, As^{3+}, CH_3Sn^{3+}	RS^+, RSe^+, RTe^+
Pu^{4+}, Ce^{3+}, Hf^{4+}	
UO_2^{2+}, $(CH_3)_2Sn^{2+}$, VO^{2+}, MoO^{3+}	I_2, Br_2, ICN, etc.
$BeMe_2$, BF_3, $B(OR)_3$	Trinitrobenzene, etc.
$Al(CH_3)_3$, $AlCl_3$, AlH_3	Chloranil, quinones etc.
RPO^{2+}, $ROPO^{2+}$	Tetracyanoethylene etc.
RSO_2^+, $ROSO_2^+$, SO_3	O, Cl, Br, I, N, RO·, RO_2·
I^{7+}, I^{5+}, Cl^{7+}, Cr^{5+}	M^0 (Metal atoms)
RCO^+, CO_2, NC^+	Bulk materials
HX (hydrogen bonding molecules)	CH_2, carbenes
Borderline	
Fe^{2+}, Co^{2+}, Ni^{2+}, Cu^{2+}, Zn^{2+}, Sb^{3+}, Bi^{3+}, Rh^{3+}, Ir^{3+}, $B(CH_3)_3$, SO_3, NO^+, Ru^{2+}, Os^{2+}, R_3C^+, $C_4H_5^+$, GaH_3^+	

HSAB classification of bases

Hard	**Soft**
H_2O, OH^-, F^-	R_2S, RSH, RS^-
$CH_3CO_2^-$, PO_4^{3-}, SO_4^{2-}	I^-, SCN^-, $S_2O_3^{2-}$
Cl^-, CO_3^{2-}, ClO_4^-, NO_3^-	R_3P, R_2As, $(RO)_3P$
ROH, RO^-, R_2O	CN^-, RNC, CO
NH_3, RNH_2, N_2H_4	C_2H_4, C_6H_6
	H^-, R^-
Borderline	
$C_6H_5NH_2$, C_6H_5N, N_3^-, Br^-, NO_2^-, SO_3^{2-}, N_2	

Scheme 1.1 HSAB classification of acids and bases[1]

It can be seen that the hardness of an element increases with its oxidation state. Thus the stabilization of an element in higher oxidation state requires hard bases as ligands.

Similarly low oxidation state requires soft bases as ligands. Some of the common electron donor groups, frequently employed in designing of drugs are depicted in Scheme 1.2.[1]

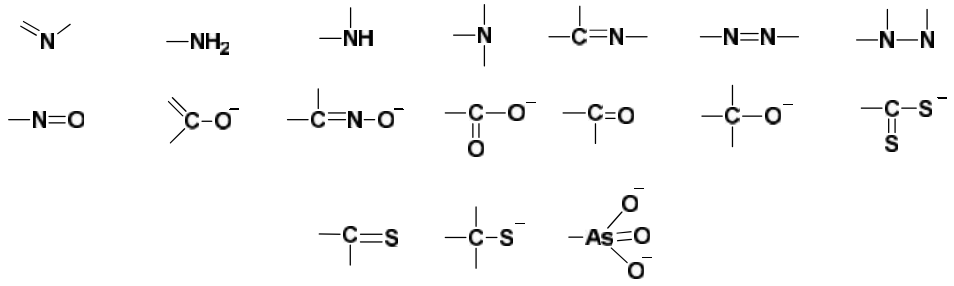

Scheme 1.2 Donor groups commonly employed in pharmaceuticals[1]

1.1.1.1. Classification of ligands

There may be several ways of classifying the ligands. Based on donor and acceptor properties, ligands may be of following types:[3]

(a) Classical donor ligands: These ligands donate the electron pair to all sorts of Lewis acids including metal ions to form the complexes e.g. NH_3 and H_2O.

(b) Nonclassical ligands: These ligands are also called π-acid ligands. These can donate the electrons to the metal in the empty d–orbitals as well as accept the electrons from the metal through π-bonding e.g. PPh_3 and CO.

Alternatively, ligands may also be classified as:

(1) **Ligands with lone pairs of electrons:** These may further be of two types.

(a) Ligands with no vacant orbitals to receive back donated electrons from metal e.g. H_2O.

(b) Ligands with vacant orbitals to receive back donated π electrons from the low oxidation state metal e.g. CO.

(2) **Ligands without lone pair of electrons:** These ligands do not have lone pairs of electrons but have π- bonding electrons e.g. ethylene.

Ligands may also be categorised *electronically* i.e. according to the number of electrons donated to the central metal atom (*when those are considered as neutral species*).[3]

(i) One electron donors: This type of ligands form a single covalent bond e.g. F and SH.

(ii) Two electron donors: This type of ligands donate a pair of electrons to form the complexes e.g. NH_3 and H_2O.

(iii) Three electron donors: This type of ligands form a covalent bond besides the donation of an electron pair e.g. an acetate ion coordinated to a metal ion by both oxygen atoms.

(iv) Four electron donors: These ligands donate two pair of electrons hence regarded as four electron donors e.g. *N*,*N*′−ethylenediamine.

Alternatively, ligands may also be classified *structurally*. Depending upon the number of donor atoms available for coordination, there may be several types of ligands in coordination chemistry like uni–, bi–, tri–, tetra–, penta–, hexadentate ligands and so on.[3] Some examples of uni– (or mono–) and multidentate (polydentate) ligands are illustrated in Table 1.1.

Table 1.1 Representative examples of some unidenate and polydentate ligands

Denticity	**Example**
Unidentate	Ammonia, water
Bidentate	*N*,*N*′−ethylenediamine, 1,10−phenanthroline
Tridentate	Terpyridine ligands
Tetradentate	Salen ligands
Pentadentate	Tetraethylenepentamine
Hexadentate	Ethylenediaminetetraacetate ($EDTA^{4-}$)

Some unidentate ligands have two or more different donor sites and may coordinate to metal ion using either of them. This type of ligands are called *ambidentate* ligands. These ligands give rise to the possibility of linkage isomerism (Scheme 1.3).[3]

M–NO_2	Nitro	M–CN	Cyano	M–SCN	*S*-Thiocyanato
M–ONO	Nitrito	M–NC	Isocyano	M–NCS	*N*-Thiocyanato

Scheme 1.3 Ambidentate ligands and their coordination modes

Furthermore, the ligands may also be classified on the basis of the nature of donor atoms like oxygen donor ligands (e.g. H_2O, Ph_3PO and SO_4^{3-}), nitrogen donor ligands (CO, η–C_5H_5, $CH_3CH{=}CH_2$) and nitrogen donor ligands (NO and NO_2^-).[3]

1.1.1.2. Special types of ligands

(a) Macrocyclic ligands

These represent a special category of polydentate ligands in which the donor atoms are constrained in a large ring encompassing the metal atom.[4] A well known example of macrocyclic ligands is polyether in which the ether oxygen atoms bind to the central metal atom in a nearly planar arrangement with the separating methylene moieties forming a crown above the ligand binding plane. A wide range of macrocyclic ligands having a conjugated π-system is also known. Phthalocyanines, porphyrins, corrins and corroles are the well known examples of such type of macrocycles. Macrocyclic ligands exhibit greater thermodynamic and kinetic stability in their complexes than the corresponding open-chain chelating ligands.[3] These ligands also exhibit the unique property of stabilizing higher oxidation states of metals such as Cu^{III} and Ni^{III} which are difficult to attain under normal conditions.[3] The properties of the complexes derived from these ligands greately depends upon the size of the cavity within the macrocycle. Among various approaches adopted for the synthesis of macrocyclic ligands, template directed synthesis and high dilution technique are the most common.[5]

(b) Clathrochelate, sepulchrate, spherand and hemispherand

Clathrochelate or cryptands are bicyclic or polycyclic multidentate macromolecules, generally containing bridgehead nitrogen atoms which form a three-dimensional cage around the metal ion.[4] These ligands exhibit selectivity for complexation of alkali and alkaline earth metal ions. Apart from the cryptands which are first synthesized and then utilized for complexation, there are other types of multicyclic ligands also, known as encapsulating ligands, which are synthesized around the metal ions and cannot release it.[3] A very well known example of such ligands is nitrogen analogs of the cryptands, known as *sepulchrates*. These are basically polyaza cage macrocyles which exhibit exceptionally strong hold on the encapsulated metal ions. These ligands bind the metal ion by six N-donors which donot leave the coordination sphere even under extremely acidic or basic conditions or with the changes of the oxidation state of the metal atom thereby permitting the study of their complexes in various oxidation states while keeping their constitution and stereochemistry unchanged.[3] There is another type of macrocylic ligands also, which is known as *spherands/hemispherands*. These ligands consist of macrocycles derived from phenyl groups arranged in a specific way to provide a preorganized cavity for complexation.

(c) Pincer ligands

Pincer ligands are terdentate ligands which are connected to the metal via at least one metal–carbon σ bond. The most common pincer scaffold is composed of an anionic aryl ring which is *ortho*, *ortho*-disubstituted with heteroatom substituents like CH_2NR_2, CH_2PR_2 or CH_2SR. These ligands coordinate with the metal centre in a η^3–*mer* fashion constructing one M─C σ bond along with the formation of two thermodynamically stable five–membered metallacycles sharing together the M─C bond. These are named as "pincer" owing to their specific binding mode. These may be represented by the general formula [2,6–

$(ECH_2)_2C_6H_3]^-$ or (ECE) where E denotes a neutral two electron donor like NR_2, PR_2, AsR_2, OR or SR and C is the anionic aryl carbon atom of the 2,6−disubstituted phenyl ring. These ligands coordinate to metals affording the complexes of general formula $[MX_n(ECE)L_m]$ which generally exhibit exceptional thermal stability along with high reactivity.[6] In these systems, the steric and electronic properties of the complexes can be efficiently tailored without any significant changes in their coordination pattern (Scheme 1.4). Organometallic complexes derived from pincer type ligands are used as catalyst in a wide variety of organic transformations and in light emitting materials.

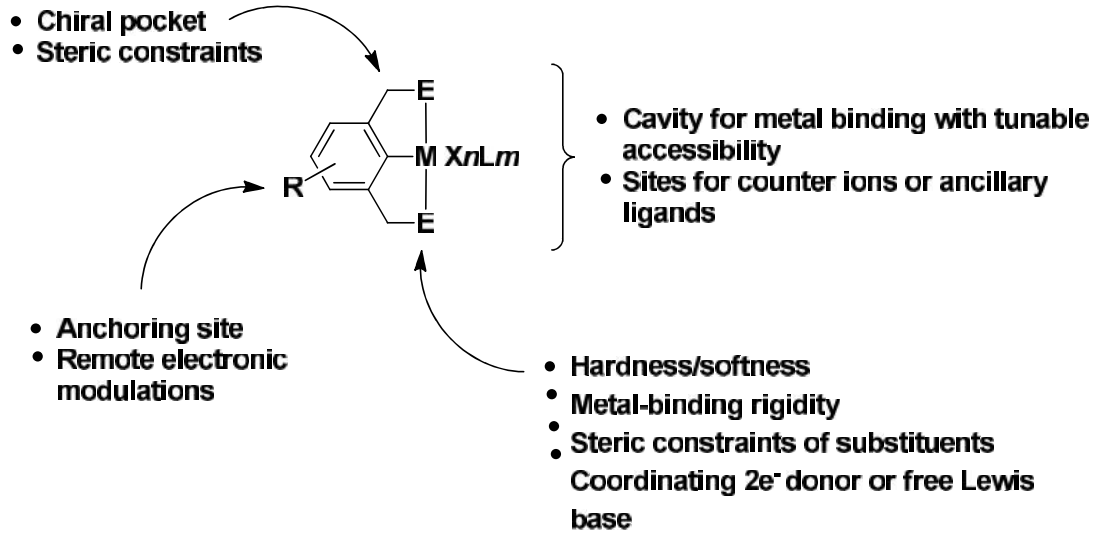

Scheme 1.4 Modification sites in pincer ligands and their effects on properties of complexes[6]

(d) Scorpionate or tripodal ligands

These are tridentate ligands in which two of the donor sites bind with metal occupying adjacent coordination sites (*pincers*) while the third donor coordinates to metal reaching over the plane containing other two donor atoms along with the metal ion (*stinger*). The overall binding mode of the ligand remains *facial* and the molecule may be visualized as being like a scorpion (*ligand*) grabbing the prey (*metal*) with its pincers before stinging it (Scheme 1.5).

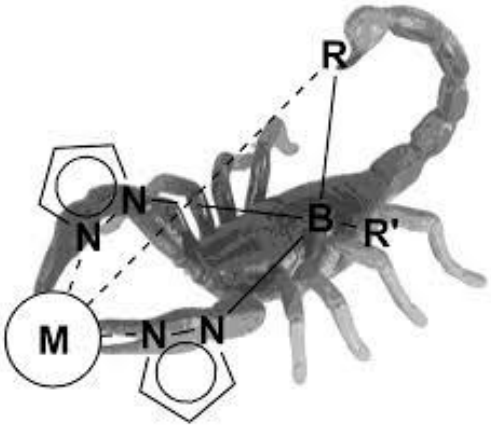

Scheme 1.5 Schematic representation of a scorpionate ligand and its structural analogy

In fact, the term "scorpionate" describes the interchange of bidentate and tridentate coordination modes of such ligands. These ligands may be boro−centric or carbo−centric depending on the nature of the central atom. The most familiar class of scorpionate ligands is Trofimenko's tris(pyrazolyl)borate or "Tp" ligands. It is important to note that variation in the steric requirements of the substituents present on 3−position of pyrazolyl ring, nearest to the metal centre, may give rise to remarkable changes in the reactivity of the ligand scaffold and properties of the resulting metal complex. However, the ligands are termed as second-generation scorpionate ligands when such steric changes at 3−position of the pyrazolyl ring lead to drastic changes in the coordination chemistry of the ligand or the metal complex.[7] Scorpionate ligands may further be classified as homoscorpionates or heteroscorpionates. Homoscorpionates contain three identical pyrazolyl based donor groups e.g. $(1-\text{pyrazolyl})_3BH^-$ and $(1-\text{pyrazolyl})_3CH$. Heteroscorpionates possess two identical pyrazolyl groups (pincers) along with a different donor group (stinger) which can bind with the metal centre.[8]

(e) Compartmental ligands

These are acyclic or cyclic, dinucleating or polynucleating ligands which exhibit the ability to selectively recognize and bind two or more metal ions in close proximity through

their in–built two or more, identical or different, adjacent or non–adjacent compartments having appropriate donor sets. In compartmental ligands with adjacent chambers, the metal ions held in close vicinity may generally communicate with each other through endogenous bridging atoms. Conversely, in the ligands composed of non–adjacent chambers, such communication between the metal centers is not possible through endogenous bridging groups and takes place through exogenous bridging groups and/or through the shape and connectivity of the entire coordination moiety.[9-10] Such ligands are widely used to synthesize dinuclear metal complexes of potential catalytic and biological interest. These ligands encompass a large variety of molecules e.g.

(a) End–off acyclic ligands: These are obtained by [1+2] condensation between a keto precursor and diamine (Scheme 1.6, A).

(b) Side–off acyclic ligands: These are prepared by [2+1] condensation between a keto–precursor and diamine followed by condensation of remaining keto groups with a primary amine (Scheme 1.6, B).

(c) Symmetric dinucleating ligands: Cyclic or acyclic molecules with similar compartments (Scheme 1.6, C).

(d) Dissymmetric dinucleating ligands: Cyclic or acyclic molecules with different compartments. These ligands are especially suited for synthesis of heterobimetallic complexes (Scheme 1.6, D).

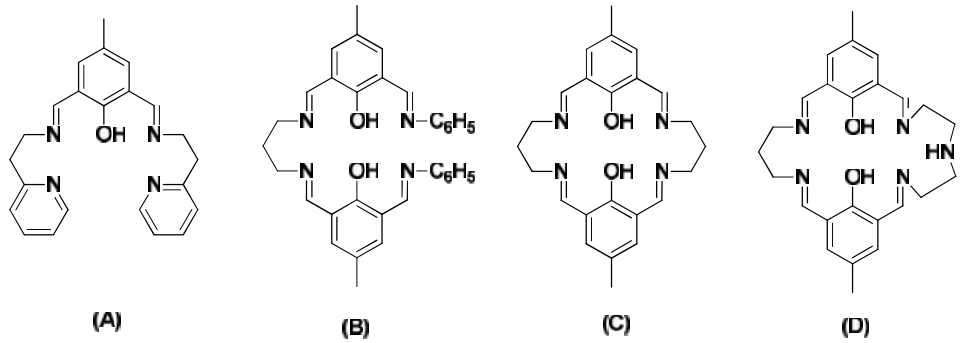

Scheme 1.6 Schematic representation of different types of compartmental ligands

(f) Hemilabile ligands

The term "Hemilabile" was first introduced by Jeffrey and Rauchfuss in 1979.[11] Many polydentate ligands are known to possess a Lewis basic moiety which can dissociate from the metal reversibly leading to the generation of a transient coordinative unsaturation over the metal ion. Such types of ligands are known as hemilabile ligands. These ligands are generally composed of the coordinating atoms which differ in their electronic nature like hard and soft donors or substitutionally inert and substitutionally labile groups. This unique feature of hemilabile ligands allows the temporary dissociation of one of the coordinating groups (*substitutionally labile*) from the metal making the room for substrate binding while the other group (*substitutionally inert*) remains firmly anchored to the metal ion. The bifunctional character of hemilabile ligands has been successfully exploited for chemical sensing as well as to stabilize some reactive unsaturated transition metal species. Complexes derived from such type of ligands are widely used for metal complex small molecule bond activation reactions and transition metal catalysis.[12]

(g) Non-innocent ligands (NILs)

The general behaviour of transition metal complexes during the course of a redox process involves oxidation or reduction of the metal centre, leaving the ligand part

unaffected. However, in some cases, ligands can also participate in the redox processes acting as a source or sink of electrons with the metal retaining its original oxidation state. Such ligands are termed as "non-innocent" or "suspect" ligands. The terms "redox–active ligands" or "redox ambi–valent ligands" have also been used as their synonyms[13] though distinctions have been made in some cases.[14] According to Jorgenson, a ligand is considered as innocent if the oxidation states in its complexes can be strictly assigned however in case of non–innocent ligands the assignment of oxidation states is ambiguous.[15] However, Chirik pointed out that appropriate assignment of the oxidation states of metals in such cases is often possible by means of modern experimental and computational methods.[14] Two types of terms are generally used to explain the oxidation state of metals in mononuclear metal complexes.[16-17]

(i) Formal oxidation state: It can be defined as "the charge remaining on the metal ion when all the ligands attached with the metal are removed in their normal, closed–shell configuration – that is with their electron pair".

(ii) Spectroscopic or physical oxidation state: It is described as "the oxidation state of the metal ion which is directly deduced with the help of various spectroscopic techniques by ascertaining its electronic configuration".

Both *formal* and *physical* oxidation states are often used interchangeably but such practice may lead to absurd or erroneous description of oxidation states in certain areas of coordination chemistry, especially in those cases where the ligands can exist in several or at least two different oxidation states available at common redox potentials. To avoid misleading descriptions, it is desirable to switch from the *formal oxidation state* to *physical oxidation state* in such cases.

The phenomenon of non–innocence is exemplified by ligands when there is very small energy difference between metal–centered and ligand–centered frontier orbitals thus enabling a ready electron transfer.[18] The ligands can participitate in electron-transfer interaction with metal center upto varying extents as represented in Scheme 1.7.[19]

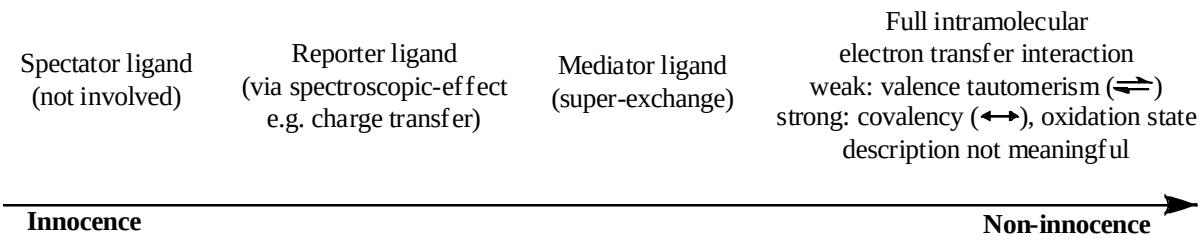

Scheme 1.7 Schematic representation of the extent of ligand involvement in charge–transfer interaction with metal center[19]

It is worthnoting that the innocence or non–innocence is not a permanent attribute of a ligand but a function of specific circumstances in certain situations.[13] Furthermore, the redox–active ligands can behave both, in an innocent or in a non–innocent way.[15] The category of non–innocent ligands encompasses a large array of molecules including bio–relevant as well as non–bio–relevant ones. Among biologically relevant redox non–innocent ligands, the prominent examples are $NO^{+/\cdot/-}$, $O_2^{0/\cdot-/2-}$, tetrapyrrole ligands such as porphyrins, chlorins and corroles, pterins, flavins and 4–centered chelate redox systems with *o*–quinone/*o*–semiquinone/catecholate,[20,21] α–iminocarbonyls or α–dithiolene/ene–1,2–dithiolate functions.[13,16] Cyanides (as in iron hydrogenases), oxo ligands (as in P–450 dependent enzymes and copper containing monooxygenases), hydrides and alkyl ligands (as in B_{12} coenzymes and methane producing nickel dependent coenzymes) are among those biologically relevant ligands which possess "*hidden*" non–innocence essential for their biochemical functioning. Several stable and transient amino acids radicals

have also been identified as localized to glycines, cysteines, tryptophans, tyrosines as well as a variety of modified tryptophan and tyrosine residues within proteins[22] which are illustrated in Scheme 1.8 along with their protein source (Table 1.2).

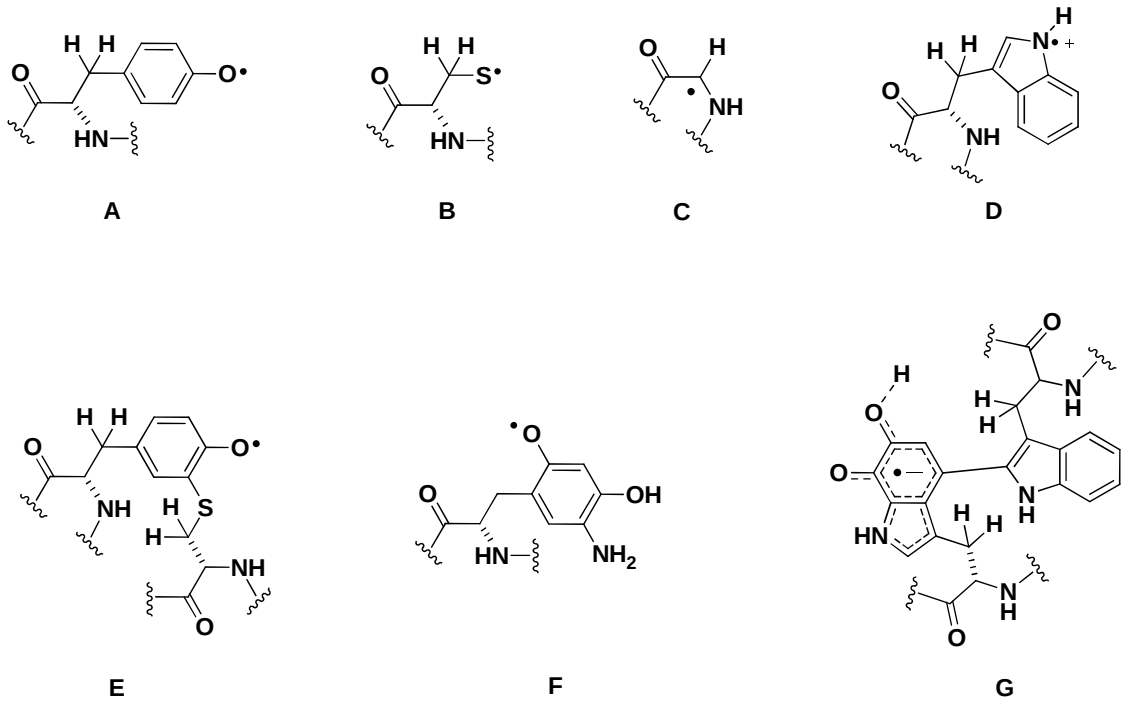

Scheme 1.8 Various amino acid radicals identified in proteins[22]

Table 1.2 Protein sources of amino acid radicals[22]

Radical	Protein Source
A	Class I ribonucleotide reductase (RNR), photosystem II, prostaglandin H synthase
B	Class II RNR
C	Class III RNR, pyruvate formate lyase
D	Cytochrome peroxidise
E	Galactose oxidase
F	Plasma amine oxidases
G	Methylamine dehydrogenases

Non–bio–relevant redox non–innocent ligands include α–diimine, α–dicarbonyl and α–azo functional 4–centered system,[13] iminepyridines,[23] bipyridines,[23] terpyridines,[23] Fischer type carbene ligands,[24] N=N containing tetrazine ligands and acceptor substitued olefins.[13,16]

The redox–active ligands may serve in several aspects:[13]

(i) As substrate of reactions (examples include O_2 or quinones/catechols in oxygenation reactions).

(ii) As reactive intermediates (like H–abstracting oxyl or oxidizing phenoxyl radical).

(iii) As controlling electron reservoirs (examples include dithiolene or porphyrin π–systems).

These ligands find their potential application in developing molecular conductors and switches,[13] molecular magnets,[13] photoactive components such as emitters and sensitizers,[13] synthetic models for metalloenzymes (*vide infra*) and in the synthetic conversions also. Ligand redox non–innocence has been proven to be a great synthetic tool offering unique opportunities to enhance reactivity and steer selectivity by modifying the properties of transition metal catalysts. A number of organometallic transformations are generally catalysed by noble and expensive transition metals like Pd, Rh and Pt which undergo oxidative addition and/or reductive elimination processes involving two–electron transfer. On the contrary, most of the inexpensive metals, mainly from the first row transition series, exhibit one electron transformations and hence are more suitable for catalyzing the radical type reactions. Utilizing redox non–innocent ligands has opened a new window in the realm of catalytic processes where low–cost transition metals can be used as surrogates for expensive metals. Now–a–days, the non–innocence of ligands is being successfully exploited

for organometallic catalysis and two complementary strategies are generally adopted for this purpose (Scheme 1.9):[24,25]

(a) Through the use of non–reactive redox–active ligands which behave as electron reservoirs inducing noble metal character (two–electron reactivity) (spectator ligand);

(b) Through the generation of reactive ligand radicals and their utilization in catalysis to impose controlled ligand–centered radical–type reactivity (actor ligand).

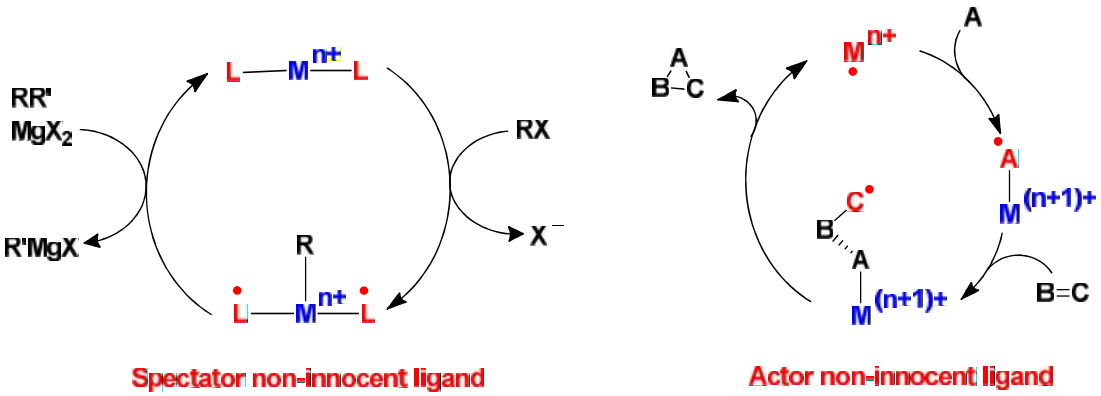

Scheme 1.9 Application of ligand redox–noninnocence in organometallic catalysis

A number of classifications have been proposed to categorize the redox–active ligands employed in catalysis and a few of them are as follows:[14]

(a) Actor versus spectator ligands: Actor ligands are those which engage directly with the substrate molecule during the catalytic process whereas spectator ligands exert their effect on the metal center which forms the site of reactivity.

(b) Closed shell *versus* open shell redox active ligands: In closed shell redox activity, the ligand exhibits redox changes in such a way that the system remains spin–paired whereas in case of open shell redox active ligands, some unpaired electron density may be present at some stage.

(c) Covert radical *versus* overt radical ligands: Covert ligand radical describes those cases where the ligand in the reactant complex is essentially spin−paired but attains radical character as the transition state of the reaction is approached. The overt ligand radical refers to those systems where the ligand possesses significant unpaired spin density even in the reactant.

1.1.2. Metals

A metal ion is another main constituent of a coordination complex which is generally responsible for substrate binding and forming the site of reactivity. The present work deals with four metals: cobalt, nickel, copper and zinc.

1.1.2.1. Cobalt (*symbol*: Co; *electronic configuration*: [Ar] $3d^7$, $4s^2$)

1.1.2.1.1. General comments[3]

Cobalt generally occurs in nature in association with Ni or As. The most important minerals of cobalt are *smaltite* ($CoAs_2$) and *cobaltite* (CoAsS). Cobalt can exhibit oxidation states from (-I) to (+V) though (I), (II) and (III) are the most common oxidation states. Among transition metal elements, the (+I) oxidation state is better represented by cobalt than any other element, except copper. Co(II) is the only d^7 ion of common occurrence and occurs in a wide range of coordination environments. The stereochemistry of Co(II) shows normal coordination numbers of 3, 4, 5 and 6 though few 8-coordinated complexes of Co(II) are also known. There are numerous simple or hydrated salts of cobalt(II), the latter being mostly pink or red in color. The color change from blue to pink due to the conversion of anhydrous form to octahedral form of Co(II) is used as moisture indicator in silica gel drying agents. Co(II) may exist in both high−spin and low−spin states but examples of low−spin octahedral Co^{II} complexes are very rare. Such complexes undergo strong Jahn−Teller distortion ($t_{2g}^6 e_g^1$) and tend to lose ligands to form low−spin tetra− or penta−coordinated species. Co(II) gives rise to

kinetically labile complexes while Co(III) complexes are kinetically inert in nature.[26-28] There are very less number of simple salts or binary compounds available for Co(III) since water reduces the uncomplexed Co(III) ions rapidly at room temperature. Co(III) can exhibit a coordination number of 4, 5 or 6 in its complexes. Most of the Co(III) complexes are octahedral though a few tetrahedral, planar and square antiprismatic complexes are also known. All known octahedral Co(III) complexes are diamagnetic in nature except $[Co(H_2O)_3F_3]$ and $[CoF_6]^{3-}$ which are paramagnetic and have four unpaired electrons. Cobalt (III) shows a special affinity for nitrogen donors like ammonia, ethylenediamine, NO_2 groups and N–bonded SCN groups.

1.1.2.1.2. Role in biosystem

Cobalt is present in vitamin B_{12} (anti–pernicious anemia factor or cyanocobalamin) in the form of diamagnetic Co^{3+} bound to a substituted corrin macrocycle. It is the only vitamin containing a metal and the nature's only organometallic compound.[4] An analogous compound 5'–deoxyadenosylcobalamin is known as coenzyme B_{12} which is needed by several enzymes including methylmalonyl CoA mutase, glutamate mutase, α–methylene–glutarate mutase, dioldehydrase, glyceroldehydrase, ethanoldeaminase, L–β–lysine mutase, D–α–lysine mutase, methane synthetase, ribonucleotide reductase, methionine synthetase, methyl transferase and acetate synthetase to exhibit their activity.[29] Numerous non–corrin cobalt containing enzymes are also known which are listed in Table 1.3.[30]

Table 1.3 Cobalt–containing proteins and their functions[30]

Protein	Source	Role of Cobalt	Cofactor content
Methionine aminopeptidase	Yeast, bacteria, animals	Hydrolysis	2 Co per subunit
Nitrile hydratase	Actinomycetes, bacteria	H_2O activation, CN–triple–bond hydration and protein folding	1 Co in each α–subunit
Glucose isomerise	Actinomycetes	Isomerization	1 Co per 4 subunit
Prolidase	Archae	Hydrolysis	1–2 Co per subunit
Cobalt transporter	Actinomycetes and yeast	Cobalt uptake	
Methylmalonyl–Co–A carboxytransferase	Bacteria	Carboxytransferation	1 Co, 1 Zn per subunit
Aldehyde decarbonylase	Algae	Decarbonylation for aldehyde	1 Co–porphyrin per αβ subunit
Lysine–2,3–aminomutase*	Bacteria	Mutation	0.5–1 Co per subunit
Bromoperoxidase	Bacteria	Bromination	≈0.35 Co per 2 subunit
Cobalt–porphyrin–containing protein	Bacteria	Electron carrier	1 Co–porphyrin per protein

* Besides cobalt, iron sulphur clusters, zinc and PLP are also found as cofactors in lysine-2,3-aminomutase

1.1.2.1.3. Applications of cobalt

(i) Tracer and therapeutics

Radioactive cobalt (^{60}Co) is widely used as a concentrated source of γ–radiations in cancer therapy, food sterilization and as radioactive tracer in wide range of processes since the natural isotope (^{59}Co) is converted to non–radioactive nickel (^{60}Ni) on the neutron bombardment leading to emission of β– and γ– radiations.[30]

(ii) Spectroscopic probes for metalloenzymes

Due to the characteristic spectroscopic properties of cobalt correlated with its stereochemistry, it is frequently used as a spectroscopic probe for metalloenzymes.[31] Several

"spectroscopically–silent" zinc containing enzymes have been successfully substituted with cobalt giving rise to still functioning enzymes which can actively respond to optical (absorption, magnetic circular dichroism) and magnetic resonance spectroscopy (NMR, EPR and ENDOR).[32] Such substitution is helpful to elucidate the coordination environment of active centres in those proteins as well as the structural and stereochemical aspects responsible for the catalytic activity of these enzymes.[30] It is documented in literature that, in some cases, substitution with cobalt resulted the restoration of the enzymatic activity whereas in some enzymes the activity got enhanced due to substitution with cobalt ion.[33]

(iii) Oxygen carrier

The metal catalysts which can activate dioxygen and promote oxygen atom transfer, possess remarkable biological importance and find potential industrial applications.[34] After the affinity of cobalt complexes towards dioxygen was realized, a number of cobalt complexes derived from dien, salen, porphyrin, pentacyano, trispyrazoleborato, tetraazamacrocylic and various other ligands have been designed and synthesized. Such molecules found their applications as spectroscopic models to elucidate the oxygen binding chemistry of heme enzymes due to their potential for irreversible or reversible binding with dioxygen and their ability to work as oxygen carriers[35] and oxygen reservoir.[36] Simultaneously, a plethora of cobalt complexes has been developed to catalyze the oxidation of various organic substrates utilizing molecular oxygen where the affinity of cobalt towards oxygen is successfully exploited (*vide infra*).

(iv) NO sensors

Sensing of nitric oxide is of immense significance due to its diversified roles in physiological processes like anticancer activity, host immune system defense, neurotransmission, and vasodilation as well as pathological processes like cancer, ischemia,

septic shock, inflammation and neurodegeneration.[37-42] Furthermore, higher doses of NO may induce inhibition of respiratory complexes, DNA damage and modification, gene mutation and cell apoptosis also.[42,43] A number of cobalt complexes including Co–DATI systems,[44,45] Co–dansyl systems [46,47] and Co–FATI systems[48] have been successfully employed for the fluorescent detection of nitric oxide.[49]

(v) Dye sensitized solar cells (DSSCs)

Most of the DSSCs utilize an iodide/triiodide redox shuttle to regenerate the oxidized dye. However, several disadvantages including large energy loss, corrosiveness and competitive absorption of light by triiodide associated with the iodide/triiodide system limit its application.[50] A number of cobalt complexes[51] with special attention to cobalt polypyridyl complexes [50-56] have been synthesized in search of alternative redox shuttle and till today, the best alternative redox shuttle is composed of Co(II/III) polypyridyl complexes.[51]

(vi) Catalysis

Fischer–Tropsch process

Fischer–Tropsch process is a widely used commercial method to synthesize hydrocarbon fuels from syngas derived from the natural gas and coal. Fischer and Tropsch proposed cobalt and iron as first catalysts for the syngas conversion[57] and commercial FT plants still utilize iron and cobalt catalysts for this purpose. Although ruthenium and nickel also show excellent catalytic properties for the hydrogenation of carbon monoxide, ruthenium is highly expensive and less abundant whereas nickel catalysts produce excessive methane which limits their commercial usage as catalysts for the FT process in large scale industries.[57] Recently, a comparison between the efficiencies of cobalt and iron catalysts for the Fischer-Tropsch process was made by Davis[58] and it was found that cobalt was more efficient catalyst

under low severity conditions whereas iron was more active under more severe conditions (higher space velocities and higher reactor pressures). Furthermore cobalt catalysts were accompanied with two major advantages over iron catalysts; (1) because of lack of the water gas shift (WGS) reaction, a process known to compete with the Fischer–Tropsch process, cobalt catalysts efficiently convert the oxygen in CO to water rather than CO_2 exhibiting higher activities than the iron catalysts; (2) cobalt catalysts can achieve the robustness if provided with a support which is a significant factor for the accomplishment of the process.[58]

Oxo process[59]

The cobalt catalyzed hydroformylation of alkenes which is also known as oxo process involves the conversion of alkenes into the corresponding aldehydes and receives considerable synthetic importance.

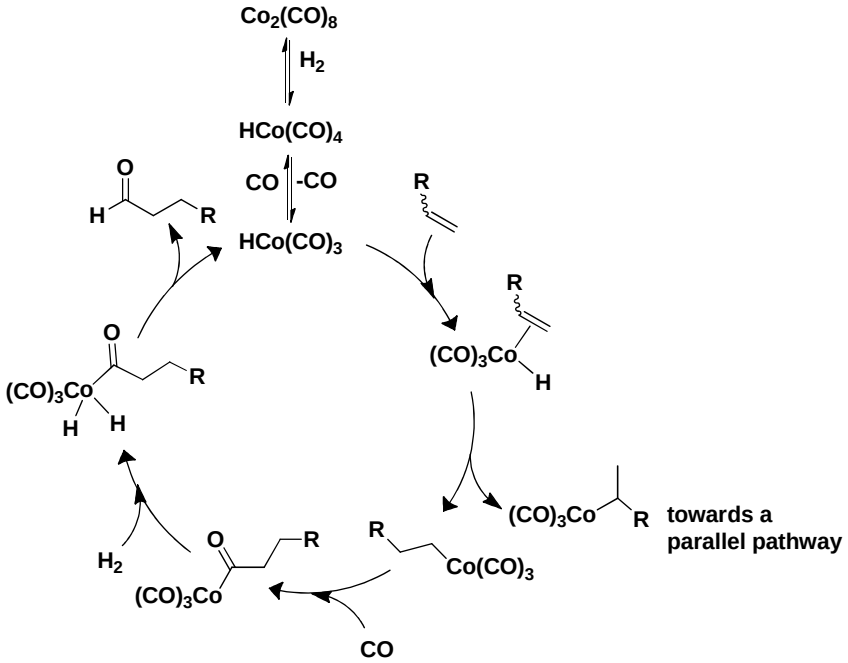

Scheme 1.10 Mechanism of cobalt catalyzed hydroformylation of alkenes[59]

The catalytic cycle involves $[Co(H)(CO)_4]$ as the oxo–cobalt catalyst. During the catalytic cycle, it loses a CO ligand giving rise to a $16e^-$ species $[Co(H)(CO)_3]$ which undergoes a number of steps including alkene coordination, hydride transfer, CO

coordination and migratory CO insertion, oxidative addition of H_2 and reductive elimination of aldehyde to regenerate the active species (Scheme 1.10).

An alternative pathway may also be operative when the reactions are carried out under stoichiometric conditions with high concentrations of cobalt (Scheme 1.11).

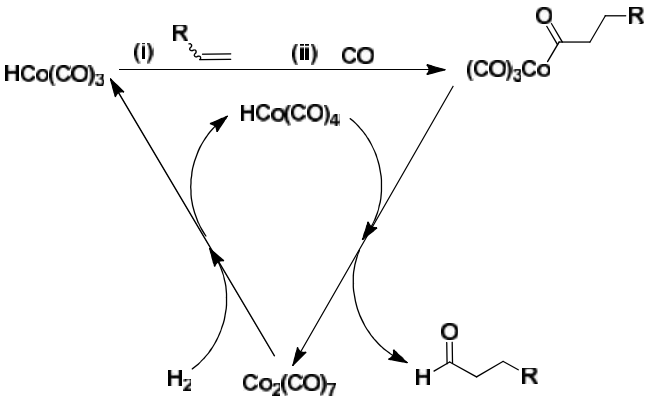

Scheme 1.11 Alternate dinuclear mechanism of hydroformylation[59]

Miscellaneous conversions

Cobalt can catalyze the oxidation of a variety of organic substrates in presence of molecular oxygen. A large number of cobalt catalysts have been developed which can promote the epoxidation of alkenes, oxidation of alkenes to alcohols and ketones, allylic oxidation, oxidative dehydrogenation of alkanes to alkenes, oxygenation of alkanes, benzylic oxidation and aromatic C–H oxidation.[60]

Splitting of water

To meet the global energy demand on one hand, and simultaneously to avoid the release of green house gases on the other, hydrogen is emerging as an alternative clean fuel. In nature, iron or nickel dependent hydrogenase enzymes generate H_2 from the aqueous media. However, this process can be also be accomplished artificially by utilizing some synthetic transition metal–based catalysts. A number of cobalt complexes have been designed and developed for this purpose.[61] Krishnan and Sutin reported the first photocatalytic system

for the generation of hydrogen through photoreduction of water utilizing $[Co(bpy)_n]^{2+}$ (n = undefined) complex as catalyst and $[Ru(bpy)_3]^{2+}$ as photosensitizer.[62] Later on, the same system exhibited simultaneous reduction of CO_2 and water driven from the visible light.[62] Rigsby et al. synthesized a family of dinuclear $Co^{III}Co^{III}$ peroxo complexes analogous to ruthenium based water oxidation catalysts. The electrochemical studies suggested that those complexes may be used as molecular electrocatalysts for oxidation of water in acidic media.[63] Chang and co−workers reported a molecular cobalt polypyridine catalyst derived from the ligand Py5Me2 which exhibited high stablility and activity for the electrocatalytic generation of hydrogen from neutral water.[64] Gray and co−workers presented a cobalt complex derived from non−innocent bis(iminopyridine) ligand as a highly active electrocatalyst for water reduction in buffered aqueous media.[65] Leung et al. reported a cobalt(II) quaterpyridine complex $[Co^{II}(qpy)(OH_2)_2]^{2+}$ (where qpy = 2,2′:6′,2′′:6′′,2′′′−quaterpyridine) as an efficient visible light−driven catalyst for the photochemical oxygen evolution through water oxidation as well as photochemical hydrogen generation through water reduction.[66]

Activation of small molecules

Nitrogen, which is abundant in the atmosphere in the form of an extremely inert molecule known as dinitrogen, is an important constituent of biomolecules. Although dinitrogen continuously enters in our body, it does not participate in the metabolism owing to its extreme inertness.[67] Furthermore, it's activation through chemical processes (like Frank−Caro cyanamide process and Haber−Bosch process) demands harsh conditions.[67] However, cobalt can bind a variety of neutral molecules including N_2[68-73] and CO_2[74] and promote their activation. Such complexes may serve as benchmark to develop efficient catalysts for reactions having considerable economic, industrial and biological importance.

1.1.2.2. Nickel (*symbol*: Ni; *electronic configuration*: [Ar] $3d^8$, $4s^2$)

1.1.2.2.1. General comments[3]

Nickel is mainly found in nature associated with arsenic, antimony and sulphur. The most important ore of nickel is *millerite* (NiS). It is also found in the form of *garnierite*, which is a magnesium–nickel silicate and the iron mineral *pyrrhotite* which contains 3 to 5% Ni. It can exhibit the oxidation states from -1 to +4 though +2 oxidation state is the most common.[75] Nickel(II) can form variety of complexes having the coordination numbers 3 to 6. Among penta–coordinated complexes of Ni(II), both trigonal bipyramidal geometry and square pyramidal geometry are common and high–spin as well as low–spin complexes of each geometry are known. There are few interesting phenomena associated with Ni(II) complexes. Ni(II) square planar complexes are known to undergo ligand association to form 5– and 6–coordinate metal complexes accompanied with the change in their spin state. In some cases the complexes undergo monomer–polymer equilibrium to expand their coordination number. Ni(II) complexes also show planar–tetrahedral equilibria where the same species exists in solution in an equilibrium distribution between the tetrahedral and square forms. Sometimes, it is possible to isolate the two forms of the species where it is termed as square–tetrahedral isomerism. Ni(II) complexes also exhibit thermochromism where temperature–dependent structural changes give rise to variations in *d–d* absorption bands. Ni(I) usually exhibits distorted octahedral or square–planar geometry whereas Ni(III) generally forms low–spin complexes with distorted–octahedral or trigonal bipyramidal geometry.[76]

1.1.2.2.2. Role in biosystem

Nickel is an essential trace element[4,77] supposed to be involved in protein structure and function.[78] In biology, nickel can catalyze a multitude of biochemical reactions including simple hydrolytic to multi–step redox reactions spanning over a wide range of redox potential of around 1.5 V. There are eight known nickel–containing enzymes till date, most of which catalyze the usage/production of gases relevant to the global carbon, nitrogen or oxygen cycles (Table 1.4).[79]

Table 1.4 Nickel containing enzymes and their functions[76]

Enzymes	**Ni center**	**Functions**
Urease	High–spin Ni^{II} dimer	$Urea + H_2O \rightarrow 2NH_3 + H_2CO_3$
Hydrogenase	NiFe center	$2H^+ + 2e^- \leftrightarrow H_2$
CO Dehydrogenase	$NiFe_4S_4$ cluster or $NiFe_4S_5$ cluster	$CO + H_2O \leftrightarrow 2H^+ + CO_2 + 2e^-$
Acetyl–CoA synthase	$NiNiFe_4S_4$ cluster	CH_3–CFeSP + CoASH + CO → CH_3–CO–SCoA + CFeSP
Methyl–CoM reductase	Ni tetrapyrrole (tetracorphin)	Methyl–SCoM + CoBSH → CH_4 + CoBS–SCoM
Superoxide Dismutase	4–5 coordinate Ni site	$2O_2^- + 2H^+ \rightarrow H_2O_2 + O_2$
Glyoxalase I	6–coordinate Ni site	Methylglyoxal + glutathione ↔ GS-derivative
Aci–reductone Dioxygenase	6–coordinate Ni site	Aci-reductone + O_2 → methylthiopropionate

1.1.2.2.3. Applications of nickel

(i) As tracer

^{63}Ni is a β–emitting radioactive isotope of nickel which has a half life of 100.1 years. ^{63}Ni has been employed successfully as tracer for several biological studies.[75]

(ii) In industries

Nickel and its complexes possess considerable significance in modern industries. Nickel is resistant to attack by air or water at ordinary temperatures hence it is used for electroplating.[3] It is also used for making Ni–Cd batteries, stainless steel and electronic equipments.[75] Nickel is used to produce a number of alloys:[75] inox steel for metallurgical and mechanic industry, cupro–nickel for manufacture of coins, chromium–nickel for cutlery, iron–nickel for magnets and copper–nickel–zinc (German silver) for ornamental and domestic objects.

(iii) In catalysis

Hydrogenation

Nickel–aluminium alloy when treated with aqueous sodium hydroxide under inert atmosphere leaches out aluminium giving rise to finely divided nickel particles known as Raney nickel. Raney nickel is widely used as hydrogenation catalyst on commercial scale in industries.[3] Finely divided nickel functions as a catalyst in the hydrogenation of vegetable oils.[80]

Ethylene oligomerization

The discovery of the "*nickel effect*" on the nature of products in $Al–R_3$ catalyzed growth reaction of ethylene by Ziegler et al. set foundation for "Ziegler catalysis" which was further developed by Wilke and others over decades.[81] Numerous Ni(II) catalysts tend to favour chain termination over propagation and to yield interal olefins which makes them suitable for various processes pertaining to dimerization of α–olefins.[81] *Shell Higher Olefin Process (SHOP)* is one of the remarkable catalytic systems which utilizes nickel based catalysts for the oligomerization of ethylene with selective formation of linear α–olefins.[81]

Activation of small molecules

Nickel also exhibits properties similar to cobalt for the coordination and activation of small molecules like N_2,[82-84] CO_2,[85,86] and H_2[83,84,87] . Hydrogen activation by catalysts derived from abundant and inexpensive metals like nickel may be significant for the development of future hydrogen–based energy storage and delivery systems. Nickel exhibits a remarkable property to occlude carbon monoxide also. It is estimated that hundred grams of nickel can absorb 500–800 mL of carbon monoxide ($Ni(CO)_4$).[75] Nickel–catalyzed hydrogenation of carbon monoxide to methane is known for a long time which is used to remove carbon monoxide from a stream of hydrogen gas on an industrial scale e.g. in the production of ammonia. Interestingly, the reverse reaction i.e. cleavage of methane (steam reforming) also proceeds *via* nickel–based catalysts.[88] Reppe utilized the nickel–carbon monoxide affinity to develop a series of homogeneous catalytic rections known as carbonylations.[88]

Splitting of water

A number of nickel complexes have been synthesized as artificial models of [NiFe] hydrogenase and nickel based functional complexes. However, no model complex of [NiFe] hydrogenase could produce hydrogen from water till date and all complexes exhibited electrocatalytic proton reduction from acids[89] however, few nickel–based functional models have shown the electrocatalytic production of hydrogen from water. McLaughlin et al. reported a nickel(II) based catalyst for visible light–driven hydrogen production from water in presence of $[Ru(bpy)_3]^{2+}$ or Eosin Y (photosensitizer) and ascorbate.[90]

Miscellaneous conversions

In addition to aforementioned processes, several nickel based catalysts have been developed to catalyze a wide range of chemical conversions including epoxidation of alkenes, Baeyer-Villiger oxidation, sulphoxidation,[60] selective hydrogenolysis of aryl ethers,[91]

Friedel–Crafts alkylation,[92] cyclo–addition reactions and cross–coupling reactions[93]. Furthermore, many reactions involving carbon–carbon bond formation can proceed with high selectivity if catalyzed by organo–nickel complexes.[88]

1.1.2.3. Copper (*symbol*: Cu; *electronic configuration*: [Ar] $3d^{10}$, $4s^1$)

1.1.2.3.1. General comments[3,94]

Copper occurs in nature in the form of sulphides, arsenides, chlorides and carbonates. It's major ores are *chalcopyrite* ($CuFeS_2$), *chalcocite* (Cu_2S), *cuprite* (Cu_2O) and *malachite* ($Cu_2CO_3(OH)_2$).[94] It shows the oxidation states from (I) to (III) though the (III) oxidation state is relatively uncommon. Copper(I) exhibits a wide range of coordination numbers including 2, 3, 4 and 5 having linear, planar, tetrahedral or distorted planar and square pyramidal geometries respectively. Copper(I) compounds are diamagnetic due to the d^{10} electronic configuration, and colorless except where the color arises from the anion or due to charge–transfer bands. Copper(II) affords a variety of complexes with the coordination numbers 3, 4, 5 and 6 with almost all possible geometries though a few hepta– or octa–coordinated complexes of Cu(II) are also known. Generally, copper(II) complexes are blue or green in color due to the presence of an unpaired electron, however, some complexes exhibit a charge–transfer band in the UV–vis spectrum which imparts them a reddish–brown color. Magnetic moments of mononuclear copper(II) complexes generally fall within the range 1.75–2.20 B.M. irrespective of their stereochemistry. Due to the d^9 configuration of Cu(II), it undergoes severe Jahn–Teller distortion when having octahedral or tetrahedral arrangement of donor atoms around it. The relative stability of Cu^I and Cu^{II} vary considerably with solvent and depend on the nature of anions when present in aqueous solutions. Most of the Cu(I) compounds undergo disproportionation to Cu(0) and Cu(II) in aqueous solutions

and the only simple compounds of Cu(I) which are stable to water are those which are insoluble in water like CuCl or CuCN. Acetonitrile solvates the Cu^{I} ion very effectively resulting in higher stability of Cu^{I} in acetonitrile than Cu^{II}. Unlike Cu^{II}, Cu^{I} forms a large number of compounds with Cu–C bond which find their application in organic synthesis.

1.1.2.3.2. Role in biosystem

Copper is the third most abundant metallic element in the human body.[3] It is known to coordinate with several kinds of biological ligands including imidazole nitrogen, amine and amide nitrogen, carboxylate oxygen and cysteine and methionine sulphur donor atoms.[95] It occurs in a variety of metalloenzymes as cofactor due to its ability to switch between Cu^{+} and Cu^{2+} at biologically relevant redox potentials. On the basis of spectroscopic properties, three classical types of active sites have been recognized in copper proteins – (i) type I copper centers or "blue copper centers" (mononuclear), (ii) type II centres or "non–blue copper centers" (mononuclear) and (iii) type III copper centers (dinuclear). However the active sites of some enzymes like laccase, ascorbate oxidase and ceruloplasmin do not strictly resemble to any of these classes and can be described as composed of trinuclear moiety having a combination of type II and type III centers. Cytochrome *c* oxidase also exhibits two another type of copper sites which may be regarded as CuA and CuB sites.[96] Few copper containing enzymes and their functions have been summarized in the Table 1.5.

Table 1.5 Copper containing enzymes and their functions[97-99]

Class	Protein	Function
Type I		
	Azurin	Electron carriers
	Pseudoazurin	
	Stellacyanin	
	Plastocyanin	
	Amicyanin	
	Auracyanin	
Type II		
	Galactose oxidase	Conversion of primary alcohol to aldehyde
	Amine oxidases	Conversion of primary amine to aldehyde
	Superoxide dismutase	Superoxide scavenging
	Lysine oxidase	Connective tissue biosynthesis
	Dopamine-β-monooxygenase	Catecholamine synthesis
Type III		
	Hemocyanin	Oxygen carrier
	Tyrosinase	Phenol oxidation, melanin synthesis
Multiple types of copper		
	Laccase	$O_2 \rightarrow H_2O$
	Ascorbate oxidases	
	Ceruloplasmin	
	Cytochrome *c* oxidase	
	Nitrite reductase	Denitrification

1.1.2.3.3. Applications of copper

(i) Copper in radiopharmaceutics and imaging

Several positron emitting radionucleides of copper have been investigated for molecular imaging purposes. ^{64}Cu decays by β^- emission and electron capture resulting in Auger electron emission and can be used for therapeutic applications.[100] ^{67}Cu can emit β^- particles and gamma photons which have been used for imaging.[100] Pyruvaldehyde–bis(4–methylthiosemicarbazonato)copper(II) (Cu^{II}(ptsm)) complexes radiolabelled with ^{62}Cu and ^{67}Cu have been recognized as ideal tracers for evaluation of cerebral and myocardial blood flow.[100]

(ii) Nitric oxide and nitroxyl sensor

Among many approaches employed to devise fluorescence NO sensor, designing an organic molecule based on *o*–phenylenediamine scaffold has been one of the most trivial strategies. Such molecules oxidize to the corresponding aryl triazole in presence of air and NO (Scheme 1.12 (a)).[101]

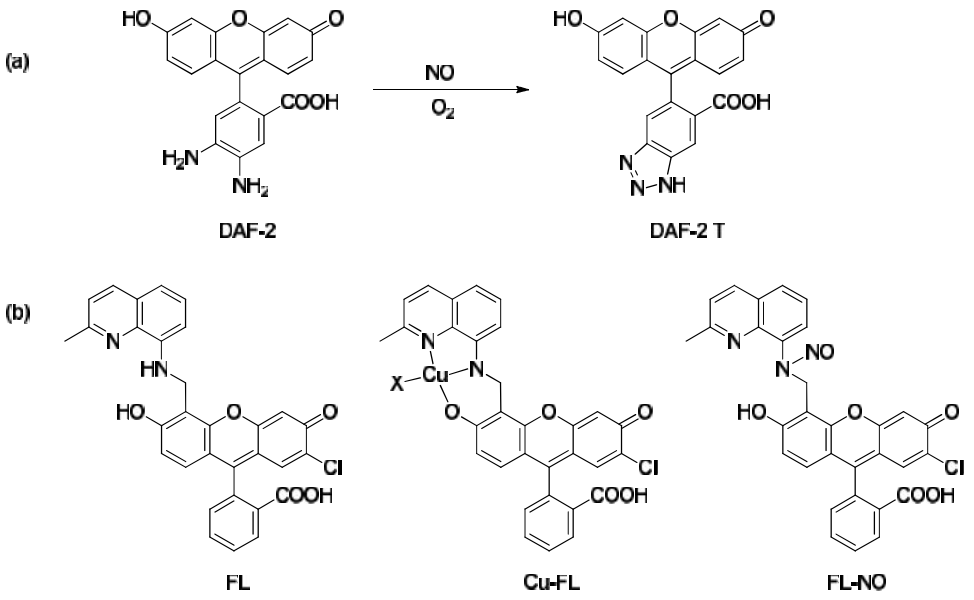

Scheme 1.12 Fluorescent probes used for the detection of NO[101]

The large difference in the electronic nature of the diamine (*electron rich*) and the triazole (*electron poor*) provides an indirect means of NO detection. One major disadvantage to use such systems is the requirement of molecular oxygen limiting the direct and real–time detection of NO by such organic moieties.[101]

In the past few years, enormous interest has emerged in developing transition metal complex based NO probes since such systems offer the promise of direct detection of NO. After reacting with NO, these complexes may undergo one of the following processes with concomitant retrieval or/and enhancement of the emission intensity:[49,102]

(a) Fluorophore displacement without metal reduction;

$$\underset{\text{"OFF"}}{FL\text{-}M^{n+}(L)} \overset{NO}{\rightleftharpoons} \underset{\textbf{"ON"}}{\textbf{FL}} + M^{n+}(L)(NO)$$

(b) Metal reduction without fluorophore displacement;

$$\underset{\text{"OFF"}}{FL\text{-}M^{n+}(L)} \xrightarrow{NO,\ ROH} \underset{\textbf{"ON"}}{\textbf{FL-M}^{(n-1)+}\textbf{(L)}} + RONO + H^{+}$$

(c) Metal reduction accompanied with fluorophore displacement

(i) $$\underset{\text{"OFF"}}{FL\text{-}M^{n+}(L)} \xrightarrow{NO} \underset{\textbf{"ON"}}{\textbf{FL (or FL-N-NO)}} + M^{(n-1)+}(L)(NO)$$

(ii) $$\underset{\text{"OFF"}}{FL\text{-}N\text{-}M^{n+}} \xrightarrow{NO} \underset{\textbf{"ON"}}{\textbf{FL-N-NO}} + M^{(n-1)+}$$

Lippard and co–workers reported a metal based NO sensor using Cu(II)–fluorescein complex as an alternative approach for the direct detection of nitric oxide in living cells (Scheme 1.12 (b)).[103] The fluorescence of the derivatized fluorescein ligand FL quenched after coordinating with the paramagnetic Cu(II) ion. In presence of nitric oxide, Cu(II) of Cu–FL underwent NO mediated reduction to Cu(I) and subsequently leading to the generation of bright nitrosylated fluorophore FL–NO by dissociation of the Cu(I):FL–NO

complex.[39,103,104] Detection of nitric oxide by similar type of mechanism has also been reported by Ford and co−workers using Cu(II) cyclam complex containing an anthracene fluorophore[105] and Zhang and co−workers using MNIP fluorophore−Cu(II) complexes (MNIP = 4−methoxy−2−(1*H*−naphtho[2,3−*d*]imidazol−2−yl)phenol).[106]

On the other hand, several copper(II) fluorophore complexes have also been devised as probes for nitric oxide which follow a different mechanism for NO detection. Although, coordination of copper(II) ion with fluorophore results the quenching of emission because of the paramagnetic nature of Cu(II), the recovery of emission properties of fluorophore is achieved here due to the reduction of Cu(II) to diamagnetic Cu(I) after reacting with NO thus enabling the direct imaging of nitric oxide.[39,107] Recently, Lippard and co−workers reported Cu(II) complexes bearing dansyl and anthracenyl fluorophore ligands as efficient probes for the detection of nitric oxide in organic and aqueous environment where the fluorescence was restored due to the reduction of Cu(II).[102] With similar approach, Yao and co−workers developed a coumarin based copper containing turn−on fluorescent probe for the detection of nitroxyl in living cells.[108]

(iii) Catalysis

Wacker process

Wacker process is an industrial process widely used for large−scale catalytic production of acetaldehyde which involves the oxidation of ethylene by a mixed−metal $PdCl_2/CuCl_2$ system in presence of O_2 and H_2O. In the catalytic cycle, palladium presents the catalytically active metal centre and switches between Pd^0 and Pd^{II} oxidation states. Cu^{II} redox co−catalyst plays an important role of oxidizing Pd^0 back to Pd^{II} with the help of dioxygen to complete the catalytic cycle.[3,109] Mixed palladium /copper systems have also

been employed to catalyze a number of other processes including cyclization of allylphenols, acetylization of alkenes and oxidation of terminal alkenes in presence of air.[110]

Miscellaneous conversions

Several chemical reactions including oxygenation of alkanes, benzylic oxidation, aromatic C–H oxidation, Baeyer–Villiger oxidation,[60] cross–coupling reactions, allylic alkylation reactions, carbene transfer reactions[93] and asymmetric Friedel–Crafts alkylation reactions[111] can also be catalyzed successfully by using copper based catalysts.

1.1.2.4. Zinc (*symbol*: Zn; *electronic configuration*: [Ar] $3d^{10}$, $4s^2$)

1.1.2.4.1. General comments[3,94]

Zinc occurs in nature as zinc sulphide, carbonate and oxides. The major ores of zinc are *sphalerite* or *zinc blende* (ZnS), *smithsonite* or *calamine* ($ZnCO_3$), *hemimorphite* ($Zn_4Si_2O_7(OH)_2.H_2O$) and *franklinite* ($(Zn,Fe)O.Fe_2O_3$).[94] Zinc typically forms Zn(II) ion which is the most common oxidation state of this element. Since, it has completely filled *d*-orbitals, it does not behave as typical transition metals and generally gives rise to diamagnetic and colorless compounds. Zinc is considered as an element of borderline hardness which generally accommodates nitrogen, oxygen or sulphur ligands.[2,112] Furthermore, It affords complexes which lack inertness and exhibit no sterochemical preferences derived from ligand field stabilization effects due to their d^{10} electronic configuration.[3] Hence, a wide range of coordination numbers and geometries are exhibited by its complexes which are mainly governed by the interplay of electronic factors, covalence and size factors.[3] Zinc(II) complexes are typically either tetrahedral or octahedral but both trigonal bipyramidal and square pyramidal five–coordinate complexes of Zn(II) are also known.[4] Coordinative flexibility associated with zinc makes the ligand exchange more facile and enables it as suitable candidate to effect a catalytic cycle.[112] The divalent zinc exhibits exceptional

stability against redox processes.[2,112] Zinc exhibits strong tendency to form covalents compounds. It is interesting to note that anionic ligands such as OH^-, OR^- or SR^- retain their nucleophilicity even after coordinating with Zn(II). Only Mn(II), Fe(III) and Cu(II) can exhibit this type of property except zinc.[112]

1.1.2.4.2. Role in biosystems

Zinc is the second most abundant metal ion in the human body and follows after iron.[3] In a multitude of enzymes, zinc plays a key role in the enzymatic catalysis, structural organization and/or regulation of functions. Till date, more than 1000 metalloenzymes are known which contain zinc at the active centre.[2] Few metalloenzymes containing zinc at the active site along with their biological functions are summarized in Table 1.6.

Table 1.6 Representative mononuclear $[\{XYZ\}Zn^{II}(OH_2)]$ zinc enzymes with their coordination motifs and functions[112]

X,Y,Z	**Enzyme**	**Function**
His, His, His	Carbonic anhydrase	Hydration of CO_2
His, His, Glu	Carboxypeptidase	Exopeptidase
	Thermolysin	Endopeptidase
	Neutral protease	Endopeptidase
His, His, Asp	Protease (*Streptomyces caespitosus*)	Endopeptiase
His, Asp, Cys	Farnesyl protein transferase	Transfer of a farnesyl isoprenoid to a cysteine residue
His, His, Cys	Bacteriophage T7 lysozyme	Cleavage of peptide bond between L–alanine and *N*–acetylmuramate moieties
His, Cys, Cys	Alcohol dehydrogenase	Oxidation of alcohols to aldehydes and ketones
	Cytidine deaminase	Hydrolytic deamination of cytidine to uridine
Cys, Cys, Cys	5–aminolevulinate dehydratase	Synthesis of porphobilinogen from 5–aminolevulinic acid

1.1.2.4.3. Applications of zinc

(i) In industries

Zinc is widely used in industries for protective coating over iron or steel (galvanizing) in order to prevent rusting and for preparing many useful alloys such as brass.[3] Zinc is also used as the negative electrode in sealed 'dry' batteries.

(ii) Dyes, stains or sensors

Inorganic transition metal complexes possessing luminescent properties are emerging as excellent biomolecular and cellular probes. Phenomena like self–quenching and homo–fluorescence resonance energy transfer (FRET) are relatively uncommon in transition metal complexes because of their larger Stoke's shifts which make them more suitable for monitoring the biological events than organic dyes.[113] Numerous research groups including Zhang and co–workers,[114] Hamachi and co–workers,[115-118] Jolliffe and co–worker,[119] Yoon and co–workers,[120] Kim and co–workers,[121] Churchill and co–workers,[122] Eisenhut and co–workers[123,124] and Zhu and co–workers[125] have studied zinc containing fluorescent molecules as staining dyes for cell organelles and biomolecule,[114,125] sensors for the recognition of anions[119] and probes for the detection of nucleoside polyphosphates,[117] FAD, NADH,[120] pyrophosphates,[121,122] pathological proteins viz. aggregated hyperphosphorylated tau proteins[115] and microscopic imaging of cellular processes like apoptosis/necrosis.[123]

(iii) Catalysis

Zinc and its complexes have also been employed to catalyze a number of reactions like asymmetric aldol reactions,[126] Henry reaction,[127,128] Reformatsky reaction,[129] cleavage of nitrone cycloaddition adducts,[130] chemoselective reduction of nitroarenes,[131] cross–Mannich reactions of carbonyl compounds[132,133] and alkylation of α–ketoesters.[134]

1.1.3. Relevance among Co, Ni, Cu and Zn

In spite of having quite contrast redox behaviour, Cu(II) and Zn(II) resemble each other in several aspects. In some instances, zinc complexes analogous to copper complexes are utilized as probes for the magnetic, spectroscopic or structural investigations.[135] Both Cu(II) and Zn(II) are substitutionally labile and possess high ionization potentials and Lewis acidity. The pK_a values of water molecules bound to Cu(II) or Zn(II) are generally found within the pH range of 7–9. These characteristics enable them as suitable candidates for the hydrolytic reactions under physiological conditions. Although, Ni(II) complexes also exhibit similar types of properties, those complexes are comparatively much less studied.[136] Moreover, substitution of zinc by the labile high–spin Co(II) ion in the spectroscopically–silent zinc containing enzymes also presents a powerful and routine experimental tool for elucidating structural and stereochemical requirements for catalytic action (vide supra) and among transition metal elements, Co(II) is known to do so with least perturbation of the enzyme structure and functions.[137] It is known that Co(II) can also exhibit coordinative flexibility similar to zinc.[2] Like Zn(II), Co(III) is also a good Lewis acid and catalyzes hydrolytic reactions with the enhancement in the rate of reactions to several orders of magnitude.[138-140] It seems quite interesting to perform a collective and comparative study of complexes derived from these four metals.

1.2. Metalloenzymes

Metalloenzymes may be considered as large, complex and sophisticated coordination compounds designed by nature to catalyze a variety of tedious biochemical reactions under mild physiological conditions with appreciably high reaction rates. These are generally composed of first–row transition metals (except Mo and W containing enzymes) coordinated with a variety of amino acid residues acting as ligands derived from the surrounding protein

scaffold. In the context of present investigation, three enzymes namely, galactose oxidase, superoxide dismutase and catechol oxidase will be discussed in detail.

1.2.1. Galactose oxidase and glyoxal oxidase

Galactose oxidase (GAO) is a small (68 kDa), monomeric, type 2–copper–containing extracellular enzyme of fungal origin which incorporates a copper–coordinated tyrosyl radical at its active site. It catalyzes two–electron oxidation of D–galactose and a broad range of primary alcohols to aldehydes coupled with the conversion of O_2 to H_2O_2 (Scheme 1.13).[141-148] A related enzyme, glyoxal oxidase (GLO), which catalyzes the oxidation of aldehydes to carboxylic acids with the concomitant reduction of O_2 to H_2O_2 (Scheme 1.13), also posssesses similar active site structure composed of a tyrosyl radical–copper catalytic motif.[143,149] The tyrosyl radical generated in the active site of galactose oxidase exhibits remarkable stability ($t_{1/2}$ = 7.2 d) which is necessary for its catalytic function, however, the tyrosyl radical generated in glyoxal oxidase is 40–fold less stable ($t_{1/2}$ = 4 h).[150]

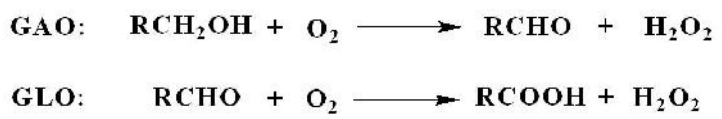

Scheme 1.13 Function of galactose oxidase (GAO) and glyoxal oxidase (GLO)

The active site in galactose oxidase comprises of a copper atom in a distorted square–pyramidal geometry where a tyrosine residue (Tyr 495) is occupying the axial position with a long Cu–O distance of 2.7 Å (Fig. 1.1).[141] Two histidine residues (His 496 and His 581), a tyrosine residue (Tyr 272) covalently cross–linked to a neighbouring cysteine residue (Cys 228) through a thioether bond resulting from the oxidative post–translational modification and an exogenous ligand (H_2O or acetate) coordinate copper in equatorial positions.[142,151-153] This thioether linkage is presumably responsible for the lowering of

tyrosyl/tyrosine redox potential[142,150,152,154] whereas the axial tyrosinate ligand Tyr 495 functions as a general base during catalysis.[155,156] A tryptophan residue Trp 290 exhibits π–stacking interactions with redox active tyrosine residue (Tyr 272) and shields the Cys–Tyr cofactor from exposure to solvent by controlling the access to the active site.[142,155]

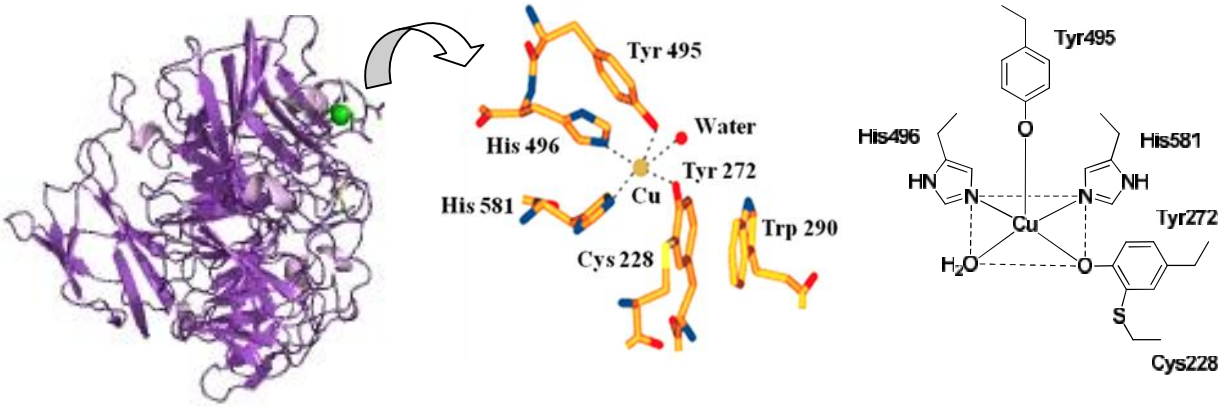

Fig. 1.1 Active site of galactose oxidase

Copper participates in the catalytic cycle through single electron Cu(I)/Cu(II) redox shuttle and the second oxidizing equivalent necessary for catalytic oxidation of alcohol is achieved from Cys cross–linked tyrosyl radical.[151] The enzyme can exist in three distinct oxidation states which can be distinguished by their characteristic spectroscopic signatures: (a) Cu^{II}–tyrosyl radical oxidized form (green, catalytically active), (b) intermediate Cu^{II}–tyrosinate form (blue, catalytically inactive) and (c) reduced Cu^{I}–tyrosine form (colorless, catalytically active).[142,155] The catalytic cycle of galactose oxidase completes in two half reactions: in the first half reaction, the alcohol substrate coordinates to the oxidized Cu^{II}–radical active site with the concomitant reduction of both redox centres (tyrosyl radical and copper(II) ion) and release of the aldehyde product; in the second half reaction, the Cu^{I}–tyrosine site binds dioxygen to regenerate the initial Cu^{II}–tyrosyl radical state with the conversion of O_2 to H_2O_2.[142] The complete catalytic mechanism is shown in Scheme 1.14.

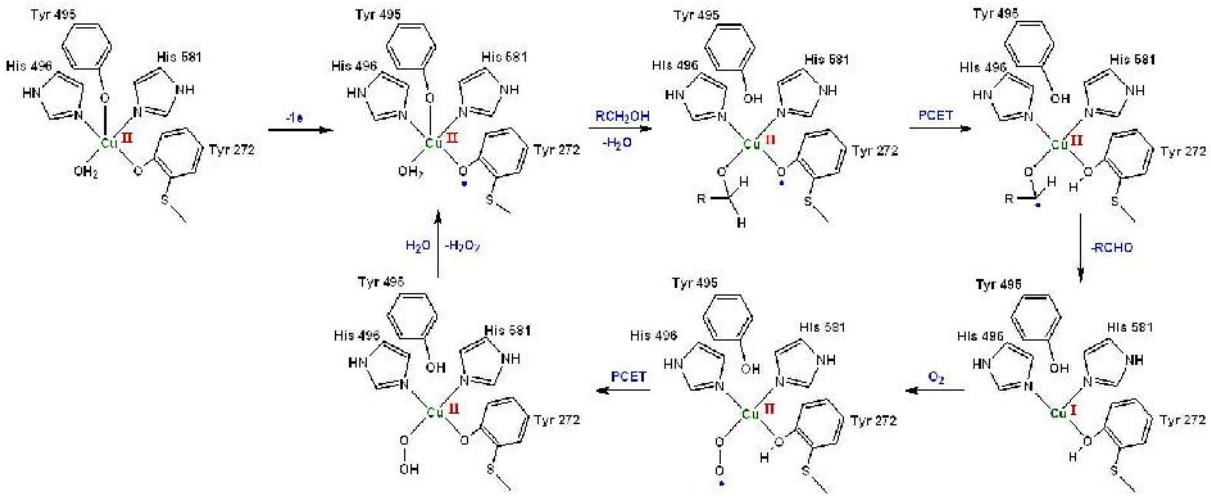

Scheme 1.14 Catalytic mechanism of galactose oxidase enzyme

Several metal–coordinated phenoxyl radicals have been characterized during the past years in order to mimic the active site of galactose oxiase which could lead to improved understanding of metal radical interactions (*vide infra*). Some of these complexes catalyzed the oxidation of organic substrates also, predominantly the alcohols, thereby exhibiting the functional mimicking of the enzyme.[144,145,157-176]

1.2.2. Superoxide dismutase

Superoxide dismutases describe the family of enzymes which play a pivotal role to prepare cellular anti–oxidant defense mechanism and combat the oxidative stress implicated in atherosclerosis and a variety of other life–threatening diseases. These enzymes exhibit the ability to convert two molecules of superoxide to one each of dioxygen and hydrogen peroxide while consuming two equivalents of H^+ during their catalytic cycle (Scheme 1.15).[177] On the basis of the type of metal–cofactor(s) present at the active site enzyme, SOD may be categorized into three major classes: Cu–Zn containing SOD, Mn or Fe containing SOD and Ni containing SOD.[177] In Cu–Zn SOD, Cu^{II} center exhibits the characteristics of type–2 copper proteins and catalyzes dismutation of superoxides by switching between +2 and +1 oxidation states (ping–pong mechanism).[178,179]

$$O_2^- + [Cu^{II}] \longrightarrow O_2 + [Cu^{I}]$$

$$O_2^- + [Cu^{I}] + 2\,H^+ \longrightarrow H_2O_2 + [Cu^{II}]$$

Scheme 1.15 The two half–reactions catalyzed by superoxide dismutase enzyme

Cu–Zn SOD is composed of two identical subunits, each possessing a bimetallic imidazolate–bridged Cu(II)–Zn(II) center in the active site (Fig. 1.2). The Cu(II) rests in a distorted square–pyramidal coordination environment with four histidines residues forming the basal plane and a water molecule occupying the fifth axial coordination site.[179] The Zn(II) ion is located about 6.2 Å apart from Cu(II) ion[180] and coordinated to three histidines and one carboxylate group in tetrahedral fashion where one of the histidine makes a bridge to the Cu(II) ion.[179]

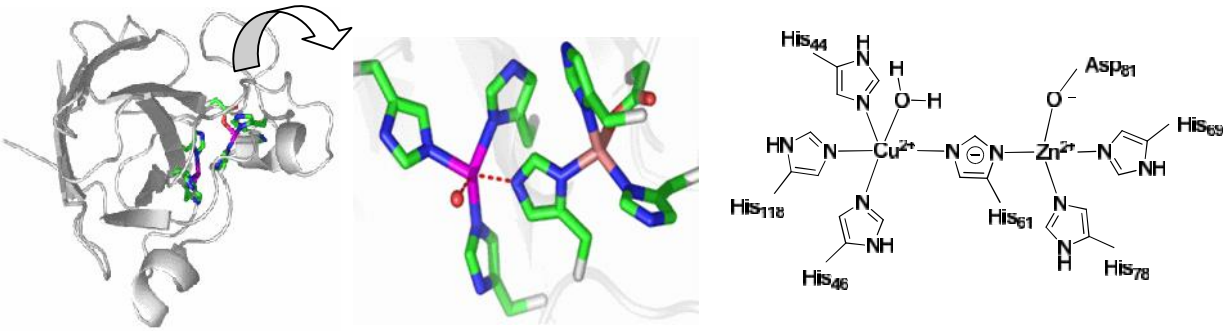

Fig. 1.2 Active site of Cu–Zn SOD enzyme

The zinc ion assists the protein to adopt the required coordination environment and provides stability to the protein.[179] The Cu(II) site presents the active centre for the enzymatic action where it directly participates in the catalytic electron transfer by changing its coordination number, arrangement of ligands and its valence state.[181] The detailed mechanism of enzymatic action is shown in Scheme 1.16.[178,179]

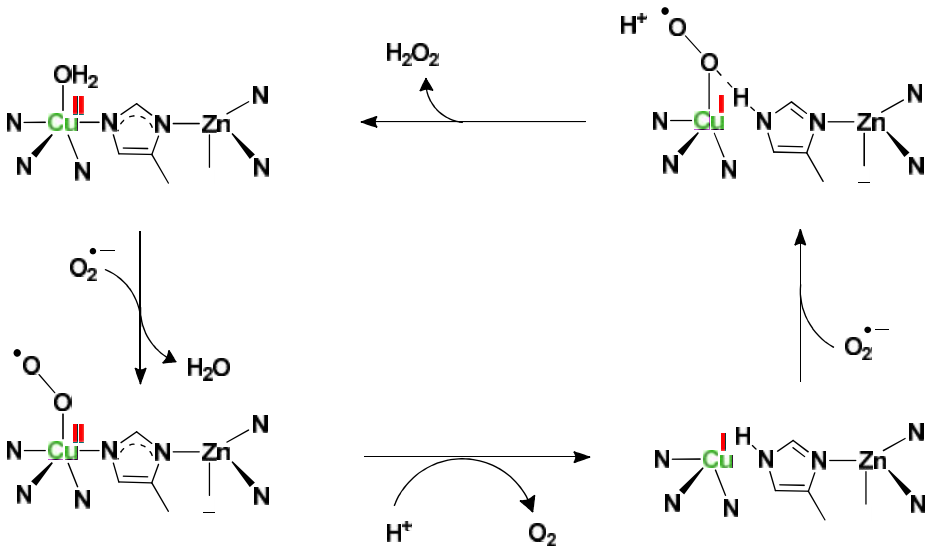

Scheme 1.16 Catalytic mechanism of superoxide dismutase enzyme

1.2.3. Catechol oxidase

Catechol oxidase, belongs to the type–3 class of dicopper proteins and resembles strongly to tyrosinase enzyme which is another member of this group. Tyrosinase exhibits two main catalytic activities: (a) hydroxylation of monophenols to *o*–diphenols, known as cresolase activity and (b) oxidation of *o*–diphenols to *o*–quinones, known as catecholase activity (Scheme 1.17). However the specificity of catechol oxidase is limited to the conversion of *o*–diphenols to *o*–quinones only.[96,182,183]

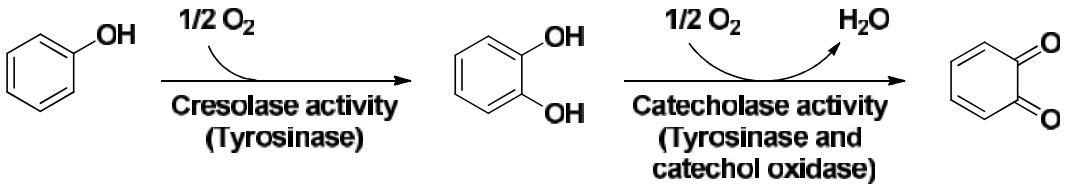

Scheme 1.17 Reaction pathway of the oxygenation and oxidation catalysed by tyrosinase and catechol oxidase

This enzyme prepares a defense mechanism for plants where the quinone products autopolymerize to form brown polyphenolic catecholmelanins. This process helps the damaged plant to protect against pathogens and insects.

The crystal structure of *I. batatas* catechol oxidase showed that it is a monomeric 39 kDa protein with dicupric Cu(II) – Cu(II) active site in the center of the four–helix bundle motif where each copper site is coordinated with three histidine residues (H 88, H 109 and H 118 for CuA and H 240, H 244 and H 274 for CuB) (Fig. 1.3).[182] One interesting feature of the active site of catechol oxidase is an unusual thioether bridge between C 92 and H 109 which is believed to create geometrical restraints over the CuA site to permit fast binding of dioxygen substrate and for optimizing the electronic structure of metal atom for the catalytic function. The *met* form of the enzyme contains both copper sites in four–coordinate trigonal pyramidal coordination environment where the fourth coordination site is occupied by a hydroxide ion bridging both copper atoms.[96]

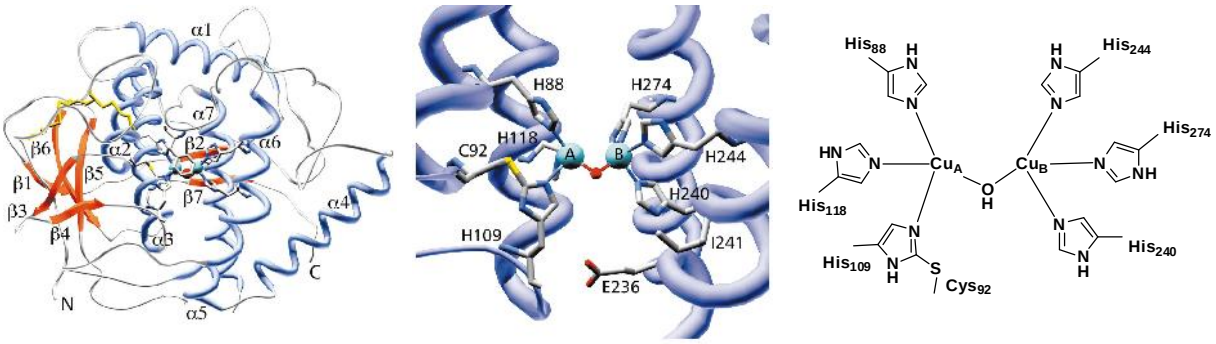

Fig. 1.3 Active site of *I. batatas* catechol oxidase[179,182]

The metal–metal separation in the *met* state is about 2.9 Å. In the *deoxy* or reduced state of enzyme, this separation increases to 4.4 Å without causing any significant changes in the conformation of protein. The reduced enzyme contains CuA in trigonal pyramidal coordination environment where a coordinating water molecule completes the coordination sphere of CuA and CuB adopts a square planar geometry with one missing coordination site.[96] On the basis of the mode of coordination of the catechol substrate to the dicopper core, two different mechanisms have been proposed for the catalytic conversion of catechol to

quinone.[184,185] Solomon and co–workers presented a mechanism involving the bidentate coordination of catechol to the dicopper centre as bridging ligand (Scheme 1.18).[186]

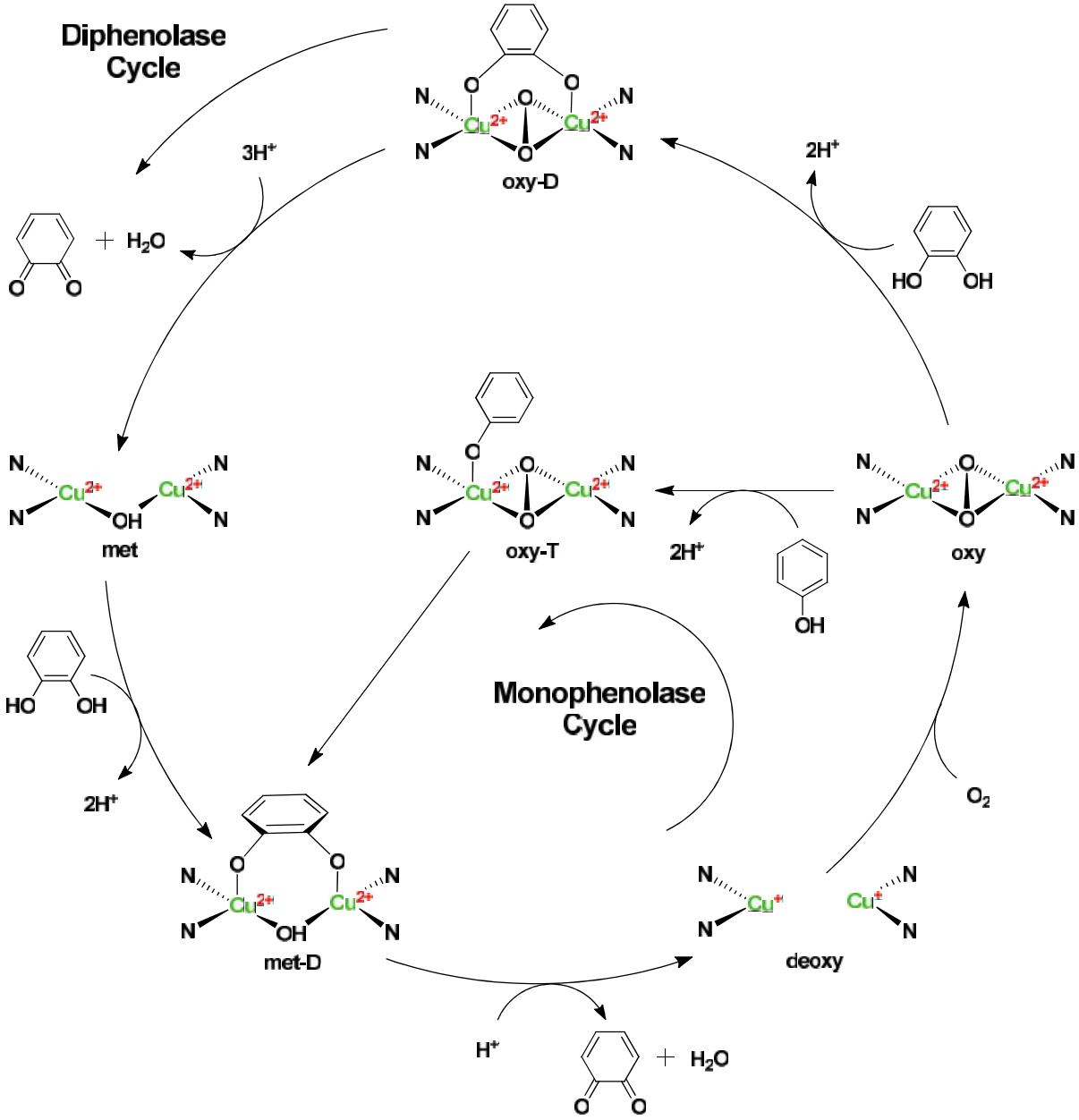

Scheme 1.18 Catalytic mechanism involving bidentate coordination of catechol

On the other hand, Krebs and co–workers suggested a monodentate asymmetric coordination of substrate to the dicopper active site (Scheme 1.19).[182]

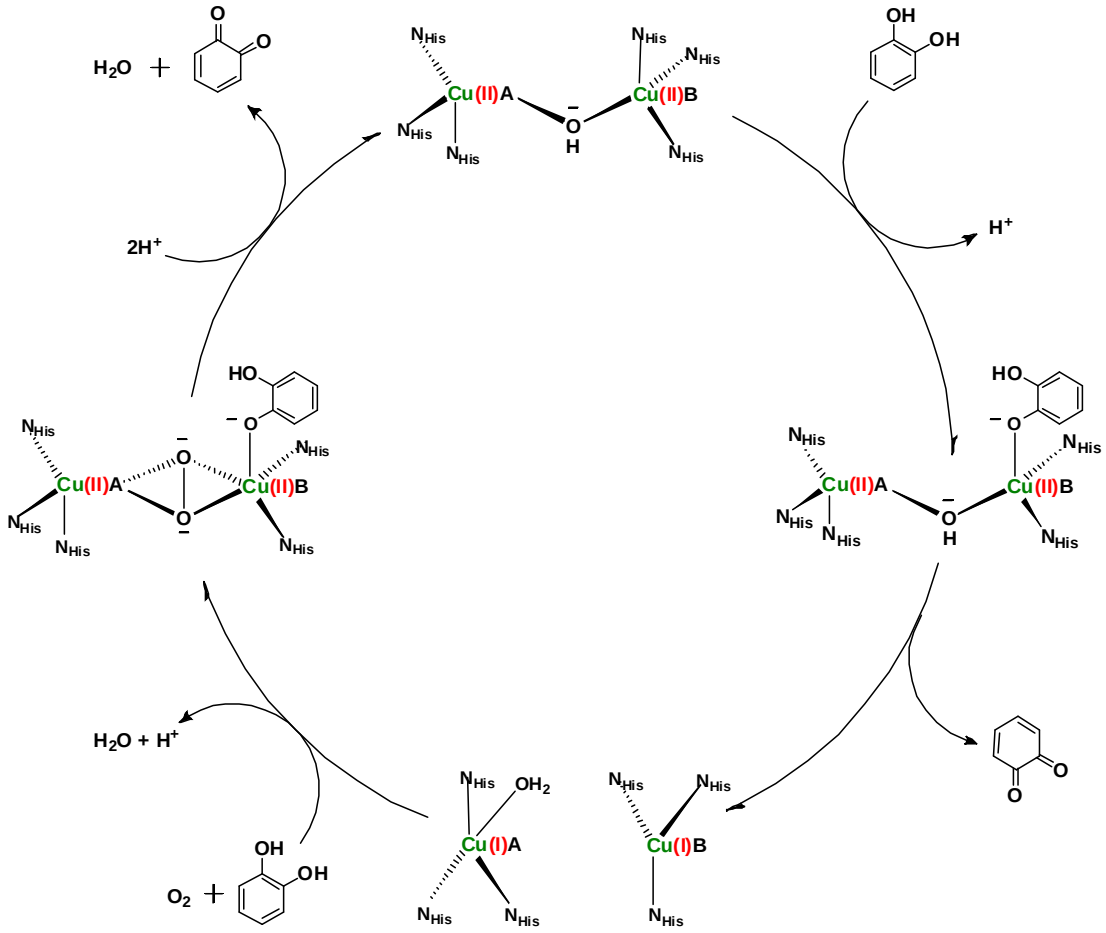

Scheme 1.19 Catalytic mechanism involving monodentate coordination of catechol

1.3. Metal complexes as enzyme models

Bio–mimetic transition metal complexes synthesized artificially may serve as structural and /or functional models (i) to investigate different aspects of steric requirements as well as the precise mechanism of enzymatic reaction,[187,188] (ii) to develop efficient catalysts for industrial applications.[189,190] These small molecule enzyme mimics can emphasize the roles of various structural factors including metal–metal distance, flexibility of the ligand, type of exogenous bridging ligand and coordination geometry around the metal ion in controlling the catalytic activity.

1.3.1. Cobalt complexes

1.3.1.1. Cobalt phenoxyl radical complexes as galactose oxidase models

Benisvy et al. reported a series of Co(II) and Co(III) complexes derived from *N*,*O*–phenol–imidazole pro–ligands which underwent ligand–based chemical oxidation to afford the corresponding phenoxyl radical species. This report presented the first example of phenoxyl radical complexes of tetra–coordinated Co(II).[191] Zats et al. also prepared a new *N*,*O*–phenol–pyrazol pro–ligand ^{pz}LH and its corresponding copper and cobalt complexes *bis*-Cu^{pz}L$_2$ and *tris*-Co^{pz}L$_3$. They showed that the pro–ligand can exist in a stable phenoxyl radical state when free or coordinated to the Cu(II) or Co(III) ions.[192] Wieghardt and co–workers reported stable phenoxyl radical complexes of Cr(III), Mn(III), Co(III) and Ni(II) derived from monoanionic tetradentate macrocyclic ligands and characterised them by electronic, resonance Raman and EPR spectroscopic techniques.[193] Arora et al. prepared a series of bis–phenolate complexes [Zn^{II}L], [Ni^{II}L], [Cu^{II}L] and [Co^{II}L] (where H_2L = 2,2′–[2,2′]bipyridinyl–6–yl–bis–4,6–di–*tert*–butylphenol) and studied their electrogenerated phenoxyl radical analogues. A diradical species [Zn^{II}L$^{\bullet\bullet}$]$^{2+}$ was obtained on electrochemical oxidation of zinc complex whereas mono–radical species were accessible in case of copper and nickel. One–electron oxidation of [Co^{II}L] gave rise to a diamagnetic Co(III) complex [Co^{III}L]$^+$ whereas two–electron oxidation afforded the paramagnetic phenoxyl radical species [Co^{III}L$^{\bullet}$]$^+$.[194] Vinck et al. also described the acid–mediated generation of an unusual and extremely robust phenoxyl radical during the activation of a well–known catalyst *N*,*N*′–bis(3,5–di–tertbutylsalicylidene)–1,2–cyclohexane–diamino Co^{II} salen complex which is widely used for the highly enantiomer–selective ring opening of racemic epoxides.[195,196] Mukherjee and co–workers synthesized four dinuclear diphenoxo–bridged cobalt(II),

nickel(II), copper(II) and zinc(II) complexes of a new tripodal ligand H_2L (H_2L = 2,4–di*tert*–butyl–6–{[(2–pyridyl)ethyl](2–hydroxybenzyl)–aminomethyl}–phenol) possessing an N_2O_2 donor set. Electrochemical oxidation of these complexes gave rise to ligand centered oxidations leading to the generation of corresponding phenoxyl radical species. DFT calculations predicted that out of the two phenolato rings present in the ligand, the ring bearing the 2,4–di*tert*–butyl group is oxidized preferably.[197]

1.3.1.2. Superoxide dismutase mimics

Cobalt(II) complexes mimicking the SOD–activity are quite rare.[198] Policar and co–workers reported two cobalt(II) complexes with the composition $[Co(L)](PF_6)_2$ (where L = 3,4,6–tri–*O*–(2–picolyl)–1,2–*O*–ethylidene–α–D–galactopyranose or 3,4,6–tri–*O*–(2–picolyl)–D–galactal) which exhibited excellent SOD–like catalytic activity.[198] Anacona and co–workers prepared bis–quinoline–bis–mercaptocobalt(II) complex $[Co(quinoline)_2(SH)_2]$ and studied its SOD–like activity where it showed the catalytic activity corresponding to 0.1% of that of native SOD.[199] In a recent report, they synthesized the cobalt(II) complex [pyrrolidinium][$Co(sulphathiazole)_3$(pyrrolidine)] which exhibited slightly improved catalytic activity towards dismutation of superoxide.[200]

1.3.1.3. Catecholase models

There is only a handful of cobalt containing catecholase mimics known to literature and most of them are lacking the description of their single crystal X–ray structures and their turnover numbers. Banerjee et al. developed a series of dinuclear cobalt complexes $[Co_2(L^1H)(H_2O)_2(OAc)_2](OAc)_2$, $[Co_2(L^2)(H_2O)_2(OAc)_2](OAc)$ and $[Co_2(L^3)(H_2O)_2(OAc)_2](OAc)$ using the ligand 2,6–bis(R–iminomethyl)–4–methyl–phenol (where R = N–ethylpiperazine for L^1, 2–ethylpyridine for L^2 and N–ethylpiperidine for L^3) as

model compounds for the met−form of active site of catecholase enzyme and determined the molecular structure of $[Co_2(L^1H)(H_2O)_2(OAc)_2](OAc)_2$ by X-ray diffraction technique.[201] All complexes exhibited excellent catecholase−like activity catalyzing oxidation of 3,5−DTBC as well as TCC to corresponding quinones. In addition, these complexes also exhibited concentration dependent nuclease activity and excellent cytotoxicity towards liver carcinoma Hep G2 cell line.[201] Majumder et al. reported a series of dinuclear mixed−valent cobalt complexes $[Co^{III}Co^{II}L(N_3)_3]\cdot CH_3CN$, $[Co^{III}Co^{II}L(OCN)_3]\cdot CH_3CN$ and $[Co^{III}Co^{II}L(\mu-CH_3COO)_2](ClO_4)$ derived from a macrocyclic ligand H_2L containing tetraimino diphenolato donors alongwith their crystal structures.[202] Among the family, only $[Co^{III}Co^{II}L(N_3)_3]\cdot CH_3CN$ exhibited catecholase like activity while other members of the family were found inactive. Furthermore, they have characterized two complex−substrate aggregates possessing monodenate catechol moiety and bidentate bridging catechol moiety. These species resembled closely to the intermediates proposed in the catalytic cycle of native enzyme.

1.3.1.4. Nitrile hydratase models

Nitrile hydratase are Co(III) or Fe(III) containing enzymes which help in the microbial assimilation of organic nitriles by converting them to the corresponding amides through M(III)−NCR, M(III)−OH, M(III)−iminol and M(III)−amide intermediates (M = Co or Fe).[203] "Very inert first−row metals such as Co(III) are only rarely encountered in bioinorganic chemistry".[204] Furthermore nitriles exhibit extreme robustness towards hydrolysis hence the artificial models for this enzyme deserve special synthetic significance.[205] Angelosante et al. also represented a cobalt complex $[NBu_4][Co(\mathbf{1})]$ (where $H_4\mathbf{1}$=N−(2−(2−mercapto−2−methylpropylcarbamoyl)propan−2−yl)−3−mercapto−3−methylbutanamide) as structural model of nitrile hydratase which exhibited precise mimicking of

unsymmetrical tetradentate plane found in the native enzyme.[206] The cysteine residues in the active site of nitrile hydratase convert to sulfenate by atmoshpheric oxygen during post–translational modifications which play a crucial role for the catalytic action of enzyme.[207] The non–S–modified enzymes were found to be inactive for the enzymatic conversion. It was also observed that oxidation of sulfenate residues to sulfinate leads to loss of activity.[207] Several cobalt containing biomimetic models have also been developed by various research groups including Kovacs and co–workers,[208,209] Masuda and co–workers[207] and Mascharak and co–workers[210,211] to highlight the role of oxygenated sulphur in the enzymatic conversion which demonstrated that the oxygenation of the sulphur ligands increases the Lewis acidity of metal ion facilitating activation of water or the substrate molecule. Kovacs and co–workers developed two biomimetic functional models namely, $[Co^{III}(S^{Me2}N_4(tren)(MeCN)](PF_6)_2$ and $[Co^{III}(O^{Me2}N_4(tren)(MeCN)](OTf)_2$ for Co–NHase which could exhibit hydrolysis of acetonitrile. Furthermore, they characterized four complexes $[Co^{III}(S^{Me2}N_4(tren)(MeCN)](PF_6)_2$, $[Co^{III}(S^{Me2}N_4(tren)(OH)](PF_6)$, $[Co^{III}(S^{Me2}N_4(tren)(NHC(O)CH_3)](PF_6)$ and $[Co^{III}(O^{Me2}N_4(tren)(NHC(OH)CH_3)](OTf)_2$ crystallographically which were analogous to the intermediates involved in the catalytic cycle of nitrile hydratase.[205]

Mascharak and co–workers reported a new route to synthesize the model complexes for mimicking the active site of nitrile hydratase.[212] The ligand PyASH (where PyASH = N–2–mercaptophenyl–2′–pyridylmethyl–enimine) having pyridine, azomethine and thiolato donors coordinated with Co(III) ion to afford complex $[Co(PyAS)_2]Cl$. They observed that $[Co(PyAS)_2]Cl$ underwent ligand centered oxidation with conversion of coordinated azomethine function to carboxamido moiety affording $(Et_4N)[Co(PyPepS)_2]$ (where $PyPepSH_2$ = N–2–mercaptophenyl–2′–pyridinecarboxamide) when reacted with OH^-.

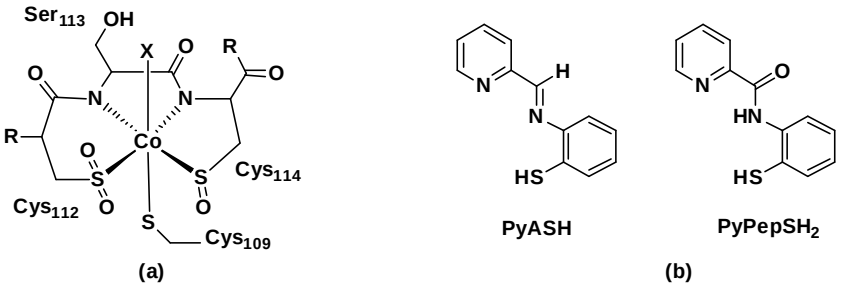

Scheme 1.20 Schematic representation of (a) active site structure of Co–NHase and (b) structures of ligands PyASH and $PyPepSH_2$

However the reaction of $[Co(PyAS)_2]Cl$ with H_2O_2 caused the oxidation of coordinated azomethine moiety to carboxamide group as well as conversion of thiolato groups to S–bound sulfinates affording the complexes $[Co(PyASO_2)(PyPepSO_2)]$ and $Na[Co(PyPepSO_2)_2]$.[212] Interestingly, no difference between initial and final oxidation state of the metal ion could be observed during such conversion.

1.3.1.5. LADH enzyme models

Corwin et al. studied bis(thiolate)cobalt(II) complexes $[Co(S–2,4,6–i–Pr_3C_6H_2)_2(Py)_2]$ and $[Co(S–2,6–i–Pr_2C_6H_3)_2(bpy)(CH_3CN)]$ as spectroscopic models for the active site of liver alcohol dehydrogenase (LADH) and supported four–coordination environment of the catalytic metal center of LADH during the catalytic mechanism.[213]

1.3.2. Nickel complexes

1.3.2.1. Nickel phenoxyl radical complexes as galactose oxidase models

Most recent advances in the field of metal–coordinated phenoxyl radicals have been achieved with nickel(II)–salen radical complexes which exhibit valence tautomerism between nickel(II)–phenoxyl radical and nickel(II)–phenolate forms. Shimazaki et al. reported such type of tautomerism in a square–planar nickel complex derived from a substituted

salicylidene ligand where the interconversion between Ni(III)−phenolate complex and Ni(II)−phenoxyl radical species was found to be temperature−dependent.[214] Experimental and theoretical studies suggest that the spin density in such complexes may or may not be localized on a single phenoxyl ring. Thomas and co−workers showed that the spin density in these radical complexes may be localized on a specific ring by controlling the acidity of the medium.[215] Shimazaki et al. reported a family of mono− and di−nuclear Ni(II) complexes derived from different N_3O−donor tripodal ligands.[216] All these complexes existed as mononuclear species in solution and gave rise to corresponding phenoxyl radical complexes upon oxidation with Ce(IV) salt at low temperature. Stack and co−workers reported the first X−ray crystal structural characterization of a Ni^{II}−ligand radical complex derived from bis(salicylidene)diamines which exhibited the contraction of the coordination sphere as compared to its unoxidized form. Theoretical calculations along with the structural and electrochemical data predicted the extensive delocalization of the oxidation locus in the whole molecule.[217] Benisvy et al. synthesized a dianionic dinickel complex $[NBu_4]_2[Ni_2(L)_2]$ (where H_3L = 3,5−di−*tert*−butyl−2−hydroxy−*N*−(2−hydroxyethyl)benzamide) which underwent two one−electron oxidation processes at low potentials leading to the formation of Ni_2−phenoxyl and Ni_2−diphenoxyl radicals.[218] Arion and co−workers prepared a novel tetradentate ligand by template condensation of 3,5−di−*tert*−butyl−2−hydroxybenzaldehyde S−methylisothiosemicarbazone with pentane−2,4−dione and triethyl orthoformate which underwent one−electron electrochemical oxidation leading to the formation of a cation−phenoxyl radical at room temperature.[219] The phenoxyl radical gained further stabilization when present in the coordinated form with Cu(II), Ni(II) or Zn(II).[219]

1.3.2.2. Superoxide dismutase mimics

On the basis of the type of metal present at the active site, superoxide dismutase enzymes may be of four types, namely, Cu/Zn–SOD, Mn–SOD, Fe–SOD and Ni–SOD. It is interesting to note that unlike Cu(II), Mn(II) and Fe(II) ions, aqueous solution of Ni(II) ions can not catalyze the dismutation of superoxide radicals.[220] However nature accomplished this process at appreciably high rates (~10^9 M^{-1} s^{-1}) utilizing NiSOD where the nickel is held in a unique coordination environment composed of two cysteine thiolates, one amino terminus, one imidazole side chain of histidine and a peptide N–donor from cysteine to achieve the appropriate Ni(III/II) redox potential of ~0.090 V vs Ag/AgCl.[220] To better understand the mechanism of Ni–SOD, several synthetic analogues have been prepared.[220] Darensbourg and co–workers synthesized the first low molecular weight Ni–SOD analogue using the ligand mmp–dachH (mmp–dachH = 1–(2–mercapto–2–methylpropyl)methyl–1,4–diazacycloheptane) which exhibited the SOD activity also.[221] Shearer and co–workers reported a square–planar Ni(II)–N_2S_2 complex (Me_4N)[Ni–BEAAM] (BEAAM = N–{2–[benzyl–(2–mercapto–2–methyl–propyl)–amino]–ethyl}–2–mercapto–2–methylpropionamide) as the first small molecule SOD analogue which exhibited precise mimicking of the Ni–SOD coordination sphere using a mixed amine/amide donor environment.[222] Harrop and co–workers prepared two model complexes (Et_4N)[Ni(nmp)(SR)] (R = C_6H_4–*p*–Cl or S^tBu) for the active site of reduced form of Ni–SOD by adopting a new route via S,S–bridge splitting of the dimeric metallosynthon $[Ni_2(nmp)_2]$ ($nmpH_2$ = *N*–(2–mercaptoethyl)picolinamide).[223] These complexes demonstrated the role of cysteine thiolate(s) for proton storage and transport during SOD catalysis.[223] Later on, Harrop and co–workers designed and constructed a nickel complex as first isolable synthetic model of

the reduced Ni–SOD active site possessing spatially and electronically accurate N_3S_2 donor environment.[224] Lee and co–workers utilized a ligand H_2BDPP (H_2BDPP = 2,6–bis(((S)–2–(diphenyl–hydroxymethyl)–1–pyrrolidinyl)methyl)pyridine) to prepare a five–coordinate Ni(II) complex [Ni(BDPP)].[225] This complex underwent oxidation with ferrocenium salts to afford a nickel(III) complex [Ni(BDPP)](PF_6). The latter complex resembled closely to the active site of oxidized Ni–SOD. Furthermore, the oxidized complex [Ni(BDPP)](PF_6) also exhibited catalytic oxidation of superoxide anion with its concomintant reduction to [Ni(BDPP)].[225] Jensen and co–workers also reported a family of penta–coordinated nickel complexes using hydrotris(3,5–dimethyl–1–pyrazolyl)borate as ligand and organoxanthate or dithiocarbamate as co–ligand.[226] These complexes exhibited the N_3S_2 donor environment around the metal center which is analogous to that found in active site of nickel–dependent superoxide dismutase enzyme. In a previous report by the same research group, a structurally related series of nickel complexes was prepared using the scorpionate ligand hydrotris(3–phenyl–5–methylpyrazolyl)borate and organoxanthate or dithiocarbamate as co–ligand which exhibited mimicking of the key properties of the reduced Ni–SOD intermediates.[227] These complexes showed equilibrium between κ^2– and κ^3–coordination modes of the scorpionate ligand framework coupled with the spin crossover.[227] The complexes underwent oxidation at fairly low potentials suitable for SOD activity.[227]

Duboc and co–workers presented a bis–amine dithiolate nickel(II) complex derived from the dianionic ligand 2,2′–(2,2′–bipyridine–6,6′–diyl)bis(1,1–diphenylethanethiol) having N_2S_2 donor set.[228] The complex exhibited metal centered electrochemical oxidation in presence of imidazole which was accompanied with the reversible apical binding of the imidazole moiety to the nickel(III) center. Although, the nickel complex under investigation did not strictly

reproduce the active site structure of Ni–SOD, it successfully exhibited the redox–dependent structural changes encountered in the catalytic cycle of the native enzyme.[228]

Nickel–thiolate complexes may undergo sulphur oxygenation when exposed to the products of the SOD catalytic cycle (dioxygen or hydrogen peroxide). However, such oxygenation process has never been observed for the coordinated thiolates in Ni–SOD in spite of its N_2S_2 coordination environment. On the basis of the reactivity studies of a nickel dianionic NiN_2S_2 complex $[Et_4N]_2[Ni(ema)]$ (ema = N,N′–ethylenebis–2–mercaptoacetamide), Darensbourg and co–workers proposed that, although the O_2 induced S–oxygenation is thermodynamically favourable, the coordinated thiolate moieties are kinetically protected by competitive SOD catalytic reaction.[229] Similar studies by Grapperhaus and co–workers using $(N_3S)Ni$ complex [N–{2–[(2–mercapto–2–methylpropyl)amino]ethyl}–1–methylimidazole–2–carboxamido]nickel(II) as a model compound revealed that H_2O_2 derived oxidation of coordinated thiolates of NiSOD is unlikely and kinetically incompetent on SOD timescale under physiological conditions.[230]

1.3.2.3. Catecholase models

A myriad of nickel complexes have also been designed and synthesized as biomimmetic models for the active site structure and/or functions of catechol oxidase. Ghosh and co–workers synthesized double phenoxide–bridged dinuclear nickel(II) complexes $[Ni_2(L^1)(NCS)_2]$, $[Ni_2(L^2)(NCS)_2]$ and $[Ni_2(L^3)(NCS)_2]$ derived from the reduced Schiff's base ligands (HL^1 = 2–[1–(3–methylamino–propylamino)–ethyl]–phenol, HL^2 = 2–[1–(2–dimethylamino–ethylamino)–ethyl]–phenol and HL^3 = 2–[1–(3–dimethylaminopropylamino)–ethyl]–phenol respectively). These complexes

exhibited functional mimicking of catecholase activity by catalyzing the aerial oxidation of 3,5–di–*tert*–butylcatechol to the corresponding quinone via complex–substrate intermediate formation. The EPR studies indicated the involvement of metal centered redox process in their catalytic cycle.[231] Chattopadhyay et al. reported a dinuclear nickel(II) complex having composition $[Ni_2(LH_2)(H_2O)_2(OH)(NO_3)](NO_3)_3$ derived from a compartmental ligand 2,6–bis(N–ethylpiperazine–iminomethyl)–4–methyl–phenol (LH) as a model compound for the met–form of active site of catechol oxidase.[232] They investigated its catecholase–like activity in methanol using 3,5–di–*tert*–butylcatechol and tetrachlorocatechol as model substrates however in acetonitrile the complex was quite inactive.[232] In a recent report, they have also presented few mononuclear nickel(II) complexes derived from NNO and NNN donor Schiff's base ligands which served as functional mimics of catecholase enzyme catalyzing the aerobic oxidation of 3,5–DTBC very efficiently.[233] Few nickel containing heterometallic complexes have also been synthesized as functional models of metalloenzymes. Ghosh and co–workers reported a family of trinuclear heterometallic complexes $[(NiL)_2Mn(NCS)_2]$, $[(NiL)_2Mn(NCO)_2]$ and $[\{NiL(EtOH)\}_2Mn(NO_2)_2]\cdot 2EtOH$ (where H_2L = N,N′–bis(salicylidene)–1,3–propanediamine) and investigated their catechol oxidase activity.[234] All three complexes exhibited excellent catalytic activity towards the oxidation of 3,5–DTBC to 3,5–DTBQ.[234]

1.3.3. Copper complexes

1.3.3.1. Copper phenoxyl radical complexes as galactose oxidase models

Various copper–coordinated phenoxyl radical species have been characterized spectroscopically as well as structurally till date. Pratt et al. synthesized bis(phenolate)–copper(II) complexes derived from salen and reduced salen ligands as model

complexes of galactose oxidase enzyme.[235] To better understand the influence of cysteine–modified tyrosine co–factor in galactose oxidase, they non–symmetrically substituted the salen and reduced salen ligands with –^{t}Bu, –S^{i}Pr and –OMe substituents which gave rise to remarkable differences in their spectroscopic and redox properties and suggested the preferential oxidation of –SMe bearing phenolate.[235] Safaei and co–workers reported a series of monomeric copper(II) complexes derived from 3,5–Bu$^{t}_{2}$–salicylaldimine (or 5–Bu$^{t}_{2}$–salicylaldimine) ligands as models of galactose oxidase active site.[236] On electrochemical oxidation, these complexes gave rise to the corresponding Cu(II) phenoxyl radical species.[236] Benisvy et al. designed and synthesized a new *N*,*O*–bidentate, phenol–imidazole pro–ligand LH (LH = 2–[2′–(4′,6′–di–*tert*–butylhydroxyphenyl)]–4,5–diphenylimidazole) which afforded the reversible generation of the corresponding phenoxyl radical species upon one–electron electrochemical oxidation.[237] They described the first X–ray crystal structure of a phenoxyl radical bound to Cu(II) ion.[237] The copper and zinc complexes also exhibited two reversible, ligand–based oxidations giving rise to corresponding mono and bis–phenoxyl radical analogues. The mono–phenoxyl species could also be generated by chemical oxidation and isolated as air–stable salts. In these complexes, the ring bearing the phenoxyl radical exhibited intramolecular π–π interactions thereby reproducing an important feature of galactose oxidase.[238] Thomas and his group also reported the crystal structure of a Cu(II)–coordinated phenoxyl radical complex and explained that the nature preferred copper in galactose oxidase due to its tendency to collect a large amount of spin density on the phenoxyl group through magnetic coupling.[173] Itoh et al. reported copper(II) and zinc(II) complexes $[M^{II}(\mathbf{L1^{\cdot}})(NO_3)]^{+}$ and $[M^{II}(\mathbf{L2^{\cdot}})(NO_3)]^{+}$ (where M = Cu, Zn; **L1H** =

2–methylthio–4–*tert*–butyl–6–[[bis[2–(2–pyridyl)ethyl]amino]methyl]phenol and **L2H** = 2,4–di–*tert*–butyl–6–[[bis[2–(2–pyridyl)ethyl]amino]methyl]phenol) as models for the active form of galactose oxidase and highlighted the role of alkylthio group in stabilizing the radical form of cofactor through electron sharing conjugative effect. [149,239] These complexes also catalyzed the hydrogen atom abstraction of 1,4–cyclohexadiene and *tert*–butyl substituted phenols giving rise to benzene and the corresponding phenoxyl radical or its C–C coupling dimer as oxidation products, respectively.[149,239] Taki et al. synthesized structurally–modified ligands by substituting the metal–binding unit $–N(CH_2CH_2Py)_2$ of these ligands with $–N(CH_2Py)_2$ and $–N(CH_2Py^{Me})_2$ and investigated its effect on the spectroscopic properties and redox potential of model complexes.[240] In another report, they also utilized a structurally related hybrid ligand to synthesize copper and zinc containing phenoxyl radical/phenolate complexes through chemical oxidation of corresponding diphenolato complexes.[241] Dasgupta et al. prepared two ternary copper(II) complexes using two modified amino acid ligands. These complexes afforded stable copper(III) coordinated phenoxyl radical complexes upon electrochemical or chemical oxidation.[242] Takaichi et al. reported a copper(II) complex bearing a non–innocent β–diketiminate ligand and studied its one and two electron oxidations giving rise to Cu(II)–coordinated phenoxyl radical complexes. These complexes exhibited the hydrogen atom abstraction ability from 1,4–cyclohexadiene but could not catalyze the oxidation of alcohol.[243]

1.3.3.2. Superoxide dismutase mimics

Reedijk and co–workers synthesized an imidazolato–bridged complex $[Cu_2(bpzbiap)Cl_3]$ (Hbpzbiap = 1,5–bis(1–pyrazolyl)–3–[bis(2–imidazolyl)methyl]azapentane) which catalyzed the dismutation of superoxide at biological pH representing a good model for superoxide

dismutase.[244] Borras and co−workers also reported dinuclear copper complexes $[Cu_2(tz-tol)_4]$ (Htz−tol = N−(thiazol−2−yl)toluenesulfonamide) and $[Cu_2(tz-naf)_4]$ (Htz−naf = N−(thiazol−2−yl)naftalenesulfonamide which displayed high SOD activity.[245] Travnicek and co−workers reported a series of mixed ligand copper(II) complexes with the composition $[Cu(Qui)(L)]BF_4 \cdot xH_2O$ (where HQui = 2−phenyl−3−hydroxy−4(1H)−quinolinone and L = 2,2′−bipyridine; 1,10−phenanthroline; bis(2−pyridyl)amine; 5−methyl−1,10−phenanthroline; 5−nitro−1,10−phenanthroline and bathophenanthroline) which exhibited promising results in SOD−activity and nuclease activity studies.[246] Patel and co−workers also reported a series of imidazolate−bridged homodinuclear Cu(II)−Cu(II) and heterodinuclear Cu(II)−Zn(II) complexes derived from 2,2′−bipyridyl or 1,10−phenantroline as possible models for superoxide dismutase.[247] All the complexes exhibited SOD−like activity near biological pH. Several copper complexes derived from the macrocyclic ligands have also been synthesized by various research groups as possible models for Cu−ZnSOD.[248-250]

1.3.3.3. Catecholase models

Synthesizing copper complexes with binucleating compartmental or non−compartmental ligands having a central phenolic moiety is of tremendous interest due to the occurrence of copper(II) ions with close proximity in the active sites of several metalloenzymes such as catecholase. Krebs and co−workers synthesized a series of dinuclear copper complexes having composition $[Cu_2(L^1)(OH)(EtOH)(H_2O)][ClO_4]_2 \cdot H_2O$, $[Cu_2(L^2)(OH)][NO_3]_2$, $[Cu_2(L^3)(OMe)(MeOH)(ClO_4)]ClO_4$, $[Cu_2(L^4)(OH)(MeOH)_2][BF_4]_2$, $[Cu_2(L^5)(OMe)][ClO_4]_2 \cdot 2MeOH$, $[Cu_2(L^6)(OMe)(MeOH)(ClO_4)]ClO_4$ and $[Cu_2(L^7)(OMe)(MeOH)(ClO_4)]ClO_4$ derived from pentadentate dinucleating ligands (HL^{1-7}) with N_4O donor sets and investigated their catecholase like activity.[251] These complexes

represented good structural mimics for the active site of met–form of native enzyme. The complexes having a coordinated piperazine group in the ligand part could also exhibit functional modeling of catechol oxidase enzyme. Later on, in another report on dinuclear Cu(II) complexes derived from structurally related ligands, it was found that catecholase activity markedly enhanced due to the involvement of an adjacent thioether group in the ligand frame.[252] Rajak and co–workers utilized two binucleating N_4O_3–coordinating heptadentate ligands (H_3L^1 = 2,6-bis[{[(2-hydroxybenzyl)(N,N-(dimethylamino)ethyl]amino}methyl]-4-methylphenol and H_3L^2 = 2,6-bis[{(2-hydroxybenzyl)(N-(2-pyridylmethyl)amino}methyl]-4-methylphenol) to prepare copper complexes $[Cu_2(L^1)(N_3)]\cdot 2H_2O$ and $[Cu_2(HL^2)(O_2CPh)(H_2O)](PhCO_2)$ where they described the steric demands as well as the effect of pH on the catecholase activity exhibited by these copper containing analogues.[253] Das and co–workers reported a series of dinuclear copper complexes $[Cu_2(H_2L2^2)(OH)(H_2O)(NO_3)](NO_3)_3\cdot 2H_2O$, $[Cu(HL1^4)(H_2O)(NO_3)]_2(NO_3)_2\cdot 2H_2O$, $[Cu(L1^1)(H_2O)(NO_3)]_2$, $[Cu_2(L2^3)(OH)(H_2O)_2](NO_3)_2$ and $[Cu_2(L2^1)(N_3)_3]$ (where L1 = 2–formyl–4–methyl–6R–iminomethyl–phenolato and L2 = 2,6–bis(R–iminomethyl)–4–methyl–phenolato; for $L1^1$ and $L2^1$, R = N–propylmorpholine; for $L2^2$, R = N–ethylpiperazine; for $L2^3$, R = N–ethylpyrrolidine, and for $L1^4$, R = N–ethylmorpholine) as structural and functional models for the active site of catechol oxidase.[254] These complexes could convert 3,5–di–*tert*–butylcatechol (3,5–DTBC) to 3,5–di–*tert*–butylbenzoquinone (3,5–DTBQ) in acetonitrile and methanol medium with extraordinarily high efficiency. Interestingly, they exhibited the formation of enzyme substrate adducts during the conversion of 3,5–DTBC to 3,5–DTBQ for the first time. Furthermore, the complex $[Cu_2(H_2L2^2)(OH)(H_2O)(NO_3)](NO_3)_3\cdot 2H_2O$ exhibited the oxidation of tetrachlorocatechol (TCC) to tetrachloro–*o*–quinone (TCQ) also which had

been reported rarely with other dinuclear copper based analogues.[251,254] Ghosh and co−workers used a tridentate, reduced Schiff's base ligand 2−[[2−(diethylamino)−ethylamino]methyl]phenol (HL) having NNO donors to synthesize a diphenoxido−bridged dinuclear copper(II) complex $[Cu_2L_2(ClO_4)_2]$. This complex afforded a double phenoxido and single hydroxido bridged dinuclear copper(II) complex $[Cu_2L_2(OH)]ClO_4$ in presence of triethylamine.[255] Both complexes represented the functional models of catecholase enzyme however $[Cu_2L_2(OH)]ClO_4$ afforded higher activity due to the presence of hydroxido group. Osorio et al. also reported two copper containing complexes $[Cu_2(\mathbf{L1})(\mu\text{-}OAc)](ClO_4)_2\cdot(CH_3)_2CHOH$ and $[Cu_2(\mathbf{L2})(\mu\text{-}OAc)](ClO_4)\cdot H_2O\cdot(CH_3)_2CHOH$ derived from the unsymmetrial ligands **L1** and **L2** (where **L1** = N′,N′,N-tris(2-pyridylmethyl)-N-(2-hydroxy-3,5-di-*tert*-butylbenzyl)-1,3-propanediamin-2-ol and **L2** = N′,N′-bis(2-pyridylmethyl)-N,N-(2-hydroxybenzyl)(2-hydroxy-3,5-di-*tert*-butylbenzyl)-1,3-propanediamin-2-ol) as functional models which exhibited catalytic promiscuity mimicking the activity of catecholase as well as hydrolases. Double electrophilic activation by introducing *tert*−butyl substituents in the ligand frame resulted higher efficiencies in catechole oxidase and hydrolase activities of the complexes.[256]

1.3.4. Zinc complexes as enzyme models

1.3.4.1. Zinc phenoxyl radical complexes as galactose oxidase models

Reedijk and co−workers reported a family of zinc(II) complexes derived from the ligands Hpyramol and Hpyrimol (Hpyramol = 4−methyl−2−(2−pyridylmethyl)aminophenol and Hpyrimol = 4−methyl−2−(2−pyridylmethylene)aminophenol) which exhibited the formation of phenoxyl radicals on electrochemical oxidation at low temperature.[257] It is interesting to note that these complexes can catalyze the oxidative cleavage of DNA and the

phenoxyl radical species were likely to be the responsible species for DNA strand scission.[257,258] Orio et al. prepared a family of octahedral zinc complexes using Schiff's and Mannich's base ligands which led to the formation of mono–phenoxyl radical species on one–electron electrochemical oxidation.[259] The quinoline derivates gave rise to most stable radicals in the series due to the efficient spin delocalization over the quinoline moiety. The diradical species could also be generated by two–electron–oxidation processes which exhibited weak magnetic coupling.[259] Franks et al. also synthesized a series of five coordinated Zn(II), Cu(II) or Ni(II) complexes derived from diphenolato Schiff base ligand having N_3O_2 donor set and studied their one and two–electron oxidations by UV–vis spectroelectrochemistry and EPR spectroscopy.[260] Zinc and copper complexes gave rise to mono and bis–phenoxyl radical species through ligand based oxidation whereas nickel complexes underwent one electron oxidation to afford Ni(III) species.[260] Kochem et al. also described a tridentate redox active α–azophenol ligand HL (HL = 2–*tert*–butyl–4–methoxy–6–(quinolin–8–ylazo)–phenol) which underwent one electron oxidation to generate primarily a hydrogen bonded phenoxyl radical whereas its reduction afforded an iminosemiquinonate radical species.[261] They showed that the ligand–centered oxidation becomes more facile and reversible when the ligand is coordinated to the zinc(II) ion. They emphasized the role of azo group in enhanced delocalization of spin density to generate phenoxyl radicals as well as semiquinonato radicals.

1.3.4.2. Catecholase models

Guha et al. reported a family of mononuclear and dinuclear zinc containing complexes $[Zn_2(H_2L^1)(OH)(H_2O)(NO_3)](NO_3)_3$, $[Zn_2L^2Cl_3]$, $[Zn_2L^3Cl_3]$, $[Zn_2(L^4)_2(CH_3COO)_2]$, $[Zn(HL^5)Cl_2]$, $[Zn(HL^6)Cl_2]$, and $[Zn(HL^7)Cl_2]$ (L^1–L^3 and L^5–L^7 = 2,6–bis(R–iminomethyl)–4–methylphenolato, where R = N–ethylpiperazine for L^1, R =

2–(N–ethyl)pyridine for L^2, R = N–ethylpyrrolidine for L^3, R = N–methylbenzene for L^5, R = 2–(N–methyl)thiophene for L^6, R = 2–(N–ethyl)thiophene for L^7, and L^4 = 2–formyl–4–methyl–6–N–methylbenzene–iminomethyl–phenolato) as models to study the radical pathway of catecholase enzyme activity exploiting the redox–inert nature of zinc ion.[262] All complexes efficiently catalysed the oxidation of 3,5–DTBC to 3,5–DTBQ under aerobic conditions. They showed that the mononuclear complexes catalyzed the oxidation of 3,5–DTBC through enzyme–substrate adducts while dinuclear complexes did not undergo such adduct formation during their catalytic activity. They suggested that these complexes followed a radical dependent pathway and supported it by EPR spectroscopy and cyclic voltammetric experiments. Furthermore, they verified the ligand centered radical generation by theoretical calculations also.

1.3.4.3. Models for liver alcohol dehydrogenase and nacreous protein

Several zinc containing complexes have also been reported as models for the active site chemistry of liver alcohol dehydrogenase, an important enzyme which biologically converts the alcohol to aldehydes and ketones. Berreau and co–workers used a ligand bmapa (N,N–bis–2–(methylthio)ethyl–N–(6–amino–2–pyridylmethyl)amine) and reported first example of mononuclear zinc methanol and DMF complexes with nitrogen/sulphur donor environment which displayed secondary hydrogen–bonding interactions similar to those found in the active site of LADH.[263] Recently, Ichikawa and co–workers reported a distorted tetrahedral zinc complex derived from the ligand L (where L = N–{tris([2–[(1–methylbenzimidazol–2–yl)ethyl]–methyl]amino)–2–oxoethyl}iminodiacetic acid) as mimic for the active site of nacreous protein and investigated its CO_2 fixation and calcification properties.[264]

1.4. DNA, DNA binding and DNA cleavage

1.4.1. Structure of DNA[29]

The three–dimensional double helical structure of DNA molecule was discovered by Watson and Crick in 1953. DNA is composed of two polynucleotide strands organized in an antiparallel arrangement and wound round each other to form a double helix. The exterior of the helix is decorated alternatively with deoxyribose sugar units and phosphate groups having two formal negative charge which are linked together by phosphodiester bonds (Fig. 1.4). The interior of helix is anchored with purine (adenine and guanine) and pyrimidine (cytosine and thymine) bases. The double helical structure of DNA is stabilized by the interstrand complementary base pairing through hydrogen bonding and π–π stacking interactions among the adjacent base pairs along the helical column.

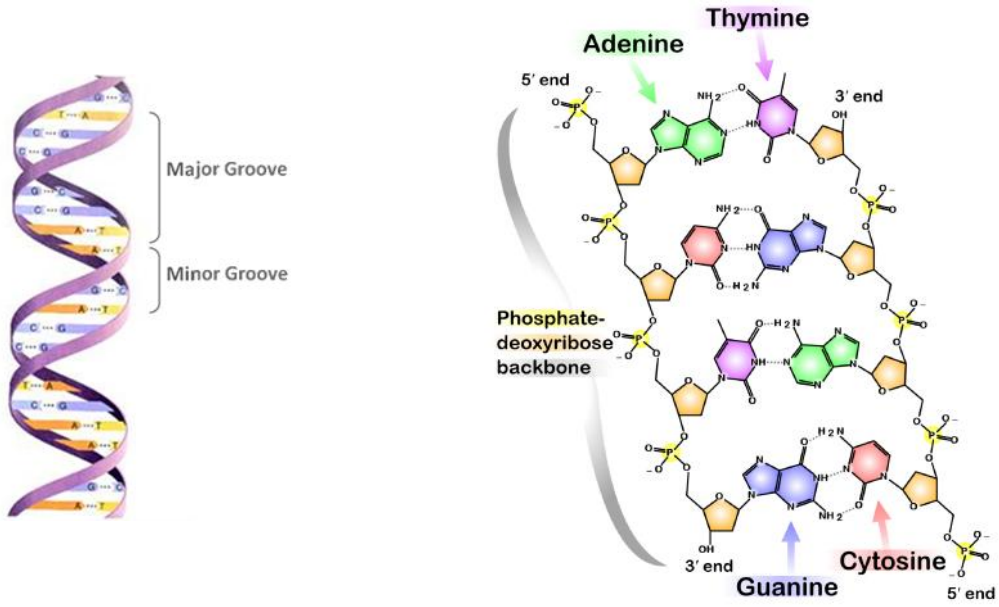

Fig. 1.4 DNA double helix and its structural components

1.4.2. DNA binding

Small molecules which can bind to DNA offer significant promise as diagnostic probes, reactive agents and therapeutics. Metal complexes can interact with DNA either

through coordination to phosphate oxygen atoms, sugar oxygen atoms, atoms of the nucleobases (N,C,O) or indirectly via their ligands. Both, strong covalent and weak non–covalent types of association of metal complexes with nucleic acids have been recognized.

1.4.2.1. Covalent Binding

Covalent type of binding generally involves the coordination of soft metal ions to the nucleophilic positions of heterocyclic bases of DNA and RNA. The preferred sites for covalent binding of metal complexes are N7 on guanine, N1 and/or N7 on adenine, N3 on cytosine, O4 on thymine and deprotonated N3 position on thymine and uracil. [29,265] A familiar example of such complexes is the anti–cancer drug *cis*–platin which interacts with polynucleotide strand through coordination of platinum center to the N7 positions of adjacent guanine bases of one strand (Fig. 1.5).[266] This results in intrastrand cross–linking between neighbouring guanine residues.

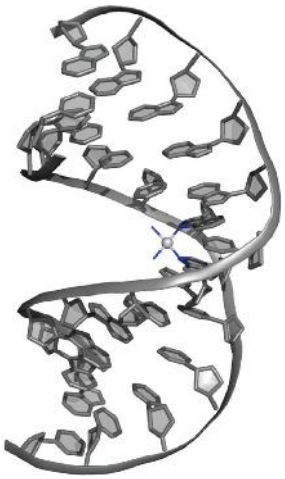

Fig. 1.5 Covalent DNA binding by *cis*–platin via intra–strand cross–linking between platinum atom and N7 atoms of adjacent guanines. Pt center is represented as light grey sphere with its four nitrogen–based ligands shown in blue[266]

In addition, transition metal complexes with lesser degree of softness may exhibit some sort of covalent binding with oxygen atoms of phosphate groups also, where the ionic

versus covalent character of interaction is mainly dictated by the metal ion involved.[29] Covalent–coordinate type of interactions with the sugar moiety are rather less common but may exist with some heavy metal compounds like osmate esters.[29] Covalent binding occurs irreversibly and affords complete inhibition of DNA processes ultimately leading to cell death.

1.4.2.2. Non-covalent binding

Non–covalent binding implies interaction of compound with DNA through hydrogen bonding, electrostatic forces, Van der Waal's forces, hydrophobic interactions or intercalation.[29] There are three fundamental modes of non–covalent DNA binding – (i) external or electrostatic interaction, (ii) groove or surface interaction and (iii) intercalation.

(i) External binding or electrostatic binding

The electrostatic interaction between positive charge of metal ion and negatively charged phosphate backbone of DNA or electron donor groups of nucleobases is referred as external binding. The strength of the binding is predominantly governed by the charge of the molecule, the ligand hydrophobicity and the total size of the ion.[267,268] This type of DNA interaction gives rise to association of DNA duplexes to form aggregates or condensed structures.[267]

(ii) Groove binding or surface binding

Groove binding involves lodging of drug molecules into the grooves of the double, triple or G–quadruplex helices of DNA (Fig. 1.6).[265] Unlike intercalators which exhibit planarity and rigidity, groove binders should have flexible structures and distort the DNA backbone to a lesser extent than that caused by intercalators.[265] Groove binding is stabilized by a combined action of electrostatic, H–bonding and Van der Waal's interactions which

brings about the drug–DNA complexes more stable than those resulted by intercalation only.[265] Groove binding of molecules with DNA may occur in two distinct ways: (i) via major groove and (ii) via minor groove. It has been observed that DNA binding proteins or gene–targeted oligonucleotides interact via major groove whereas small and cresent shaped molecules bind through the minor groove of helix.[267] Major groove binders possess multiple interaction sites and exhibit comparatively stronger binding ability with guest molecules. In terms of size, flexibility, electrostatic potential and water bonding properties, minor grooves may serve as better receptors for small, flat and cationic DNA binding molecules.[267] As a general rule, minor groove binding molecules cause little or no perturbation in the structure of DNA which is reflected by little or no change in the DNA circular dichroism.[267] Distamycin, metallobleomycins and Sigman's bis(1,10–phenanthroline)copper(I) complex are excellent examples of such molecules which bind DNA through minor grooves.[269]

(iii) Intercalation

Intercalation was first reported by Lerman in 1961.[270] It may be defined as irreversible sandwiching of a molecule between the adjacent base pairs of the DNA base stack, stabilized by π–π stacking interactions, dipole–dipole interactions and hydrogen bonding interactions with planar aromatic bases (Fig. 1.6). Slight unwinding of the helix at the intercalation site, stiffening of the helix, lengthening of DNA equal to the height of one base pair and enhanced DNA stability are main consequences of the DNA intercalation event.[270] However, no bending or kinking results after intercalation and the overall structure of DNA remains unperturbed.[270] Intercalating ligands and metal complexes should possess extended planar aromatic ring system of suitable size and chemical nature to slot between base pairs. Examples include planar organic moieties such as ethidium, daunomycin and metal complexes bearing planar aromatic ligands like phen (1,10–phenanthroline), phe

(9,10–phenanthrenequinone diimine) or dppz (dipyrido[3,2–*a*:2′,3′–*c*]phenazine).[270] Coordinative saturation, rigidity and inertness for substitution are important characteristics of metallointercalators which make them suitable for intercalation and hamper their coordination with DNA.[270]

In addition to these three fundamental modes, alternative modes for DNA interaction may also exist. Insertion is one of these alternative pathways which involves binding with DNA helix through separation and displacement of base pairs. Metalloinsertors contain a planar aromatic ligand which can act as a π–stacking replacement in the DNA base stack and eject the bases of a single base pair.[269] Very recently, Barton and co–workers posited the first example of molecules exhibiting this type of DNA binding.[269]

Fig. 1.6 The binding modes of metal complexes with DNA: Groove binding, metallointercalator and metalloinsertor[270]

1.4.3. DNA cleavage or nuclease

Nucleases are the enzymes which serve as excellent biological tools to destroy foreign nucleic acids and, to excise and repair the mutations in DNA in order to maintain the integrity of the genetic substances. However, nucleic acid strand scission may also arise from the

exposure of cell to free radical species. In general, modification of nucleic acids may occur mainly by two major pathways: (i) nucleophilic pathway, and (ii) oxidative pathway.

(i) Nucleophilic pathway

The nucleophilic cleavage begins with the attack of a nucleophile on the phosphorus atom of phosphodiester moiety to form a trigonal bipyramidal transition state having the attacking nucleophile and the departing alkoxide on apical positions which ultimately ends up with the cleavage of phosphodiester bond (Scheme 1.21). This process is known as *nucleic acid hydrolysis* when water or hydroxide ion acts as nucleophile. On the other hand, when the nucleophile is an alcohol or alkoxide, the process is termed as *transesterification*.[136] The uncatalyzed hydrolysis of phosphate esters is exceedingly slow under physiological conditions. The remarkable stability of phosphodiester bonds renders the hydrolysis of nucleic acids quite challenging. The extreme kinetic inertness of DNA and RNA towards nucleophilic cleavage derives from strong repulsion between the potential nucleophiles and highly negatively charged backbones of nucleic acids.[136] Furthermore, formation of the requisite transition state for nucleophilc cleavage is also strongly unfavoured by base stacking interactions.[136] The active sites of most nucleases contains divalent cation like Mg^{2+}, Ca^{2+}, Mn^{2+} or Zn^{2+}. The presence of these cations greately enhances the hydrolysis of phosphate ester by activating them towards nucleophilic attack via charge neutralization as well as by assisting the departure of the alkoxide leaving group through stabilizing interactions.[136]

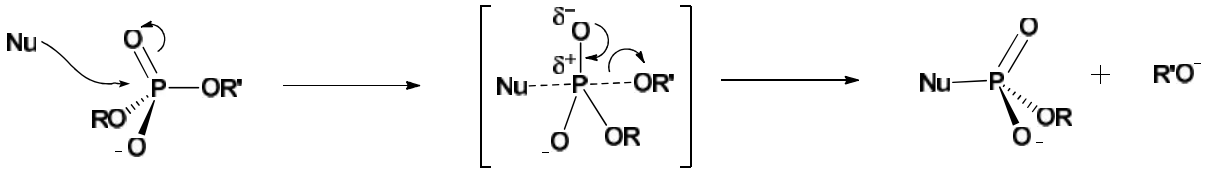

Scheme 1.21 Associate mechanism for nucleophilic cleavage of phosphate diester[136]

(ii) Oxidative pathway

In biology, oxidative cleavage generally involves oxidation of sugar moiety and/or the nucleobases by reactive intermediates of intracellular or extracellular origin which ultimately lead to the strand scission. However, redox−active transition metal complexes can also mediate DNA oxidation by generating such intermediates through redox−cycling in presence of oxidants/reductants or with out any assisting agents. These reactive intermediates generally include reactive oxygen species (ROS) like hydroxyl radical (HO˙), superoxide anion (O_2^-), hydrogen peroxide (H_2O_2) and singlet oxygen ($^1O_2$).[271] Hydroxy radical is an extremely strong oxidant which can abstract hydrogen from any carbon of the pentose sugar. It can add to the double bonds of DNA bases and abstract hydrogens from various positions of nucleobases as shown in Scheme 1.22.

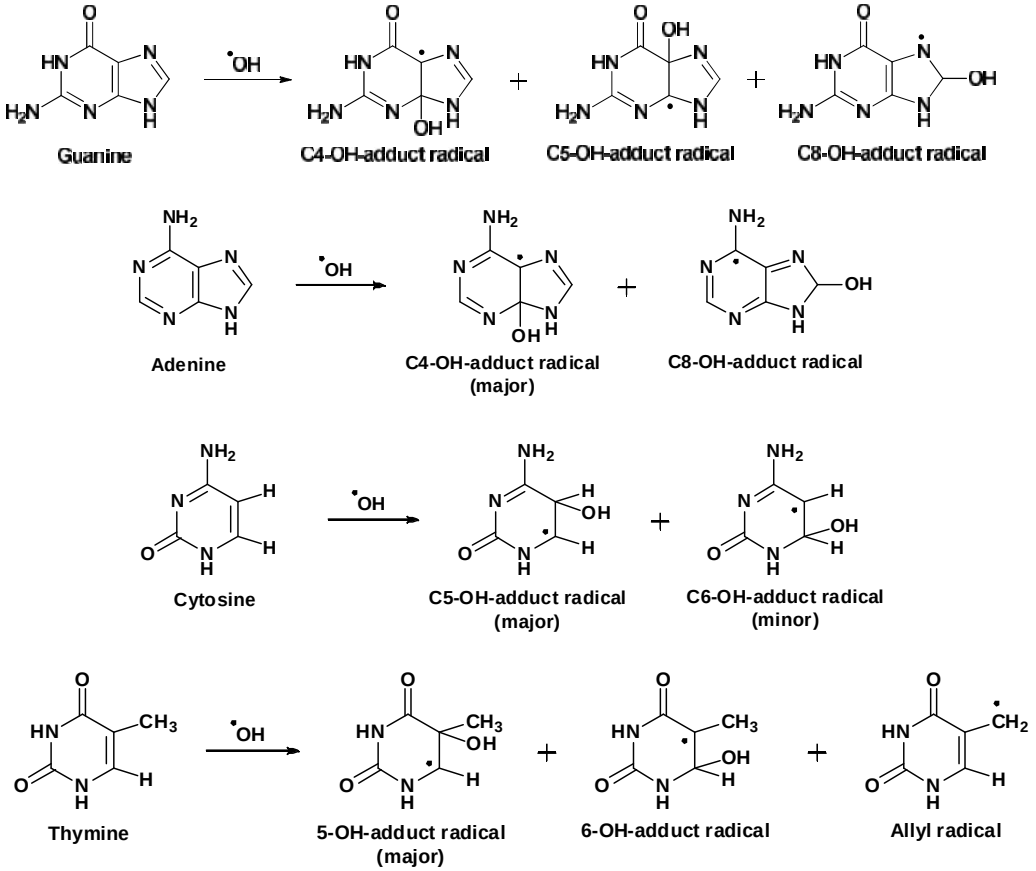

Scheme 1.22 Preferred sites of oxidation in nucleobases by reactive oxygen species[272]

The C–centered radicals of sugar moiety and C– or N– centered radicals of DNA bases generated this way, may then undergo further reactions resulting in a variety of final products.[272] Singlet oxygen can also cleave DNA oxidatively with energy transfer.[271] Furthermore, reactive metal–oxo species (RMOS) e.g. end–on and side–on peroxo/superoxo metal species (M–OH/M–OOH) and metal oxo species (M=O) may also cause DNA cleavage at specific sites through binding with DNA in selective ways.[271]

The oxidative modification of DNA can also be induced by photochemical methods where reactive intermediates responsible for the DNA cleavage are generated by photo–irradiation.[273] This type of cleavage is termed as *photo-induced DNA cleavage* which is extensively used for clinical applications like photodynamic therapy.

1.5. Metal complexes as artificial metallonucleases

The biomimetic molecules which bind nucleic acids and catalytically cleave them can be regarded as chemical nucleases. Such molecules are of paramount importance for elucidating the genetic mechanism of natural nucleases as well as for the development of footprinting and chemotherapeutic agents, gene regulation, mapping of protein and cancer therapy.

1.5.1. Cobalt complexes as artificial nucleases

Cobalt is one of the promising metals to develop artificial metallonucleases due to its biological relevance, natural occurrence in the nucleolytic enzymes,[28,33,274-276] and its extreme potential to catalyze hydrolytic reactions[138,277]. A large number of cobalt complexes have been synthesized and investigated for their DNA binding and DNA cleavage ability. There are several reports for cobalt complex–mediated photolytic cleavage of DNA[278-283] however those exhibiting hydrolytic or oxidative type of cleavage are relatively lesser in number. Nair and co–workers prepared a Co(II) complex $[Co(bzimpy)_2]$ (where bzimpy =

2,6–bis(benzimidazol–2–yl)pyridine monoanion) which exhibited moderate surface binding with DNA and gave rise to the nicking of plasmid DNA upon photoexcitation in the MLCT region of the complex.[278] Kumbhar and co–workers reported a family of *cis*–dichloro bis diimine Co(III) complexes with the compositions $[Co(LL)_2Cl_2]Cl$ (where LL = N,N′–ethylenediamine (en), 2,2′–bipyridine (bpy), 1,10–phenanthroline (phen), 1,10–phenanthroline–5,6–dione (phendione) and dipyrido[3,2–a:2′,3′–c]phenazine (dppz)).[283] These complexes interacted with DNA in a covalent fashion or through intercalation and showed efficient photoclevage of pBR322 DNA.[283] Qian et al. synthesized three water soluble di–cobalt(III) complexes of 1,4,7–triazacyclononane–N–acetate which exhibited double–stranded cleavage of pBR322 DNA *via* hydrolytic pathway.[284] Xu et al. also reported a family of *cis*–aquahydoxo–tetraamine–cobalt(III) complexes and evaluated their efficiency to promote hydrolytic cleavage of DNA.[285] Indumathy et al. prepared Co(II) and Co(III) complexes derived from a tridentate ligand imidazole–terpyridine (Itpy) which exhibited DNA binding through intercalation and catalyzed oxidative DNA cleavage in presence of ascorbic acid and /or hydrogen peroxide.[286] Ng and co–workers presented the first report of oxidative DNA cleavage by a cobalt chelated amino acid complex *mer*–tris(β–alaninato)cobalt(III).[287] The complex showed efficient nuclease activity in presence of ascorbic acid. The DNA cleavage was mediated by ascorbate free radicals generated through one electron transfer from ascorbate ions to the metal complex.

1.5.2. Nickel complexes as artificial nucleases

There are very scanty reports regarding nickel(II) complexes exhibiting nuclease activity.[232] Kong and co–workers reported a family of Schiff's base tetraazamacrocyclic oxamido Ni(II) complexes which could bind with DNA by partial intercalative and groove binding modes.[288] Furthermore, all complexes afforded oxidative cleavage of plasmid DNA

in presence of H_2O_2. Mariappan and co–workers synthesized a nickel(II) complex [Ni(daasal)] derived from a salen–functionalized ligand H_2daasal (H_2daasal = *N*,*N*′–Bis(salicylidene)–9–(3,4–diaminophenyl)acridine) possessing the salen and acridine intercalating moieties linked together.[289] These complexes exhibited intercalative interaction with CT DNA and promoted the cleavage of pBR322 DNA upon irradiation under terminal oxidant oxone.[289] Chattopadhyay et al. reported a dinuclear nickel(II) complex derived from a compartmental ligand 2,6–bis(*N*–ethylpiperazine–iminomethyl)–4–methyl–phenol which exhibited hydroxyl radical–mediated DNA cleavage through a self–activating mechanism.[232] Anbu et al. also reported a series of macrocyclic binuclear Ni(II) complexes and investigated their DNA binding and DNA cleavage properties.[290] The complexes interacted with DNA through electrostatic binding mode or intercalation and promoted hydrolytic cleavage in presence of H_2O_2. Reddy and Rao demonstrated the intercalative binding of ternary nickel(II) complexes [Ni^{II}(en)(HisLeu)] and [Ni^{II}(hist)(HisLeu)] (where en = ethylenediamine; hist = histamine and HisLeu = histidylleucine) with DNA and their hydrolytic DNA–cleaving properties.[291] Wang et al. studied the DNA binding and cleavage properties of a nickel(II) complex [Ni(phen)(pha)$(H_2O)_3$] (phen = 1,10–phenanthroline; pha = *o*–phthalate) and found that it could intercalate into the DNA base pairs and cleave supercoiled DNA in presence of H_2O_2.[292]

1.5.3. Copper complexes as artificial nucleases

Copper possesses high affinity for nucleobases and exhibits biologically accessible redox potentials which has invoked considerable interest for its application as artificial metallonucleases.[293] The first example was put forward by Sigman and co–workers as copper complexes of 1,10–phenanthroline which showed efficient double–strand DNA cleavage in presence of molecular oxygen and reducing agent.[294] Palaniandavar and co–workers utilized

several ligands with varying donor sets to synthesize mixed ligand copper(II) complexes[295-298] and explored the influence of diimine co–ligands on their DNA binding and cleavage properties. Investigation of nuclease activity of such complexes afforded DNA strand scission mostly via an oxidative and/or hydrolytic mechanism though few of them exhibited the photonuclease also when irradiated with the light of appropriate wavelength. Many of these complexes showed excellent cytotoxicity against various cancer cell lines including human breast cancer cell lines (MCF–7) and human cervical epidermoid carcinoma cell lines (ME–180).[296] Currently, they have reported a series of copper(II) complexes having NNO and NNN donor ligands which exhibited covalent mode of binding with DNA through the replacement of easily removable choride ions by DNA nucleobases.[299] Interestingly, these complexes catalyzed the cleavage of DNA very efficiently and completely degraded the SC DNA to undetectable fragments. Furthermore, these complexes also exhibited remarkable cytotoxicity selectively killing the cancer cells[299]. Guo and co–workers reported a novel ternary copper(II) complex $[Cu(phen)(L–Thr)(H_2O)](ClO_4)$ (where phen = 1,10–phenanthroline and L–Thr = L–threonine) which could bind DNA through intercalative mode and exhibited oxidative scission of pBR322 DNA.[300] The complex exhibited potent cytotoxic effects against human leukemia cell line (HL–60) and human stomach cancer cell line (SGC–7901).[300] They also reported trinuclear copper(II) complex Cu_3–L (L = *N*,*N*,*N*′,*N*′,*N*′′,*N*′′–hexakis(2–pyridyl)–1,3,5–tris(aminomethyl)benzene) which exhibited more efficient oxidative DNA strand scission at the same $[Cu^{2+}]$ concentration than its corresponding mononuclear analogue.[301] The higher nucleolytic ability was attributed to the possible synergism between the copper(II) centers. Reedijk and co–workers showed an unusual and outstanding copper–mediated DNA cleavage by a square–planar cytotoxic $[Cu^{II}(pyrimol)Cl]$ complex (HPyrimol =

4–methyl–2–*N*–(2–pyridylmethylene)aminophenol).[302] Mechanistic studies confirmed that DNA was cleaved through a "self-activating" oxidative mechanism without any involvement of diffusible radical species in DNA scission.

1.5.4. Zinc complexes as artificial nucleases

Strong Lewis acidity, rapid ligand exchange properties, well–defined coordination geometries and physiological relevance of the zinc metal ion, altogether enable it as the best suited metal ion for the development of artificial metallonucleases.[303] Many mono– and multinuclear zinc complexes have also been studied for their potential to act as artificial nucleolytic agents. Due to the redox inactive nature of zinc ion, it predominantly affords the hydrolytic type of DNA cleavage. However, oxidative scission of DNA strands has also been acheived in few cases where the ligands can exhibit redox–innocence upto some extent.[135,258] Reedijk and co–workers observed a unique ligand–based oxidative DNA cleavage by Zn(II) complexes derived from Hpyramol and Hpyrimol ligands (where Hpyramol = 4–methyl–2–*N*–(2–pyridylmethyl)aminophenol and Hpyrimol = 4–methyl–2–*N*–(2–pyridylmethylene)aminophenol) mediated by non–diffusible phenoxyl radical species.[258] Boseggia et al. reported a series of *cis*–*cis*–triaminocyclohexane Zn(II) complex–anthraquinone intercalator conjugates as hydrolytic cleaving agents of plasmid DNA where the conjugation of the metal complex with DNA targeting unit gave rise to a 15–fold increase of the cleavage efficiency with respect to the metal complex alone.[303] Mao and co–workers prepared guanidinium–functionalized zinc complexes which could exhibit sequence specific DNA binding and efficient cleavage of plasmid DNA in presence of hydrogen peroxide.[304] Bochu and co–workers showed that zinc(II)–quercetin complex can also catalyze the hydrolytic cleavage of plasmid DNA producing single and double strand breaks.[305] Jiang et al. synthesized zinc(II) terpyridine complexes $[Zn(atpy)_2(PF_6)_2]$ and

$[Zn(ttpy)_2(PF_6)_2]$ (where atpy = 4′–p–N9′–adeninylmethylphenyl–2,2′:6,2′′–terpyridine and ttpy = 4′–p–tolyl–2,2′:6,2′′–terpyridine) and evaluated the impact of adenine moiety incorporated in the ligand frame on their DNA binding modes and nuclease ability.[306] These complexes exhibited potent in vitro cytotoxic properties against various human cancer cell lines including HeLa, HepG2, PC–3 and MCF–7 cell lines. Qian and co–workers synthesized mono– and di–nuclear zinc(II) complexes derived from a tridentate ligand with NNN donor set and investigated their DNA binding and DNA cleavage properties.[307] The complexes interacted with DNA in a partial intercalative mode and efficiently promoted the double–stranded cleavage of DNA through hydrolytic mechanism.[307]

1.6. Protein models, protein binding and protein cleavage

1.6.1. Structure of albumin and binding sites

Studies regarding modes of drug–protein interactions are of enormous significance for the development of chemotherapeutic agents because such interactions greately influence the absorption, distribution, metabolism and excretion properties of drugs.[293] BSA is frequently used as a protein model for protein interaction studies becuase of its low cost, ready availability along with its structural homology with HSA.[308] BSA and HSA consist of single peptide chain with 607 and 585 amino acids respectively, and possess very similar sequence and conformations. These are composed of three homologous helical domains (I–III) which are further subdivided into A and B subdomains. A striking difference between the structures of BSA and HSA is the distance between subdomains IIA and IIB. Two primary drug binding sites have been recognized in the structure of serum albumins. These are known as *Sudlow site I* and *Sudlow site II* and located in subdomains IIA and IIIA respectively (Fig. 1.7). Sudlow site I shows preference for large heterocyclic and negatively charged compounds whereas Sudlow site II exhibits affinity for small aromatic carboxylic acids.[309] However,

presence of other or secondary binding sites in the albumin molecule can not be excluded. In fact, one highly specific binding site for polycyclic aromatic hydrocarbon epoxides and as many as six for fatty acids have been identified.[309]

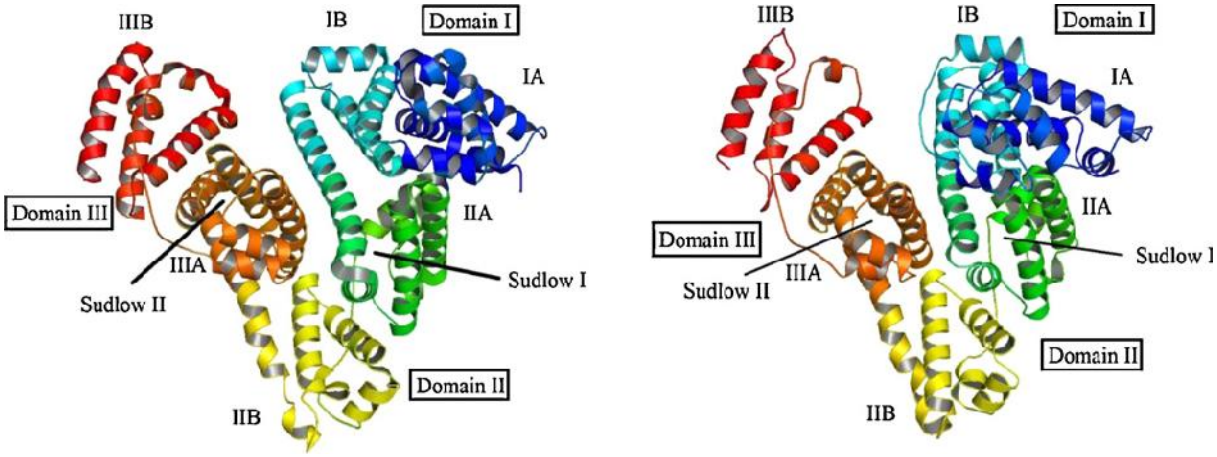

Fig. 1.7 Ribbon representation of the structure of HSA (left) and BSA (right)[309]

The process of binding may be reversible as well as irreversible. Reversible binding is stabilized by weak chemical interactions like hydrogen bonding, hydrophobic interactions, van der Waal's forces and ionic interactions. Surface donor groups in albumins such as histidine or methionine may also coordinate with metal complexes substituting some labile groups and give rise to irreversible covalent binding.[310] However, this type of binding is rare and known to induce carcinogenicity, teratogenicity and tissue or organ toxicity. A number of techniques like UV–vis spectrophotometry, fluorimetry, circular dichroism spectroscopy, equilibrium dialysis and electrochemistry can be employed to study the molecular interactions of drugs with serum albumins.[309] Among these techniques, fluorescence spectroscopy has been particularly useful to investigate the nature of the binding sites as well as their specificity and affinity towards particular ligands.[309]

1.6.2. Protein Cleavage or protease

The enzymes which can hydrolyze the peptide linkages present within the protein molecules are regarded as a proteases. Proteases can be divided into two classes; (a) *exopeptidases* which can split off only single amino acids by cleaving the peptide bonds adjacent to the termini of the peptide chain e.g. aminopeptidases and carboxypeptidase A and (b) *endopeptidases* which can hydrolyze any peptide linkage irrespective of its position in the peptide chain e.g. trypsin, chymotrypsin and pepsin.

Free radicals mediated oxidative modification of proteins by reactive oxygen species (ROS) may also give rise to fragmentation of polypeptide chain, generation of protein–protein cross linkage and oxidation of amino acid side chains.[311] Accumulation of oxidized protein is implicated in a variety of physiological disorders including muscular dystrophy, amyotrophic lateral sclerosis, Alzheimer's disease, respiratory distress syndrome, cataractogenesis, progeria, rheumatoid arthritis, and Werner's syndrome.[311,312] Oxidative modification of protein is also known to cause diabetes, atherosclerosis, Parkinson's disease, cystic fibrosis, ulcerative colitis and pulmonary dysfunction.[311,312] Increased production of reactive oxygen species (ROS) due to stress, aging or diseases leads to the accumulation of oxidized protein. Unlike, irreversibly damaged proteins, extensively oxidized proteins cannot be degraded by 20S proteasomes and vacuolar proteases and form aggregates by cross–linking. This impairs the 20S proteasome and mitochondrial function which enhances the ROS production in turn (Scheme 1.23).[313]

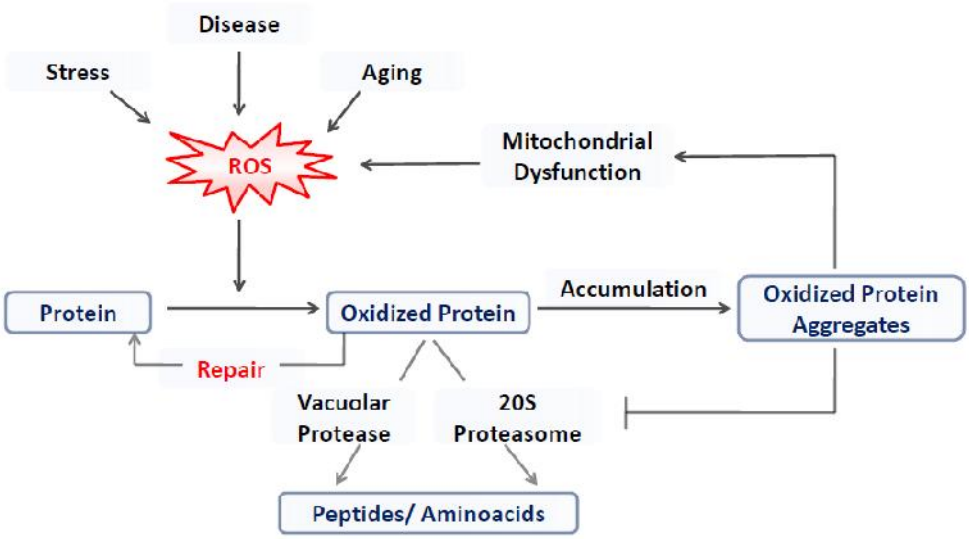

Scheme 1.23 Protein oxidation and proteolysis of oxidized proteins[313]

Oxidation of proteins is mainly initiated by $^{\cdot}OH$–dependent α–hydrogen atom abstraction of amino acid residues to form a carbon centered radical which, in turn, undergoes a series of steps mediated by Fe^{2+} or $HO_2^{\cdot}$ to generate alkoxyl radicals in presence of oxygen. The alkoxyl radical produced this way, follows either *diamide pathway* to produce peptide fragments possessing diamide and isocyanate structures respectively, or the ~J*amidation pathway* leading to the peptide fragments having amide and *N*–α–ketoacyl structures respectively (Scheme 1.24).[312]

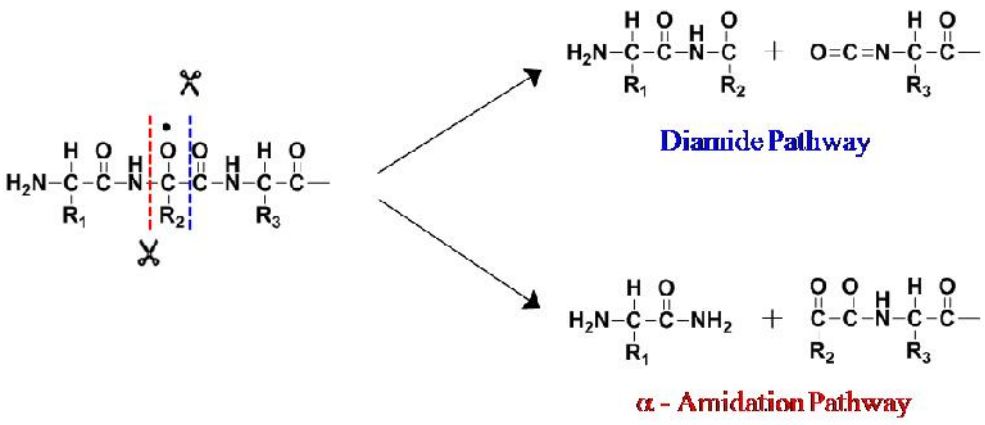

Scheme 1.24 Pathways for peptide bond cleavage[312]

Aromatic amino acid residues are among the preferred targets for ROS–mediated oxidation (Table 1.7). ROS attack on glutamyl, aspartyl and prolyl side chains may also lead to peptide bond cleavage giving rise to scission of protein backbone.[312]

Table 1.7 Amino acid residues most prone to oxidation and oxidation products[312]

Amino acids	Oxidation products
Arginine	Glutamic semialdehyde
Cysteine	Disulphides, cysteic acid
Glutamyl	Oxalic acid, pyruvic acid
Histidine	2-Oxohistidine, asparagine, aspartic acid
Lysine	α-Aminoadipic semialdehyde
Methionine	Methionine sulphoxide, methionine sulphone
Phenylalanine	2,3-Dihydroxyphenylalanine, 2-, 3-, and 4-hydroxyphenylalanine
Proline	2-Pyrrolidone, 4- and 5-hydroxyproline pyroglutamic acid, glutamic semialdehyde
Threonine	2-Amino-3-ketobutyric acid
Tryptophan	2-, 4-, 5-, 6-, and 7-Hydroxytryptophan, nitrotryptophan, kynurenine, 3-hydroxykynurinine, formylkynurinine
Tyrosine	3,4-Dihydroxyphenylalanine, tyrosine-tyrosine cross-linkages, Tyr-*O*-Tyr, cross-linked nitrotyrosine

1.7. Metal complexes as artificial metalloproteases

The molecules which can bind at the active site of the disease related proteins with high affinity and high selectivity have been employed as conventional drugs for a long time to control and regulate their functions.[314] However, catalytically cleaving the peptide backbone of malignant proteins may also be an effective treatment for the diseases related to the protein pathogens. For this purpose target selective artificial proteases have been developed which can recognize the disease related proteins or oligomers and cause their catalytic cleavage. This gives rise to the inactivation of target protein and the cleavage agent is regenerated (Fig. 1.8).

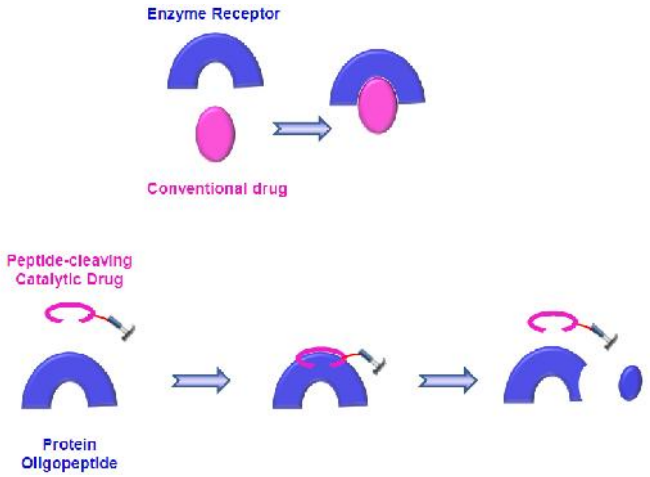

Fig. 1.8 Conventional drugs vs peptide–cleaving catalytic drugs

These molecules offer additional advantages over the conventional drugs since these do not require strong binding and offer reduced drug dosage with less side effects.[315] Furthermore, conventional drugs can not be developed for amyloidogenic proteins or oligopeptides which do not have active site.[316] Such complexes may provide a potential therapeutic alternative for the treatment of amyloidoses (Alzheimer's disease, Type–2 diabetes mellitus, Parkinson's disease, mad cow's disease, spongiform encephalopathies etc.).

1.7.1. Cobalt complexes as artificial metalloproteases

Suh et al. reported a family of target selective metalloproteases containing Co(III) complexes of cyclen as the catalytic center.[317,318] These compounds exhibited efficient cleavage of h–IAPP (human Islet Amyloid PolyPeptide) oligomers and few of them catalyzed the hydrolysis of Aβ_{42} oligomers also. As a follow up, they prepared cobalt(III) aqua complex of 1–oxa–4,7,10–triazacyclododecane which exhibited higher proteolytic activity due to the enhancement of Lewis acidity of Co(III) center.[316] Kumar and co–workers exhibited the regioselective exopeptidase activity of pentammineaquocobalt(III) chloride and tetramminediaquocobalt(III) chloride over chicken hen egg lysozyme under mild physiological conditions.[319] They also investigated a series of polyamine cobalt(III)

complexes and showed that these complexes could catalyze the photocleavage of the peptide backbone of lysozyme.[320] Chakravarty and co–workers synthesized a cobalt(III) complex $[Co(pnt)(dppz)_2](NO_3)_2$ (where pnt = pyridine–2–thiol; dppz = dipyrido[3,2–a:2′,3′–c]phenazine) which exhibited non–specific BSA or lysozyme protein cleavage activity when illuminated with UV–light of 365 nm. Investigation of the mechanism revealed the involvement of hydroxyl radical and singlet oxygen in protein scission.[321]

1.7.2. Copper complexes as artificial metalloproteases

Burstyn and his group reported a copper(II) complex $Cu([9]aneN_3)Cl_2$ derived from a macrocyclic ligand which set the first example for complexes catalyzing hydrolysis of proteins as well as phosphodiester bonds near physiological pH conditions.[322] de Oliveira et al. synthesized two mononuclear copper(II) complexes $[Cu(HL^1)Cl_2]$ and $[Cu(L^1)Cl]$ (HL^1 = 2–[(bis(pyridylmethyl)amino)methyl]–4–methyl–6–formylphenol) and showed site–specific protein cleavage using BSA and *Taq* DNA polymerase enzyme as the model substrate.[323] The scission of protein backbone was achieved through hydrolytic mechanism at micromolar concentrations of complexes and under mild physiological conditions. Palaniandavar and co–workers synthesized the mixed–ligand copper(II) complex $[Cu(tdp)(tmp)](ClO_4)$ (where H(tdp) = 2–[(2–(2–hydroxyethylamino)ethylimino)methyl]phenol and tmp = 3,4,7,8–tetramethyl–1,10–phenanthroline) which showed rapid site–specific protease activity with BSA and lysozyme at micromolar concentrations and under mild physiological conditions.[324] They also reported a series of mononuclear mixed ligand copper(II) complexes $[Cu(bba)(diimine)](ClO_4)_2$ (bba = N,N–bis(benzimidazol–2–ylmethyl)amine, diimine = 2,2–bipyridine, 1,10–phenanthroline, 5,6–dimethyl–1,10–phenanthroline or dipyrido[3,2–d:2,3–f]–quinoxaline which exhibited the oxidative DNA cleavage as well as BSA protein cleavage activity in presence of H_2O_2 as activating agent.[294] In a recent report,

they synthesized a series of mononuclear mixed–ligand copper(II) complexes derived from a tridentate ligand pmdt (where pmdt = N,N,N′,N′′,N′′–pentamethyldiethylenetriamine) and several diimine co–ligands.[293] They explored the effect of hydrophobicity of ligands on DNA and protein binding and cleavage activity as well as cytotoxicity of these complexes. Suh and co–workers investigated the proteolytic activity of Cu(II)–oxacyclen complex (oxacyclen = 1–oxa–4,7,10–triazacyclododecane) using albumin, γ–globulin and myoglobin as model substrates and compared their activity with that of Cu(II)–cyclen complex (cyclen = 1,4,7,10–tetraazacyclododecane).[325] The enhancement in proteolytic activity was attributed to the increased Lewis acidity of Cu(II) ion in Cu(II)–oxacyclen complex.[325] The reactivity and selectivity of these complexes was further enhanced by positioning an aldehyde group in close proximity to the copper(II) oxacyclen center which was proposed to form imine bonds with the ammonium groups located on the surface of protein.[326,327] Chakravarty and co–workers reported a family of metal complexes having composition $[M(Tp^{Ph})(py–nap)]ClO_4$ (where M = Co(II), Cu(II) or Zn(II); TpPh = tris(3–phenylpyrazoly)borate anionic ligand and py–nap = pyridyl ligand bearing a naphthalimide chromophore moiety).[328] All the complexes exhibited DNA cleavage activity when irradiated with UV–A or near–IR light. Under photochemical conditions, cobalt and copper complexes exhibited protein cleavage activity also when bovine serum albumin was used as the model substrate. They also synthesized few copper(II) complexes derived from a reduced Schiff's base ligand having a ferrocene pendant moiety and 1,10–phenanthroline or dipyrido[3,2–*a*:2′,3′–*c*]phenazine coligands. The complexes displayed red–light induced oxidative DNA strand scission or/and UV–A light induced oxidative cleavage of bovine serum albumin.[329] Nair and co–workers utilized the copper(II) complex of 2,6–bis(benzimidazol–2–yl)pyridine as artificial metallopeptidase which could bind with

histidine residues of domain III in BSA and catalyzed the site−specific protein cleavage under aerobic conditions.[330]

1.8. Present Investigation

1.8.1. Synthesis of ligands and metal complexes

Series of complexes using different transition metals like copper, zinc, cobalt and nickel were synthesized and characterized by different spectroscopic measurements namely IR, UV−visible, NMR and ESI−mass spectral techniques. Structures of representative complexes were authenticated using X−ray diffraction technique. Cyclic voltammetric experiments were performed over these complexes (excluding zinc) to investigate their redox properties. The ligands used to prepare the complexes are summarized in Scheme 1.25.

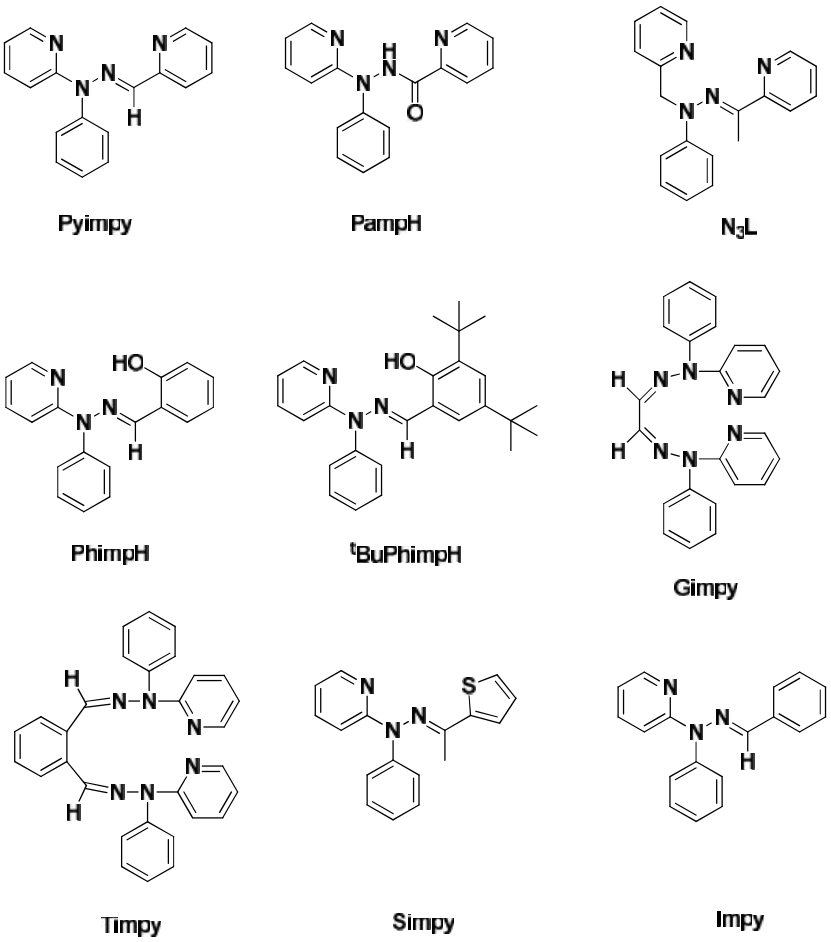

Scheme 1.25 Ligands used in the present thesis

Various types of biological activities including DNA interaction studies, nuclease activity, superoxide dismutase activity, phenoxyl radical generation, catecholase activity, protein interaction studies, protein cleavage activity and anticancer activity were also examined for these complexes. Many of the complexes exhibited excellent biological activities. The effect of donor atoms and ligand structure was explored using various types of ligands.

1.8.2. Description of activity studies

1.8.2.1. Generation of phenoxyl radical complexes: Relevance to galactose oxidase

Generation of a stable tyrosyl radical at the active site of galactose oxidase and glyoxal oxidase is the key step for their catalytic activity. To mimic these enzymes, we generated the phenoxyl radical complexes *in situ* through chemical oxidation of phenolato complexes by adding $(NH_4)_2[Ce^{IV}(NO_3)_6]$ (CAN) into a CH_3CN or DMF solution at different temperatures. The formation of the phenoxyl radical species was ascertained by the change in color, the characteristic bands in UV–visible spectra and EPR spectra of corresponding radical complexes. The decomposition of phenoxyl radical species with time was followed by UV−visible spectroscopy.

1.8.2.2. Superoxide dismutase activity

Dismutation of superoxide is a redox process hence electrochemical behaviour of all complexes was examined prior to investigate their SOD–like activity. For any model complex (M), the redox potential should fall in between one−electron reduction potential for oxygen (-0.16 V vs. NHE, -0.40 V vs. SCE, pH 7.0) and one−electron reduction potential of superoxide radical (0.89 V vs. NHE, 0.65 V vs. SCE, pH 7.0) in order to exhibit the SOD activity[331] i.e.

$$E_o\, O_2/O_2^- < E_o\, M^{(n+1)+}/M^{n+} < E_o\, O_2^-/O_2^{2-}$$

McCord–Fridovich (McCF) method was employed to determine the SOD activity of complexes which involves the enzymatic generation of superoxide radicals by xanthine/xanthine oxidase system in presence of cytochrome C (cyt c) or nitro blue tetrazolium (NBT) indicators.[331] The assay is based on the competition between SOD/SOD mimic and the redox active indicator for superoxide radicals.[331] In the experiments, steady state low levels of superoxide ions were maintained in the reaction medium using xanthine/xanthine oxidase system. The experiments were carried out in presence of a fixed concentration of nitro blue tetrazolium (NBT) indicator which gets reduced by superoxide ions and produces a blue formazan dye after reduction. Reduction of NBT was followed spectrophometrically by measuring its absorbance at 560 nm. The relative amounts of superoxide ions present in the reaction medium were estimated indirectly by measuring the concentration of reduced NBT produced by the reaction between superoxide ions and NBT. IC_{50} value of a compound for SOD activity has been described as the concentration of that particular compound required for 50% inhibition of NBT–reduction by superoxide ions.

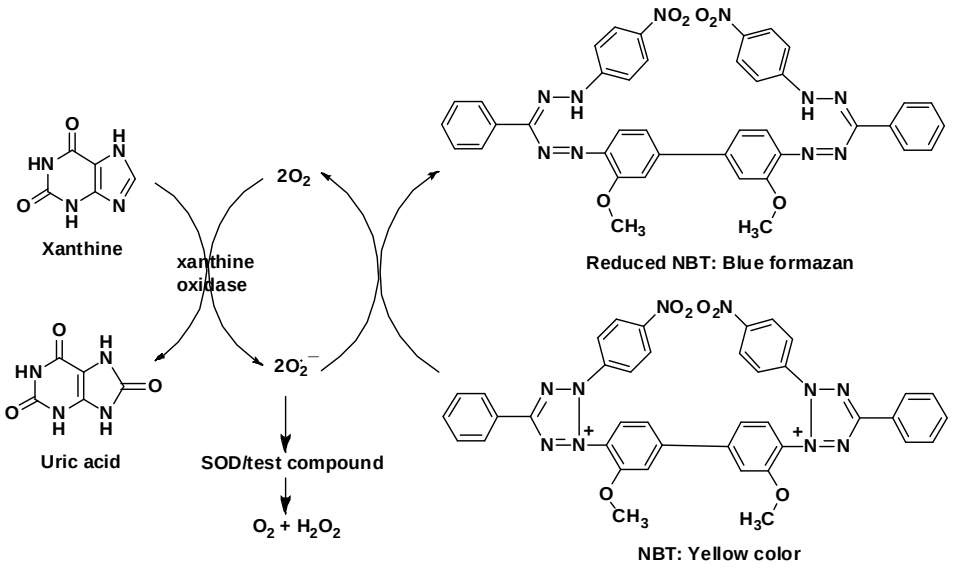

Scheme 1.26 Principle of SOD activity determination by NBT assay

1.8.2.3. DNA interaction studies

The mode of DNA interaction was investigated by absorption titration, fluorescence quenching and circular dichroism spectral studies. We performed DNA interaction studies in 0.1 M phosphate buffer (pH = 7.2) and sometimes dimethylformamide, methanol or actonitrile was added for better solubility of complexes. Stability of the complexes was investigated in phosphate buffer (pH = 7.2) for 6 h to 3 days, prior to begin the DNA interaction experiment. The DNA binding experiments were carried out in 0.1 M phosphate buffer (pH 7.2) using a solution of calf thymus DNA (CT–DNA) which showed the ratio of UV–visible absorbance at 260 and 280 nm (A_{260}/A_{280}) of *ca.* 1.8, indicating that the CT-DNA was sufficiently protein free.[332] The concentration of DNA solution was determined by measuring its absorbance at 260 nm and the extinction coefficient ε_{260} was taken as 6600 $M^{-1}cm^{-1}$ as reported in the literature.[332]

DNA interaction studies were investigated by absorbance titration experiments where a fixed concentration of complex was titrated with varying CTJDNA concentration in 0.1 M phosphate buffer (pH 7.2). The binding constants (K_b) were determined from a plot of [DNA]/($£_a - £_f$) vs. [DNA] using the equation:[332]

$$[DNA]/(£_a - £_f) = [DNA]/(£_b - £_f) + [K_b(£_a - £_b)]^{-1} \quad (1.1)$$

where [DNA] represents the concentration of DNA in base pairs. The apparent absorption coefficients $£_a$, $£_f$ and $£_b$ represent A_{obs}/[Complex], the extinction coefficient of free complexes and the extinction coefficient of complexes in fully bound form, respectively. The binding mode of metal complexes with CT–DNA can be predicted by observing the changes in the absorption spectra as well as the order of binding constant (K_b). Hypochromicity for charge transfer transition without bathochromic shift indicates interaction between the surface or

groove of DNA and metal complexes.[269,333-335] Hypochromicity accompanied with bathochromic shift shows the intercalative mode of binding.[336-338] Hyperchromicity predicts electrostatic interaction of metal complexes with DNA.[339,340] The binding constants (K_b) of various metal complexes follow the order – groove or surface binder < intercalator < metalloinsertor.[341]

In order to get better insight into the DNA binding event, competitive binding of ethidium bromide vs. test compounds with DNA was investigated using fluorescence spectroscopy. Ethidium bromide (EB) emits intense fluorescence in presence of DNA due to its strong intercalation between adjacent DNA−base pairs. Addition of complexes to the EB-DNA mixture may lead to the quenching of enhanced fluorescence of ethidium bromide indicating their competitive binding with DNA. Fluorescence quenching experiments were carried out by successive addition of complexes to the DNA (25 µM) solutions pretreated with 5−10 µM ethidium bromide (EB) in 0.1 M phosphate buffer (pH 7.2). The samples were excited at 250 nm and emissions were recorded within the range of 400−700 nm. Stern−Volmer quenching constants were calculated using equation 1.2.[332]

$$I_0/I = 1 + K_{sv}[Q] \qquad (1.2)$$

Where I_0 and I represent the emission intensities in the absence and presence of complex respectively and [Q] is the concentration of quencher (metal complex). K_{sv} is the linear SternJVolmer constant which is given by the ratio of slope to intercept in the plot of I_0/I versus [Q]. The order of SternJVolmer constant (K_{sv}) can predict the mode of binding with DNA and it follows the order: groove or surface binder < intercalator < metalloinsertor.

Circular dichroism (CD) spectroscopic technique is a sensitive and significant tool to monitor the conformational changes of DNA in solution. The CD spectrum of CT−DNA in

the range 225–300 nm exhibits one positive band at 278 nm due to base stacking and one negative band at 246 nm due to helicity.[332] To investigate the mode of DNA interaction by metal complexes, CD spectra of CT–DNA in absence and presence of complexes were recorded with a 0.1 cm pathJlength cuvette after 10 min incubation at 25 °C. The concentration of the complexes and CTJDNA were 50 and 200 μM respectively. The mode of interaction of metal complexes with DNA can be elucidated on the basis of change in molar ellipticity values and shifting in the position of positive and negative bands. No shift in the wavelengths of positive and negative bands indicates that the conformation of DNA remains largely unaltered after binding with the metal complex.

1.8.2.4. Nuclease activity

The cleavage of supercoiled (SC) plasmid DNA may give rise to nicked circular (NC) and linear circular (LC) forms which are separated on the basis of their sizes. However the relative migration rates of these three types also depend upon applied voltage, buffer concentration, agarose concentration and the amount of superhelical twists in DNA. The rate of migration is highest for the supercoiled form and lowest for the nicked form while the linear form runs in the middle. After electrophoresis, gel is stained with ethidium bromide and visualized using Gel–Doc system. The relative amounts of supercoiled, nicked and linear forms are determined by comparing the intensities of the individual bands.

Cleavage of plasmid DNA was monitored by agarose gel electrophoresis in TrisJboric acidJEDTA (TBE) buffer (pH = 8.4). Supercoiled pBR322 DNA was incubated with test complexes in 0.1 M phosphate buffer (pH = 7.2) at 37 °C for varying time periods. The oxidative DNA cleavage by complexes was studied in presence of varying concentrations of H_2O_2 (oxidizing agent) or 2Jmercaptoethanol (BME) (reducing agent).

To investigate the mechanism of nuclease activity, DNA cleavage experiments were carried out in presence of variety of standard radical scavengers and reaction inhibitors like DMSO, D_2O, ethanol, urea (20 mM), NaN_3 (20 mM), L–histidine (20 mM), catalase (10 U) and neocuproine (400 μM).[258,336,342,343] After incubation, the reaction was quenched by adding loading buffer (25% bromophenol blue and 30% glycerol) to each vial. Electrophoresis of the DNA cleavage products was performed in Tris–boric acid–EDTA (TBE) buffer at 60 V for 2 h over an agarose gel (0.8%) containing 0.4 μg/mL of ethidium bromide (EB). The fragments were identified by placing the stained gel under an illuminated UV lamp and photographed using Gel–documentation system.

1.8.2.5. Cell viability assay

Cell viability is the determination of living or dead cells, based on a total cell sample by treating cells with a cytotoxic compound. The cells may undergo necrosis, in which they lose membrane integrity and die rapidly as a result of cell lysis. The cells can stop actively growing and dividing (a decrease in cell viability), or the cells can activate a genetic program of controlled cell death (apoptosis). Cytotoxicity can be monitored using the MTT ((3–(4, 5–dimethylthiazol–2–yl)–2, 5–diphenyltetrazoliumbromide), a yellow tetrazole) assay. This assay measures the reducing potential of the cell using a colorimetric reaction. Viable cells will reduce the yellow MTT reagent to formazan dye of purple color. The absorbance of this colored solution can be quantified by measuring at a certain wavelength (usually between 500 and 600 nm) by a spectrophotometer. This reduction takes place only when mitochondrial reductase enzymes are active and therefore conversion can be directly related to the number of viable cells. When the amount of purple formazan produced by cells treated with an agent is compared with the amount of formazan produced by untreated control cells, the effectiveness of the agent in causing death of the cell can be calculated.

MTT assay was carried out according to the procedure described by Mosmann et al.[344] using COS, DU–45, C127–I, MCF–7 and C3H10T1/2 cell lines. 5–Fluorouracil was used as a positive anticancer drug in this experiment. The cells were maintained in tissue culture plate in DMEM supplemented with 10% fetal bovine serum (FBS), 1× antibiotic–antimycotic solution and 2 mM glutamine at 37°C in humidified atmosphere in a CO_2 incubator. During all the experiments the cells were within passage number about 12–20 for all cell lines except COS–1 which was in its 30–35 passage. In brief, 5×10^3 cells in 200 µL of medium were seeded in 96–well plates (Griener, Germany) and grown under normal conditions. Serial dilutions of all compounds initially ranging from 0–100 µM in DMSO were added to the monolayer in triplicates. The final DMSO concentration used for all dilutions was 0.1% which was used as vehicle control. Cultures were assayed after 24 h by the addition of 0.5 mg/mL MTT and incubating for 4 h at 37 °C. The MTTJcontaining medium was aspirated and 200 µL of DMSO and 25 µL of Sorensen glycine buffer (0.1 M glycine and 0.1 M NaCl, pH 10.5) were added to lyse the cells and solubilize the water insoluble formazan. Absorbance values of the lysates were determined on a Fluostar optima (BMG Labtech, Germany) microplate reader at 570 nm. The percentage inhibition was calculated as:

$$\frac{\text{Mean OD of vehicle treated cells – mean OD of treated cells}}{\text{Mean OD of vehicle treated cells}} \times 100$$

The IC_{50} values were calculated using graph pad prism, version 5.02 software.

1.8.2.6. Protein interaction studies

The mode of protein interaction was investigated by absorption spectral studies, tryptophan intrinsic fluorescence quenching experiments and circular dichroism spectral studies using BSA as the model protein substrates. The stock solutions of BSA were prepared by dissolving solid BSA (1×10^{-4} mol L^{-1}) in 0.1 M phosphate buffer at pH 7.2 and stored at

0–4 °C for three days under dark conditions and then diluting with 0.1 M phosphate buffer (pH 7.2) to the desired concentration. The concentration of protein solution was determined from the absorption spectral data using the molar absorptivity value of ε_{280} = 44720 for BSA.[345]

Intrinsic fluorescence of protein molecules is due to the aromatic amino acid residues *viz.* tryptophan, tyrosine and phenylalanine. The tryptophan resiudes can be excited solely at 295 nm whereas at 280 nm both tyrosine and tryptophan residues are excited. Binding behaviour of proteins can be investigated by monitoring the changes in wavelength of emission maximum (λ_{ex}) at 340 nm along with the change in the emission intensity.[346] Quenching of the intrinsic fluorescence of tryptophan residues in BSA was carried out using metal complexes as quencher molecules. BSA solution (2×10^{-6} M) in 0.1 M phosphate buffer (pH 7.2) with 2% DMF was equilibrated for 30 min at room temperature and the emission spectrum was recorded between 300 and 600 nm using the excitation wavelength of 295 nm, exclusively for tryptophan residues.[346] Incremental additions of the quenchers were made to the BSA solution followed by an incubation period of 2 min after each successive addition and spectra were recorded. Binding behaviour of the quencher molecules with serum albumins was compared using Stern–Volmer and Scatchard graphs.[347] The Stern–Volmer equation is represented as

$$F_0/F = 1 + K_q \tau_0 [Q] = 1 + K_{sv} [Q] \qquad (1.3)$$

where F_0 and F represent the emission intensity of serum albumin before and after the addition of quenchers respectively, K_q is the quenching rate constant and τ_0 denotes the average life–time of BSA without quencher (~10^{-8} s), K_{sv} represents the Stern–Volmer quenching constant and [Q] is the concentration of quencher.

The Scatchard equation may be represented as[348]

$$\log (F_0\text{-}F)/F = \log K + n \log [Q] \quad (1.4)$$

where F_0 and F represent the emission intensity of serum albumin before and after the addition of quenchers respectively, K is the association binding constant and n is the number of binding sites per albumin molecule. Scatchard plots were given as double logarithm regression curve of log $(F_0\text{-}F)/F$ vs. log [Q] and the values of K and n were calculated by the intercept and slope of these curves respectively.

CD spectroscopic technique can be successfully employed to probe the conformational changes in the secondary structure of proteins induced by interactions with small molecules. Typical CD spectroscopic signals of BSA include one double humped negative band and one positive band within the region of 190–260 nm which represent the α–helical structure of albumin. Circular dichroism (CD) spectra of BSA in absence and presence of metal complexes were recorded with a 0.1 cm path length cuvette after 15 min incubation at 25 °C with three scans averaged for each CD spectrum. The concentrations of the complexes and BSA were 10 μM and 1 μM respectively.

1.8.2.7. Protein cleavage studies

Protein cleavage experiments were carried out by incubating BSA (15 μM) with test compounds (10–100 μM) in 10% DMF: 1 M HEPES buffer at pH 7.2 for 20 h at 50 °C. In order to identify the role of ROS in protein scission, standard radical scavengers like DMSO (20%), glycerol (20%), NaN_3 (20 mM) and catalase (10 U) were introduced. After the completion of the incubation period, an aliquot was mixed with loading buffer (100 mM Tris–HCl (pH 6.8), 4% (w/v) sodium dodecyl sulphate (SDS), 20% (v/v) glycerol, 200 mM dithiothreitol (DTT) and 0.2% (w/v) bromophenol blue) and the protein solutions were then

denatured by heating to boil for 3 min. Incubated protein samples were then subjected to a discontinuous SDS–PAGE (having 2% acrylamide for the stacking gel and 10% acrylamide for the separation gel) in a Genei vertical gel electrophoresis apparatus. The electrophoresis was performed at 50 V for stacking gel and 100 V for separation gel. Coomassie Brilliant Blue R–250 solution was used for staining the gels which were subsequently destained with a water/methanol/acetic acid (1:5:4) mixture for 3 h. The gels, after destaining, were scanned with gel–documentation system and images were reproduced without further processing.

1.8.2.8. Catecholase activity

The catecholase activity of the complexes was evaluated by the catalytic oxidation of 3,5–DTBC. 3,5–DTBC is widely used as a model substrate for catecholase activity due to its low redox potential which facilitates its oxidation to quinone and its bulky substituents rendering the further oxidation reactions slower.[256] The reactions were initiated by treating the test compounds (~10^{-5} M solutions) with 100 equiv of 3,5–DTBC in dioxygen saturated methanol at 25 °C and time–dependent changes were monitored by UV–visible spectroscopy. The progress of the oxidation reaction was demonstrated by gradual increment in the intensity of absorption band near 400 nm (ε = 1900 $M^{-1}cm^{-1}$) due to the formation of 3,5–DTBQ. The material, reagents, synthetic procedures and experimental details for complexes will be described in the respective chapters.

1.8.3. Summary of present investigation

The **First chapter** presents an introduction to coordination chemistry of various types of ligands as well as to the general properties of few first row transition metals. Role of ligand to determine the chemical properties and biological activities of various coordination complexes is thoroughly discussed. A number of ligands were discussed which were used for the structural/functional mimicking of the active sites of various metalloenzymes. Continuous

efforts have been made by several research groups to develop economical and potential catalysts for organic and organometallic synthesis mainly derived from the first row metals. An account of such attempts will be made in the first chapter of the thesis emphasizing the role of the ligands. The various chemical methods and spectroscopic techniques used were comprehensively summarized in this chapter.

In **chapter two**, we have described the synthesis and characterization of mononuclear cobalt complexes namely $[Co(Pyimpy)Cl_2]$ (**1a**), $[Co(Pyimpy)_2](ClO_4)_2$ (**1b**), $[Co(Pamp)Cl_2]$ (**2a**) and $[Co(Pamp)_2](ClO_4)$ (**2b**) (where Pyimpy = 1−phenyl−1−(pyridin−2−yl)−2−(pyridin−2−ylmethylene)hydrazine; PampH = N'−phenyl−N'−(pyridin−2−yl)picolinohydrazide and H stands for the dissociable proton). All the complexes were characterized by elemental analysis, conductivity measurements, IR, electronic absorption spectral and NMR spectroscopic methods as well as ESI−mass spectrometry. The spin−state of the complexes was determined by magnetic moment measurements. The molecular structure of complex **1a** was authenticated using X−ray diffraction study. Redox behavior of the metal complexes was investigated through electrochemical methods. DNA interaction studies over all the complexes were performed using absorption spectral technique, emission spectroscopy and circular dichroic methods. Investigation of DNA cleavage activity was accomplished in presence of activators and the mechanism was established using various types of scavengers. Superoxide dismutase (SOD) activity of the complexes was assayed by xanthine/xanthine oxidase/nitroblue tetrazolium assay and a correlation was developed with the DNA cleavage activity.

Chapter three describes the synthesis and characterization of a tridentate ligand N_3L (where N_3L=2−((1−phenyl−2−(1−(pyridin−2−yl)ethylidene)hydrazinyl)methyl)pyridine) and its mononuclear metal complexes of copper, zinc, cobalt and nickel namely $[Cu(N_3L)Cl_2]$

(**3a**), $[Cu(N_3L)_2](ClO_4)_2$ (**3b**), $[Zn(N_3L)Cl_2]$ (**4a**), $[Zn(N_3L)_2](ClO_4)_2$ (**4b**), $[Co(N_3L)Cl_2]$ (**5a**), $[Co(N_3L)_2](ClO_4)_2$ (**5b**), $[Ni(N_3L)Cl_2]$ (**6a**) and $[Ni(N_3L)_2](ClO_4)_2$ (**6b**) respectively. All the complexes were characterized using the standard spectroscopic methods. The structures of complexes **3a** and **5a** were established by X-ray diffraction methods. Cyclic voltammetric experiments were performed to examine the redox properties of the metal complexes. All the complexes were found to be stable in the buffer solutions at physiological pH and subjected to DNA interaction studies by absorption spectroscopy, emission spectroscopy and circular dichroism spectroscopy. The complexes represent the rare kind of complexes which bind covalently with nucleic acids and the mechanism has been established by titration with potential small ligands using absorption spectral technique. The complexes were investigated for their capability to cleave DNA in absence and presence of external agents and the mechanism was determined using inhibition experiments involving radical scavengers. Binding of these complexes with albumin namely, Bovine serum albumin (BSA) was investigated using UV–visible and fluorescence spectroscopy as well as by circular dichroic method. The mechanism of binding with protein was explored by the titration of these complexes with amino acids using electronic absorption spectroscopy and a covalent attachment of metal complexes with the amino acids side chains was observed. Various constants were calculated to compare the DNA binding affinity as well as protein binding propensity of all the complexes. The family represents novel examples of complexes which are still less explored and highly desirable for *in vivo* applications.

In **chapter four**, two mononuclear cobalt complexes namely $[Co(Phimp)_2](ClO_4)\cdot CH_3CN$ (**7**·CH_3CN) and $[Co(^tBuPhimp)_2](ClO_4)$ (**8**) derived from tridentate ligands PhimpH and ^{t}BuPhimpH (PhimpH = 2–((2–phenyl–2–(pyridin–2–yl)hydrazono)methyl)phenol and ^{t}BuPhimpH =

2,4–di–*tert*–butyl–6–((2–phenyl–2–(pyridin–2–yl)hydrazono)methyl)phenol where H stands for the dissociable proton) were synthesized. The resultant complexes were characterized by elemental analysis, conductivity measurements, IR, UV–visible and NMR spectral studies and ESI–mass spectrometric technique. X–ray crystallographic studies were performed to determine the molecular structure of the representative complex **7**·CH_3CN. These complexes gave rise to the phenoxyl radical species in solution in presence of external oxidizing agents due to the non–innocent character of the ligands. Such species are very much significant to understand the mechanism of galactose oxidase enzyme. Generation of phenoxyl radical species was confirmed by UV–visible and EPR spectroscopy. Cyclic voltammetric experiments indicated the ligand centered oxidation and stabilization of the resulting species by the introduction of tertiary–butyl groups in the ligand frame. The complexes were subjected to DNA cleavage activity and the complex **8** was found to be very efficient for DNA cleavage leading to extensive DNA degradation. Protein interaction studies of these complexes were performed by tryptophan fluorescence quenching assay using BSA as a protein model. Protease activity of both complexes was scrutinized and complex **8** was found to be efficient in protein cleavage also. The anticancer activities of these complexes were also studied against various cell lines and promising results were obtained for complex **8**.

In **chapter five**, the synthesis of nickel complexes $[Ni(Phimp)_2]\cdot 3H_2O\cdot CH_3OH$ (**9a**·$3H_2O\cdot CH_3OH$), [Ni(Phimp)Cl] (**9b**), $[Ni(Phimp)(Pyimpy)](ClO_4)\cdot H_2O$ (**9c**·H_2O), $[Ni(^tBuPhimp)_2]$ (**10a**), [Ni(^{t}BuPhimp)Cl] (**10b**), and $[Ni(^tBuPhimp)(Pyimpy)](ClO_4)$ (**10c**) was described. All the complexes were characterized using the standard spectroscopic methods. The molecular structures of the complexes **9a**·$3H_2O\cdot CH_3OH$ and **9c**·H_2O were determined using X–ray diffraction methods. The redox behavior of these complexes was investigated using cyclic voltammetry. The ability of the complexes to generate phenoxyl

radical species in solution by chemical oxidation was investigated. DNA and protein interaction studies of these complexes were accomplished in this chapter. Nuclease activity of these complexes and its mechanism was also investigated.

In **chapter six**, the fluorescence properties of two ligands Gimpy and Timpy (where Gimpy = 1,2–bis(2–phenyl–2–(pyridin–2–yl)hydrozono)ethane and Timpy = 1,2–bis((2–phenyl–2–(pyridin–2–yl)hydrozono)methyl)benzene) were examined in presence of various transition metal ions in solution and enhancement in fluorescence was observed in presence of Ni^{2+}. To confirm the binding mode of these ligands, nickel complexes of these ligands namely $[(Ni(Gimpy)(\mu–Cl))_2](ClO_4)_2$ (**11**) and $[(Ni(Timpy)(\mu–Cl))_2](ClO_4)_2\cdot 2(CH_3)_2CO$ (**12**$\cdot 2(CH_3)_2CO$) were synthesized. These complexes were characterized by elemental analysis, conductivity measurements, electronic absorption, ESI–MS and IR spectral studies. Cyclic voltammetric experiments were performed to investigate the redox behavior of these complexes. Molecular structures of Gimpy and complex **12** were determined using X–ray crystallography.

Chapter seven presents the synthesis of dinuclear copper and cobalt complexes namely $[\{Cu(Simpy)(\mu–Cl)Cl\}_2]\cdot 4H_2O$ (**13a**$\cdot 4H_2O$), $[\{Co(Simpy)(\mu–Cl)Cl\}_2]$ (**13b**), $[\{Cu(Impy)(\mu–Cl)Cl\}_2]$ (**14a**) and $[\{Co(Impy)(\mu–Cl)Cl\}_2]$ (**14b**) derived from two bindentate ligands Simpy and Impy (Simpy = 2–(1–phenyl–2–(1–(thiophen–2–yl)ethylidene)hydrazinyl)pyridine and Impy = 2–(2–benzylidene–1–phenylhydrazinyl)pyridine). We have characterized these complexes by elemental analysis, conductivity measurements, IR and UV–visible spectroscopy, and ESI–Mass spectrometric method. Molecular structures of complexes **13**$\cdot 4H_2O$ and **14** were

authenticated using X–ray diffraction studies. The complexes were examined for the catecholase activity as well as DNA cleavage activity.

1.9. Measurements

Several physical and spectroscopic techniques have been utilized for the characterization of synthesized compounds and investigation of their properties which have been described in detail in the subsequent chapters. These are briefly described below.

(i) Elemental analyses

The measurements of the C, H, N contents of the samples were carried out with the help of Elementar Vario EL III elemental analyser which utilizes thermal conductivity data for gas (CO_2, H_2O, N_2) analysis.

(ii) Infrared spectroscopy

IR spectra were recorded as KBr pellets with Thermo Nikolet Nexus FT–IR spectrometer, using 16 scans and reported in cm^{-1}.

(iii) Mass spectrometry

Electro–Spray Ionization (ESI) mass spectra of the complexes were recorded as acetonitrile solutions under positive or negative ion mode with the help of a Bruker MicroTOF–QII mass spectrometer.

(iv) NMR spectroscopy

^{1}H and ^{13}C NMR spectra were recorded on Bruker AVANCE, 500.13 MHz spectrometer. The chemical shifts for all NMR spectra were related to internal standard Me_4Si for all residual protium in the deutrated solvents.

(v) EPR spectroscopy

EPR measurements (CW XJband (9.4 GHz)) were carried out with a Bruker Elexsys E500 series using the Bruker ER4122 SHQE cavity. The spectra at 120 K were recorded with an Oxford ESR900 helium continuous flow cryostat. All spectra were recorded with 0.5 mT modulation amplitude and 2 mW powers.

(vi) Conductometer

Molar conductivities were determined in DMF and acetonitrile solutions (at 10^{-3} M) at 25 °C with a Systronics 304 conductometer.

(vii) Magnetic moment

Magnetic susceptibilities were determined at room temperature with Vibrating Sample Magnetometer model 155, using nickel as a standard. Diamagnetic corrections were carried out with Pascal's increments.[349]

(viii) SQUID magnetometer

SQUID magnetic measurements were carried out on crystalline samples with a Quantum Design MPMS XL SQUID magnetometer at temperature ranging from 3 to 300 K under an applied magnetic field of 5000 G.

(ix) UVJVisible spectrophotometer

Electronic absorption spectra were recorded in phosphate buffer (pH = 7.2), acetonitrile and methanol as solvents with a SHIMADZU, UV–2450 UV–visible spectrophotometer. For better solubility, 5–10% DMF was used when spectra were recorded in phosphate buffer. A matched pair of quartz cell of path length 1 cm was used.

(x) Fluorescence spectrophotometer

Emission spectra were recorded with SHIMADZU, RF−5301 PC spectrofluorophotometer. Solution preparations were same as those for electronic spectral experiments.

(xi) Circular dichroism

Circular dichroism spectra of DNA and BSA were obtained by using a Chirascan circular dichroism spectrometer operating at 25 ^{o}C. The regions 220−320 nm and 190−260 nm were scanned using a cuvette of 1 mm path length to obtain the spectra of DNA and BSA respectively. The complexes were incubated with CT DNA and BSA for 10 min in phosphate buffer (pH = 7.2). Due to the lesser solubility of some complexes in buffer, 5−10 % of methanol was used.

(xii) Cyclic voltammetry

Cyclic voltammetry measurements were performed in different solvents such as DMF, dichloromethane and acetonitrile using a CH−600C electroanalyzer with a conventional three−electrode arrangement consisting of Ag(s)/AgCl electrode as reference electrode, glassy carbon as working electrode and platinum wire as auxiliary electrode. Tetrabutylammonium perchlorate (TBAP) (0.1 M) was used as the supporting electrolyte and complex concentration of 10^{-3} M was used for experiments. All experiments were performed at room temperature. Solutions were thoroughly degassed with nitrogen prior to begin the experiments, and nitrogen atmosphere was maintained during the measurements. The $E_{1/2}$ (aE) values for ferrocene/ferrocenium couple vs. Ag/AgCl were determined under the same experimental conditions which were found to be +0.420 V (0.075 V), +0.509 V (0.125 V) and +0.498 V (0.090 V) in acetonitrile, dichloromethane and dimethylformamide respectively.

(xiii) XJRay structure determination

The X–ray data collection and processing for ligands and complexes were performed on Bruker Kappa Apex–II CCD diffractometer by using graphite monochromated Mo–Kα radiation (λ = 0.71070 Å). Crystal structures were solved by direct methods. Structure solution, refinement and data output were carried out with the SHELXTL program.[350,351] All non–hydrogen atoms were refined anisotropically. Hydrogen atoms were placed in geometrically calculated positions and refined using a riding model. Images were created with DIAMOND and MERCURY programs.[352-353]

R1, *wR2* and goodness–of–fit (GOF) are expressed by following equations respectively.

$$R1 = \Sigma \| F_o | - | F_c \| / \Sigma F_o | \quad (1.5)$$

$$wR2 = [\Sigma[w(F_o^2 - F_c^2)^2] / \Sigma[w(F_o^2)^2]]^{1/2} \quad (1.6)$$

$$^{a}GOF = [\Sigma[w(F_o^2 - F_c^2)^2] / M - N)]^{1/2} \quad (1.7)$$

where, M = number of reflections, N = number of parameters refined

Specific details for each compound will be given in the concerned chapter.

(xiv) Gel documentation

DNA fragments were identified by placing the gel under an illuminated UV lamp and photographed by using gel documentation system (BIO RAD).

(xv) Chemical and solvents

The chemicals and solvents used were analytical grade and most of thm were used as obtained. The standard purification methods were followed wherever required.

2.1. Introduction

In the recent years, artificial DNA binding and cleaving agents have been a subject of tremendous interest due to their potential applications in gene regulation, mapping of proteins, probing of DNA specific structures and cancer therapy.[136,271] *cis*–Diamminedichloroplatinum(II) (*cis*–platin) is one of the most effective chemotherapeutic agents used to cure various types of cancers like testicular cancer, ovarian cancer, oropharyngeal carcinoma, cervical carcinoma, lymphoma, osteosarcoma, bladder carcinoma, neuroblastoma and melanoma.[354] In spite of its efficiency in the treatment of cancers, *cis*Jplatin also exhibits some serious side effects such as nephrotoxicity, neurotoxicity, bone marrow suppression and emetogenesis.[354] Moreover some tumors can acquire immunity against *cis*–platin. This led to the discovery of new platinum based anticancer drugs like carboplatin, oxaliplatin, nedaplatin, lobaplatin and heptaplatin which have also been used clinically.[354] Considerable efforts have been made to develop anticancer agents from first row transition elements due to their lesser toxicity and in this regard, copper and iron got much attention. Copper possesses high affinity for nucleobases and exhibits biologically accessible redox properties.[293,355] Iron–bleomycin causes DNA damage and clinically used for cancer treatment.[356,357] Several iron complexes are known to exhibit DNA interaction and nuclease activity.[358-360] On the other–hand cobalt, a constituent of vitamin B_{12} and one of the essential elements in biosystem[4] received less attention.[361-363] Several cobalt polypyridyl complexes have been investigated for DNA interaction and nuclease activity studies[280-282,286,287,364-370] however, reports for oxidative cleavages are few.[286,287,371-374] In the present study, we have explored the coordination chemistry of cobalt because it possesses several interesting properties. First, usual oxidation states of +2 and +3 in cobalt complexes

give rise to kinetically labile and kinetically inert complexes respectively.[26-28] Second, cobalt(III) is a strong Lewis acid and exhibits ligand exchange properties. Third, Co(III) has important role in catalytic hydrolysis of phosphate esters.[277] Hettich and co−workers reported that Co(III) complexes are known to be most effective catalysts for hydrolytic cleavage of amides, esters and phosphates.[138] Fourth, cobalt ion is present in natural nucleases [28,33,275,276] or sometimes required for the activity of nucleases[277,375-378]. There are reports that substitution of zinc by cobalt in several nucleases may result the enhancement of the enzyme activity.[33] Fifth, DNA cleaving properties of cobalt complexes are sometimes similar to ruthenium complexes.[361] Moreover, antiproliferative activity of the cobalt complexes was determined in MCF−7 and MDA−MB−231 human breast cancer cells and very promising results were obtained.[379]

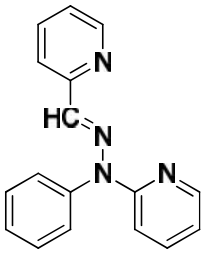

Pyimpy

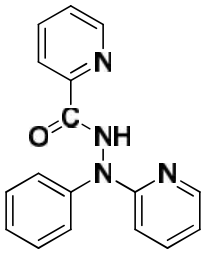

PampH

Scheme 2.1 Schematic drawing of ligand Pyimpy and PampH

Hence, in this chapter we have synthesized and characterized a series of cobalt complexes with two meridional tridentate ligands, namely Pyimpy and PampH (Scheme 2.1). Molecular structure of the representative complex [Co(Pyimpy)Cl_2] (**1a**) was determined by X−ray crystallography. Structures of the complexes derived from PampH were established by NMR spectroscopy. Redox properties of the complexes were examined by cyclic voltammetric experiments. Superoxide dismutase (SOD) activity of the complexes

was assayed by xanthine/xanthine oxidase/nitroblue tetrazolium assay. Numerous small molecule SOD mimics are known in the literature which can exhibit excellent antitumor activity and can serve as potential anticancer agents.[380] This prompted us to investigate the DNA interaction properties of these complexes by various spectroscopic techniques along with their nuclease activity studies. The mechanism of the nuclease activity was also examined in presence of various radical scavengers. In this chapter, the necessity of a redox–active metal centre for superoxide scavenging as well as nuclease activity of complexes was scrutinized in the light of some reported results.

2.2. Results and discussion

2.2.1. Synthesis and characterization of the ligands

The ligand Pyimpy was obtained by condensation reaction between a 1:1 mixture of 2–(1–phenylhydrazinyl)pyridine and pyridine–2–aldehyde in methanolic solution following a reported procedure.[381] Synthetic scheme representing the synthesis of ligand Pyimpy is shown in Scheme 2.2.

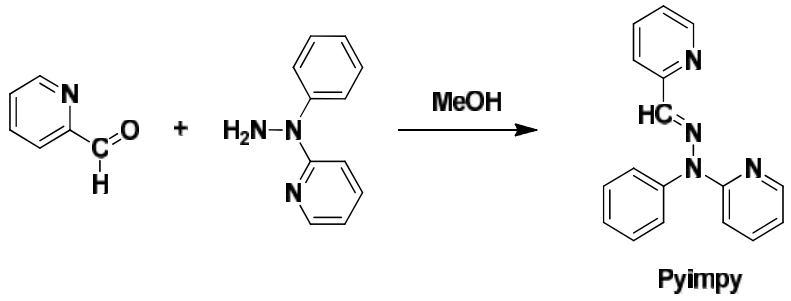

Scheme 2.2 Schematic representation of synthesis of ligand Pyimpy

The ligand PampH (H stands for dissociable hydrogen atom) was prepared by condensation reaction between a 1:1 mixture of 2–(1–phenylhydrazinyl)pyridine and

picolinic acid in dimethylformamide solution following a reported procedure.[381] Synthetic scheme representing the synthesis of ligand Pyimpy is shown in Scheme 2.3.

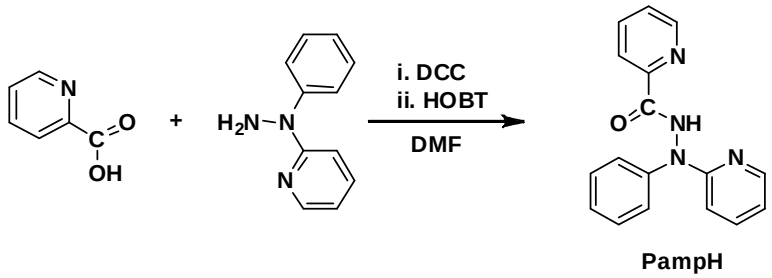

Scheme 2.3 Schematic representation of synthesis of ligand PampH

We want to mention here that both the ligands chosen for the study in this chapter are exactly similar except having only one difference. Pyimpy is having an imine nitrogen (soft donor atom) along with two pyridine nitrogen donors whereas PampH possesses a carboxamide nitrogen donor (hard donor atom) with two pyridyl nitrogens available for coordination.

2.2.2. Synthesis and characterization of cobalt complexes

Complexes $[Co(Pyimpy)Cl_2]$ (**1a**) and $[Co(Pyimpy)_2](ClO_4)_2$ (**1b**) were synthesized by the reaction of $CoCl_2.6H_2O$ and ligand Pyimpy in 1:1 and 1:2 molar ratio respectively. Complexes $[Co(Pamp)Cl_2]$ (**2a**) and $[Co(Pamp)_2](ClO_4)$ (**2b**) were synthesized by two different methods. Complex **2a** was isolated as green solid by the reaction of deprotonated ligand with $CoCl_2{\cdot}6H_2O$ (1:1) in aerobic conditions. The reaction gave rise to the oxidation of metal centre indicating the coordination of carboxamido nitrogen to the metal centre because deprotonated carboxamide nitrogen stabilizes higher oxidation state of metal ions[382,383] and oxygen acts as oxidizing agent during such reactions. This was also supported by spectroscopic and electrochemical studies (*vide infra*). Complex $[Co(Pamp)_2](ClO_4)$ (**2b**)

was prepared by the reaction of deprotonated ligand with $CoCl_2 \cdot 6H_2O$ (2:1) in aerobic conditions. Brown coloured microcrystalline complex was isolated and characterized (described in method A). It is important to note here that the reaction of $CoCl_2 \cdot 6H_2O$ and PampH also afforded complexes **2a** and **2b** in presence of air (described in method B). These data indicated that under aerobic conditions, cobalt ion was efficient in deprotonating the ligand due to its Lewis acidity. We may or may not need a deprotonating agent (sodium hydride here) for the deprotonation of amide nitrogen for the synthesis of complexes **2a** and **2b**.[383,384] All the complexes were synthesized in good yields (50–80%). The synthetic procedures of complexes are summarized in Scheme 2.4.

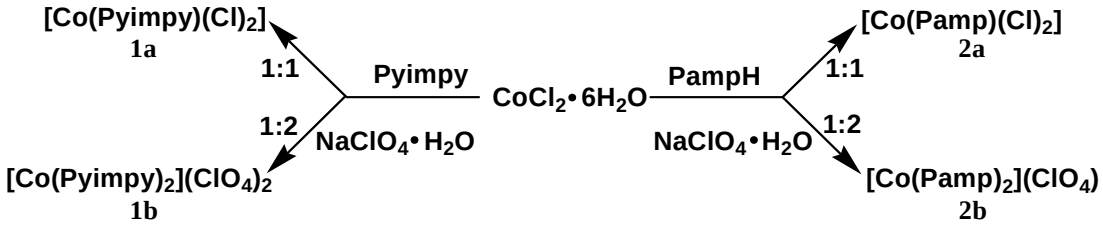

Scheme 2.4 Schematic drawing of synthesis of complexes **1–2**

Table 2.1 Data for yield, elemental analysis, IR, conductivity and magnetic moment

Complex	Yield %	Elemental analysis			IR data (cm^{-1})[a]	Conductivity i_M (t^- $^1cm^2mol^{-1}$)[b]	Magnetic moment (μ_B)
		C	H	N	¬C=N		
1a	81	50.29	3.62	13.93	1596	17 (neutral)	4.60
1b	59	50.45	3.56	13.85	1599, 1088, 625	141 (1:2)	4.54
2a	54	48.32	3.34	13.52	1655	30 (neutral)	-
2b	82	55.14	3.79	15.16	1655, 1096, 623	60 (1:1)	-

[a]KBr pellets, [b]Solvent: dimethylformamide

(i) IR spectral studies

In complexes **1a** and **1b**, coordination of azomethine nitrogen was supported by shifting of ¬$_{C=N}$ to higher frequencies by 18–21 cm^{-1} as compared to those of free ligands (1578 cm^{-1}) in IR spectra.[385] Complexes **2a** and **2b** afforded the carbonyl stretching frequency ¬$_{C=O}$ nearly 1655 cm^{-1}. The decrease in the carbonyl stretching frequencies as compared to free ligand by 40 cm^{-1} clearly expressed the coordination of carboxamido nitrogen. The disappearance of the peak at 3354 cm^{-1} which was assigned to be N–H stretching frequency in PampH as well as shifting of $\nu_{C=O}$ to lower wavenumbers indicated its coordination in the deprotonated form.[386] Complex **1b** and **2b** showed IR bands near 1092 cm^{-1} and 1096 cm^{-1} respectively, together with band near 625 cm^{-1}. These data suggested the presence of non–coordinated perchlorate ion in **1b** and **2b**.[332]

(ii) Electronic properties

Intense absorption bands were observed in the UV–visible spectra of all cobalt complexes between 200–250 nm region. These bands were assigned as π–π* intraligand transitions (Fig. 2.1, Table 2.2).

Table 2.2 UV–visible spectral data of complexes **1–2**

Complex	$^{a}\lambda_{max}$/nm (£/M^{-1}cm^{-1})[a]
1a	204 (29400), 230 (12360), 249 (10340), 278 (8040), 359 (13160), 458 (206)
1b	206 (49200), 230 (30540), 249 sh (24540), 291 (19760), 358 (29400), 461 (600)
2a	208 (48400), 242 (19380), 267 (14800), 394 (12900), 512 (392)
2b	214 (71580), 240 (42680), 264 (33300), 398 (22000), 512 (800)

[a]UV–visible data recorded in methanol

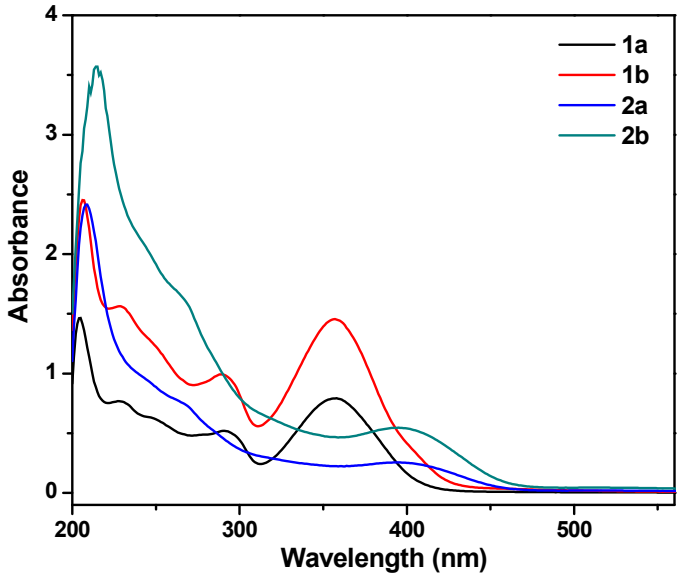

Fig. 2.1 UV–visible spectra of complexes **1–2** (50 μM) in methanol

The absorption bands in the range 358–398 nm found in UV–vis spectra of all complexes in methanol were accompanied with high molar extinction coefficient values which suggested that these bands were of charge transfer type (Fig. 2.1, Table 2.2).

(iii) NMR spectroscopy

The structures of the complexes **2a** and **2b** were established by ^{1}H and ^{13}C NMR spectral studies. The ^{1}H and ^{13}C NMR spectra of complexes **2a** and **2b** are illustrated in Fig. 2.2–2.3 and Fig. 2.4–2.5 respectively. These spectra suggested that the complexes **2a** and **2b** are diamagnetic in nature and give rise to Co^{3+} low spin complexes.

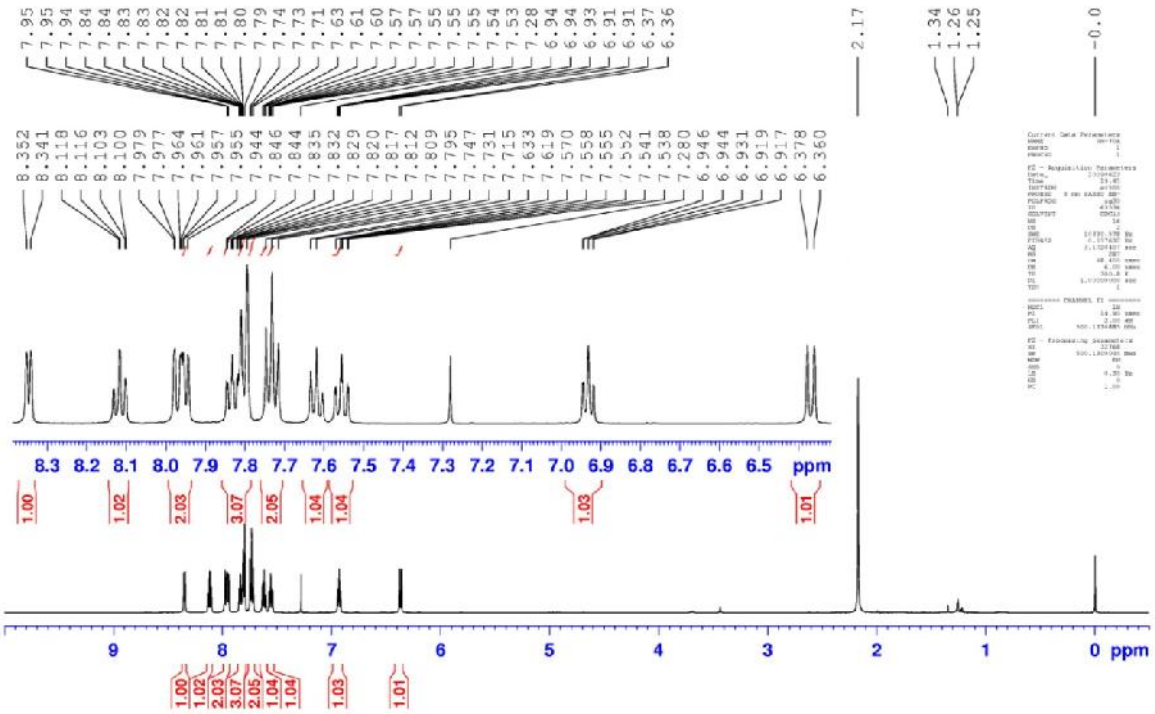

Fig. 2.2 ^{1}H NMR spectrum of complex **2a** in $CDCl_3$

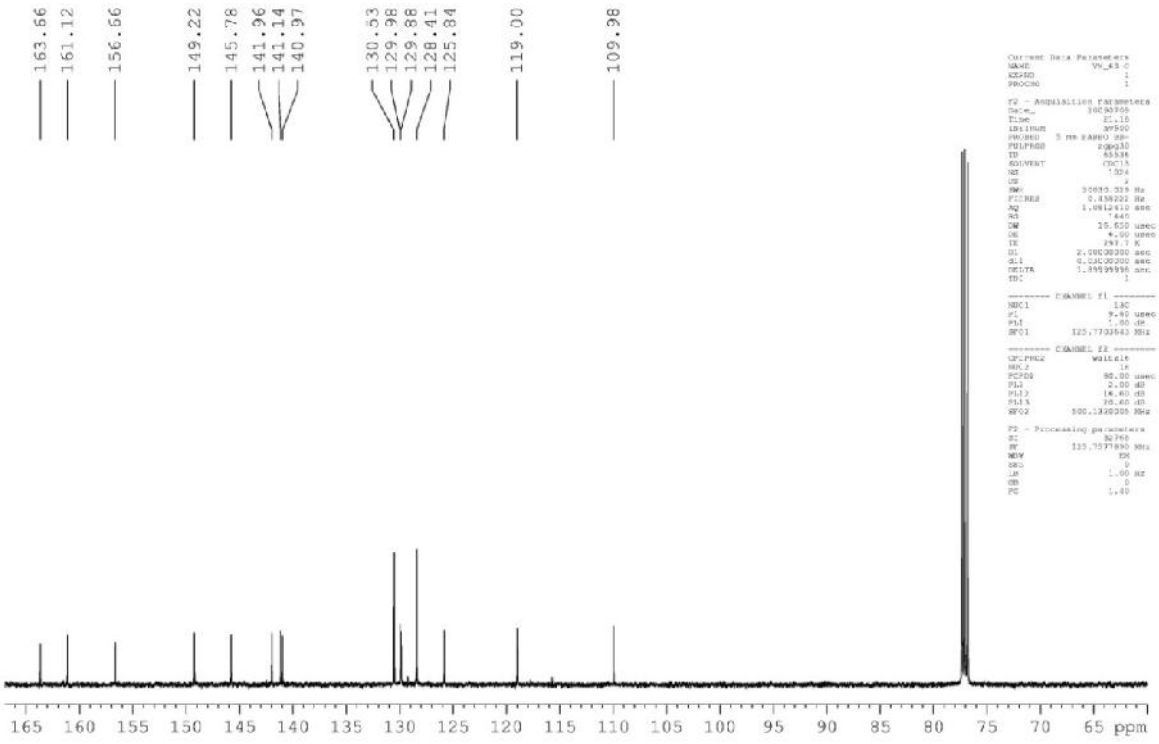

Fig. 2.3 ^{13}C NMR spectrum of complex **2a** in $CDCl_3$

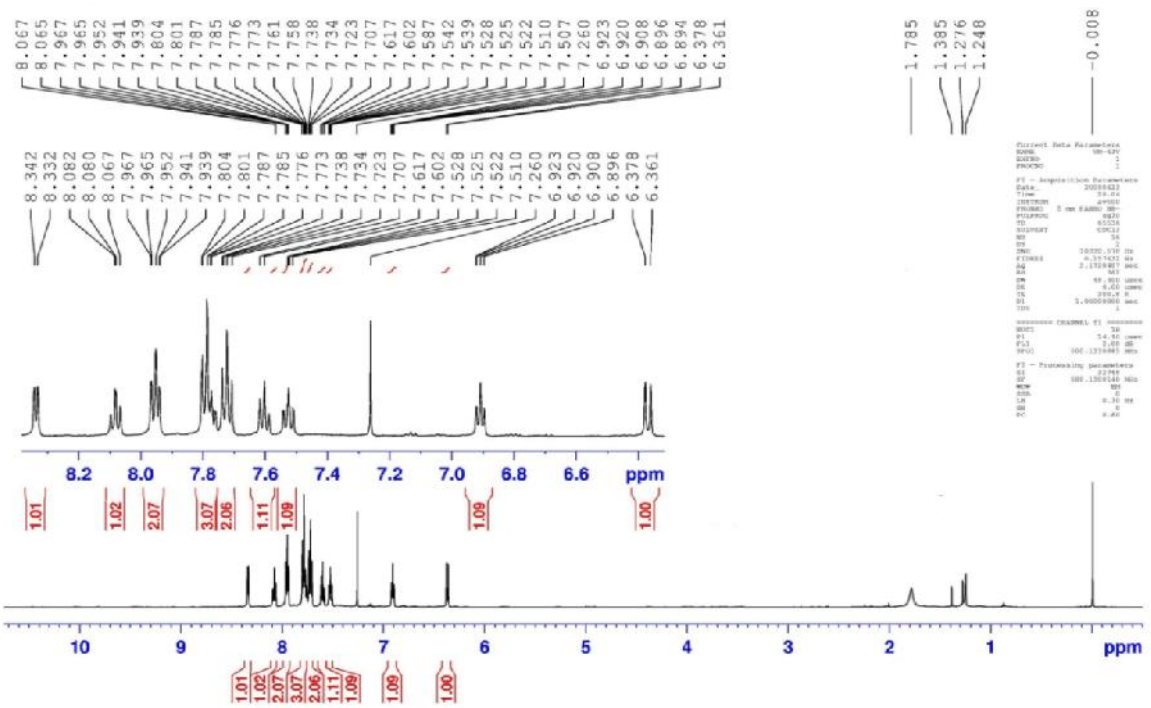

Fig. 2.4 ^{1}H NMR spectrum of complex **2b** in $CDCl_3$

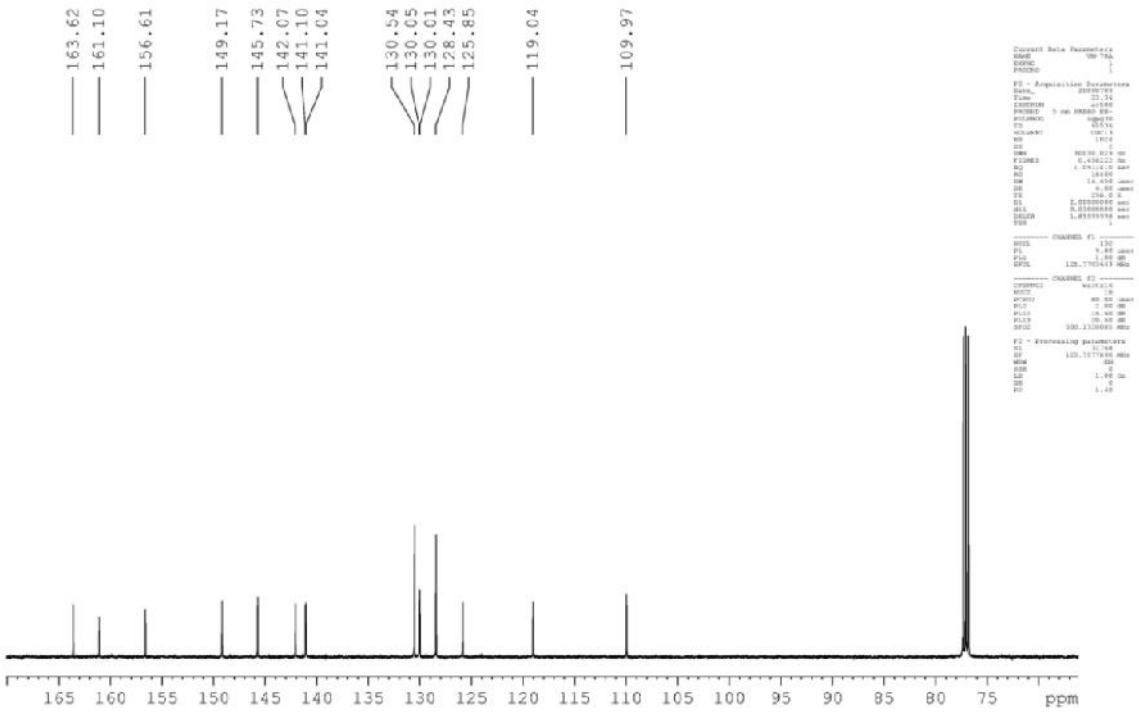

Fig. 2.5 ^{13}C NMR spectrum of complex **2b** in $CDCl_3$

(iv) ESIJMass spectrometry

The complexes **1a**, **1b** and **2b** were subjected to ESI–mass spectrometric analysis in acetonitrile: water (1:1) mixture and analyzed in positive or negative mode. The electro–spray ionization mass spectrum (ESI–MS) of **1a** showed a peak with m/z value of 402.08 probably due to the formation of [**1a**-H^+]$^-$ anion with loss of a proton (Fig. 2.6). The ESI–MS spectrum of **1b** exhibited two peaks with m/z values of 706.11 (relative intensity 4.5%) and 303.58 (relative intensity 100%) which were assigned to the formation of [**1b**-(ClO_4)]$^+$ and [**1b**-2(ClO_4)]$^{2+}$ cations due to the loss of one and two perchlorate anions (Fig. 2.7) respectively. However in case of **2b** only one peak was observed with m/z value of 637.15 (relative intensity 100%) assigned to the formation of [**2b**-(ClO_4)]$^+$ cation by the loss of perchlorate anion present outside the coordination sphere (Fig. 2.8).

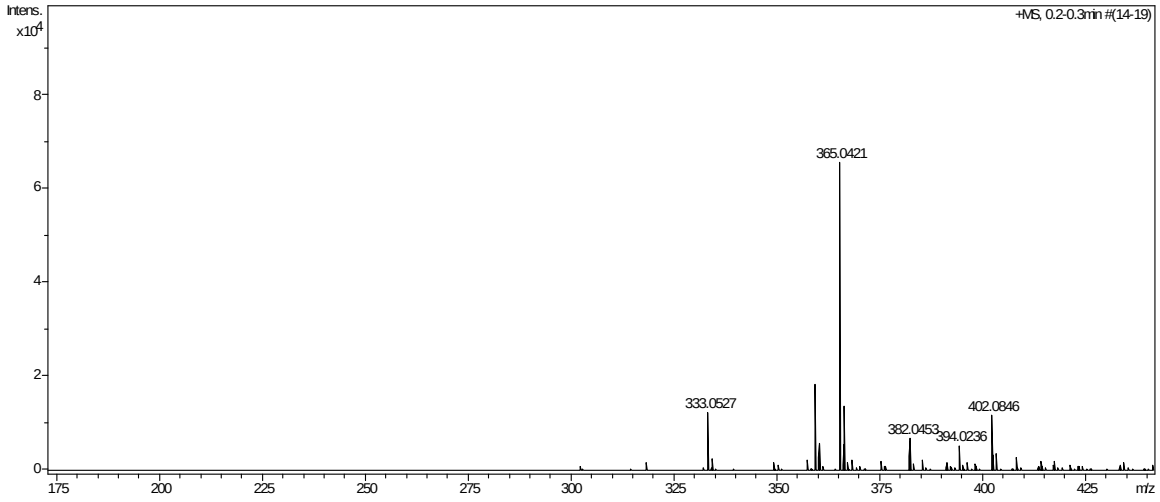

Fig. 2.6 The ESI–MS spectrum of [Co(Pyimpy)Cl_2] (**1a**) in acetonitrile showing the peaks at (m/z) 402.08 corresponding to [M-H^+]$^-$ anion

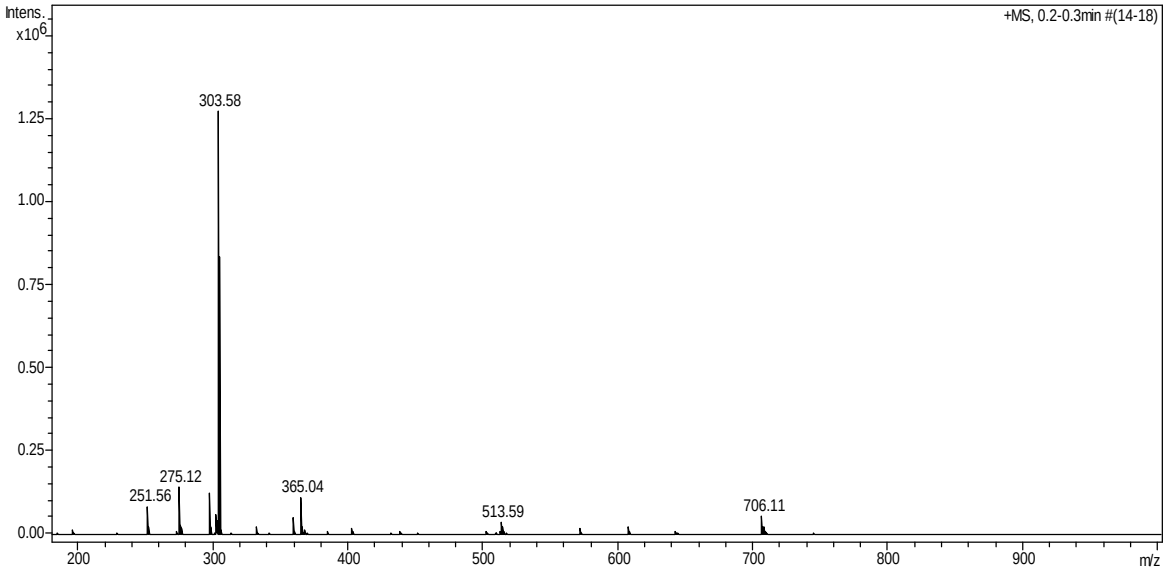

Fig. 2.7 The ESI–MS spectrum of $[Co(Pyimpy)_2](ClO_4)_2$ (**1b**) in acetonitrile showing the peaks at (m/z) 706.11 and 303.58 corresponding to $[M\text{-}(ClO_4)]^+$ and $[M\text{-}2(ClO_4)]^{2+}$ cations respectively

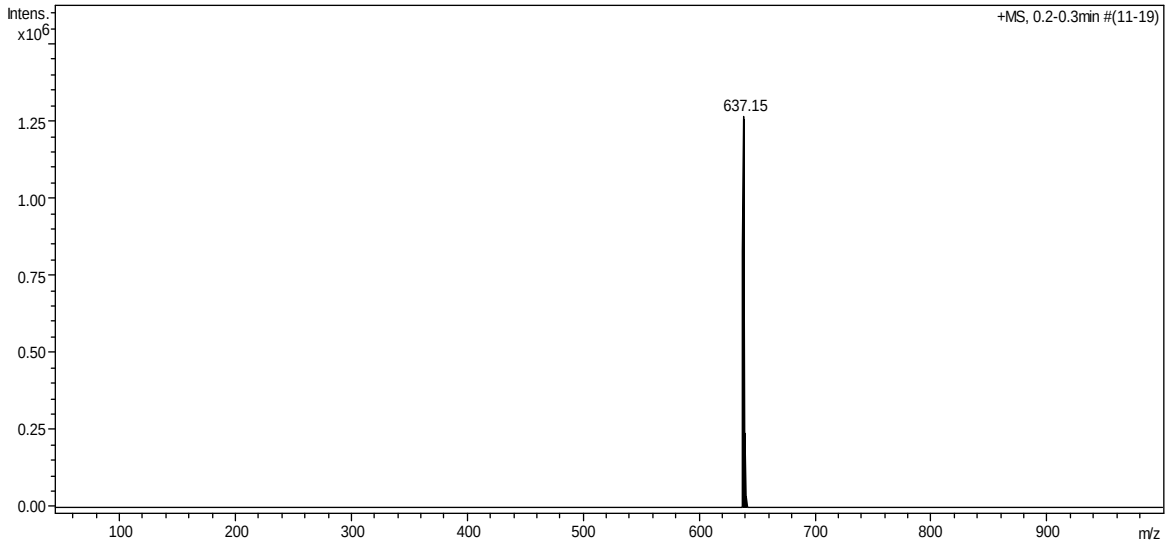

Fig. 2.8 The ESI–MS spectrum of $[Co(Pamp)_2]ClO_4$ (**2b**) in acetonitrile showing the peak at (m/z) 637.15 corresponding to $[M\text{-}(ClO_4)]^+$ cation

(v) Conductivity measurements

The molar conductivity measurements for complexes **1a** and **2a** in DMF solution (*ca.* 10^{-3} M) gave rise to neutral electrolytic behavior with conductivity values of 17 and 30 $\Omega^{-1}cm^2mol^{-1}$ respectively at 25 °C. Complex **1b** afforded molar conductivity values of 141 $\Omega^{-1}cm^2mol^{-1}$ (at 25 °C) indicating bi–univalent electrolytic behavior whereas **2b** afforded 60 $\Omega^{-1}cm^2mol^{-1}$ (at 25 °C) indicating uni–univalent electrolytic behavior.[387]

(vi) Magnetic moment studies

Magnetic susceptibility measurements for complexes **1a** and **1b** at room temperature suggested the presence of three unpaired electrons at the cobalt(II) centre.[388] The carboxamido nitrogen donor stabilizes the higher oxidation states so complexes **2a** and **2b** showed the Co(III) centres and these two complexes were found to be diamagnetic with low–spin d^6 electronic configuration. These data are consistent with the NMR spectral data of complexes **2a** and **2b** (Fig. 2.2–2.5).

2.2.3. Description of molecular structure

In order to confirm mode of coordination of the ligand Pyimpy with cobalt, crystals were grown for complex **1a** by the diffusion of acetone in the methanolic solution and molecular structure was determined by XJray diffraction studies. ORTEP representation of the metal coordination environment in complex **1a** is displayed in Fig. 2.9. Selected bond lengths and bond angles are listed in Table 2.3. Two pyridine nitrogen donors (N_{Py}) and one azomethine nitrogen (N_{Im}) was bound to the cobalt centre in **1a** in meridional fashion (Fig. 2.9). The equatorial plane of the coordination sphere consists of two pyridine nitrogens (N_{Py}), one azomethine nitrogen (N_{Im}) and Cl atom while the axial position is occupied by other Cl atom.

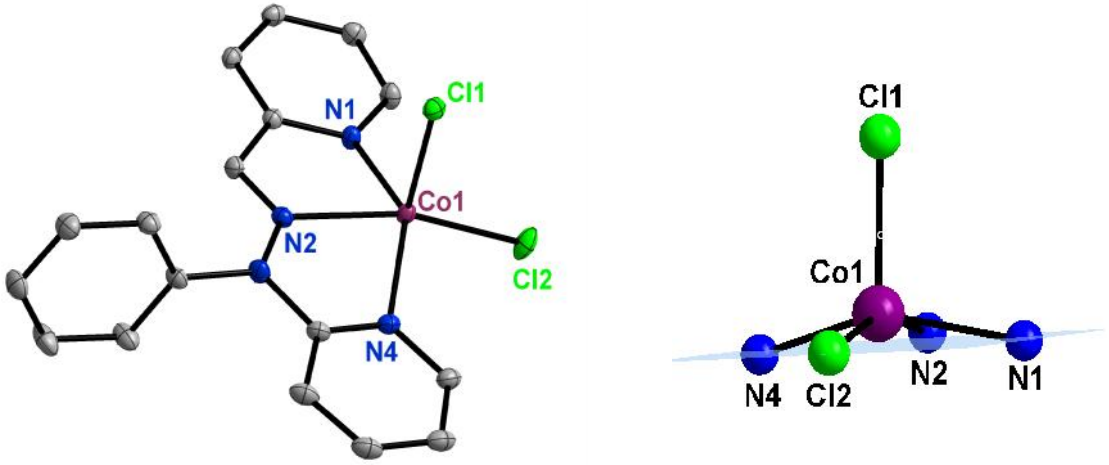

(a) (b)

Fig. 2.9 (a) ORTEP representation of the crystal structure of [Co(Pyimpy)Cl_2] (**1a**) showing atom numbering scheme and displacement ellipsoid (50% probability level). Hydrogen atoms are omitted for clarity; (b) square pyramidal disposition of donor atoms around metal centre

Table 2.3 Selected bond lengths (Å) and bond angles (˚) for **1a**

Bond lengths (Å)		Bond angles (˚)	
Co(1)−N(1)	2.0956(17)	N(1)−Co(1)−N(4)	142.23(7)
Co(1)−N(2)	2.1190(17)	N(1)−Co(1)−N(2)	75.26(7)
Co(1)−N(4)	2.0992(18)	N(4)−Co(1)−N(2)	73.67(7)
Co(1)−Cl(1)	2.3152(6)	N(1)−Co(1)−Cl(2)	100.25(5)
Co(1)−Cl(2)	2.2844(6)	N(4)−Co(1)−Cl(2)	101.77(5)
		N(1)−Co(1)−Cl(1)	99.38(5)
		N(4)−Co(1)−Cl(1)	103.39(5)
		N(2)−Co(1)−Cl(1)	93.46(5)
		Cl(2)−Co(1)−Cl(1)	106.20(2)
		N(2)−Co(1)−Cl(2)	160.32(5)

The ligand biting angles at the metal centre were 75.26^o (N(1)−Co(1)−N(2)) and 73.67^o (N(4)−Co(1)−N(2)) in complex **1a** and the other two angles with Cl2 were 100.25^o and 101.77^o. Structural index parameters calculation (τ = 0.30) showed the distorted square

pyramidal geometry.[135] Two pyridine and imine nitrogen distances from Co(II) centre were consistent with the reported data for high−spin Co(II) complexes.[389-391] These data were consistent with the magnetic moment data (4.60 B.M.) described earlier (*vide supra*). The axial Co−Cl1 distance 2.315 Å was found to be longer than the equatorial Co−Cl2 distance 2.284 Å due to Jahn−Teller distortion which are consistent with the literature values.[392] The Co(II) centre is 0.424 Å above the plane generated by the coordinated N1, N2, N4 and Cl2 atoms. The ligand Pyimpy has three six−membered rings; among them, the two pyridine rings are coplanar with the imine function whereas the other phenyl ring is roughly perpendicular (85.55°) to the ligand binding plane.

Non−covalent interactions like πJstacking interactions with aryl hydrogen and hydrogen bonding network are important in supramolecular chemistry and crystal engineering.[393] In complex **1a**, the axial Cl atom showed hydrogen bonding interaction with the hydrogen atoms of two pyridine and one phenyl rings of neighboring molecules and the distances are 2.666, 2.760 and 2.878 Å respectively. However the equatorial Cl showed the hydrogen boding interactions with the hydrogen atoms of two phenyl rings and one pyridine ring of the neighboring molecules with the bond distances 2.896, 2.780 and 2.773 Å respectively (Fig. 2.10). Interestingly, weak π–π stacking interactions were observed between the pyridine rings of two neighboring molecules affording the centroid to centroid distance of 3.636 Å (Fig. 2.11) which is lesser than those reported by Yin and co−workers.[394] The interaction of the axial Cl ion with pyridine hydrogen at a distance of 2.878 Å helps for π–π interactions. These hydrogen bonding and π–π interactions generated a supramolecular polymer like species. All types of hydrogen bonding interactions found in

the crystal structure of **1a** are documented in Table 2.4. Packing diagrams of the molecule and a three-dimensional network is shown in Fig. 2.12.

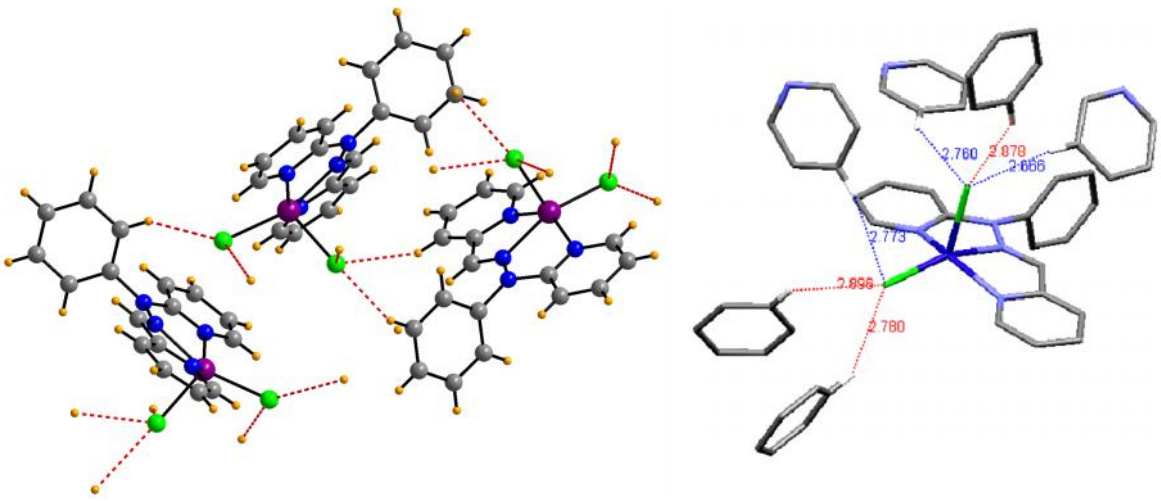

(a) (b)

Fig. 2.10 (a) Intermolecular hydrogen bonding network in [Co(Pyimpy)$(Cl)_2$] (**1a**); (b) another view (hydrogen atoms are omitted for clarity)

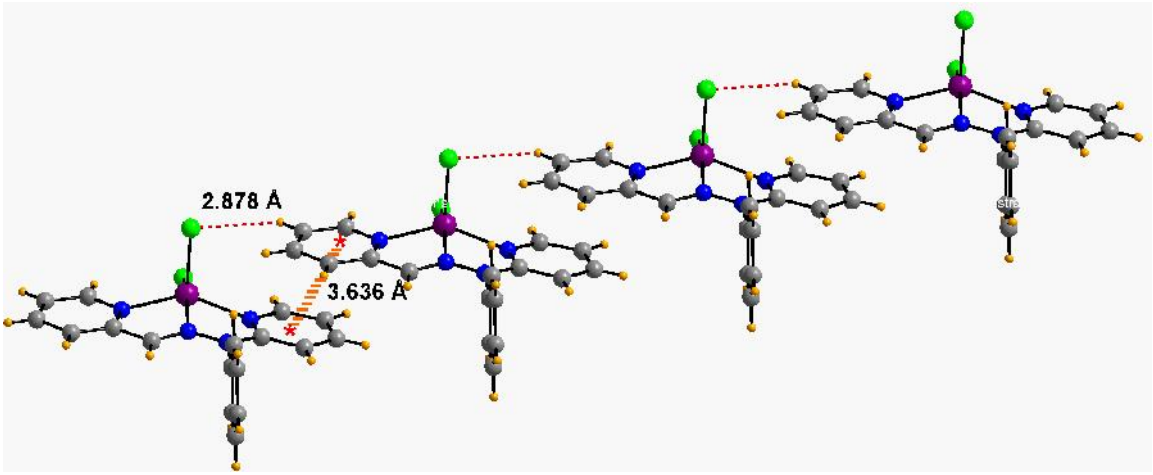

Fig. 2.11 Intermolecular hydrogen bonding network and π–stacking interactions in [Co(Pyimpy)$(Cl)_2$] (**1a**) giving rise to supramolecular polymer–like species

Table 2.4 Hydrogen–bonding geometries for **1a**

D─H.....A	D─H (Å)	D.....A (Å)	H.....A (Å)	D─H.....A (˚)
C1─H1.....Cl2[a]	0.930(2)	3.503(2)	2.932(1)	120.99(13)
C17─H17.....Cl2 [a]	0.930(2)	3.530(2)	2.947(1)	122.02(14)
C2─H2.....Cl1[b]	0.930(2)	3.522(2)	2.760(1)	139.88(13)
C4─H4.....Cl1[c]	0.930(2)	3.531(2)	2.667	154.87(12)
C10─H10.....Cl2[d]	0.930(2)	3.652(2)	2.896(1)	139.27(13)
C11─H11.....Cl1[e]	0.930(2)	3.686(2)	2.878	146.10(15)
C12─H12.....Cl2[f]	0.930(2)	3.575(2)	2.780(1)	144.06(15)
C15─H12.....Cl2[g]	0.930(2)	3.689(2)	2.773(1)	168.39(15)

Symmetry codes: (a) x,y,z; (b) x-1,+y,+z; (c) x-1/2,-y+1/2,-z; (d) -x+1/2+1,-y+1,+z-1/2; (e) x,+y+1,+z; (f) -x+1,+y+1/2,-z+1/2; (g) -x+2,+y+1/2,-z+1/2

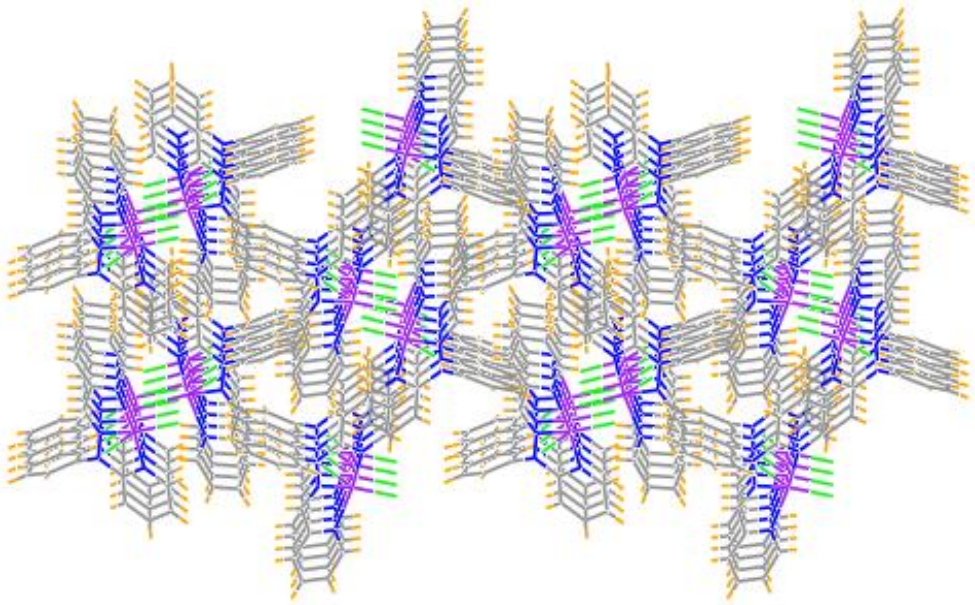

Fig. 2.12 Packing diagram in crystal structure of [Co(Pyimpy)$(Cl)_2$] (**1a**)

2.2.4. Electrochemistry

The redox properties of all the complexes were investigated through cyclic voltammetric experiments in acetonitrile using Ag/AgCl as reference electrode. The

electrochemical data for all the complexes are described in Table 2.5 and all the voltammograms are shown in Fig. 2.13.

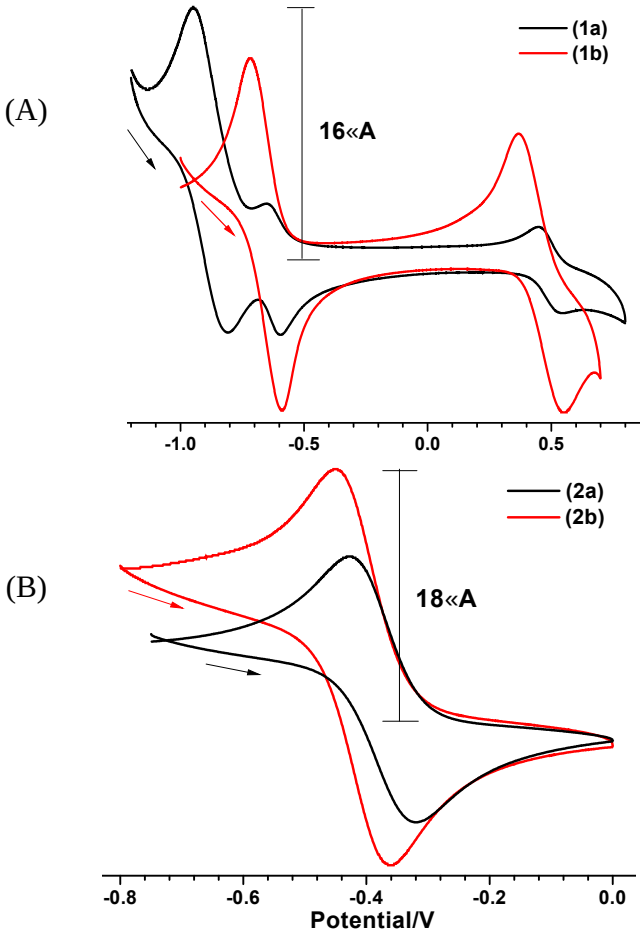

Fig. 2.13 Cyclic voltammograms of 10^{-3} M solutions of **1**–**2** in acetonitrile (10^{-3} M) vs. Ag/AgCl in presence of 0.1 M tetrabutylammonium perchlorate as supporting electrolyte; scan rate: 0.1 V/s

Two different types of voltammograms were observed for these complexes. **1a** and **1b** gave rise to voltammograms of type A and **2a** and **2b** gave rise to voltammograms of type B respectively. In case of **1a** the quasireversible redox couples were found near $E_{1/2}$ values of +0.487 V, −0.630 V and −0.879 V vs. Ag/AgCl. $E_{1/2}$ values of +0.487 V and −0.630 V were designated as Co^{3+}/Co^{2+} and Co^{2+}/Co^{1+} redox couples respectively. The quasi–reversible

redox couple near $E_{1/2}$ values of −0.879 V vs. Ag/AgCl furnished greater current height compared to other two couples found for this complex. We have investigated each couple individually scanning in between +0.300 V and +0.650 V, –0.700 V and –0.500 V and –1.100 V and –0.650 V respectively and the results are shown in Fig. 2.14 (*vide infra*).

Table 2.5 Redox potentials for complexes **1– 2** at 298 K vs. Ag/AgCl

Complex			Co(II/I)		Co(III/II)	
	$E_{1/2}$[b] (V)	ΔE_p[c] (mV)	$E_{1/2}$[b] (V)	ΔE_p[c] (mV)	$E_{1/2}$[b] (V)	ΔE_p[c] (mV)
1a	–0.879	118	–0.630	67	0.487	114
1b	—	—	–0.653	130	0.459	182
2a	—	—	—	—	-0.373	107
2b	—	—	—	—	-0.407	88

[a]$E_{1/2} = 0.5(E_{pa} + E_{pc})$, [b]$\Delta E_p = (E_{pa} – E_{pc})$, [c]Solvent: acetonitrile

The $E_{1/2}$ value found near −0.879 V vs. Ag/AgCl could probably be due to ligand centered reduction or any other species generated in the solution. We investigated the redox property of the ligand in acetonitrile as well as an acetonitrile solution containing ligand and $ZnCl_2$ in 1:1 ratio separately; we were unable to find any redox couple in that range which could authenticate ligand centered reduction. Hence at this point we speculated that the redox couple is probably due to some other species generated in the solution. Similar to **1a**, $E_{1/2}$ values of +0.459 V and −0.653 V vs. Ag/AgCl electrode for **1b** were designated as Co^{3+}/Co^{2+} and Co^{2+}/Co^{1+} redox couples respectively. Investigation of literature revealed that our Co^{3+}/Co^{2+} data is closer to the value reported by Slattery and co–worker.[395] However, the positive potential values are higher than that of similar complexes reported in the literature.[396-399] Cyclic voltammogram of **2a** and **2b** displayed single quasi–reversible redox couple (type B in Fig. 2.13) with $E_{1/2}$ values in the range −0.373 V to −0.407 V vs. Ag/AgCl

electrode. These data are similar to the data obtained by Mascharak and co–workers[382] and are due to the Co^{3+}/Co^{2+} couple.

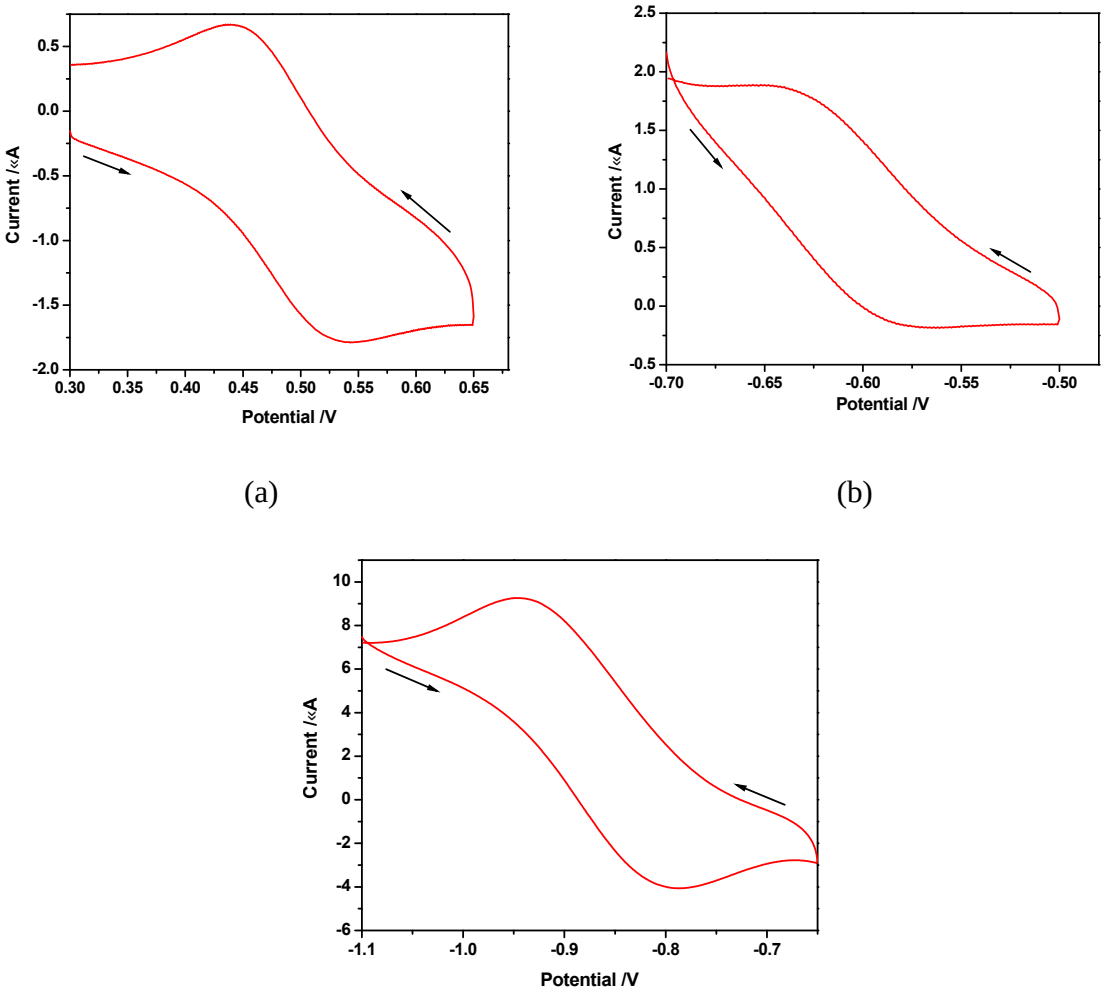

Fig. 2.14 Cyclic voltammograms of solution of **1a** (10^{-3} M) in acetonitrile exhibiting individual redox couples obtained by scanning within the potential ranges (a) +0.300 V and +0.650 V, (b) -0.700 V and -0.500 V, and (c) -1.100 V and -0.650 V respectively; 0.1 M TBAP was used as a supporting electrolyte, glassy–carbon as a working electrode and Ag/AgCl as reference electrode; scan rate 0.1 V/s

2.2.5. Superoxide dismutase activity studies

The electrochemical behaviors of these complexes showed that all these complexes are redox–active which prompted us to study their superoxide scavenging ability. McCord

Fridovich (McCF) assay was performed to investigate the SOD–like activity of this series of complexes and complexes **1a** and **1b** were found to be active towards the dismutation of the superoxide radicals. The $O_2^{\cdot -}$ radicals were generated in the reaction medium by the xanthine/xanthine oxidase system and the SOD activity was determined from the reduction of nitroblue tetrazolium by these radicals. Appearance of a formazan color accompanied the reduction of NBT which could be monitored spectrophotometrically by the enhancement in absorbance at 560 nm. Presence of a second molecule in the reaction medium able to react with superoxide radicals could establish a competition with NBT and may inhibit its reduction which is an indirect measure of the SOD–like activity exhibited by complexes. The rate of absorption change was determined for all complexes and the IC_{50} values were obtained by plotting the rate of NBT reduction (along Y–axis) versus the concentration of test solution (along X–axis) (Fig. 2.15).

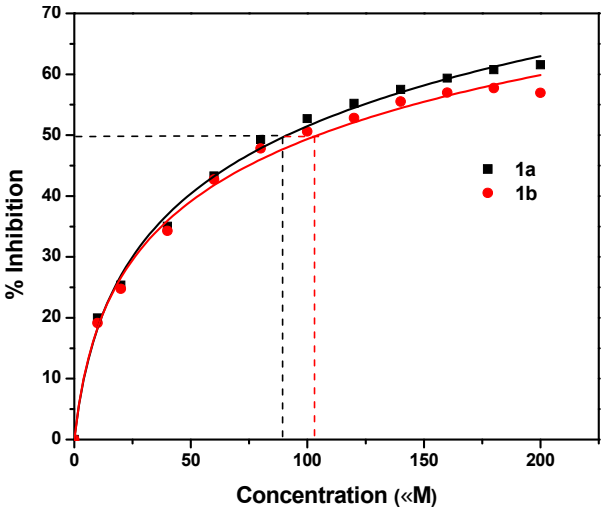

Fig. 2.15 SOD activity of complexes **1a** and **2a** by xanthine/xanthine oxidase–nitro blue tetrazolium assay with an incubation time of 10 min

The IC_{50} value for **1a** and **1b** were found to be 85 ± 3 μM and 105 ± 5 μM whereas only 10–12% inhibition could be obtained with **2a** and **2b** even at very high concentration of the complexes (500 μM). Similar superoxide scavenging activity by Co(II) complexes was observed by Anacona and co–workers (IC_{50} values 1000 μM and 580 μM).[199,200]

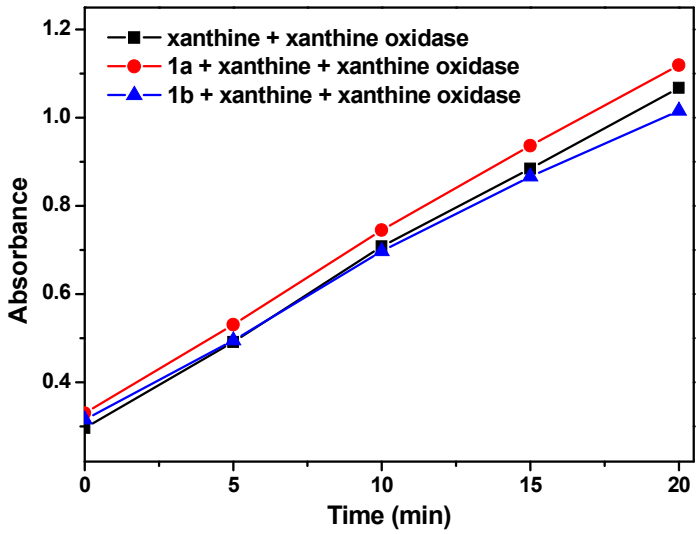

Fig. 2.16 Absorption spectral changes exhibiting the uric acid formation in phosphate buffer (pH 7.8) containing 1% dimethylformamide (DMF). Equal concentration of complexes was maintained in both (sample and reference) cuvettes. [xanthine] = 200 μM, [xanthine oxidase] = 2.1 mU/mL, [Complex] = 100 μM. Incubation time was varied from 0 min to 20 min

As control experiments, we have monitored the rate of change in absorbance at 295 nm and found negligible spectral change at this wavelength due to the presence of the complex **1a** or **1b** (Fig. 2.16). The increase in absorbance at 295 nm is due to the uric acid formation by the action of xanthine oxidase (XO) enzyme on xanthine (X). Hence it was concluded that the SOD mimics here are not directly inhibiting the action of the enzyme on the substrate. Further, the control experiments in Fig. 2.17 suggested that **1a** and **1b** are neither decomposing in the under experimental conditions nor those are participating in any reaction with NBT.

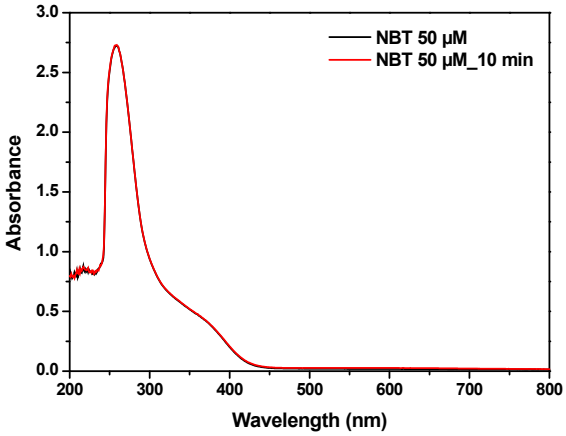
NBT 50 μM
NBT 50 μM_10 min
Absorbance
Wavelength (nm)

(a)

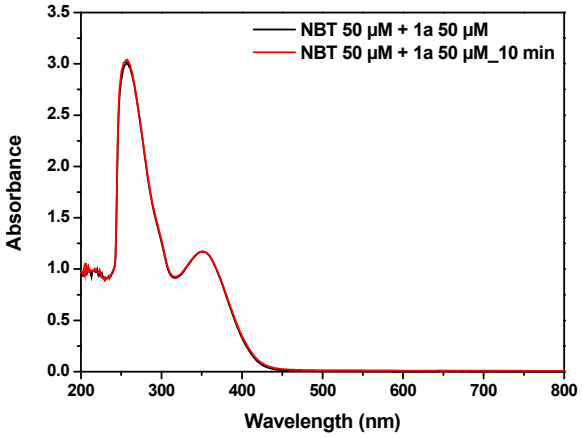
NBT 50 μM + 1a 50 μM
NBT 50 μM + 1a 50 μM_10 min
Absorbance
Wavelength (nm)

(b)

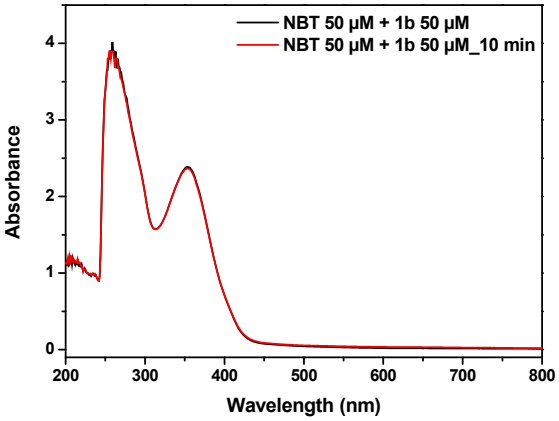
NBT 50 μM + 1b 50 μM
NBT 50 μM + 1b 50 μM_10 min
Absorbance
Wavelength (nm)

(c)

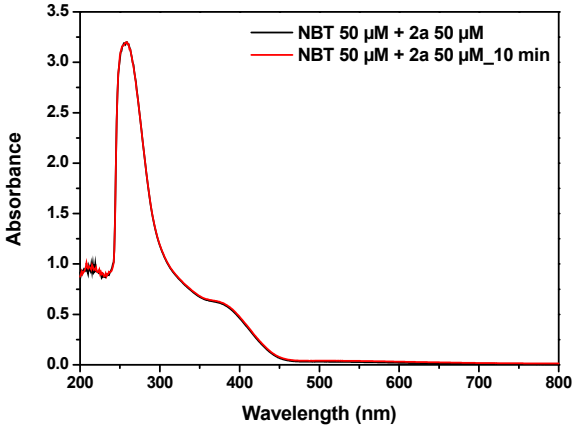
NBT 50 μM + 2a 50 μM
NBT 50 μM + 2a 50 μM_10 min
Absorbance
Wavelength (nm)

(d)

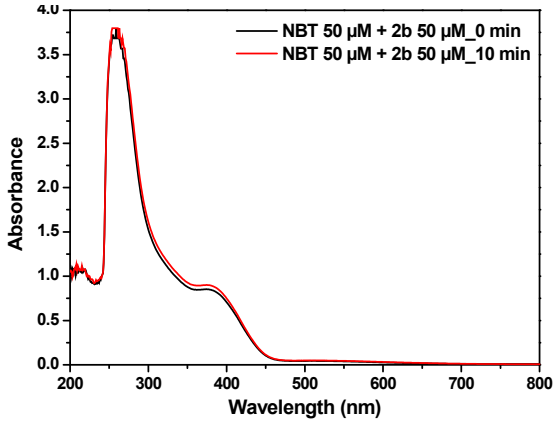
NBT 50 μM + 2b 50 μM_0 min
NBT 50 μM + 2b 50 μM_10 min
Absorbance
Wavelength (nm)

(e)

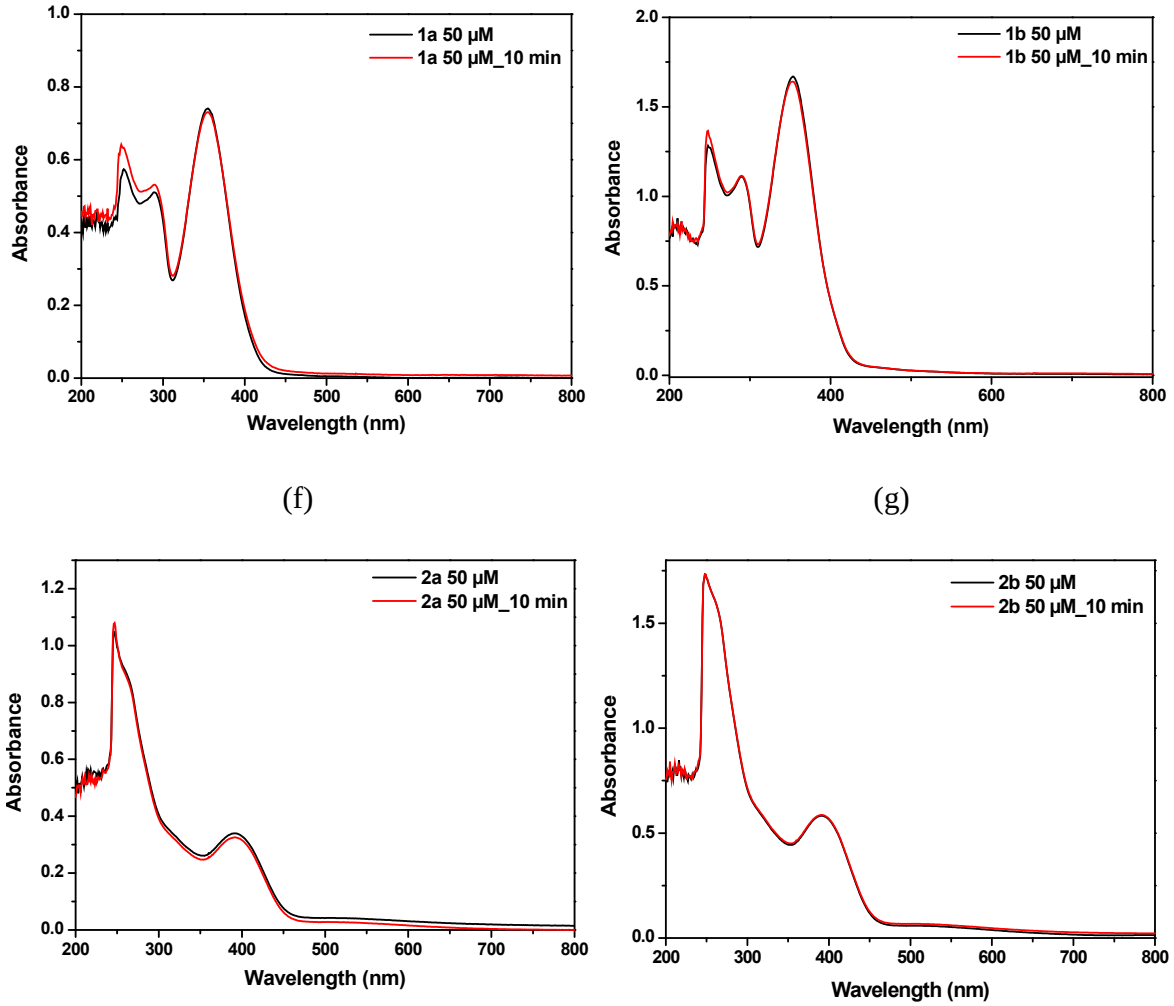

Fig. 2.17 Electronic absorption spectrum exhibiting negligible change in the absorption profile of NBT (50 µM) due to incubation or presence of complex

(a) No change in absorption profile of NBT after incubation in absence of any complex

(b) – (e) No change in absorption profile of NBT after incubation with **1a**, **1b**, **2a** and **2b** (all 50 µM) respectively

(f) – (i) No change in absorption profile of **1a**, **1b**, **2a** and **2b** (50 µM) respectively after incubation

2.2.6. DNA binding studies

The DNA binding properties of the cobalt complexes were studied using the electronic absorption spectroscopic technique. We performed the DNA binding studies in 0.1 M phosphate buffer (pH 7.2) so it was necessary to check the stability of these complexes in buffer. Little change in absorbance was observed after 3 days. A small change in absorbance without any considerable shift in wavelengths (λ_{max}) predicted the stability of these cobalt complexes in the above buffer solution. To investigate the DNA binding properties, the absorption spectra of complexes in the absence and presence of calf thymus DNA (CT–DNA) at different concentrations were recorded. As the concentration of CT–DNA was increased, the absorption spectra of complexes **1a** and **1b** underwent a blue shift (~20 nm) leading to the generation of a new peak in the spectra. The spectral changes exhibited by **1a** and **1b** with increasing concentration of CT–DNA are depicted in Fig. 2.18.

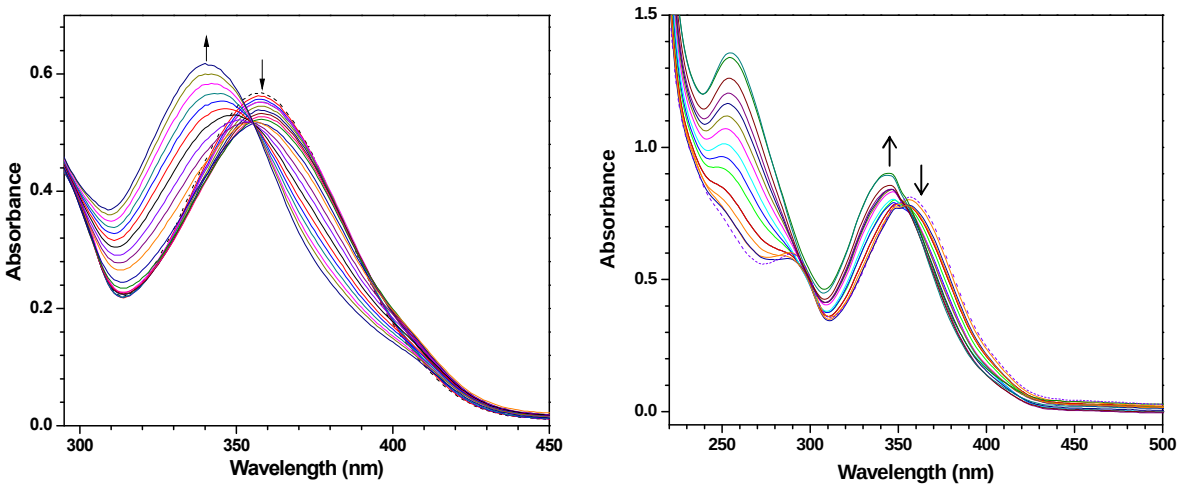

(a) (b)

Fig. 2.18 Absorption spectra of cobalt complexes in the presence of increasing amounts of DNA in 0.1 M phosphate buffer (pH 7.2) (a) [**1a**] = 50 µM, [DNA] = 0–116.5 µM and (b) [**1b**] = 40 µM, [DNA] = 0–93 µM. Dotted line represents the spectrum in the absence of DNA

The intrinsic binding constants K_b for all complexes have been determined according to the reported procedures[332] and shown in Table 2.6. The observed binding constants for these complexes are smaller than those of classical intercalators and metallointercalators where binding constant was reported to be in the order of 10^6–10^7 M^{-1}.[278,400]

Table 2.6 Binding constants (K_b) and Stern–Volmer constants (K_{SV}) for complexes **1-2**

Complex	K_b (M^{-1})	K_{sv} (M^{-1})
1a	1.15×10^4	2.98×10^4
1b	4.23×10^4	7.33×10^4
2a	5.06×10^4	5.14×10^4
2b	3.27×10^4	9.99×10^4

This type of spectral changes resulting into the formation of a new band is indicative of the generation of a new species possibly due to the covalent interaction between the complexes and DNA.[401-403] Investigation of literature revealed that cobalt complexes may bind covalently with N7 of guanine bases in DNA.[283] Hence we predict that a new species generated due to the attachment of Co(II) complexes with nucleic bases of DNA during DNA interaction studies. Control experiments with complexes **1a** and **1b** precluded any possibility of direct coordination of metal centre with phosphate backbone of DNA (Fig. 2.19). The formation of new species was also supported by the reverse titration experiments where a fixed concentration of DNA was titrated with increasing concentrations of the complex **1a**. The spectral changes during the reverse titration experiments are shown in the Fig. 2.20. At lower concentration of the complex, the spectrum is characteristic of the new species which is dominated by the CT band of the complex at higher concentrations.

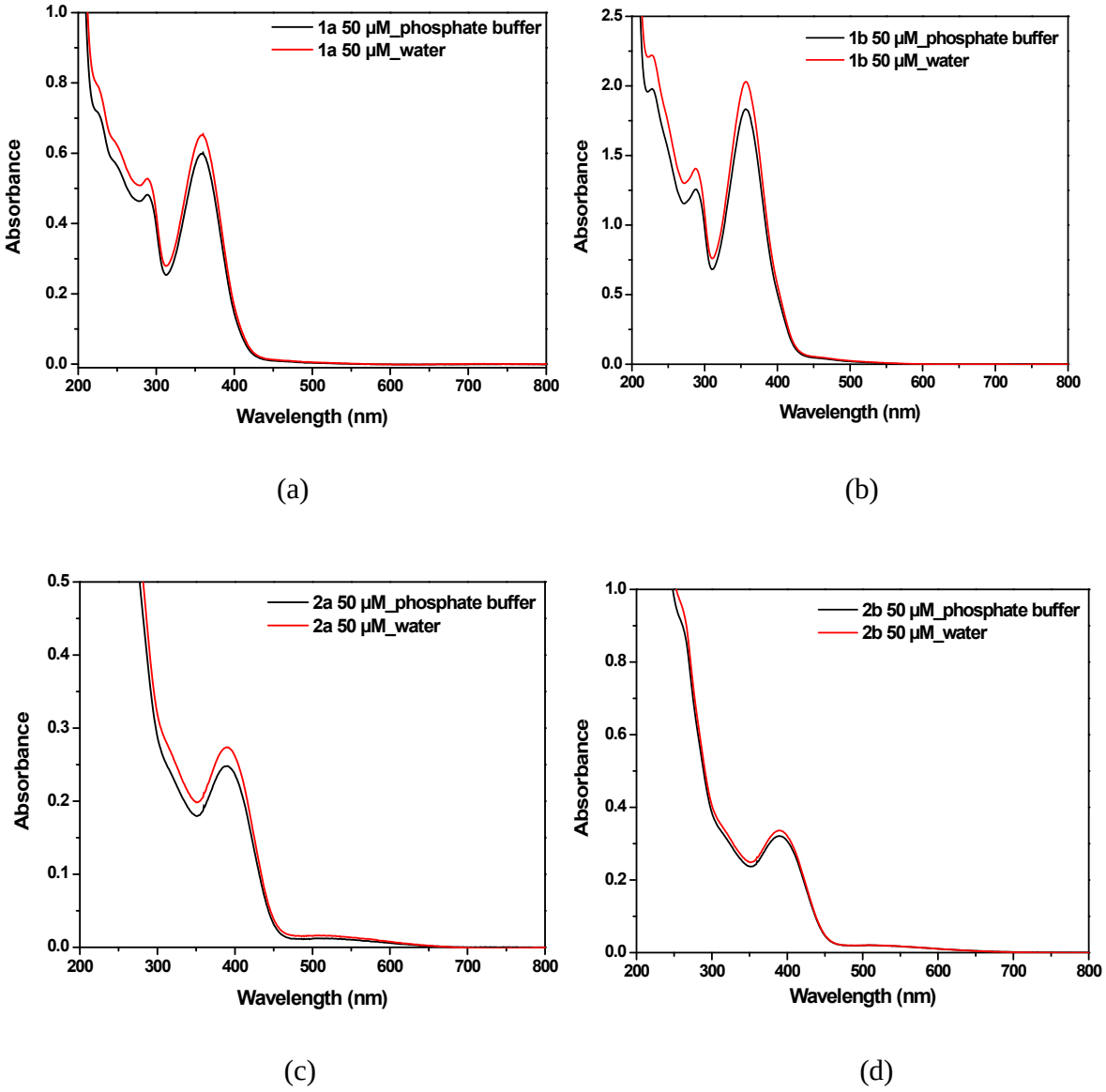

Fig. 2.19 Electronic absorption spectrum of complexes (a) **1a**, (b) **1b**, (c) **2a** and (d) **2b** in phosphate buffer (pH 7.2) and water exhibiting no spectral shift

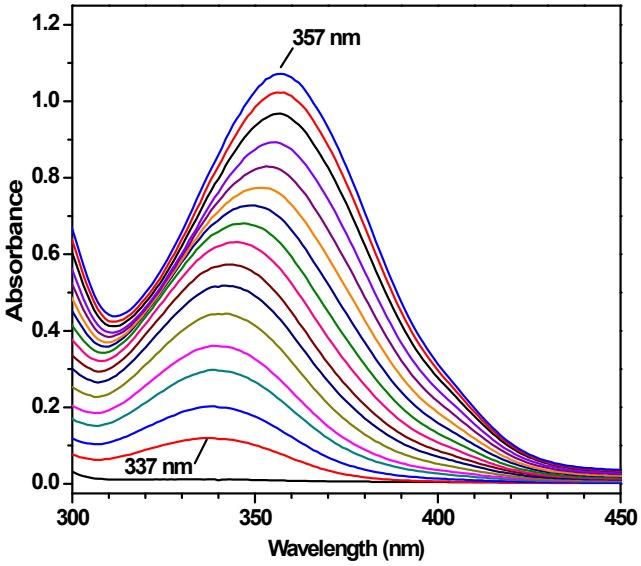

Fig. 2.20 Reverse titration experiment of CT–DNA with complex **1a** in 0.1 M phosphate buffer (pH 7.2) showing a shift of 20 nm in UV–vis spectrum. [DNA] = 120 μM and [**1a**] = 0–64 μM respectively

However absorption spectra for **2a** and **2b** exhibited only hypochromism without any shift in the wavelength values which indicated that these complexes interacted with DNA quite differently from **1a** and **1b** (Fig. 2.21) probably due to the presence of Co(III) in **2a** and **2b**.

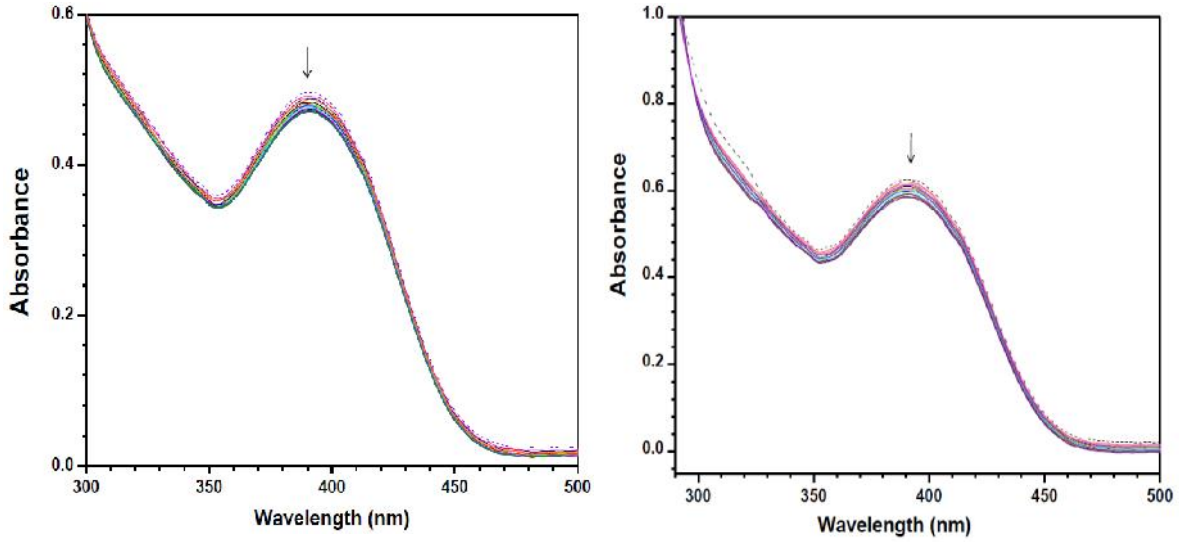

(a) (b)

Fig. 2.21 Absorption spectra of cobalt complexes in the presence of increasing amounts of DNA in 0.1 M phosphate buffer (pH 7.2) (a) [**2a**] = 100 µM, [DNA] = 0–123 µM, (b) [**2b**] = 80 µM, [DNA] = 0–80 µM. Dotted line represents the spectrum in the absence of DNA

To get better insight into DNA binding event, we examined the competitive binding of ethidium bromide vs. cobalt complexes with DNA. Ethidium bromide (EB) emits intense fluorescence in presence of DNA due to its strong intercalation between the DNA base pairs. The enhanced fluorescence can be quenched by the addition of the metal complexes to the EBJDNA mixture which competitively bind to DNA resulting in the reduction in emission intensity. The fluorescence quenching curve of ethidium bromide bound to DNA by complexes **1J2** are shown in Fig. 2.22. The Stern−Volmer quenching constants (K_{sv}) for all complexes were obtained by Stern−Volmer plots which are described in Table 2.6. These values are lesser than those reported for metallointercalators.[347] The K_{sv} values for these complexes indicated that the **1b** and **2b** exhibited higher extent of quenching as compared to **1a** and **2a** probably due to bis complexation of the ligand. The Stern–Volmer plots for all complexes are illustrated in Fig. 2.23.

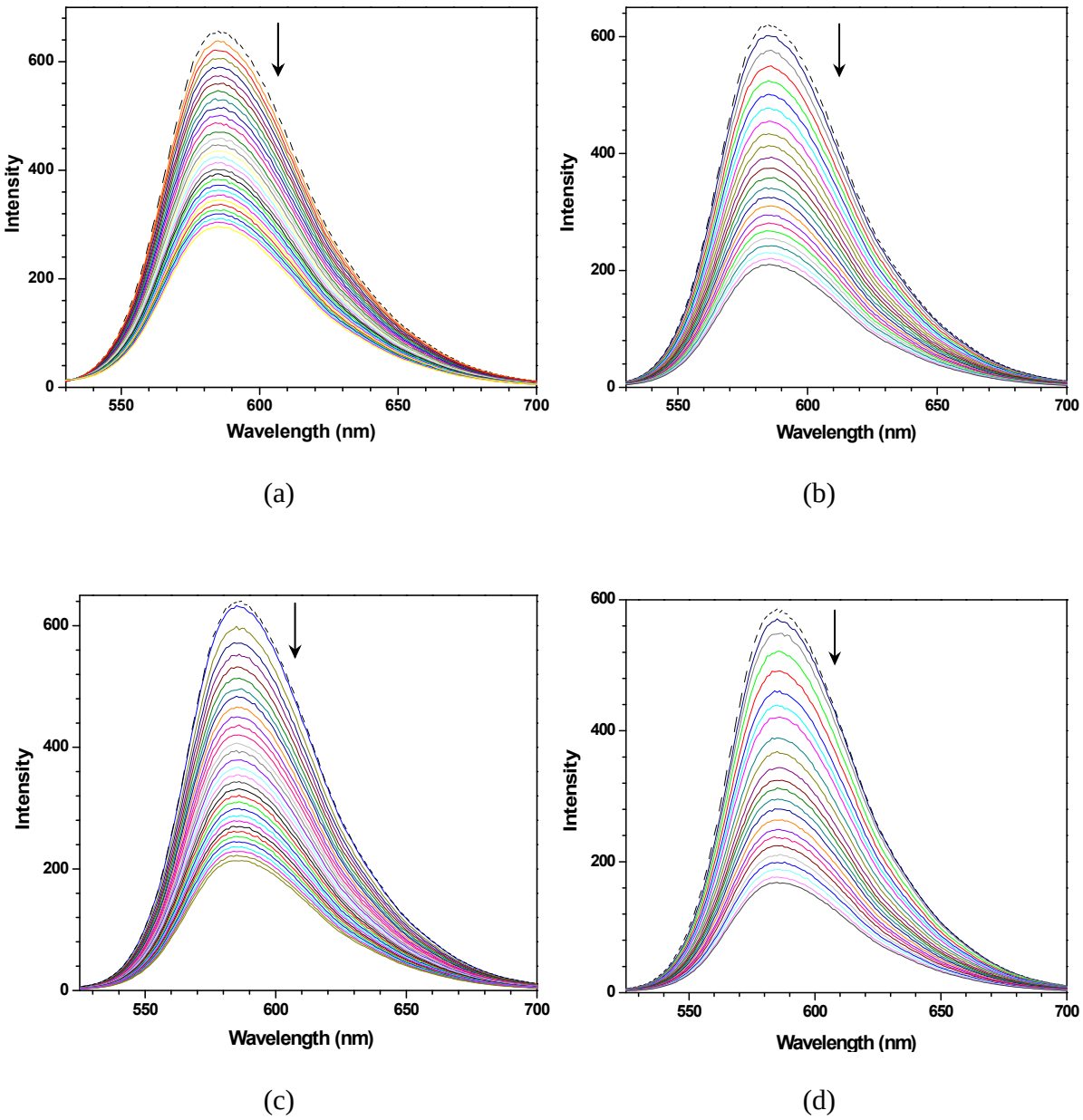

Fig. 2.22 Fluorescence emission spectra of the EB−DNA in presence of cobalt complexes in 0.1 M phosphate buffer (pH 7.2). λ_{ex} = 250 nm and λ_{em} = 585 nm. [EB] = 5 μM, [DNA] = 25 μM, (a) [**1a**] = 0–45.7 μM, (b) [**1b**] = 0–35.5 μM, (c) [**2a**] = 0–48.7 μM and (d) [**2b**] = 0–35.5 μM. Dotted line represents the spectrum in the absence of complex

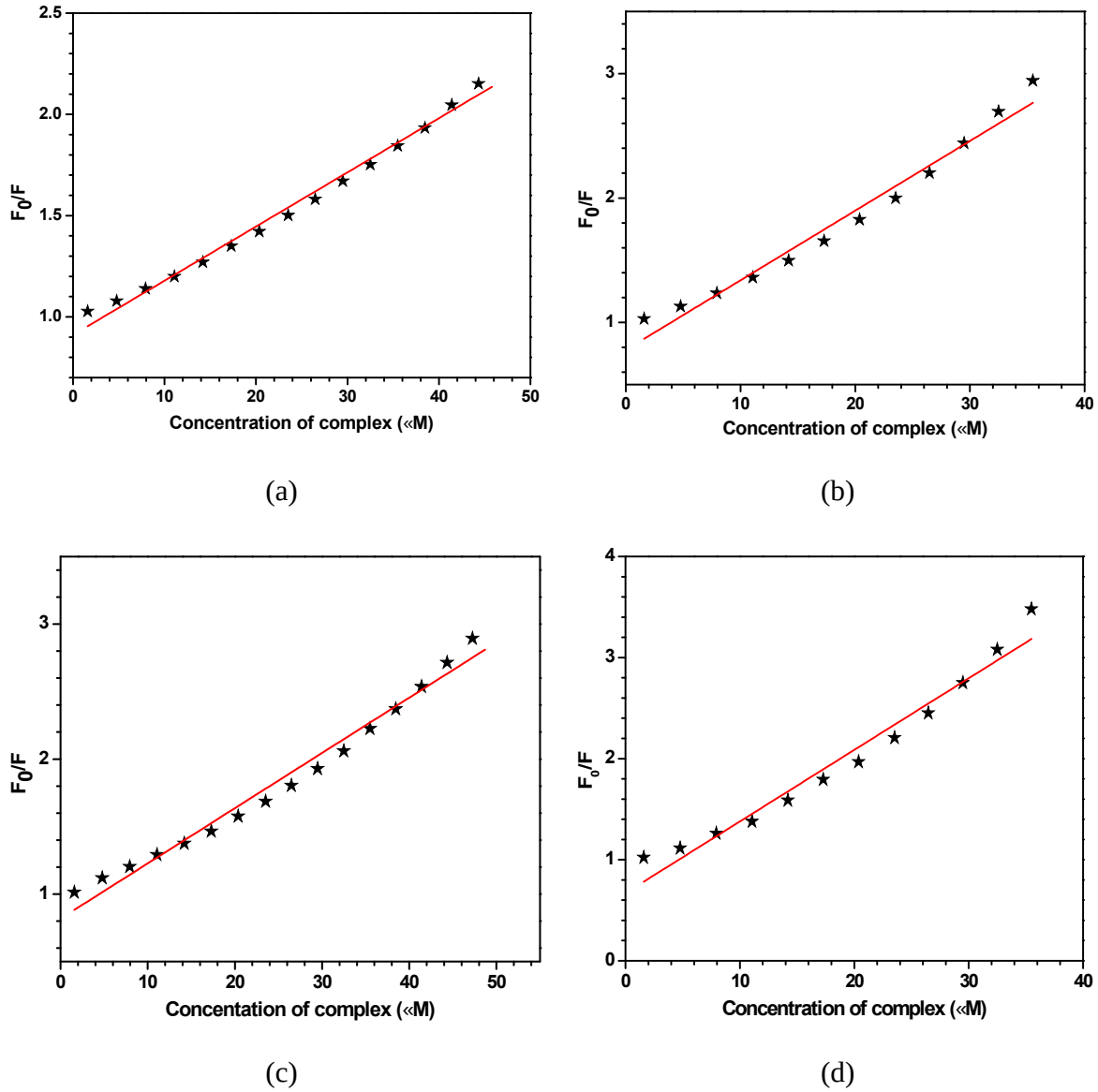

Fig. 2.23 Stern–Volmer plots for complexes (a) **1a**, (b) **1b**, (c) **2a** and (d) **2b**

CD spectroscopic technique was employed to detect the possible conformational changes of DNA induced by its interaction with metal complexes. The CD spectrum of CT–DNA was recorded in the range 225–300 nm in 0.1 M phosphate buffer (pH 7.2) and it has been found that there were one positive band at 278 nm due to base stacking and one negative band at 246 nm due to helicity. The examination of Fig. 2.24 indicates that the

positive band slightly increased in intensity and the negative band decreased in intensity after binding of **1a** with DNA, however no considerable shift in λ_{max} could be observed. A very small decrease in the intensity of positive band and a small increase in the intensity of negative band was observed when the DNA was incubated with **2a** (Fig. 2.24). However, the spectrum of DNA was almost unaffected by the presence of **1b** or **2b** (Fig. 2.24). These data indicated that the DNA did not undergo any appreciable conformational change after the DNA binding event.[403]

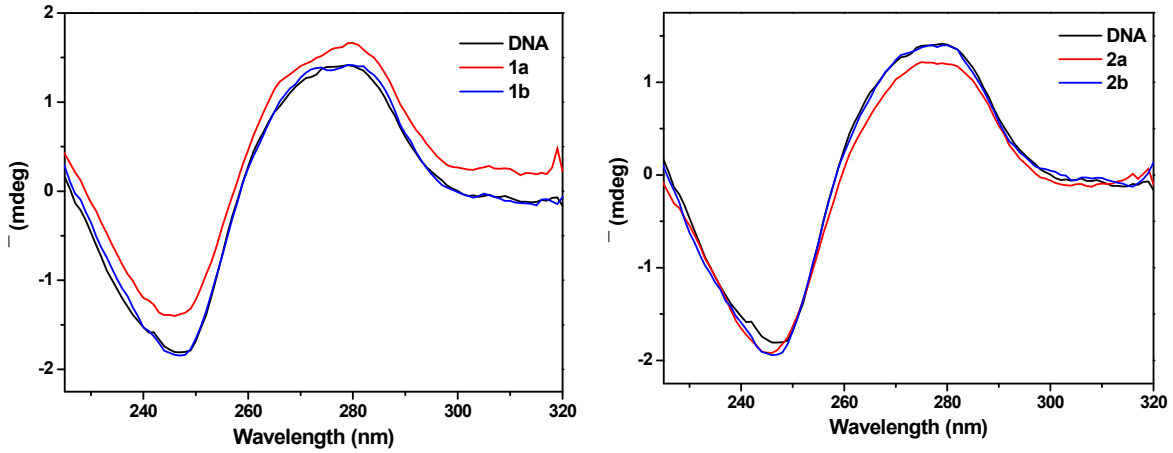

(a) (b)

Fig. 2.24 Circular dichroism spectra in 0.1 M phosphate buffer (pH 7.2) after 10 min incubation at 25 °C. (**a**) CT–DNA and its interaction with complexes **1a** and **1b** (**b**) CT–DNA and its interaction with complexes **2a** and **2b**

Results of the absorption spectral studies, competitive binding assay and circular dichroic spectral studies collectively suggested an external binding mode with DNA for complexes **2a** and **2b**.

2.2.7. Nuclease activity

Investigation of literature revealed that the complexes which contain a redox–active metal centre and interact with DNA covalently could exhibit excellent nuclease activity.[381]

The complexes **1a** and **1b** exhibited new species generation probably via covalent interaction with DNA which prompted us to extend our DNA interaction studies by examining the nuclease activity of these complexes. The cleavage of supercoiled pBR322 DNA (100 ng) by these complexes was analyzed by monitoring the conversion of supercoiled form (SC) to nicked circular (NC) and linear (LC) forms and the gel electrophoretic separation of the three forms is shown in Fig. 2.25, 2.26 and 2.27.

DNA cleavage experiments were performed in the presence of an oxidizing agent (H_2O_2) and a reducing agent (2–mercaptoethanol or BME). In the absence of an oxidizing or reducing agent, **1a** and **1b** could not exhibit (may be negligible) any nuclease activity (Fig. 2.25, lanes 4 and 10 respectively). However both the complexes showed excellent nuclease activity in presence of H_2O_2 as well as BME (Fig. 2.25, lanes 5–6 and 11–12 respectively) and it was found that the nuclease activity was more pronounced in presence of H_2O_2 than BME. Interestingly, the whole DNA got converted to NC as well as LC forms in the presence of H_2O_2 at a minimum of 50 µM concentration of these complexes. It is clear from Fig. 2.25 that **1a** showed better nuclease activity as compared to **1b**. However we did not observe any NC or LC form of DNA in case of complexes **2a** and **2b** exhibiting their inefficiency to cleave DNA (Fig. 2.25, lanes 7–9 and 13–15 respectively). Hence efficient nuclease activity was afforded by all Co(II) complexes in presence of oxidizing or reducing agents whereas no such activity could be observed with the Co(III) complexes. In the control experiment, H_2O_2 and 2–mercaptoethanol did not exhibit any cleavage in the absence of cobalt complexes (Fig. 2.25, lanes 2, 3).

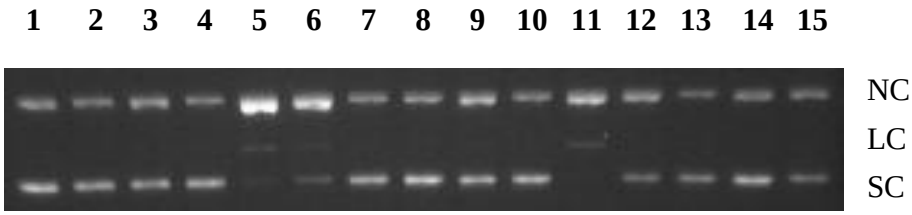

Fig. 2.25 Gel electrophoresis separations showing the cleavage of supercoiled pBR322 DNA (100 ng) by complexes **1a, 2a, 1b** and **2b** in presence of H_2O_2 (200 µM) and BME (200 µM). Samples were incubated at 37 °C for 2 h. Lane 1, DNA control; lane 2, DNA + H_2O_2; lane 3, DNA + BME; lane 4, DNA + **1a** (50 µM); lane 5, DNA + **1a** (50 µM) + H_2O_2; lane 6, DNA + **1a** (50 µM) + BME; lane 7, DNA + **2a** (50 µM); lane 8, DNA + **2a** (50 µM) + H_2O_2; lane 9, DNA + **2a** (50 µM) + BME; lane 10, DNA + **1b** (50 µM); lane 11, DNA + **1b** (50 µM) + H_2O_2; lane 12, DNA + **1b** (50 µM) + BME; lane 13, DNA + **2b** (50 µM); lane 14, DNA + **2b** (50 µM) + H_2O_2; lane 15, DNA + **2b** (50 µM) + BME

Small molecule SOD mimics prove to be potent agents for cleaving the DNA. Interestingly, in the previous reports, manganese complexes with ligand PampH bearing the carboxamido functionality exhibited excellent DNA cleavage whereas those with Pyimpy showed no nuclease activity.[381] For these complexes, it was found that the complexes which were capable of dismuting superoxide, exhibited the DNA cleavage activity also. This may be due to the redox potentials of manganese complexes derived from PampH which significantly differ from those of complexes derived from Pyimpy. In the present report, the Co(III) complex derived from PampH showed no nuclease activity whereas Co(II) complexes of Pyimpy showed excellent nuclease activity which is in contradiction to the previously reported results.[381]

In order to see the effect of incubation time on the nuclease activity of these complexes, we have performed gel electrophoresis experiments with **1a** by varying the incubation time over 15–90 min. Interestingly, conversion of SC form to NC form increased progressively with the increase in the incubation time (Fig. 2.26, lanes 4–6 and 7–9).

Furthermore, the extent of cleavage also increased with the increasing concentration of H_2O_2 (Fig. 2.26, lanes 13–15).

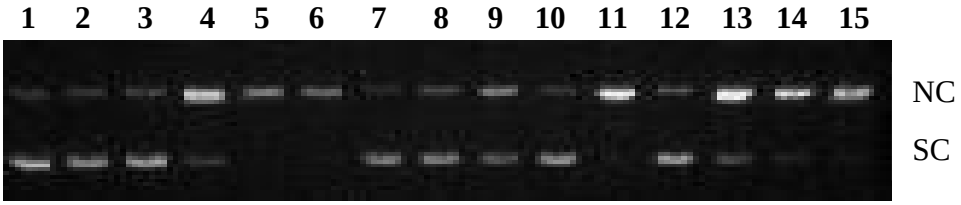

Fig. 2.26 Gel electrophoresis separation showing the cleavage of supercoiled pBR 322 DNA (100 ng) by complexes **1a** and **1b** (100 μM). The samples were incubated at 37 ˚C for 2 h except wherever mentioned. Lane 1, DNA; lane 2, DNA + H_2O_2 (200 μM); lane 3, DNA + BME (200 μM); lanes 4–6, DNA + **1a +** H_2O_2 (200 μM) (incubation time 15 min, 60 min and 90 min respectively); lanes 7–9, DNA + **1a +** BME (200 μM) (incubation time 15 min, 60 min and 90 min respectively); lane 10, DNA + **1b**; lane 11, DNA + **1b** + H_2O_2 (200 μM); lane 12, DNA + **1b** + BME (200 μM); lane 13, DNA + **1a** + H_2O_2 (25 μM); lane 14, DNA + **1a** + H_2O_2 (50 μM); lane 15, DNA + **1a** + H_2O_2 (100 μM)

Role of diffusible radical species can be diagnosed by monitoring the quenching of DNA cleavage in the presence of radical scavengers in solution. Standard radical scavengers were added to the reaction of complex **1a** with H_2O_2 during DNA cleavage experiments. Analysis of the data obtained from the gel electrophoresis revealed that the presence of NaN_3 and L–histidine in the reaction system led to the significant inhibition in nuclease activity (Fig. 2.27, lanes 5 and 7). These data indicated that singlet oxygen and/or singlet oxygen like species may be responsible for the DNA cleavage. However, no enhancement in cleavage activity could be observed in presence of D_2O (Fig. 2.27, lane 6).[403] It was also observed, although to a lesser extent, that inhibition of nuclease activity occurred in presence of DMSO and EtOH which are known to be hydroxyl radical scavengers. A similar inhibition was also observed in presence of catalase. Hence the possible role of hydroxyl radical as well as peroxide ion in DNA cleavage could not be ruled out.

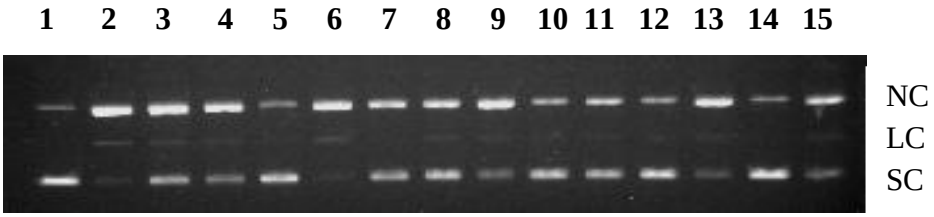

Fig. 2.27 Gel electrophoresis separations showing the cleavage of supercoiled pBR322 DNA (100 ng) by complex **1a** (50 µM) in presence of H_2O_2 (200 µM) and BME (200 µM). Samples were incubated at 37 °C for 2 h. Lane 1, DNA; lane 2, DNA + **1a** + H_2O_2; lanes 3-8, DNA + **1a** + H_2O_2 + DMSO, ethanol, NaN_3, D_2O, L- histidine (20 mM) and catalase (10 U) respectively; lane 9, DNA + **1a** + BME; lanes 10-15, DNA + **1a** + BME + DMSO, ethanol, NaN_3, D_2O, L–histidine (20 mM) and catalase (10 U) respectively

2.3. Conclusions

The following are the principal findings and conclusions of our present study. Cobalt(II) and cobalt(III) complexes of ligands Pyimpy and PampH respectively, were synthesized and characterized by spectroscopic studies. Molecular structure of [Co(Pyimpy)Cl_2] (**1a**), determined by X–ray crystallography afforded high–spin Co(II) center. Electrochemical studies afforded Co(II)/Co(III) and Co(I)/Co(II) redox couple for complexes [Co(Pyimpy)Cl_2] (**1a**) and [Co(Pyimpy)$_2$](ClO_4)$_2$ (**1b**). On the other hand, only Co(III)/Co(II) redox couple was found for complexes [Co(Pamp)Cl_2] (**2a**) and [Co(Pamp)$_2$](ClO_4) (**2b**). In the superoxide scavenging activity by NBT assay, complex **1a** and **1b** afforded IC_{50} values of 85± 3 µM and 105 ± 3 µM respectively. However we found that complexes **2a** and **2b** exhibited very poor activity. DNA interaction studies indicated external and/or surface binding of all the complexes. Interestingly, **1a** was efficient in DNA cleavage activity in presence of H_2O_2 as well as BME. Although **1b** also showed this type of nuclease activity but the efficiency of **1a** was better than **1b**. Complexes **2a** and **2b** neither exhibited SOD activity nor the nuclease activity. Mechanistic studies indicated possible role of reactive oxygen species (ROS) in the DNA cleavage catalyzed by **1a** and **1b**.

Investigation of results of the present report and those of other structurally related complexes (Table 2.7) clearly expressed that once the complex responds to superoxide scavenging activity, the complex will also be efficient in DNA cleavage activity in presence of H_2O_2 or BME.

Table 2.7 Summary of SOD activity and nuclease activity of complexes

S. No.	Complex	SOD activity	Nuclease activity	Reference
1.	$[Mn(Pyimpy)_2](ClO_4)_2$	Not effective	No	381
2.	$[Mn(Me–Pyimpy)_2](ClO_4)_2$	Not effective	No	381
3.	$[Mn(Pamp)_2](ClO_4)$	~3.73 μM	Yes	381
4.	$[Mn(Phimp)_2]$	~0.29 μM	Yes	332
5.	$[Mn(Phimp)_2](ClO_4)$	~0.39 μM	Yes	332
6.	$[Mn(N–Phimp)_2](ClO_4)$	~1.12 μM	Yes	332
7.	$[Cu(Pyimpy)(H_2O)](ClO_4)_2$	~7.41 μM	Yes	403
8.	$[Cu(Pyimpy)Cl_2]$	~4.92 μM	Yes	403
9.	$[Cu(Phimp)(H_2O)]_2(ClO_4)_2$	~11.20 μM	Yes	404
10.	$[Cu(Phimp)_2]$	~8.31 μM	Yes	404
11.	$[Co(Pyimpy)Cl_2]$	~85 μM	Yes	Present work
12.	$[Co(Pyimpy)_2](ClO_4)_2$	~105 μM	Yes	Present work
13.	$[Co(Pamp)Cl_2]$	Not effective	No	Present work
14.	$[Co(Pamp)_2](ClO_4)$	Not effective	No	Present work

2.4. Experimental section

2.4.1 Reagents and materials

Analytical grade reagents Phenylhydrazine, 2–mercaptoethanol, hydrogen peroxide (S. D. Fine, Mumbai, India), sodium azide (Sigma Aldrich, Steinheim, Germany), picolinic acid (Wilson Laboratories, Mumbai, India), 1–hydroxybenzotriazol, sodium perchlorate monohydrate (Himedia Laboratories Pvt. Ltd., Mumbai, India), dicyclohexylcarbodiimide (SRL, Mumbai, India), ethylenediaminetetraacetic acid, cobalt chloride hexahydrate (Merck Limited, Mumbai, India), pyridine–2–aldehyde, sodium hydride and 2–chloropyridine (Acros organics, USA) were used as obtained. The supercoiled pBR322 DNA and CT DNA

were purchased from Bangalore Genei (India) and stored at 4 °C. Agarose (molecular biology grade) and ethidium bromide were obtained from Sigma Aldrich. Xanthine, nitro blue tetrazolium (NBT) and catalase were obtained from Himedia and xanthine oxidase (XO) from bovine milk was purchased from Sigma. Tris(hydroxymethyl)aminomethane–HCl (Tris–HCl) buffer and phosphate buffer were prepared in deionised water. Solvents used for spectroscopic studies were HPLC grade and purified by standard procedures before use.

2.4.2. Synthesis of ligands

Synthesis of 1-phenyl-1-(pyridin-2-yl)-2-(pyridin-2-ylmethylene)hydrazine (Pyimpy) and N'-phenyl-N'-(pyridin-2-yl)picolinohydrazide (PampH)

Ligands Pyimpy and PampH were prepared according to the reported procedures.[381]

2.4.3. Synthesis of cobalt complexes

Caution! Perchlorate salts of metal complexes with organic ligands are potentially explosive. Only a small amount of material should be prepared and handled with caution.

Synthesis of [Co(Pyimpy)Cl_2] (1a)

A batch of $CoCl_2 \cdot 6H_2O$ (0.238 g, 1 mmol) was dissolved in 5 mL of tetrahydrofuran. After stirring for 5 min, a batch of ligand (Pyimpy) (0.274 g, 1 mmol) dissolved in 15 mL of tetrahydrofuran was added dropwise. The color of the solution changed from blue to green and resulted into the precipitation of a green solid. After 3 h of stirring, the solid was filtered and washed thoroughly with excess of tetrahydrofuran and dried *in vacuo*. The complex was recrystallized in methanol: tetrahydrofuran mixture. Yield: 81%. *Anal*. (%) Calcd. for $C_{17}H_{14}Cl_2CoN_4$: C, 50.52; H, 3.49; N, 13.86. Found: C, 50.29; H, 3.62; N, 13.93. Selected

IR data (KBr, ν_{max}/cm^{-1}): 1596, $\nu_{C=N}$; μ_{eff} (297 K): 4.60 μ_B. $\Lambda_M/\Omega^{-1}cm^2mol^{-1}$ (DMF): 17 (1:1). UV–visible [CH_3OH, λ_{max}/nm ($\varepsilon/M^{-1}cm^{-1}$)]: 230 (12360), 249 (10340), 278 (8040), 359 (13160). ESI–MS (acetonitrile, neg.): m/z 402.08 [$M\text{-}H^+$].

Synthesis of $[Co(Pyimpy)_2](ClO_4)_2$ (1b)

A batch of ligand (Pyimpy) (0.274 g, 1 mmol) was dissolved in 10 mL of methanol. After stirring for 10 min, a batch of $CoCl_2{\cdot}6H_2O$ (0.119 g, 0.5 mmol) in 10 mL of methanol was added dropwise to the above stirring solution. The colour of the solution changed to red. After 30 min of stirring, a batch of sodium perchlorate monohydrate (0.154 g, 1.1 mmol) dissolved in 5 mL of methanol was added and stirred for 2 h. An orange solid precipitated which was filtered, washed with small amount of methanol, successively with diethyl ether and dried *in vacuo*. Yield: 59%. *Anal*. (%) Calcd. for $C_{34}H_{28}Cl_2CoN_8O_8$: C, 50.64; H, 3.50; N, 13.89. Found: C, 50.45; H, 3.56; N, 13.85. Selected IR data (KBr,ν_{max}/cm^{-1}): 1599, $\nu_{C=N}$; 1088, 625, ν_{ClO4}^-. μ_{eff} (297 K): 4.54 μ_B. $\Lambda_M/\Omega^{-1}cm^2mol^{-1}$ (DMF): 141 (1:2). UV–visible [CH_3OH, λ_{max}/nm ($\varepsilon/M^{-1}cm^{-1}$)]: 230 (30540), 249 sh (24540), 291 (19760), 358 (29400). ESI–MS (acetonitrile, pos.): m/z 706.11 (4.5%) $[M\text{-}(ClO_4)]^+$, m/z 303.58 (100%) $[M\text{-}2(ClO_4)]^{2+}$.

Synthesis of $[Co(Pamp)Cl_2]$ (2a)

Method A: A batch of ligand (PampH) (0.290 g, 1 mmol) was dissolved in 10 mL of methanol. After stirring for 5 min, a batch of sodium hydride (0.024 g, 1 mmol) was added to this solution and stirred for 1 h. This deprotonated ligand solution was added dropwise to a continuously stirred solution of $CoCl_2{\cdot}6H_2O$ (0.262 g, 1.1 mmol) dissolved in 5 mL of methanol. After 4 h of strirring, volume was reduced to 5 mL under reduced pressure. A green solid separated out which was washed with very small amount of methanol,

successively with diethyl ether and dried *in vacuo*. The complex was then recrystallized in methanol. Yield: 37%. *Anal*. (%) Calcd. for $C_{17}H_{13}Cl_2CoN_4O$: C, 48.71; H, 3.13; N, 13.37. Found: C, 48.32; H, 3.34; N, 13.52. Selected IR data (KBr,ν_{max}/cm^{-1}): 1655, $\nu_{C=O;}$. $\Lambda_M/\Omega^{-1}cm^2mol^{-1}$ (DMF): 30. UV–visible [CH_3OH, λ_{max}/nm ($\varepsilon/M^{-1}cm^{-1}$)]: 394 (12900). ^{1}H NMR (500 MHz, δ/ppm, $CDCl_3$): 8.35 (d, J=5.5 Hz, 1 H), 8.11 (t, J=7.5 Hz, 1 H), 7.96 (dd, 2 H), 7.82 (m, 3H), 7.73 (t, J=8 Hz, 2 H), 7.62 (t, J=7 Hz, 1 H), 7.55 (t, 1 H), 6.93 (t, J=6.5 Hz, 1H), 6.37 (d, J=9 Hz, 1H), ^{13}C NMR (500 MHz, δ/ppm, $CDCl_3$): 163.62, 161.10, 156.61, 149.17, 145.73, 142.07, 141.10, 141.04, 130.54, 130.05, 130.01, 128.43, 125.85, 119.04, 109.97.

Method B: A batch of $CoCl_2{\cdot}6H_2O$ (0.262 g, 1.1 mmol) was dissolved in 5 mL of methanol. After stirring for 5 min, a batch of ligand (PampH) (0.290 g, 1 mmol) dissolved in 10 mL of methanol was added dropwise to the above stirring solution and stirring was continued to 4 h. A green solid separated out which was washed with small amount of methanol, successively with diethyl ether and dried *in vacuo*. The complex was then recrystallized in methanol. Yield: 54%.

Synthesis of $[Co(Pamp)_2]ClO_4$ (2b)

Method A: A batch of ligand (PampH) (0.145 g, 0.5 mmol) was dissolved in 5 mL of acetonitrile. After stirring for 5 min, a batch of sodium hydride (0.012 g, 0.5 mmol) was added to the stirred solution and stirred for 1 h. A batch of $CoCl_2{\cdot}6H_2O$ (0.060 g, 0.25 mmol) in 5 mL of acetonitrile was added dropwise to the above stirred solution. The colour of the solution changed to red. After 30 min of stirring, the solution was filtered. A batch of sodium perchlorate monohydrate (0.042 g, 0.3 mmol) dissolved in 2 mL of acetonitrile was added to the filtrate. After 4 h of stirring the solution was evaporated to dryness *in vacuo*.

The brown solid obtained was recrystallised in dichloromethane: methanol mixture. Yield: 82%. *Anal*. (%) Calcd. for $C_{34}H_{26}ClCoN_8O_6$: C, 55.41; H, 3.56; N, 15.20. Found: C, 55.14; H, 3.79; N, 15.16. Selected IR data (KBr,ν_{max}/cm^{-1}): 1655, $\nu_{C=O}$; 1096, 623, ν_{ClO4}^{-}. $\Lambda_M/\Omega^{-1}cm^2mol^{-1}$ (DMF): 60 (1:1). UV−visible [CH_3OH, λ_{max}/nm ($\varepsilon/M^{-1}cm^{-1}$)]: 398 (22000). ^{1}H NMR (500 MHz, δ/ppm, $CDCl_3$): 8.34 (d, J=6 Hz, 1 H), 8.08 (t, J=6.5 Hz, 1 H), 7.95 (t, J=6 Hz, 2 H), 7.78 (m, 3H), 7.72 (t, 2 H), 7.61 (t, 1 H), 7.52 (t, 1 H), 6.90 (t, J=6 Hz, 1H), 6.37 (d, J=8.5 Hz, 1H). ^{13}C NMR (500 MHz, δ/ppm, $CDCl_3$): 163.66, 161.12, 156.66, 149.22, 145.78, 141.96, 141.14, 140.97, 130.53, 129.98, 129.88, 128.41, 125.84, 119, 109.98. ESI−MS (acetonitrile, pos.): m/z 637.15 (100 %) $[M-(ClO_4)]^+$.

Method B: A batch of ligand (PampH) (0.145 g, 0.5 mmol) was dissolved in 5 mL of acetonitrile. A batch of $CoCl_2{\cdot}6H_2O$ (0.060 g, 0.25 mmol) dissolved in 10 mL of acetonitrile was added dropwise to the above stirred solution. The colour of the solution changed to red. After 2 h of stirring, a batch of sodium perchlorate monohydrate (0.042 g, 0.3 mmol) dissolved in 2 mL of acetonitrile was added to reaction mixture and stirring was continued for additional 2 h followed by filtration of the reaction mixture. The filtrate was evaporated to dryness *in vacuo*. The brown solid obtained was recrystallised in dichloromethane: methanol mixture. Yield: 68%.

2.4.4. X–ray crystallography

The X–ray data collection and processing for **1a** was carried out on Bruker Kappa Apex–II CCD diffractometer by using graphite monochromated Mo–Kα radiation (λ = 0.71073 Å) at 293 K. Crystal structure was solved by direct methods. Structure solution, refinement and data output were carried out with the SHELXTL program.[351] All non–hydrogen atoms were refined anisotropically. Hydrogen atoms were placed in geometrically

calculated positions and refined using a riding model. Graphics were created with the DIAMOND[352] and MERCURY[353] programs.

Table 2.8 Crystal data and data collection parameters for **1a**

Empirical formula	$C_{17}H_{14}Cl_2N_4Co$
Formula weight ($gmol^{-1}$)	404.17
Temperature /K	293(2)
λ (Å) (Mo-Kα)	0.71073
Crystal system	Orthorhombic
Space group	*P212121*
a (Å)	8.4008(6)
b (Å)	10.0715(7)
c (Å)	19.8632(12)
~ (°)	90.000
γ (°)	90.000
β (°)	90.00
V ($Å^3$)	1680.6(2)
Z	4
ρ_{calc} (gcm^{-3})	1.597
F(000)	820
Theta range for data collection	2.05−32.85
Index ranges	$-12 < h < 8$, $-15 < k < 9$, $-30 < l < 27$
Refinement method	Full matrix least–squares on F^2
Data/restraints/parameters	6115/0/218
GOF[a] on F^2	0.734
R_1[b] [$I > 2\sigma(I)$]	0.0364
R_1[all data]	0.0307
wR_2[c] [$I > 2\sigma(I)$]	0.0973
wR_2 [all data]	0.0774

2.4.5. Superoxide dismutase assay

To investigate the ability of complexes (**1**–**2**) towards dismutation of superoxide radicals, McCord−Fridovich assays were performed and the inhibition of NBT reduction by superoxide radicals was monitored. Experiment was started by the addition of 2.1 mU/mL xanthine oxidase to the reaction system containing 0.2 mM xanthine, 0.6 mM NBT, 1000 U/mL catalase and varying concentration of complexes in 0.1 M phosphate buffer (pH 7.8).

The measurements were started after 10 min incubation and each experiment was performed in duplicate. The degree of NBT reduction was monitored by measuring the absorbance at 560 nm. IC_{50} value for SOD activity was defined as the concentration of the compound for 50% inhibition of NBT reduction by superoxide radicals generated in the reaction system.

2.4.6. DNA binding and cleavage experiments

DNA binding experiments were carried out in 0.1 M phosphate buffer (pH 7.2) with complex concentration of 40–100 μM varying the CT–DNA concentration from 0–135 μM. Fluorescence quenching experiments were carried out by successive additions of the cobalt complexes as quencher molecules to the DNA (25 μM) solutions containing 5 μM ethidium bromide (EB) in 0.1 M phosphate buffer (pH 7.2). These samples were excited at 250 nm and emissions were observed between 500 and 700 nm. Circular dichroism (CD) spectra of CT–DNA in absence and presence of the cobalt complexes were recorded with a 0.1 cm path-length cuvette after 10 min incubation at 25 °C. The concentration of CT–DNA and complexes were 200 and 50 μM respectively.

Agarose gel electrophoresis experiments were carried out to investigate the nuclease activity of the cobalt complexes. Supercoiled pBR322 DNA (100 ng) in Tris–boric acid–EDTA (TBE) buffer (pH 8.2) was treated with cobalt complexes (50–200 μM) in the presence or absence of additives. The oxidative DNA cleavage by the complexes were studied in the presence of H_2O_2 (200 μM, oxidizing agent) or 2–mercaptoethanol (200 μM, reducing agent) and DMSO, ethanol, NaN_3, D_2O, L–histidine (20 mM each) and catalase (10 U). The samples were incubated for 15 min to 2 h at 37 °C followed by the addition of loading buffer (25% bromophenol blue and 30% glycerol) and then subjected to gel electrophoresis.

3.1. Introduction

Transition metal complexes are widely used as efficient catalysts (*chapter 1*) for several chemical and biochemical transformations due to their cationic character, high charge density, strong Lewis acidity, tunable coordination geometries, versatile redox chemistry and unique spectroscopic properties.[28,405] Their interaction with biomolecules like DNA and RNA is of enormous importance and has led to the development of a wide range of foot–printing agents, electrochemical probes and chemotherapeutic agents.[269] One of the most prominent examples of such complexes is *cis*Jplatin, a well known anticancer drug, which binds covalently at N7 position of the guanine nucleobases (*chapter 1*).[266] Although, there is a large number of anticancer agents which exhibit non–covalent interactions with DNA, examples of covalent attachment with DNA are still rare.[299,406] These agents cause deformation in the structure of DNA and hamper its replication process. However, the mode of action of metal based drugs is not yet clear and demands further investigations.[407]

Moreover, several metal based artificial nucleases have also been developed which can either oxidize the sugar moiety and/or nucleobases of nucleic acids (oxidative cleavage) or catalyze the hydrolysis of phosphodiester back bone of DNA (hydrolytic cleavage) (*chapter 1*). Metallonucleases exhibiting hydrolytic type of cleavage receive special importance since these generally do not require the addition of external agents (activator). This makes them suitable for *in vivo* applications and the fragments produced after cleavage are more amenable for further enzymatic manipulations.[408] Redox inertness,[2,112] strong Lewis acidity, ligand exchange properties and negligible energy barrier for stereochemical changes altogether make Zn(II) the best suited ion in this regard[136,303,307] among other biologically relevant metal ions which is also reflected in the nature's selection of metal ions

for hydrolases.[29,348] Till today, very few examples of zinc containing metallonucleases[303,307] or other metals–based catalytic agents have been reported which exhibit DNA cleavage activity via a hydrolytic pathway or self–activating mechanism thus providing enough room for further exploration.[409-416] In the development of anticancer drugs, nucleic acids have been the most trivial targets for binding and cleavage processes (*classical targets*). In the similar way, targeting proteins may also be significant to develop new and effective anticancer agents as suggested by high occurrence of alternations in the genes coding for the proteins in tumor cells (*non classical targets*).[297] One of such targets is the cancer suppressor p53 protein which is responsible for the regulation of cell growth by controlling programmed cell death (PCD).[417]

Moreover, interaction of plasma proteins with various metal based drugs has been implicated in a variety of pharmacological and biological processes. Serum proteins, specifically serum albumin and serum transferrin are known to bind various types of bioactive molecules chiefly by hydrophilic, hydrophobic and ionic interactions[418] and are responsible for the transport of various metal ions and metallodrugs through the blood channels. Bioavalilability, biodistribution and pharmacokinetics of many drugs is contingent upon their affinity to serum albumins thus directly influencing their concentration in the blood and in the binding sites, as well as their efficacy.[419] Protein interaction studies may be significant to reveal the structural aspects for designing new and more efficient drugs and for fixing their dose limits since weak binding with serum proteins results in poor distribution of drug while strong binding decreases the concentration of free drug in plasma.[345] Binding of metal complexes to protein molecules may also give rise to artificial metalloenzymes, known as *hybrids* where the metal complexes are encaged in a protein

scaffold in order to induce selectivity by providing a well suited second coordination sphere to the molecule.[420,421] The hybrids offer additional advantages since these possess the properties of the protein chain along with the activity of the artificial prosthetic group thus serving as the functional metalloprotein. Presence of protein scaffolds in these conjugates very often results with the enhancement of activity of the inorganic metal complex[422,423] and gives rise to highly economical and biocompatible catalysts useful in green industrial catalysis, pharmaceuticals, electrochemical biosensors, contrast agents, probes for protein structure and energy production[424] as well as metalloenzymes exhibiting non–natural catalytic activity. On the other hand there are several examples in the literature that metal complexes can also bind competitively to a protein binding pocket resulting with inhibition of their enzymatic function.[425] However, reports for the protein interaction of metal complexes are relatively scarce and this area is mainly dominated by the organic moieties.[426]

The present piece of work stems from our interest in metal based pharmaceutics which could decipher the precise mechanism of drug–biomolecule interactions and can foster the better understanding to develop new and more efficient drugs. A new tridentate meridional ligand N_3L (2–((1–phenyl–2–(1–(pyridin–2–yl)ethylidene)hydrazinyl)methyl)pyridine) having NNN donor set was synthesized and characterized by various spectroscopic techniques. The ligand afforded a series of mononuclear metal complexes (M = Cu, Zn, Co, Ni) (**3J6** respectively) which was characterized by elemental anlaysis, conductivity measurements, UV–visible, IR and NMR spectroscopy and ESI–mass spectrometry. The molecular structures of $[Cu(N_3L)Cl_2]$ (**3a**) and $[Co(N_3L)Cl_2]$ (**5a**) were determined by X–ray crystallography. Redox behavior of the complexes was investigated by cyclic voltammetry. DNA interaction

studies on these complexes were carried out using various spectroscopic techniques which predicted covalent type of binding probably via coordination of nucleobases with the metal centre. The complexes were also subjected to the protein interactions studies using BSA as a model substrate. A covalent type of binding was observed between surface donor groups of protein and the metal centers of the complexes. Nuclease activity of these compounds was explored and their mechanisms using various radical scavengers as well as through the anaerobic experiments were also investigated.

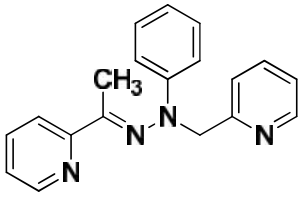

N_3L

Scheme 3.1 Schematic representation of the structure of ligand (N_3L)

3.2. Results and discussion

3.2.1. Synthesis and characterization of the ligand

The ligand N_3L was synthesized by two different procedures which are summarized in Schemes 3.2 and 3.3 respectively.

Procedure A

This method consists of the synthesis of 2−((1−phenylhydrazinyl)methyl)pyridine in the first step followed by its condensation with methyl−2−pyridylketone in next step. 2−((1−phenylhydrazinyl)methyl)pyridine was prepared through the deprotonation of phenylhydrazine by sodium hydride in toluene and the reaction of its sodium salt with 2−chloromethylpyridine free base (picolyl chloride).

2–((1–phenylhydrazinyl)methyl)pyridine prepared this way, was then subjected to the condensation reaction with methyl–2–pyridylketone in presence of some traces of concentrated sulphuric acid to afford the ligand 2–((1–phenyl–2–(1–(pyridin–2–yl)ethylidene)hydrazinyl)methyl)pyridine (N_3L) (Scheme 3.2).

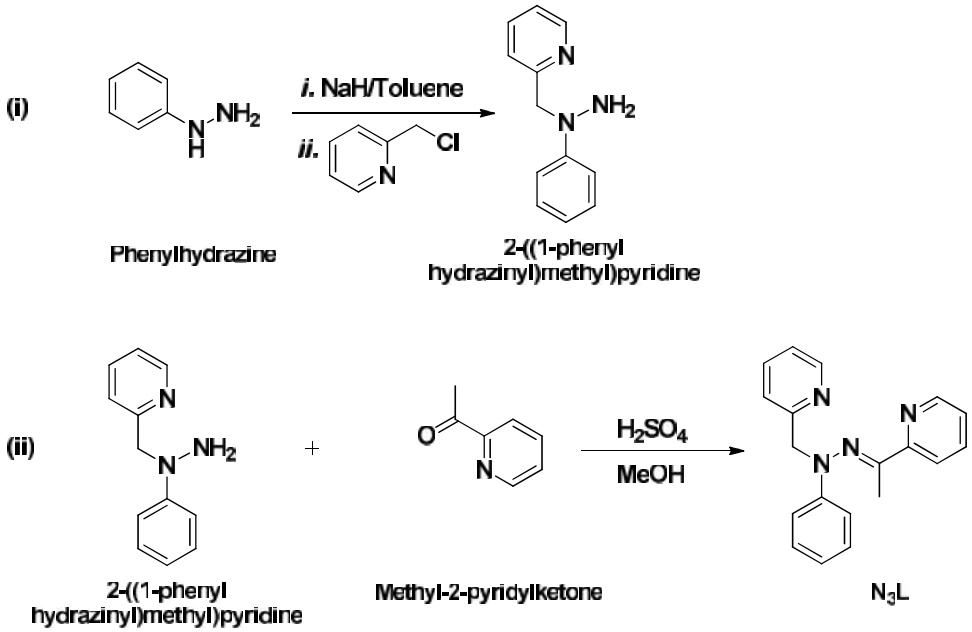

Scheme 3.2 Schematic representation of the synthesis of ligand N_3L by procedure 'A'

Procedure B

This procedure consists of the acid catalyzed condensation of methyl–2–pyridylketone and phenylhydrazine in methanol to prepare a Schiff base 2–(1–(2–phenylhydrazono)ethyl)pyridine in the first step followed by its substitution reaction over 2–chloromethylpyridine (picolyl chloride) free base to afford the ligand 2–((1–phenyl–2–(1–(pyridin–2–yl)ethylidene)hydrazinyl)methyl)pyridine (N_3L) (Scheme 3.3).

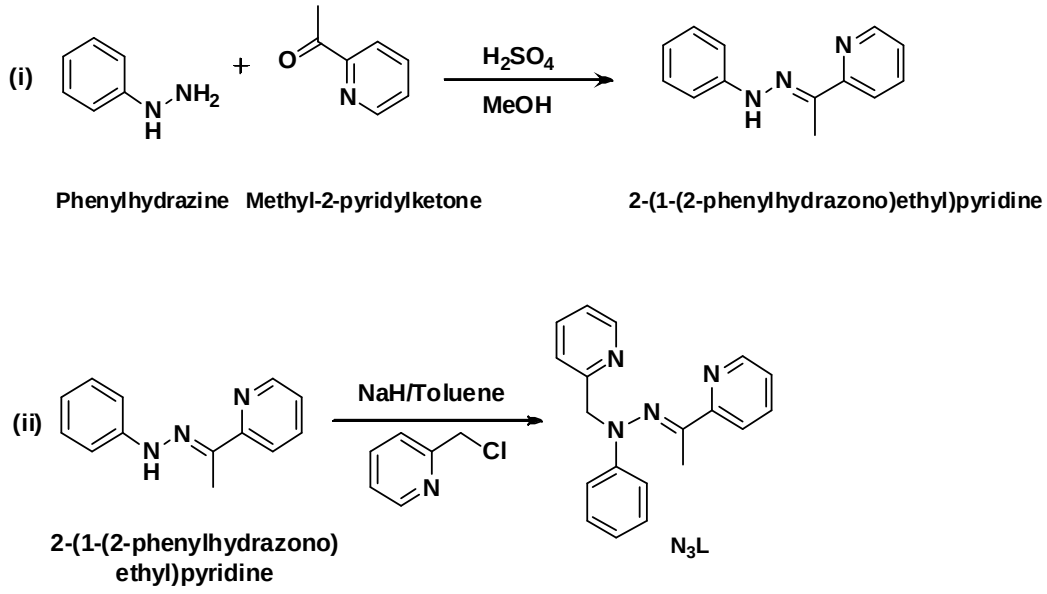

Scheme 3.3 Schematic representation of the synthesis of ligand N_3L by procedure 'B'

Both procedures afforded the product as red–yellow oil which was purified through column chromatography and method 'B' was preferred to method 'A' due to the higher yield of product (ligand) in the former.

The ligand was characterized by various physical and spectroscopic techniques including elemental analysis, IR, UV-visible and NMR spectroscopy as well as by ESI–mass spectrometry and the data are respresented in Tables 3.1 and 3.2. The IR spectrum of N_3L showed a peak near 1593 cm^{-1} which was assigned to the stretching frequency of azomethine function (─CH=N─). The absorption spectrum of the ligand exhibited intense bands near 251 (15056), 279 (6040) and 341 (5914) nm arising from $\pi-\pi^*$ and $n-\pi^*$ transitions (*vide infra*). All NMR spectra (including ^1H, ^{13}C and DEPT–NMR) of the ligand N_3L are represented in Figures 3.1–3.6. Proton NMR spectrum of the ligand in deuterated chloroform exhibited two sharp singlets near 2.35 ppm for three protons and 5.04 ppm for two protons predicting the presence of methyl and methylene groups, respectively, which

was further supported by the occurrence of corresponding peaks in ^{13}C NMR spectrum near 16.43 ppm and 63.86 ppm (Fig. 3.1 and 3.2 respectively). DEPT−135 NMR experiment can be used to differentiate between the carbons having even and odd number of protons. A downward peak near 63.86 ppm in DEPT−135 NMR spectrum of ligand suggested the presence of two protons attached to this carbon again confirming the presence of methylene group (Fig. 3.3). The disappearance of two peaks near 16.43 and 63.86 ppm in DEPT−90 NMR spectrum further confirmed that these peaks were due to a methyl and a methylene group respectively (Fig. 3.4). Vanishing of the signals near 149.84, 155.95, 159.00 and 163.71 in all DEPT−NMR spectra indicated that these signals belonged to the quaternary carbons and these did not possess any hydrogen attached to them (Fig. 3.3–3.5).

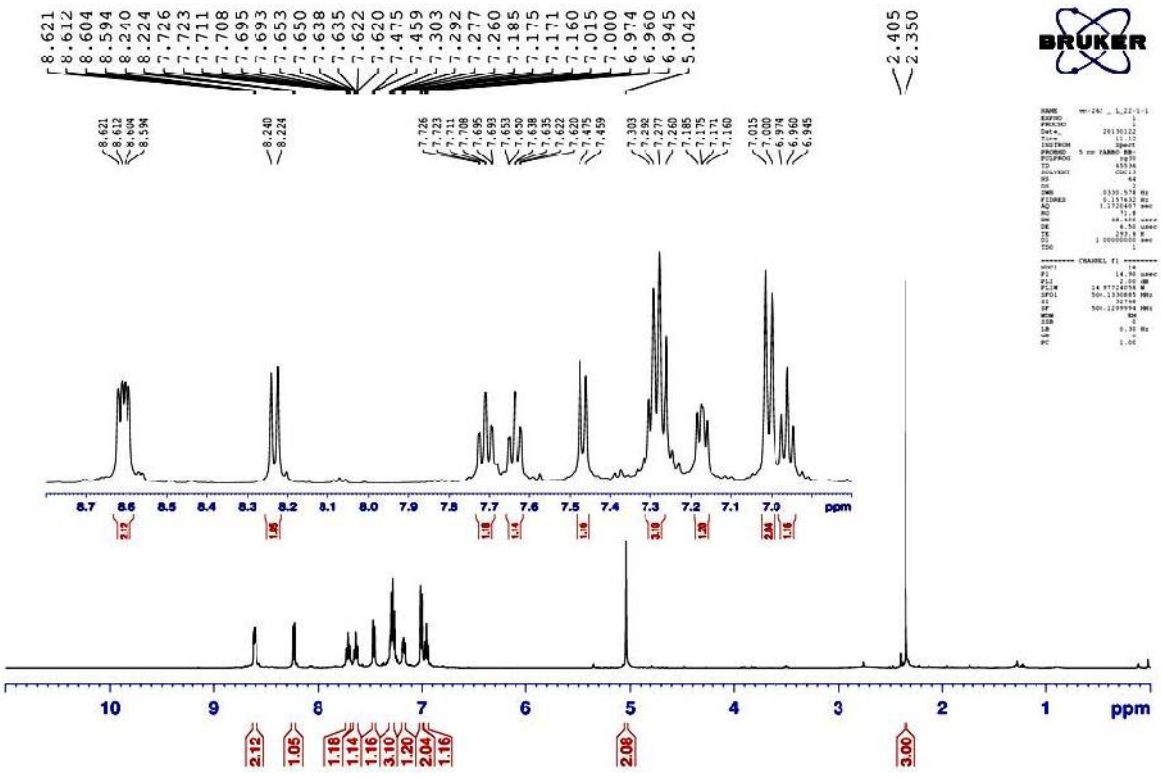

Fig. 3.1 ^{1}H NMR spectrum of ligand N_3L in $CDCl_3$

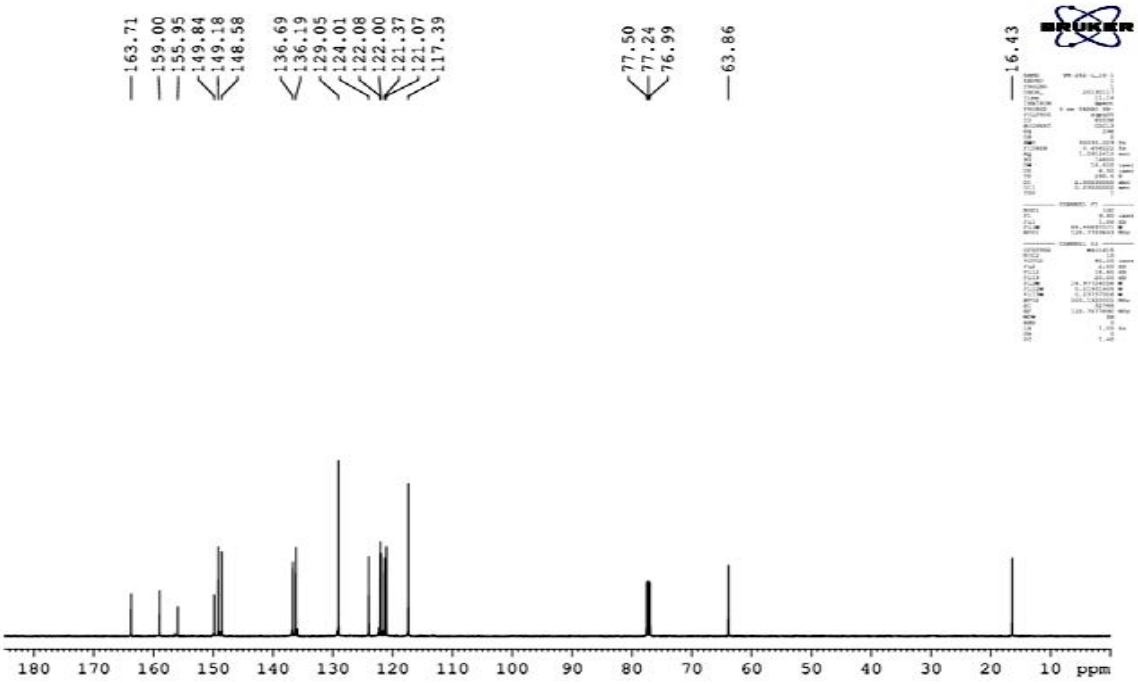

Fig. 3.2 ^{13}C NMR spectrum of ligand N_3L in $CDCl_3$

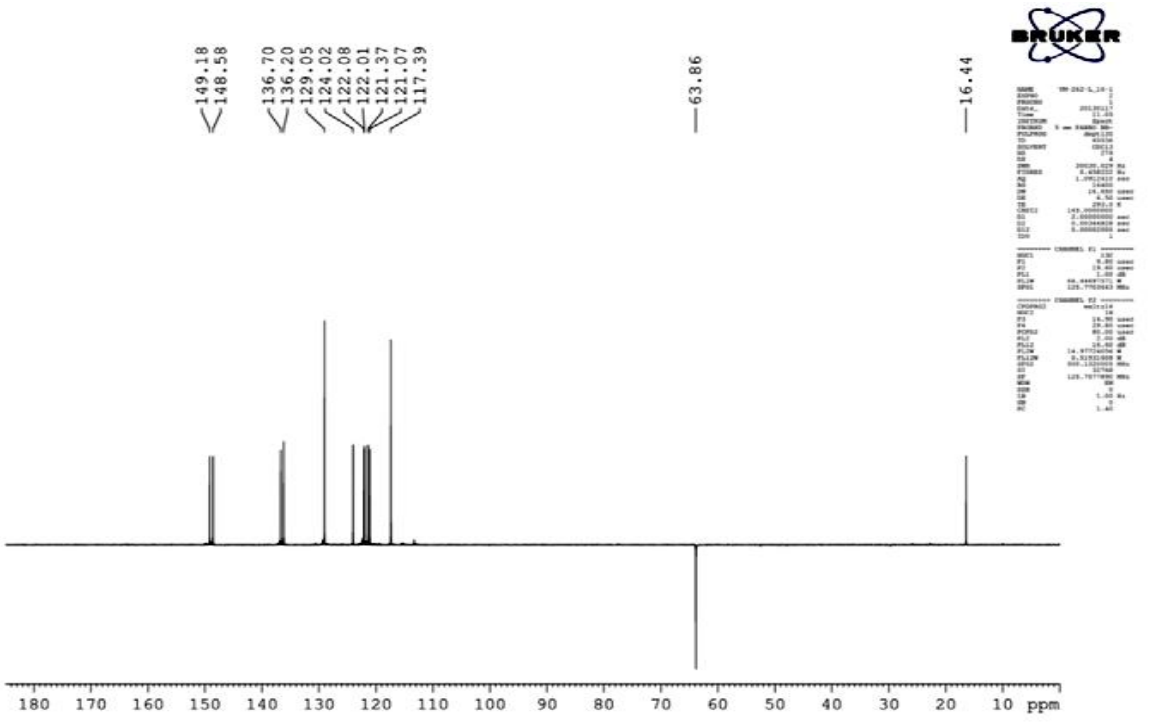

Fig. 3.3 DEPT-135 NMR spectrum of ligand N_3L in $CDCl_3$

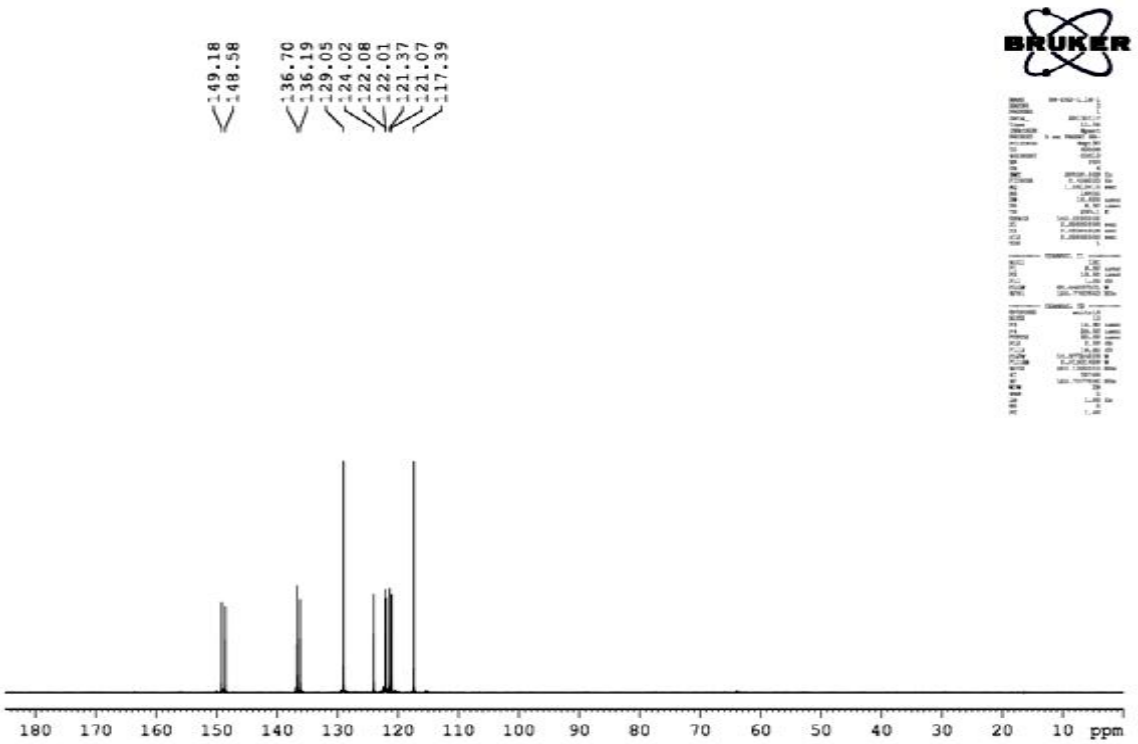

Fig. 3.4 DEPT−90 NMR spectrum of ligand N_3L in $CDCl_3$

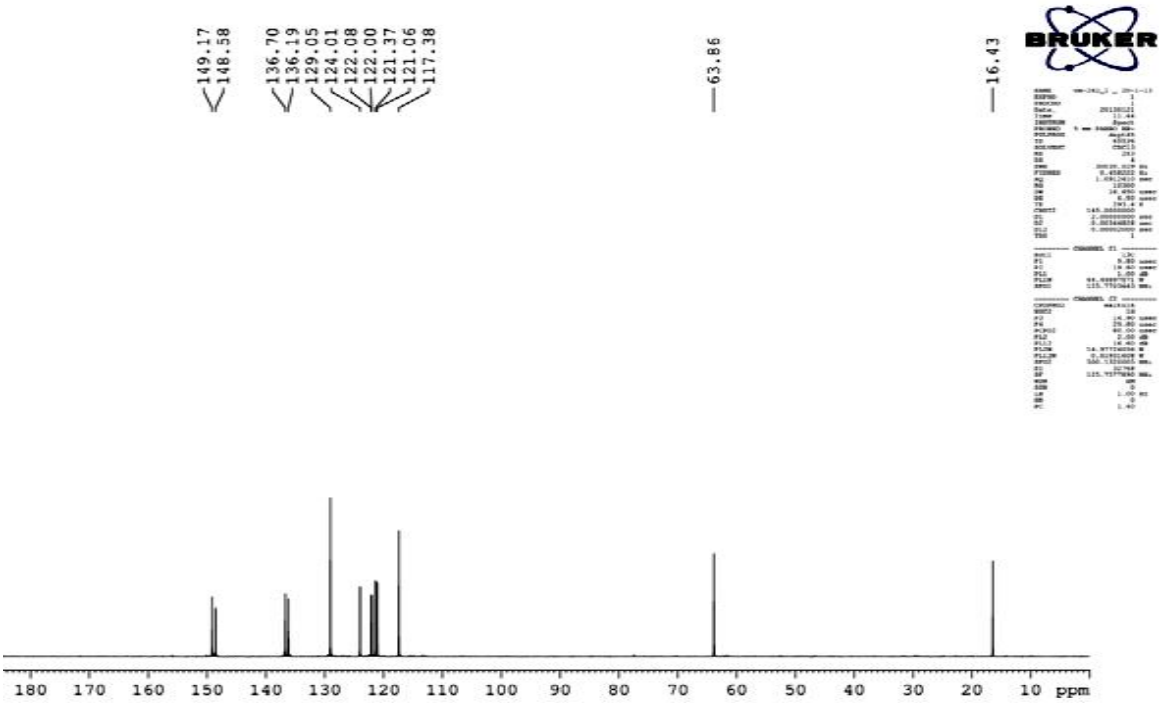

Fig. 3.5 DEPT−45 NMR spectrum of ligand N_3L in $CDCl_3$

The ESI–MS spectrum of N_3L is shown in the Fig. 3.6 which exhibited a peak with m/z value of 325.14 due to the formation of sodium adduct $[M+Na]^+$ (here M = ligand).

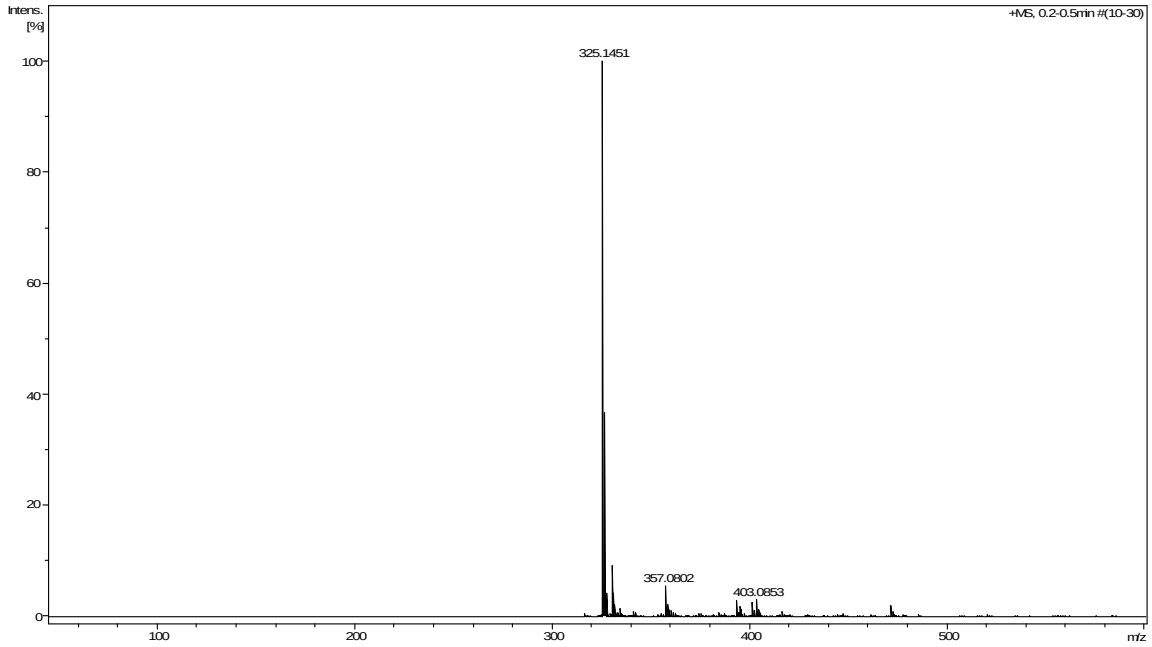

Fig. 3.6 The ESI–MS spectrum of ligand N_3L in acetonitrile under positive mode exhibiting the peak at (m/z) 325.14 corresponding to $[M+Na]^+$ cation

3.2.2. Synthesis and characterization of metal complexes

All the mono complexes $[M(N_3L)Cl_2]$ (M = Cu, Zn, Co and Ni; **3a**, **4a**, **5a** and **6a** respectively) were synthesized by the reaction of ligand (N_3L) and corresponding metal chloride salts in 1:1 molar ratio through the gradual addition of ligand to the metal salt solution. The bis complexes of copper and zinc $[M(N_3L)_2](ClO_4)_2$ (M = Cu, Zn; **3b** and **4b** respectively) were synthesized by the reaction of corresponding metal perchlorate salts with ligand in 1:2 molar ratio. However, the bis complexes of cobalt and nickel $[M(N_3L)_2](ClO_4)_2$ (M = Co and Ni; **5b** and **6b** respectively) were prepared using the respective metal chloride salts and stoichiometric amount of sodium perchlorate was charged in the reaction to provide the perchlorate ions as counter anions. All the reactions were performed in open

atmosphere and ended up with good yields. The synthetic strategy for preparing the metal complexes is illustrated in Scheme 3.4.

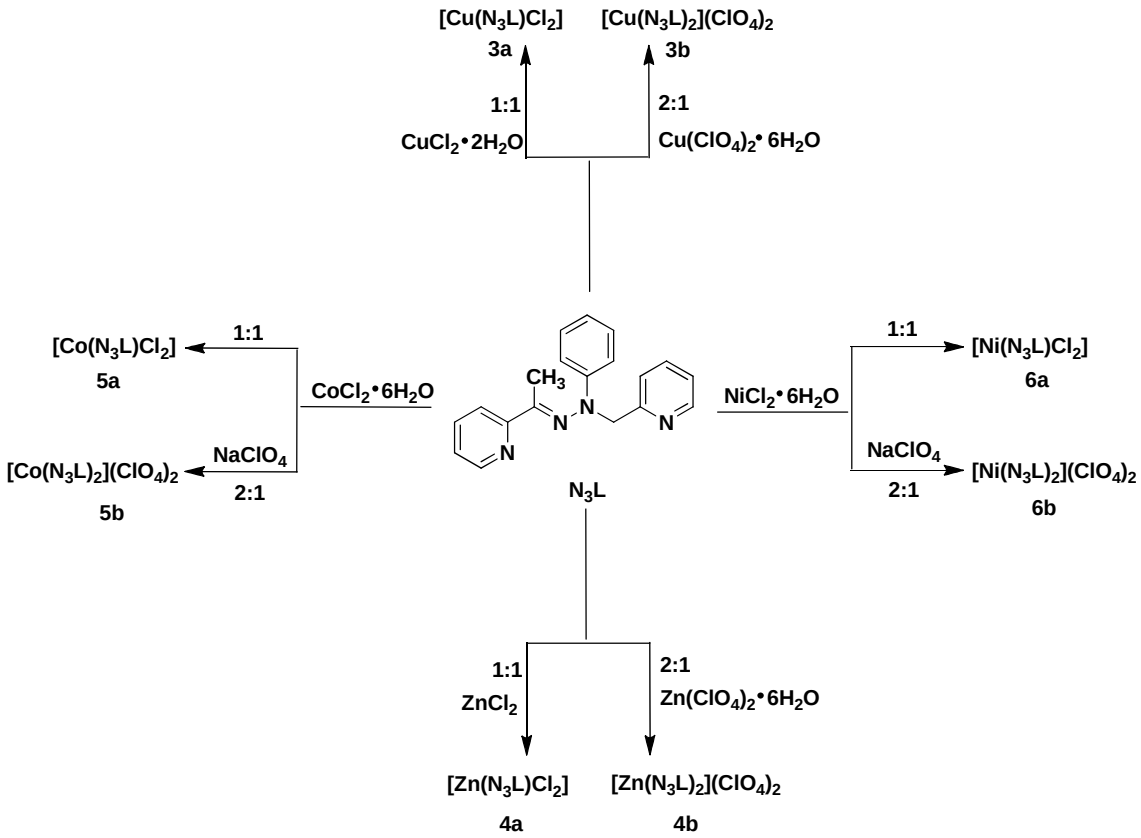

Scheme 3.4 Schematic representation of the synthesis of complexes **3-6**

Table 3.1 Data for yield, elemental analysis, IR, conductivity and magnetic moment

Complex	Yield %	Elemental analysis			Selected IR data (cm^{-1})[a]	Conductivity i_M ($t^{-1}cm^2mol^{-1}$)[b]	Magnetic moment (μ_B)
		C	H	N			
N_3L	70	75.47	5.84	18.65	1594	–	–
3a	77	52.35	4.32	12.70	1595,1659	23 (neutral)	1.75
3b	78	53.21	4.30	12.69	1596,1658	136 (1:2)	1.82
4a	73	52.50	4.19	12.70	1598,1639	9 (neutral)	–
4b	79	52.68	4.06	12.98	1594,1640	104 (1:2)	–
5a	72	53.01	4.19	12.85	1600,1646	23 (neutral)	4.34
5b	76	53.19	4.43	12.88	1604,1642	122 (1:2)	4.47
6a	52	53.51	4.64	13.02	1595,1624	49 (neutral)	3.15
6b	76	53.70	4.12	12.71	1602,1640	106 (1:2)	3.18

[a]KBr pellets, [b]Solvent: dimethylformamide

(i) IR spectral studies

In most of the complexes, the $\nu_{(-HC=N-)}$ was shifted to higher frequencies[385] as compared to the free ligand (1596 cm^{-1}) along with the appearance of a new peak within the range between 1624–1659 cm^{-1} suggesting the ligation of the azomethine nitrogen to the metal centres (Table 3.1). All the bis complexes exhibited an unsplitted peak near 1090 cm^{-1} along with a peak near 624 cm^{-1} in IR spectrum indicating the presence of non–coordinating perchlorate ion outside the coordination sphere.[332]

(ii) Electronic properties

Intense absorption bands were observed between 200–300 nm in the UV–visible spectra of all metal complexes. These bands were assigned as intra–ligand π–π* transitions (Table 3.2).

Table 3.2 UV–visible spectral data of ligand (N_3L) and complexes **3-6**

Complex	$^{a}\lambda_{max}$/nm (£/$M^{-1}cm^{-1}$)[a]
N_3L	251 (15056), 279 (6040), 341 (5914)
3a	239 (23964), 250 (22536), 286 (9430), 353 (6084), 395 (4508), 551 (706)
3b	238 (31436), 286 (12908), 344 (11976), 432 (2590)
4a	245 (13406), 258 (14168), 285 (5700), 374 (5332)
4b	246 (27656), 253 (28360), 285 (10240), 358 (8714)
5a	212 (17182), 215 (16576), 217 (15240), 245 (14560), 347 (3720), 407 (2736)
5b	246 (25500), 344 (8370), 406 (4140)
6a	242 (15940), 253 (15270), 280 (6970), 357 (3532), 402 (3064), 545 (228)
6b	242 (28160), 255 (26240), 347 (10598), 410 (5200), 543 (278)

[a]UV–visible data recorded in methanol

The absorption bands in the range 340–560 nm found in the UV–visible spectra of all metal complexes were accompanied with high molar extinction coefficient values which were assigned as ligand to metal charge transfer transitions.[427-430] The bands encountered in the lower energy end of the spectra (>500 nm) were assigned as d–d transitions due to their

low extinction values. The absorption spectra of ligand (N_3L) as well as the metal complexes (**3**-**6**) are given in Figure 3.7.

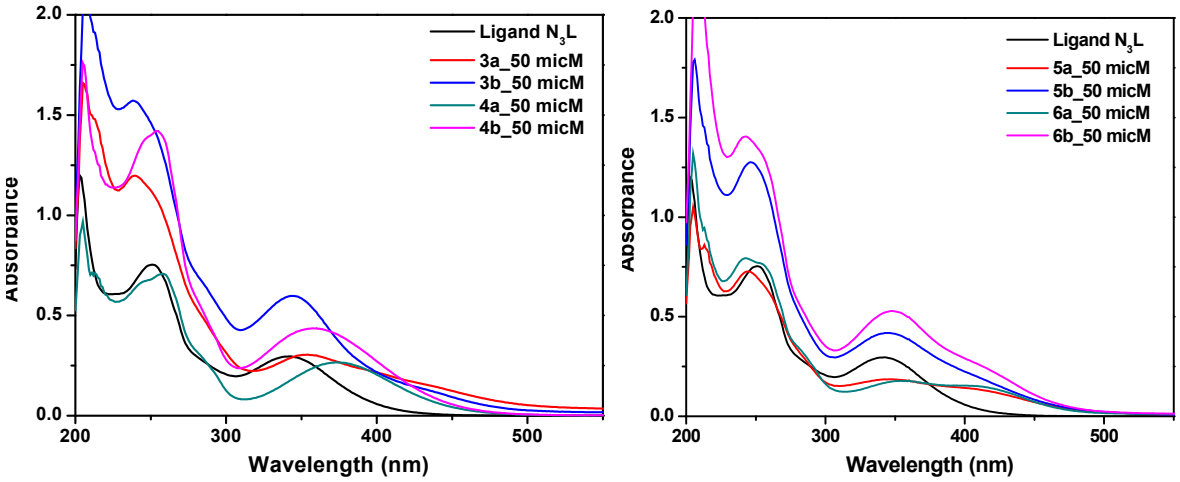

(a) (b)

Fig. 3.7 Quantitative UV–visible spectra of ligand and complexes (50 μM) in methanolic solution (a) **3aJb** and **4a**–**b**; (b) **5aJb** and **6a**–**b**

(iii) NMR spectroscopy

The diamagnetic zinc complexes **4a** and **4b** afforded clear NMR spectra however the peaks underwent little chemical shift as compared to those of the free ligand which indicated the coordination of the ligand with zinc ion. All ^{1}H and ^{13}C NMR spectral data (including DEPT) for **4a** and **4b** are represented below (Figures 3.8–3.13).

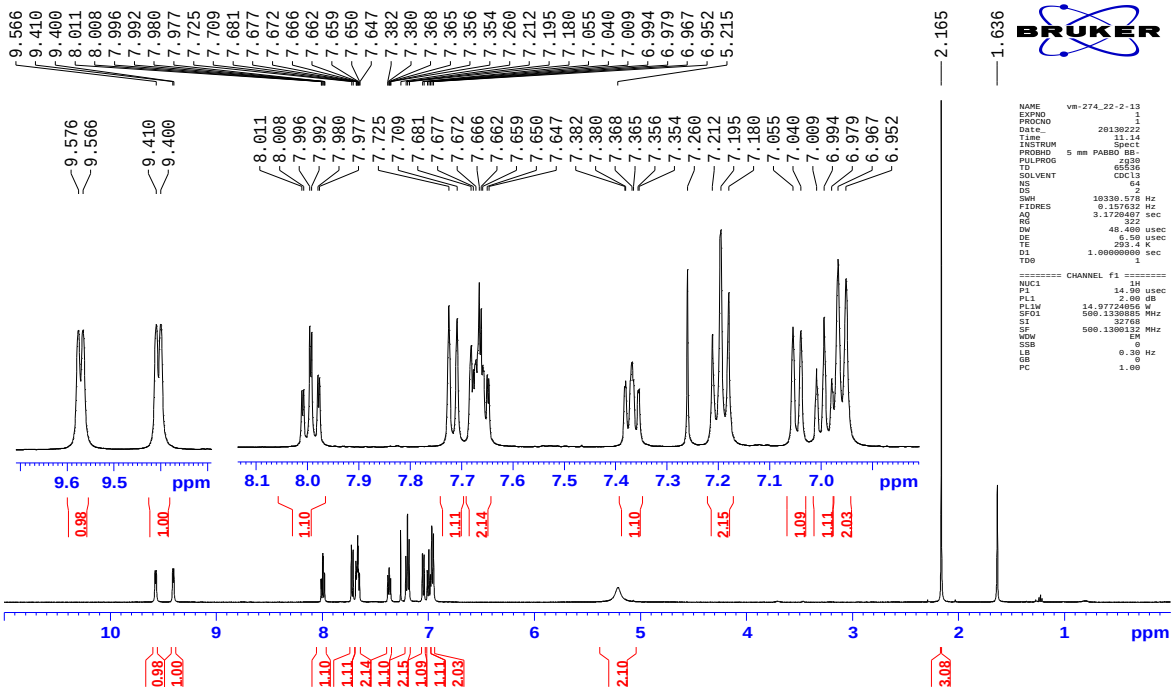

Fig. 3.8 ^{1}H NMR spectrum of **4a** in $CDCl_3$

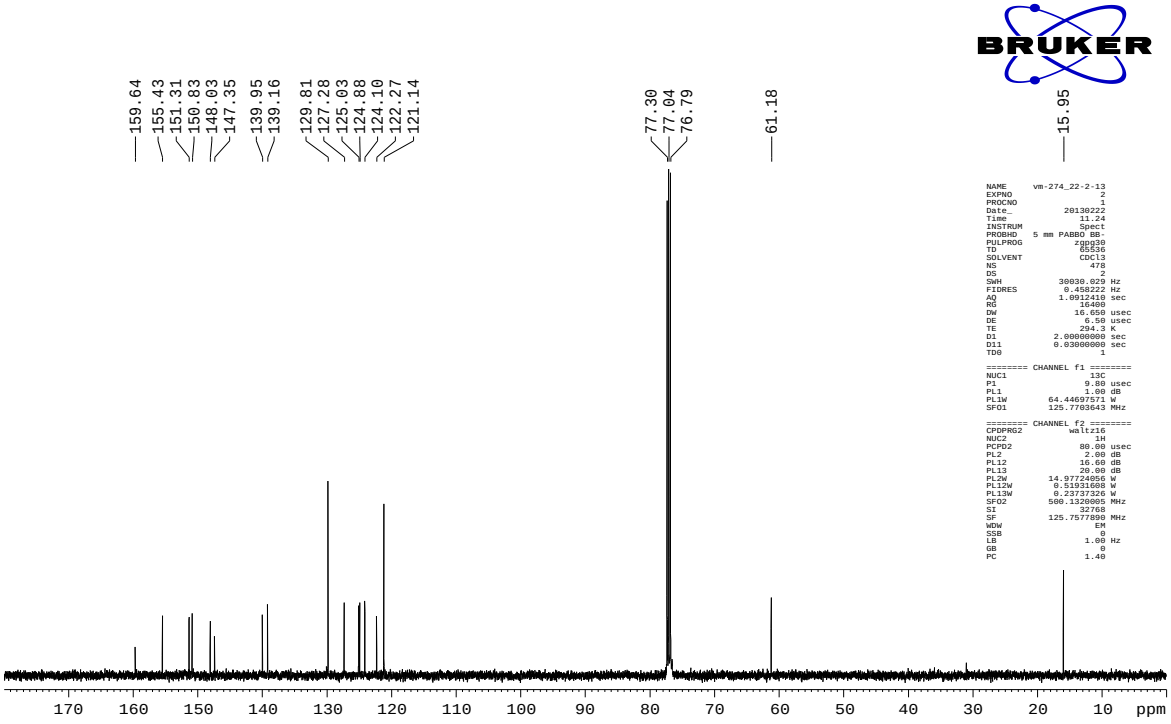

Fig. 3.9 ^{13}C NMR spectrum of **4a** in $CDCl_3$

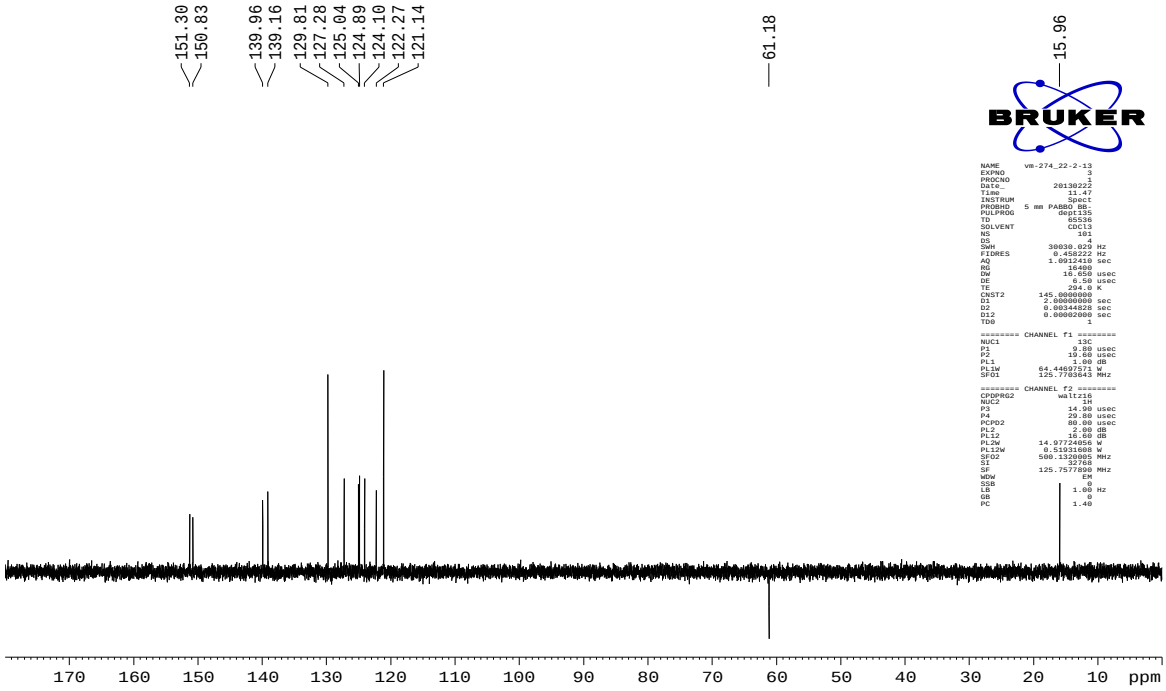

Fig. 3.10 DEPT–135 NMR spectrum of **4a** in $CDCl_3$

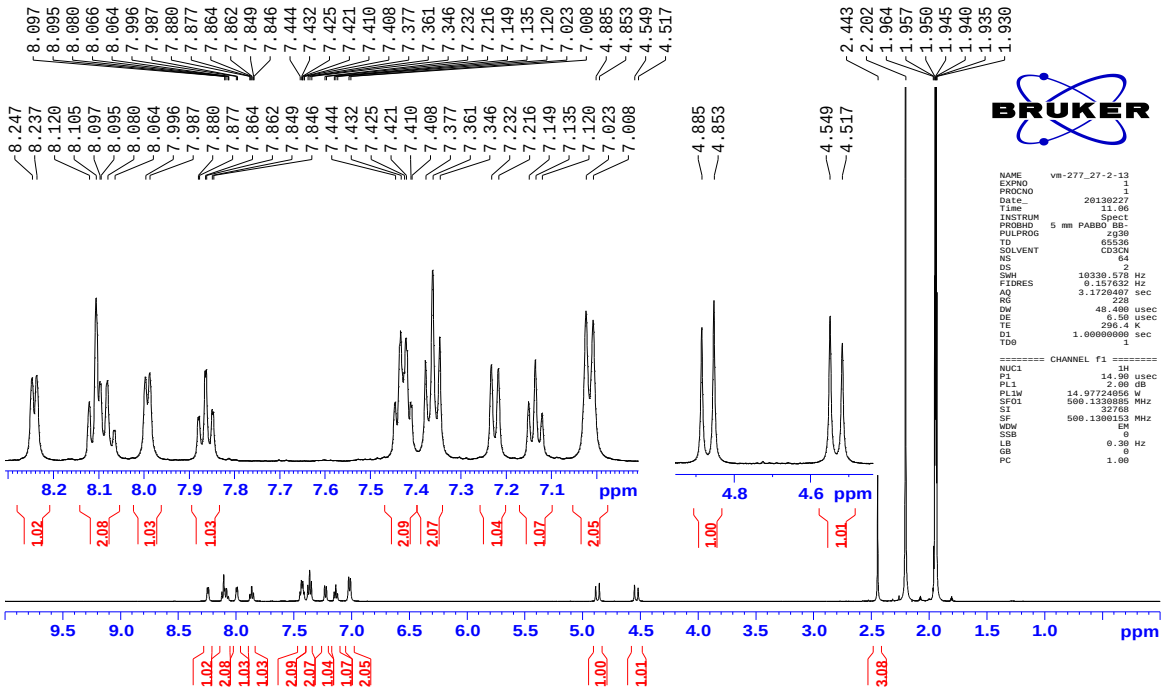

Fig. 3.11 ^{1}H NMR spectrum of **4b** in CD_3CN

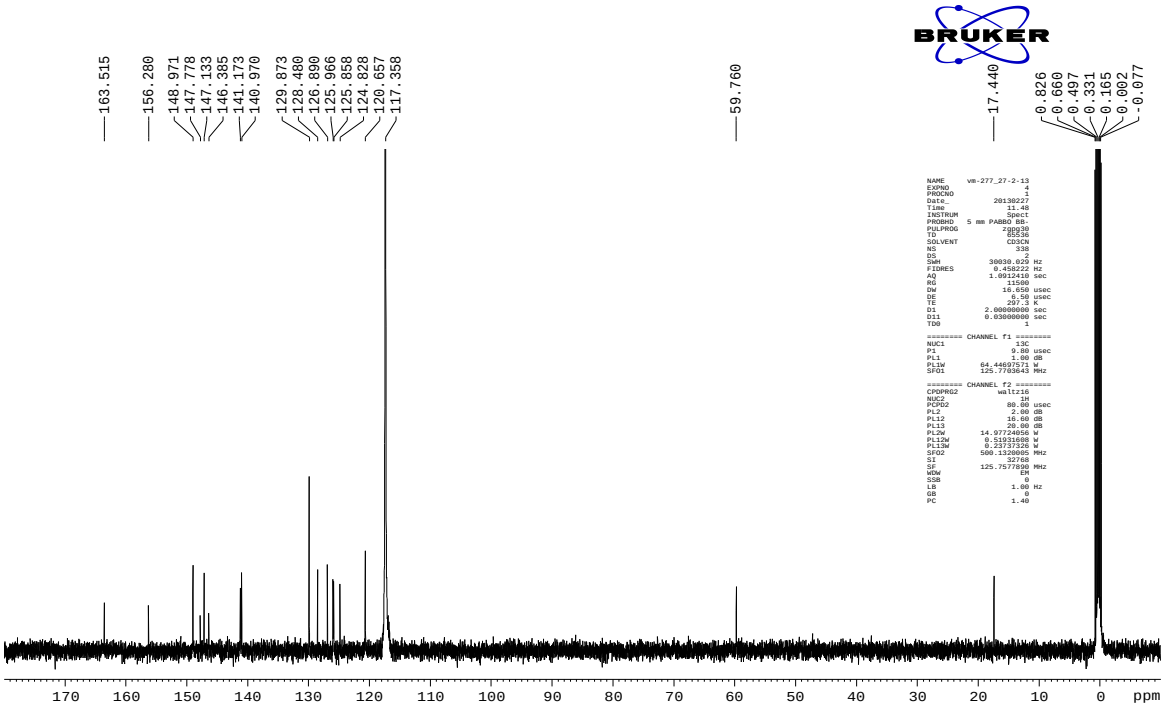

Fig. 3.12 ^{13}C NMR spectrum of **4b** in CD_3CN

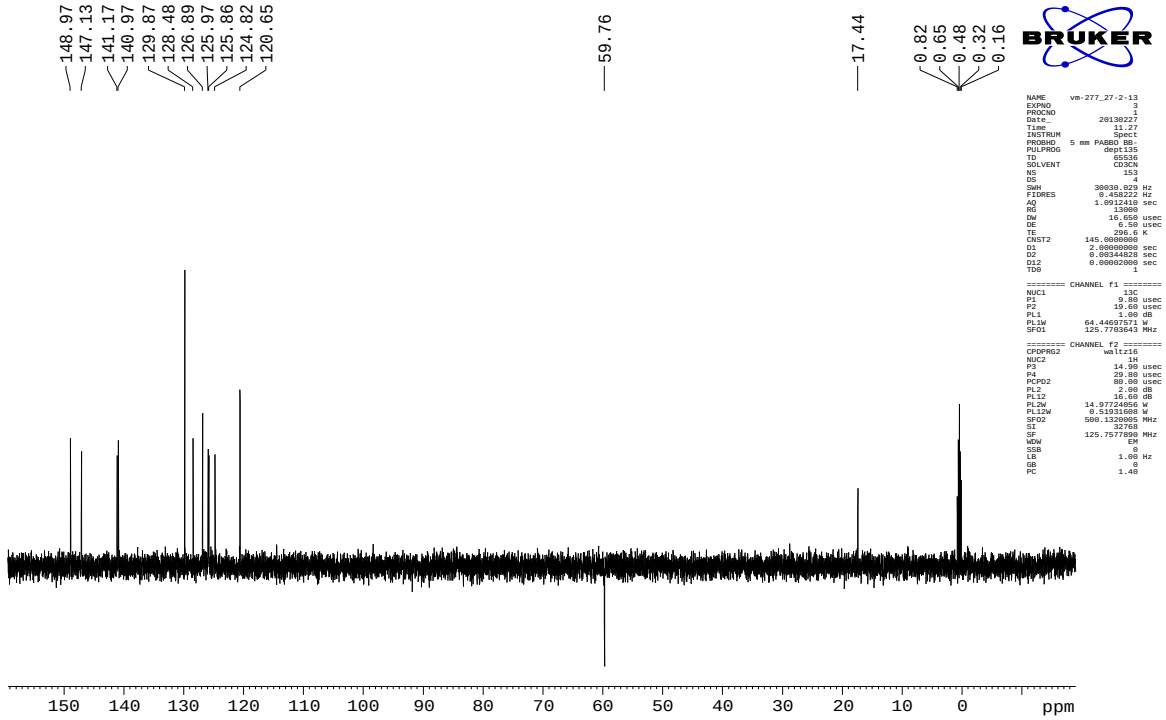

Fig. 3.13 DEPT–135 NMR spectrum of **4b** in CD_3CN

(iv) ESIJmass spectrometry

The ESI–mass spectra of all the complexes are illustrated in Figures 3.14–3.21. Mass spectra of all the mono complexes namely **3a**, **4a**, **5a** and **6a** exhibited intense peaks at their corresponding m/z values due to the formation of $[M\text{-}Cl]^+$ cations after the loss of one chloride ion. $[Zn(N_3L)Cl_2]$ (**4a**) and $[Co(N_3L)Cl_2]$ (**5a**) showed additional peaks with m/z values of 459.00 and 454.00 respectively, in their mass spectra due to the formation of $[M+Na]^+$ cations (Figures 3.16 and 3.18). All bis complexes exhibited sequential dissociation of the perchlorate ions present outside the coordination sphere thus giving rise to two peaks at their respective m/z values due to the formation of $[M\text{-}(ClO_4)]^+$ and $[M\text{-}2(ClO_4)]^{2+}$ cations (Figures 3.15, 3.17, 3.19 and 3.21) respectively. Some additional peaks due to the generation of $[M\text{-}2(ClO_4)\text{-}L+Cl]^+$ type of cations were also observed.

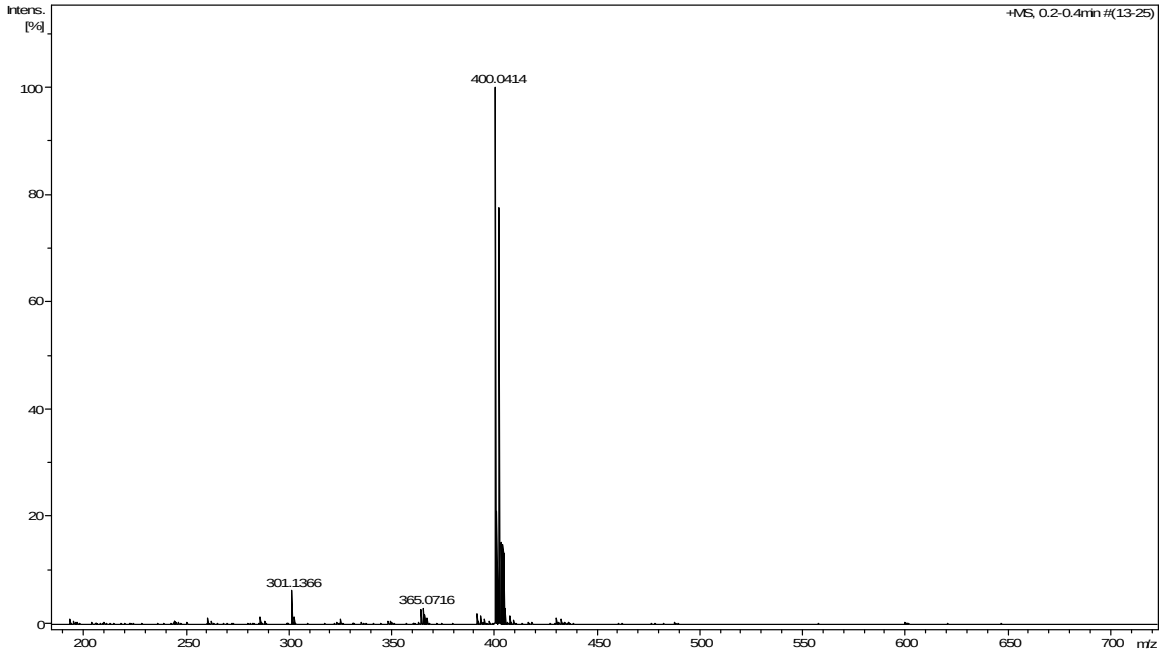

Fig. 3.14 The ESI–Mass spectrum of **3a** in acetonitrile under positive mode exhibiting the peaks at (m/z) 400.04 corresponding to $[M\text{-}Cl]^+$ cation

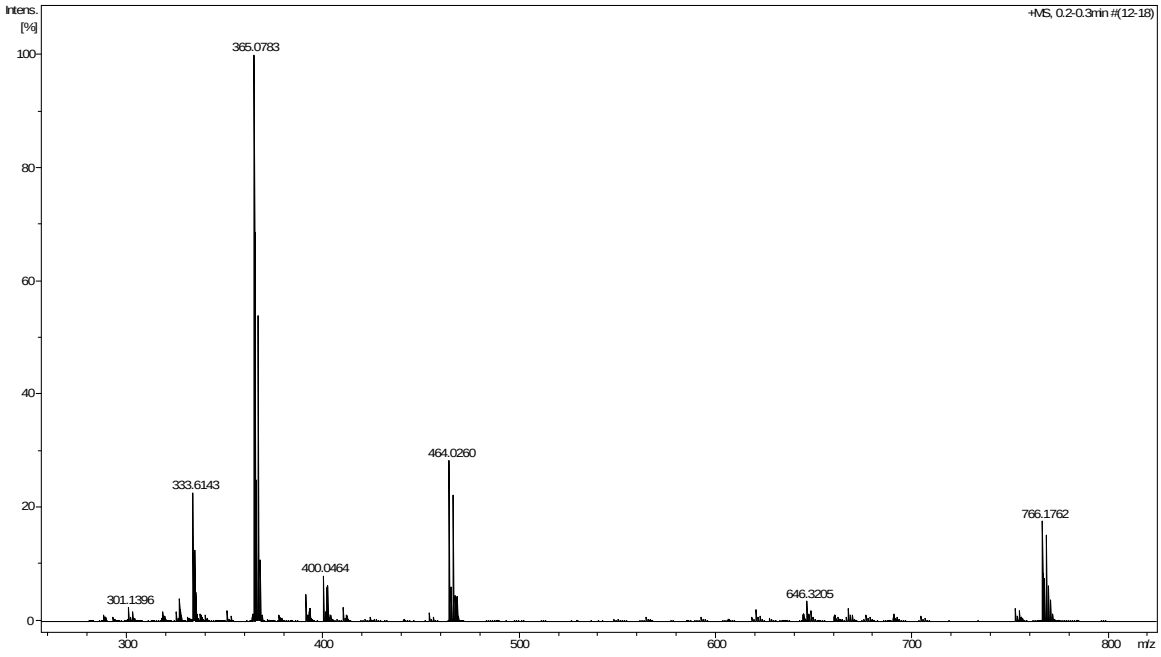

Fig. 3.15 The ESI–Mass spectrum of **3b** in acetonitrile under positive mode exhibiting the peaks at (m/z) 766.17, 333.61 and 400.04 corresponding to $[M-(ClO_4)]^+$, $[M-2(ClO_4)]^{2+}$ and $[M-2(ClO_4)-L+Cl]^+$ cations respectively

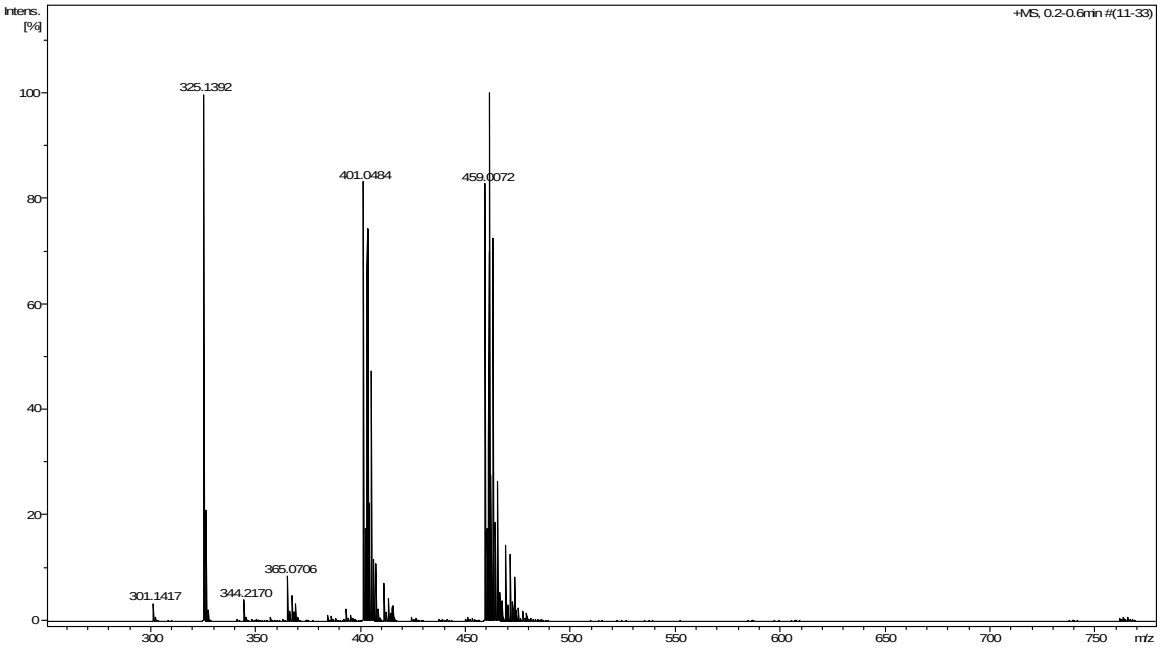

Fig. 3.16 The ESI–Mass spectrum of **4a** in acetonitrile under positive mode exhibiting the peaks at (m/z) 459.00 and 401.04 corresponding to $[M+Na]^+$ and $[M-Cl]^+$ cations respectively

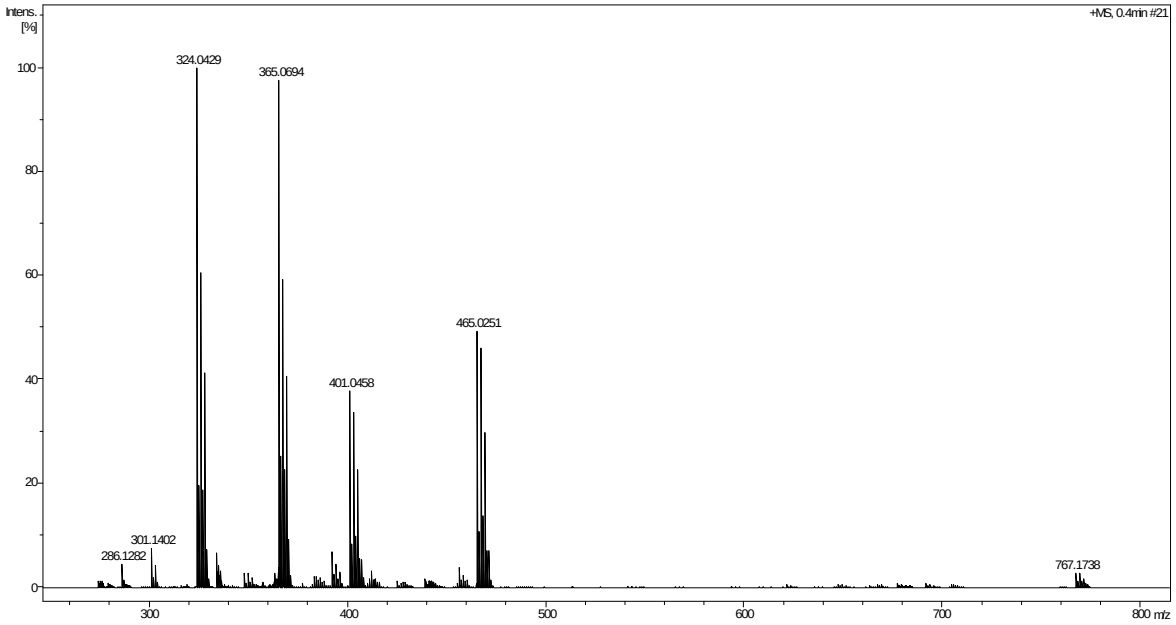

Fig. 3.17 The ESI–Mass spectrum of **4b** in acetonitrile under positive mode exhibiting the peaks at (m/z) 767.17 and 401.04 corresponding to $[M-(ClO_4)]^+$ and $[M-2(ClO_4)-L+Cl]^+$ cations respectively

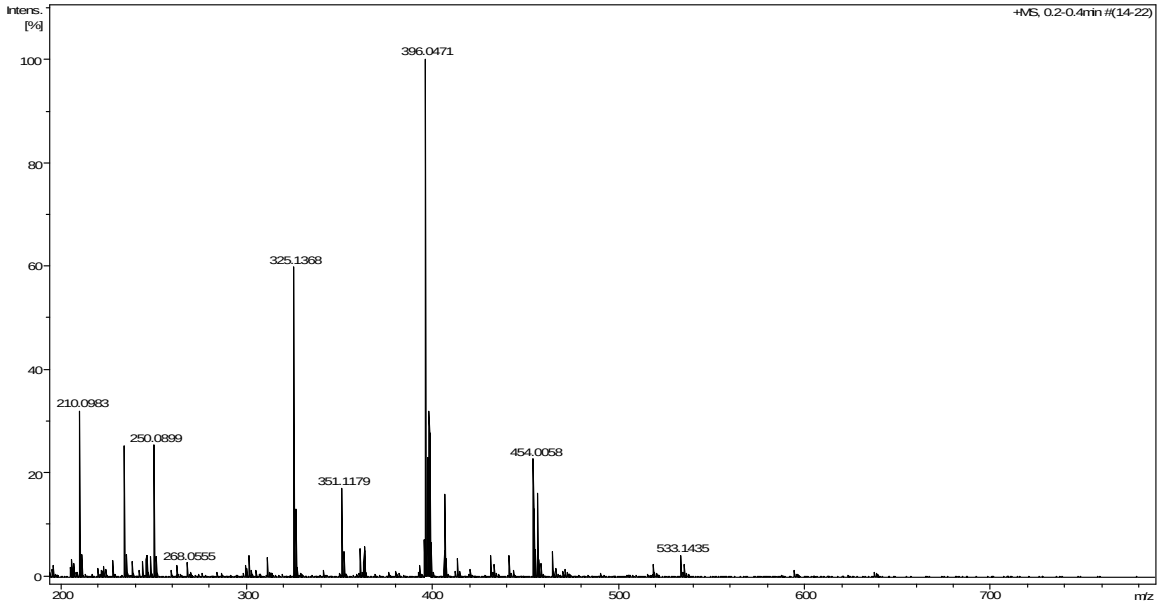

Fig. 3.18 The ESI–Mass spectrum of **5a** in acetonitrile under positive mode exhibiting the peaks at (m/z) 454.00 and 396.04 corresponding to $[M+Na]^+$ and $[M-Cl]^+$ cations respectively

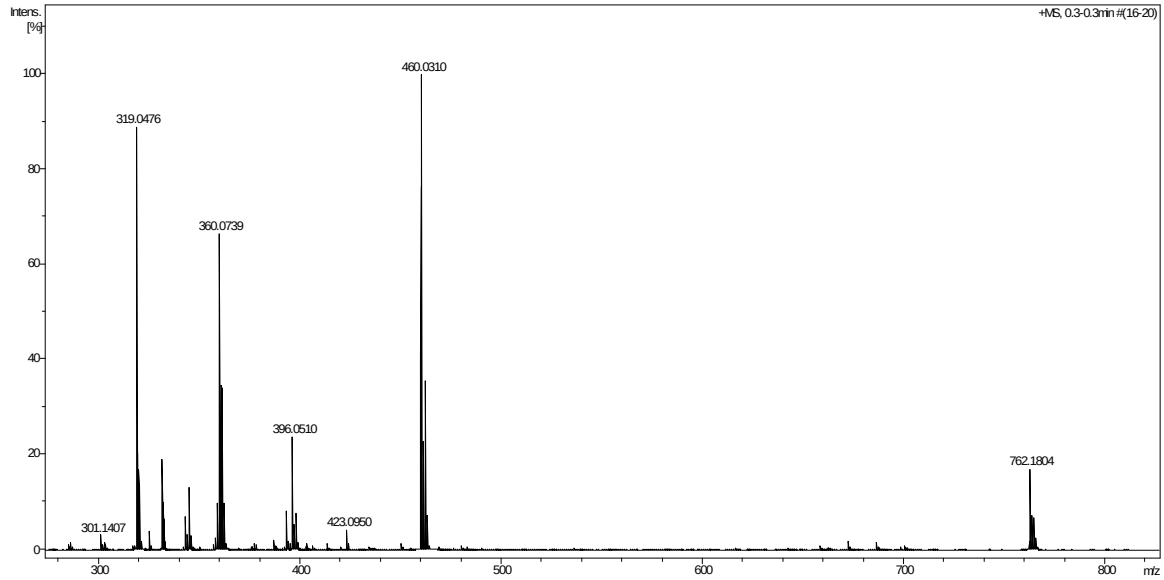

Fig. 3.19 The ESI–MS spectrum of **5b** in acetonitrile under positive mode exhibiting the peaks at (m/z) 762.18, 396.05 and 331.61 corresponding to $[M-(ClO_4)]^+$, $[M-2(ClO_4)-L+Cl]^+$ and $[M-2(ClO_4)]^{2+}$ cations respectively

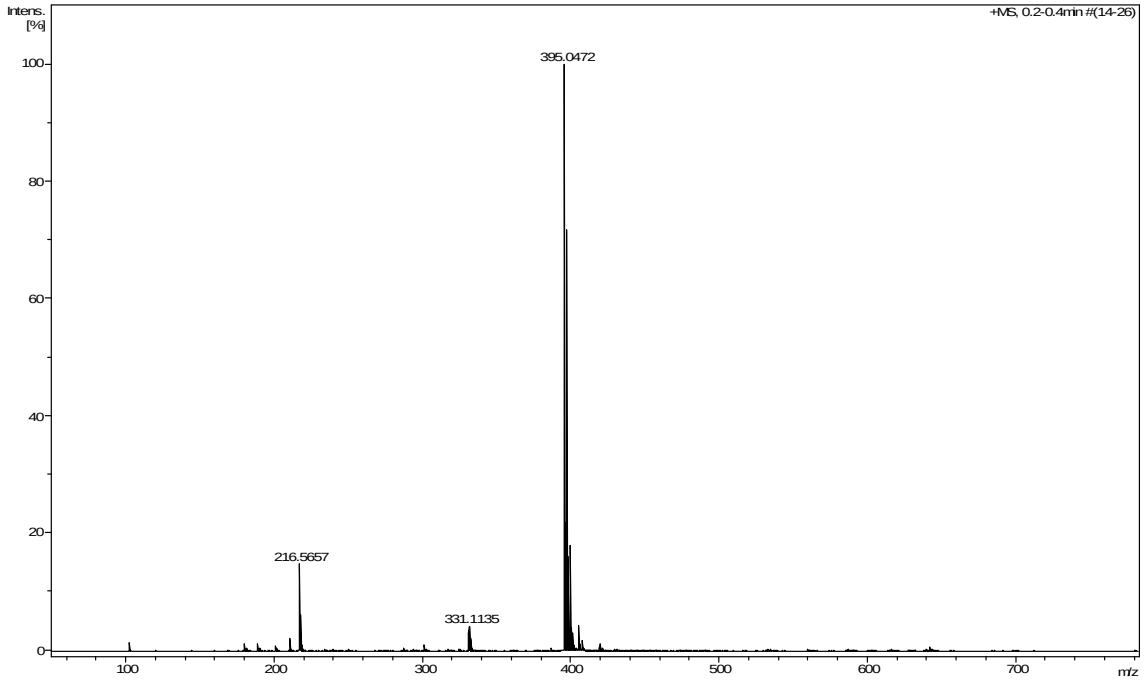

Fig. 3.20 The ESI–MS spectrum of **6a** in acetonitrile under positive mode exhibiting the peaks at (m/z) 395.04 corresponding to $[M-Cl]^+$ cation

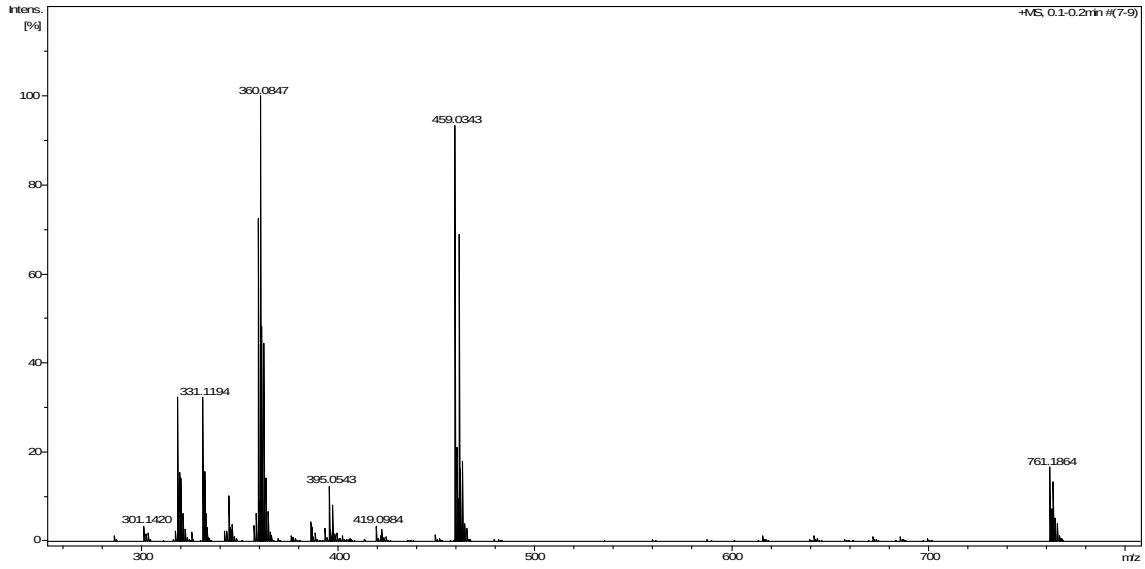

Fig. 3.21 The ESI–MS spectrum of **6b** in acetonitrile under positive mode exhibiting the peaks at (m/z) 761.18, 459.03, 395.05 and 331.11 corresponding to $[M-(ClO_4)]^+$, $[M-(ClO_4)-L]^+$, $[M-2(ClO_4)-L+Cl]^+$and $[M-2(ClO_4)]^{2+}$ respectively

(v) Conductivity measurements

Molar conductivity values in DMF solution (*ca.* 10^{-3} M) for all the mono complexes (**3a**, **4a**, **5a** and **6a**) were found to be within the range 9─49 Ω^{-1} cm^2 M^{-1} at 25° C suggesting their neutral and non–electrolyte behaviour in solution.[387] The bis complexes (**3b**, **4b**, **5b** and **6b**) exhibited molar conductivity values in DMF (25° C) within the range 104─136 Ω^{-1} cm^2 M^{-1} indicating their bi–univalent behaviour in solution (Table 3.1).[387]

(vi) Magnetic moment studies

Magnetic susceptibility measurements at room temperature afforded the magnetic moment values of 1.75 B. M. and 1.82 B. M. for copper complexes **3a** and **3b** respectively, suggesting the presence of one unpaired electron in these complexes.[403,431] Similar experiments with cobalt complexes **5a** and **5b** afforded the magnetic moment values of 4.34 B. M. and 4.47 B. M. respectively, suggesting the presence of three unpaired electrons. Hence it was concluded that **5a** and **5b** have Co^{2+} in high spin state similar to the complexes

1a and **1b** derived from the ligand (Pyimpy) with similar type of donor atoms *(chapter 2).*[431-433] The magnetic moment values for nickel complexes **6a** and **6b** were found to be 3.15 B. M. and 3.18 B. M. respectively, indicating the presence of two unpaired electrons.[432-434]

3.2.3. Description of molecular structures

In order to confirm the mode of coordination of the ligand N_3L, the molecular structures of complexes **3a** and **5a** were authenticated by X-ray diffraction methods. X–ray diffraction quality crystals of **3a** were achieved by slow evaporation of methanolic solution of the complex (**3a**). Crystals of **5a** suitable for X-ray diffraction studies were obtained by diffusion of diethyl ether in dichloromethane solution of complex (**5a**). The ORTEP representations of complexes **3a** and **5a** are included in Figures 3.22 and 3.23 respectively and their selected bond lengths and bond angles are listed in Table 3.3.

Both complexes (**3a** and **5a**) possessed the central metal ion in a penta–coordination donor environment and exhibited very similar geometries having trigonal bipyramidal dispositions of the donor atoms around the metal centres. In both structures, the imine nitrogen N(3) of the ligand along with two chloride ions Cl(1) and Cl(2) forms the equatorial plane and the pyridine nitrogens N(1) and N(4) are occupying the axial positions. The N(1)─M─N(4) moiety in both structures deviates significantly from linearity (N(1)─M─N(4) moiety: 170.12(11) Å for copper (**3a**), 166.60(27) Å for cobalt (**5a**)). The structural index parameters (τ) for **3a** and **5a** were calculated and found to be 0.695 and 0.708 respectively thus ascertaining their trigonal bipyramidal geometry having some distortion towards the square–pyramidal.[135] In both structures, Cl(1) which is close to the

phenyl ring exhibited comparatively longer bond distances than Cl(2), probably, due to Jahn–Teller distortion.

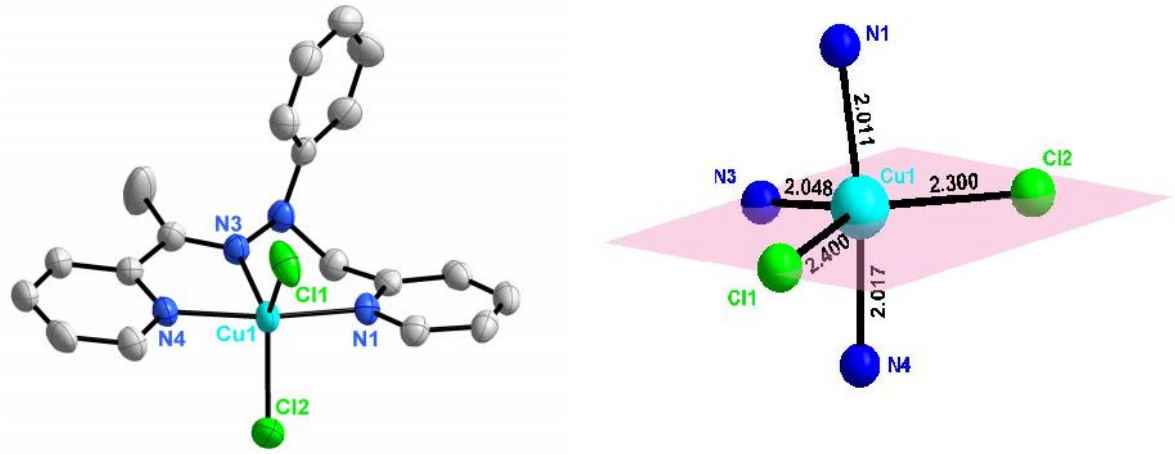

(a) (b)

Fig. 3.22 (a) ORTEP representation of the crystal structure of $[Cu(N_3L)Cl_2]$ (**3a**) showing atom numbering scheme and displacement ellipsoid (50% probability level). Hydrogen atoms are omitted for clarity; (b) trigonal bipyramidal disposition of donor atoms showing the bond distances from the metal centre

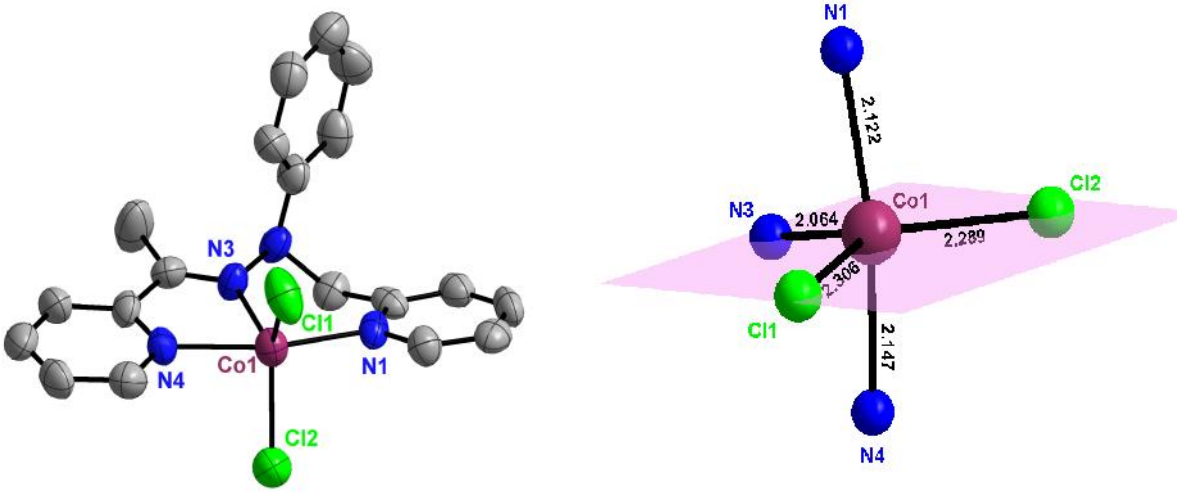

(a) (b)

Fig. 3.23 (a) ORTEP representation of the crystal structure of $[Co(N_3L)Cl_2]$ (**5a**) showing atom numbering scheme and displacement ellipsoid (50% probability level). Hydrogen atoms are omitted for clarity; (b) trigonal bipyramidal disposition of donor atoms showing the bond distances from the metal centre

Table 3.3 Selected bond lengths (Å) and angles (˚) for **3a** and **5a**

Bond lengths (Å)		Bond angles (˚)	
		3a	
Cu(1)−N(1)	2.0109(28)	N(3)−Cu(1)−N(1)	92.412(116)
Cu(1)−N(4)	2.0174(28)	N(3)−Cu(1)−N(4)	77.831(118)
Cu(1)−N(3)	2.0482(31)	N(1)−Cu(1)−N(4)	170.124(113)
Cu(1)−Cl(2)	2.3000(13)	N(1)−Cu(1)−Cl(2)	93.534(94)
Cu(1)−Cl(1)	2.3995(12)	N(4)−Cu(1)−Cl(2)	93.755(94)
		N(1)−Cu(1)−Cl(1)	94.156(91)
		N(3)−Cu(1)−Cl(1)	111.782(90)
		N(4)−Cu(1)−Cl(1)	88.153(91)
		Cl(2)−Cu(1)−Cl(1)	118.819(49)
		N(3)−Cu(1)−Cl(2)	128.373(93)
		5a	
Co(1)−N(1)	2.1222(70)	N(3)−Co(1)−N(1)	91.909(283)
Co(1)−N(3)	2.0637(77)	N(3)−Co(1)−N(4)	74.755(288)
Co(1)−N(4)	2.1470(72)	N(1)−Co(1)−N(4)	166.595(269)
Co(1)−Cl(1)	2.3060(27)	N(1)−Co(1)−Cl(2)	95.567(230)
Co(1)−Cl(2)	2.2892(31)	N(4)−Co(1)−Cl(2)	92.040(232)
		N(1)−Co(1)−Cl(1)	96.429(211)
		N(3)−Co(1)−Cl(1)	115.733(213)
		N(4)−Co(1)−Cl(1)	88.370(209)
		Cl(2)−Co(1)−Cl(1)	124.073(115)
		N(3)−Co(1)−Cl(2)	118.191(244)

(i) Structure of $[Cu(N_3L)Cl_2]$ (3a)

The compound **3a** crystallized in the centrosymmetric monoclinic space group C2/c with Z=8. The ligand coordinated to copper(II) ion by two pyridine nitrogen donor atoms (N_{py}) and one azomethine nitrogen (N_{im}) atom affording a meridional spanning of the ligand around the copper centre. The dihedral angle between the mean planes of two chelating pyridyl rings was found to be 15.02°. The phenyl ring is almost perpendicular to the plane formed by N(1), N(3), N(4) donors and the copper(II) ion with an angle of 84.06°. The

pyridine nitrogen distances from Cu(II) centre are 2.011 and 2.07 Å which are consistent with the literature values for other copper(II) complexes having similar type of ligands.[403,435-437] However, the Cu(II)–imine distance was found to be 2.048 Å which is slightly lower than the distances observed by Neves and co–workers in copper complexes having similar types of donor atoms.[438] The mean Cu(II)─Cl distance is 2.350 Å which is consistent with the literature values.[403,435-437] The ligand biting angles are 92.412° and 77.831° and the Cu(II) ion is sitting 0.029 Å above the ligand binding plane. The bite size Cl(1)─Cl(2) distance for the copper complex (**3a**) is found to be 4.046 Å which is remarkably consistent with those reported for other copper molecules known to bind DNA in a covalent mode like 3.936 and 4.020 Å for $[Cu(L^1)Cl_2]$ and 3.836 Å for $[Cu(L^2)Cl_2]$ (where L^1 = *N*,*N*–dimethyl–*N*′–((6–methyl)pyrid–2–ylmethyl)ethylenediamine and L^2 = *N*,*N*–dimethyl–*N*′–(pyrid–2–ylmethyl)ethylenediamine) respectively.[406]

Non–covalent interactions involving aromatic rings such as π–stacking and CH─π interactions as well as hydrogen bonding are significant in crystal engineering, supramolecular chemistry, material science, molecular biology and drug design.[393,439-440] Examination of the packing diagram revealed three types of non–covalent interactions. Firstly, alkyl/aryl hydrogen–chlorine hydrogen bonding interactions; in complex **3a**, the Cl(1) atom is showing intermolecular hydrogen bonding interactions with phenyl hydrogen (H8) of one molecule and one of the methylene protons (H6A) of the same molecule as well as pyridyl hydrogen (H17) of another molecule with the distances 2.740, 2.753 and 2.768Å respectively (Fig. 3.24). Cl(2) is also participating in the intermolecular hydrogen bonding and shows interactions with pyridyl hydrogens of neighbouring molecules (H18 and H19 of

one molecule and H3 of another molecule) with distances of 2.983, 3.068, and 3.095 Å respectively (Fig. 3.25).

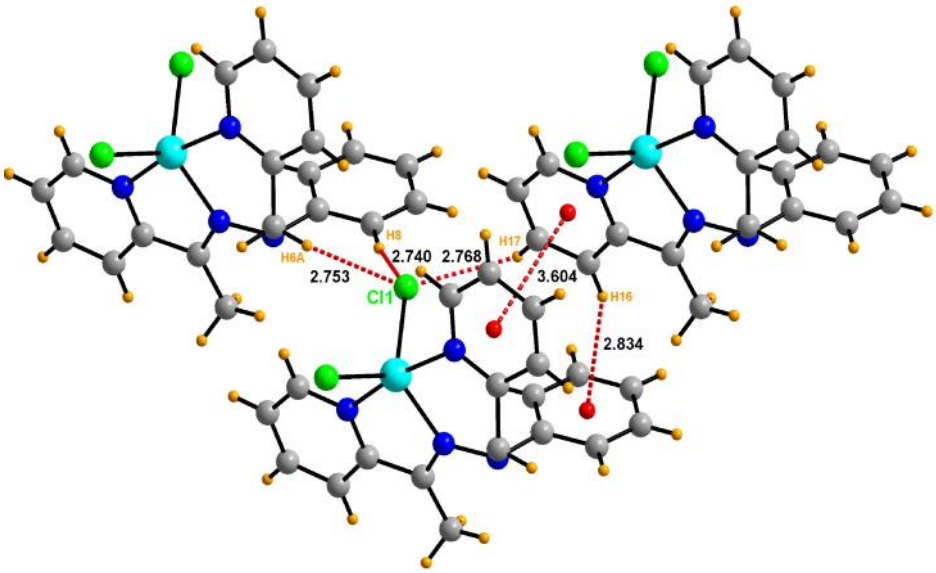

Fig. 3.24 Three dimensional network in **3a** exhibiting hydrogen bonding, π–π interactions and C–H···π interactions

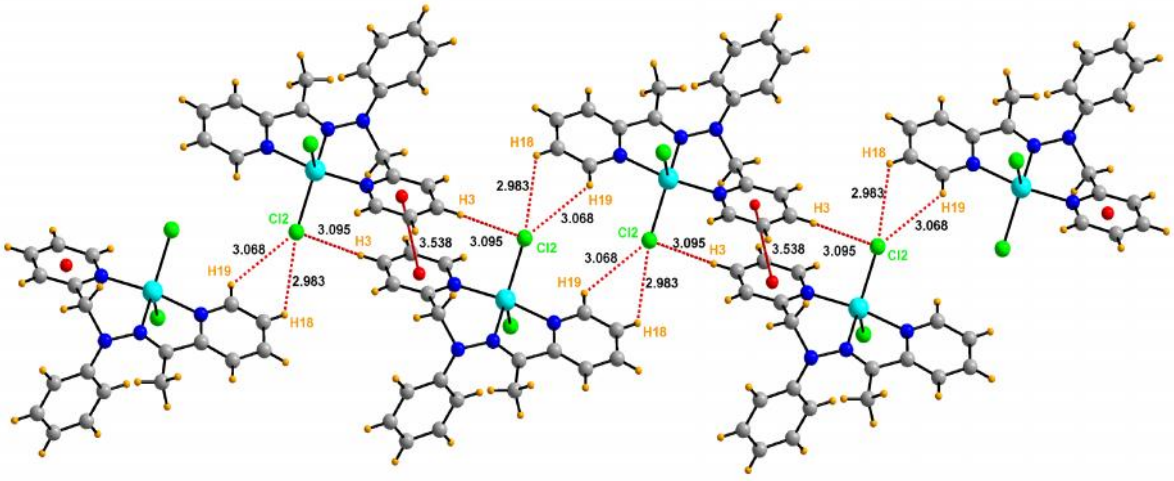

Fig. 3.25 Three dimensional hydrogen bonding network in the crystal structure of **3a** affording a supramolecular chain–like structure

List of selected hydrogen bonding interactions encountered in **3a** is given in Table 3.4.

Table 3.4 Hydrogen–bonding geometries for **3a**

D─H···A	D─H (Å)	D···A (Å)	H···A (Å)	D─H···A (˚)
C1─H1···Cl1[a]	0.930(4)	3.380(4)	2.995(1)	106.57(25)
C12─H12···N3[a]	0.930(5)	2.780(6)	2.457(3)	100.40(30)
C14─H14A···N2[a]	0.960(6)	2.795(7)	2.366(3)	106.57(37)
C8─H8···Cl1[b]	0.930(4)	3.638(4)	2.740(1)	162.62(26)
C6─H6A···Cl1[b]	0.970(4)	3.719(4)	2.753(1)	173.83(22)
C18─H18···Cl2[c]	0.930(4)	3.526(5)	2.985(1)	118.66(27)
C17─H17···Cl1[d]	0.930(4)	3.440(5)	2.768(1)	129.97(27)

Symmetry Equivalents: (a) x,y,z; (b) x+1/2,+y+1/2,+z; (c) –x-1/2,-y+1/2+1,-z+1; (d) x-1/2,+y+1/2,+z

Secondly, the interactions between aryl hydrogens and phenyl ring (C─H---π interaction) with a distance of 2.834 Ǻ from the centroid (Fig. 3.24) of phenyl ring. Thirdly, the pyridine rings of same sides of two neighbouring molecules (comprising of N1, C1, C2, C3, C4 and C5 atoms) exhibited π-stacking interactions with a centroid to centroid distance of 3.538 Å. A weak π-stacking interaction is also observed between the pyridine rings of opposite sides of two neighboring molecules with a centroid to centroid distance of 3.604 Å.

The intermolecular hydrogen bonding interactions arising from Cl(2) are giving rise to a supramolecular chain like structure which is also complemented by the π-stacking interactions (3.538 Ǻ) between the similar pyridine rings of two neighbouring molecules (Fig. 3.25). Similarly, another supramolecular polymer like structure is held by hydrogen bonding of a chlorine atom with pyridine hydrogen along with the π-stacking interactions between the pyridine rings of opposite sides in two neighbouring molecules (Fig. 3.26). The packing diagram of **3a** is illustrated in Fig. 3.27.

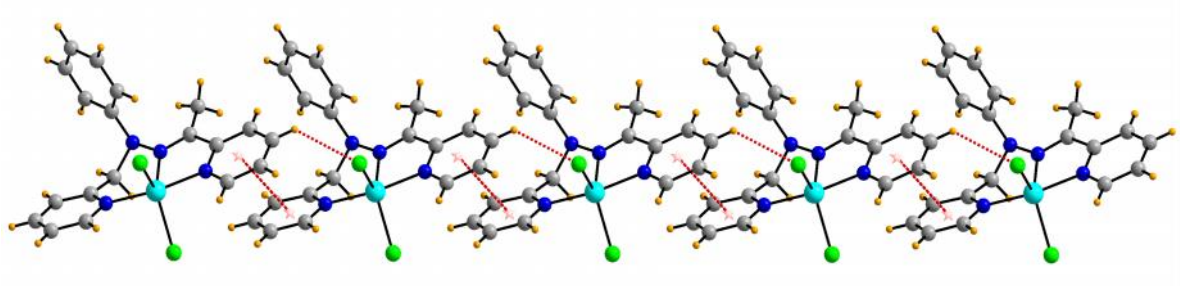

Fig. 3.26 Intermolecular hydrogen bonding network in $[Cu(N_3L)Cl_2]$ (**3a**)

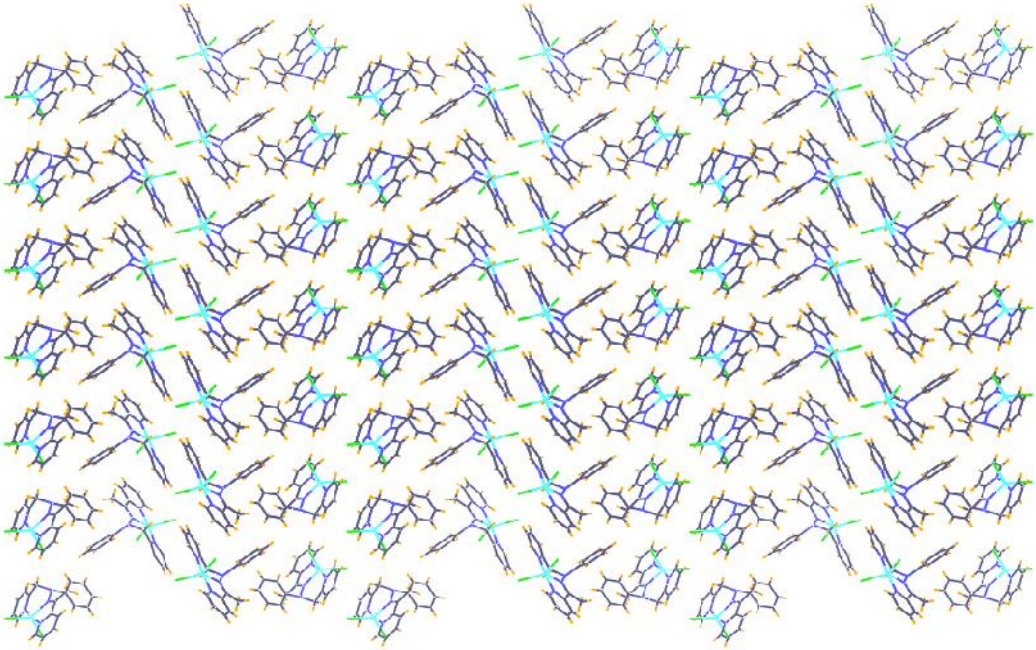

Fig. 3.27 Packing diagram in crystal structure of $[Cu(N_3L)Cl_2]$ (**3a**)

(ii) Structure of $[Co(N_3L)Cl_2]$ (5a)

The structural features of **5a** were found to be very much similar to those of **3a**. The compound $[Co(N_3L)Cl_2]$ (**5a**) crystallizes in the monoclinic space group C2/c with Z=8. The ligand binds with metal by two pyridine nitrogen donor atoms (N_{py}) and one azomethine nitrogen (N_{im}) affording a meridional spanning of the ligand around the metal centre. The dihedral angle between the mean planes of two chelating pyridyl rings is 14.22°. The phenyl

ring is almost perpendicular to the plane formed by N(1), N(3), N(4) donors and the metal ion Co(1) with an angle of 85.16°. Two pyridine and imine nitrogen distances from Co(II) centre are consistent with the literature values for high−spin cobalt(II) complexes and those observed in the crystal structure of **1a** (*chapter 2*).[441,442] The mean Co(II)─Cl distance is 2.298 Å which is consistent with reported values.[441-443] The ligand biting angles are 91.91° and 74.76° and the Co(II) ion is sitting 0.029 Å above the ligand binding plane. The bite size Cl(1)─Cl(2) distance for the cobalt complex is 4.059 Å which is comparable to that found in copper complex **3a** and considerably larger than the reported values for other molecules known to bind DNA in a covalent mode like 3.240 Å for $[Co(phendione)_2Cl_2]Cl$, 3.350 Å for *cis*-diammine dichloro platinum(II) and 3.490 Å for *cis*-diimine dichloro ruthenium(II).[283]

Non-covalent interactions found in the crystal structure of **5a** are very much similar to those observed for **3a** and are illustrated in Fig. 3.28. Three types of non-covalent interactions are visible in the crystal structure of **5a**. Firstly, alkyl/aryl hydrogen-chlorine hydrogen bonding interactions; the Cl(1) atom is showing intermolecular hydrogen bonding interactions with phenyl hydrogen (H8) of one molecule and one of the methylene protons (H6A) of the same molecule as well as pyridyl hydrogen (H17) of another molecule with the distances 2.784, 2.824 and 2.878 Å respectively (Fig. 3.28). Cl(2) is also participating in the intermolecular hydrogen bonding interactions with pyridyl hydrogens of neighbouring molecules (H18 and H19 of one molecule; H2 and H3 of other molecules) with distances of 3.095, 3.048, 2.994 and 3.088 Å respectively (Fig. 3.29). List of selected hydrogen bonding interactions is given in Table 3.5.

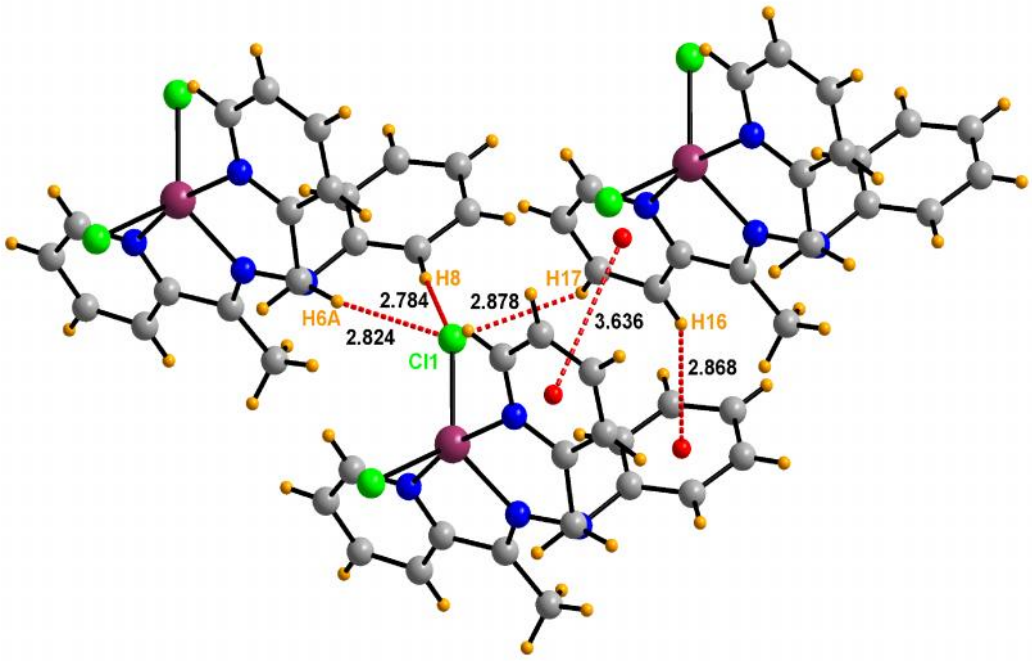

Fig. 3.28 Three dimensional network in **5a** exhibiting hydrogen bonding, π–π interactions and C–H···π interactions

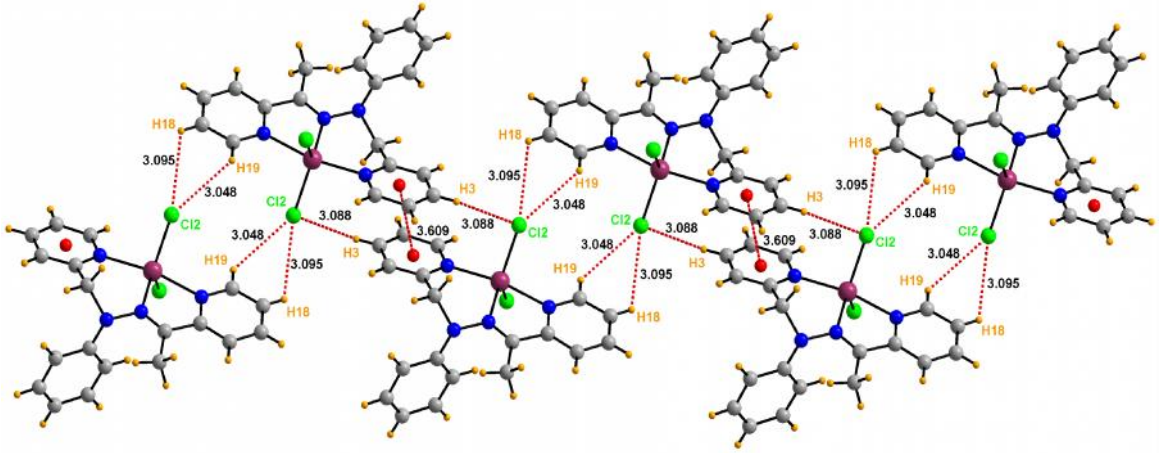

Fig. 3.29 Three dimensional hydrogen bonding network in the crystal structure of **5a** affording a supramolecular chain–like structure

Table 3.5 Hydrogen–bonding geometries for **5a**

D─H···A	D─H (Å)	D···A (Å)	H···A (Å)	D─H···A (˚)
C12─H12···N3[a]	0.930 (2)	2.767 (7)	2.427 (2)	101.54 (1)
C14─H14C···N2[a]	0.960	2.776 (7)	2.349 (4)	106.30 (1)
C2─H2···Cl2[b]	0.930 (1)	3.685 (4)	2.994 (2)	132.24 (1)
C8─H8···Cl1[c]	0.930 (2)	3.698 (11)	2.785 (9)	167.29 (1)
C6─H6A···Cl1[c]	0.970 (1)	3.783 (4)	2.824 (3)	169.69 (1)
C17─H17···Cl1[d]	0.930 (2)	3.531 (7)	2.878 (9)	128.35 (1)

Symmetry Equivalents: (a) x,y,z; (b) x+1/2,+y-1/2,+z; (c) x+1/2,+y+1/2,+z; (d) x-1/2,+y+1/2,+z

Secondly, the interactions between aryl hydrogens and phenyl ring (C─H···π interaction) with a distance of 2.868 Å from the centroid (Fig. 3.28) of phenyl ring. Thirdly, the pyridine rings of same sides of two neighbouring molecules (comprising of N1, C1, C2, C3, C4 and C5 atoms) exhibited π-stacking interactions with a centroid to centroid distance of 3.609 Å. A weak π-stacking interaction is also observed between the pyridine rings of opposite sides of two neighboring molecules with a centroid to centroid distance of 3.636 Å. Interestingly, these distances (2.878 Å for hydrogen bonding and 3.636 Å for π-stacking) are exactly similar to the values reported for the cobalt complex [Co(Pyimpy)Cl_2] (**1a**) (*chapter 2*) derived from a similar ligand (Pyimpy).

The intermolecular hydrogen bonding interactions arising from Cl(2) are giving rise to a supramolecular chain like structure which is also complemented by the π-stacking interactions (3.609 Å) between the similar pyridine rings of two neighbouring molecules (Fig. 3.29). Similarly, another supramolecular polymer like structure is held by hydrogen bonding of chlorine atoms with pyridine hydrogens along with the π-stacking interactions

between the pyridine rings of opposite sides in two neighbouring molecules (Fig. 3.30). The packing diagram of **3a** is illustrated in Fig. 3.31.

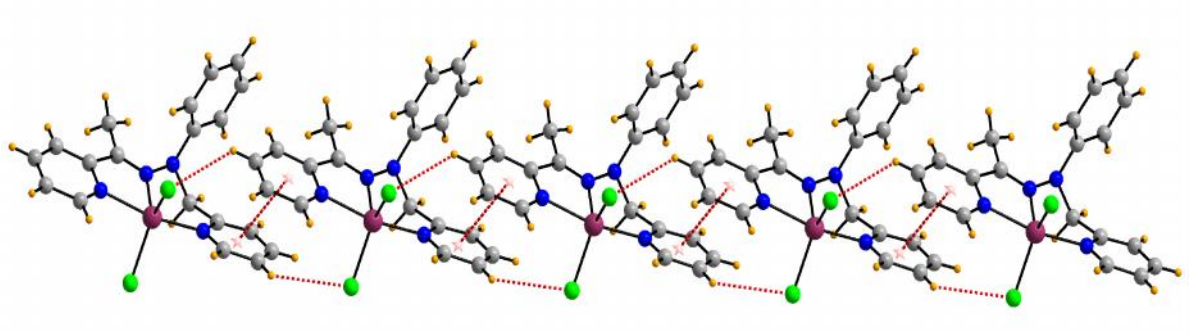

Fig. 3.30 Intermolecular hydrogen bonding network in the crystal structure of **5a**

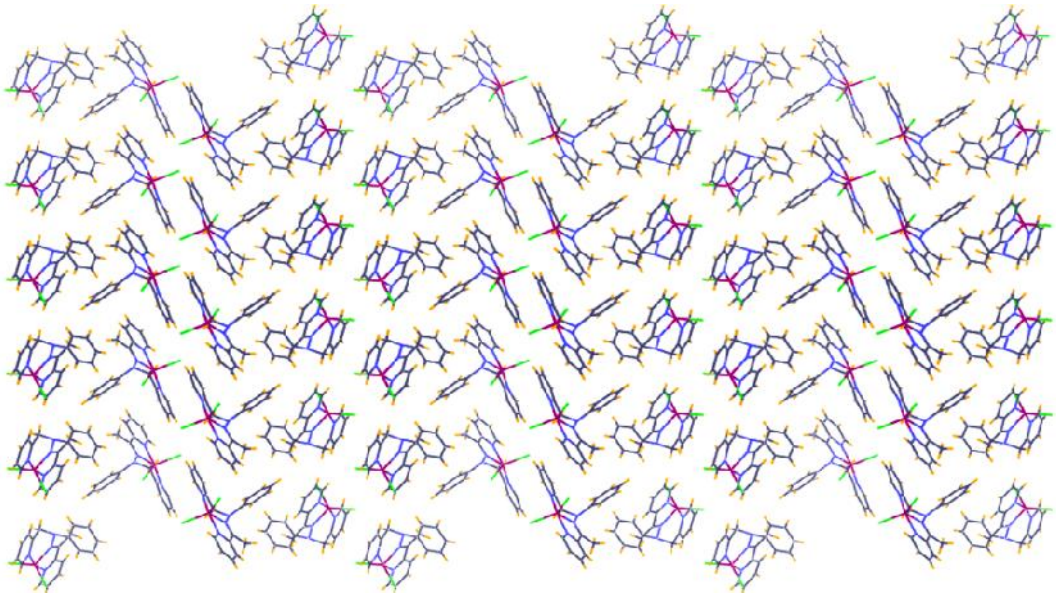

Fig. 3.31 Packing diagram in crystal structure of **5a**

3.2.4. Electrochemistry

The redox properties of copper (**3a** and **3b**), cobalt (**5a** and **5b**) and nickel (**6a** and **6b**) complexes were investigated through cyclic voltammetry within the potential range -1.200

V to +1.200 V vs Ag/AgCl under nitrogen atmosphere at 298 K. The cyclic voltammetric experiments were performed at a scan rate of 0.1 V/s in dichloromethane or acetonitrile in presence of 0.1 M tetrabutylammonium perchlorate (TBAP) as supporting electrolyte using Ag/AgCl as reference electrode, glassy carbon as working electrode and platinum wire as auxiliary electrode. The ferrocene/ferrocenium couple occurred at $E_{1/2}$ = +0.51 (125) V versus Ag/AgCl in acetonitrile and $E_{1/2}$ = +0.42 (75) V versus Ag/AgCl in acetonitrile under same experimental conditions. The electrochemical data for these complexes are described in Table 3.6. and their voltammograms are shown in Figures 3.32, 3.33 and 3.34 respectively.

Table 3.6 Redox potentials for complexes **3**, **5** and **6** at 298 K vs. Ag/AgCl

Complex	M(II/I)		M(III/II)	
	$E_{1/2}$[c] (V)	ΔE_p[d] (mV)	$E_{1/2}$[c] (V)	ΔE_p[d] (mV)
3a[b]	-0.028	137	—	—
3b[a]	-0.329	144	0.168	91
5a[a]	-0.952	174	0.597	398
5b[a]	-0.791	71	0.743	104
6a[a]	-0.789	100	—	—
6b[b]	-0.804	—	—	—

measured in [a]acetonitrile or [b]dichloromethane with 0.1 M tetrabutylammonium perchlorate (TBAP), [c]$E_{1/2} = 0.5(E_{pa} + E_{pc})$, [d]$\Delta E_p = (E_{pa} - E_{pc})$

Two different types of voltammograms were observed for copper complexes **3a** and **3b** respectively. For complex **3a**, a quasi–reversible redox couple was found in dichloromethane near $E_{1/2}$ value of -0.028 V vs. Ag/AgCl which was designated as Cu^{II}/Cu^{I} redox couple.[402,444,445] In case of complex **3b**, no well-resolved voltammogram could be obtained in dichloromethane, however, two major redox processes were recognized when the experiment was accomplished in acetonitrile. The cyclic voltammogram of **3b** in acetonitrile consisted of a reversible redox couple near $E_{1/2}$ value of +0.168 V vs. Ag/AgCl

along with a quasi–reversible redox couple found near $E_{1/2}$ values of -0.329 V vs. Ag/AgCl which were assigned as Cu^{II}/Cu^{I} and Cu^{I}/Cu^{0} redox couples respectively.[403,446,447] The reduced Cu^{0} is adsorbed on the electrode surface which is evidenced by the narrow width of the anodic response with a large peak current.[448]

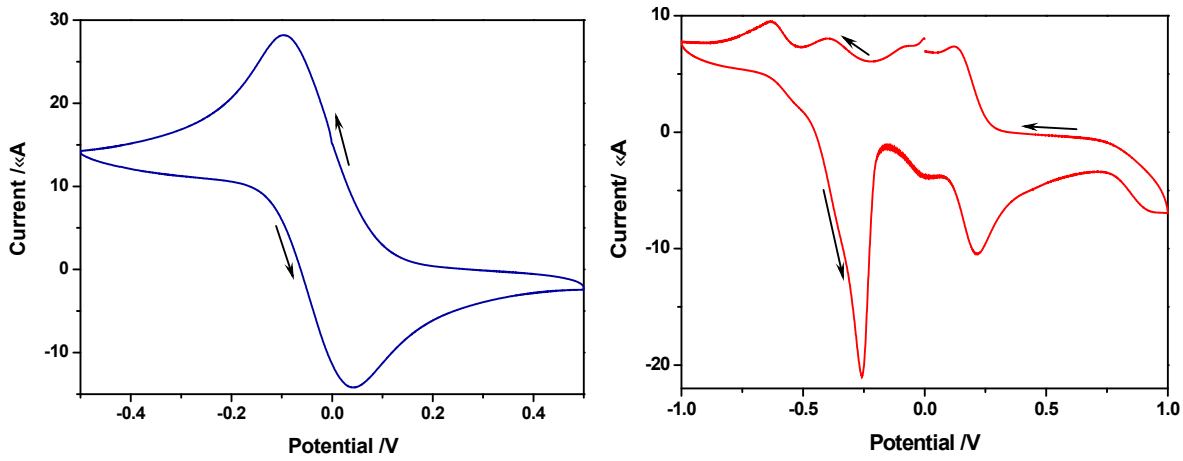

(a) (b)

Fig. 3.32 Cyclic voltammograms of 10^{-3} M solutions of (a) $[Cu(N_3L)Cl_2]$ (**3a**) in dichloromethane and (b) $[Cu(N_3L)_2](ClO_4)_2$ (**3b**) in acetonitrile, respectively, in presence of 0.1 M TBAP as a supporting electrolyte, glassy-carbon as a working electrode and Ag/AgCl as reference electrode; scan rate 0.1 V/s

The cobalt complexes **5a** and **5b** showed very much similar redox behavior in acetonitrile and their voltammograms comprised of two major redox couples probably due to a Co^{II}/Co^{III} oxidation process and a Co^{II}/Co^{I} reduction process respectively.[369,449-451] In case of **5a**, the quasi–reversible Co^{III}/Co^{II} redox couple was found near $E_{1/2}$ value of +0.597 V vs. Ag/AgCl and another quasi–reversible Co^{II}/Co^{I} redox couple was found near $E_{1/2}$ value of -0.952 V vs. Ag/AgCl. For complex **5b**, the quasi–reversible Co^{III}/Co^{II} redox couple was centered near $E_{1/2}$ value of +0.743 V vs. Ag/AgCl whereas a reversible Co^{II}/Co^{I} redox couple was found near $E_{1/2}$ value of -0.791 V vs. Ag/AgCl. These couples could also

be visualized in dichloromethane, though, with lesser reversibility and at slightly positively shifted potential values.

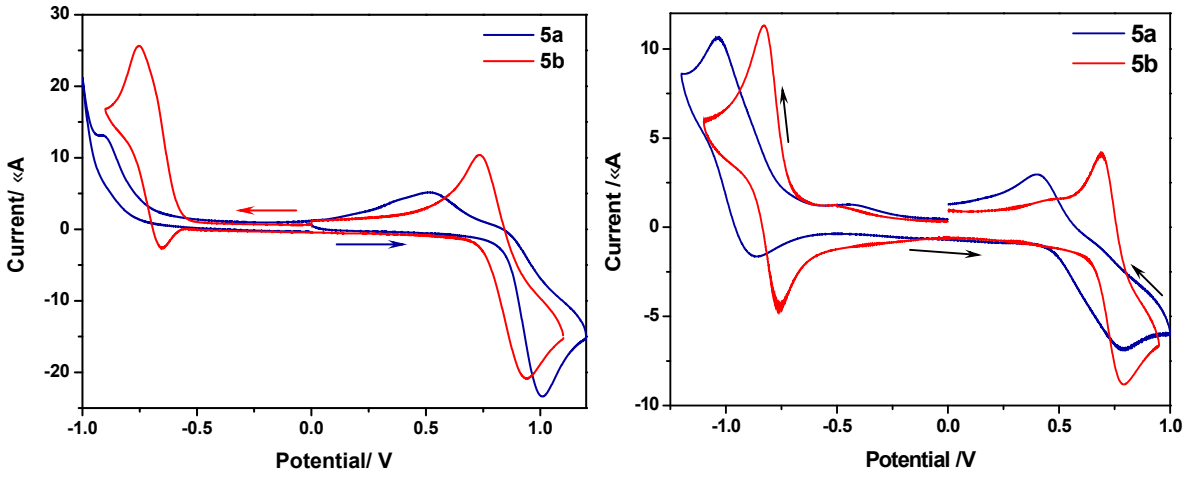

(a) (b)

Fig. 3.33 Cyclic voltammograms of 10^{-3} M solutions of $[Co(N_3L)Cl_2]$ (**5a**) and $[Co(N_3L)_2](ClO_4)_2$ (**5b**) in (a) dichloromethane (b) acetonitrile in presence of 0.1 M TBAP as a supporting electrolyte, glassy-carbon as a working electrode and Ag/AgCl as reference electrode; scan rate 0.1 V/s

For nickel complexes **6a** and **6b**, no Ni^{III}/Ni^{II} redox couple could be observed and their voltammograms consisted of only a single redox couple due to the Ni^{II}/Ni^{I} redox process. The complex **6a** exhibited quasi–reversible Ni^{III}/Ni^{II} redox couple with the $E_{1/2}$ value of -0.789 V vs Ag/AgCl in acetonitrile. We could not observe any distinct redox process for the complex **6b** in acetonitrile, however, the complex (**6b**) showed one irreversible redox couple in dichloromethane with the *E*pc value of -0.804 V vs Ag/AgCl which was ascribed to a Ni^{II}/Ni^{I} redox process. These potential values are comparatively less negative than the values reported by Halcrow et al.[446] and Drew et al.[452] for structurally analogous compounds.

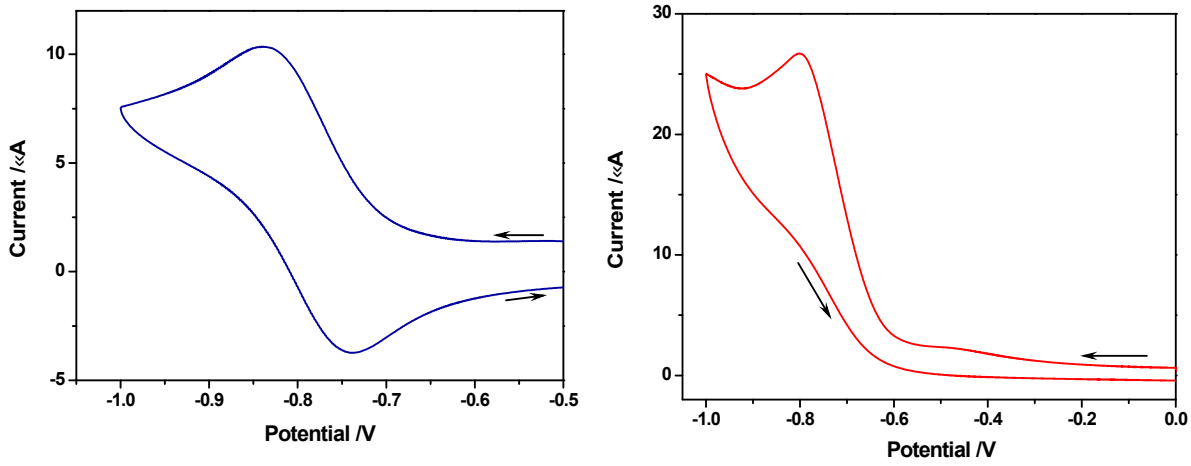

(a) (b)

Fig. 3.34 Cyclic voltammograms of a 10^{-3} M solution of (a) $[Ni(N_3L)Cl_2]$ (**6a**) in acetonitrile and (b) $[Ni(N_3L)_2](ClO_4)_2$ (**6b**) in dichloromethane, respectively, in presence of 0.1 M TBAP as a supporting electrolyte, glassy-carbon as a working electrode and Ag/AgCl as reference electrode; scan rate 0.1 V/s

3.2.5. Superoxide dismutase activity studies

The electrochemical data of complexes **3a** and **3b** ascertained their redox−active nature. Their potential values were found to be fairly within the range as observed for small molecule SOD mimics[381] which prompted us to study their superoxide dismutase scavenging ability. McCord Fridovich (McCF) assay was performed to investigate their SOD−like activity[381,403,404] and both complexes were found to be active towards the dismutation of superoxide radicals. The IC_{50} values for the complexes were obtained by plotting percentage inhibition of NBT reduction (along Y-axis) vs the concentration of test solution (along X−axis) (Fig. 3.35. (a) and (b)) and listed in Table 3.11.

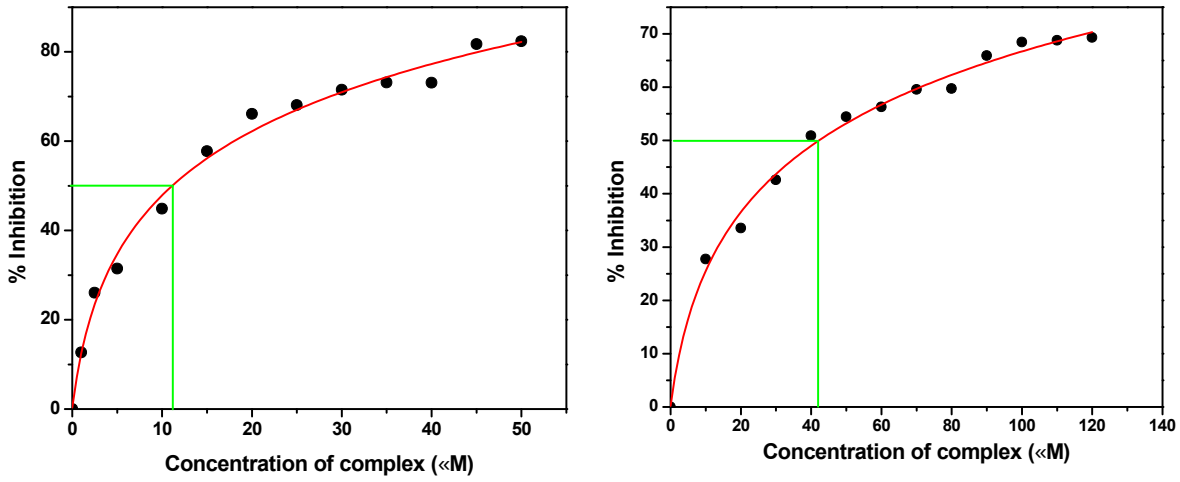

(a) (b)

Fig. 3.35 SOD activity of complex (a) **3a** and (b) **3b** by xanthine/xanthine oxidase–nitro blue tetrazolium assay with an incubation time of 10 min

Table 3.7 SOD activity of complexes **3a** and **3b** as assessed by NBT assay

Complex	**IC_{50} (μM)[a]**
$[Cu(N_3L)Cl_2]$ (**3a**)	11.1 ± 0.5
$[Cu(N_3L)_2](ClO_4)_2$ (**3b**)	41.7 ± 1.0
$CuCl_2.2H_2O$	18.2 ± 1.0
Native CuZn SOD[404]	0.04

[a]SOD by xanthine-xanthine oxidase/NBT assay

From Table 3.11, it is clear that **3a** is more efficient for the dismutation of superoxide ions than **3b** or $CuCl_2$ but less active than analogous compound derived from Pyimpy.[403]

3.2.6. DNA interaction studies

Stability of the metal complexes in aqueous solution is one of the key criteria to be monitored prior to investigate their nuclease and anticancer activity.[453] We performed all the biological activity studies in 0.1 M phosphate buffer so it was necessary to check the stability of our complexes in these buffers. Little change in absorbance was observed after 2 days. A small change in absorbance of whole spectrum without any considerable shift in

wavelengths (λ_{max}) predicted the stability of these metal complexes in buffer solution (Fig. 3.36–3.39).

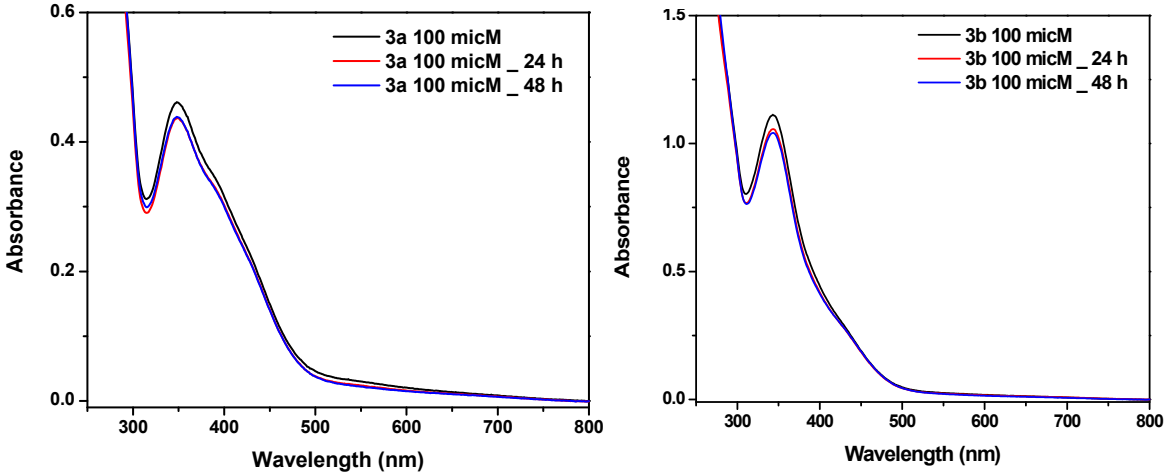

(a) (b)

Fig. 3.36 Absorption spectra of (a) **3a** (100 µM) and (b) **3b** (100 µM) in phosphate buffer (pH 7.2) containing 10% DMF exhibiting no shift in wavelength over 48 h

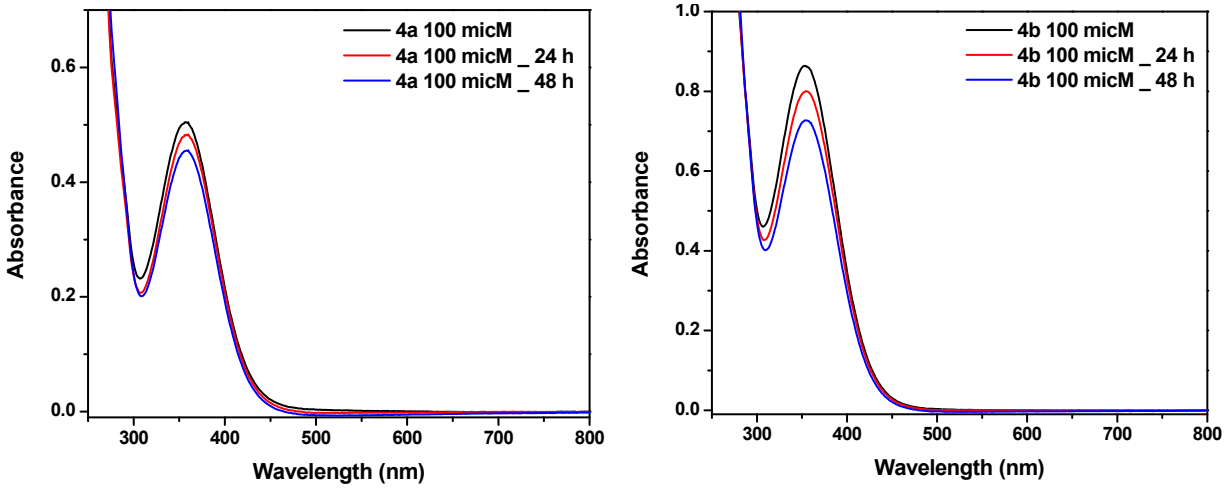

(a) (b)

Fig. 3.37 Absorption spectra of (a) **4a** (100 µM) (b) **4b** (100 µM) in phosphate buffer (pH 7.2) containing 10% DMF exhibiting no shift in wavelength over 48 h

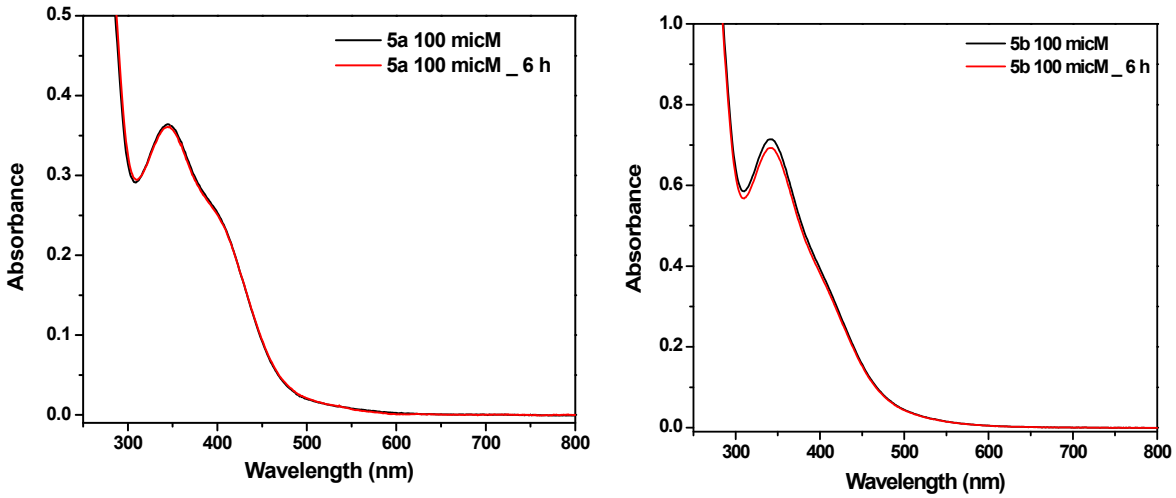

(a) (b)

Fig. 3.38 Absorption spectra of (a) **5a** (100 µM) and (b) **5b** (100 µM) in phosphate buffer (pH 7.2) containing 10% DMF exhibiting no shift in wavelength over 6 h

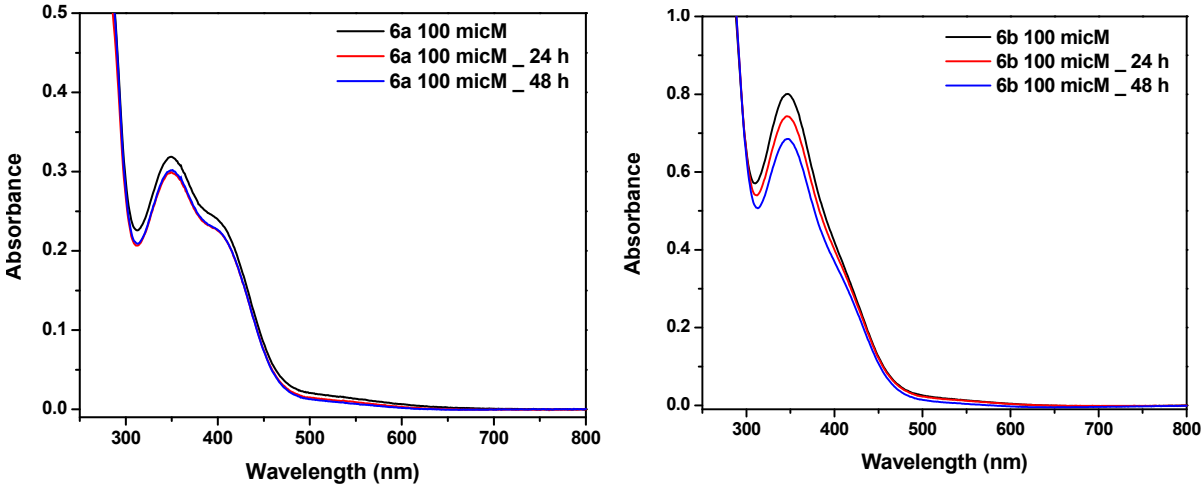

(a) (b)

Fig. 3.39 Absorption spectra of (a) **6a** (100 µM) and (b) **6b** (100 µM) in phosphate buffer (pH 7.2) containing 10% DMF exhibiting no shift in wavelength over 48 h

The slight decrease in absorbance may probably be due to the slow precipitation of the compounds.[454] The cobalt complexes exhibited some changes in the absorption maxima

after 24 h however the complexes were fairly stable on the experimental time scale (4h–6h) (Fig. 3.38).

Electronic absorption technique was used to investigate the DNA binding behaviour of metal complexes. To accomplish this, a fixed concentration of metal complexes was titrated with increasing concentration of CT–DNA at physiological pH and the spectral changes were monitored. The absorption spectra of all complex in absence and presence of different concentrations of CT–DNA are shown in Fig. 3.40–3.47. With increasing concentration of DNA, absorption spectra of all complexes underwent some changes characterized by (a) significant blue shifts; (b) remarkable hypochromism in the charge transfer bands and (c) change in the overall profile of spectrum.

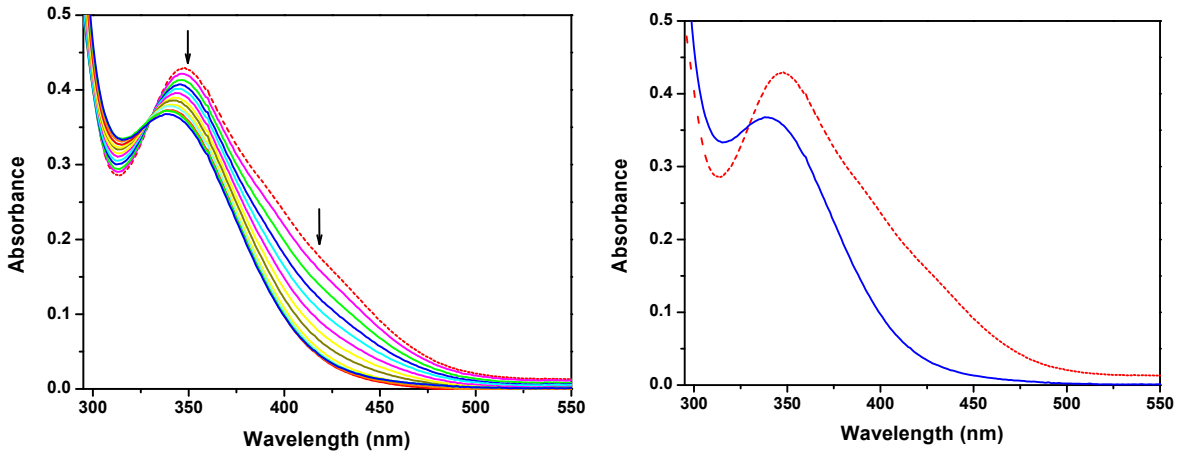

(a) (b)

Fig. 3.40 Absorption spectral changes of complex (a) **3a** (70 µM) in 0.1 M phosphate buffer (pH 7.2) in the presence of increasing amounts of DNA (0 – 447 µM) (b) hypsochromic shift with DNA between the initial and final spectra. Dotted line represents the spectrum in the absence of DNA

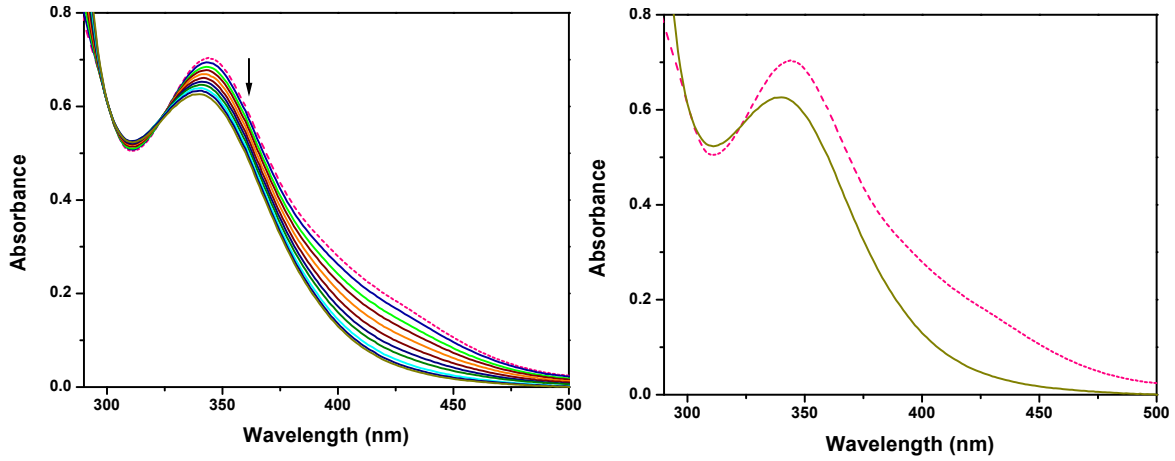

(a) (b)

Fig. 3.41 Absorption spectral changes of complex (a) **3b** (70 µM) in 0.1 M phosphate buffer (pH 7.2) in the presence of increasing amounts of DNA (0 – 500 µM) (b) hypsochromic shift with DNA between the initial and final spectra. Dotted line represents the spectrum in the absence of DNA

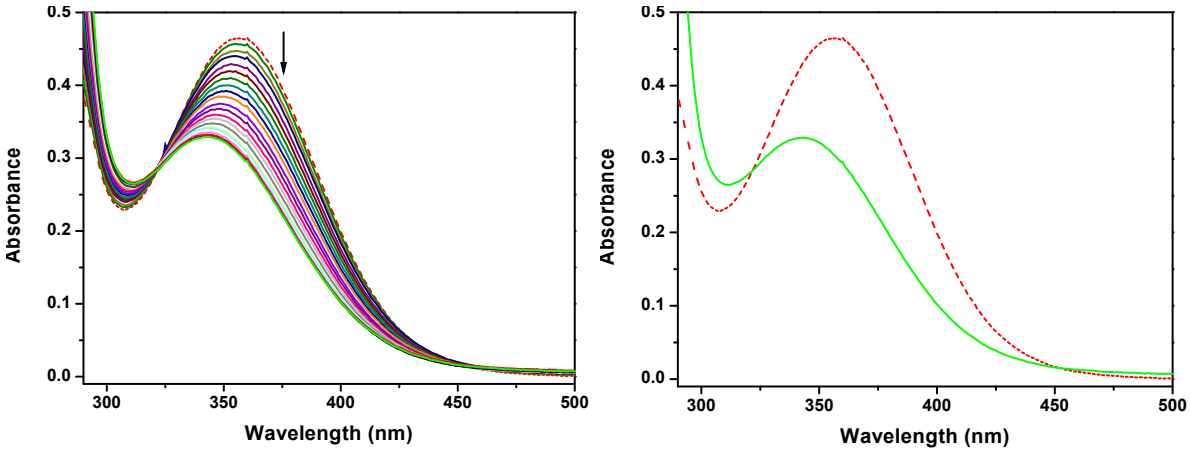

(a) (b)

Fig. 3.42 Absorption spectral changes of complex (a) **4a** (70 µM) in 0.1 M phosphate buffer (pH 7.2) in the presence of increasing amounts of DNA (0 – 698 µM) (b) hypsochromic shift with DNA between the initial and final spectra. Dotted line represents the spectrum in the absence of DNA

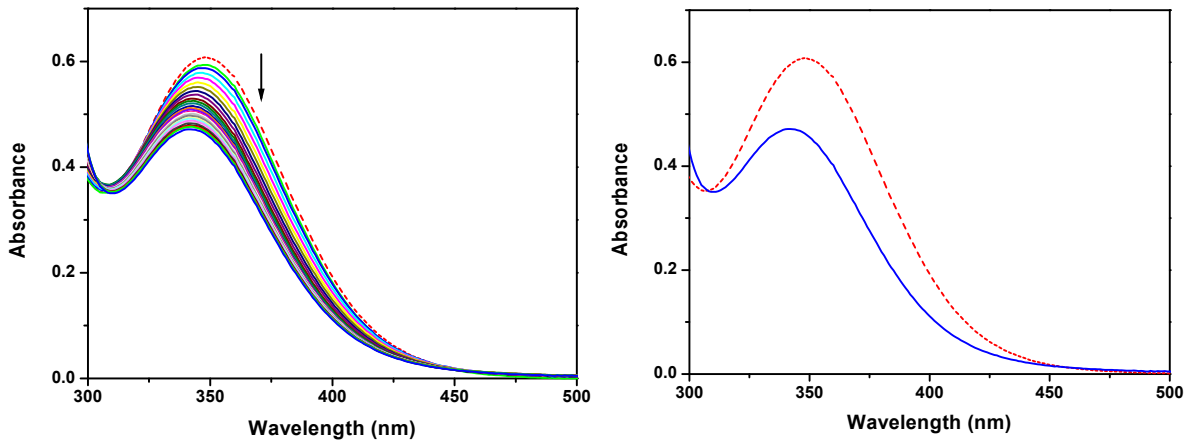

(a) (b)

Fig. 3.43 Absorption spectral changes of complex (a) **4b** (70 µM) in 0.1 M phosphate buffer (pH 7.2) in the presence of increasing amounts of DNA (0 – 385 µM) (b) hypsochromic shift with DNA between the initial and final spectra. Dotted line represents the spectrum in the absence of DNA

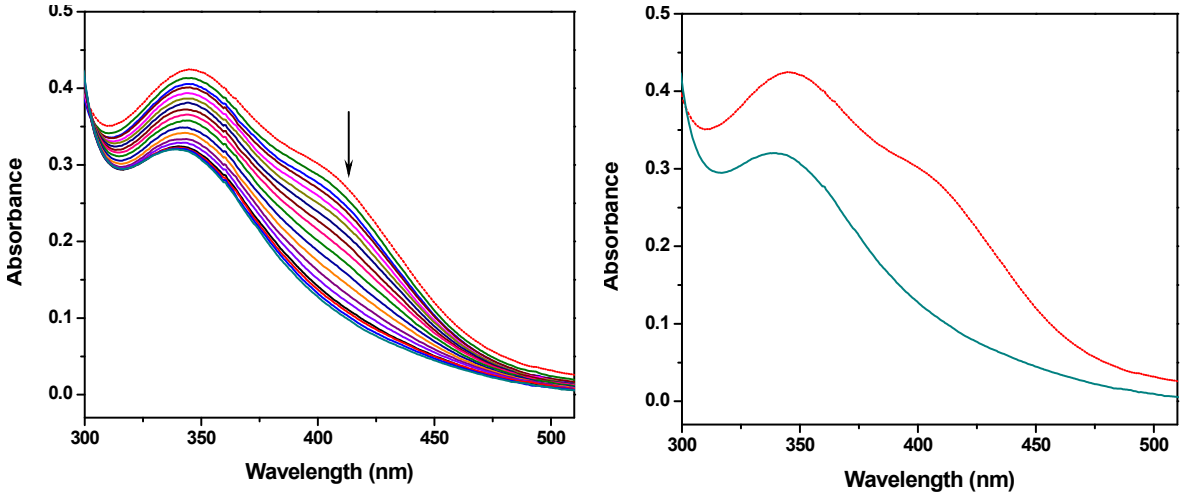

(a) (b)

Fig. 3.44 Absorption spectral changes of complex (a) **5a** (100 µM) in 0.1 M phosphate buffer (pH 7.2) in the presence of increasing amounts of DNA (0 – 316 µM) (b) hypsochromic shift with DNA between the initial and final spectra. Dotted line represents the spectrum in the absence of DNA

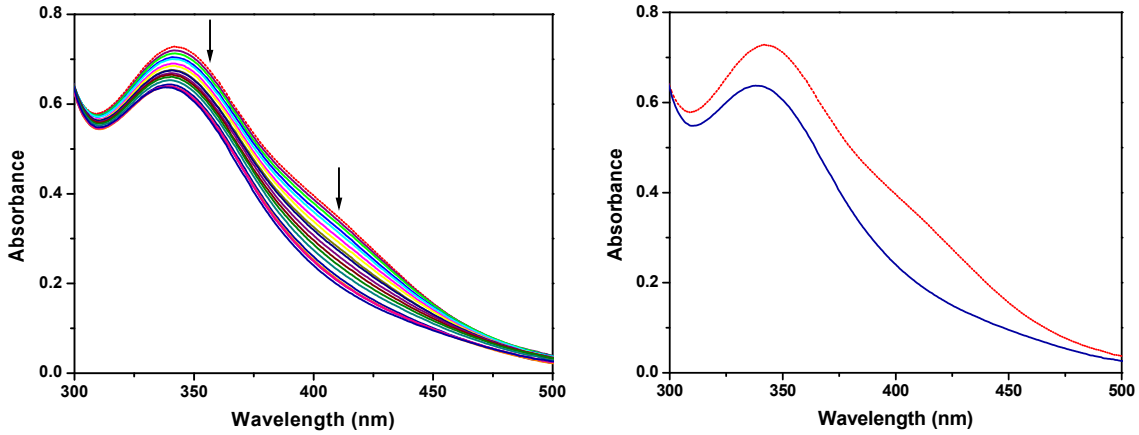

(a) (b)

Fig. 3.45 Absorption spectral changes of complex (a) **5b** (100 µM) in 0.1 M phosphate buffer (pH 7.2) in the presence of increasing amounts of DNA (0 – 501 µM) (b) hypsochromic shift with DNA between the initial and final spectra. Dotted line represents the spectrum in the absence of DNA

Similar type of experiment with **6a** afforded similar spectral changes, however, with hyperchromism at one band (342 nm) and hypochromism on another band (350 nm) accompanied by the generation of an isosbestic point near 368 nm.

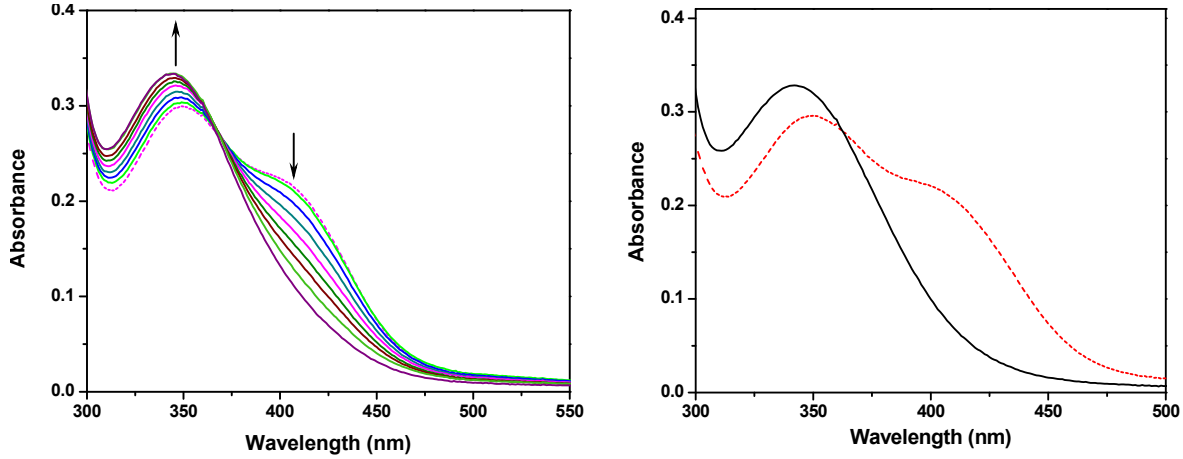

(a) (b)

Fig. 3.46 Absorption spectral changes of complex (a) **6a** (100 µM) in 0.1 M phosphate buffer (pH 7.2) in the presence of increasing amounts of DNA (0 – 546 µM) (b) hypsochromic shift with DNA between the initial and final spectra. Dotted line represents the spectrum in the absence of DNA

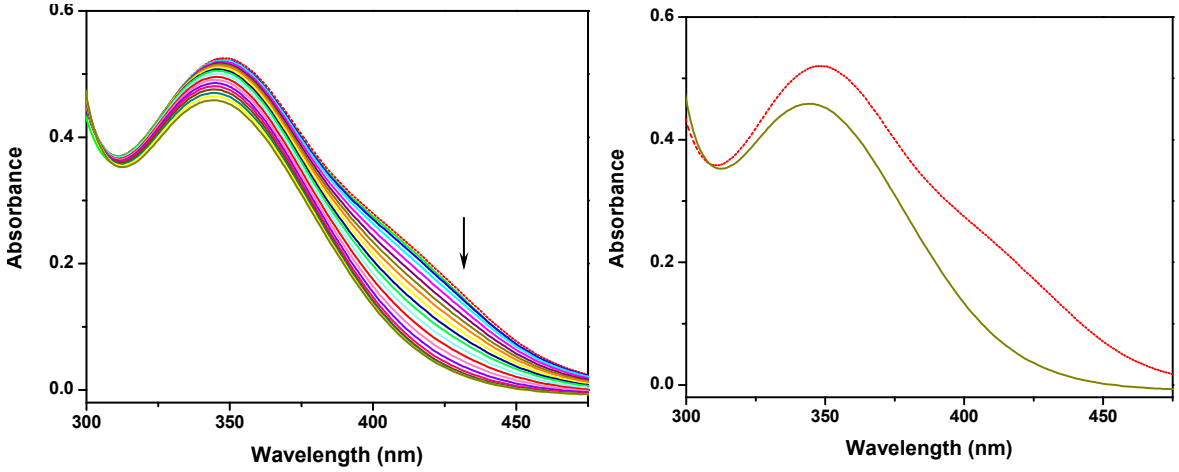

(a) (b)

Fig. 3.47 Absorption spectral changes of complex (a) **6b** (70 µM) in 0.1 M phosphate buffer (pH 7.2) in the presence of increasing amounts of DNA (0 – 348 µM) (b) hypsochromic shift with DNA between the initial and final spectra. Dotted line represents the spectrum in the absence of DNA

The absorption spectral behaviour of the present series of complexes with DNA is summarized in Table 3.8.

Table 3.8 Summary of the DNA binding events

Complex	$^{a}_{max}$ (nm)	Type of Change	a^{a}_{max} (nm)
3a	347–339 419	Hypochromism, Hypsochromism Hypochromism	8
3b	344–339 416	Hypochromism, Hypsochromism Hypochromism	5
4a	357–342	Hypochromism, Hypsochromism	15
4b	349–341	Hypochromism, Hypsochromism	8
5a	346–337 401	Hypochromism, Hypsochromism Hypochromism	9
5b	342–338 401	Hypochromism, Hypsochromism Hypochromism	4
6a	350–342 404	Hyperchromism, Hypsochromism Hypochromism	8
6b	348–344 410	Hypochromism, Hypsochromism Hypochromism	4

It can be noticed that all mono complex exhibited larger spectral shifts than corresponding bis complexes during DNA binding event. Zinc complexes afforded highest shifts among the family probably due to the lowest CFSE values indicating that CFSE may be one of the important factors determining the DNA binding affinity of complexes.[455] The binding constants for all complexes are listed in Table 3.9.

Table 3.9 Binding constants and Stern–Volmer constants for DNA interaction studies

Complex	K_b (M^{-1})	K_{SV} (M^{-1})
3a	5.31×10^3	9.01×10^4
3b	2.48×10^3	1.97×10^5
4a	2.44×10^3	4.90×10^4
4b	6.78×10^3	6.34×10^4
5a	3.95×10^3	5.79×10^4
5b	5.58×10^3	1.09×10^5
6a	3.32×10^3	5.74×10^4
6b	2.44×10^4	1.02×10^5

A myriad of complexes is known which can intercalate between the base pairs of DNA giving rise to the shifts in the absorption bands of complexes. However the intercalative mode of interaction between the present series of metal complexes and DNA was unlikely since intercalation is evident when hypochromism is accompanied by red shift in the absorption spectrum without any change in the spectrum profile.[336-338,348,456-461] Furthermore, the binding constants calculated for the complexes [$\sim 10^3$–10^4] were much lower than those of classical intercalators and metallointercalators [$\sim 10^6$–10^7] indicating their non–intercalative mode of interaction.[462]

Recalling from the previous reports[401-403] including *Chapter 2*, such type of DNA interaction has been investigated for complexes derived from a meridional ligand, Pyimpy,

where binding of complexes at nucleobases was proposed leading to the generation of a new species. However, in that case, spectral shifts were much pronounced and resulted with generation of a new peak in the spectrum with formation of an isosbestic point. It is well established that nucleobases can bind covalently with metal complexes and preferred binding sites are N7 for guanine, N1 and/or N7 for adenine, N3 for cytosine and O4 for thymine.[265] It is also known that the presence of labile ligands in the coordination sphere of a metal ion may facilitate their substitution by nucleobases while interacting with nucleic acids.[454,463] Changes in the spectrum profile, generally accompanied with a remarkable hypsochromic shift at the charge transfer band of the metal complexes, is characteristic of the covalent bond formation with DNA most probably at the guanine or adenine nucleobases.[337,406,464] Hence, it was inferred that the complexes underwent coordination to the nucleobases during DNA binding experiments ultimately giving rise to aforesaid changes in the absorption spectra.

Investigation of the literature revealed that the metal complexes which are known to form coordinate–covalent bonds with DNA, bind predominantly at adenine or guanine nucleobases.[417,465,466] Absorption spectral changes near charge transfer bands of metal complexes during their titration with small ligands like guanosine-5′-monophosphate (GMP) and adenosine-5′-monophosphate (AMP) may provide some additional grounds for covalent binding with nucleobases.[337,406,467] The complex $[Zn(N_3L)Cl_2]$ (**4a**) was chosen as a representative complex for these titrations since highest spectral shift was observed for this complex among whole family. A fixed concentration of **4a** (100 μM) was titrated with increasing concentration of nucleotides and spectra were recorded. The absorption spectral changes of **4a** with increasing concentration of AMP and GMP are illustrated in Fig. 3.48. It

is evident that the spectrum underwent pronounced blue shift with hypochromism at higher concentration of AMP (470 µM). These data suggest that the complex is probably coordinating with the adenine nucleobases during the DNA interaction event. However, no distinct spectral shift could be observed even at 10−fold higher concentration of GMP (4760 µM). No change in the spectrum in presence of GMP precluded any possibility of binding of complexes with guanine nucleobases.

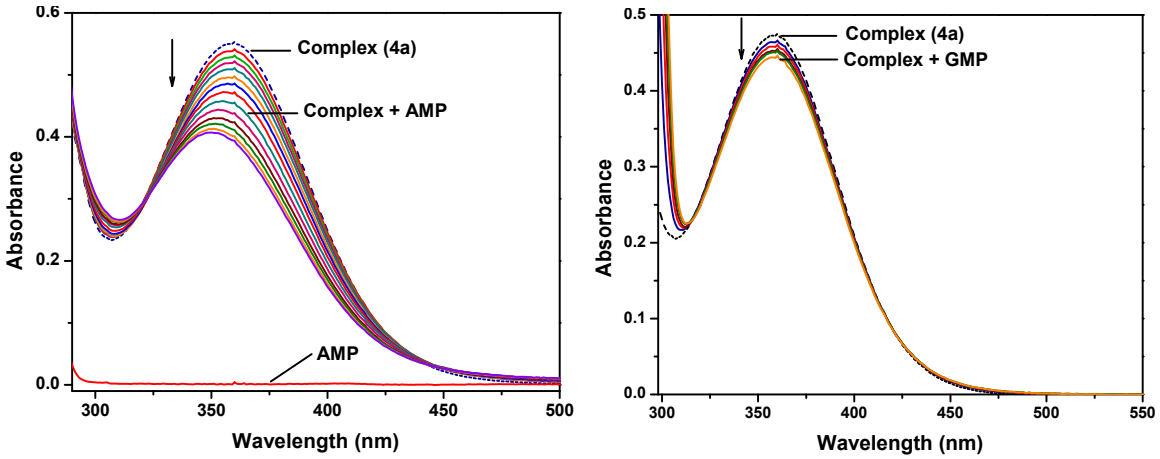

(a) (b)

Fig. 3.48 Absorption spectral changes exhibiting (a) a hypsochromic shift of ~11 nm after incremental addition of AMP (470 µM) and (b) no shift in wavelength after incremental addition of GMP (4760 µM) to the complex **4a** (100 µM) in 0.1 M phosphate buffer (pH 7.2) containing 10% DMF. The dotted line represents the spectrum of the complex in absence of nucleotide. AMP (500 µM) did not show any absorption within the experimental wavelength range. Each successive addition was followed by 3 min incubation

Absorption spectral studies of the present series of complexes with DNA prompted us to investigate their DNA binding properties using emission spectral technique by the competitive binding experiment using ethidium bromide (EtBr) as intercalator. Ethidium bromide is non−emissive in the buffer medium due to the quenching of fluorescence by solvent molecules. It forms soluble complexes with nucleic acids through strong

intercalation of the phenenthridinium ring between the adjacent base pairs giving rise to enhancement in fluorescence.[347] When the complexes were added to the CT−DNA solution pretreated with ethidium bromide, reduction in emission intensity was observed. It is well established that the enhanced emission of ethidium bromide may be quenched by addition of a second DNA binding molecule which can either replace the DNA−bound EtBr (intercalation) or accept an excited state electron from EtBr giving rise to the reduction in the emission intensity.[336] The fluorescence quenching curves and the Stern−Volmer plots for the complexes **3J6** are represented in Figures 3.49–3.56.

Stern−Volmer quenching constants (K_{SV}) were calculated from the slope of the regression curve and listed in Table 3.9. All bis− complexes exhibited stronger binding propensity with DNA as compared to the corresponding mono− complexes and the copper complexes showed highest binding affinity among the whole family (Table 3.9). Quenching of EtBr bound to DNA by metal complexes showed good agreement with the linear Stern−Volmer equation. However, Stern−Volmer plot for complex **6b** showed positive deviation from linearity at higher concentration of the complex (quencher) (see Fig. 3.56 b). This may either be due to the existence of additional binding sites or combined quenching involving both static and dynamic processes occuring at higher concentration of the quencher.[468]

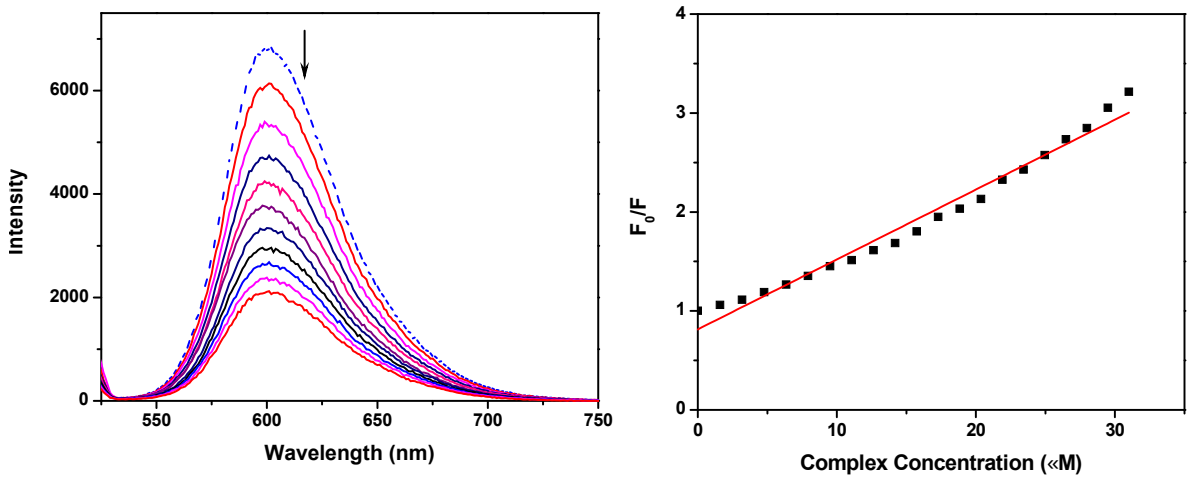

(a) (b)

Fig. 3.49 (a) Fluorescence emission spectra of CT–DNA in presence of complex **3a** in 0.1 M phosphate buffer (pH 7.2) containing 2% DMF. [DNA] = 38.12 ─ 36.94 µM, [**3a**] = 0 ─ 31.01 µM, λ_{ex} = 250 nm and λ_{em} = 600 nm. Dotted line represents the spectrum in the absence of **3a** (b) Stern–Volmer plot for complex **3a**

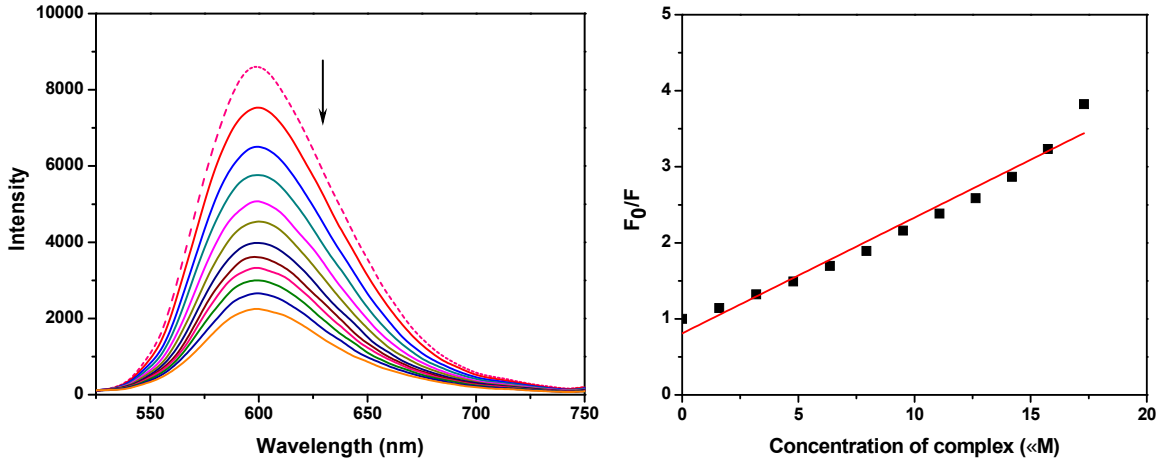

(a) (b)

Fig. 3.50 (a) Fluorescence emission spectra of CT–DNA in presence of complex **3b** in 0.1 M phosphate buffer (pH 7.2) containing 2% DMF. [**3b**] = 25.87 ─ 25.42 µM, [**3b**] = 0 ─ 17.29 µM, λ_{ex} = 250 nm and λ_{em} = 600 nm. Dotted line represents the spectrum in the absence of complex (b) Stern–Volmer plot for complex **3b**

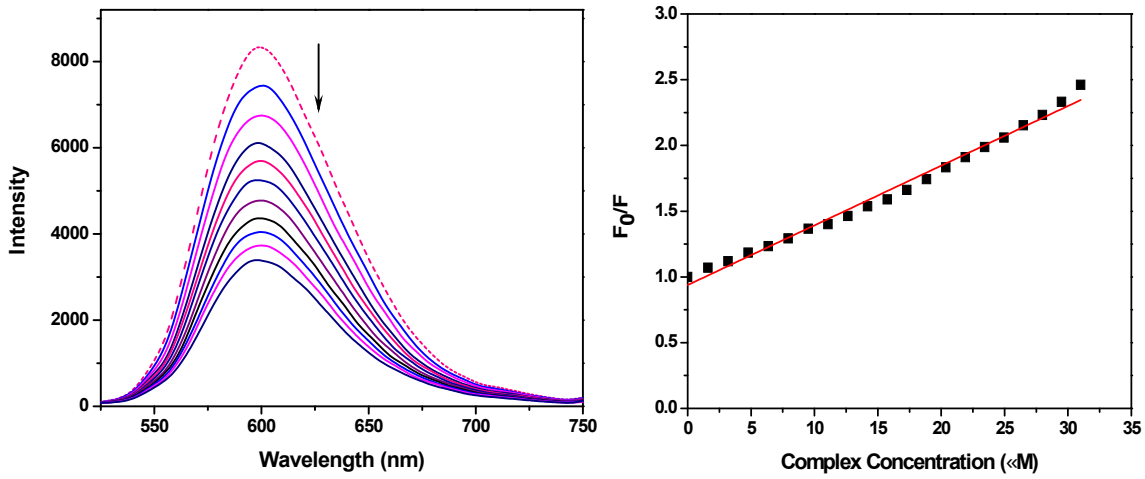

(a) (b)

Fig. 3.51 (a) Fluorescence emission spectra of CT–DNA in presence of complex **4a** in 0.1 M phosphate buffer (pH 7.2) containing 2% DMF. [DNA] = 25.87 ─ 25.07 µM, [**4a**] = 0 ─ 31.01 µM, λ_{ex} = 250 nm and λ_{em} = 600 nm. Dotted line represents the spectrum in the absence of complex **4a** (b) Stern–Volmer plot for complex **4a**

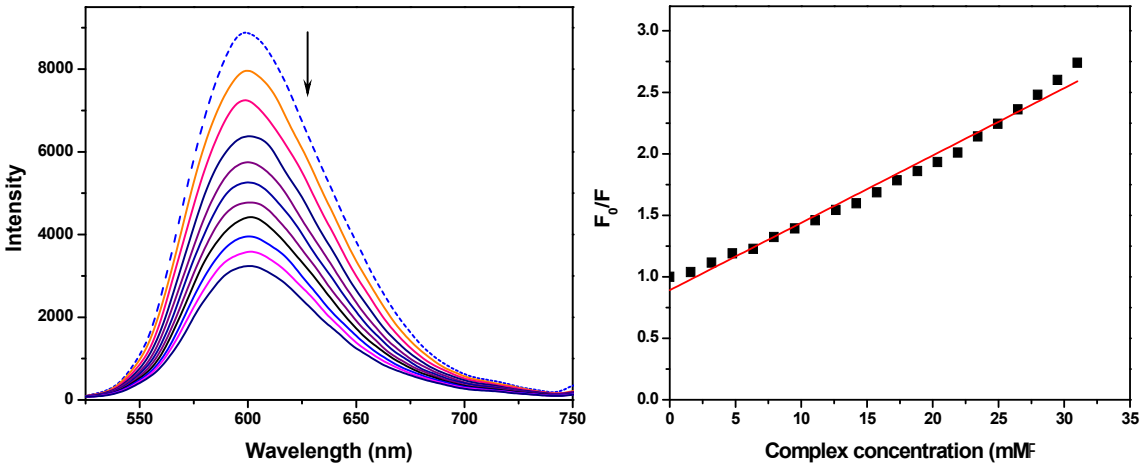

(a) (b)

Fig. 3.52 (a) Fluorescence emission spectra of CT–DNA in presence of complex **4b** in 0.1 M phosphate buffer (pH 7.2) containing 2% DMF. [DNA] = 25.87 ─ 25.07 µM, [**4b**] = 0 ─ 31.01 µM, λ_{ex} = 250 nm and λ_{em} = 600 nm. Dotted line represents the spectrum in the absence of complex **4b**; (b) Stern–Volmer plot for complex **4b**

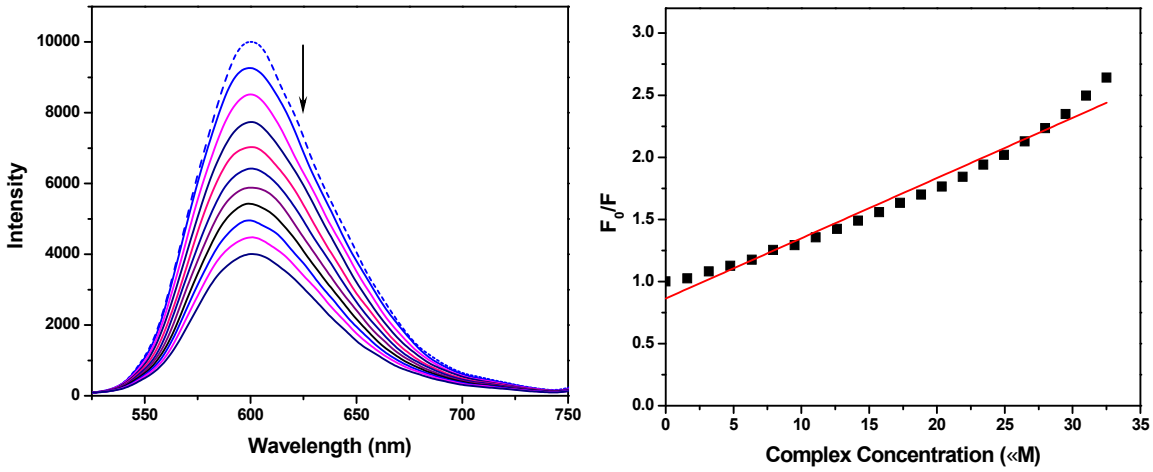

(a) (b)

Fig. 3.53 (a) Fluorescence emission spectra of CT–DNA in presence of complex **5a** in 0.1 M phosphate buffer (pH 7.2) containing 2% DMF. [DNA] = 25.87 ─ 25.03 µM, [**5a**] = 0 ─ 31.01 µM, λ_{ex} = 250 nm and λ_{em} = 600 nm. Dotted line represents the spectrum in the absence of complex **5a**; (b) Stern–Volmer plot for **5a**

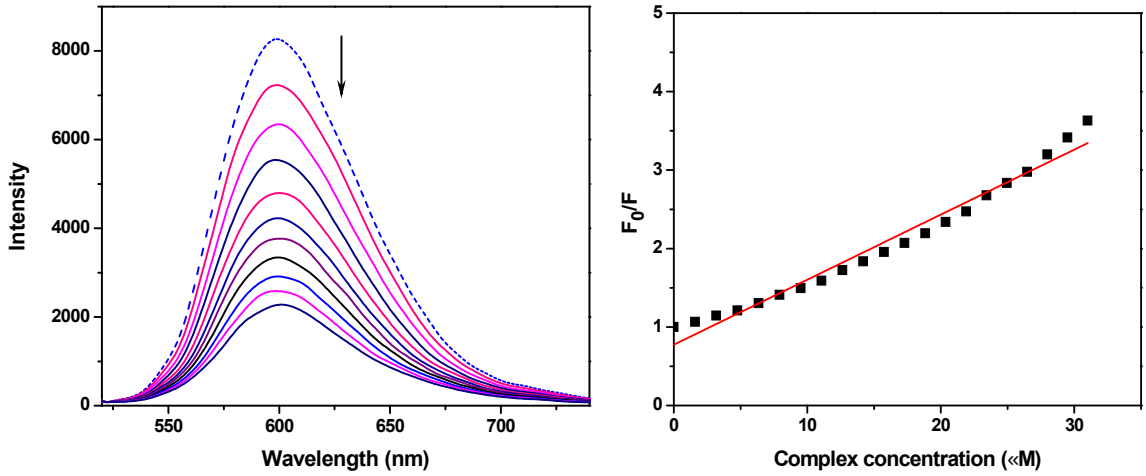

(a) (b)

Fig. 3.54 (a) Fluorescence emission spectra of CT–DNA in presence of complex **5b** in 0.1 M phosphate buffer (pH 7.2) containing 2% DMF. [DNA] = 25.87 ─ 25.07 µM, [**5b**] = 0 ─ 31.01 µM, λ_{ex} = 250 nm and λ_{em} = 600 nm. Dotted line represents the spectrum in the absence of complex **5b**; (b) Stern–Volmer plot for **5b**

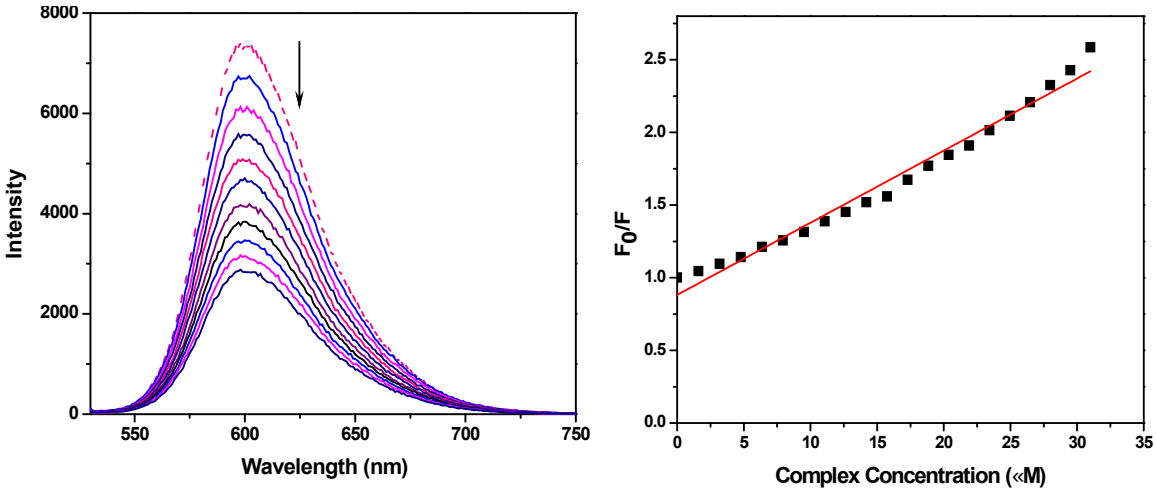

(a) (b)

Fig. 3.55 (a) Fluorescence emission spectra of CT–DNA in presence of complex **6a** in 0.1 M phosphate buffer (pH 7.2) containing 2% DMF. [DNA] = 38.12 ─ 36.93 µM, [**6a**] = 0 ─ 31.01 µM, λ_{ex} = 250 nm and λ_{em} = 600 nm. Dotted line represents the spectrum in the absence of complex **6a**; (b) Stern–Volmer plot for **6a**

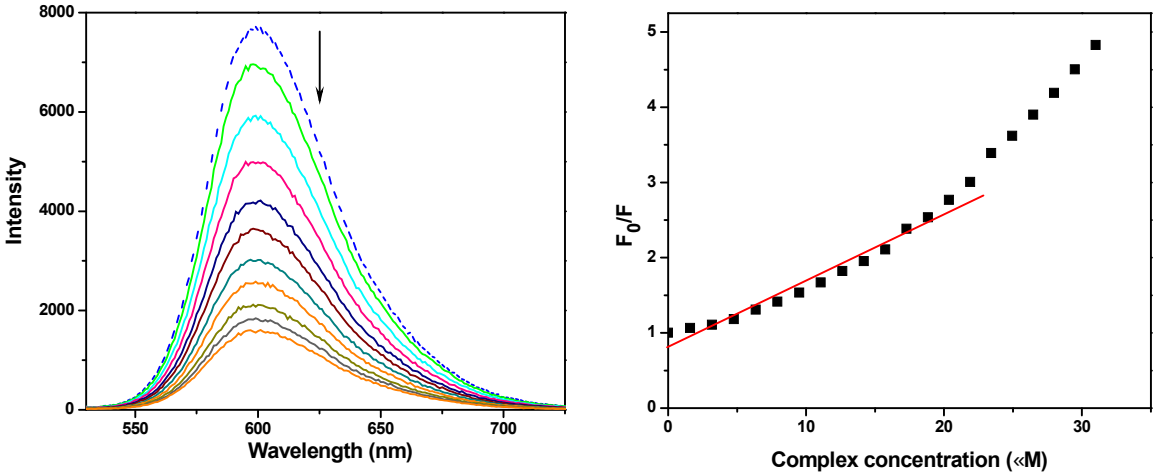

(a) (b)

Fig. 3.56 (a) Fluorescence emission spectra of CT–DNA in presence of complex **6b** in 0.1 M phosphate buffer (pH 7.2) containing 2% DMF. [DNA] = 38.12 ─ 36.94 µM, [**6b**] = 0 ─ 31.01 µM, λ_{ex} = 250 nm and λ_{em} = 600 nm. Dotted line represents the spectrum in the absence of complex **6b**; (b) Stern–Volmer plot for **6b**

Circular Dichroism (CD) is a sensitive technique for probing the conformational changes in DNA induced by foreign DNA binding agents. The CD spectrum of CT–DNA exhibits one positive band near 275 nm due to base stacking and one negative band near 248 nm due to helicity which are characteristic of the right handed B–conformation of DNA. The CD–spectral changes of DNA in presence of complexes **3**–**6** are illustrated in the Fig. 3.57.

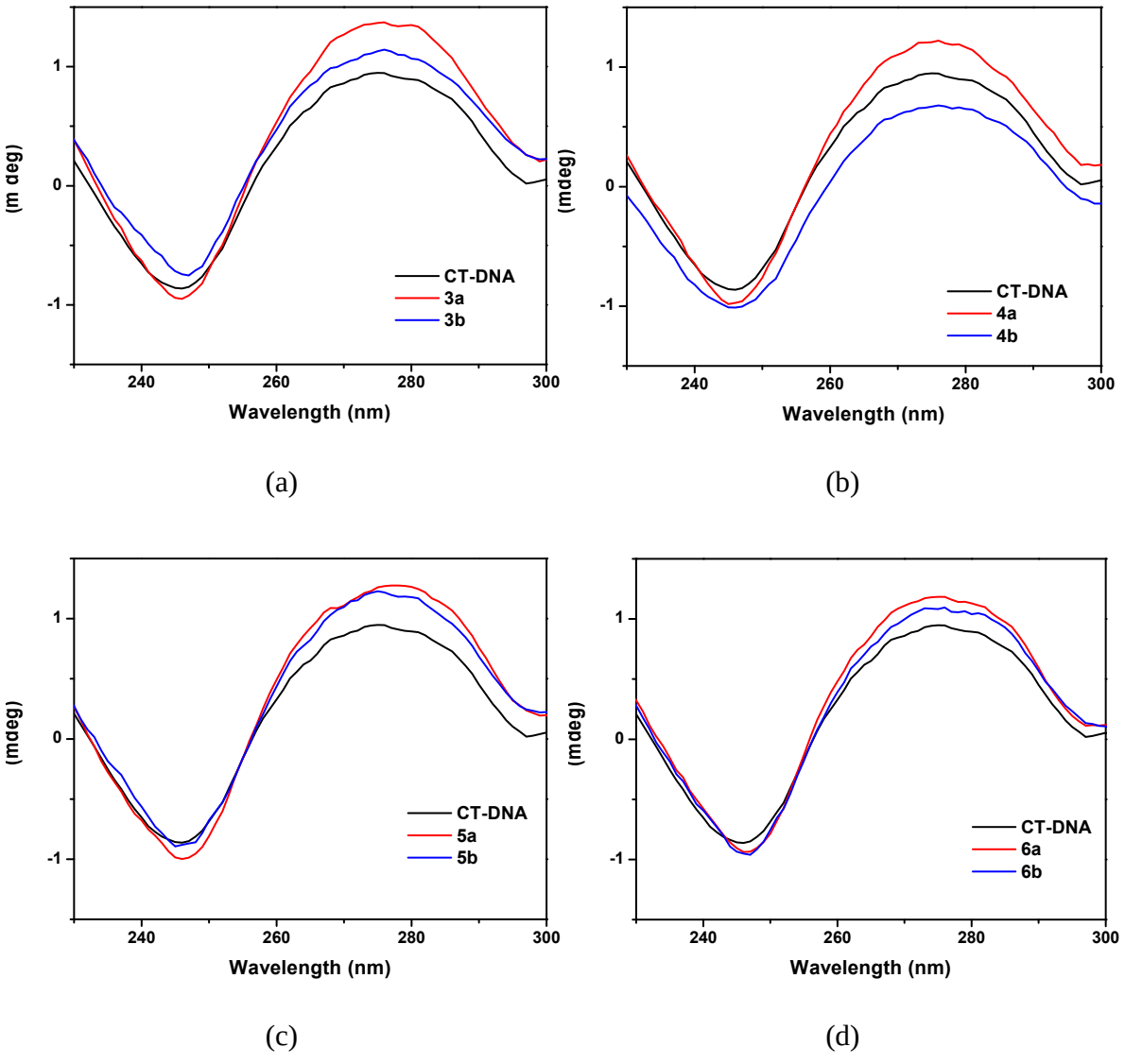

Fig. 3.57 Circular dichroism spectra of CT–DNA and its interaction with complexes (a) **3a** and **3b**, (b) **4a** and **4b**, (c) **5a** and **5b** and (d) **6a** and **6b** in 0.1 M phosphate buffer (pH 7.2) after 15 min incubation at 298 K

The intensity of the negative band was almost unaffected by incubation of DNA with metal complexes, however, little change in the intensity of positive band was observed without any considerable shift in the wavelength. Occurrence of no significant red or blue shift predicted that the conformation of secondary structure of DNA remained largely unaltered after the DNA binding event[348] though little enhancement in the stacking interactions could not be ruled out. It is well established that classical intercalators cause significant changes in intensities of both, positive and negative bands due to enhancement of base stacking and stabilization of helicity whereas small molecules exhibiting groove binding or electrostatic interactions with DNA cause no perturbations.[355,455] Hence CD spectroscopic experiments support a non−intercalative mode of interaction with DNA for the present series of complexes. These data are consistent with the results inferred from the absorption spectral titrations and competitive binding experiments.

3.2.7. Nuclease activity

The nuclease activity of the complexes **3J6** was investigated by agarose gel electrophoresis by monitoring their ability to convert the supercoiled (SC) form (*Form I*) of plasmid to nicked (NC) form (*Form II*) and/or linear (LC) form (*Form III*) under physiological conditions. The nuclease activity of the copper complex **3a** was studied in absence as well as in presence of oxidizing (H_2O_2) and reducing agents (BME) and result are shown in Fig. 3.58 (a) and (b). The complex **3a** exhibited concentration dependent DNA strand scission even in the absences of activators (H_2O_2 or BME) when incubated with DNA (70 ng) for 2.5 h at a concentration of 100 µM or higher. The amount of SC form decreased and that of NC form increased progressively with increasing complex concentration however no LC form could be observed even at higher concentrations of **3a** (500 µM) (Fig.

3.58 (a), lanes 1–7). Introduction of activators like H_2O_2 and BME caused considerable enhancement in the DNA cleavage activity with concomitant appearance of the LC form also (Fig. 3.58 (a), lanes 8–15) and cleavage was found to be more efficient in presence of H_2O_2 than BME. It was observed that DNA cleavage propensity of **3a** at a concentration of 50 µM with H_2O_2 (200 µM) was comparable to that of 500 µM of **3a** alone (Fig. 3.58 (a), lanes 7-8).

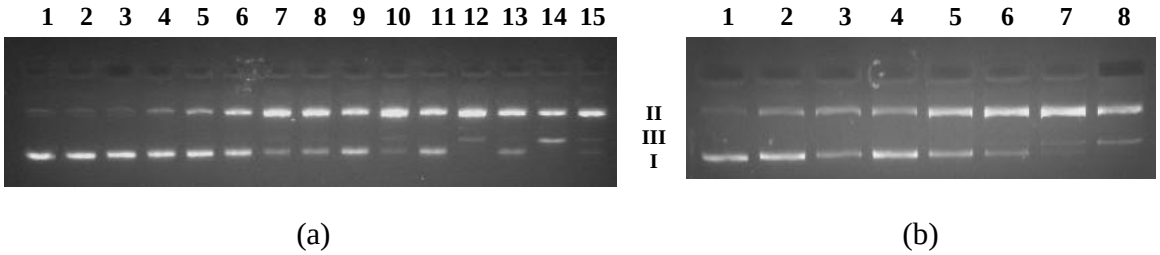

(a) (b)

Fig. 3.58 Gel electrophoresis separations showing cleavage of supercoiled pBR322 DNA (70 ng) by complex **3a** (a) in absence and presence of H_2O_2 (200 µM) and BME (200 µM). Lane 1, DNA control; lane 2, DNA + H_2O_2; lane 3, DNA + BME; lanes 4-7, DNA + **3a** (50, 100, 200 and 500 µM respectively); lanes 8, 10, 12, 14, DNA + H_2O_2 + **3a** (50, 100, 200 and 500 µM respectively); lanes 9, 11, 13, 15, DNA + BME + **3a** (50, 100, 200 and 500 µM respectively); (b) in presence of H_2O_2. Lane 1, DNA control; lane 2─8, DNA + **3a** (50 µM) + H_2O_2 (20 µM, 50 µM, 100 µM, 250 µM, 500 µM, 1 mM and 2 mM respectively). Samples were incubated at 37 °C for 2.5 h in 0.1 M phosphate buffer containing 10% DMF

The extent of cleavage was found to depend on the concentration of H_2O_2 (Fig. 3.58 (b), lanes 2–8) as well and rises gradually with the amount of H_2O_2. It is worth mentioning that H_2O_2 and BME alone did not exhibit any DNA strand scission activity in the control experiments (Fig. 3.58 (a), lanes 2–3).

Similar type of DNA cleavage was found in case of **3b** and the extent of cleavage enhanced in presence of activators (Fig. 3.59 (a)). However **3b** was less efficient than **3a** and no LC form could be seen even at higher concentrations of **3b** with H_2O_2.

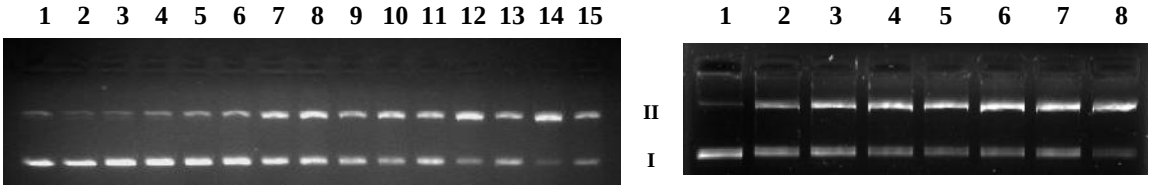

(a) (b)

Fig. 3.59 Gel electrophoresis separations showing cleavage of supercoiled pBR322 DNA (70 ng) by complex **3b** (a) in absence and presence of H_2O_2 (200 µM) and BME (200 µM). Samples were incubated at 37 °C for 2.5 h in 0.1 M phosphate buffer containing 10% DMF. Lane 1, DNA control; lane 2, DNA + H_2O_2; lane 3, DNA + BME; lanes 4-7, DNA + **3b** (50, 100, 200 and 500 µM respectively); lanes 8, 10, 12, 14, DNA + H_2O_2 + **3b** (50, 100, 200 and 500 µM respectively); lanes 9, 11, 13, 15, DNA + BME + **3b** (50, 100, 200 and 500 µM respectively); (b) in presence of H_2O_2 (200 µM). Samples were incubated at 37 °C for varying intervals in 0.1 M phosphate buffer containing 10% DMF. Lane 1, DNA control; lane 2–8, DNA + **3b** (50 µM) + H_2O_2 with incubation time 5 min, 15 min, 30 min, 60 min, 90 min, 120 min and 150 min respectively

Under similar experimental conditions, a time–dependent nuclease activity was also observed for the copper complexes. It is clearly seen in Fig. 3.59 (b) that the concentration of SC form decreased and the concentration of NC form increased gradually with time.

Similar complexes derived from zinc (**4a** and **4b**) also afforded concentration dependent nuclease activity when incubated for longer periods with DNA (Fig. 3.60) and no requirement for any activator (such as H_2O_2) was observed for this processs.

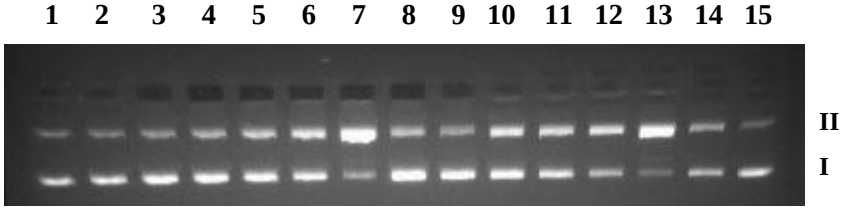

Fig. 3.60 Gel electrophoresis separations showing the cleavage of supercoiled pBR322 DNA (70 ng) by complexes **4a** and **4b**. Samples were incubated at 37 °C for 24 h in 0.1 M phosphate buffer containing 10% DMF. Lane 1, DNA control; lanes 2-7, DNA + **4a** (50 µM, 100 µM, 250 µM, 500 µM, 1 mM and 2 mM respectively); lanes 8-13, DNA + **4b** (50 µM, 100 µM, 250 µM, 500 µM, 1 mM and 2 mM respectively), lane14, DNA + ligand [N_3L] (2 mM); lane 15, DNA + $ZnCl_2$ (2 mM)

As the concentration of metal complexes was increased, a progressive increment in the amount of NC form was observed without generation of any LC form (Fig. 3.60; for **4a** and **4b**: lanes 2-7, and lanes 8-13, respectively). This indicated that no direct double strand scission is happening and the cleavage occurred on only one strand of DNA.

It is important to note that the cobalt complex **5a** could not show any cleavage through self–activating mechanism and no NC or LC form could be seen when incubated in absence of H_2O_2 and BME (Fig. 3.61 (a), lanes 4–7). The complex showed single strand cleavage in presence of H_2O_2 (Fig. 3.61 (a), lanes 8, 10, 12 and 14) however, no such cleavage could be observed when **5a** was incubated with BME (Fig. 3.61 (a), lanes 9, 11, 13 and 15).

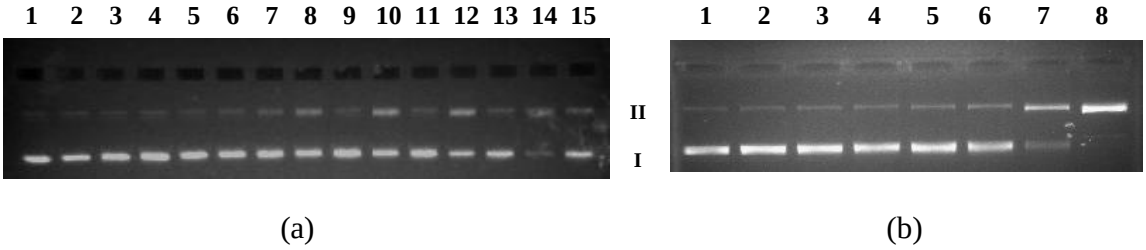

Fig. 3.61 Gel electrophoresis separations showing the cleavage of supercoiled pBR322 DNA (70 ng) by complex **5a** (a) in absence and presence of H_2O_2 (200 µM) and BME (200 µM). Lane 1, DNA control; lane 2, DNA + H_2O_2; lane 3, DNA + BME; lanes 4-7, DNA + **5a** (50, 100, 200 and 500 µM respectively); lanes 8, 10, 12, 14, DNA + H_2O_2 + **5a** (50, 100, 200 and 500 µM respectively); lanes 9, 11, 13, 15, DNA + BME + **5a** (50, 100, 200 and 500 µM respectively); (b) in presence of varying amount of H_2O_2. Lane 1, DNA control; lane 2–8, DNA + **5a** (50 µM) + H_2O_2 (20 µM, 50 µM, 100 µM, 250 µM, 500 µM, 1 mM and 2 mM respectively). Samples were incubated at 37 °C for 2.5 h in 0.1 M phosphate buffer containing 10% DMF

The extent of cleavage was found to depend on the concentration of **5a** as well as H_2O_2 (Fig. 3.61 (b)).

Interestingly, the bis– complex **5b** was able to exhibit self–activated nicking of SC plasmid DNA, though, to a lesser extent than the corresponding copper complexes (Fig.

3.62; lanes 4–7). The nicking enhanced in presence of H_2O_2 however no effect of presence of BME was observed on strand scission by **5b** (Fig. 3.62; lanes 8–15).

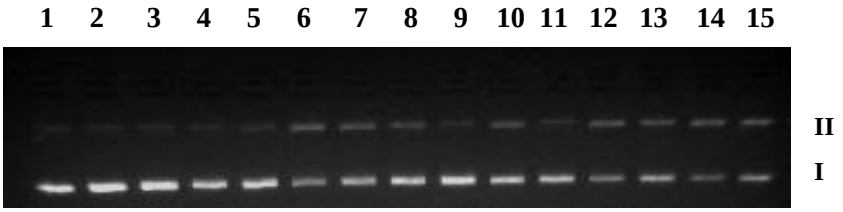

Fig. 3.62 Gel electrophoresis separations showing the cleavage of supercoiled pBR322 DNA (70 ng) by complex **5b** in absence and presence of H_2O_2 (200 µM) and BME (200 µM). Samples were incubated at 37 °C for 2.5 h in 0.1 M phosphate buffer containing 10% DMF. Lane 1, DNA control; lane 2, DNA + H_2O_2; lane 3, DNA + BME; lanes 4-7, DNA + **5b** (50, 100, 200 and 500 µM respectively); lanes 8, 10, 12, 14, DNA + H_2O_2 + **5b** (50, 100, 200 and 500 µM respectively); lanes 9, 11, 13, 15, DNA + BME + **5b** (50, 100, 200 and 500 µM respectively)

The nickel complexes **6a** and **6b** were found to be very less efficient exhibiting negligible DNA cleavage activity (Fig. 3.63). Results of the nuclease activity of complexes **3J6** (**a** and **b**) are summarized in Table 3.10.

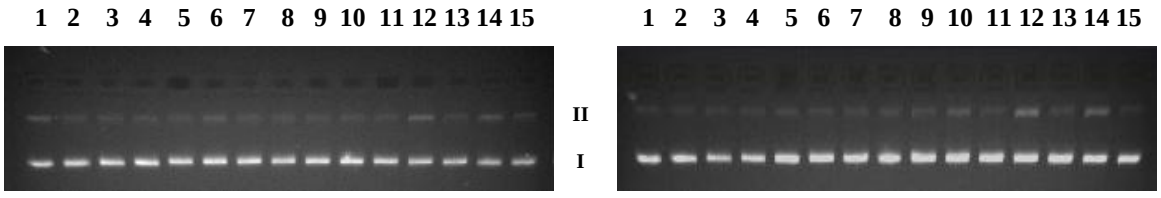

(a) (b)

Fig. 3.63 Gel electrophoresis separations showing negligible cleavage of supercoiled pBR322 DNA (70 ng) in absence and presence of H_2O_2 (200 µM) and BME (200 µM) by complexes (a) **6a** and (b) **6b**; Lane 1, DNA control; lane 2, DNA + H_2O_2; lane 3, DNA + BME; lanes 4-7, DNA + complex (50, 100, 200 and 500 µM respectively); lanes 8, 10, 12, 14, DNA + H_2O_2 + complex (50, 100, 200 and 500 µM respectively); lanes 9, 11, 13, 15, DNA + BME + complex (50, 100, 200 and 500 µM respectively). Samples were incubated at 37 °C for 2.5 h in 0.1 M phosphate buffer containing 10% DMF

Table 3.10 Summary of DNA cleavage activity studies

Complex	Nuclease	Mechanism
3a	✓	Self-activation
3b	✓	Self-activation
4a	✓	Hydrolytic cleavage
4b	✓	Hydrolytic cleavage
5a	✓	Oxidative cleavage
5b	✓	Self-activation
6a	×	–
6b	×	–

To establish the role of various reactive oxygen species (hydroxyl radical, singlet oxygen and peroxy radical) in DNA strand scission mechanism, DNA cleavage experiments were performed in presence of potential radical scavengers. Results of the inhibition studies for complex **3a** are manifested in Fig. 3.64. DMSO, ethanol and urea did not exhibit any inhibition of nuclease activity catalyzed by **3a** suggesting that the cleavage was not mediated by hydroxyl radicals (Fig. 3.64, lanes 5–7). However, significant inhibition was observed in presence of NaN_3 as well as L–histidine (Fig. 3.64, lanes 8–9) with little enhancement in DNA cleavage in presence of D_2O (Fig. 3.64, lane 10). These facts collectively suggested that singlet oxygen and/or singlet oxygen like species are responsible for DNA damage by copper complex **3a**. Activation of molecular oxygen may generate peroxide species also which is evident from the inhibition in presence of catalase enzyme (10 U) (Fig. 3.64, lane 11). Several copper containing nucleases especially those which exhibit self–activating mechanism are known to undergo Cu(II)→Cu(I) reduction in the absence of an external reducing agent with the concomitant activation of molecular oxygen. This process gives rise to the generation of reactive oxygen species leading to DNA cleavage and such electron transfer is known to originate from the coordinated ligand to Cu^{2+}.[342] Hence, investigation of

cleavage mechanism for such complexes in presence of specific Cu(I) chelators, such as neocuproine, becomes highly desirable. Fig. 3.64 shows that appreciable inhibition of conversion of SC form to NC form was achieved when neocuproine was added to the reaction mixture (lane 12). This implies that the cleavage process is governed by a redox dependent pathway and Cu(I) is playing a key role in this process. Furthermore, nuclease activity of complexes exhibiting the electrostatic binding with DNA depends on the ionic strength of the rection medium. Increased salt concentration would neutralize negative charges in DNA, thereby, decreasing the electrostatic interactions and giving rise to inhibition of nuclease activity.[469] When NaCl (400 µM) was added, no change in the plasmid DNA cleavage pattern was observed thus ruling out the electrostatic mode of binding for these complexes (Fig. 3.64, lane 13).

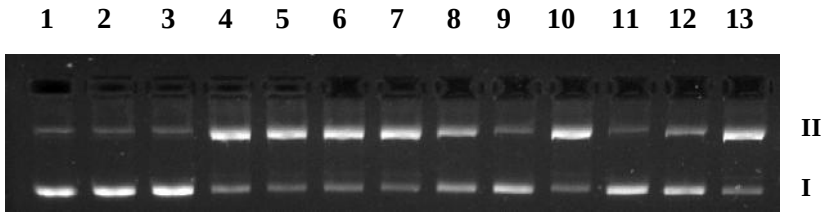

Fig. 3.64 Gel electrophoresis separations showing the cleavage of supercoiled pBR322 DNA (70 ng) by complex **3a** in presence of H_2O_2 (200 µM). Samples were incubated at 37 °C for 2.5 h in 0.1 M phosphate buffer containing 10% DMF. Lane 1, DNA control; lane 2, DNA + ligand [N_3L] (50 µM); lane 3, DNA + ligand [N_3L] (50 µM) + H_2O_2; lanes 4, DNA + **3a** (50 µM) + H_2O_2; lanes 5-9, DNA + **3a** (50 µM) + H_2O_2 + DMSO, ethanol, urea, sodium azide and L-histidine (20 mM each) respectively; lane 10, DNA + **3a** (50 µM) + D_2O (10%); lane 11, DNA + **3a** (50 µM) + catalase (10 U); lanes 12-13; DNA + **3a** (50 µM) + neocuproine and sodium chloride respectively (400 µM each)

A similar mechanism was observed for the self–activated DNA cleavage mediated by **3a** in absence of activator (Fig. 3.65).

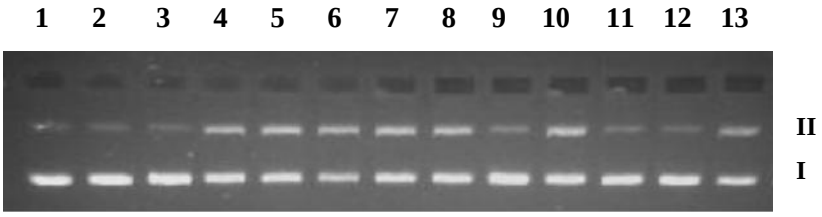

Fig. 3.65 Gel electrophoresis separations showing the cleavage of supercoiled pBR322 DNA (70 ng) by complex **3a** in absence of H_2O_2 and BME. Samples were incubated at 37 °C for 2.5 h in 0.1 M phosphate buffer containing 10% DMF. Lane 1, DNA control; lane 2, DNA + DMF (10 %); lane 3, DNA + ligand [N_3L] (200 µM); lanes 4, DNA + **3a** (200 µM); lanes 5-9, DNA + **3a** (200 µM) + DMSO, ethanol, urea, sodium azide and L-histidine (20 mM each) respectively; lane 10, DNA + **3a** (200 µM) + D_2O (10 %); lane 11, DNA + **3a** (200 µM) + catalase (10 U); lanes 12-13; DNA + **3a** (200 µM) + neocuproine and sodium chloride respectively (400 µM each)

Nuclease activity of **4a** was also investigated in presence of different radical scavengers and the results are illustrated in Fig. 3.66.

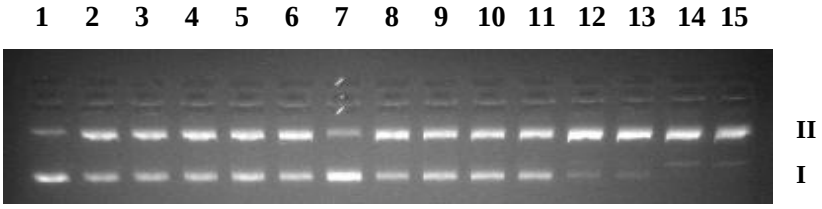

Fig. 3.66 Gel electrophoresis separations showing the cleavage of supercoiled pBR322 DNA (70 ng) by complex **4a**. Samples were incubated at 37 °C for 18 h in 0.1 M phosphate buffer containing 10% DMF. Lane 1, DNA control; lanes 2-5, DNA + **4a** (1 mM) + DMSO, ethanol, urea and sodium azide (20 mM each) respectively; lane 6, DNA + **4a** (1mM) + D_2O (10%); lane 7, DNA + **4a** (1 mM) + L-histidine (20 mM); lane 8, DNA + **4a** (1 mM) + catalase (10 U); lane 9, DNA + **4a** (1 mM) + sodium chloride (400 µM); lanes 10-11, DNA + **4a** (1 mM); lanes 12-13, DNA + **4a** (2 mM); lanes 14-15, DNA + **4a** (5 mM); lanes 11, 13 and 15 represent cleavage in exclusion of air *(anaerobic conditions)*

Addition of DMSO, ethanol, urea (hydroxyl radical scavengers), NaN_3 (singlet oxygen scavenger) and catalase (peroxide ion scavenger) did not show any inhibition of DNA strand scission (Fig. 3.66, lanes 2–5 and 8 respectively). Furthermore, no enhancement of DNA cleavage was obtained due to the addition of D_2O (singlet oxygen stabilizer) (Fig. 3.66, lane

6). Hence the possibility of generation of these ROS was ruled out. Increased ionic strength of the reaction medium also, did not affect the nuclease activity (Fig. 3.66, lane 9). Interestingly, considerable inhibition of the nuclease activity was observed in presence of higher amounts of L–histidine (Fig. 3.66, lane 7). We want to mention here that this family of complexes exhibited covalent type of binding with L–histidine as evident from the absorption spectral experiments (*vide infra*). It is expected that L–histidine probably blocked some vacant or labile coordination sites in **4a** thereby rendering the resulting species incapable to interact with DNA and hence giving rise to inhibition in DNA cleavage activity. This fact also suggests that binding of the complex **4a** with DNA is a key step for the expression of nuclease activity (hydrolytic cleavage) and the cleavage is not mediated by any type of diffusible radical species in solution.

To gain further insight into the mechanism of nuclease activity of zinc complexes, we performed the DNA cleavage experiment under anaerobic conditions (Fig. 3.66, lanes 11, 13 and 15). However, no change in the efficiency of strand scission was observed in anaerobic conditions and the complexes showed efficient DNA cleavage even in the exclusion of air. These data indicated non–involvement of molecular oxygen or any oxygen derived species in DNA cleavage mediated by zinc complexes. It is important to note that zinc does not exhibit redox chemistry hence it can catalyze DNA cleavage only through a hydrolytic mechanism.[470] Results of the inhibition studies including anaerobic DNA cleavage and redox–inertness of zinc ion strongly support that a hydrolytic mechanism is operative for **4a** and **4b**.

Inhibition experiments for complex **5a** showed that there was negligible effect on the ratio of amounts of NC and SC forms of plasmid in presence of various hydroxyl radical

scavengers viz. DMSO, ethanol and urea (Fig. 3.67, lanes 3–5) indicating that hydroxyl radicals are not responsible for the DNA cleavage.

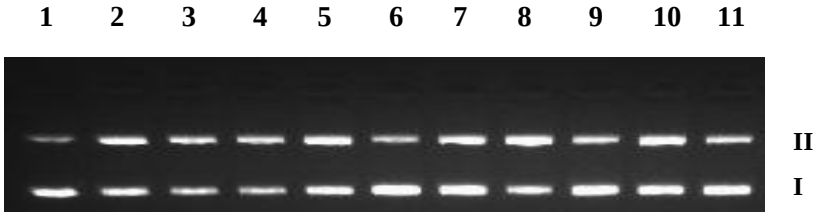

Fig. 3.67 Gel electrophoresis separations showing the cleavage of supercoiled pBR322 DNA (70 ng) by complex **5a** (200 µM) in presence of H_2O_2 (200 µM). Samples were incubated at 37 °C for 2.5 h in 0.1 M phosphate buffer containing 10% DMF. Lane 1, DNA control; lane 2, DNA + **5a** + H_2O_2; lanes 3-7, DNA + **5a** + H_2O_2 + DMSO, ethanol, urea, sodium azide and L-histidine (20 mM each) respectively; lane 8, DNA + **5a** + H_2O_2 + D_2O (10%); lane 9, DNA + **5a** + H_2O_2 + catalase (10 U); lane 10, DNA + **5a** + H_2O_2 + sodium chloride (400 µM), lane 11, DNA + ligand [N_3L] (200 µM) + H_2O_2

Inhibition in presence of sodium azide together with the enhancement in presence of D_2O suggested a vital role of singlet oxygen and/or singlet oxygen like species in nuclease activity (Fig. 3.67, lanes 6 and 8 respectively). Possibility of peroxide generation in solution leading to DNA damage could also not be discarded since considerable inhibition of strand scission was achieved with catalase (Fig. 3.67, lane 9). Increased ionic strength could not lead to any significant inhibition suggesting that the complex did not bind DNA predominantly through electrostatic interaction (Fig. 3.67, lane 10).

3.2.8. Protein interaction studies

Bovine serum albumin is frequently used as protein model for protein interaction studies due to its abundance and low cost, ease of purification, stability, medically important and unusual ligand binding properties and more significantly since bovine serum albumin is structurally homologous to human serum albumin possessing almost 76% sequence identity with HSA.[345,471,472] Binding of metal complexes with BSA as protein model was investigated

using various spectroscopic methods including UV−vis spectroscopy, emission spectroscopy and circular dichroic studies.

To investigate the interaction between protein and metal complexes, the complex **6a** was chosen as a representative of the series. A known concentration of **6a** (100 µM) was incubated with BSA (100 µM) and absorption spectral changes were monitored after different time intervals. The absorption spectra of **6a** in the absence and presence of BSA are illustrated in Fig. 3.68.

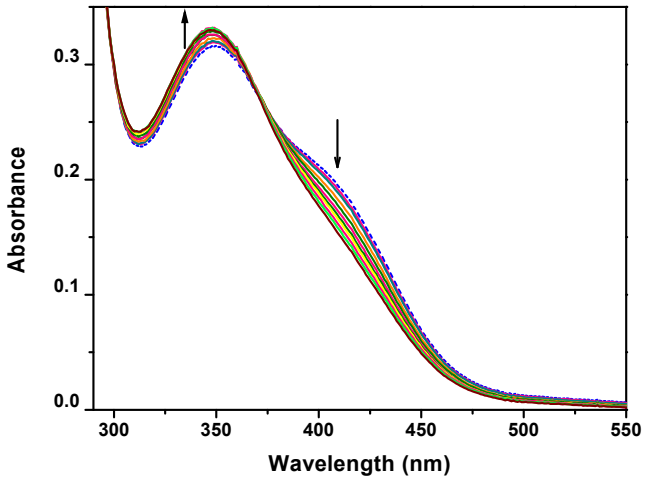

Fig. 3.68 Difference absorption spectral changes between BSA (100 µM) containing **6a** (100 µM) and BSA solution (100 µM) exhibiting a hypsochromic shift of 3 nm (350 nm to 347 nm) after an incubation for 50 min in 0.1 M phosphate buffer (pH 7.2) containing 10% DMF

The complex interacted with BSA exhibiting the spectral changes similar to those observed during the DNA binding experiment (*vide supra*) with the formation of an isosbestic point near 370 nm. These observations indicate that the metal complex underwent changes in the primary coordination sphere of the metal atom through direct protein coordination and more precisely, probably through the coordination with albumin side chains.[345,422,473-475] In case of protein interaction, **6a** exhibited lesser degree of

hypochromism than that observed during DNA interaction, which may be attributed to the lesser number as well as availability of the side chains in BSA for covalent binding with complexes. However, which side chains in albumin binds preferentially to the complexes still remains a point of interest. Surface donor groups in albumins, such as histidine and methionine residues may bind with metal complexes accompanied by the replacement of chloride or other labile groups.[310] Titrations of these amino acids with the metal complexes at their charge transfer bands may provide better insight into their BSA binding event. Absorption spectral changes for the complexes $[Zn(N_3L)Cl_2]$ (**4a**) and $[Ni(N_3L)Cl_2]$ (**6a**) with increasing concentrations of histidine in phosphate buffer (pH 7.2) are shown in Fig. 3.69 and 3.70.

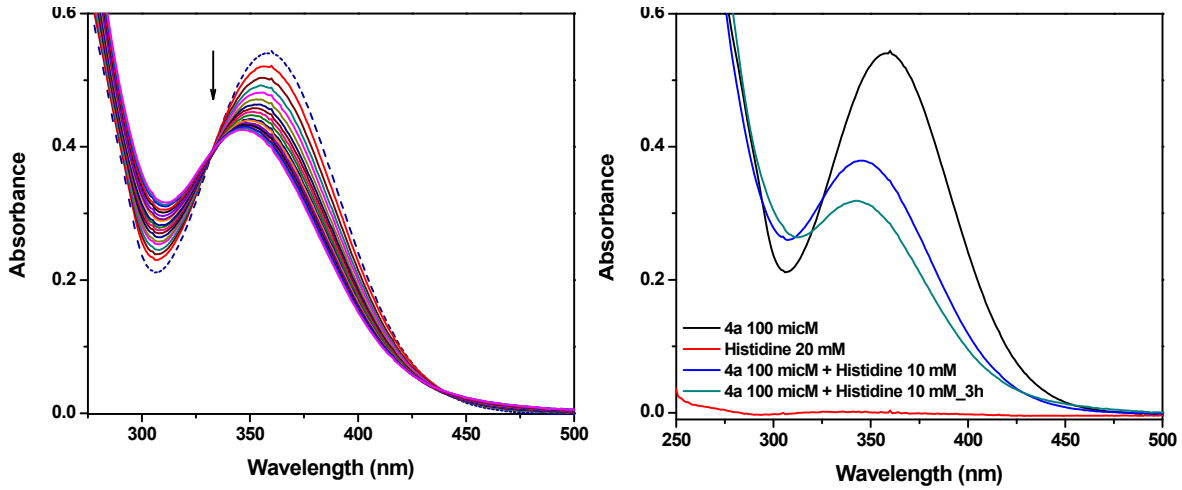

(a) (b)

Fig. 3.69 (a) Absorption spectral changes exhibiting a hypsochromic shift of ~12 nm after incremental addition of L-histidine to the complex **4a** (100 µM) in 0.1 M phosphate buffer (pH 7.2) containing 10% DMF. The dotted line represents the spectrum of the complex in absence of L-histidine; (b) Spectral shift encountered in the absorption profile of complex **4a** (100 µM) after addition of excess of L-histidine (10 mM) and on incubation for 3 h

The complex **4a** exhibited significant hypsochromic shift with the formation of an isosbestic point near 333 nm, as the concentration of L–histidine was increased (up to 3.5 mM) in solution. These data suggest the coordination of metal ion in **4a** with histidine.

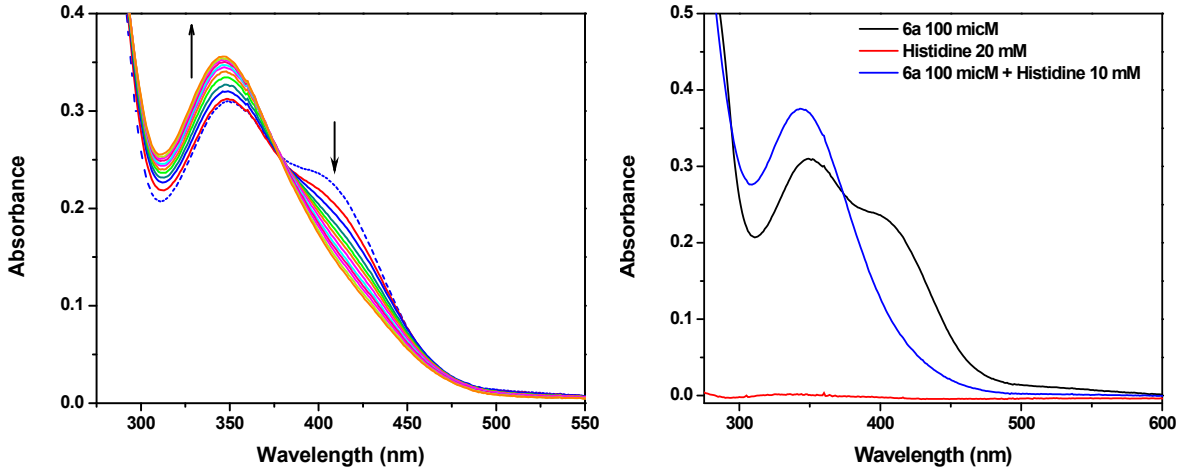

(a) (b)

Fig. 3.70 (a) Absorption spectral changes exhibiting a hypsochromic shift of ~5 nm along with the formation of isosbestic point near 379 nm after incremental addition of L–histidine to the complex **6a** (100 µM) in 0.1 M phosphate buffer (pH 7.2) containing 10% DMF. The dotted line represents the spectrum of the complex in absence of L–histidine; (b) Spectral shift encountered in the absorption profile of complex **6a** (100 µM) after addition of excess of L–histidine (10 mM)

However, in case of complex **6a**, little blue shift in the charge transfer band at 349 nm accompanied by the formation of an isosbestic point at 378 nm was observed at higher concentrations of L–histidine (2.2 mM). We want to emphasize here that these spectral changes are similar to those observed during the BSA interaction studies of these complexes. These data clearly indicated the covalent type of binding between these complexes and BSA, probably at the histidine residues however the possibility of coordination of other side chains can not be ignored.

Binding behaviour of the metal complexes with serum albumins can be investigated by the tryptophan fluorescence quenching experiment.[347] Trp 134 and Trp 213 residues of BSA can be selectively excited at 295 nm and the emission intensity is highly dependent on the degree of exposure of these tryptophan side chains to polar environment as well as their proximity to various quenching groups like protonated carbonyl and protonated imidazole, tyrosinate anions and deprotonated ε–amino groups. In order to study the protein binding propensity of the complexes (**3J6**), a fixed concentration of albumin was titrated with increasing concentrations of the metal complexes and the changes in emission intensity were monitored. Binding of metal complexes with albumin led to significant decrease in emission intensity with increasing concentration of metal complexes. The fluorescence quenching curves, Stern–Volmer plots and Scatchard plots for all complexes are illustrated in Figures 3.71–3.78.

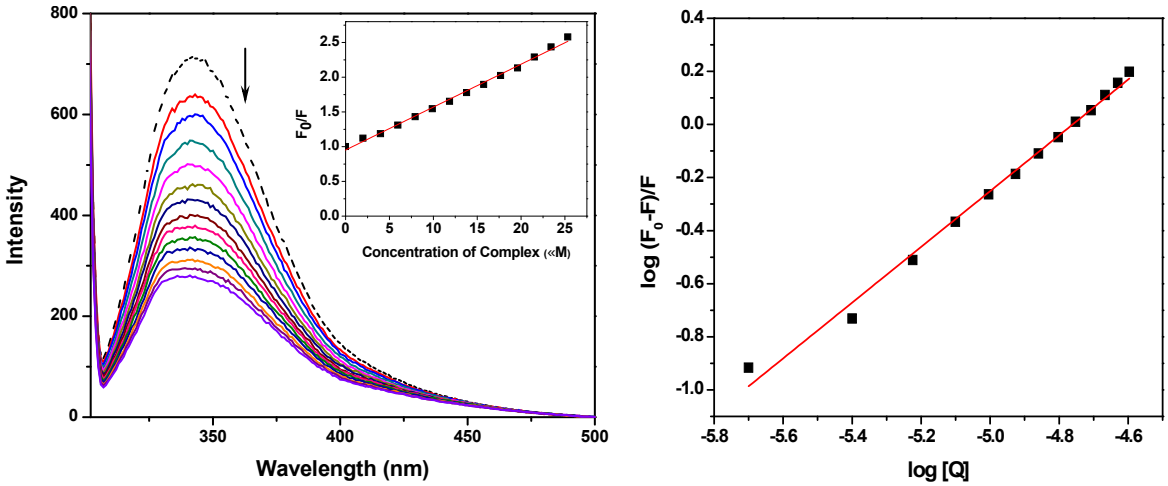

(a) (b)

Fig. 3.71 (a) Fluorescence emission spectra of BSA in presence of complex **3a** in 0.1 M phosphate buffer (pH 7.2) containing 2% DMF. [BSA] = 2 μM, [**3a**] = 0–25.34 μM, λ_{ex} = 295 nm and λ_{em} = 344 nm. Dotted line represents the spectrum in the absence of complex; inset: Stern–Volmer plot of complex **3a**; (b) Plot of log (F_0-F)/F vs. log [Q] for complex **3a**

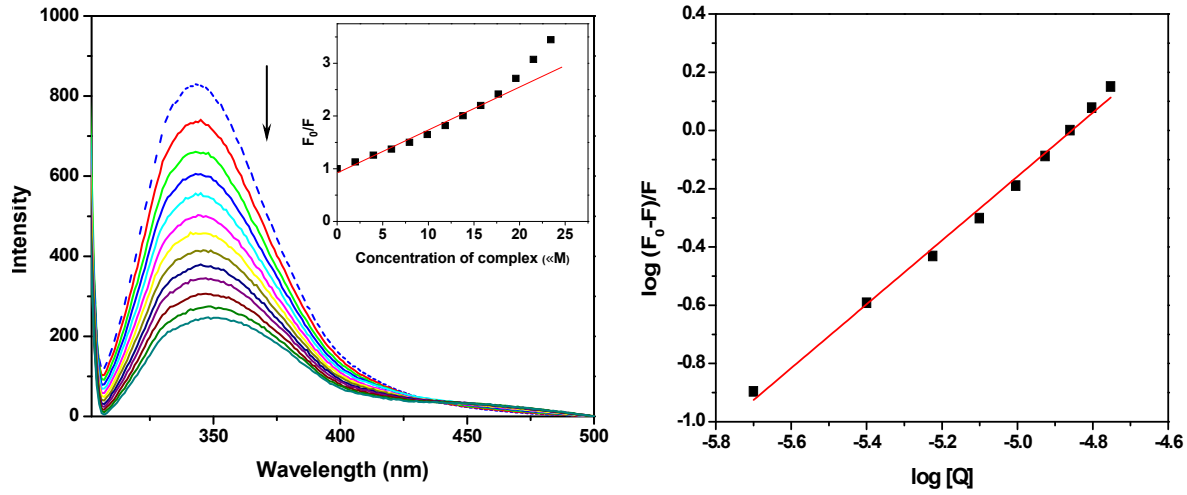

(a) (b)

Fig. 3.72 (a) Fluorescence emission spectra of BSA in presence of complex **3b** in 0.1 M phosphate buffer (pH 7.2) containing 2% DMF. [BSA] = 2 μM, [**3b**] = 0–23.43 μM, λ_{ex} = 295 nm and λ_{em} = 344 nm. Dotted line represents the spectrum in the absence of complex; inset: Stern–Volmer plot of complex **3b**; (b) Plot of log (F_0-F)/F vs. log [Q] for **3b**

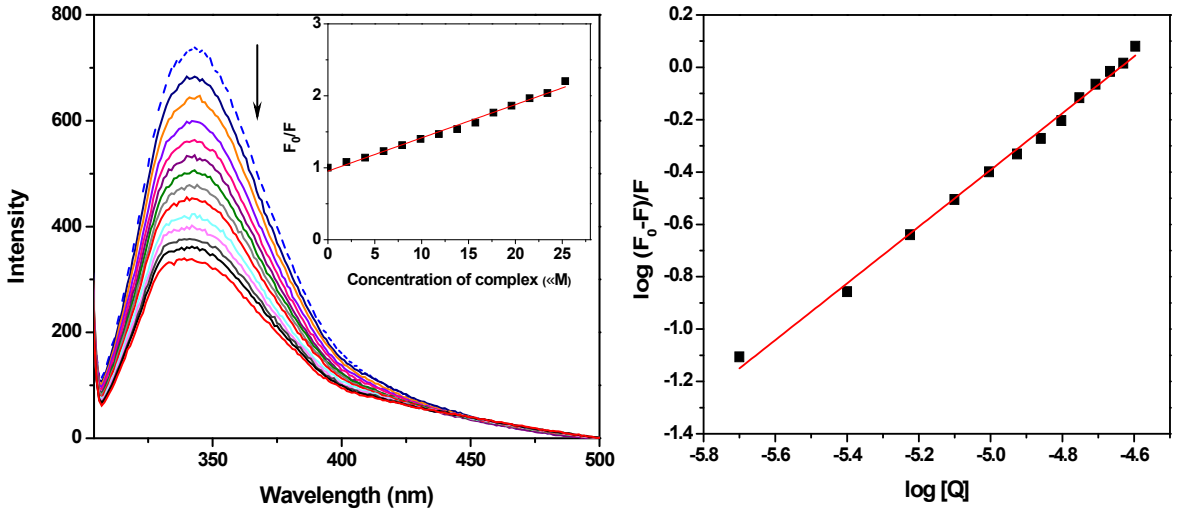

(a) (b)

Fig. 3.73 (a) Fluorescence emission spectra of BSA in presence of complex **4a** in 0.1 M phosphate buffer (pH 7.2) containing 2% DMF. [BSA] = 2 μM, [complex] = 0–25.34 μM, λ_{ex} = 295 nm and λ_{em} = 344 nm. Dotted line represents the spectrum in the absence of complex; inset: Stern–Volmer plot of complex **4a**; (b) Plot of log (F_0-F)/F vs. log [Q] for **4a**

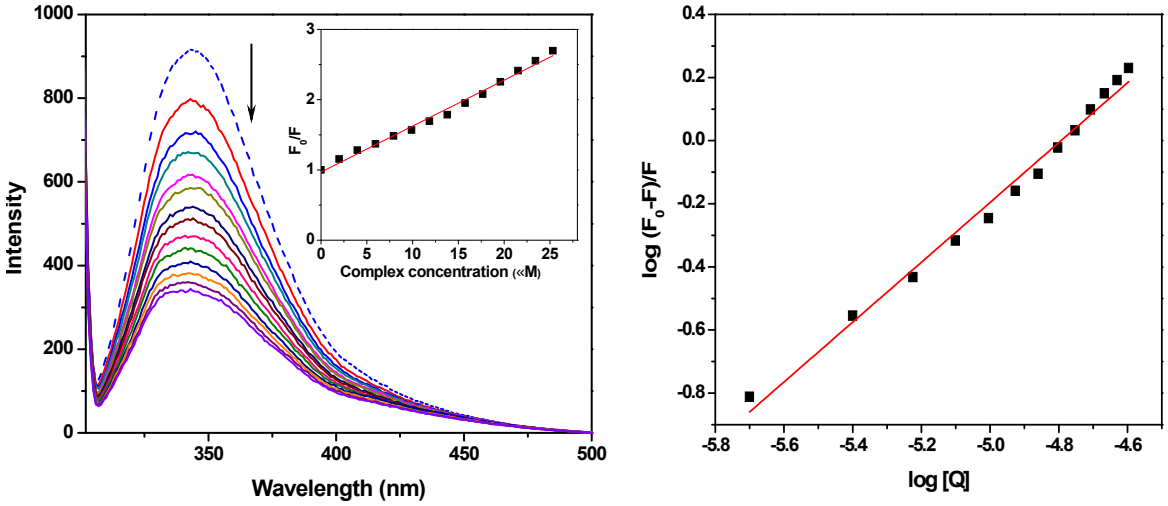

(a) (b)

Fig. 3.74 (a) Fluorescence emission spectra of BSA in presence of complex **4b** in 0.1 M phosphate buffer (pH 7.2) containing 2% DMF. [BSA] = 2 μM, [**4b**] = 0–25.34 μM, λ_{ex} = 295 nm and λ_{em} = 344 nm. Dotted line represents the spectrum in the absence of complex inset: Stern–Volmer plot of complex **4b**; (b) Plot of log (F_0-F)/F vs. log [Q] for **4b**

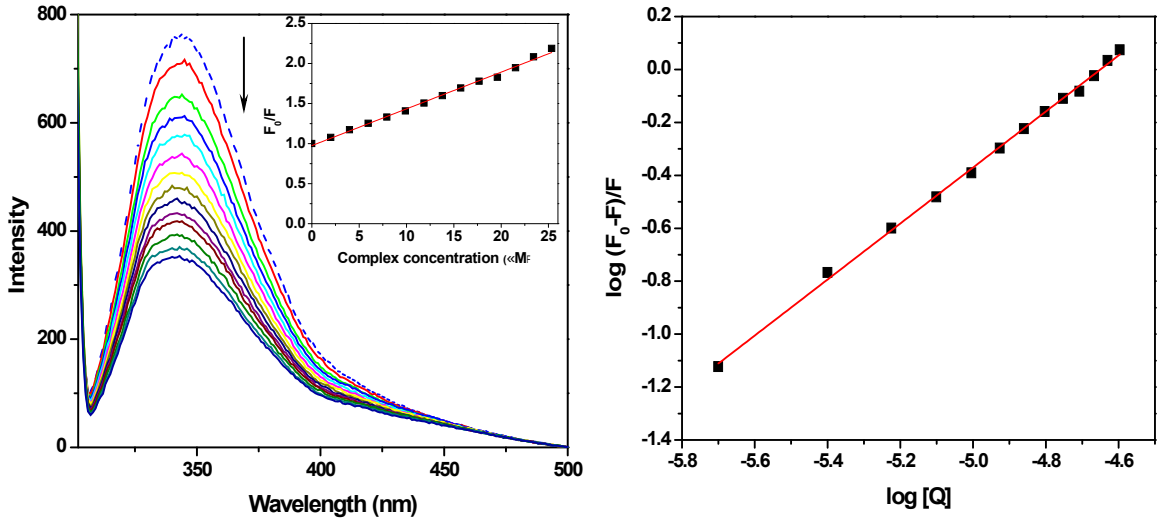

(a) (b)

Fig. 3.75 (a) Fluorescence emission spectra of BSA in presence of complex **5a** in 0.1 M phosphate buffer (pH 7.2) containing 2% DMF. [BSA] = 2 μM, [**5a**] = 0–25.34 μM, λ_{ex} = 295 nm and λ_{em} = 344 nm. Dotted line represents the spectrum in the absence of complex inset: Stern–Volmer plot of complex **5a**; (b) Plot of log (F_0-F)/F vs. log [Q] for **5a**

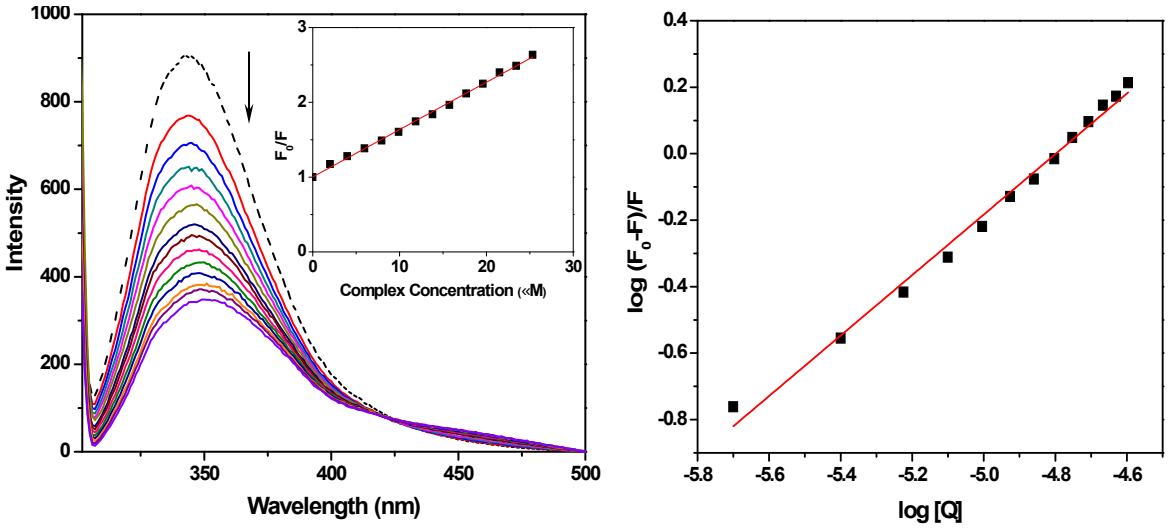

(a) (b)

Fig. 3.76 (a) Fluorescence emission spectra of BSA in presence of complex **5b** in 0.1 M phosphate buffer (pH 7.2) containing 2% DMF. [BSA] = 2 μM, [**5b**] = 0–25.34 μM, λ_{ex} = 295 nm and λ_{em} = 344 nm. Dotted line represents the spectrum in the absence of complex; inset: Stern–Volmer plot of complex **5b**; (b) Plot of log (F_0-F)/F vs. log [Q] for **5b**

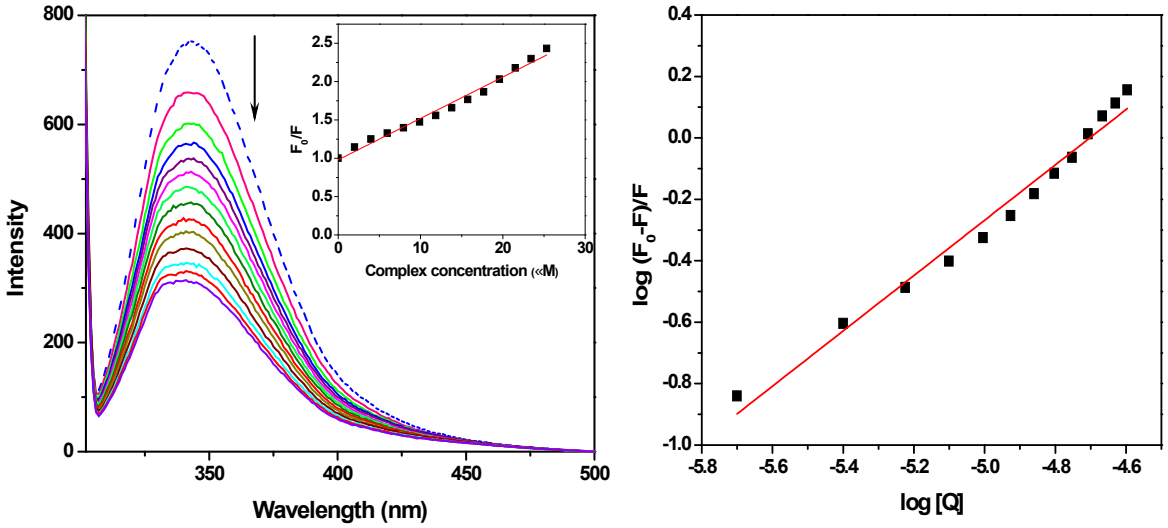

(a) (b)

Fig. 3.77 (a) Fluorescence emission spectra of BSA in presence of complex **6a** in 0.1 M phosphate buffer (pH 7.2) containing 2% DMF. [BSA] = 2 μM, [**6a**] = 0–25.34 μM, λ_{ex} = 295 nm and λ_{em} = 344 nm. Dotted line represents the spectrum in the absence of complex inset: Stern–Volmer plot of complex **6a**; (b) Plot of log (F_0-F)/F vs. log [Q] for **6a**

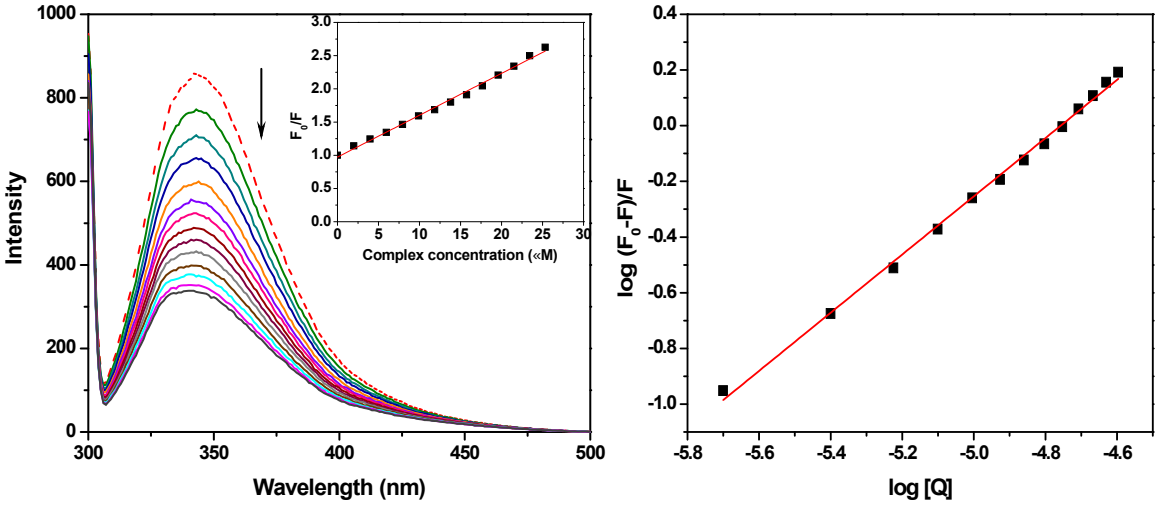

(a) (b)

Fig. 3.78 (a) Fluorescence emission spectra of BSA in presence of complex **6b** in 0.1 M phosphate buffer (pH 7.2) containing 2% DMF. [BSA] = 2 μM, [**6b**] = 0–25.34 μM, λ_{ex} = 295 nm and λ_{em} = 344 nm. Dotted line represents the spectrum in the absence of complex; inset: Stern–Volmer plot of complex **6b**; (b) Plot of log (F_0-F)/F vs. log [Q] for **6b**

These data clearly indicate that the protein underwent considerable changes in its secondary structure as a consequence of binding with metal complex. Quenching of fluorescence may occur by two types of mechanisms; (a) dynamic quenching which is characterized by the close vicinity of fluorophore and quencher molecule during the transient excited state formation; and (b) static quenching which features the ground state fluorophore–quencher complex formation. The K_q values for all the complexes are listed in Table 3.11. These values are much higher than the maximum scatter collision–quenching constants (~10^{10} $M^{-1}s^{-1}$) for biopolymer fluorescence suggesting that a static quenching mechanism was prevalent.[348] Binding constants (*K*) and the number of binding sites (*n*) for the complexes **3J6** were determined by applying the Scatchard equation (*Chapter 1*) and

calculating the slope and intercept from the Scatchard plots. From Table 3.11 it is evident that the zinc complexes exhibited highest binding affinities with albumin in the series.

Table 3.11 Stern–Volmer quenching constants, binding constants and number of binding sites for interactions of complexes **3J6** (**a** and **b**) with BSA

Complex	K_{SV} (M^{-1})	K_q (M^{-1})	K (M^{-1})	n
3a	6.49×10^4	6.49×10^{12}	1.00×10^5	1.05
3b	9.26×10^4	9.26×10^{12}	2.10×10^5	1.09
4a	4.85×10^4	4.85×10^{12}	1.05×10^5	1.08
4b	6.74×10^4	6.74×10^{12}	3.49×10^5	0.95
5a	4.71×10^4	4.71×10^{12}	8.33×10^4	1.06
5b	6.31×10^4	6.31×10^{12}	2.32×10^4	0.91
6a	5.51×10^4	5.51×10^{12}	1.71×10^4	0.90
6b	6.47×10^4	6.47×10^{12}	9.38×10^4	1.05

CD spectroscopy is another sensitive tool to explore the conformational changes in the secondary structure of proteins induced due to the interaction with small molecules. Typical CD spectroscopic signals of BSA include one double humped negative band and one positive band within the region of 190─260 nm which represent the α–helical structure of albumin.[476] To monitor the conformational changes in BSA induced by metal complexes, BSA solution was incubated with complexes **3J6** in the molar ratio 1:10 for 15 min and spectra were recorded. CD spectral changes of BSA due to the interaction with metal complexes (**3**–**6**) are illustrated in Fig. 3.79. Little changes in the ellipticity were observed without any shift in the wavelengths (λ_{max}) suggesting that some sort of interaction indeed exists between BSA and metal complexes. These data indicated that BSA did not undergo any significant conformational change and the α–helical structure of albumin was maintained even after binding with the metal complexes.[476]

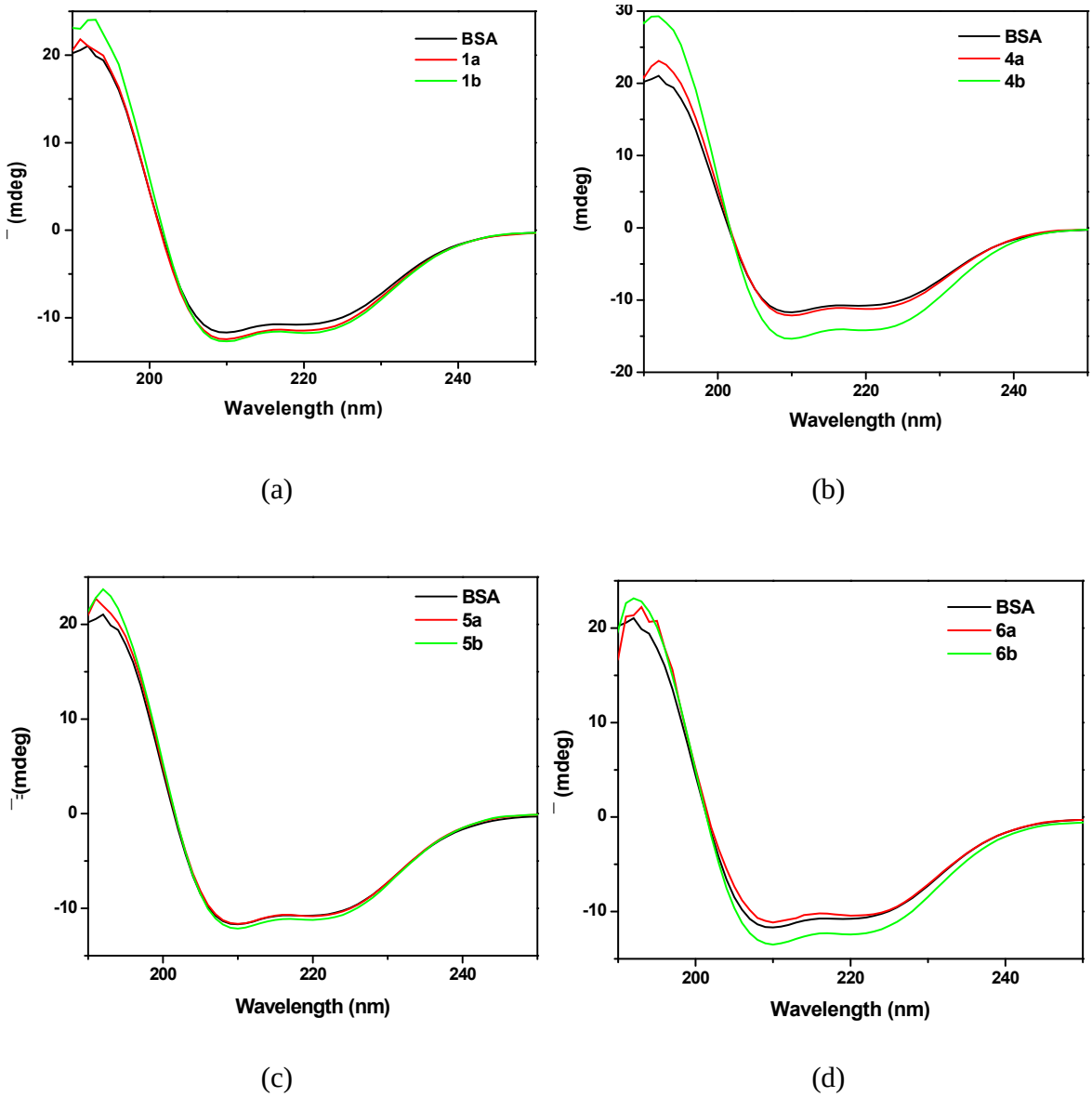

Fig. 3.79 Circular dichroism spectra of BSA and its interaction with complexes (a) **3a** and **3b**, (b) **4a** and **4b**, (c) **5a** and **5b** and (d) **6a** and **6b** in 0.1 M phosphate buffer (pH 7.2) after 15 min incubation at 25 °C

3.3. Conclusions

A family of mononuclear copper, zinc, cobalt and nickel complexes derived from a new tridentate ligand (N_3L) having NNN donor set has been synthesized and characterized by various physical and spectroscopic techniques. X–ray diffraction studies authenticated the

structures of representative complexes **3a** and **5a** and exhibited the meridional spanning of the ligand around the metal centre. Redox behavior of the metal complexes (except zinc) was examined through electrochemical investigations. Complexes **3a** and **3b** exhibited superoxide scavenging activity in xanthine/xanthine oxidase nitroblue tetrazolium (NBT) assay and **3a** was found to be more efficient in superoxide scavenging than **3b**. DNA interaction studies predicted covalent type of binding between metal complexes and DNA nucleobases. Nuclease activity of the metal complexes was examined and their mechanisms were also established. Copper complexes catalyzed the cleavage of plasmid DNA through self–activating mechanism whereas zinc complexes exhibited a hydrolytic type of DNA cleavage. Protein interaction properties of the complexes were also explored through electronic absorption spectroscopy, fluorescence spectroscopy and circular dichroism which suggested covalent type of binding of the metal center with the surface donor groups of BSA.

3.4. Experimental Section

3.4.1 Reagents and materials

Analytical grade reagents phenylhydrazine, 2–mercaptoethanol, hydrogenperoxide (S. D. Fine, Mumbai, India), sodium azide and 2–chloromethylpyridine hydrochloride (Sigma Aldrich, Steinheim, Germany), methyl–2–pyridyl ketone, sodium perchlorate monohydrate, adenosine–5′–monophosphate free acid, guanosine–5′–monophoshate disodium salt (Himedia Laboratories Pvt. Ltd., Mumbai, India), L–histidine (Sisco Research Laboratories Pvt. Ltd., Mumbai, India), ethylenediaminetetraacetic acid, cobalt chloride hexahydrate, nickel chloride hexahydrate, copper chloride dihydrate, zinc chloride anhydrous (Merck Limited, Mumbai, India), copper perchlorate hexahydrate, zinc perchlorate hexahydrate and

sodium hydride (Acros organics, USA) were used as obtained. The supercoiled pBR322 DNA and CT–DNA were purchased from Bangalore Genei (India) and stored at 4 °C. Agarose (molecular biology grade), ethidium bromide and bovine serum albumin were obtained from Sigma Aldrich. Tris(hydroxymethyl)aminomethane–HCl (Tris–HCl) buffer and phosphate buffer were prepared in deionised water. Stock solutions of all the metal complexes were prepared in dimethylformamide. Solvents used for spectroscopic studies were HPLC grade and purified by standard procedures before use.

3.4.2. Synthesis of ligand

Caution ! The handling of the free base 2–(chloromethyl)pyridine and its solution should be performed in a well–ventilated fume hood. Skin and eye contact should be carefully avoided since the compound is an aggressive skin irritant and can cause bronchial irritation as well.

Synthesis of Schiff's base (2J(1J(2Jphenylhydrazono)ethyl)pyridine)

Schiff's base (2–(1–(2–phenylhydrazono)ethyl)pyridine) was prepared by the condensation of phenyl hydrazine and methyl–2–pyridylketone in methanol containing traces of concentrated H_2SO_4.

Synthesis of 2J((1JphenylJ2J(1J(pyridinJ2Jyl)ethylidene)hydrazinyl)methyl)pyridine (N_3L)

The Schiff's base 2–(1–(2–phenylhydrazono)ethyl)pyridine (1.05 g, 5 mmol) was dissolved in 20 mL of toluene by heating. Then 1.5 equivalents of NaH (1.90 g, 7.5 mmol) were added to it with stirring and refluxed at 90° C for 2 h. In a separate flask 2-chloromethylpyridine hydrochloride (0.98 g, 6 mmol) was neutralised in excess of triethylamine for 2 h. Then triethylamine was evaporated *in vacuo* and the sticky residue left

over was taken in toluene and acetonitrile (2:1) mixture. The solution was filtered and the filtrate was added to the deprotonated Schiff's base. The reaction was allowed to continue at this temperature for 12 h. After completion, reaction mixture was filtered and evaporated to dryness. The reaction mixture was extracted several times with toluene and dried over anhydrous sodium sulphate. Then the dry filtrate was purified by column chromatography over silica to afford the compound as red yellow oil. Yield: 1.057 g (70%); ESI-MS (acetonitrile, pos.): m/z 325.14 (100%) $[M+Na]^+$. Selected IR data: 1594 ($\nu_{C=N}$), 1571, 1491, 783, 752, 696, 622, UV-visible [CH_3OH, λ_{max}/nm ($\varepsilon/M^{-1}cm^{-1}$)]: 251 (15056), 279 (6040), 341 (5914); ^{1}H NMR (500 MHz, δ/ppm, $CDCl_3$): 8.608 (dd, J=4.5 Hz, 8.75 Hz, 2H), 8.232 (d, J=8 Hz, 1H), 7.710 (t, J=7.75 Hz, 1H), 7.637 (t, J=7.75 Hz, 1H), 7.467 (d, J=8Hz, 1H), 7.290 (m, 3H), 7.173 (dd, J= 5 Hz, 7.25 Hz, 1H), 7.007 (d, J=7.5, 2H), 6.960 (t, J=7.5 Hz, 1H), 5.042 (s, 2H), 2.35 (s, 3H); ^{13}C NMR (500 MHz, δ/ppm, $CDCl_3$): 163.71, 159.00, 155.95, 149.84, 149.18, 148.58, 136.69, 136.19, 129.05, 124.01, 122.08, 122.00, 121.37, 121.07, 117.39, 63.86, 16.43; DEPT-45 NMR (500 MHz, δ/ppm, $CDCl_3$): 149.17, 148.58, 136.70, 136.19, 129.05, 124.01, 122.08, 122.00, 121.37, 121.06, 117.38, 63.86, 16.43; DEPT-90 NMR (500 MHz, δ/ppm, $CDCl_3$): 149.18, 148.58, 136.70, 136.19, 129.05, 124.02, 122.08, 122.01, 121.37, 121.07, 117.39; DEPT-135 NMR (500 MHz, δ/ppm, $CDCl_3$): 149.18, 148.58, 136.69, 136.20, 129.05, 124.02, 122.08, 122.01, 121.37, 121.07, 117.39, 63.86 (CH_2), 16.43.

3.4.3. Synthesis of metal complexes

Caution! Perchlorate salts of metal complexes with organic ligands are potentially explosive. Only small quantities of these compounds should be prepared and handled with proper protection.

Synthesis of $[Cu(N_3L)Cl_2]$ (3a)

A batch of ligand N_3L (0.15 g, 0.5 mmol) was dissolved in 10 mL methanol and a batch of $CuCl_2{\cdot}2H_2O$ (0.09 g, 0.5 mmol) dissolved in 1 mL of methanol was added to it with vigorous stirring in one slot. The resulting brown solution was stirred overnight. The green solid obtained was filtered and dried. The filtrate was kept in a conical flask to develop the X-ray diffraction quality crystals of the compound on slow evaporation. Anal. Calc. for $C_{19}H_{18}N_4Cl_2Cu$ C, 52.24; H, 4.15; N, 12.83, Found C, 52.35; H, 4.32; N, 12.70; Yield: 0.167 g (77%); $\Lambda_M/\Omega^{-1}cm^2mol^{-1}$ (DMF): 23, Selected IR data (KBr, ν_{max}/cm^{-1}): 1659, 1595 ($\nu_{C=N}$), 1493. UV-visible [CH_3OH, λ_{max}/nm ($\varepsilon/M^{-1}cm^{-1}$)]: 239 (23964), 250 (22536), 286 (9430), 353 (6084), 395 (4508), 551 (706); ESI-MS (acetonitrile, pos.): m/z 400.04 (100%) $[M - Cl]^+$.

Synthesis of $[Cu(N_3L)_2](ClO_4)_2$ (3b)

A batch of ligand N_3L (0.30 g, 1.0 mmol) was dissolved in 10 mL of ethanol. To this stirring solution of ligand, a batch of $Cu(ClO_4)_2{\cdot}6H_2O$ (0.19 g, 0.5 mmol) dissolved in 2 mL of ethanol was added dropwise with constant stirring to afford a brown solution. The reaction was stirred overnight and a dark brown precipitate was observed in the reaction mixture. The solid was filtered and washed with some amount of ethanol followed by diethylether. Anal. Calc. for $C_{38}H_{36}N_8O_8Cl_2Cu$ C, 52.63; H, 4.18; N, 12.92, Found C, 53.21; H, 4.30; N, 12.69; Yield: 0.338 g (78%); $\Lambda_M/\Omega^{-1}cm^2mol^{-1}$ (DMF): 136; Selected IR data (KBr, ν_{max}/cm^{-1}): 1638, 1596 ($\nu_{C=N}$), 1491, 1107, 623 (ν_{ClO4}^-); UV-visible [CH_3OH, λ_{max}/nm ($\varepsilon/M^{-1}cm^{-1}$)]: 238 (31436), 286 (12908), 344 (11976), 432 (2590); ESI-MS (acetonitrile, pos.): m/z 766.17 (17.8%) $[M-(ClO_4)]^+$, 400.04 (7.9%) $[M-2(ClO_4)-L+Cl]^+$, 333.61 (22.6%) $[M-2(ClO_4)]^{2+}$.

Synthesis of $[Zn(N_3L)Cl_2]$ (4a)

A batch of anhydrous $ZnCl_2$ (0.07 g, 0.5 mmol) was dissolved in 5 mL of methanol and the solution was kept on vigorous stirring. Then a batch of ligand (0.150 g, 0.5 mmol) dissolved in 15 mL of ethanol was added to the above solution dropwise over a period of 1 h with continuous stirring resulting in a yellow precipitate. The reaction mixture was stirred for 3 h and the solid was isolated by filtration, washed with little ethanol, subsequently with diethylether and dried. Anal. Calc. for $C_{19}H_{18}N_4Cl_2Zn$ C, 52.02; H, 4.14; N, 12.77 Found C, 52.50; H, 4.19; N, 12.70; Yield: 0.159 g (73%); $\Lambda_M/\Omega^{-1}cm^2mol^{-1}$ (DMF): 9, Selected IR data (KBr, ν_{max}/cm^{-1}): 1639, 1598 ($\nu_{C=N}$), 1492. UV-visible [CH_3OH, λ_{max}/nm ($\varepsilon/M^{-1}cm^{-1}$)]: 245 (13406), 258 (14168), 285 (5700), 374 (5332); ESI-MS (acetonitrile, pos.): m/z 459.00 (83%) $[M + Na]^+$, 401.04 (83.6%) $[M - Cl]^+$; ^1H NMR (500 MHz, δ/ppm, $CDCl_3$): 9.571 (d, J=5 Hz, 1H), 9.405 (d, J=5Hz, 1H), 7.994 (t, J=7.75 Hz, 1H), 7.664 (2H, m), 7.717 (d, J=8 Hz, 1H), 7.368 (t, J= 6.5 Hz, 1H), 7.196 (t, J=8 Hz, 2H), 7.047 (d, J= 7.5 Hz, 1H), 6.994 (t, J=7.5 Hz, 1H), 6.959 (d, J=7.5 Hz, 2H), 5.215 (s, 2H), 2.165 (s, 3H); ^{13}C NMR (500 MHz, δ/ppm, $CDCl_3$): 159.64, 155.43, 151.31, 150.83, 148.03, 147.35, 139.95, 139.16, 129.81, 127.28, 125.03, 124.88, 124.10, 122.27, 121.14, 61.18, 15.95; DEPT-135 NMR (500 MHz, δ/ppm, $CDCl_3$): 151.30, 150.83, 139.96, 139.16, 129.81, 127.28, 125.04, 124.89, 124.10, 122.27, 121.14, 61.18 (CH_2), 15.96 (CH_3).

Synthesis of $[Zn(N_3L)_2](ClO_4)_2$ (4b)

A batch of $Zn(ClO_4)_2 \cdot 6H_2O$ (0.09 g, 0.25 mmol) was dissolved in 5 mL of methanol. To this solution a batch of ligand N_3L (0.15 g, 0.50 mmol) dissolved in 3 mL of methanol was added dropwise with constant stirring followed by the addition of 10 mL of ethanol. The reaction mixture was stirred for 4 h and the yellow precipitate obtained was filtered, washed

with some amount of ethanol and subsequently with diethylether. Anal. Calc. for $C_{38}H_{36}N_8O_8Cl_2Zn$ C, 52.52; H, 4.18; N, 12.89, Found C, 52.68; H, 4.06; N, 12.98; Yield: 0.171 g (79%); $\Lambda_M/\Omega^{-1}cm^2mol^{-1}$ (DMF): 104, Selected IR data (KBr, ν_{max}/cm^{-1}): 1640, 1594 ($\nu_{C=N}$), 1489, 1091, 624 (ν_{ClO4}^-). UV-visible [CH_3OH, λ_{max}/nm ($\varepsilon/M^{-1}cm^{-1}$)]: 246 (27656), 253 (28360), 285 (10240), 358 (8714); ESI-MS (acetonitrile, pos.): m/z 767.17 (2.8%) $[M-(ClO_4)]^+$, 401.04 (37.8%) $[M-2(ClO_4)-L+Cl]^+$; ^1H NMR (500 MHz, δ/ppm, CD_3CN): 8.242 (d, J=5Hz, 1H), 8.064-8.120 (m, 2H), 7.992 (d, J=4.5 Hz, 1H), 7.863 (t, J=7.75 Hz, 1H), 7.426 (q, J=5.5 Hz, 2H), 7.360 (t, J=8 Hz, 2 H), 7.224 (d, J=8 Hz, 1H), 7.135 (t, J=7.5 Hz, 1H), 7.015 (d, J=7.5 Hz, 2H), 4.869 (d, J=16 Hz, 1 H), 4.533 (d, J=16 Hz, 1 H), 2.443 (s, 3H); ^{13}C NMR (500 MHz, δ/ppm, CD_3CN): 163.52, 156.28, 148.97, 147.78, 147.13, 146.39, 141.17, 140.97, 129.87, 128.48, 126.89, 125.97, 125.86, 124.83, 120.66, 117.36, 59.76, 17.44; DEPT-135 NMR (500 MHz, δ/ppm, CD_3CN): 148.97, 147.13, 141.17, 140.97, 129.87, 128.48, 126.89, 125.97, 125.86, 124.82, 120.65, 59.76, 17.44.

Synthesis of $[Co(N_3L)Cl_2]$ (5a)

A batch of $CoCl_2·6H_2O$ (0.119 g, 0.5 mmol) was added in 5 mL of tetrahydrofuran and the solution was kept on vigorous stirring. Now, a batch of ligand (0.150 g, 0.5 mmol) dissolved in 10 mL of tetrahydrofuran was added to the above solution dropwise over a period of 1 h with continuous stirring. A green solution was obtained turning brown after overnight stirring. The brown solid was isolated by filtration which was washed with some amount of tetrahydrofuran, followed by diethyl ether and dried. Diffusion of diethylether in dichloromethane solution of the complex resulted with X-ray quality crystals. Anal. Calc. for $C_{19}H_{18}N_4Cl_2Co$ C, 52.80; H, 4.20; N, 12.96. Found C, 53.01; H, 4.19; N, 12.85; Yield: 0.156 g (72%); $\Lambda_M/\Omega^{-1}cm^2mol^{-1}$ (DMF): 23, Selected IR data (KBr, ν_{max}/cm^{-1}): 1646, 1600

($\nu_{C=N}$), 1493. UV-visible [CH_3OH, λ_{max}/nm ($\varepsilon/M^{-1}cm^{-1}$)]: 212 (17182), 215 (16576), 217 (15240), 245 (14560), 347 (3720), 407 (2736); ESI-MS (acetonitrile, pos.): m/z 454.00 (23 %) $[M+Na]^+$, 396.04 (100 %) $[M - Cl]^+$.

Synthesis of $[Co(N_3L)_2](ClO_4)_2$ (5b)

A batch of ligand N_3L (0.30 g, 1.0 mmol) was dissolved in 10 mL of methanol. To the stirring solution of ligand, $CoCl_2 \cdot 6H_2O$ (0.119 g, 0.5 mmol) dissolved in 2 mL of methanol was added dropwise to afford a red solution. The reaction solution was stirred for 2 h followed by the addition of a batch of sodium perchlorate monohydrate (0.14 g, 1.0 mmol). A yellow solid was obtained by filtration which was washed with little amount of ethanol and subsequently with diethylether. Anal. Calc. for $C_{38}H_{36}N_8O_8Cl_2Co$ C, 52.91; H, 4.21; N, 12.99, Found C, 53.19; H, 4.43; N, 12.88; Yield: 0.326 g (76%); $\Lambda_M/\Omega^{-1}cm^2mol^{-1}$ (DMF): 122; Selected IR data (KBr, ν_{max}/cm^{-1}): 1642, 1604 ($\nu_{C=N}$), 1488, 1090, 624 (ν_{ClO4^-}). UV-visible [CH_3OH, λ_{max}/nm ($\varepsilon/M^{-1}cm^{-1}$)]: 246 (25500), 344 (8370), 406 (4140); ESI-MS (acetonitrile, pos.): m/z (m/z) 762.18 (16.9%) $[M-(ClO_4)]^+$, 396.05 (23.7%) $[M-2(ClO_4)-L+Cl]^+$, 331.61 (18.9%) $[M-2(ClO_4)]^{2+}$.

Synthesis of $[Ni(N_3L)Cl_2]$ (6a)

A batch of $NiCl_2 \cdot 6H_2O$ (0.12 g, 0.5 mmol) was dissolved in 10 mL of methanol and the solution was kept on vigorous stirring. Now, a batch of ligand (0.15 g, 0.5 mmol) dissolved in 15 mL of acetone was added to the above solution dropwise over a period of 1 h with continuous stirring, resulting in a yellow solution. The reaction mixture was stirred overnight and a yellow brown precipitate was obtained which was isolated by filtration, washed with little methanol, subsequently with diethylether and dried. Anal. Calc. for $C_{19}H_{18}N_4Cl_2Ni$ C, 52.83; H, 4.20; N, 12.97, Found C, 53.51; H, 4.64; N, 13.02; Yield: 0.113

g (52%); $\Lambda_M/\Omega^{-1}cm^2mol^{-1}$ (DMF): 49, Selected IR data (KBr, ν_{max}/cm^{-1}): 1623, 1595 ($\nu_{C=N}$), 1492. UV-visible [CH_3OH, λ_{max}/nm ($\varepsilon/M^{-1}cm^{-1}$)]: 242 (15940), 253 (15270), 280 (6970), 357 (3532), 402 (3064), 545 (228); ESI-MS (acetonitrile, pos.): m/z 395.04 (100%) $[M - Cl]^+$.

Synthesis of $[Ni(N_3L)_2](ClO_4)_2$ (6b)

A batch of ligand N_3L (0.15 g, 0.5 mmol) was dissolved in 10 mL of methanol. To this solution of ligand, $NiCl_2{\cdot}6H_2O$ (0.06 g, 0.25 mmol) dissolved in 1 mL of methanol was added dropwise with constant stirring to afford a deep red solution. The reaction mixture was stirred overnight followed by the addition of a batch of sodium perchlorate monohydrate (0.07 g, 0.5 mmol) dissolved in 1 mL of methanol. After 5 min of stirring, a deep yellow solid was obtained which was washed with some amount of methanol after filtration. Anal. Calc. for $C_{38}H_{36}N_8O_8Cl_2Ni$ C, 52.93; H, 4.21; N, 12.99, Found C, 53.70; H, 4.12; N, 12.71; Yield: 0.164 g (76%); $\Lambda_M/\Omega^{-1}cm^2mol^{-1}$ (DMF): 106, Selected IR data (KBr, ν_{max}/cm^{-1}): 1640, 1602 ($\nu_{C=N}$), 1492, 1091, 624 (ν_{ClO4^-}), UV-visible [CH_3OH, λ_{max}/nm ($\varepsilon/M^{-1}cm^{-1}$)]: 242 (28160), 255 (26240), 347 (10598), 410 (5200), 543 (278); ESI-MS (acetonitrile, pos.): m/z 761.18 (16.8%) $[M-(ClO_4)]^+$, 459.03 (93.5%) $[M-(ClO_4)-L]^+$, 395.05 (12.5%) $[M-2(ClO_4)-L+Cl]^+$, 331.11 (32.5%) $[M-2(ClO_4)]^{2+}$.

3.4.4. X–ray crystallography

The X–ray data collection and processing for $[Cu(N_3L)Cl_2]$ (**3a**) and $[Co(N_3L)Cl_2]$ **(5a)** were performed on Bruker Kappa Apex–II CCD diffractometer by using graphite monochromated Mo–Kα radiation (λ = 0.71073 Å) at 296 K to a maximum $^-$ range of 28°. All the data were corrected for Lorentzian, polarization and absorption effects. Crystal structures were solved by direct methods. Structure solution, full matrix least–squares

refinement on F^2 and data output were carried out with the SHELXTL program.[351] All non–hydrogen atoms were refined anisotropically. Hydrogen atoms were placed in geometrically calculated positions and refined using a riding model. Images were created with the DIAMOND[352] and MERCURY[353] programs. The matrix parameters for the crystals of **3a** and **5a** are given in Table 3.12.

Table 3.12 Crystal data and structure refinement details for $[Cu(N_3L)Cl_2]$ (**3a**) and $[Co(N_3L)Cl_2]$ (**5a**)

	3a	**5a**
Empirical formula	$C_{19}H_{18}N_4Cl_2Cu$	$C_{19}H_{18}N_4Cl_2Co$
Formula weight ($gmol^{-1}$)	436.82	432.20
Temperature /K	296(2)	296 (2)
λ (Å) (Mo-Kα)	0.71073	0.71073
Crystal system	Monoclinic	Monoclinic
Space group	*C 2/c*	*C 2/c*
a (Å)	13.3346(4)	13.4763(16)
b (Å)	10.0729(4)	10.2817(12)
c (Å)	28.0319(12)	27.649(3)
~ (˚)	90.00	90.00
γ (˚)	90.112(14)	90.646(8)
β (˚)	90.00	90.00
V ($Å^3$)	3765.2(2)	3830.8(8)
Z	8	8
ρ_{calc} (gcm^{-3})	1.541	1.499
F(000)	1784	1768.0
Theta range for data collection	1.45─25.0	1.47─25.0
Index ranges	$-14 < h < 15$, $-11 < k < 10$, $-33 < l < 33$	$-15 < h < 16$, $-12 < k < 12$, $-32 < l < 32$
Refinement method	Full matrix least–squares on F^2	Full matrix least–squares on F^2
Data/restraints/parameters	2058/0/236	3359/0/236
GOF[a] on F^2	1.087	1.070
R_1[b] [$I > 2\sigma(I)$]	0.0332	0.0846
R_1[all data]	0.0500	0.2039
wR_2[c] [$I > 2\sigma(I)$]	0.0870	0.1850
wR_2 [all data]	0.1121	0.2390

3.4.5. Superoxide dismutase assay

To investigate the ability of complexes (**3a** and **3b**) for the dismutation of superoxide radicals, McCord–Fridovich assays were performed and the inhibition of NBT reduction by superoxide radicals was monitored. Experiment was started by the addition of 2.1 mU/mL xanthine oxidase to the reaction system containing 0.2 mM xanthine, 0.6 mM NBT, 1000 U/mL catalase and varying concentration of complexes in 0.1 M phosphate buffer (pH 7.8). The measurements were started after 10 min incubation and each experiment was performed in duplicate. The degree of NBT reduction was monitored by measuring the absorbance at 560 nm. IC_{50} value for SOD activity was defined as the concentration of the compound for 50% inhibition of NBT reduction by superoxide radicals generated in the reaction system.

3.4.6. DNA binding and cleavage experiments

DNA binding experiments were carried out in 0.1 M phosphate buffer (pH 7.2) using a solution of calf thymus (CT) DNA which gave a ratio of UV–vis absorbance at 260 and 280 nm (A_{260}/A_{280}) of *ca.* 1.8, indicating that the CT–DNA was sufficiently protein free.[332,404] The concentration of DNA solution was determined by measuring its optical density at 260 nm and the extinction coefficient ε_{260} was taken 6600 cm^{-1} as reported in the literature.[332,404] Absorption titration experiments were carried out with complex concentration of 70─100 µM varying the CT–DNA concentration from 0─700 µM in 0.1 M phosphate buffer (pH 7.2). The binding constants K_b were determined according to the reported method.[332,404] Fluorescence quenching experiments were carried out by the successive addition of the metal complexes to the DNA (25 µM) solutions containing 5 µM ethidium bromide (EB) in 0.1 M phosphate buffer (pH 7.2) and the reaction mixture was incubated for 2 min after each successive addition of the quencher molecules. These samples were excited at 250 nm and

emissions were observed between 500 and 700 nm. Stern–Volmer quenching constants K_{sv} were calculated according to the reported procedure.[332,404] Circular dichroism (CD) spectra of CT–DNA in absence and presence of metal complexes were recorded with a 0.1 cm path-length cuvette after 15 min incubation at 25 °C with three scans averaged for each CD spectrum. The concentration of the complexes and CT–DNA were 50 and 200 μM respectively.

Cleavage of plasmid DNA was monitored by using agarose gel electrophoresis. Supercoiled pBR322 DNA (70 ng) in Tris–boric acid–EDTA (TBE) buffer (pH 8.2) was treated with metal complexes (50─200 μM for **3**,**5** and **6**; 50 μM─2 mM for **4**) in presence or absence of additives. The oxidative DNA cleavage by the complexes was studied in the presence of H_2O_2 (20 μM–2 mM, oxidizing agent) or 2–mercaptoethanol (200 μM, reducing agent) and mechanistic details were explored using DMSO, ethanol, urea, NaN_3, L- histidine (20 mM each), D_2O (10%), Neocuproine (400 μM), NaCl (400 μM) and catalase (10 U) as scavenging agents. Anaerobic conditions were maintained according to the method as reported earlier.[477] The samples were incubated for 5 min to 2.5 h (upto 24 h for **4**) at 37 °C followed by the addition of loading buffer (25% bromophenol blue and 30% glycerol) prior to the gel electrophoresis.

3.4.7. Protein binding experiments

The stock solutions of BSA were prepared by dissolving solid BSA (1×10^{-4} mol L^{-1}) in 0.1 M phosphate buffer at pH 7.2 and stored at 0─4 °C for three days under dark conditions and then diluting with 0.1 M phosphate buffer (pH 7.2) to the desired concentration. The concentration of protein solution was determined from the absorption spectral data using the molar absorptivity value of ε_{280} = 44720 for BSA.[345] Quenching of the intrinsic fluorescence

of tryptophan residues of BSA was carried out using metal complexes as quencher molecules. BSA solution (2×10^{-6} M) in 0.1 M phosphate buffer (pH 7.2) with 2% DMF was equilibrated for 30 min at room temperature and the emission spectrum was recorded between 300 and 600 nm using the excitation wavelength of 295 nm which is selective for tryptophan residues.[346] Incremental additions of the quenchers were made to the BSA solution followed by an incubation period of 2 min after each successive addition and the spectra were recorded. Binding behaviors of the quencher molecules with serum albumin were compared using the Stern–Volmer and Scatchard graphs.[347] Circular dichroism (CD) spectra of BSA in absence and presence of metal complexes were recorded with a 0.1 cm pathJlength cuvette after 15 min incubation at 25 °C with three scans averaged for each CD spectrum. The concentration of the complexes and BSA were 10 and 1 μM respectively.

4.1. Introduction

The coordination chemistry of phenoxyl radicals has in recent years been intensively studied due to their occurrence in the catalytic cycle of some copper containing enzymes such as galactose oxidase and glyoxal oxidase.[147,166,191,192,240] In relevance with copper chemistry, the cobalt complexes having ligands containing phenolato donor(s) can also undergo ligand centered oxidation affording phenoxyl radical complexes.[191,193,197,478,479] A wide range of model complexes afford the phenoxyl radical species only at low temperatures and those affording such species at room temperature are lesser in number. Oxygen and/or solvent play an important role in the decomposition process of the radical species which may or may not be accompanied by the regeneration of the precursor complex.[135] In the native enzyme, the tyrosyl radical is stabilized by a thioether group present at the ortho position to the tyrosinate oxygen and obtained via post–translational modification (*Chapter 1*). However, in case of metal complexes, phenoxyl radicals can be stabilized by incorporating a thioether group and/or bulky alkyl groups in the phenyl ring bearing phenolato function.[141,196,219,477,480]

Metal complexes which can generate phenoxyl radicals have been employed as catalysts for the oxidation of organic substrates[481] as well as for biological activities like SOD activity and DNA cleavage.[135,404,477] It has also been observed that the incorporation of radical stabilizing groups may induce or dramatically enhance the efficiency of such catalysts.[477] However, to the best of our knowledge, there is no report of amide bond hydrolysis or protein cleavage activity exhibited by such complexes.

In the present endeavour, we have chosen biologically relevant cobalt metal ion due to its interesting coordination chemistry and unique chemical properties as well as due to its occurrence in the natural nucleases (*Chapter 2*). Moreover, investigation of literature revealed that cobalt complexes have been frequently being employed for the hydrolysis of amide bonds.[482,483]

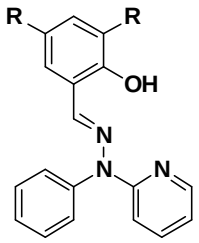

R = H; PhimpH
R = *tert*-Bu; ^{t}BuPhimpH

Scheme 4.1 Schematic drawing of ligand PhimpH and ^{t}BuPhimpH

Hence we have synthesized cobalt complexes $[Co(Phimp)_2]ClO_4 \cdot CH_3CN$ (**7**·CH_3CN) and $[Co(^{t}BuPhimp)_2]ClO_4$ (**8**) derived from two tridentate meridional ligands namely PhimpH and ^{t}BuPhimpH (where H implies the dissociable hydrogen; Scheme 4.1). The complexes were characterized by several physical and spectroscopic techniques and redox properties of these complexes were investigated by cyclic voltammetric experiments. Molecular structure of **7**·CH_3CN was authenticated by X–ray crystallography. Phenoxyl radical analogs of these complexes were generated by chemical oxidation and their decomposition mechanisms were scrutinized. DNA interaction and DNA cleavage properties of these complexes were investigated and their mechanism was also established. Anticancer activity of these complexes against various cell lines were determined and compared. Protein interaction propensities of these complexes were explored using BSA as a protein model and their sites of binding in the albumin molecule were predicted by site–marking experiments. Protein cleavage activities of both complexes were investigated and mechanism of protein cleavage was explored in presence of various radical scavengers.

4.2. Results and discussion

4.2.1. Synthesis and characterization of the ligands

The ligands PhimpH and ^{t}BuPhimpH were obtained by the condensation reaction between a 1:1 mixture of 2–(1–phenylhydrazinyl)pyridine and 2–hydroxybenzaldehyde or

3,5–di–*tert*–butyl–2–hydroxybenzaldehyde respectively, in methanolic solutions following the reported procedures.[332,477] Synthetic scheme representing the syntheses of PhimpH and ^{t}BuPhimpH is illustrated in Scheme 4.2.

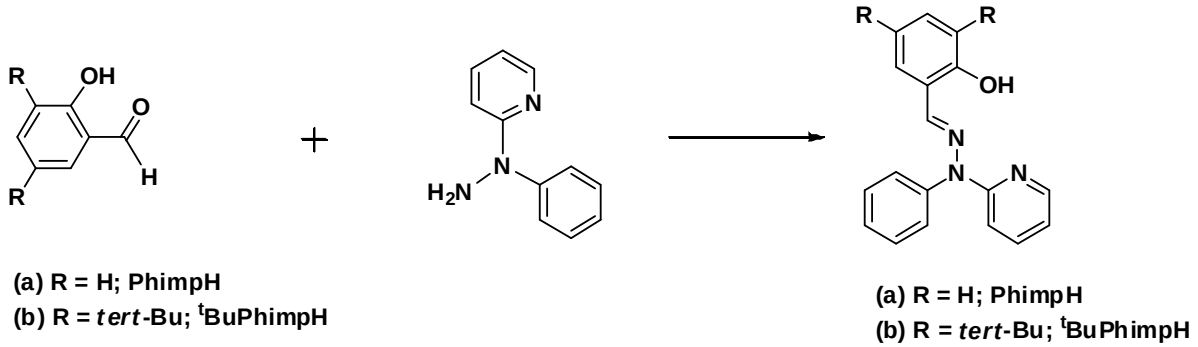

Scheme 4.2 Schematic representation of syntheses of ligands PhimpH and ^{t}BuPhimpH

4.2.2. Synthesis and characterization of cobalt complexes

The complexes $[Co(Phimp)_2]ClO_4{\cdot}CH_3CN$ (**7**·CH_3CN) and $[Co(^{t}BuPhimp)_2]ClO_4$ (**8**) were synthesized by the reaction of $CoCl_2{\cdot}6H_2O$ and deprotonated ligand $Phimp^{-}$ or $^{t}BuPhimp^{-}$ respectively, in 1:2 molar ratio in acetonitrile solution. In both cases, the reactions were performed under aerobic conditions. Both reactions resulted with the oxidation of metal center indicating the coordination of phenolato oxygen to the metal ion in the deprotonated form since deprotonated phenolato oxygen stabilizes higher oxidation state of the metal ions. It is worthmentioning that the atmospheric oxygen serves as oxidizing agent during such reactions. All attempts to isolate cobalt complexes derived from PhimpH and ^{t}BuPhimH with mono speciation resulted only bis complexes **7**·CH_3CN and **8** respectively. Both complexes were isolated in good yields. Synthetic procedures for complexes **7**·CH_3CN and **8** are summarized in Scheme 4.3.

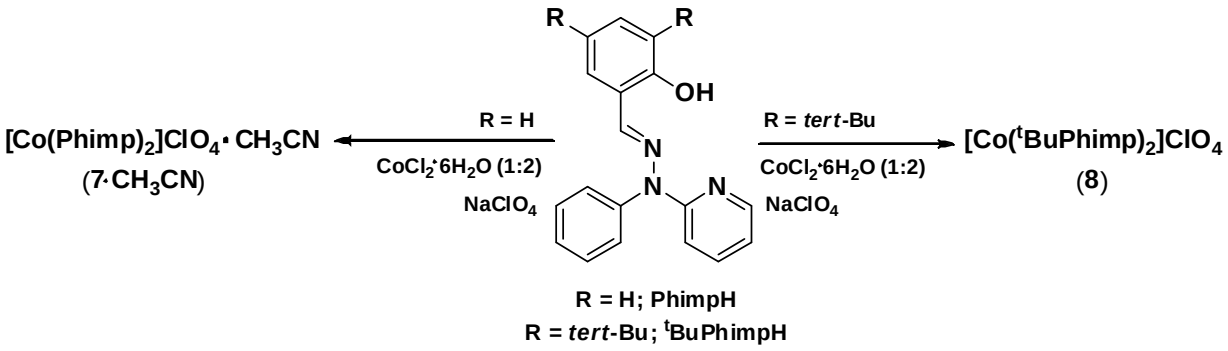

Scheme 4.3 Schematic representation of syntheses of complexes **7**·CH_3CN and **8**

Table 4.1 Data for yield, elemental analysis, IR and conductivity

Complex	Yield %	Elemental analysis			Selected IR data (cm^{-1})[a]	Conductivity Λ_M ($\Omega^{-1}cm^2mol^{-1}$)
		C	H	N		
7·CH_3CN	81	59.14	3.74	11.52	1613, 1092, 623	131[b], 62[c]
8	78	64.77	6.27	8.83	1610, 1077, 623	88[b], 41[c]

[a]KBr pallets, solvents: [b]acetonitrile, [c]dimethylformamide

(i) IR spectral studies

IR spectra of complexes **7**·CH_3CN and **8**, exhibited only weak shifting in $\nu_{(C=N)}$ (2–5 cm^{-1}) due to the coordination of azomethine nitrogen with cobalt ion. However, disappearance of the peak near 3450 cm^{-1} predicted the coordination of ligands in their deprotonated form. The complexes **7**·CH_3CN and **8** showed unsplitted IR bands near 1092 and 1077 cm^{-1} respectively along with a peak near 623 cm^{-1}. These data suggested the presence of a non–coordinating perchlorate ion outside their coordination sphere.[332]

(ii) Electronic properties

Intense absorption bands were observed in the UV–visible spectra of both complexes (**7**·CH_3CN and **8**) between 200–330 nm region. These bands were assigned as π–π* intra–ligand transitions (Fig. 4.1, Table 4.2).

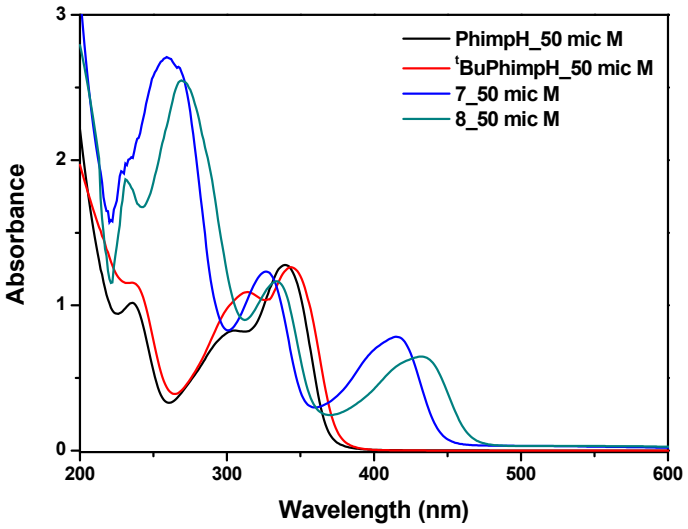

Fig. 4.1 UV–visible spectra of ligands (PhimpH and ^{t}BuPhimpH) and their complexes **7**·CH_3CN and **8** (50 µM) in acetonitrile

The absorption bands found in the range 415–432 nm in UV–visible spectra of complexes in acetonitrile were accompanied with high molar extinction coefficient values and assigned as phenolate to metal charge transfer transitions (Fig. 4.1, Table 4.2).[484] The absorption bands observed in the spectra near 495 nm and 545 nm for complexes **7**·CH_3CN and **8** respectively were assigned as originating from d–d transitions probably due to their low molar extinction coefficient values.[484]

Table 4.2 UV–visible spectral data of complexes **7**·CH_3CN and **8**

Complex	$^{a}_{max}$**/nm (£/M^{-1}cm^{-1})**^{a}
7·CH_3CN	259 (54400), 326 (24880), 415 (15600), 495 (680)
8	269 (50940), 332 (23560), 431 (12880), 545 (640)

^{a}UV–visible data recorded in acetonitrile

(iii) NMR spectroscopy

The structures of the complexes **7**·CH_3CN and **8** were established by ^{1}H and ^{13}C NMR spectral studies. The ^{1}H and ^{13}C NMR spectra of **7**·CH_3CN and **8** are illustrated in Figures 4.2–4.3 and Figures 4.4–4.5 respectively.

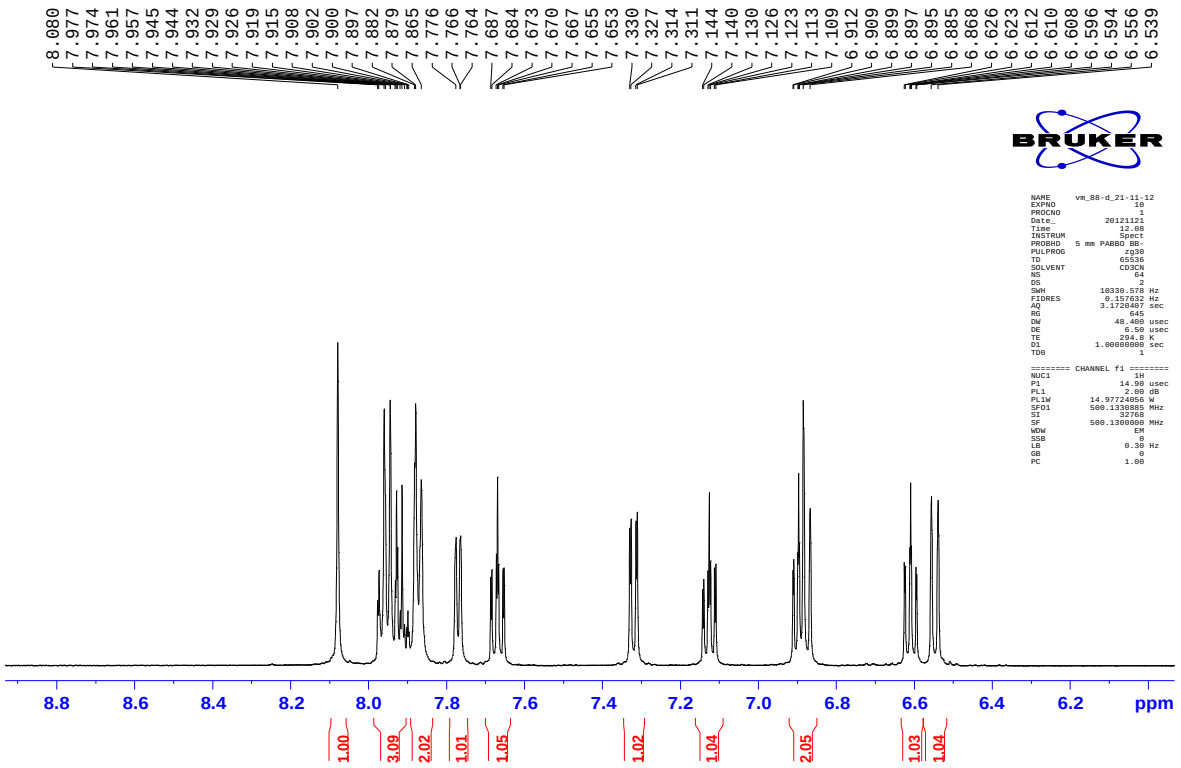

Fig. 4.2 ^{1}H NMR spectrum of **7**·CH_3CN in CD_3CN

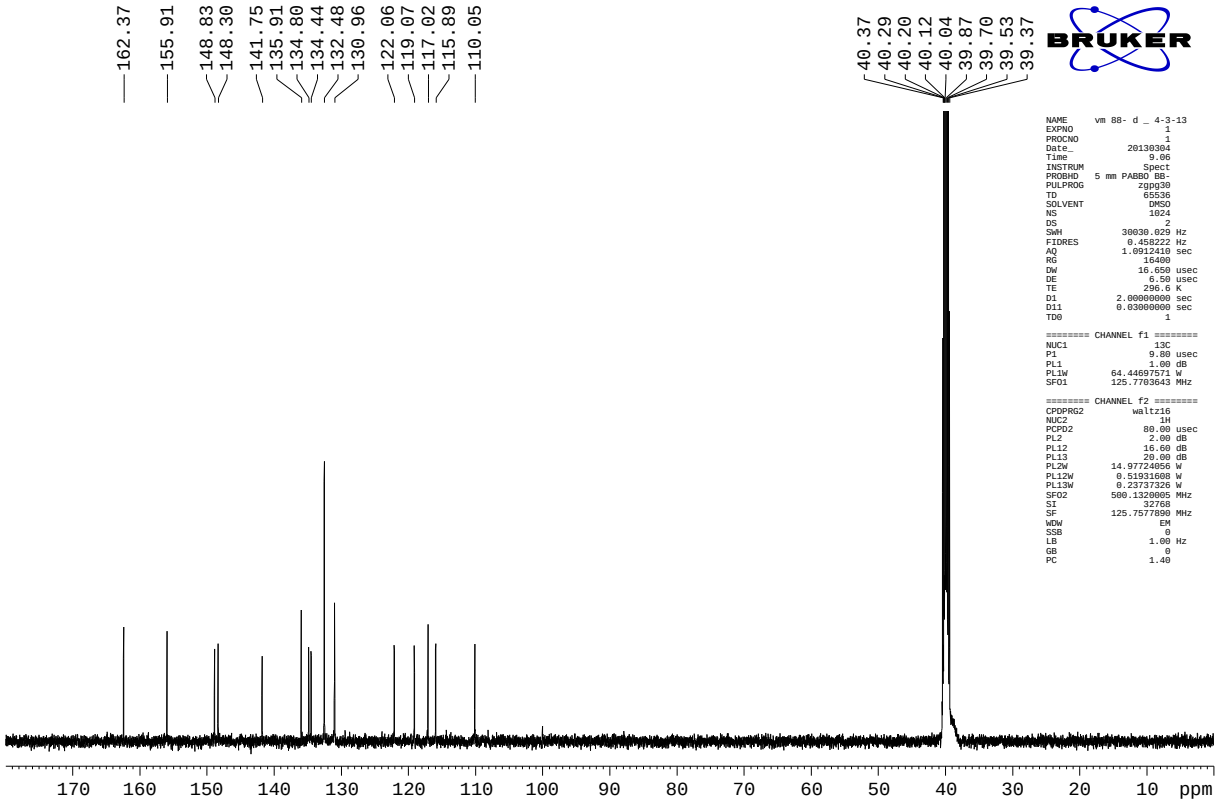

Fig. 4.3 ^{13}C NMR Spectrum of **7**·CH_3CN in $(CD_3)_2SO$

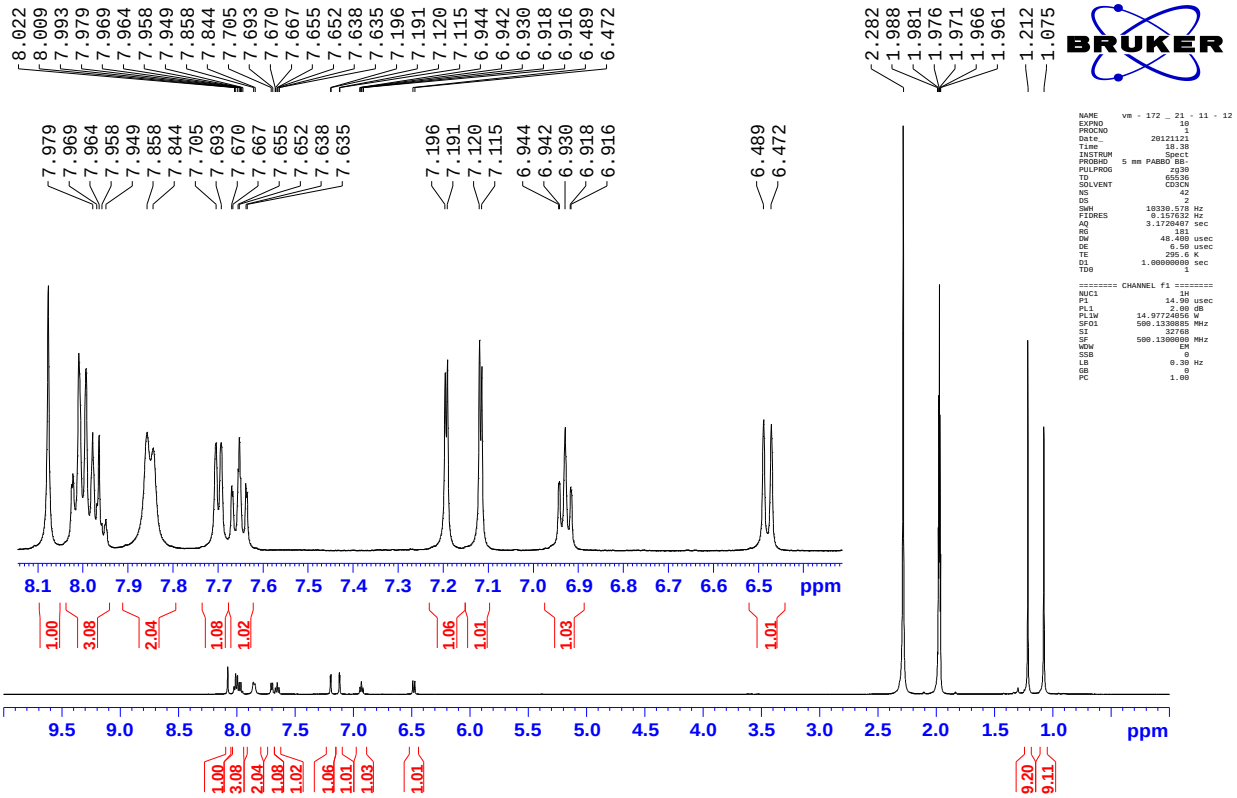

Fig. 4.4 ^{1}H NMR spectrum of **8** in CD_3CN

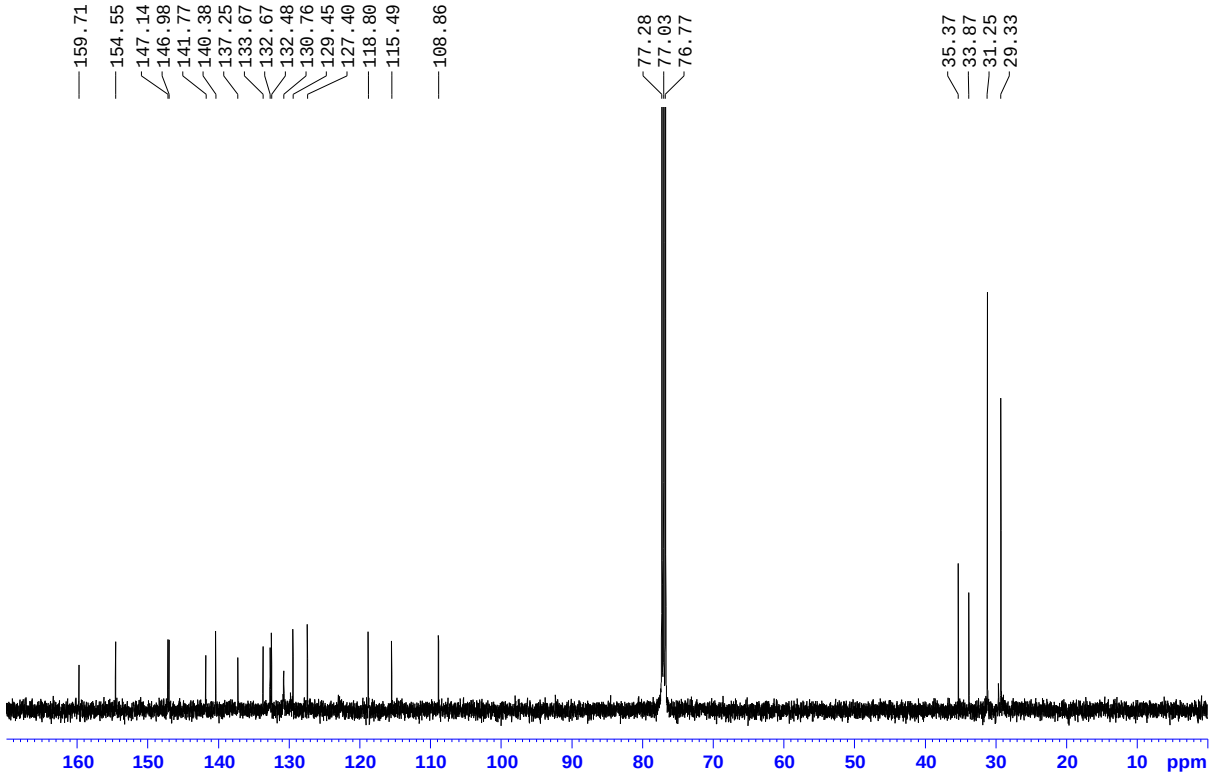

Fig. 4.5 ^{13}C NMR Spectrum of **8** in $CDCl_3$

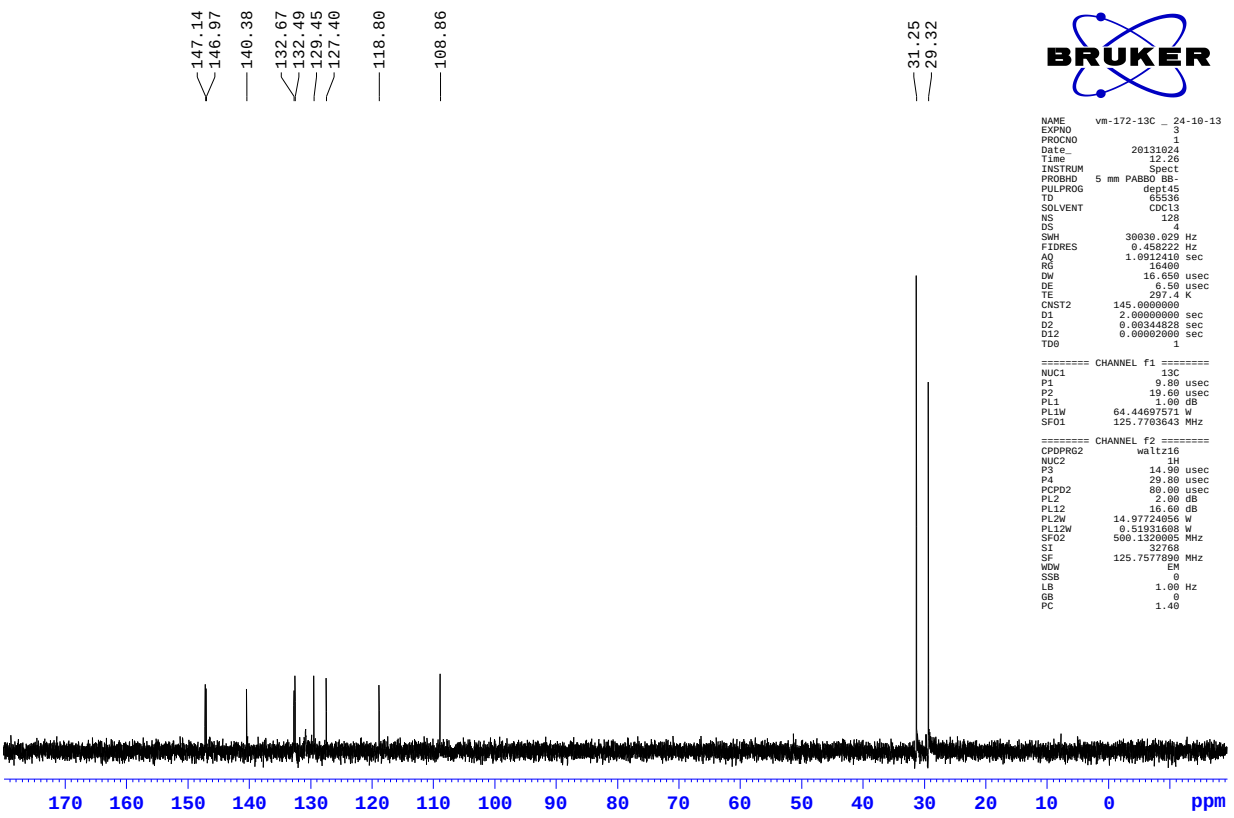

Fig. 4.6 DEPT–45 NMR Spectrum of **8** in $CDCl_3$

DEPT–45 NMR spectrum of **8** indicating the positions of quaternary carbons (vanished off from the spectrum) is represented in Fig. 4.6. These spectra suggested that **7**·CH_3CN and **8** are diamagnetic in nature and give rise to Co^{3+} low–spin complexes.

(iv) ESIJMass spectrometry

The complexes **7**·CH_3CN and **8** were subjected to ESI–mass spectrometric analysis in acetonitrile : water (1:1) mixture and analyzed under positive mode. The ESI–mass spectrum of **7**·CH_3CN showed a peak with m/z value of 635.15 (relative intensity 100%) probably due to the formation of $[\mathbf{7}–ClO_4]^+$ cation with the loss of one perchlorate ion present outside the coordination sphere (Fig. 4.7). The ESI-Mass spectrum of **8** exhibited a peak with m/z value of 859.40 (relative intensity 100%) which was assigned to the formation of $[\mathbf{8}–ClO_4]^+$ cation after losing one non–coordinated perchlorate anion (Fig. 4.8).

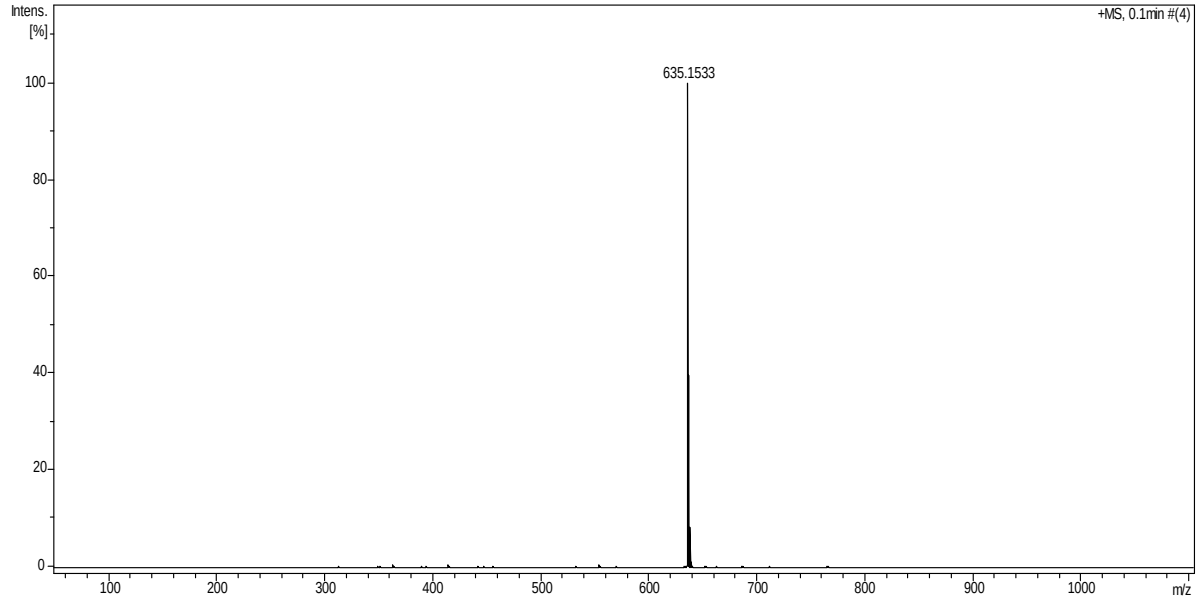

Fig. 4.7 ESI–mass spectrum of **7**·CH_3CN exhibiting the peak at m/z 635.15 due to the formation of [**7**-ClO_4]$^+$ cation

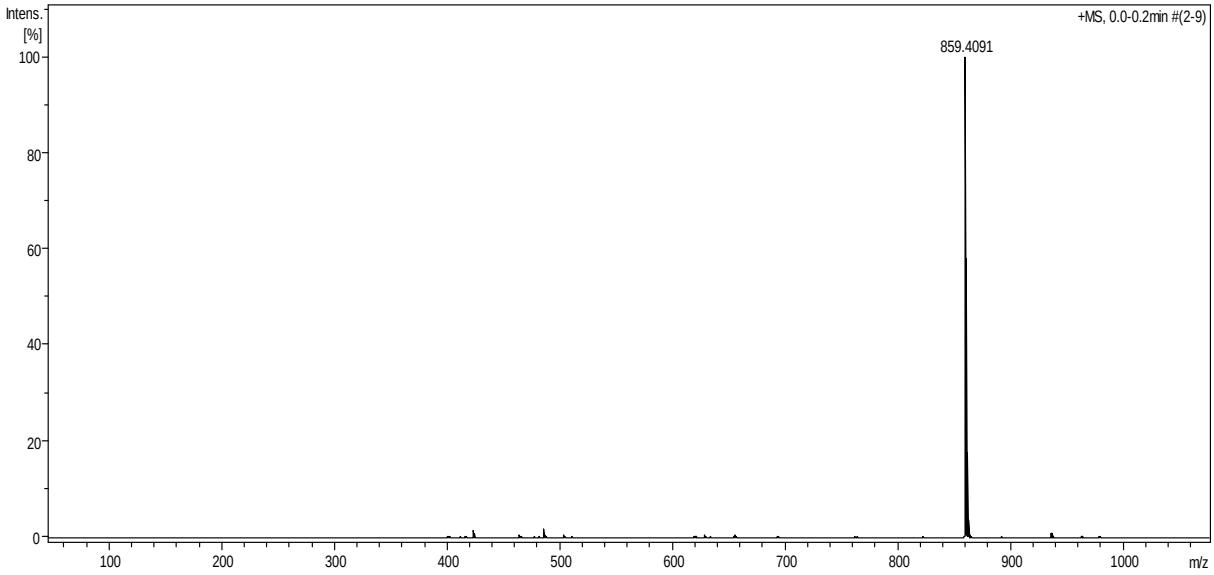

Fig. 4.8 ESI-mass spectrum of **8** exhibiting the peak at m/z 859.40 due to the generation of [**8**-ClO_4]$^+$ cation

(v) Conductivity measurements

The molar conductivity measurements for the complex **7**·CH_3CN gave rise to uni–univalent electrolyte behaviour with conductivity values of 131 and 62 $\Omega^{-1}cm^2mol^{-1}$ in

acetonitrile and dimethylformamide solutions respectively.[387] However conductivity values afforded by complex **8** in acetonitrile and dimethylformamide solutions were found to be 41 and 88 $\Omega^{-1}cm^2mol^{-1}$ which were lower than the values expected for a uni–univalent electrolyte.[387]

4.2.3. Description of molecular structure

The single crystals of the representative complex **7**·CH_3CN were grown by slow evaporation of acetonitrile solution of the complex and the molecular structure was determined by X–ray diffraction technique. The compound crystallized in the space group *P 21/n*. ORTEP representation of the molecular structure and the metal coordination environment in complex **7**·CH_3CN are displayed in Fig. 4.9. Selected bond lengths and bond angles are shown in Table 4.3.

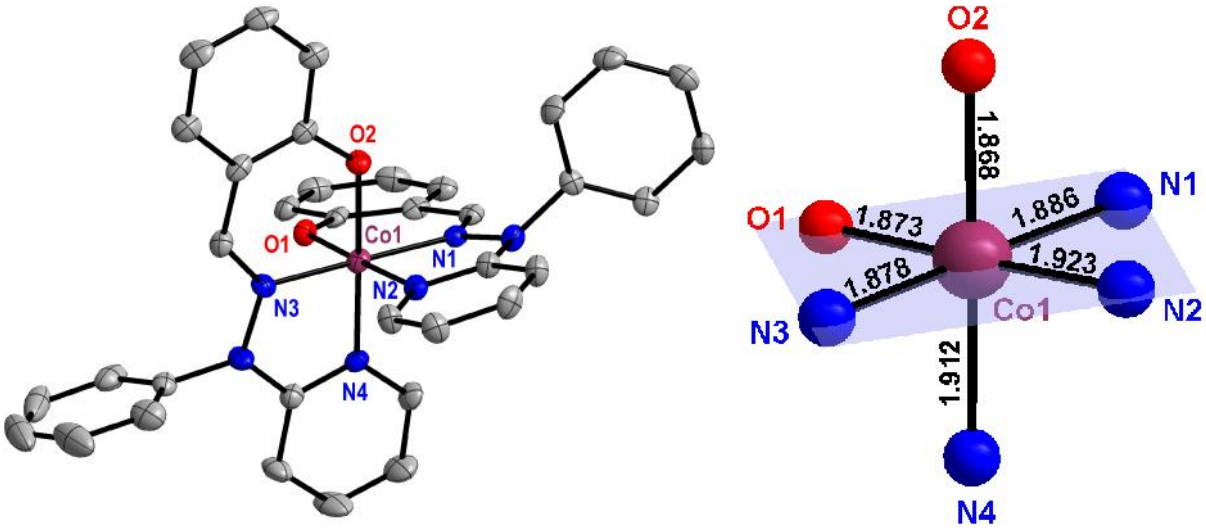

(a) (b)

Fig. 4.9 (a) ORTEP representation of the crystal structure of $[Co(Phimp)_2]ClO_4$·CH_3CN (**7**·CH_3CN) showing atom numbering scheme and displacement ellipsoid (50% probability level). Hydrogen atoms, perchlorate anion and the solvent molecule are omitted for clarity; (b) octahedral disposition of donor atoms showing the bond distances from metal centre

Table 4.3 Selected bond lengths [Å] and bond angles [deg] for complex **7**·CH_3CN

Bond Lengths [Å]	
Co(1) –O(1)	1.8725(33)
Co(1) –O(2)	1.8676(30)
Co(1) –N(1)	1.8859(36)
Co(1) –N(2)	1.9234(40)
Co(1) –N(3)	1.8784(36)
Co(1) –N(4)	1.9116(35)
Bond Angles [deg]	
O(1)–Co(1)–O(2)	90.628(130)
O(1)–Co(1)–N(1)	95.457(147)
O(1)–Co(1)–N(2)	178.407(146)
O(1)–Co(1)–N(3)	86.792(146)
O(1)–Co(1)–N(4)	88.605(143)
O(2)–Co(1)–N(1)	83.986(142)
O(2)–Co(1)–N(2)	88.594(141)
O(2)–Co(1)–N(3)	95.666(143)
O(2)–Co(1)–N(4)	178.985(141)
N(1)–Co(1)–N(2)	83.080(163)
N(1)–Co(1)–N(3)	177.725(169)
N(1)–Co(1)–N(4)	96.747(158)
N(2)–Co(1)–N(3)	94.667(163)
N(2)–Co(1)–N(4)	92.190(152)
N(3)–Co(1)–N(4)	83.629(157)

In the crystal structure of **7**·CH_3CN, one pyridine nitrogen donor (N_{py}), one azomethine nitrogen donor (N_{im}) and one deprotonated phenolato donor (O_{ph}) bind to Co(III) in the meridional fashion. All the bond distances between metal centre and donor atoms were found to be consistent with the literature values.[478,485-487] The overall coordination environment around the metal center consisted of two *cis* phenolato oxygens, two *trans* azomethine nitrogens and two *cis* pyridine nitrogen donors affording slightly distorted octahedral geometry. The distortion in the geometry was manifested by the angles N1–Co1–N2 (83.08°) and N3–Co1–N4 (83.62°) deviating significantly from the ideal values of 90° for an octahedral geometry. The phenyl rings were almost perpendicular to the ligand binding

planes with the angles (phenyl ring vs. meridional plane) of 84.68° and 85.20°. Interestingly, one of the phenyl rings was comparatively more bent and forms larger angle with the ligand binding plane than the second phenyl ring. An acetonitrile molecule was also present in the crystal lattice as solvent of crystallization lying at the crystallographic symmetry axis. Non–covalent interactions receive special importance in supramolecular chemistry and crystal engineering.[393,439-440] Crystal structure of **7**·CH_3CN exhibited several hydrogen–bonding interactions which are listed in detail in Table 4.4.

Table 4.4 Hydrogen bonding geometries for **7**·CH_3CN

DJH···A	**DJH (Å)**	**D···A (Å)**	**H···A (Å)**	**DJH···A (˚)**
C2JH2···O3	0.930	3.647^{i}	2.973^{i}	$130.62(1)^{i}$
C2JH2···O4	0.930	3.565^{i}	2.684^{i}	$158.38(2)^{i}$
C14JH14···O2	0.930	3.537^{i}	2.794^{i}	$137.61(2)^{i}$
C19JH19···N3	0.930	3.023^{i}	2.565^{i}	$110.76(1)^{i}$
C19JH19···N5	0.930	3.530^{i}	2.906^{i}	$125.65(1)^{i}$
C32JH32···O5	0.930	3.377^{i}	2.849^{i}	$117.17(1)^{i}$
C33JH33···O5	0.930	3.240^{i}	2.573^{i}	$129.09(1)^{i}$
C38JH38···N1	0.930	3.059^{i}	2.584^{i}	$112.20(1)^{i}$
C10JH10···O5	0.930	3.347^{ii}	2.652^{ii}	$132.05(1)^{ii}$
C11JH11···O1	0.930	3.489^{ii}	2.650^{ii}	$150.37(1)^{ii}$
C7JH7···O4	0.930	3.405^{ii}	2.617^{ii}	$142.84(1)^{ii}$
C7JH7···O5	0.930	3.068^{ii}	2.756^{ii}	$100.71(1)^{ii}$
C38JH38···O5	0.930	3.332^{ii}	2.428^{ii}	$163.82(2)^{ii}$
C17JH17···O3	0.930	3.243^{iii}	2.436^{iii}	$145.19(1)^{iii}$
C19JH19···O6	0.930	3.088^{iv}	2.363^{iv}	$134.65(1)^{iv}$
C24JH24···O3	0.930	3.485^{iv}	2.763^{iv}	$135.19(1)^{iv}$
C26JH26···O3	0.930	3.407^{iv}	2.675^{iv}	$136.17(1)^{iv}$
C29JH29···O6	0.930	3.294^{iv}	2.563^{iv}	$135.74(1)^{iv}$

Symmetry codes: (i) x, y, z; (ii) x-1, +y, +z; (iii) –x+1/2, +y-1/2, -z+1/2; (iv) -x+1/2+1, +y-1/2, -z+1/2

In **7**·CH_3CN, each perchlorate anion is surrounded by four molecules of **7** and weak hydrogen–bonding interactions ranging from 2.363 Å to 2.849 Å were observed between perchlorate oxygens and aryl hydrogens of pyridine ring, phenyl ring and the ring bearing the phenolato oxygen (Fig. 4.10). Moreover, a network of C–H···π interactions was also observed in the crystal structure of **7**·CH_3CN. The crystal structure of **7**·CH_3CN exhibited extensive C–H···π interactions ranging from 2.653 Å to 3.355 Å which gave rise to a cavity–like structure composed of six molecules of **7** (Fig. 4.11). The three–dimensional packing diagram of **7**·CH_3CN is shown in Fig. 4.12.

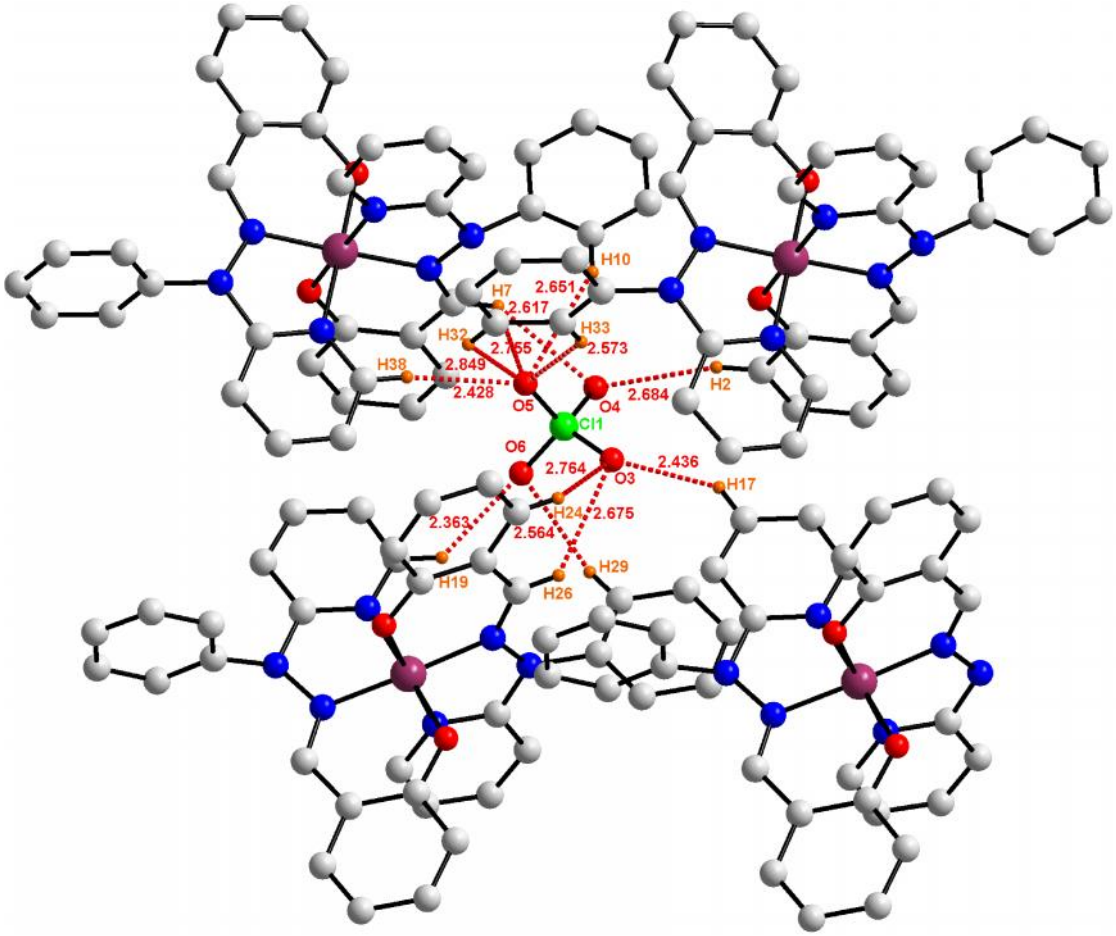

Fig. 4.10 Hydrogen–bonding interaction network between aryl hydrogens and perchlorate anions in the crystal structure of **7**·CH_3CN

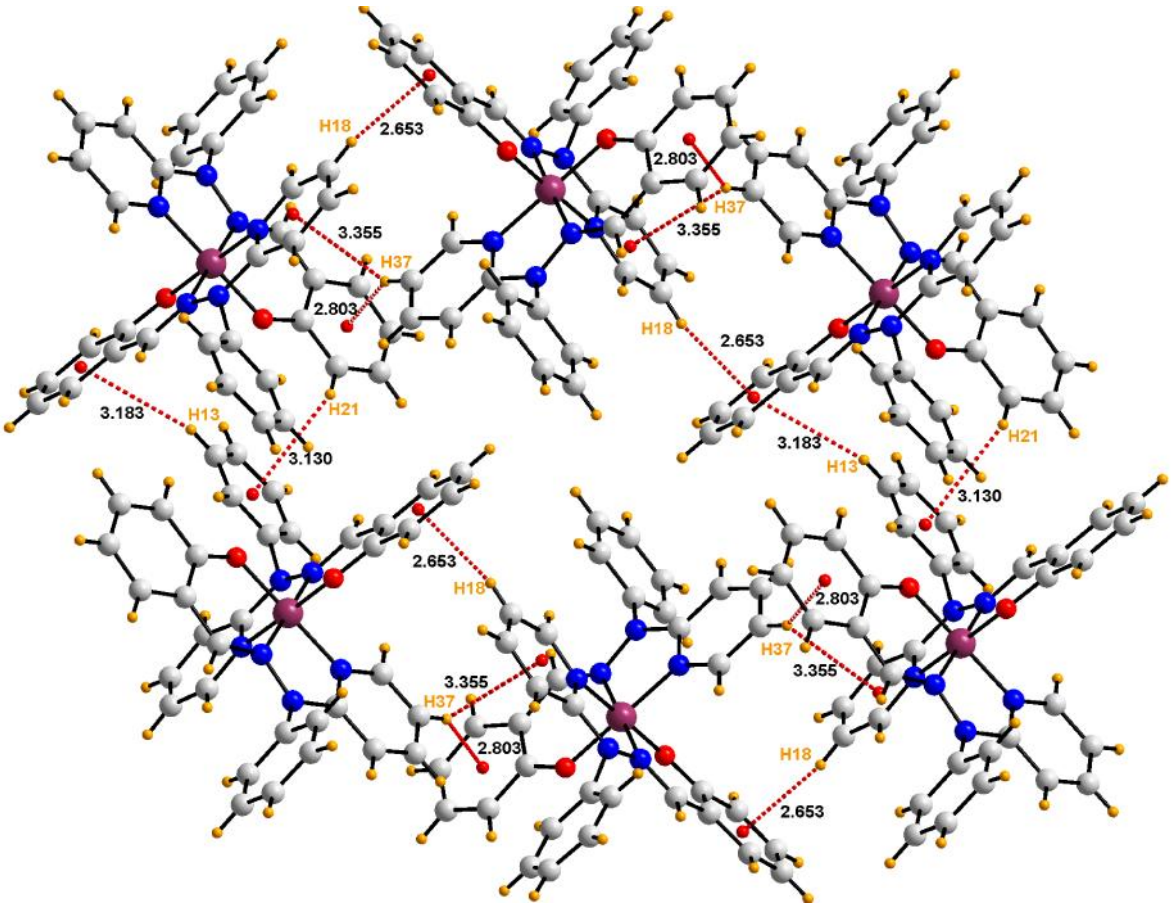

Fig. 4.11 Extensive C–H···π interactions in the crystal structure of **7**·CH_3CN

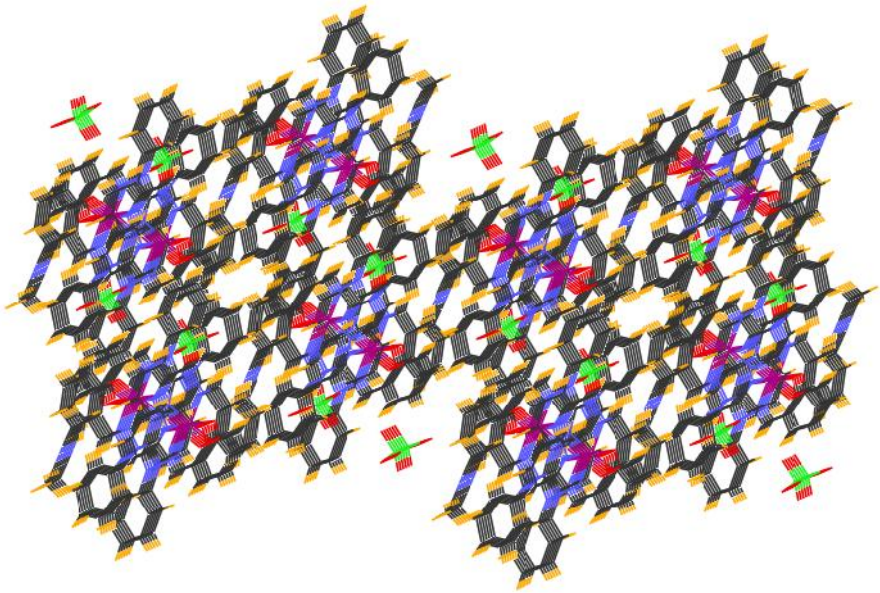

Fig. 4.12 Three–dimensional packing diagram of **7**·CH_3CN

4.2.4. Electrochemical studies

The electrochemical profiles of the complexes were investigated in acetonitrile at room temperature by cyclic voltammetry using Ag/AgCl as reference electrode, glassy carbon as working electrode and platinum wire as auxiliary electrode. The solutions were thoroughly degassed with nitrogen prior to the beginning of experiments. The cyclic voltammograms were recorded within the potential range of −1.500 V to +1.500 V vs. Ag/AgCl using tetrabutylammonium perchlorate (TBAP) as supporting electrolyte and shown in Fig. 4.13. The voltammetric data of all redox processes are documented in Table 4.5.

The cyclic voltammogram of **7**·CH_3CN displayed a quasi−reversible cathodic peak with $E_{1/2}$ and ΔE values of -0.338 V and 0.397 V vs. Ag/AgCl which was ascribed to the reduction of metal centre (CoIII/CoII) (Table 4.5).[488] Another peak was found in the anodic region with $E_{1/2}$ and ΔE values of +1.180 V and 0.204 V respectively which was assigned as the ligand centered oxidation process (Table 4.5).[488] The complex **8** also showed very much similar electrochemical behavior. Cyclic voltammogram of **8** comprised of two redox processes; the first quasi−reversible peak in cathodic region with $E_{1/2}$ and ΔE values of -0.333 V and 0.636 V vs. Ag/AgCl respectively represented Co(III)/Co(II) redox process[488] and the second reversible peak in anodic region with $E_{1/2}$ and ΔE values of +1.111 V and 0.073 V vs. Ag/AgCl respectively was assigned as the ligand centered oxidation (Table 4.5).[477,488] The potential values for anodic processes fall within the reported range for the conversion of coordinated phenolates into phenoxyl radical species and thus suggest the electrochemical generation of metal−coordinated phenoxyl radical species $[\mathbf{7}]^{\bullet+}$ and $[\mathbf{8}]^{\bullet+}$ respectively.[488]

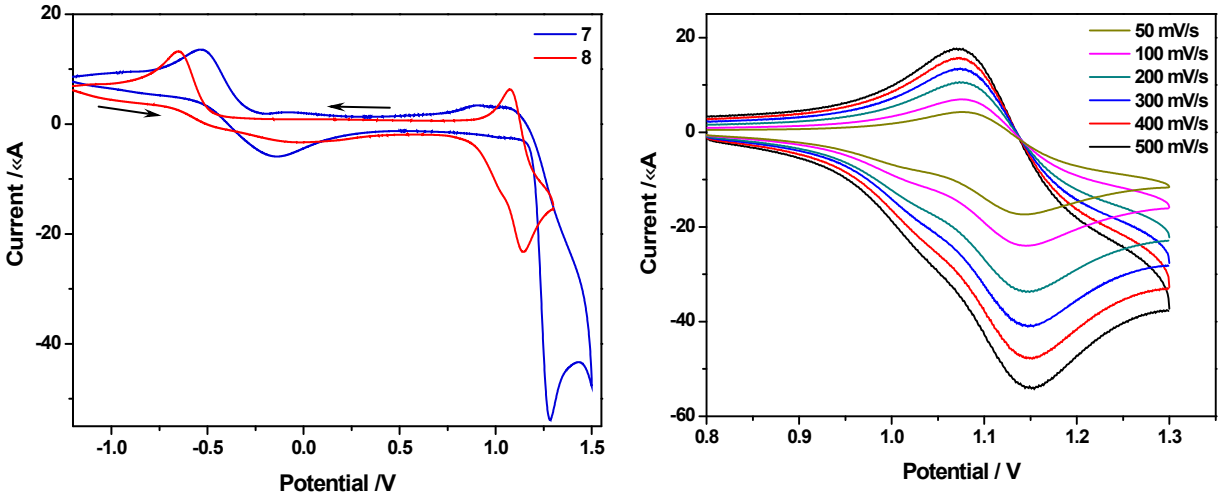

(a) (b)

Fig. 4.13 (a) Cyclic voltammograms of **7**·CH_3CN and **8** in acetonitrile (10^{-3} M) vs. Ag/AgCl at 298 K in presence of 0.1 M tetrabutylammonium perchlorate as supporting electrolyte; scan rate 0.1 V/s. (b) Cyclic voltammograms of **8** at different scan rates i.e. 0.05, 0.1, 0.2, 0.3, 0.4 and 0.5 V/s respectively

Table 4.5 Redox potentials for complexes **7**·CH_3CN and **8** at 298 K vs. Ag/AgCl

Complex	Co^{III}/Co^{II}		L^{+}/L^{0}	
	$E_{1/2}$[a] (V)	ΔE_p[b] (mV)	$E_{1/2}$[a] (V)	ΔE_p[b] (mV)
7·CH_3CN	-0.338	397	+1.180	204
8	-0.333	636	+1.111	73

measured in acetonitrile with 0.1 M TBAP, [a]$E_{1/2} = 0.5(E_{pa} + E_{pc})$, [b]$\Delta Ep = (E_{pa} - E_{pc})$

Two important facts could be observed by comparing these voltammograms: (a) metal centered reduction process ($Co^{III} \rightarrow Co^{II}$) occurred at comparatively more negative potential value in complex **8** due to the introduction of *tert*-butyl groups in the ligand frame. It seems obvious since electron donating substituents would increase the electron density around metal centre thereby rendering the metal centered reduction process less facile and thus increasing the negative value of potential for the reduction of metal center.[488] (b) reversibility of the peaks decreased for the metal centered reduction process in complex **8** while the reversibility was improved for ligand–centered oxidation due to the presence of radical–stabilizing *tert*-

butyl groups. We have recorded the voltammograms for complex **8** in anodic region with repeatitive scans at different scan rates ranging from 0.05 V/s to 0.5 V/s and found negligible change in the ΔE value for the ligand–centered redox process (Fig. 4.13).

4.2.5. Generation of phenoxyl radical species

Metal complexes derived from the ligands having phenolato donors may undergo ligand–centered oxidation giving rise to phenoxyl radical species. Such complexes may serve as small molecule functional mimics for galactose oxidase and glyoxal oxidase enzymes (*Chapter 1*). Generation of phenoxyl radical species by chemical oxidation of **7**·CH_3CN and **8** in acetonitrile solution was monitored at 298 K by electronic absorption spectroscopy. Addition of two equivalents of ceric ammonium nitrate ($(NH_4)_2[Ce^{IV}(NO_3)_6]$ or CAN) to the acetonitrile solution of complex **7**·CH_3CN afforded only enhancement in the intensity of the bands associated with phenolate–to–cobalt charge transfer transition with λ_{max} at 415 nm and d–d transition with λ_{max} at 495 nm without formation of any new band in the spectrum. However, addition of CAN to the solution of complex **8** in acetonitrile resulted the shifting of phenolate–to–cobalt charge transfer band from 433 nm to 415 nm and disappearance of the d–d band with λ_{max} at 545 nm (Fig. 4.14 a). Furthermore, two new bands appeared in the spectrum: one with λ_{max} at 562 nm and another extending into the NIR region (Fig. 4.14 a).

The intensity of these bands was enhanced by the addition of CAN upto six equivalents. These spectral changes are in accordance with those reported for phenoxyl radicals derived from cobalt complexes and thus predict the formation of phenoxyl radical species $[\mathbf{8}]^{\bullet+}$ through ligand oxidation in complex **8**.[143,193] The colour of the solutions changed from light brown and green to dark red after oxidation of complexes **7**·CH_3CN and **8** respectively.

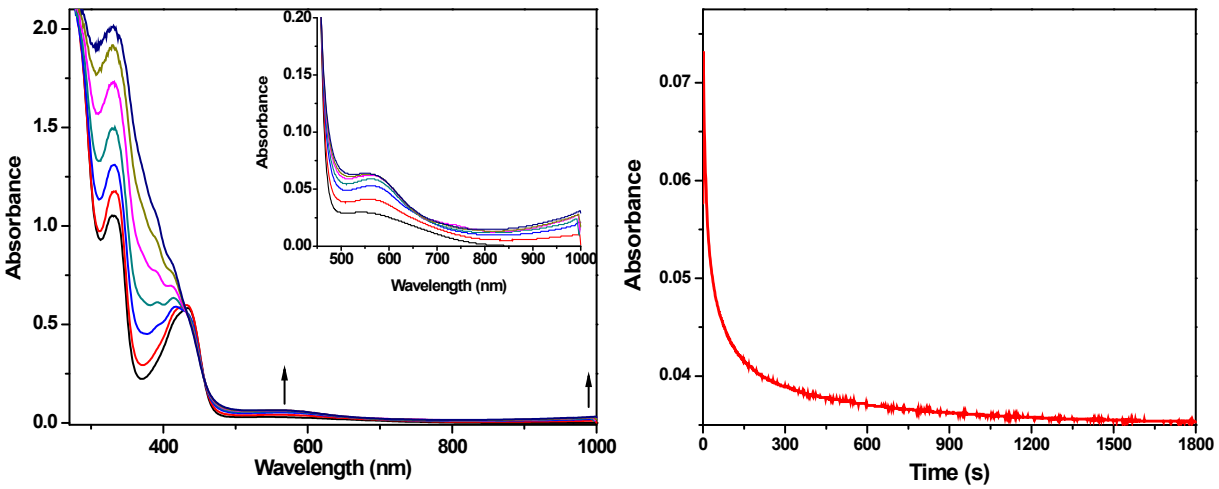

(a) (b)

Fig. 4.14 (a) Absorption spectral changes upon oxidation of complex **8** (5×10^{-5} M) with CAN upto six equivalents in CH_3CN at 298 K; (b) time course of decomposition of $[\mathbf{8}]^{\bullet+}$ monitored at 562 nm

The phenoxyl radical species $[\mathbf{8}]^{\bullet+}$ was genetared at room temperature which decomposed completely within ~10 min without regenerating the parent complex **8**. However, it is important to note that generation of corresponding radical species from complex **7**·CH_3CN could not be confirmed at room temperature by electronic absorption spectral studies probably due to the absence of radical stabilizing groups. The decomposition of $[\mathbf{8}]^{\bullet+}$ was monitored by a time dependent study at 562 nm and results are shown in Fig. 4.14 (b). These data indicated that the decomposition of $[\mathbf{8}]^{\bullet+}$ is probably following a second–order pathway. Purging of oxygen into the solution containing $[\mathbf{8}]^{\bullet+}$ could not bring about any change in the rate of decomposition hence we speculated that possibly the solvent is playing a major role in the decomposition process.

The absorption spectrum of **7**·CH_3CN in acetonitrile showed the bands at 415 nm and 495 nm which are the characteristic bands of phenoxyl radical complex so we tried to record the EPR spectrum of solid as well as CH_3CN solution of **7**·CH_3CN; however, we were unable to get any distinct signal corresponding to radical species in the solid form. The X–band EPR spectrum of phenoxyl radical complexes derived from frozen solutions of **7**·CH_3CN and **8** in

CH_3CN at 120 K are shown in Fig. 4.15. The EPR spectra exhibited isotropic sharp signals at g = 2.000 and 1.997 for phenoxyl radical complexes derived from **7**·CH_3CN and **8** respectively which feature a free electron typical for the phenoxyl radical (S = ½) species.[143,194,478,488,489] The single sharp isotropic signal indicated the absence of coupling due to benzylic proton, imine nitrogens or cobalt ion.[135]

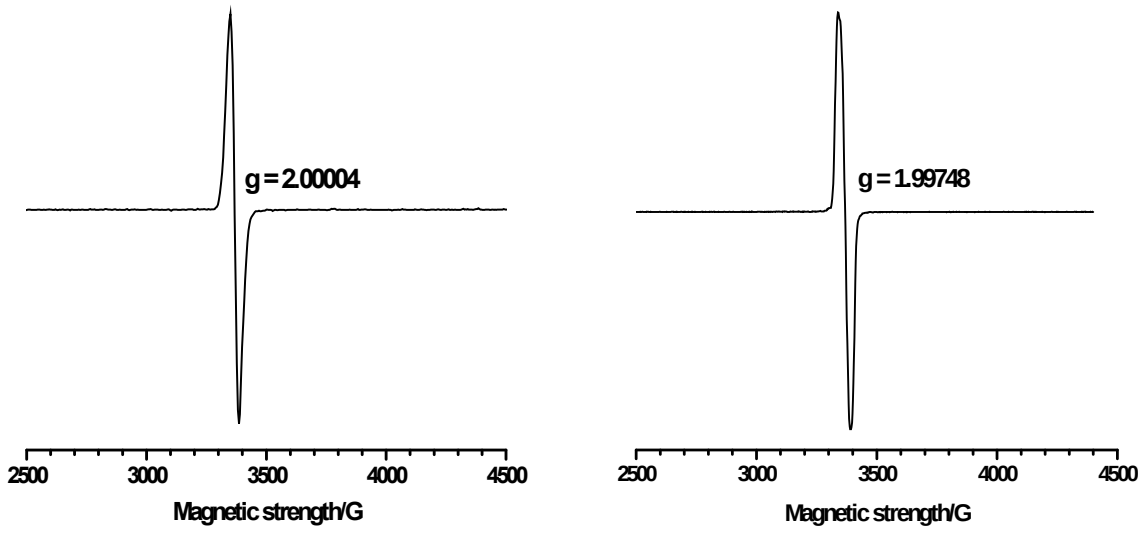

(a) (b)

Fig. 4.15 X–band EPR spectra of phenoxyl radical complexes derived from frozen solutions of (a) **7**·CH_3CN and (b) **8** in CH_3CN at 120 K

4.2.6. DNA interaction studies

Absorption spectral changes of complexes **7**·CH_3CN and **8** could not be monitored in presence of CT–DNA due to slow precipitation of complexes in buffer with time. Hence, the DNA binding properties of complexes **7**·CH_3CN and **8** were studied only by fluorescence emission spectroscopy and circular dichroism. During competitive binding experiments, solutions of metal complexes were added gradually to the CT–DNA solution pretreated with ethidium bromide. The enhanced fluorescence of ethidium bromide : DNA mixture arising from the intercalation of ethidium between the base pairs of DNA got quenched in presence of metal complexes. The fluorescence quenching curves of ethidium bromide bound to DNA

by complexes **7**·CH_3CN and **8** and their Stern–Volmer plots are shown in Fig. 4.16. Stern–Volmer plot for **7**·CH_3CN was close to linearity whereas plot for complex **8** showed positive deviation from linearity at higher concentration of quencher complex. This indicates either the existence of additional binding sites or a combined quenching involving both static and dynamic processes occurring at higher concentrations of quencher molecule.[468]

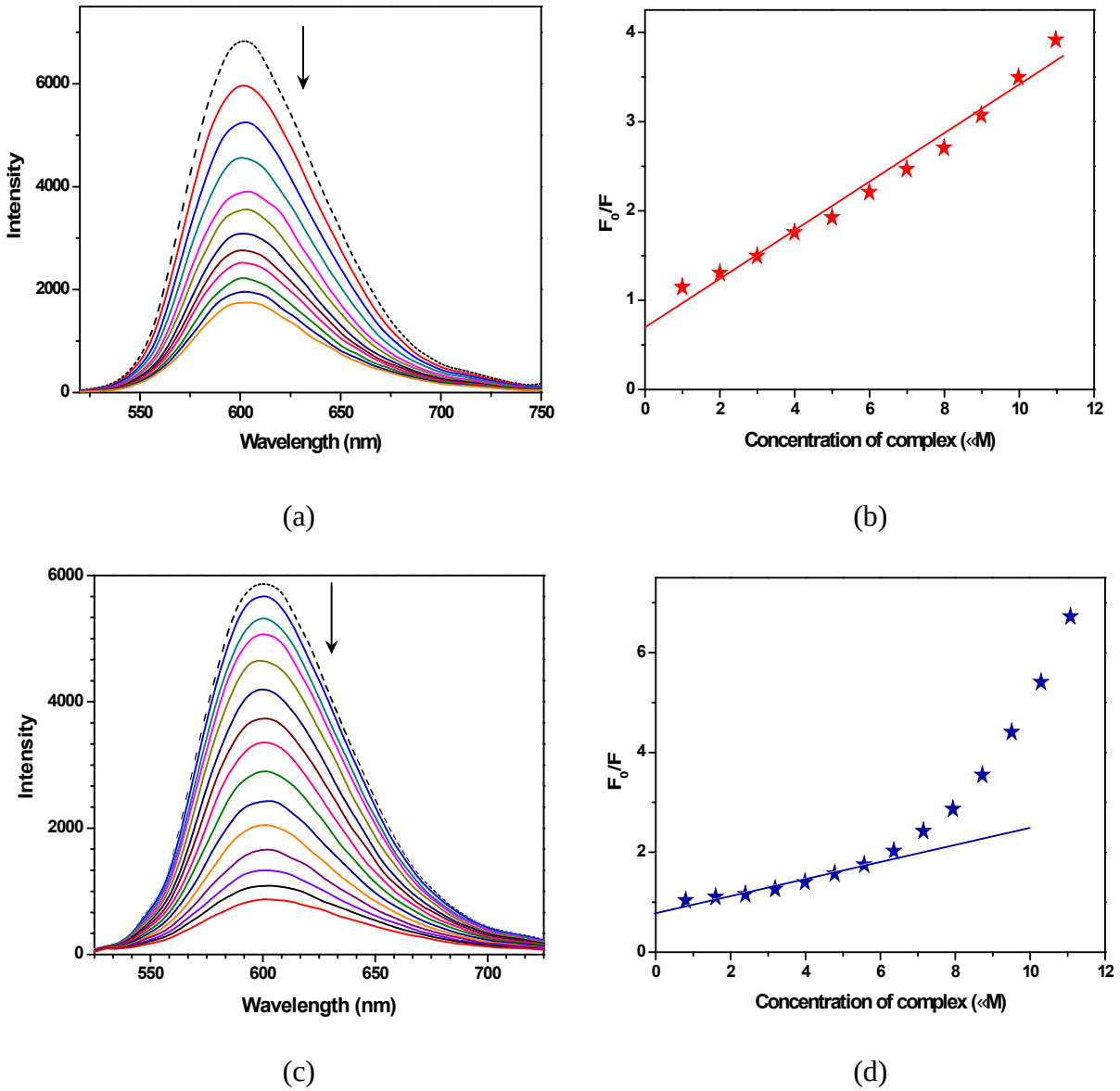

Fig. 4.16 Emission spectral changes of EB−DNA in the absence (dotted line) and presence of cobalt complexes (solid lines) in 0.1 M phosphate buffer (pH 7.2) containing 2% DMF. λ_{ex} = 250 nm; λ_{em} = 585 nm. [EB] = 5 μM, [DNA] = 25 μM, (a) [**7**] = 0–10.97 μM, (c) [**8**] = 0–11.07 μM; (b) and (d) Stern–Volmer plots for complexes **7**·CH_3CN and **8** respectively

The Stern–Volmer quenching constants (K_{SV}) for both complexes were calculated using linear Stern–Volmer equation (*Chapter 1*) and listed in Table 4.6. These values are lesser than those reported for metallointercalators[347] thus predicting a non–intercalative mode of binding for these complexes with DNA. Hence there is no possibility of displacement of intercalatively bound ethidium bromide by these complexes.

Table 4.6 Stern–Volmer quenching constants of **7**·CH_3CN and **8** with DNA

Complex	K_{SV} (M^{-1})
7·CH_3CN	3.92×10^5
8	2.18×10^5

If the quenching occurred by photo–electron transfer mechanism, then the ability of these complexes to quench the enhanced emission of intercalatively bound ethidium bromide should depend on the reducibility of Co(III) complexes which is possibly reflected through the higher binding constant of **7**·CH_3CN (for Co(III) → Co(II) process: E_p = -0.541 V vs. Ag/AgCl for **7**·CH_3CN; E_p = -0.655 V vs. Ag/AgCl for **8**).[299]

In order to get better insight into the DNA binding event, CD–spectral changes of CT–DNA in presence of complexes **7**·CH_3CN and **8** were monitored within the wavelength range of 200–300 nm (Fig. 4.17). In the absence of complexes, CT–DNA exhibited one positive band near 275 nm due to base stacking and one negative band near 248 nm due to helicity which are characteristic of the right handed B-conformation of DNA (*Chapter 1*).[332] Incubation of DNA with metal complexes afforded only little change in the intensity of positive and negative bands without any considerable shift in the wavelength. Absence of any remarkable red or blue shift indicated that the conformation of secondary structure of DNA remained largely unaltered after the DNA binding event.

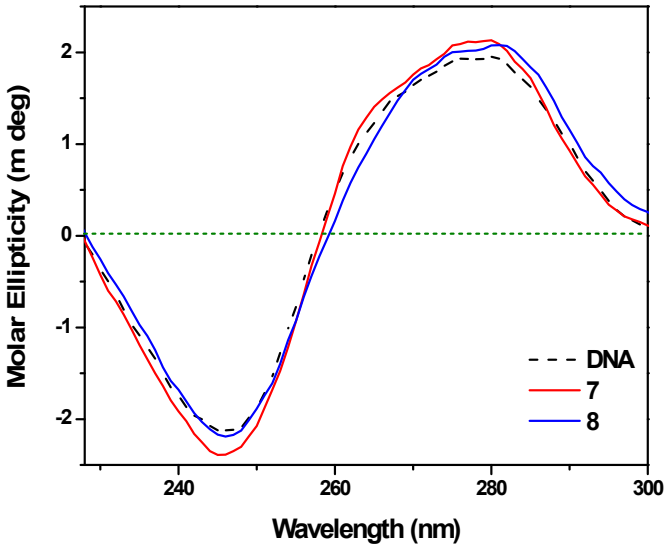

Fig. 4.17 Circular dichroism spectra of CT–DNA in presence of complexes **7**·CH_3CN and **8** in 0.1 M phosphate buffer (pH 7.2) after 10 min incubation at 298 K

Investigation of literature revealed that classical intercalators cause significant changes in the intensities of both, positive and negative bands due to the enhancement of base stacking and stabilization of helicity whereas small molecules exhibiting groove binding or electrostatic interactions with DNA cause no perturbations.[355,455] Hence, CD spectroscopic experiments supported a non–intercalative mode of interaction with DNA for these cobalt complexes which is consistent with the data obtained through competitive binding experiments.

4.2.7. Nuclease Activity

Transition metal complexes can also be used as artificial nucleases since they can activate molecular oxygen and generate reactive oxygen species (ROS) in solution. Nuclease activity of cobalt complexes **7**·CH_3CN and **8** was analyzed by agarose gel electrophoresis under physiological conditions. DNA cleavage experiments of **7**·CH_3CN were performed in absence as well as presence of oxidizing (H_2O_2, 200 μM) and reducing agents (BME, 200 μM) and results are shown in Fig. 4.18. On the basis of gel electrophoresis data, following important observations were made. First, **7**·CH_3CN does not participate itself in nuclease

activity even at high concentrations (100 μM). Second, no nuclease activity was observed for **7**·CH_3CN even in the presence of external oxidizing or reducing agents.

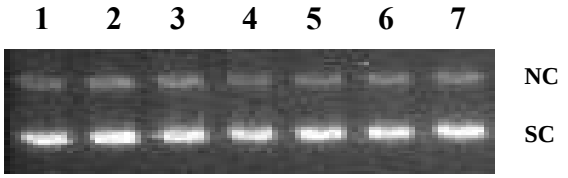

Fig. 4.18 Gel electrophoretogram of DNA incubated with **7**·CH_3CN at 37 °C for 1.5 h. DMF (5%) was used for the better solubility of the complex. Keys: Lane 1, DNA control; lane 2, DNA + H_2O_2 (200 μM); lane 3, DNA + BME (200 μM); lane 4–5, DNA + **7**·CH_3CN (50 and 100 μM respectively); Lane 6, DNA + **7**·CH_3CN (100 μM) + H_2O_2 (200 μM); Lane 7, DNA + **7**·CH_3CN (100 μM) + BME (200 μM)

Conversely, the complex **8** exhibited excellent nuclease activity even in the absence of any oxidizing or reducing agent with simultaneous decrease in the amounts of SC and NC forms. A progressive vanishing of both SC and NC bands was observed as the concentration of **8** or the incubation period was increased. This type of vanishing may be due to the extensive oxidative degradation of DNA resulting from the cleavage at multiple sites.[490] Although enhancement of the extent of DNA cleavage was observed with longer incubation periods, 5 min of incubation was found to be sufficient to see the nuclease activity while using a complex concentration of 25 μM (Fig. 4.19 b, lanes 9–15). On the other hand, increasing concentrations of **8** also caused the enhancement of nuclease activity (Fig. 4.19. lanes 2–7) though the complex concentration as low as 5 μM was enough to catalyze the DNA strand scission if incubated for 1.5 h. From the gel electrophoresis data of complexes **7**·CH_3CN and **8**, it is evident that the introduction of radical stabilizing *tert*–butyl groups in the ligand frame imparted the complex with DNA cleaving ability through a self–activating mechanism. These results are similar to those reported for analogous copper compounds where the *tert*–butyl groups in the ligand architecture were suspected to play an important

role in self–activated DNA cleavage mediated by singlet oxygen and/or singlet oxygen like species generated in solution.[477]

To establish the roles of various reactive oxygen species (ROS) in DNA strand scission mechanism, we have performed the DNA cleavage experiments in presence of potential radical scavengers. Results of the inhibition studies for complex **8** are manifested in Fig. 4.20.

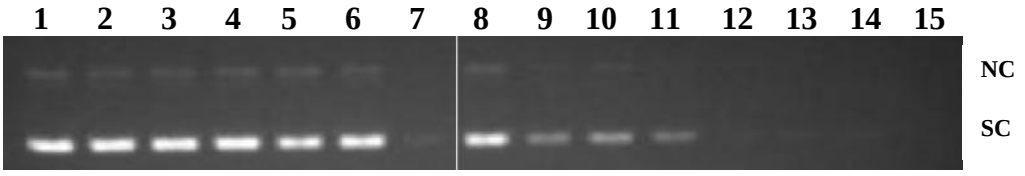

Fig. 4.19 Gel electrophoresis separation showing the cleavage of pBR322 DNA by complex **8**. All lanes except lane 1 and 5 contain 5% DMF. Keys: (a) Incubation was done at 37°C for 1.5 h (Lanes 1–7). Lane 1, DNA control; lane 2, DNA + DMF (5%); lane 3, DNA + PhimpH (50 µM); lane 4, DNA + ^{t}BuPhimpH (50 µM); lane 5, DNA + $CoCl_2 \cdot 6H_2O$ (25 µM); lane 6, DNA + **7**·CH_3CN (25 µM); lane 7, DNA + **8** (25 µM); (b) Lane 8, DNA control; lanes 9–15, DNA + **8** (25 µM). Samples were incubated at 37°C for 5, 10, 20, 30, 45, 60, 90 min respectively (lanes 9–15)

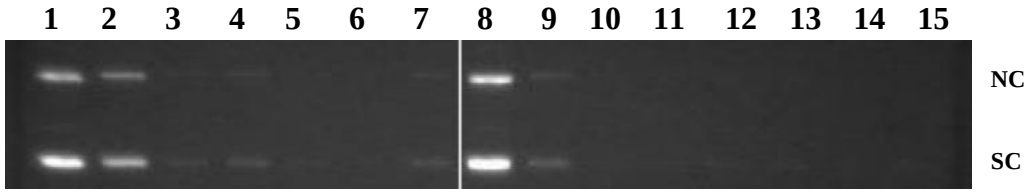

Fig. 4.20 Gel electrophoresis separation showing the cleavage of pBR322 DNA by complex **8**. All lanes except lane 1 contain 5% DMF. Samples were incubated at 37°C for 1.5 h. Keys: (a) Lane 1, DNA control; lanes 2–7, DNA + **8** (5, 10, 20, 30, 40 and 50 µM respectively); (b) Lane 8, DNA control; lane 9, DNA + **8** (25 µM); lanes 10–15, DNA + **8** (25 µM) + DMSO, ethanol, urea, NaN_3, L–histidine (20 mM each) and catalase (10 U) respectively

Interestingly, none of the scavengers could show any inhibition of nuclease activity. These data suggested that the DNA cleavage is either not mediated by singlet oxygen, hydroxyl

radicals or peroxide radicals or these are not the only species responsible for the DNA cleavage. Investigation of literature revealed that metal–bound oxo species like [M–OH], [M–OOH] and [M=O] may also cause efficient DNA cleavage.[271] In fact, several iron and copper complexes have shown excellent nuclease activity mediated by metal bound reactive oxygen radical species generated in solution.[403,491] Considering the inherent affinity of cobalt(III) complexes for dioxygen[492] along with their potential towards its activation[493] or reduction[494-496] and the involvement of Co(III)–$OO^{\bullet}$ species in DNA cleavage[497], we proposed that hypervalent metal bound oxygen radical species might be responsible for the DNA strand scission.

4.2.8. Protein interaction studies

Non–covalent binding of complexes with serum albumins offer great promise for the development of efficient therapeutics since such interactions are reversible and assist to retain the activity of complexes during blood circulation.[498] Binding behaviours of the metal complexes **7**·CH_3CN and **8** with albumins were investigated by the tryptophan fluorescence quenching experiment using bovine serum albumin (BSA) as model substrate. Trp 134 and Trp 213 residues of BSA were selectively excited at 295 nm and the emission spectra were recorded which showed maxima near 344 nm. In order to study the protein binding properties of complexes, a fixed concentration of albumin was titrated with increasing concentrations of the metal complexes and the changes in the emission intensity were monitored. Binding of metal complexes with albumin led to significant decrease in the emission intensity and considerable red shift in the spectrum with increasing concentrations of **7**·CH_3CN and **8**. The fluorescence quenching curves of complexes **7**·CH_3CN and **8** are illustrated in Fig. 4.21 (a) and (b) respectively.

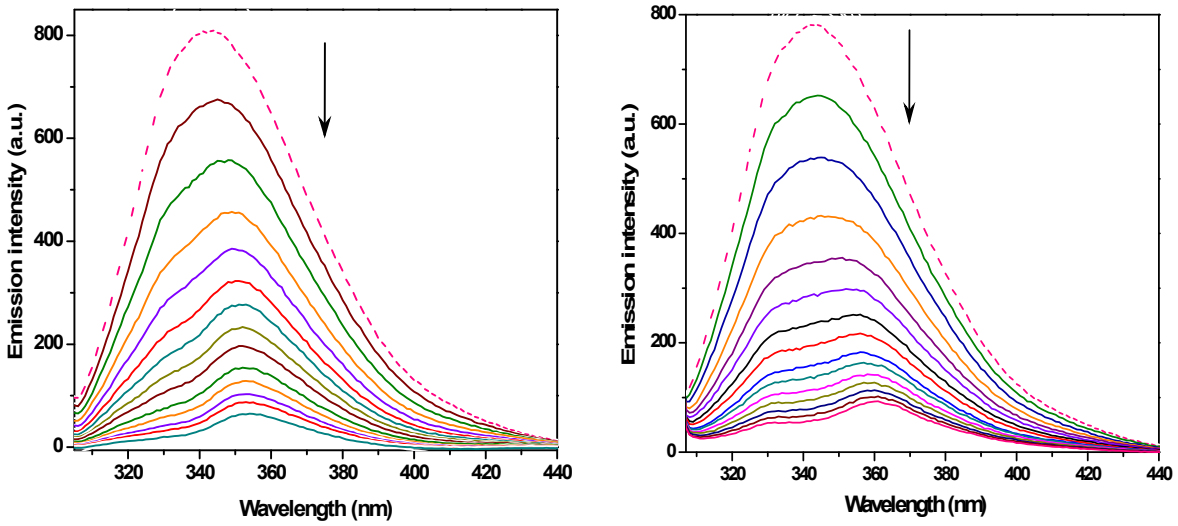

(a) (b)

Fig. 4.21 Emission spectra of BSA in the absence (dotted lines) and presence of complexes **7**·CH_3CN and **8** (solid lines) respectively, in 0.1 M phosphate buffer containing 2% DMF; (a) [BSA] = 2 µM, [**7**] = 0–40 µM; (b) [BSA] = 2 µM, [**8**] = 0–22 µM. Arrows show the intensity changes with increasing concentration of metal complexes

It is noteworthy that the emission intensity of tryptophan residues in BSA can be affected by changes in the polarity of the environment, conformational transitions, subunit association, substrate binding or denaturation.[498] These data clearly indicated that the protein underwent considerable changes in its secondary structure as a consequence of binding with metal complexes. Stern–Volmer plots and Scatchard plots for complexes **7**·CH_3CN and **8** are represented in Fig. 4.22 and 4.23 respectively and K_{SV} values are listed in Table 4.7. The K_q values for both complexes are higher than the maximum scatter collision-quenching constants (~10^{10} $M^{-1}s^{-1}$) for biopolymer fluorescence indicating that a static quenching mechanism for these complexes was prevalent (Table 4.7).[348] Binding constants (K) and the number of binding sites (n) were calculated by applying Scatchard equation (*Chapter 1*) and calculating the slopes and intercepts from Scatchard plots. These data suggested relatively higher binding affinity of complex **8** for protein molecules which may be attributed to the enhanced hydrophobicity of the ^{t}BuPhimpH ligand.[294]

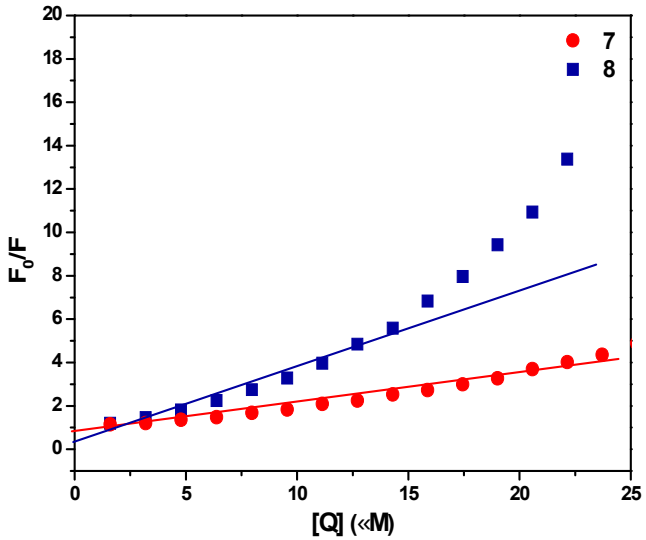

Fig. 4.22 Stern–Volmer plots exhibiting the interaction of complexes **7**·CH_3CN and **8** with BSA

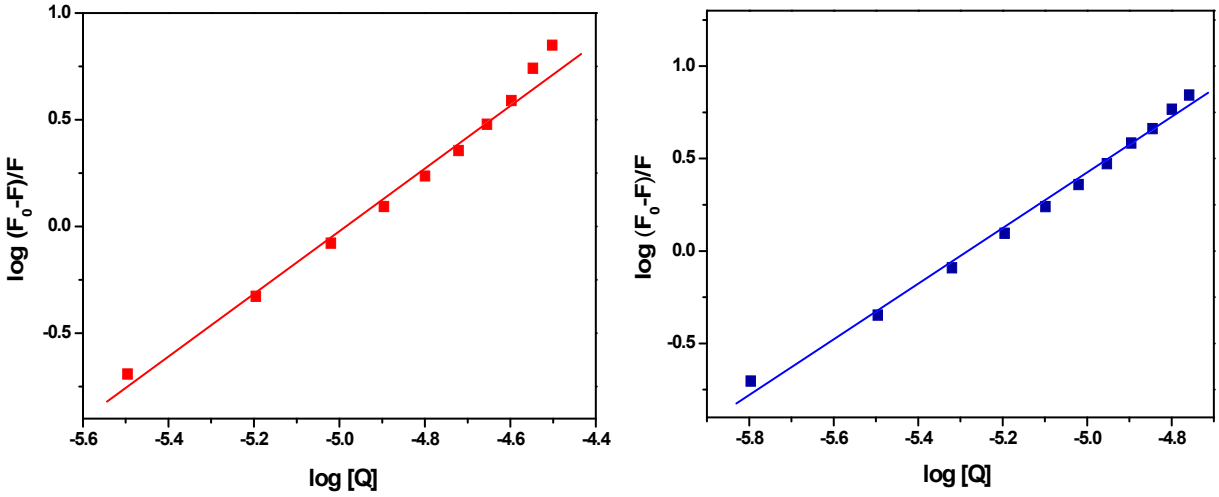

(a) (b)

Fig. 4.23 Scatchard plots for the interaction of complexes (a) **7**·CH_3CN and (b) **8** with BSA

Table 4.7 Stern–Volmer quenching constants, binding constants and number of binding sites for the interaction of **7**·CH_3CN and **8** with BSA

Complex	K_{SV} (M^{-1})		K_q (M^{-1})	K (M^{-1})	n
	(with ibuprofen)	(without ibuprofen)			
7·CH_3CN	1.37×10^5	1.62×10^5	1.62×10^{13}	2.20×10^7	1.47
8	3.72×10^5	1.09×10^6	1.09×10^{14}	8.64×10^7	1.50

In order to explore the preferential binding sites of these complexes in BSA, we endeavored to perform the competitive binding experiments in presence of different site markers viz. warfarin for site I and ibuprofen for site II respectively.

Warfarin is one of the best characterized drugs which bind preferentially to the site I located in subdomain IIA near Trp-213 residue in BSA and Trp-214 in HSA.[345,499] In the free state, it exhibits only weak emission with λ_{max} at 378 nm when excited at 335 nm. However, binding of warfarin with the albumin molecule gives rise to enhancement in the emission intensity.[499] The enhanced fluorescence of SA bound warfarin can be quenched by a second molecule possessing affinity for site I. The emission spectral behaviour of SA bound warfarin in presence of complexes **7**·CH_3CN and **8** at different molar ratios is represented in Figures 4.24 (a) and 4.25 (a) respectively.

It is evident that the strong fluorescence of warfarin bound to protein, got quenched in presence of cobalt complexes **7**·CH_3CN and **8** which may be attributed to the reduction in warfarin–binding capacity at the primary binding site of serum albumin. These data support the binding of cobalt complexes **7**·CH_3CN and **8** in the proximity of Trp–213 residue, within warfarin site I located in subdomain IIA.[499]

To investigate the binding affinities of cobalt complexes **7**·CH_3CN and **8** for site II, we carried out competitive binding experiment with ibuprofen (Figures 4.24 (b) and 4.25 (b) respectively).[500] The results are demonstrated in the form of modified Stern–Volmer plots and illustrated in Fig. 4.26. In the control experiments, metal complexes and ibuprofen itself showed negligible emission intensity under identical experimental conditions. In case of **7**·CH_3CN, the fluorescence properties of metal complex–BSA system underwent considerable changes in the presence of ibuprofen (Fig. 4.26 a).

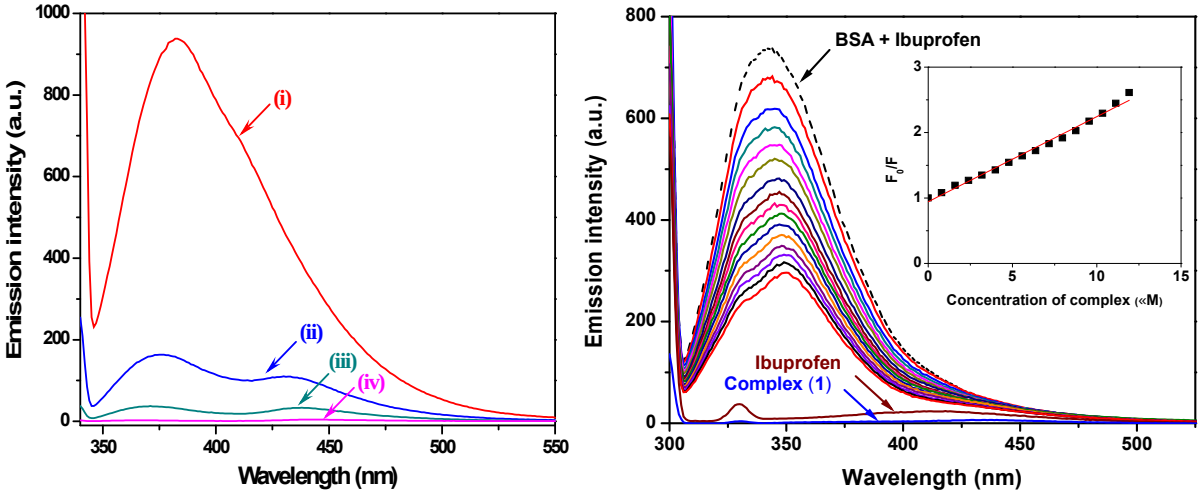

(a) (b)

Fig. 4.24 Fluorescence emission spectra of (a) warfarin (80 μM) and BSA (40 μM) equilibrated for 1 h in phoshphate buffer (pH 7.2) containing 10% DMF in (i) absence or (ii–iv) presence of complex **7**·CH_3CN (ii) 40 μM, (iii) 80 μM and (iv) 160 μM respectively; λ_{ex} = 335 nm, λ_{em} = 378 nm. (b) BSA (2 μM) treated with the site marker ibuprofen (2 μM) in 0.1 M phoshphate buffer (pH 7.2) containing 2% DMF in absence (dotted line) and presence of complex **7**·CH_3CN. [**7**] = 0 – 11.928 μM; λ_{ex} = 295 nm, λ_{em} = 344 nm; incubation time = 2 min. Ibuprofen (2 μM) and complex **7**·CH_3CN (100 μM) exhibited negligible emission intensity under similar experimental conditions, inset: Stern–Volmer plot for **7**·CH_3CN

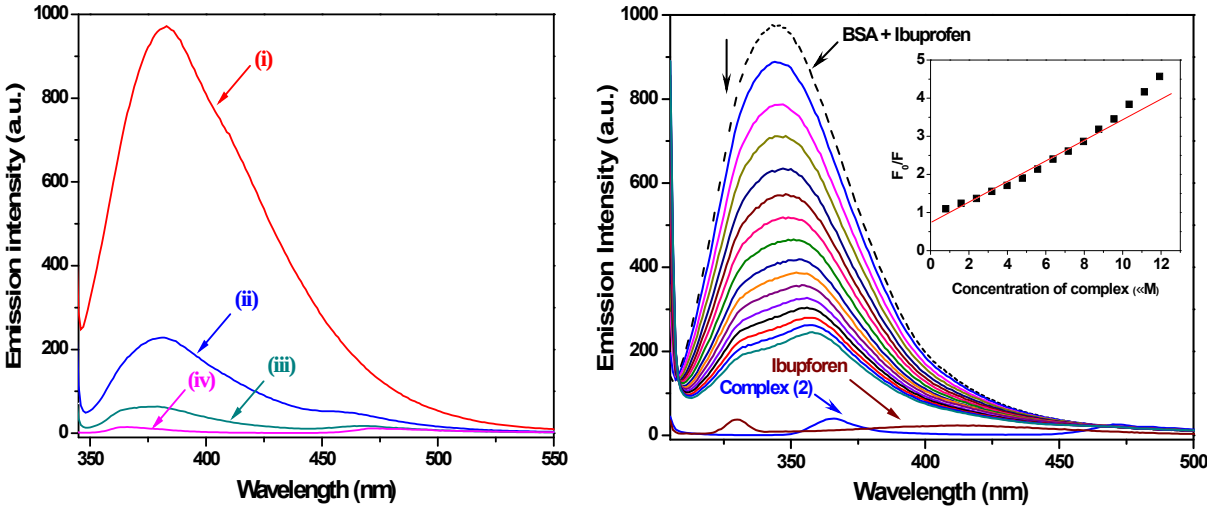

(a) (b)

Fig. 4.25 Fluorescence emission spectra of (a) warfarin (80 μM) and BSA (40 μM) equilibrated for 1 h in phoshphate buffer (pH 7.2) containing 10% DMF in (i) absence or (ii–iv) presence of complex **8** (ii) 40 μM, (iii) 80 μM and (iv) 160 μM respectively; λ_{ex} = 335 nm, λ_{em} = 378 nm, (b) BSA (2 μM) treated with the site marker ibuprofen (2 μM) in 0.1 M phoshphate buffer (pH 7.2) containing 2% DMF in absence (dotted line) and presence of complex **8**. [**8**] = 0 – 11.928 μM; λ_{ex} = 295 nm, λ_{em} = 344 nm; incubation time = 2 min. Ibuprofen (2 μM) and complex **7** (100 μM) exhibited negligible emission intensity under similar experimental conditions, inset: Stern–Volmer plot for complex **8**

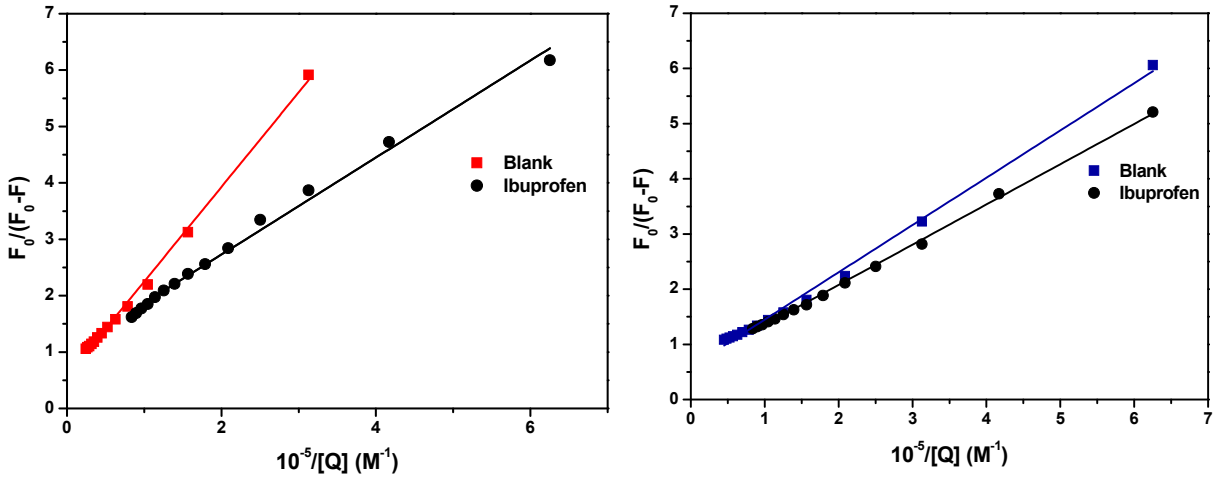

(a) (b)

Fig. 4.26 Modified Stern–Volmer plots of complexes (a) **7**·CH_3CN and (b) **8** in the absence and presence of ibuprofen respectively

The observed changes in emission spectral properties of **7**·CH_3CN bound BSA induced by ibuprofen can be rationalized in terms of binding of cobalt complex (**7**·CH_3CN) to site II.[500] Hence it was concluded that **7**·CH_3CN could bind to the warfarin binding site (site I) as well as ibuprofen binding site (site II) during protein interaction event. On the other hand, fluorescence properties of metal complex (**8**)–BSA system were almost the same in the absence or presence of ibuprofen suggesting that the complex had no appreciable binding affinity for site II (Fig. 4.26 b).[500]

4.2.9. Protein cleavage activity

The ability of complexes **7**·CH_3CN and **8** to cleave peptide bonds was examined in the absence of any external activator by SDS–PAGE using BSA as substrate. The protein (15 μM) was incubated at 50 °C with varying concentrations of complexes **7**·CH_3CN and **8** for 20 h and then subjected to SDS–PAGE. The results of protease activity are represented in Fig. 4.27.

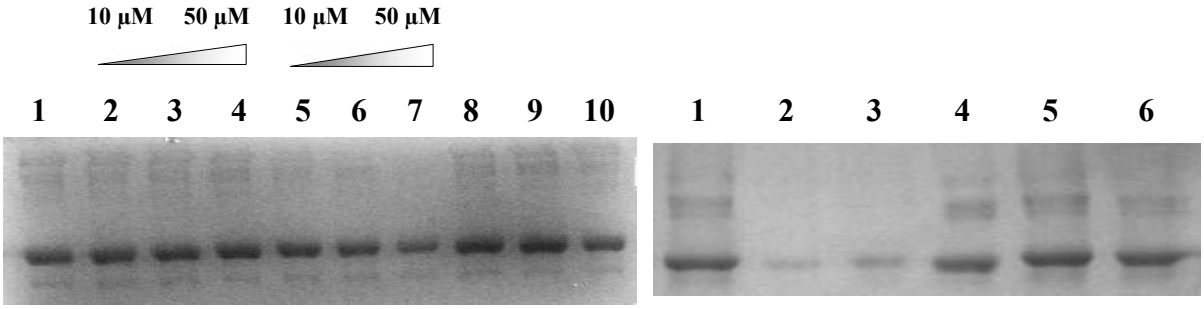

(a) (b)

Fig. 4.27 SDS–PAGE separation showing the cleavage of bovine serum albumin (BSA) by complex **8** in HEPES buffer (10 mM, pH 7.3). Incubation was done at 50°C for 20 h. Keys: (a) Lane 1, BSA (15 μM) control; lanes 2–4, BSA (15 μM) + **7** (10, 25 and 50 μM respectively); lanes 5–7, BSA (15 μM) + **8** (10, 25 and 50 μM respectively); lane 8, BSA + Phimph (50 μM); lane 9, BSA + ^{t}BuPhimph (50 μM) and lane 10, BSA + $CoCl_2 \cdot 6H_2O$ (50 μM); (b) Lane 1, BSA (15 μM) control; lane 2, BSA (15 μM) + **8** (100 μM); lanes 3–6, BSA (15 μM) + **8** (100 μM) + DMSO (20%), glycerol (20%), NaN_3 (20 mM) and catalase (10 U) respectively

The complex **7**·CH_3CN was found as inefficient for protein cleavage activity (Fig. 4.27 (a), lanes 2–4). However, a concentration dependent smearing or fading of BSA band was observed in presence of complex **8** suggesting that the binding of complex **8** to BSA gave rise to its cleavage into very small fragments (Fig. 4.27 (a), lanes 5–7).[293,294] It is important to note that almost whole BSA band got vanished when a concentration of 100 μM of complex **8** was used (Fig. 4.27 (b), lane 2). The higher protein cleavage activity of complex **8** may be attributed to the hydrophobic *tert*–butyl substituents which recognize the more exposed hydrophobic regions of protein and facilitate the protein cleavage.[294] In the control experiments, the ligands alone or the metal salt itself could not exhibit any protease–like activity (Fig. 4.27 (a), lanes 8–10). Inhibition experiments in presence of various potential radical scavengers confirmed the oxidative nature of the protein cleavage activity exhibited by complex **8.** A complete inhibition of protein cleavage activity was observed in presence of glycerol, NaN_3, and catalase (Fig. 4.27 (b), lanes 4–6) which indicated the role of hydroxyl radicals, singlet oxygen (or singlet oxygen like species) and peroxide radicals respectively, in

protease activity.[294,501] Hence it was concluded that the protein cleavage activity exhibited by complex **8** was mediated by reactive oxygen species (ROS) generated in the solution.

4.2.10. Cytotoxicity studies

Efficient DNA degradation and protein cleavage activity exhibited by cobalt complex **8** prompted us to investigate the anticancer properties of these complexes against various cancer cell lines. Both compounds were screened *in vitro* for their cytotoxicities against breast cancer (C127–I, MCF–7) cell lines, prostrate cancer (DU–145) cell lines and murine embryonic mesenchymal cell lines (C3H10T1/2) within the concentration range of 1–100 μM through MTT assay. The results of MTT assays are summarized in Table 4.7 and compared in terms of their relative toxicities (Fig. 4.28). IC_{50} values of both complexes for normal cell COS–1 were also determined and included in Table 4.8. These IC_{50} values were compared with those of 5–fluorouracil under identical experimental conditions, which has been used as a positive control during these investigations.[502]

Both complexes showed different levels of cytotoxicity against different types of cell lines, however, these compounds afforded better results than the metal salt itself ($CoCl_2·6H_2O$) or the positive control (5–fluorouracil) in each case. It is clear from Fig. 4.28 that complex **8** possessed an overall higher efficiency than complex **7**·CH_3CN.

Table 4.8 The levels of cytotoxicity *in vitro* exhibited by complexes **7**·CH_3CN and **8**

Cell lines	**7**·CH_3CN	**8**	$CoCl_2·6H_2O$	5JFluorouracil
COS	~68.64 μM	~33.84 μM	~149.10 μM	~228.00 μM
DUJ145	~46.48 μM	~39.00 μM	~287.40 μM	~446.00 μM
C127-I	~39.63 μM	~14.13 μM	~157.20 μM	~270.00 μM
MCF-7	~76.68 μM	~54.07 μM	~269.20 μM	~180.00 μM
C3H10T1/2	~33.57 μM	~33.42 μM	~293.00 μM	~55.28 μM

The data are expressed in terms of IC_{50} values as extrapolated from the MTT assays.

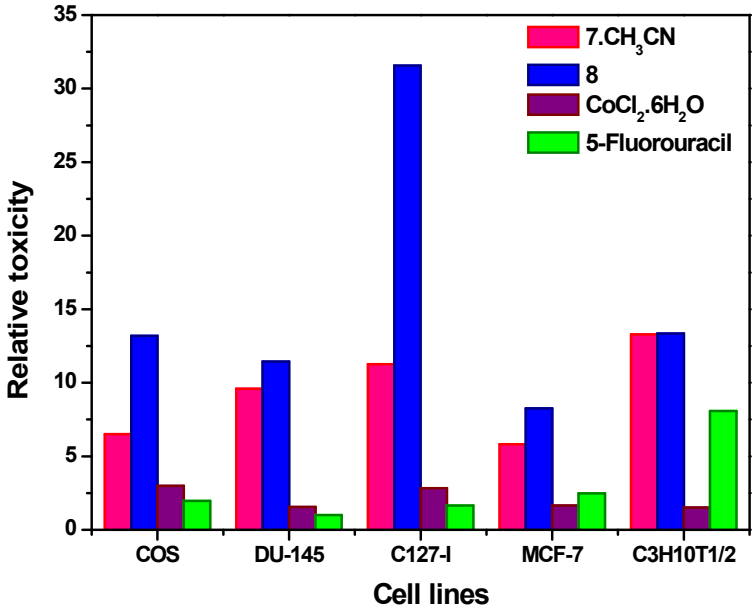

Fig. 4.28 Histogram of relative toxicities of complexes **7**·CH_3CN and **8**, $CoCl_2·6H_2O$ and 5–fluorouracil against various cell lines. Relative toxicities of the compounds were described as the ratios of the reciprocals of their IC_{50} values determined by MTT assay

Furthermore, both compounds were found to be more active particularly against C127–I cell line, affording around 7–fold (for complex **7**·CH_3CN) and 19–fold (for complex **8**) higher potencies than the anticancer drug–5–fluorouracil.

4.3. Conclusions

We synthesized mononuclear cobalt complexes with phenolato oxygen donor ligands as well as their phenoxyl radical analogues through chemical oxidation and characterized them by UV–visible, EPR and electrochemical studies. This report presents a novel example of mononuclear cobalt complexes, where phenoxyl radical was stabilized without any radical stabilizing group in the phenyl ring bearing phenolato oxygen. Furthermore, DNA binding properties and nuclease activities of the parent complexes were also investigated and extensive DNA degradation was observed probably due to the cleavage at multiple sites in DNA. We observed that the introduction of radical stabilizing *tert*-butyl group in the ligand frame made a significant contribution and enabled the complex to cleave DNA via

self–activation. The complexes also showed excellent anticancer activities as determined by cell viability assays. Protein interaction properties of these complexes were investigated with BSA and the binding sites were explored in presence of different site markers. The complexes were also analysed for their proteolytic activities over bovine serum albumin and the complex anchored with *tert*-butyl groups in the ligand part was found to be highly efficient for protein cleavage which again highlighted the role of *tert*–butyl groups in imparting the self–activating mechanism. To the best of our knowledge, this is one of the rare examples of mononuclear cobalt complexes which cleave DNA as well as protein through a self–activation mechanism.

4.4. Experimental section

4.4.1. Reagents and materials

Analytical grade reagents phenylhydrazine (S. D. Fine, Mumbai, India), salicylaldehyde (Sisco Research Laboratories Pvt. Ltd., Mumbai, India), sodium azide, warfarin, ibuprofen, 3,5–di–*tert*–butyl–2–hydroxybenzaldehyde (Sigma Aldrich, Steinheim, Germany), sodium perchlorate monohydrate (Himedia Laboratories Pvt. Ltd., Mumbai, India), ethylenediaminetetraacetic acid, cobalt chloride hexahydrate (Merck Limited, Mumbai, India), sodium hydride and 2–chloropyridine (Acros organics, USA) were used as obtained. The supercoiled pBR322 DNA and CT–DNA were purchased from Bangalore Genei (India) and stored at 4 °C. Agarose (molecular biology grade), ethidium bromide and bovine serum albumin were obtained from Sigma Aldrich. Tris(hydroxymethyl)aminomethane–HCl (Tris–HCl) buffer, phosphate buffer and HEPES buffer were prepared in deionised water. The stock solutions of BSA were prepared as described in *Chapter 1*. Stock solutions of ibuprofen, warfarin and complexes **7**·CH_3CN and **8** were prepared in dimethylformamide. Solvents used for spectroscopic studies were HPLC grade and purified by standard procedures before use. All cell lines used in the present study were obtained from National Center for Cell Sciences, Pune, India. The cells were maintained in tissue

culture plate in DMEM supplemented with 10% FBS, 1× antibiotic–antimycotic solution and 2 mM glutamine at 37 °C with a humidified atmosphere in a CO_2 incubator. During all the experiments the cells were within passage number about 12–20 for all cell lines except COS–1 which was in its 30–35 passage.

4.4.2. Synthesis of ligands

Synthesis of 2J((2JphenylJ2J(pyridinJ2Jyl)hydazono)methyl)phenol (PhimpH) and 2,4Jdi-*tert*JbutylJ6J((phenyl(pyridinJ2Jyl)hydazono)methyl)phenol (^{t}BuPhimpH)

The ligands PhimpH and ^{t}BuPhimpH were prepared by following the reported procedures.[332,477]

4.4.3. Synthesis of cobalt complexes

Caution! Perchlorate salts of metal complexes with organic ligands are potentially explosive. Only small quantities of these compounds should be prepared and handled with proper protection.

Synthesis of $[Co(Phimp)_2]ClO_4 \cdot CH_3CN$ ($7 \cdot CH_3CN$)

A batch of ligand (PhimpH) (0.150 g, 0.52 mmol) was dissolved in 10 mL of acetonitrile. After stirring for 5 min, sodium hydride (0.015 g, 0.62 mmol) was added to the stirred solution and stirred for 30 min to form a precipitate. A batch of $CoCl_2 \cdot 6H_2O$ (0.050 g, 0.21 mmol) dissolved in 10 mL of acetonitrile was added dropwise to the above stirred solution. The colour of the solution changed to dark red. After 2 h of stirring in an unstoppered flask, a batch of sodium perchlorate monohydrate (0.035 g, 0.25 mmol) dissolved in 2 mL of acetonitrile was added and stirred for 3 h. The solution was filtered and the filtrate was kept for slow evaporation to afford brown–red crystals. Yield: (0.594 g) 81%. Anal. Calc. For $C_{36}H_{28}N_6O_6ClCo$ C, 58.83; H, 3.84; N, 11.43; Found: C, 59.14; H, 3.74; N, 11.52; Selected IR data (KBr, ν_{max}/cm^{-1}): 1613, $\nu_{C=N}$; 1092, 623, ν_{ClO4^-}. $\Lambda_M/\Omega^{-1}cm^2mol^{-1}$ (Acetonitrile): 131;

(DMF): 62 (1:1). UV–visible [CH_3CN, λ_{max}/nm ($\varepsilon/M^{-1}cm^{-1}$)]: 259 (54400), 326 (24880), 415 (15600), 495 (680); ESI–MS (acetonitrile, pos.): m/z 635.15 (100%) $[M\text{-}ClO_4]^+$; ^1H NMR (500 MHz, δ/ppm, CD_3CN): 8.080 (s, 1H), 7.977–7.897 (m, 3H), 7.880 (s, 1H), 7.865 (s, 1H), 7.770 (d, J=5.5 Hz, 1H), 7.670 (t, J=7.75 Hz, 1H), 7.320 (d, J=8 Hz, 1H), 7.126 (t, J=7.75 Hz, 1H), 6.912–6.868 (m, 2H), 6.610 (t, J=7.5 Hz, 1H), 6.547 (d, 1H); ^{13}C NMR (500 MHz, δ/ppm, $(CD_3)_2SO$): 162.37, 155.91, 148.83, 148.30, 141.75, 135.91, 134.80, 134.44, 132.48, 130.96, 122.06, 119.07, 117.02, 115.89, 110.05

Synthesis of $[Co(^tBuPhimp)_2]ClO_4$ (8)

A batch of ligand (^{t}BuPhimpH) (0.400 g, 1 mmol) was dissolved in 10 mL of acetonitrile. After stirring for 5 min, sodium hydride (0.035 g, 1.5 mmol) was added to the solution and stirred for 30 min to form a yellow turbid solution. A batch of $CoCl_2{\cdot}6H_2O$ (0.119 g, 0.5 mmol) dissolved in 10 mL of acetonitrile was added dropwise to the above stirred solution. After 1 h of stirring, sodium perchlorate monohydrate (0.070 g, 0.5 mmol) dissolved in 2 mL of acetonitrile was added. The reaction mixture was allowed to stir for 5 h and then the solvent was removed under reduced pressure. The residual mass was dissolved in dichloromethane and the solution was filtered. The green solution was evaporated to dryness and the solid mass obtained was purified by column chromatography over silica and eluted with dichloromethane. Yield: (0.746 g) 78%. Anal. Calc. For $C_{52}H_{60}N_6O_6ClCo$ C, 65.09; H, 6.30; N, 8.76; Found: C, 64.77; H, 6.27; N, 8.83; Selected IR data (KBr, ν_{max}/cm^{-1}):, 1610, $\nu_{C=N}$; 1077, 623, ν_{ClO4^-}. $\Lambda_M/\Omega^{-1}cm^2mol^{-1}$ (Acetonitrile) 88; (DMF): 41. UV–visible [CH_3CN, λ_{max}/nm ($\varepsilon/M^{-1}cm^{-1}$)]: 269 (50940), 332 (23560), 431 (12880), 545 (640); ESI–MS (acetonitrile, pos.): m/z 859.40 (100%) $[M\text{-}ClO_4]^+$; ^1H NMR (500 MHz, δ/ppm, CD_3CN): 8.077 (s, 1H), 8.025-7.949 (m, 3H), 7.858 (s, 1H), 7.844 (s, 1H), 7.699 (d, J=6 Hz, 1H), 7.653 (dt, J=8.5 Hz, 1.5 Hz, 1H), 7.193 (d, J=2.5 Hz, 1H), 7.117 (d, J=2.5 Hz, 1H), 6.930 (dt, J=6.5

Hz, 1 Hz, 1H), 6.480 (d, J=8.5 Hz, 1H), 1.212 (s, 9H), 1.075 (s, 9H); ^{13}C NMR (500 MHz, δ/ppm, $CDCl_3$): 159.71, 154.55, 147.14, 146.98, 141.77, 140.38, 137.25, 133.67, 132.67, 132.48, 130.76, 129.45, 127.40, 118.80, 115.49, 108.86, 35.37, 33.87, 31.25, 29.33; DEPT–45 NMR (500 MHz, δ/ppm, $CDCl_3$): 147.14, 146.97, 140.38, 132.67, 132.49, 129.45, 127.40, 118.80, 108.86, 31.25, 29.32.

4.4.4. X–ray crystallography

The X–ray data collection and processing for $[Co(Phimp)_2]ClO_4 \cdot CH_3CN$ (**7**$\cdot CH_3CN$) were performed on Bruker Kappa Apex–II CCD diffractometer by using graphite monochromated Mo–Kα radiation (λ = 0.71073 Å) at 296 K to a maximum $^{-}$ range of 26°.

Table 4.9 Crystal data and structure refinement details for complex **7**$\cdot CH_3CN$

Empirical formula	$C_{76}H_{62}N_{13}O_{12}Cl_2Co_2$
Formula weight ($gmol^{-1}$)	1538.15
Temperature /K	296(2)
λ (Å) (Mo-Kα)	0.71073
Crystal system	Monoclinic
Space group	*P 21/n*
a (Å)	9.8116(11)
b (Å)	16.5103(18)
c (Å)	21.387(3)
~ (°)	90.00
β (°)	101.971(5)
γ (°)	90.00
V ($Å^3$)	3389.2(7)
Z	2
Crystal size (mm)	0.25 × 0.21 × 0.17
F(000)	1586
Theta range for data	2.45–26.46
Index ranges	-12< *h*< 10,-20<*k* <20,-26<*l*<26
Refinement method	Full matrix least–squares on F^2
Data/restraints/parameters	6987/154/477
GOF on F^2	1.070
*R*1[$I > 2\sigma(I)$]	0.0655
*R*1[all data]	0.1247
*wR*2 [$I > 2\sigma(I)$]	0.1555
*wR*2 [all data]	0.1884

The crystal data and structure refinement details for $[Co(Phimp)_2]ClO_4 \cdot CH_3CN$ (**7**$\cdot CH_3CN$) are given in Table 4.9.

4.4.5. DNA binding and cleavage experiments

Fluorescence quenching experiments were carried out by successive addition of metal complexes (0–11 μM) to the DNA (25 μM) solutions containing 5 μM ethidium bromide (EB) in 0.1 M phosphate buffer (pH 7.2) and the reaction mixture was incubated for 2 min after each successive addition of quencher molecules. For better solubility of complexes 2% DMF was used. These samples were excited at 250 nm and emissions were observed between 500 and 700 nm. Stern–Volmer quenching constants K_{SV} were calculated according to the reported procedure.[332,404] Circular dichroism (CD) spectra of CT–DNA in absence and presence of metal complexes were recorded with a 0.1 cm pathJlength cuvette after 15 min incubation at 25 °C with three scans averaged for each CD spectrum. The concentration of the complexes and CT–DNA were 50 and 200 μM respectively.

Cleavage of plasmid DNA was monitored by using agarose gel electrophoresis. Supercoiled pBR322 DNA (70 ng) in Tris–boric acid–EDTA (TBE) buffer (pH 8.2) was treated with metal complexes (50─100 μM for **7**$\cdot CH_3CN$; 5 μM─50 μM for **8**) in the absence or presence of additives like H_2O_2 (200 μM) and BME (200 μM). The mechanism of DNA cleavage by complex **8** was studied in presence of DMSO, ethanol, urea, NaN_3, L–histidine (20 mM each) and catalase (10 U) as scavenging agents. The samples were incubated for 5 min to 1.5 h at 37 °C followed by the addition of loading buffer (25% bromophenol blue and 30% glycerol) prior to the gel electrophoresis. The details regarding the procedures of DNA binding and DNA cleavage experiments have been described in *Chapter 1*.

4.4.6. Protein binding and cleavage experiments

The stock solutions of BSA were prepared by dissolving solid BSA (1×10^{-4} mol L^{-1}) in 0.1 M phosphate buffer at pH 7.2, storing at 0─4 °C for three days under dark conditions and then diluting with 0.1 M phosphate buffer (pH 7.2) to the desired concentration. The concentration of protein solution was determined from the absorption spectral data using the molar absorptivity value of ε_{280} = 44720 for BSA.[345] Quenching of the intrinsic fluorescence of tryptophan residues of BSA was carried out using metal complexes as quencher molecules. BSA solution (2×10^{-6} M) in 0.1 M phosphate buffer (pH 7.2) with 2% DMF was equilibrated for 30 min at room temperature and the emission spectrum was recorded between 300 and 600 nm using the excitation wavelength of 295 nm which is selective for tryptophan residues.[346] Incremental additions of the quenchers (0–40 μM for complex **7**·CH_3CN, 0–22 μM for complex **8**) were made to the BSA solution followed by an incubation period of 2 min after each successive addition and the spectra were recorded. Binding behaviors of the quencher molecules with serum albumin were compared using the Stern–Volmer and Scatchard graphs.[347] In order to investigate the binding site of metal complexes, site marking experiments were carried out in presence of warfarin and ibuprofen (for site I and site II respectively). For this purpose, BSA was equilibrated with warfarin ([BSA] = 40 μM; [warfarin] = 80 μM) or ibuprofen ([BSA] = [ibuprofen] = 2 μM) in 0.1 M phosphate buffer (pH = 7.2) for 1 h at 25 °C and emission spectral changes were recorded in presence of varying concentrations of metal complexes.[499,500]

Protein cleavage experiments were performed by incubating BSA (15 μM) with complexes **7**·CH_3CN and **8** (10–50 μM) in 10 mM HEPES buffer (pH 7.3) containing 10% DMF for 20 h at 50 °C. After the completion of the incubation period, an aliquot was mixed with loading buffer containing 100 mM Tris HCl (pH 6.8), 4% (w/v) sodiumdodecyl

sulphate, 0.2% (w/v) bromophenol blue, 20% (v/v) glycerol and 200 mM dithiothreitol. After the denaturation of protein solution, samples were subjected to SDS–PAGE. In order to investigate the role of ROS (reactive oxygen species) in protease activity, potential radical scavengers like DMSO (20%), glycerol (20%), NaN_3 (20 mM) and catalase (10 U) were introduced during incubation. The details of protein interaction and protein cleavage experiments have been described in *Chapter 1*.

4.4.7. Cell viability assay

MTT assay was carried out according to the procedure described by Mosmann et al.[344] using COS, DU–45, C127–I, MCF–7 and C3H10T1/2 cell lines. 5–Fluorouracil was used as a positive anticancer drug in this experiment. The cells were maintained in tissue culture plate in DMEM supplemented with 10% fetal bovine serum (FBS), 1× antibiotic–antimycotic solution and 2 mM glutamine at 37 °C in humidified atmosphere in a CO_2 incubator. During all the experiments, the cells were within passage number about 12–20 for all cell lines except COS–1 which was in its 30–35 passage. Detailed experimental procedure of cell viability assay has already been described in *Chapter 1*.

5.1. Introduction

Metal coordinated radical species are known to play key roles in a variety of biological processes. Majority of the recent investigations in the realm of metal–coordinated phenoxyl radicals are focused to the precise description of electronic structure of such species and exploration of the locus of oxidation during their generation.[214,215,218,260,503] It is important to note that the electronic distribution in the oxidized forms of metal–phenolate complexes is mainly governed by the nature of metal ion.[214] Among them, nickel coordinated radicals have always been fascinating the researchers by their intriguing properties. Interestingly, square–planar Ni(II)–N_2O_2 complexes of non–innocent salen ligands afford corresponding Ni(II)–phenoxyl radical species on one–electron oxidation where the location of the radical can be controlled by rational designing of the ligands through substituent group variation and pH modification.[215,503] Furthermore, nickel(II) complexes derived from tetraanionic diamido–diphenoxo ligands exhibit duality in their behaviors and give rise to nickel(III) complexes as well as nickel(II)–coordinated phenoxyl radical species on one–electron oxidation.[503] This behavior results from the similarity of energies of ligand–based and metal–based redox active orbitals in the complexes and may be described as a function of nature of the ligand field as well as temperature of the system.[260] Additionally, certain degree of solvent dependency of the oxidation processes has also been observed in tetra–coordinated Ni(II)–phenolate complexes.[260] Ni(II)–bisphenolate complexes possessing octahedral coordination environment pose a subtle balance between the states arising from ligand and metal centered oxidations respectively.[260] Investigation of the literature revealed that certain Ni(II) systems derived from salen or porphyrin ligands may exhibit a temperature–dependent tautomerism between a high–valent metal–phenolate or a

metal–coordinated phenoxyl radical state.[214] Hence the properties of nickel(II)–phenoxyl radical complexes are rather peculiar and deserve further attention.[503]

In this chapter, we have synthesized and characterized a series of mononuclear nickel(II) complexes derived from meridional tridentate ligands Pyimpy (*Chapter 2*, Scheme 2.1), PhimpH and ^{t}BuPhimpH (*Chapter 4*, Scheme 4.1). Molecular structures of the representative complexes $[Ni(Phimp)_2]\cdot 3H_2O\cdot CH_3OH$ (**9a**$\cdot 3H_2O\cdot CH_3OH$) and $[Ni(Phimp)(Pyimpy)](ClO_4)\cdot H_2O$ (**9c**$\cdot H_2O$) were determined by X–ray crystallography. These complexes gave rise to phenoxyl radical species through ligand centered oxidation which were characterized by UV–vis and EPR spectroscopy. Redox behavior of the nickel complexes was also investigated by cyclic voltammetric experiments. DNA interaction properties of these complexes were examined by various spectroscopic techniques and their nuclease activity was also investigated. The mechanism of nuclease activity was established by inhibition experiments involving potential radical scavengers. Protein interaction studies on these complexes were accomplished using BSA and their sites of binding in BSA were explored through site marking experiments.

5.2. Results and discussion

5.2.1. Synthesis and characterization of ligands

The ligands Pyimpy, PhimpH and ^{t}BuPhimpH were prepared as described in *Chapter 2* and *Chapter 4*.

5.2.2. Synthesis and characterization of nickel complexes

Complexes $[Ni(Phimp)_2]$ (**9a**) and [Ni(Phimp)Cl] (**9b**) were prepared by the reaction of $NiCl_2\cdot 6H_2O$ and deprotonated ligand ($Phimp^{-}$) in 1:2 and 1:1 molar ratios respectively. For the synthesis of complex $[Ni(Phimp)(Pyimpy)]ClO_4$ (**9c**), the complex **9b** was used as the

starting material and the ligand Pyimpy was charged in 1:1 molar ratio. One equivalent of sodium perchlorate was added in the reaction mixture to provide the counter anion for charge neutralization. The complexes [Ni(^{t}BuPhimp)$_2$] (**10a**), [Ni(^{t}BuPhimp)Cl] (**10b**) and [Ni(Phimp)(Pyimpy)]ClO_4 (**10c**) were synthesized in similar manner using ^{t}BuPhimpH as ligand in place of PhimpH. All the reactions were performed in open atmosphere and the complexes were obtained in good yields. The synthetic procedures of nickel complexes are summarized in Scheme 5.1.

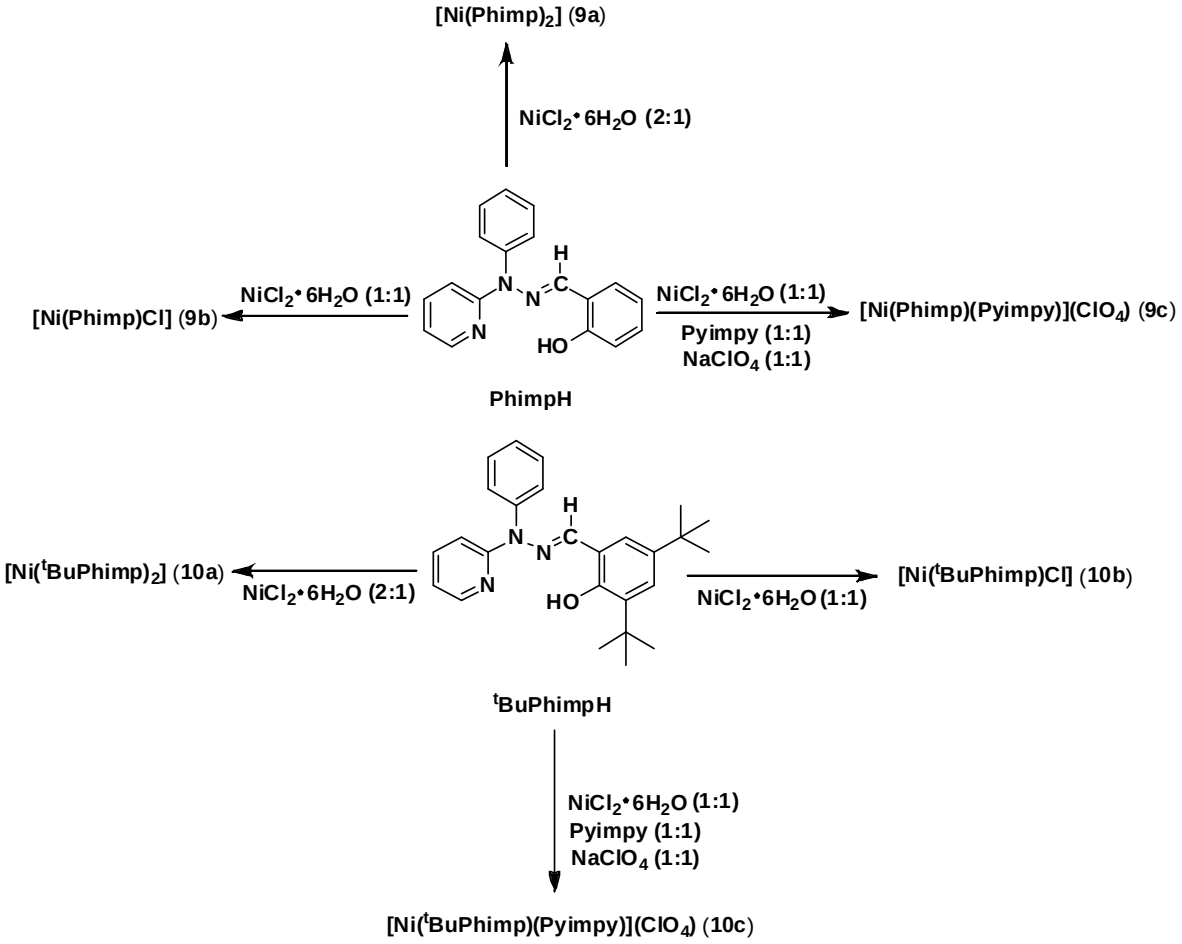

Scheme 5.1 Schematic drawing of synthesis of complexes **9** and **10**

Table 5.1 Data for yield, elemental analysis, IR, conductivity and magnetic moment

Complex	Yield %	Elemental analysis			IR data (cm^{-1})[a]	Conductivity i_M ($t^{-1}cm^2mol^{-1}$)[b]	Magnetic moment (μ_B)
		C	H	N	¬C=N		
9a	91	61.27	5.24	11.79	1602	1	2.95
9b	95	55.94	3.80	11.56	1602	51	J
9c	60	57.27	4.32	13.20	1602, 1098, 623	66	3.20
10a	91	72.15	6.90	9.92	1607	135	3.17
10b	51	64.02	6.23	8.39	1607	25	–
10c	57	62.57	5.45	11.34	1607, 1101, 623	65	3.42

[a]KBr pellets, [b]Solvent: dimethylformamide

(i) IR spectral studies

IR spectra of nickel complexes **9a**, **9b** and **9c** exhibited only weak shifting to lower wavenumbers in $\nu_{(C=N)}$ (~5 cm^{-1}) as compared to the free ligand due to the coordination of azomethine nitrogen with nickel ion. However, the complexes **10a**, **10b** and **10c** exhibited remarkable shifts in $\nu_{(C=N)}$ to higher wavenumbers (~20 cm^{-1}) as compared to the free ligand in their IR spectra. In IR spectra of all complexes, disappearance of the peak near 3450 cm^{-1} predicted the coordination of phenolato oxygen in the deprotonated form. Presence of two sharp peaks near 1439 and 1236 cm^{-1} respectively, in the IR spectra of complexes **9c** and **10c** probably indicated the presence of Pyimpy in the coordinated form. The complexes **9c** and **10c** showed unsplitted IR bands near 1098 and 1101 cm^{-1} respectively, along with a peak near 623 cm^{-1}. These data suggested the presence of a non–coordinating perchlorate ion outside their coordination sphere.[332]

(ii) Electronic properties

Intense absorption bands were observed in the UV–visible spectra of all nickel complexes between 200–300 nm region. These bands were assigned as π–π* intra–ligand transitions (Fig. 5.1, Table 5.2). The absorption bands with λ_{max} between 350–450 nm found

in the UV–visible spectra of all complexes in methanol were accompanied with high molar extinction coefficient values which suggested that these bands were originating from ligand to metal charge transfer transitions (LMCT).[216,504] It is important to note that the complex **10a** exhibited charge transfer bands associated with considerably low values of extinction coefficients among the series in spite of its bis speciation which probably indicates that the electronic structure of **10a** is remarkably different from those of other members of the series (Table 5.2).

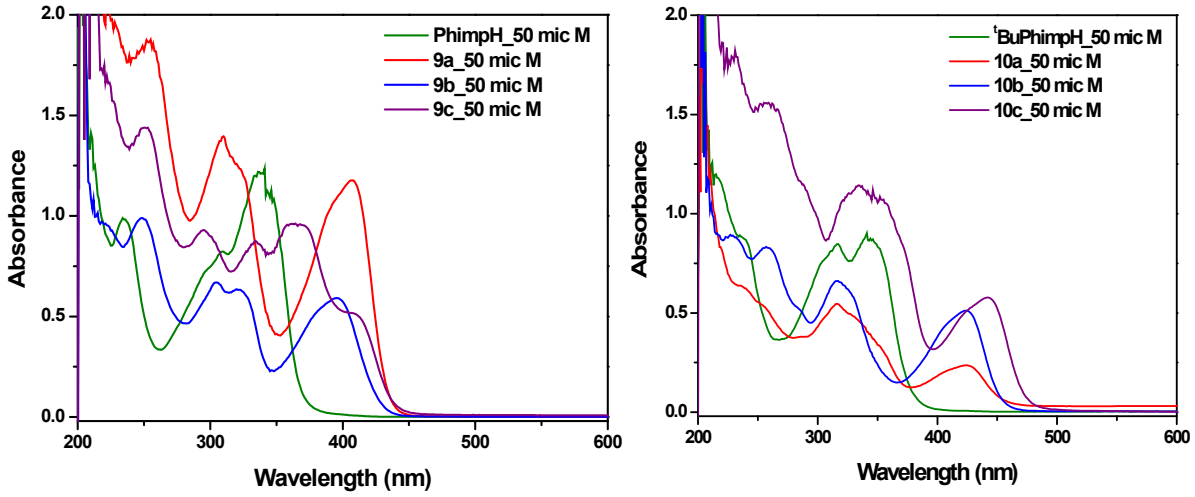

(a) (b)

Fig. 5.1 UV–visible spectra of complexes **9-10** (50 μM) in methanol

Table 5.2 UV–visible spectral data of complexes **9–10**

Complex	$^{a}\lambda_{max}$**/nm (£/M^{-1}cm^{-1})**[a]
9a·3H_2O·CH_3OH	255 (37740), 311 (28220), 324 *sh* (24720), 393 *sh* (21440), 407 (23740)
9b	249 (20080), 304 (13500), 320 (12860), 395 (11880)
9c·H_2O	251 (28900), 294 (18620), 334 (17480), 364 (19180), 408 (10260)
10a	235 (12800), 255 (10820), 316 (10940), 332 (9540), 425 (4920)
10b	228 (17940), 257 (16780), 282 *sh* (10780), 316 (13280), 407 (8940), 425 (10260)
10c	257 (31160), 286 *sh* (23160), 333 (22900), 353 (21580), 423 *sh* (10120), 442 (11680)

[a]UV–visible data recorded in methanol

(iii) ESIJMass spectroscopy

The nickel complexes **9-10** (**a**, **b** and **c**) were subjected to ESI–Mass spectrometric analysis in acetonitrile:water (1:1) mixture and analyzed under positive mode. The ESI–Mass spectrum of complex **9a** showed two major peaks with m/z values of 635.16 (relative intensity 100%) and 657.14 (relative intensity 6.6%) due to the formation of $[M+H]^+$ and $[M+Na]^+$ cations respectively (Fig. 5.2). In case of complex **9b**, two peaks were observed with (m/z) values of 346.04 (relative intensity 100%) and 404.00 (relative intensity 3.4%) corresponding to the generation of $[M-Cl]^+$ cation due to the loss of one chloride ion and $[M+Na]^+$ cations respectively (Fig. 5.3). ESI–Mass spectrum of complex **9c** consisted of only single peak at (m/z) value of 620.16 (relative intensity 100%) suggesting the formation of $[M-ClO_4]^+$ cation by losing one perchlorate anion present outside the coordination sphere (Fig. 5.4).

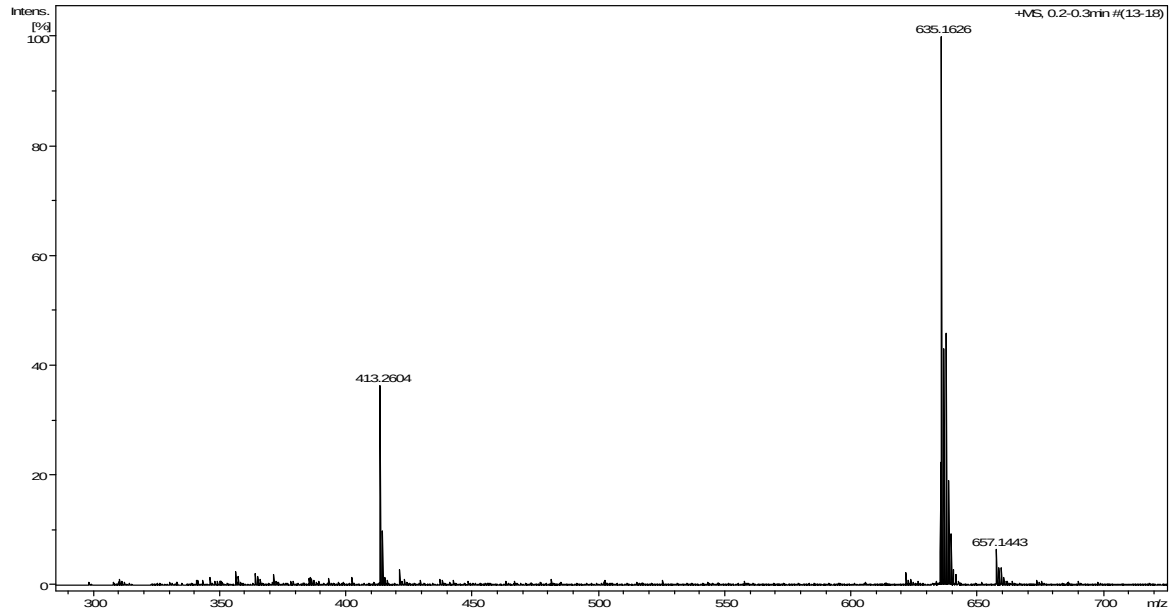

Fig. 5.2 The ESI–mass spectrum of $[Ni(Phimp)_2]$ (**9a**) in acetonitrile under positive mode showing the peak at (m/z) 635.16 (relative intensity 100%) and (m/z) 657.14 (relative intensity 6.6%) corresponding to the formation of $[M+H]^+$ and $[M+Na]^+$ cations respectively

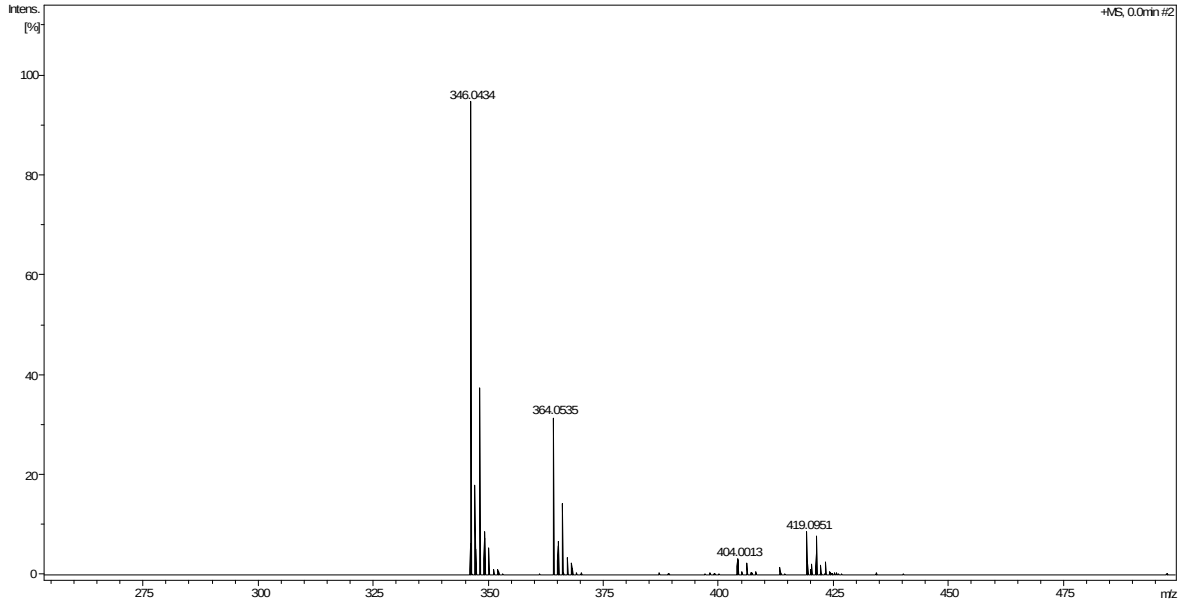

Fig. 5.3 The ESI–mass spectrum of [Ni(Phimp)Cl] (**9b**) in acetonitrile under positive mode showing the peaks at (m/z) 346.04 (relative intensity 100%) and (m/z) 404.00 (relative intensity 3.4%) corresponding to the formation of $[M\text{-}Cl]^+$ and $[M+Na]^+$ cations respectively

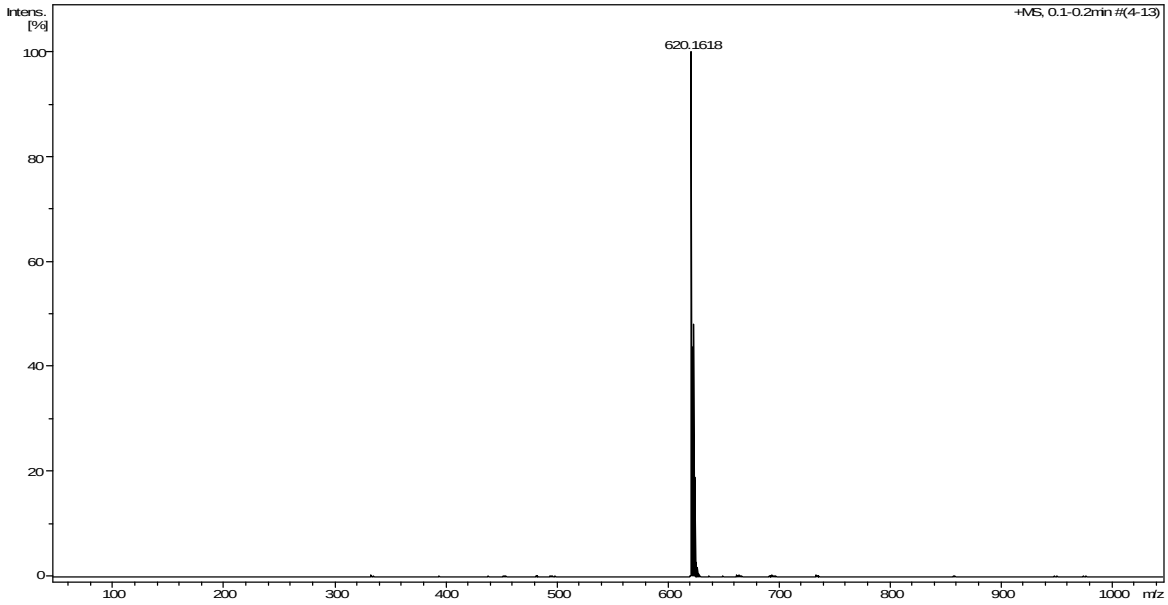

Fig. 5.4 The ESI–mass spectrum of $[Ni(Phimp)(Pyimpy)]ClO_4$ (**9c**) in acetonitrile under positive mode showing the peak at (m/z) 620.16 (relative intensity 100%) corresponding to the formation of $[M\text{-}ClO_4]^+$ cation

ESI-Mass spectrum of **10a** showed a peak at (m/z) value of 858.40 (relative intensity 100%) which may probably be ascribed to the formation of $[M]^+$ cation (Fig. 5.5). The peak present at (m/z) value of 458.16 (relative intensity 100%) in the ESI–Mass spectrum of complex **10b** indicated the formation of $[M\text{-}Cl]^+$ cation by the loss of one coordinated chloride anion (Fig. 5.6). ESI–Mass spectrum of the nickel complex **10c** showed a peak with (m/z) value of 732.28 (relative intensity 100%) which warranted the generation of $[M\text{-}ClO_4]^+$ cation by the loss of one perchlorate anion present outside the coordination sphere (Fig. 5.7).

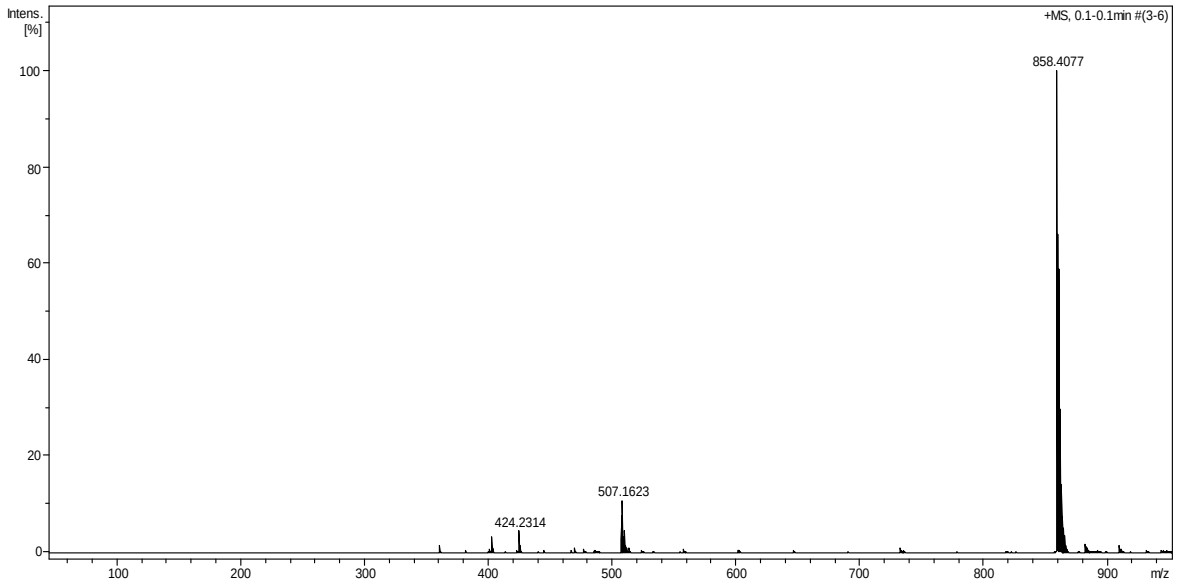

Fig. 5.5 The ESI–mass spectrum of $[Ni(^tBuPhimp)_2]$ (**10a**) in acetonitrile under positive mode showing the peak at (m/z) 858.40 (relative intensity 100%) corresponding to the formation of $[M]^+$ cation

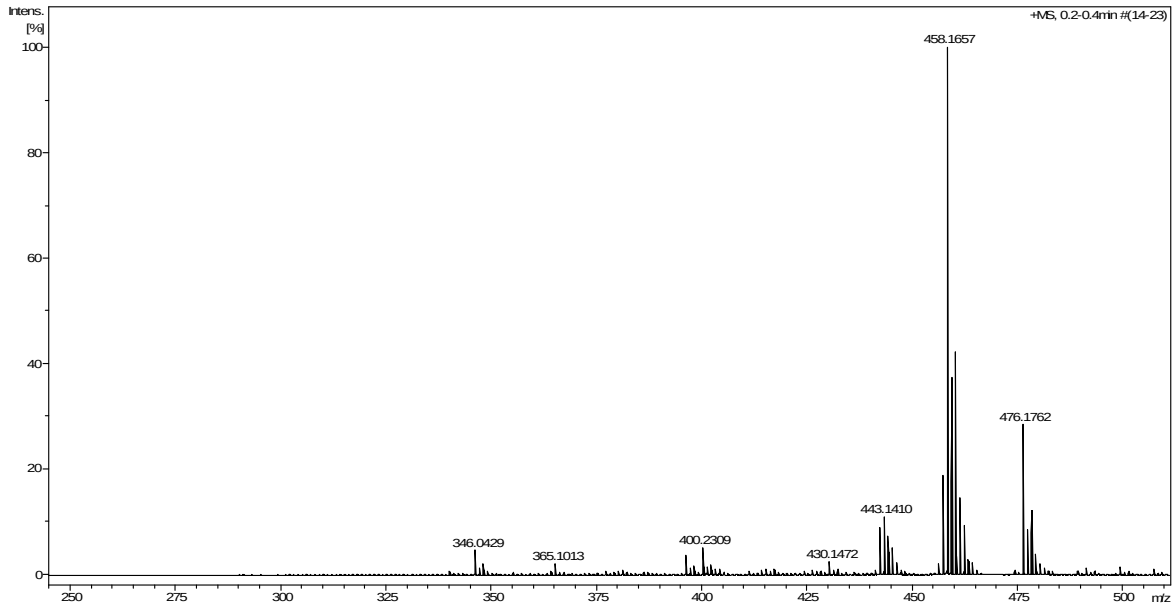

Fig. 5.6 The ESI–mass spectrum of [Ni(^{t}BuPhimp)Cl] (**10b**) in acetonitrile under positive mode showing the peak at (m/z) 458.16 (relative intensity 100%) corresponding to the formation of $[M\text{-}Cl]^+$ cation

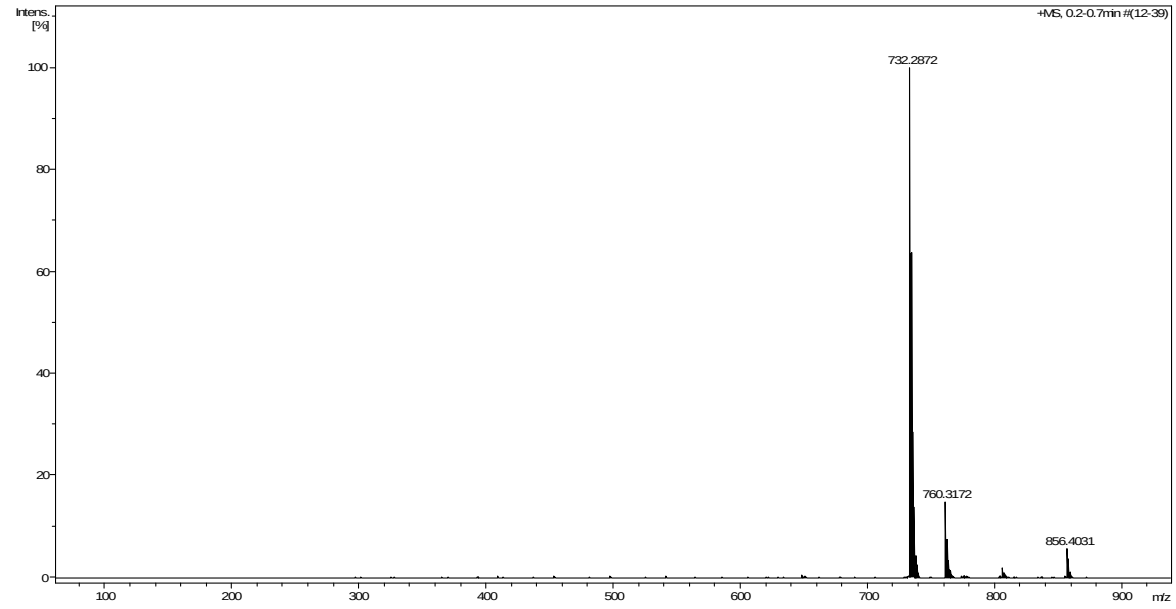

Fig. 5.7 The ESI–mass spectrum of [Ni(Phimp)(^{t}BuPyimpy)]ClO_4 (**10c**) in acetonitrile under positive mode showing the peak at (m/z) 732.28 (relative intensity 100%) corresponding to the formation of $[M\text{-}ClO_4]^+$ cation

(iv) Conductivity measurements

The molar conductivity measurements at room temperature for complexes **9a** and **9c** in DMF solution (*ca.* 10^{-3} M) gave rise to their neutral electrolytic behavior with conductivity values of 1 and 51 $\Omega^{-1}cm^2mol^{-1}$ respectively.[387] Complex **9c** afforded the conductivity value of 66 $\Omega^{-1}cm^2mol^{-1}$ at room temperature indicating its uni-univalent electrolytic behavior due to the presence of one non–coordinating perchlorate anion outside the coordination sphere.[387] The complex **10a** showed much higher value for conductivity (135 $\Omega^{-1}cm^2mol^{-1}$) in DMF solution than expected for a neutral complex.[387] The molar conductivity values for complexes **10b** and **10c** were found to be 25 and 65 $\Omega^{-1}cm^2mol^{-1}$ respectively. These data suggested their neutral (**10b**) and uni–univalent (**10c**) electrolytic nature in solution similar to that exhibited by **9b** and **9c** respectively.[387]

(v) Magnetic moment studies

Solid state magnetic susceptibility measurements for complexes **9a**, **9c**, **10a** and **10c** at room temperature fall within the range of 2.95–3.42 B. M. which suggested the presence of two unpaired electrons at Ni(II) center. These values were found to be much higher than the spin only value (2.83 B. M.) but consistent with those reported for other Ni(II) complexes.[505] The complexes **9b** and **10b** were found to be diamagnetic in nature indicating square–planar coordination environment of Ni(II) in these complexes.

5.2.3. Description of molecular structures

To confirm the mode of coordination of ligands with the Ni(II) center, single crystals of $[Ni(Phimp)_2]\cdot 3H_2O\cdot CH_3OH$ (**9a**$\cdot 3H_2O\cdot CH_3OH$) and $[Ni(Phimp)(Pyimpy)](ClO_4)\cdot H_2O$ (**9c**$\cdot H_2O$) were grown and subjected to X–ray diffraction studies. X–ray quality crystals of **9a**$\cdot 3H_2O\cdot CH_3OH$ were grown by slow evaporation of the solution of compound in

dichloromethane:methanol (9:1) mixture. The asymmetric unit of **9a**·$3H_2O$·CH_3OH comprises half of the mononuclear Ni(II) molecule **9a** being located about the center of inversion, three water molecules and one methanol molecule as lattice molecules of solvation. ORTEP representation of the molecular structure of **9a**·$3H_2O$·CH_3OH is shown in Fig. 5.8. The complex **9a**·$3H_2O$·CH_3OH consists of Ni(II) ion held in pseudo-octahedral coordination environment. The metal ion is encompassed by two deprotonated PhimpH ($Phimp^-$) ligands which coordinate through imine nitrogen (N1), pyridine nitrogen (N2) and oxygen atom (O1) of the phenolato group. Selected bond distances and bond angles in **9a**·$3H_2O$·CH_3OH are listed in Table 5.3. The Ni(II)–$O_{phenolate}$ (Ni–$O^{a\ or\ b}$(1)), Ni(II)–N_{imine} (Ni–$N^{a\ or\ b}$(1)) and Ni–$N_{pyridine}$ (Ni–$N^{a\ or\ b}$(2)) bond distances were found to be 2.021 Å, 2.025 Å and 2.096 Å respectively which are typical for high–spin nickel(II) pseudo-octahedral complexes.[506] The ligands are arranged in a meridional fashion around the metal center which enforces a *cis*–orientation of the phenolate moieties [O^a(1)−Ni(1)−O^b(1) bond angle is 94.975(78)°; symmetry codes (a) x, y, z; (b) y, x, 0.5-z]. The imine nitrogens are arranged *trans*J to each other with N^a(1)−Ni(1)−N^b(1) bond angle equal to 173.957 (102)°. The N^a(2)−Ni(1)−N^b(2) bond angle was found to be 87.645(83)° indicating a mutually *cis*–orientation of the pyridine nitrogen atoms in two ligands. The octahedral geometry of the complex is considerably distorted and the distortion is manifested by the bond angles $N^{a\ or\ b}$(1)−Ni(1)−$N^{b\ or\ a}$(2) (78.512°) and $O^{a\ or\ b}$(1)−Ni(1)−$N^{b\ or\ a}$(2) (167.751°). These bond angles differ significantly from the ideal values of 90° and 180° for a perfectly octahedral geometry. The phenyl rings were almost perpendicular with the ligand binding plane affording the angle (phenyl ring vs. meridional plane) of 88.30°.

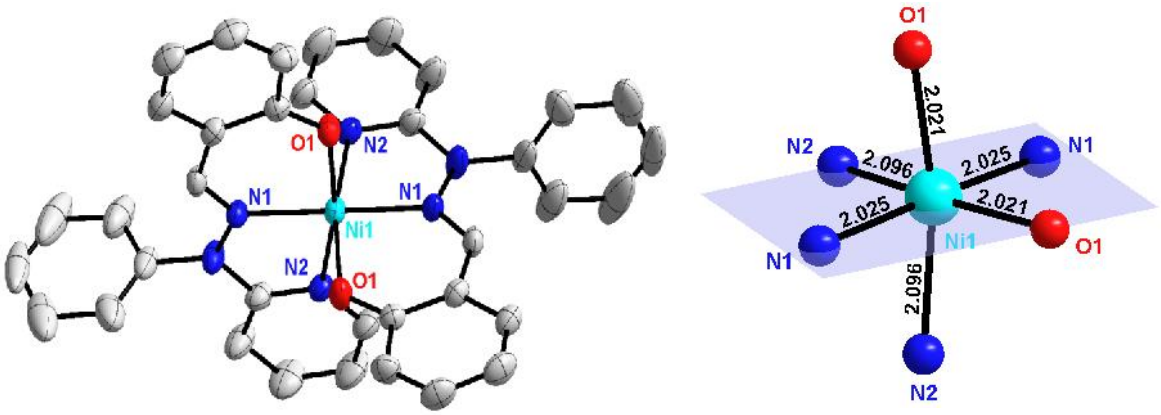

(a) (b)

Fig. 5.8 (a) ORTEP representation of the crystal structure of $[Ni(Phimp)_2]\cdot 3H_2O\cdot CH_3OH$ (**9a**$\cdot 3H_2O\cdot CH_3OH$) showing atom numbering scheme and displacement ellipsoid (50% probability level). Hydrogen atoms and solvent molecules are omitted for clarity; (b) octahedral disposition of donor atoms around metal center

Table 5.3 Selected bond lengths (Å) and angles (˚) for $[Ni(Phimp)_2]\cdot 3H_2O\cdot CH_3OH$ (**9a**$\cdot 3H_2O\cdot CH_3OH$)

Bond lengths (Å)		**Bond angles (˚)**	
$Ni(1)-N(1)^a$	2.0247 (30)	$N^a(1)-Ni(1)-N^b(1)$	173.957 (102)
$Ni(1)-N(1)^b$	2.0247 (30)	$N^b(1)-Ni(1)-N^b(2)$	97.071 (90)
$Ni(1)-N(2)^a$	2.0958 (19)	$N^a(1)-Ni(1)-N^b(2)$	78.512 (88)
$Ni(1)-N(2)^b$	2.0958 (19)	$N^b(1)-Ni(1)-N^a(2)$	78.512 (96)
$Ni(1)-O(1)^a$	2.0207 (18)	$N^a(1)-Ni(1)-N^a(2)$	97.071 (94)
$Ni(1)-O(1)^b$	2.0208 (18)	$N^a(2)-Ni(1)-N^b(2)$	87.645 (83)
		$O^b(1)-Ni(1)-N^b(1)$	89.902 (84)
		$O^b(1)-Ni(1)-N^a(1)$	94.184 (82)
		$O^a(1)-Ni(1)-N^b(1)$	94.184 (86)
		$O^a(1)-Ni(1)-N^a(1)$	89.902 (84)
		$O^b(1)-Ni(1)-N^b(2)$	89.878 (80)
		$O^b(1)-Ni(1)-N^a(2)$	167.751 (80)
		$O^a(1)-Ni(1)-N^b(2)$	167.751 (79)
		$O^a(1)-Ni(1)-N^a(2)$	89.878 (82)
		$O^a(1)-Ni(1)-O^b(1)$	94.975 (78)

Symmetry equivalents: (a) x, y, z; (b) y, x, 0.5-z

The crystal structure of **9a**$\cdot 3H_2O\cdot CH_3OH$ featured a large number of non–covalent interactions including C–H···π interactions and hydrogen–bonding which consolidated a

three–dimensional architecture. The phenolato oxygen atoms in one molecule exhibited weak inter–molecular interactions with the phenyl hydrogen atoms of another molecule (Fig. 5.9). Furthermore, methanol molecules present in the crystal lattice also showed hydrogen bonding interactions (O–H···O interactions) with the phenolato oxygens (Fig. 5.9). The rings bearing the phenolato functions in **9a**·$3H_2O$·CH_3OH were found to be associated with one another through extensive C–H···π (phenyl) interactions which are holding the molecules in a "star"–shaped geometry (Fig. 5.10 a) and giving rise to a "loop" like structure (Fig. 5.10 b). The geometric parameters characterizing all sorts of hydrogen bonding interactions are included in Table 5.4. The crystal packing in **9a**·$3H_2O$·CH_3OH viewed along axis–*c* is represented in Fig. 5.11.

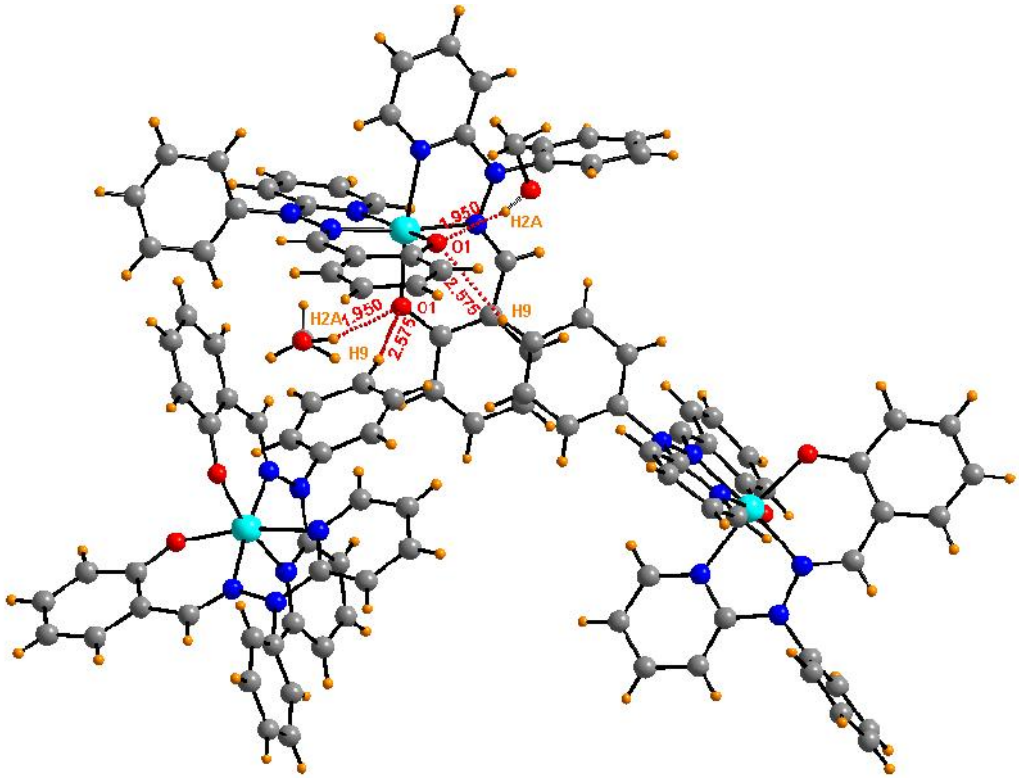

Fig. 5.9 Hydrogen–bonding network in crystals of [Ni(Phimp)$_2$]·$3H_2O$·CH_3OH (**9a**·$3H_2O$·CH_3OH)

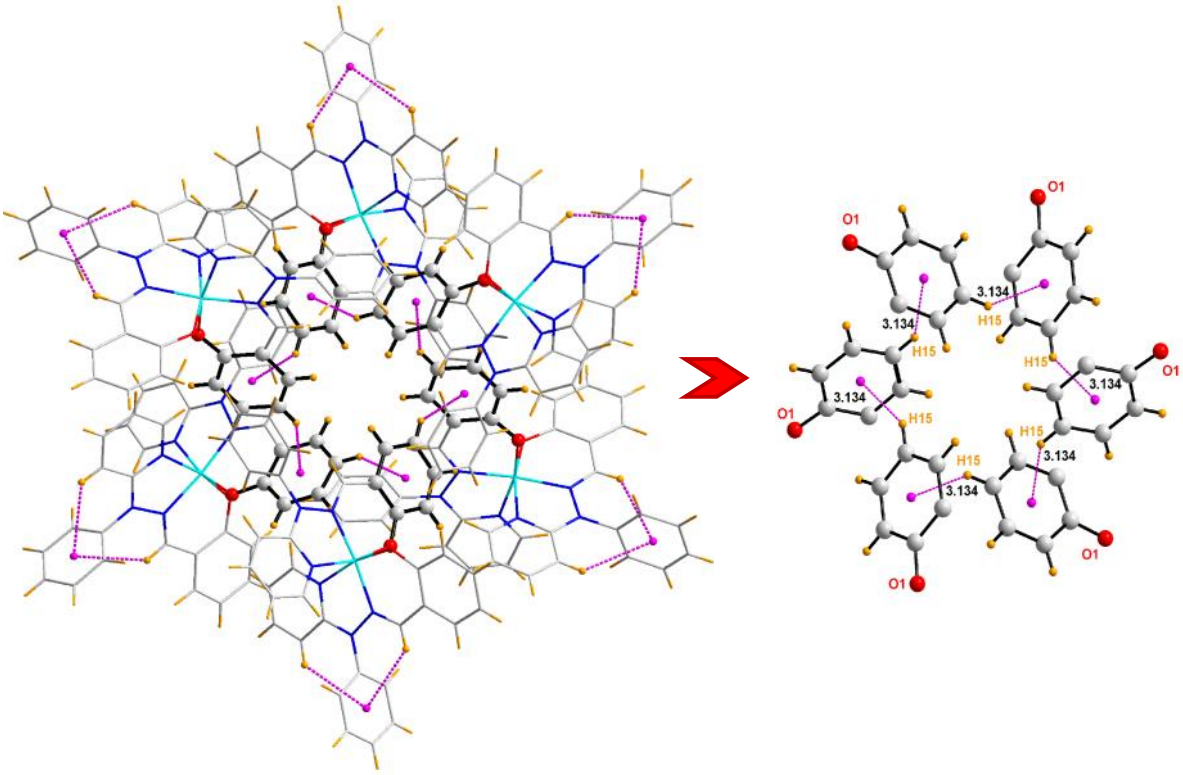

(a) (b)

Fig. 5.10 Diagrammatic representation of extensive C–H···π interactions in crystals of $[Ni(Phimp)_2]\cdot 3H_2O\cdot CH_3OH$ (**9a**·$3H_2O\cdot CH_3OH$) forming a loop like structure within star-shaped geometry

Table 5.4 Hydrogen–bonding interactions for $[Ni(Phimp)_2]\cdot 3H_2O\cdot CH_3OH$ (**9a**·$3H_2O\cdot CH_3OH$)

DJH···A	**DJH (Å)**	**D···A (Å)**	**H···A (Å)**	**DJH···A (˚)**
C17JH17···O2	0.930(4)	3.496(6)^{i}	2.950(4)^{i}	118.94(25)^{i}
C1JH1···N1	0.930(4)	3.295(4)^{i}	2.791(2)^{i}	115.10(22)^{i}
O2JH2A···O1	0.820(4)	2.734(5)^{i}	1.952(2)^{i}	159.46(28)^{i}
C7JH7···O2	0.930(5)	3.753(7)^{ii}	2.935(5)^{ii}	147.53(30)^{ii}
C8JH8···O4	0.930(8)	3.707(15)^{iii}	2.893(14)^{iii}	146.96(54)^{iii}
C9JH9···O1	0.930(11)	3.480(11)^{iii}	2.576(3)^{iii}	163.95(56)^{iii}
C8JH8···O2	0.930(8)	3.560(11)^{iii}	2.780(5)^{iii}	142.12(50)^{iii}

Symmetry equivalents: (i) x,y,z; (ii) y,+x,-z+1/2; (iii) –x+1,-x+y,-z+1/2

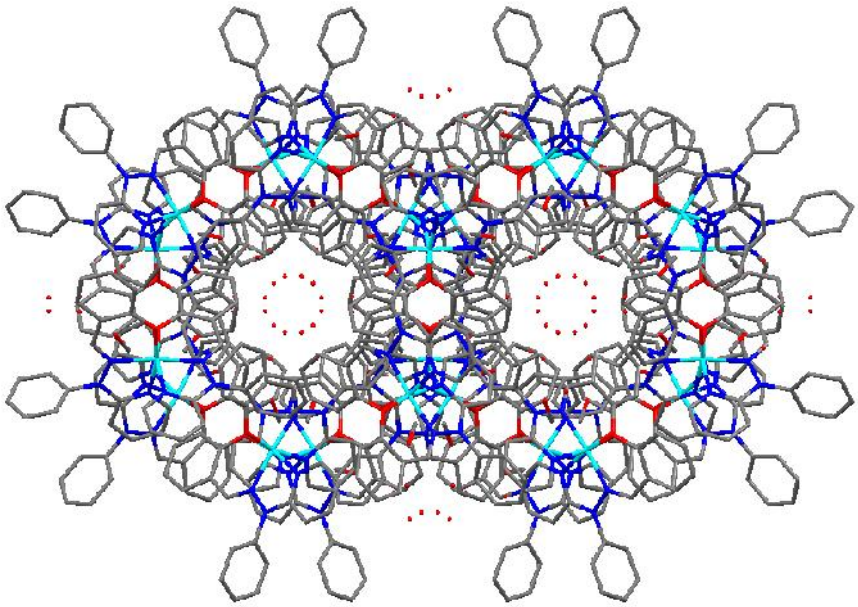

Fig. 5.11 A view of packing in projection down the '*c*'–axis in the unit cells of [Ni(Phimp)(Pyimpy)](ClO_4)·H_2O (**9c**·H_2O)

Single crystals of [Ni(Phimp)(Pyimpy)](ClO_4)·H_2O (**9c**·H_2O) for X–ray diffraction studies were developed by slow evaporation of the methanolic solution of compound. ORTEP representation of the molecular structure of **9c**·H_2O is shown in Fig. 5.12. In the mixed–ligand complex **9c**·H_2O, Ni(II) adopted a pseudo-octahedral geometry where three of the coordination sites were occupied by the deprotonated ligand $Phimp^-$ coordinating through phenolato oxygen, imine nitrogen and pyridine nitrogen donors. The remaining three coordination site were defined by the neutral ligand Pyimpy which coordinated to Ni(II) through two pyridine and one imine nitrogen donors. Selected bond distances and bond angles in **9c**·H_2O are listed in Table 5.5. All bond distances were found consistent with those of **9a**·$3H_2O$·CH_3OH and the reported values for analogous compounds representing a high–spin Ni(II) ion in pseudo–octahedral geometry.[506] The N(II)–N_{imine} and N(II)–$N_{pyridine}$

bond distances for the ligand $Phimp^{-}$ were comparatively shorter than those observed for the ligand Pyimpy.

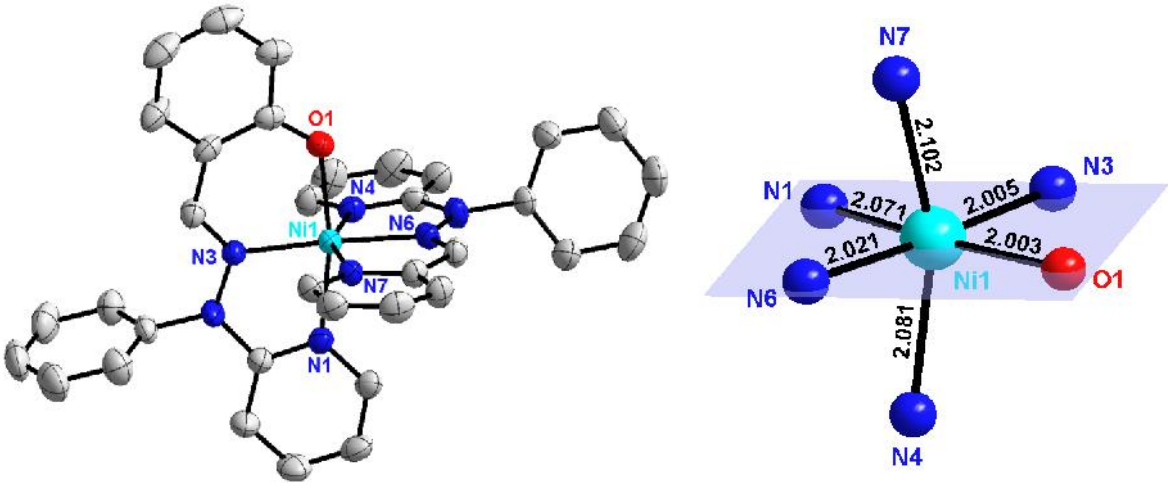

(a) (b)

Fig. 5.12 (a) ORTEP representation of crystal structure of [Ni(Phimp)(Pyimpy)](ClO_4)·H_2O (**9c**·H_2O) showing atom numbering scheme and displacement ellipsoid (50% probability level). Hydrogen atoms, perchlorate counter anion and solvent molecule are omitted for clarity; (b) octahedral disposition of donor atoms around metal center

Table 5.5 Selected bond lengths (Å) and angles (˚) for [Ni(Phimp)(Pyimpy)](ClO_4)·H_2O (**9c**·H_2O)

Bond lengths (Å)		**Bond angles (˚)**	
Ni(1)−N(1)	2.0709 (31)	N(1)−Ni(1)−N(4)	89.435 (109)
Ni(1)−N(3)	2.0045 (22)	N(1)−Ni(1)−N(7)	93.625 (110)
Ni(1)−N(4)	2.0814 (30)	N(3)−Ni(1)−N(6)	176.683 (113)
Ni(1)−N(6)	2.0214 (30)	N(3)−Ni(1)−N(1)	78.872 (112)
Ni(1)−N(7)	2.1016 (27)	N(3)−Ni(1)−N(4)	104.476 (119)
Ni(1)−O(1)	2.0026 (26)	N(3)−Ni(1)−N(7)	99.782 (115)
		N(6)−Ni(1)−N(1)	98.448 (122)
		N(6)−Ni(1)−N(4)	77.336 (119)
		N(6)−Ni(1)−N(7)	78.352 (119)
		N(4)−Ni(1)−N(7)	155.683 (112)
		O(1)−Ni(1)−N(3)	90.236 (99)
		O(1)−Ni(1)−N(6)	92.541 (103)
		O(1)−Ni(1)−N(1)	168.676 (106)
		O(1)−Ni(1)−N(4)	90.317 (105)
		O(1)−Ni(1)−N(7)	91.256 (104)

Symmetry equivalents: x, y, z

Both ligands exhibited meridional spanning around the metal center affording mutally *cis*– orientations among phenolato oxygen and pyridine nitrogens. The imine nitrogens in $Phimp^{-}$ and Pyimpywere arranged in mutually *trans*– orientation. The octahedral geometry in complex **9c**·H_2O exhibited considerable distortion which could be manifested by the bond angles N(6)−Ni(1)−N(4) (77.33°), N(3)−Ni(1)−N(4) (104.47°), N(4)−Ni(1)−N(7) (155.68°) and O(1)−Ni(1)−N(1) (168.67°). The phenyl rings were almost perpendicular with the ligand binding planes forming the angles (phenyl ring vs. meridional plane) of 72.04° in Pyimpy and 79.07° in $Phimp^{-}$ respectively. One perchlorate anion providing the charge balance to the nickel cation and a lattice water molecule of solvation were also present in the crystal lattice.

Several non–covalent interactions could also be observed in the crystal structure of **9c**·H_2O. These included hydrogen bonding interactions and π–stacking interactions. The crystal packing may be described as comprising of columns of complex cations interconnected by complex-C–H···O(perchlorate) interactions (Fig. 5.13).

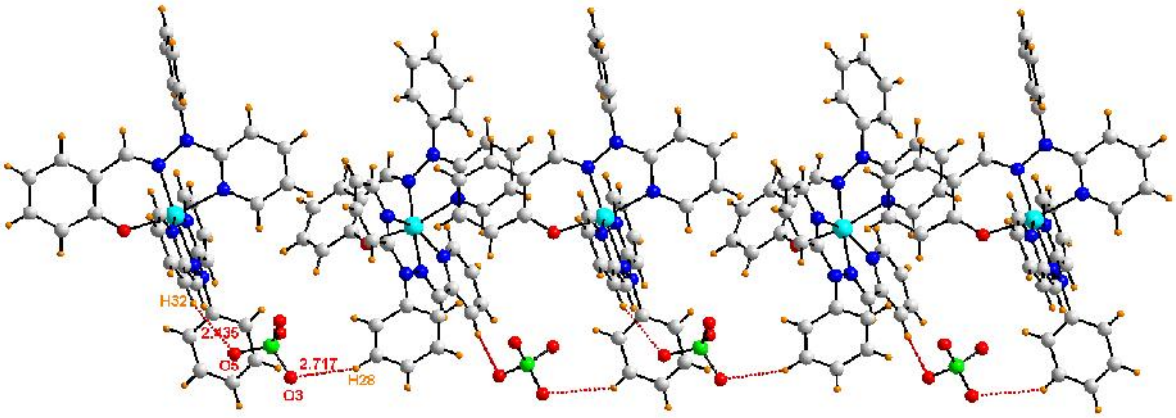

Fig. 5.13 Diagrammatic representation of hydrogen bonding network between aryl hydrogens and perchlorate oxygens in the unit cells of [Ni(Phimp)(Pyimpy)](ClO_4)·H_2O (**9c**·H_2O)

These columns were further inter–linked through hydrogen bonding interactions of aryl hydrogens with perchlorate oxygens (Fig. 5.14). This association was also complemented by π–π stacking interactions (3.763 Å) between pyridine rings of Pyimpy bearing the imine moieties (Fig. 5.14). The three–dimensional packing diagram of **9c**·H_2O viewed along axis–*a* is represented in Fig. 5.15. The geometric parameters characterizing all sorts of hydrogen bonding interactions are included in Table 5.6.

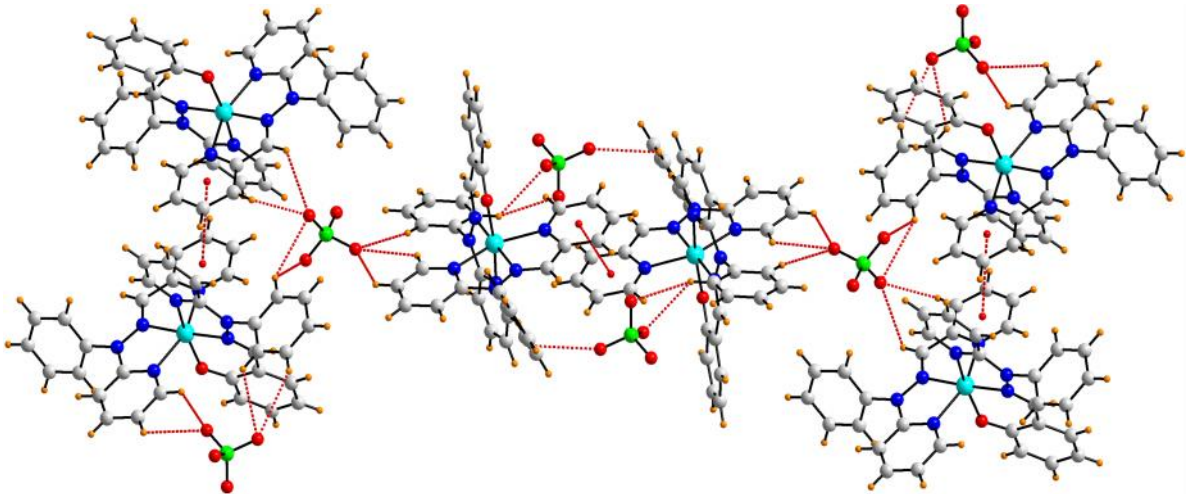

Fig. 5.14 Hydrogen bonding network and π–stacking interactions in the crystal structure of [Ni(Phimp)(Pyimpy)](ClO_4)·H_2O (**9c**·H_2O)

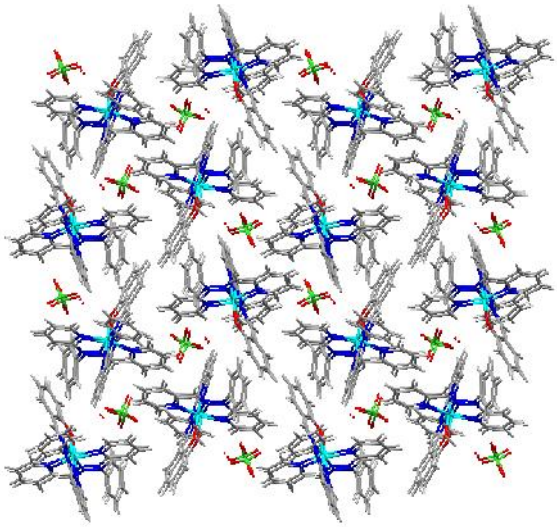

Fig. 5.15 A view of packing in projection down the '*a*'–axis in the unit cells of [Ni(Phimp)(Pyimpy)](ClO_4)·H_2O (**9c**·H_2O)

Table 5.6 Hydrogen–bonding interactions for [Ni(Phimp)(Pyimpy)](ClO_4)·H_2O (**9c**·H_2O)

DJH···A	DJH (Å)	D···A (Å)	H···A (Å)	DJH···A (˚)
C1JH1···N6	0.930(4)	3.335(5)^{i}	2.837(3)^{i}	114.77(24)^{i}
C35JH35···N3	0.930(4)	3.432(5)^{i}	2.958(3)^{i}	113.14(24)^{i}
C2JH2···O6	0.930(4)	3.305(6)^{ii}	2.799(4)^{ii}	115.27(29)^{ii}
C32JH32···O5	0.930(4)	3.314(6)^{ii}	2.434(4)^{ii}	157.81(27)^{ii}
C1JH1···O6	0.930(4)	3.224(5)^{ii}	2.612(4)^{ii}	123.93(25)^{ii}
C25JH25···O2	0.930(5)	3.324(7)^{ii}	2.851(6)^{ii}	112.82(29)^{ii}
C2JH2···O1	0.930(4)	3.796(5)^{iii}	2.929(2)^{iii}	155.58(25)^{iii}
C4JH4···O5	0.930(4)	3.318(6)^{iv}	2.799(5)^{iv}	116.32(27)^{iv}
C3JH3···O3	0.930(5)	3.614(7)^{iv}	2.830(5)^{iv}	142.66(29)^{iv}
C3JH3···O5	0.930(5)	3.411(7)^{iv}	2.971(5)^{iv}	110.58(31)^{iv}
C7JH7···O4	0.930(4)	3.463(7)^{v}	2.764(5)^{v}	132.71(30)^{v}
C34JH34···O6	0.930(4)	3.580(7)^{v}	2.671(5)^{v}	165.85(28)^{v}
C7JH7···O5	0.930(4)	3.629(7)^{v}	2.866(5)^{v}	140.09(30)^{v}
C35JH35···O4	0.930(4)	3.555(6)^{v}	2.763(4)^{v}	143.70(26)^{v}
C10JH10···O2	0.930(5)	3.501(8)^{vi}	2.866(6)^{vi}	126.55(36)^{vi}
C10JH10···O6	0.930(5)	3.811(7)^{vi}	2.899(5)^{vi}	167.00(33)^{vi}
C11JH11···O3	0.930(4)	3.669(6)^{vi}	2.757(5)^{vi}	167.04(28)^{vi}
C20JH20···O3	0.930(5)	3.559(7)^{vi}	2.949(4)^{vi}	124.49(34)^{vi}
C19JH19···O3	0.930(4)	3.528(6)^{vi}	2.861(4)^{vi}	129.64(28)^{vi}
C11JH11···O2	0.930(4)	3.548(7)^{vi}	2.970(6)^{vi}	121.72(28)^{vi}
C33JH33···N1	0.930(4)	3.715(5)^{vii}	2.952(3)^{vii}	140.16(27)^{vii}
C28JH28···O3	0.930(6)	3.471(7)^{viii}	2.717(4)^{viii}	138.77(35)^{viii}
C29JH29···O4	0.930(4)	3.606(7)^{viii}	2.924(5)^{viii}	131.30(28)^{viii}

Symmetry equivalents: (i) x,y,z; (ii) -x+1,-y+1,-z; (iii) x,-y+1/2+1,+z-1/2; (iv) -x+2,-y+1,-z; (v) x,+y+1,+z; (vi) -x+2,+y+1/2,-z+1/2; (vii) -x+1,-y+2,-z; (viii) -x+1,+y+1/2,-z+1/2

5.2.4. Electrochemical studies

To investigate the redox behaviour of nickel complexes **9-10** (a, b and c) at room temperature, cyclic voltammetric experiments were carried out under nitrogen atmosphere within the potential range -1.750 V to +1.750 V at a scan rate of 0.1 V/s using Ag/AgCl as reference electrode, glassy carbon as working electrode and platinum wire as auxiliary electrode. Fig. 5.16 (a) and (b) show the cyclic voltammograms of ca. 10^{-3} M acetonitrile

solutions of **9a**·$3H_2O$·CH_3OH and **10a** in the potential range +1.250 V to -1.250 V respectively. In spite of poor solubility of **10a**, we were successful to examine its redox behaviour in acetonitrile.

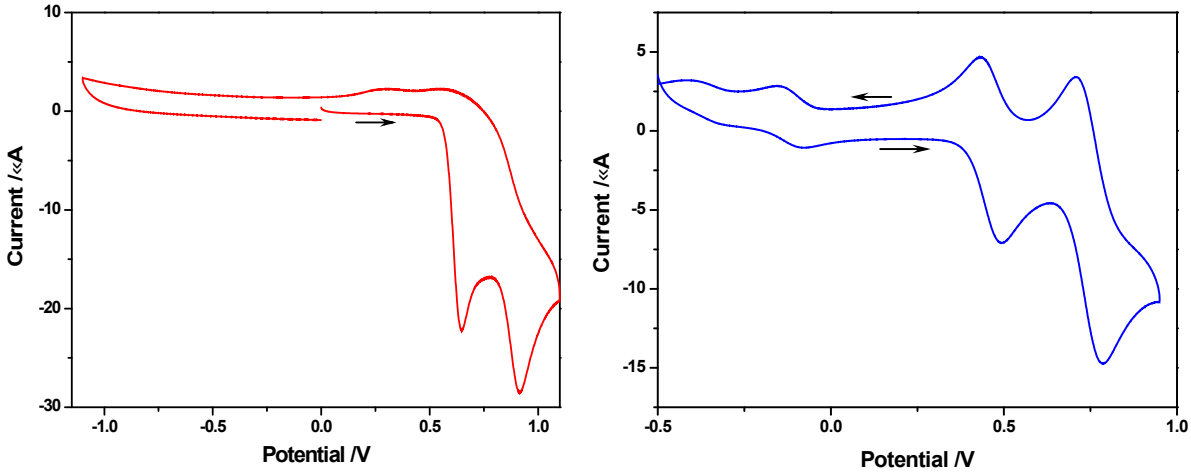

(a) (b)

Fig. 5.16 Cyclic voltammograms of 10^{-3} M solutions of (a) **9a**·$3H_2O$·CH_3OH and (b) **10a** in acetonitrile at 298 K under nitrogen atmosphere in presence of 0.1 M TBAP as a supporting electrolyte, glassy-carbon was used as working electrode, Ag/AgCl as reference electrode and platinum wire as auxiliary electrode; scan rate 0.1 V/s

The complexes **9a**·$3H_2O$·CH_3OH and **10a** exhibited two consecutive redox responses in anodic region. For **9a**·$3H_2O$·CH_3OH, the peaks were quite irreversible (E_p = +0.648 and 0.915 V vs. Ag/AgCl respectively, Table 5.7) however the reversibility of these processes enhanced appreciably on the introduction of *tert*–butyl groups in **10a** ($E_{1/2}$ = 0.460 and 0.746 V vs Ag/AgCl respectively, Table 5.7). These processes were assigned as ligand–centered oxidation, probably giving rise to mono– and bis–phenoxyl radical species successively. These potential values were found consistent with those reported for analogous octahedral Ni(II)–bis phenolate complexes.[507] It appeared that the oxidation of one phenolate moiety was influenced by the oxidation of the other phenolate moiety which was evident from the

large separation between half–wave potentials of both processes in **10a** (0.286 V).[507] These observations indicated that the coordination sphere of Ni(II) in these complexes might undergo considerable structural rearrangement after oxidation and strong electrochemical communication existed between the two chemically equivalent phenolate groups in these complexes.[507] The only reversible redox process with $E_{1/2}$ value of -0.117 V vs. Ag/AgCl exhibited by complex **10a** in the cathodic region was ascribed to the metal centered reduction ($Ni^{II} \rightarrow Ni^{I}$) (Fig. 5.16, b), however, no corresponding redox process could be observed for complex **9a**·$3H_2O$·CH_3OH (Fig. 5.16, a).

The solubility constraints of complex **9b** in acetonitrile limited the investigation of its electrochemical properties in acetonitrile. Hence we studied its electrochemical behaviour in dimethylformamide which is illustrated in Fig. 5.17 (a). The voltammogram comprised two irreversible peaks with the E_p values of 0.907 V vs. Ag/AgCl and +1.178 V vs. Ag/AgCl respectively. Additionally, a quasi–reversible peak was also found in the cathodic region with $E_{1/2}$ value of -1.012 V vs. Ag/AgCl. The electrochemical profile of complex **10b** within the potential range of -1.600 V to +1.000 V vs. Ag/AgCl in acetonitrile is shown in Fig. 5.17 (b). The voltammgram consisted of two reversible redox responses in the anodic region with $E_{1/2}$ values of 0.463 V vs. Ag/AgCl and 0.737 V vs. Ag/AgCl respectively. These values are similar to those observed for complex **10a** in the anodic region (Fig. 5.16, b). However, the redox couple observed in the cathodic region was quasi–reversible with $E_{1/2}$ value of -0.964 V vs. Ag/AgCl. The former peaks in the anodic region might be attributed to the ligand–centered oxidation giving rise to the phenoxyl radical species. However, the latter peak in the anodic region associated with increased current heights are probably arising from the rearrangement of the coordination sphere after first oxidation processs which is giving

rise to new species in solution presumably with bis– speciation. It is likely for the locus of oxidation in both processes to be ligand centered since *tert*-butyl groups are expected to enhance the reversibility of ligand–centered oxidation processes. It is notable that the half–wave potential for the redox process observed for complex **10b** in the cathodic region differs significantly from that of complex **10a** which indicates that the reduction in not metal–centered in case of **10b**. Hence, the single cathodic process observed in the voltammograms of **9b** and **10b** was attributed to a ligand–centered reduction process.

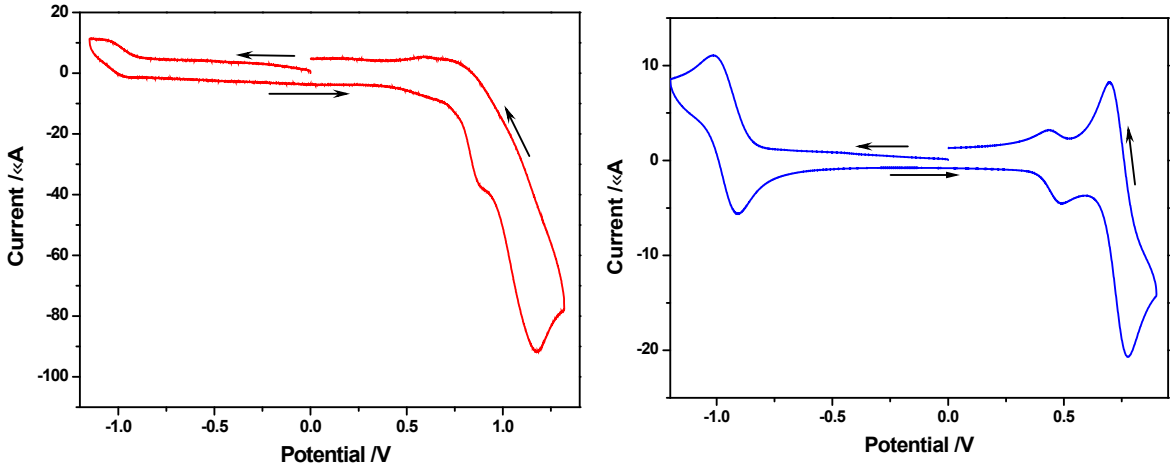

(a) (b)

Fig. 5.17 Cyclic voltammograms of 10^{-3} M solutions of (a) **9b** in dimethylformamide and (b) **10b** in acetonitrile at 298 K under nitrogen atmosphere in presence of 0.1 M TBAP as supporting electrolyte, glassy-carbon was used as working electrode, Ag/AgCl as reference electrode and platinum wire as auxiliary electrode; scan rate 0.1 V/s

The electrochemical profiles of the complexes **9c**·H_2O and **10c** in acetonitrile within the potential range of -1.750 V to +1.000 V vs. Ag/AgCl are represented in Figures 5.18 (a) and (b) respectively.

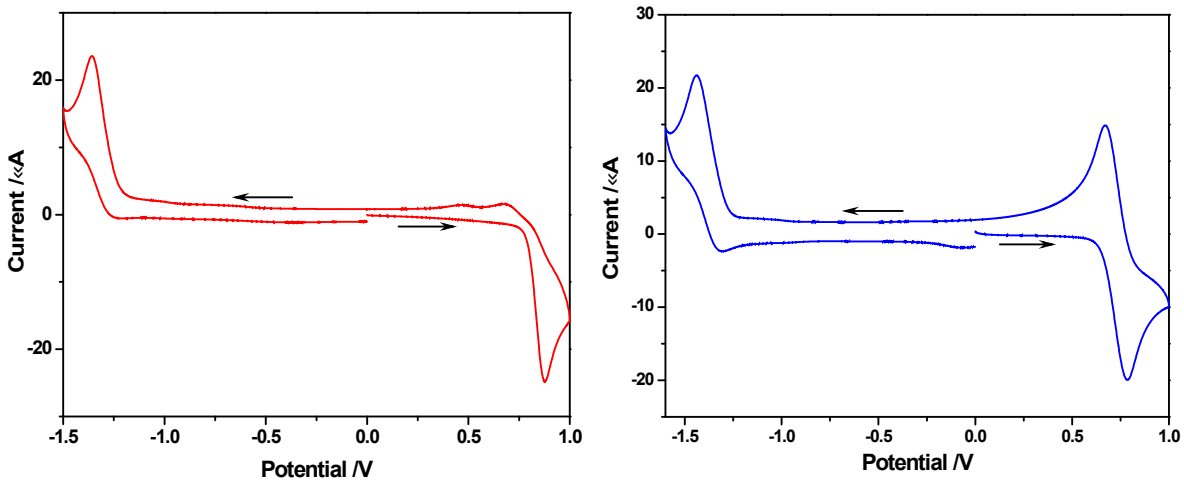

(a) (b)

Fig. 5.18 Cyclic voltammograms of 10^{-3} M solutions of (a) **9c**·H_2O and (b) **10c** in acetonitrile at 298 K under nitrogen atmosphere in presence of 0.1 M TBAP as a supporting electrolyte, glassy-carbon was used as working electrode, Ag/AgCl as reference electrode and platinum wire as auxiliary electrode; scan rate 0.1 V/s

Table 5.7 Electrochemical data of complexes **9-10** (a, b and c) at 298 K vs Ag/AgCl

Complex	$[^2L]/[^2L^{\bullet}]^-$		Ni^{II}/Ni^{I}		$[^1L^{\bullet}]^+/[^1L]$		$[^1L^{\bullet\bullet}]^{2+}/[^1L^{\bullet}]^+$	
	$E_{1/2}$[c] (V)	ΔE_p[d] (mV)	$E_{1/2}$[c] (V)	ΔE_p[d] (mV)	$E_{1/2}$[c] (V)	ΔE_p[d] (mV)	$E_{1/2}$[c] (V)	ΔE_p[d] (mV)
9a·$3H_2O$·CH_3OH[a]	–	–	–	–	0.648[e]	–	0.915[e]	–
9b[b]	-1.012	106	–	–	0.907[e]	–	1.178[e]	–
9c·H_2O[a]	-1.357[e]	–	–	–	–	–	0.878[e]	–
10a[a]	–	–	-0.117	79	0.460	62	0.746	80
10b[a]	-0.964	114	–	–	0.463	52	0.737	82
10c[a]	-1.374	137	–	–	–	–	0.723	115

Measured in [a]acetonitrile and [b]dimethylformamide with 0.1 M tetrabutylammonium perchlorate (TBAP); scan rate = 0.1 V/s; [c]$E_{1/2}$ = 1/2 (E_{pa} + E_{pc}); [d]ΔE_p = (E_{pa} – E_{pc}); [e] Due to the irreversible nature, only single potential values are given for these redox processes. [1]L implies the coordinated $Phimp^-$ whereas [2]L represents the coordinated $Phimp^-$ (for **9b** and **10b**) or the coordinated Pyimpy ligand (for **9c**·H_2O and **10c**).

The complex **9c**·H_2O exhibited an irreversible peak in the cathodic region with the E_p value near -1.357 V vs. Ag/AgCl and another irreversible peak in the anodic region with the E_p

value near +0.878 V vs. Ag/AgCl. These peaks probably define the reduction of the neutral ligand (Pyimpy) and oxidation of the monoanionic ligand part ($Phimp^{-}$) respectively, which is substantiated by the theoretical calculations also (*vide infra*). However, in case of complex **10c**, the peaks representing the ligand–centered reduction (Pyimpy) and ligand–centered oxidation processes ($Phimp^{-}$) were quasi–reversible with the $E_{1/2}$ values of -1.374 V and 0.723 V vs. Ag/AgCl respectively (Table 5.7).

5.2.5. Theoretical calculations

Density functional theory (DFT) calculations were also performed using the complex **9c**·H_2O as representative of the series. The results are illustrated in the form of contour plots of HOMO and LUMO which are shown in Figures 5.19 (a) and (b) respectively.

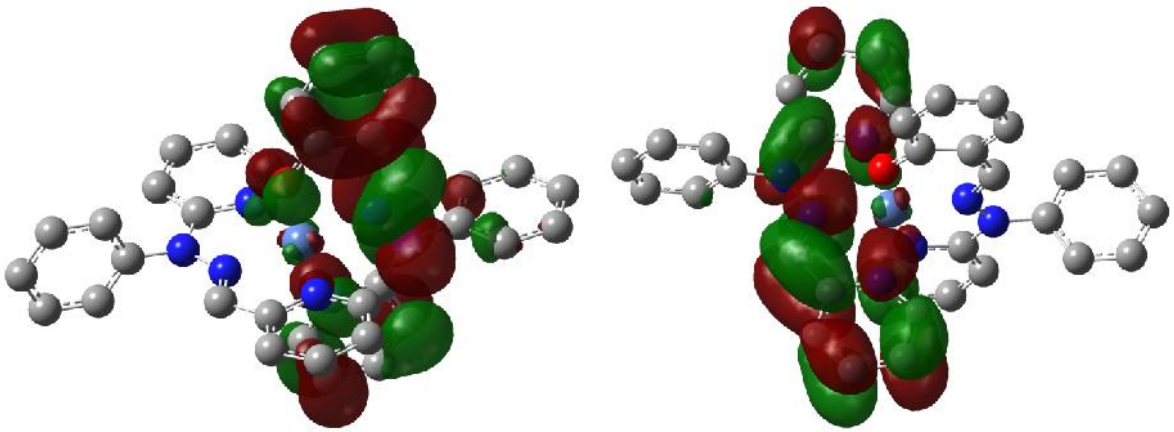

(a) (b)

Fig. 5.19 Contour plots of (a) HOMO and (b) LUMO in **9c**·H_2O

The shape and distribution of (α–) HOMO orbital in complex **9c**·H_2O clearly indicated that the redox site responsible for the first oxidation event is largely composed of the ligand part ($Phimp^{-}$) and the major contribution comes from the ring bearing the phenolate moiety (Fig. 5.19, a). It is evident from Fig. 5.19 (b) that LUMO is primarily composed of coordinated

Pyimpy and delocalized in entire ligand binding plane which is probably forming the locus for reduction process in **9c**·H_2O. These results are consistent with the voltammetric data of **9c**·H_2O (Fig. 5.18, a).

5.2.6. Generation of phenoxyl radical species

Electrochemical investigations and theoretical calculations suggested that this family of complexes may give rise to phenoxyl radical species through ligand–centered oxidation which prompted us to examine and characterize these species by means of spectroscopic techniques. Electronic absorption spectral changes of nickel complexes **9**(**a**, **b** and **c**) (50 μM) in presence of varying amounts of ceric ammonium nitrate (CAN) in acetonitrile at 298 K are shown in Fig. 5.20. Complex **9a**·$3H_2O$·CH_3OH and **9c**·H_2O exhibited very much similar spectral behaviour on oxidation with one–electron oxidant (CAN) and gave rise to two new intense bands in their absorption spectra, one band near 435–455 nm and another band centered at 709 nm (Fig. 5.20, (a) and (e) respectively, Table 5.8). It is important to note that the intense π–π* transitions of a phenoxyl radical generally appear within 390–480 nm region.[194,506,507] Furthermore, the spectral features of oxidized complexes derived from **9a**·$3H_2O$·CH_3OH and **9c**·H_2O closely resemble with those exhibited by phenoxyl radical analogues of bis–phenolate Ni(II) octahedral complexes.[506] Hence, these bands were characterized as originating from π–π* transitions and ligand–to–ligand charge transfer (LLCT) transitions in phenoxyl radical complexes.[194,197]

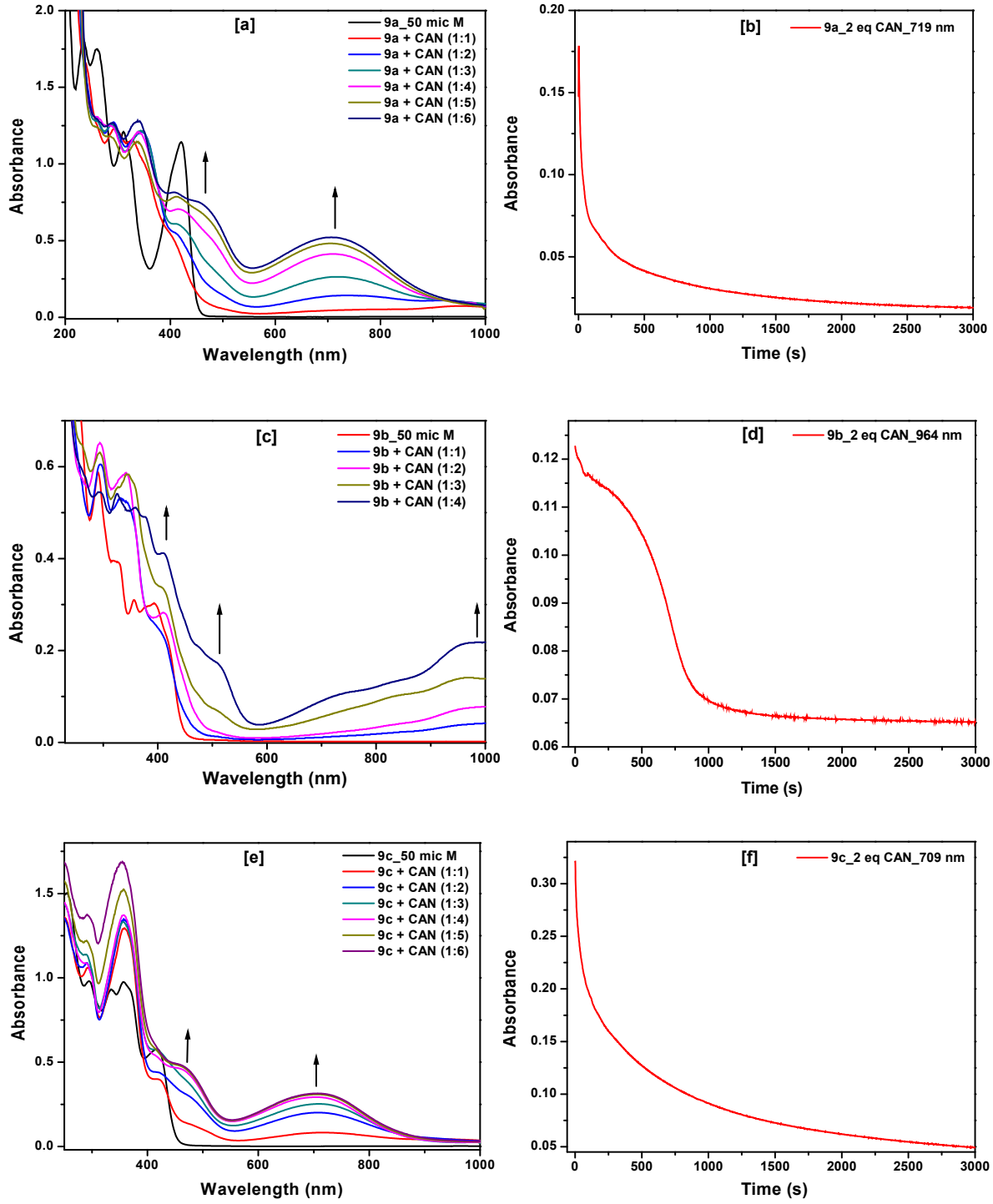

Fig. 5.20 Absorption spectral changes upon oxidation of (a) **9a**; (c) **9b**; and (e) **9c** (50 μM each) with varying equivalents of CAN in CH_3CN at 298 K; (b) time course of decomposition of phenoxyl radical analogues derived from (b) **9a**; (d) **9b**; and (f) **9c** monitored at 719, 964 and 709 nm respectively

However, the complex **9b** exhibited quite different spectral behavior after oxidation. It is evident from Fig. 5.20 (e) that oxidation of complex **9b** in acetonitrile at 298 K resulted with the appearance of new bands in the absorption spectrum over the entire visible range and extending into the NIR region (Table 5.8). The existence of well–resolved transitions over entire visible spectrum accompanied with an intense NIR feature is the evidence for the phenoxyl–radical character of oxidized species.[508] The decomposition of the oxidized species was monitored with repetitive scans and the results are represented in Fig. 5.21. Interestingly, the spectral changes largely reproduced the absorption spectral characteristics of the oxidized species derived from complexes **9a**·$3H_2O$·CH_3OH and **9c**·H_2O. On the basis of these data, we concluded that the phenoxyl radical complex **[9b$^{\bullet}$]**$^{+}$ gave rise to a new species during decomposition, presumably having bis– speciation, through considerable structural rearrangement.

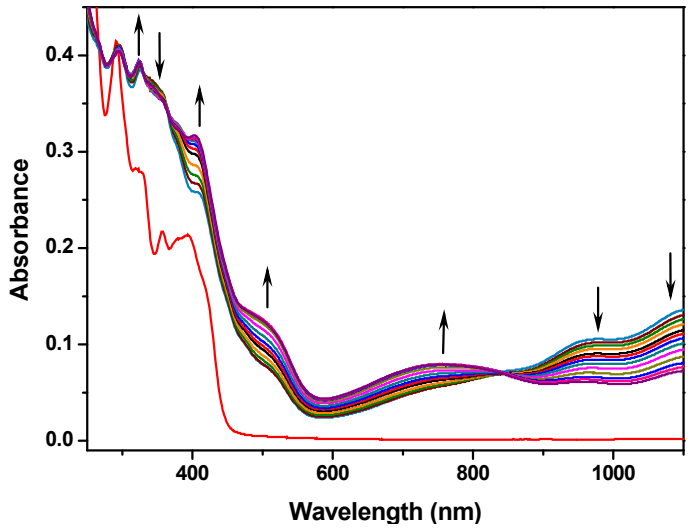

Fig. 5.21 Repetitive scans exhibiting absorption spectral changes of phenoxyl complex derived from **9b** (50 μM) in acetonitrile at 298 K

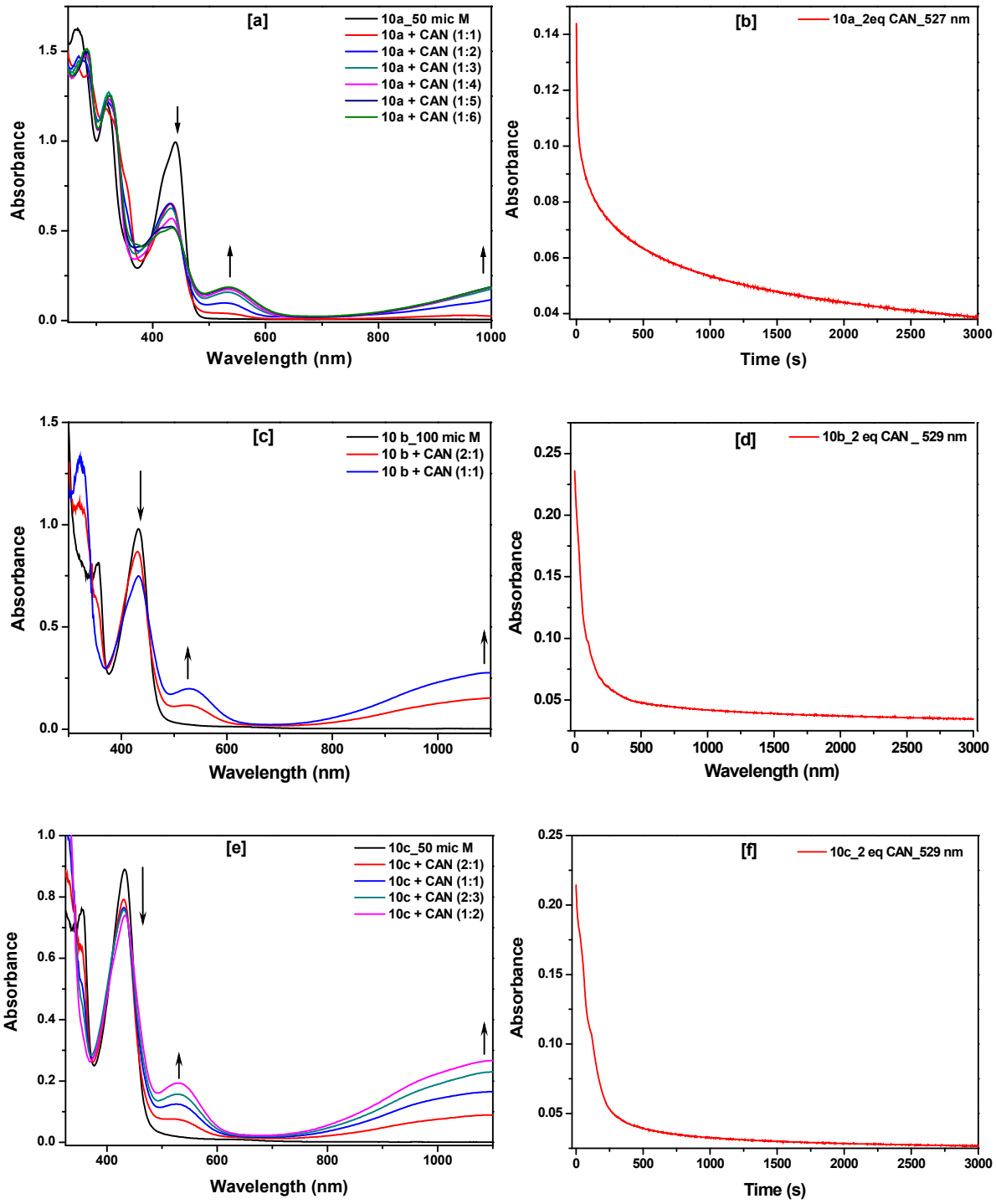

Fig. 5.22 Absorption spectral changes upon oxidation of (a) **10a** (50 μM); (c) **10b** (100 μM); and (e) **10c** (50 μM) with varying equivalents of CAN in CH_3CN at 298 K; (b) time course of decomposition of phenoxyl radical analogues derived from (b) **10a**; (d) **10b**; and (f) **10c** monitored at 527, 529 and 529 nm respectively

The absorption spectral features arising from the chemical oxidation of nickel complexes **10a**, **10b** and **10c** in acetonitrile solution at 298 K were found to be very much similar with one another and shown in Fig. 5.22 (a), (c) and (e) respectively. The intense π–π* transitions of a phenoxyl radical generally appear within 390–480 nm region.[194,506,507] As the initial complexes (**10a**, **10b** and **10c**) already possessed strong absorption bands in this region, it is difficult to predict unambiguously a ligand–based rather than metal–based oxidation in these cases. However, the spectra consisted of intense bands near 530 nm and the bands extending into the NIR region which are consistent with the spectral characteristics of other nickel(II) phenoxyl radical complexes.[506-508] These observations are probably indicative of transitions that imply delocalized phenoxyl radical orbitals[508] and the bands observed in the NIR region may be attributed to inter–valence charge transfer (IVCT) transitions.[509] The absorption spectral data of phenoxyl radical analogues **[10a$^{\bullet}$]$^{+}$**, **[10b$^{\bullet}$]$^{+}$** and **[10c$^{\bullet}$]$^{+}$** have been listed in Table 5.8.

Table 5.8 Electronic absorption spectral data of phenoxyl radical complexes

Complex	**$^{a}\lambda_{max}$/nm (£/M^{-1}cm^{-1})^{a}**
[9a$^{\bullet}$]$^{+}$	291 (25540), 339 (25620), 406 (16380), 441 (15200), 709 (10360)
[9b$^{\bullet}$]$^{+}$	353 (33840), 417 (8340), 455 (9900), 709 (6340)
[9c$^{\bullet}$]$^{+}$	376 (9854), 407 (8220), 476 *sh* (4180), 504 (3540), 763 (2240), 855 *sh* (2780), NIR band
[10a$^{\bullet}$]$^{+}$	282 (30498), 322 (25540), 416 *sh* (9936), 434 (10552), 535 (3840), NIR band
[10b$^{\bullet}$]$^{+}$	322 (26720), 407 *sh* (11508), 432 (15014), 527 (4020), NIR band
[10c$^{\bullet}$]$^{+}$	320 (24850), 411 *sh* (14760), 432 (11472), 531 (3920), NIR band

[a]Solvent : acetonitrile

It is important to note that purging of oxygen into the solutions containing oxidized species of nickel complexes could not bring about any change in their rates of decomposition which is probably indicating that the solvent is playing a major role in the decomposition process.

In order to confirm the facts deduced by the absorption spectral data as well as to explore the locus of oxidation more precisely, we analyzed the oxidation products of complexes **10a** and **10b** in acetonitrile by ESR spectroscopy. The X–band EPR spectra of both complexes in acetonitrile at 110 K feature a sharp isotropic signal with g_{iso} = 2.18 (Fig. 5.23). It is important to note that the "*g*" values typical for Ni(III) complexes fall within the range of 2.13–2.17.[217,503] In general, $S = 1/2$ d^7 low–spin Ni(III) complexes are characterized by anisotropic signals at around $g = 2.2$ and $g = 2.0$.[216,507,510] However no signals with $g = 2.0$ could be observed in the present investigation which precluded any possibility for the metal–centered oxidation.[216] This fact was further attested by the isotropic nature of EPR signals which rules out the existence of a Ni(III) complex (Fig. 5.23).[507,509]

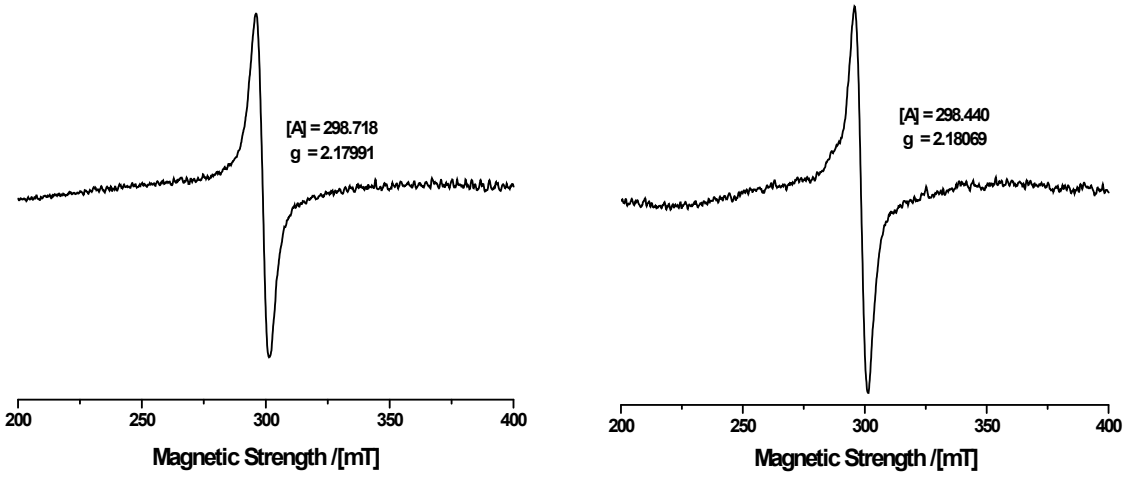

(a) (b)

Fig. 5.23 X–band EPR spectra of phenoxyl radical complexes derived from frozen solutions of (a) **10a** and (b) **10b** in CH_3CN at 110 K

In fact, the shape and position of the ESR signals obtained during the oxidation of complexes **10a** and **10b** resemble closely with those reported by Shimazaki et al.[216] and Rotthaus et al.[506,507] for their Ni(II)–coordinated phenoxyl radical complexes (*g* =

2.21–2.23). This unusual behavior could be interpreted as arising from the magnetic interactions between a phenoxyl radical and a d^8 high–spin Ni(II) center.[507]

5.2.7. DNA interaction studies

DNA interaction studies of these complexes were performed by electronic absorption spectroscopy, competitive binding assay and circular dichroism spectroscopy. Stability of the metal complexes in aqueous solution is one of the key criteria to be monitored prior to investigate their DNA binding properties and nuclease activities.[453] The nickel complexes **9a**·$3H_2O$·CH_3OH, **9b** and **9c**·H_2O were found fairly stable in aqueous solutions. A fixed concentration of these complexes was titrated with increasing concentrations of CT–DNA at physiological pH and absorption spectral changes were monitored. The UV-visible spectal profiles of complexes **9a**·$3H_2O$·CH_3OH, **9b** and **9c**·H_2O in presence of varying concentrations of CT–DNA are depicted in Figures 5.24 (a), (b) and (c) respectively. It is evident that the interaction of nickel complexes with CT–DNA led to considerable hypochromism in their charge transfer bands. However, a significant red shift of about 12 nm accompanied with the formation of an isosbestic point near 394 nm could also be observed in case of complex **9b**. The binding constants for these complexes were calculated as described in previous chapters and listed in Table 5.9. These values are much lower than those reported for classical intercalators and metallo–intercalators [~10^6–10^7] thereby suggesting a non–intercalative or partial intercalative mode of interaction with CT–DNA for these complexes.[462] The aqueous solutions of the complexes **10a**, **10b** and **10c** exhibited rapid change in the absorbance on standing which was rationalized as the precipitation of these complexes from their aqueous solutions. Hence, DNA binding behavior of these complexes could not be investigated by electronic absorption spectral technique.

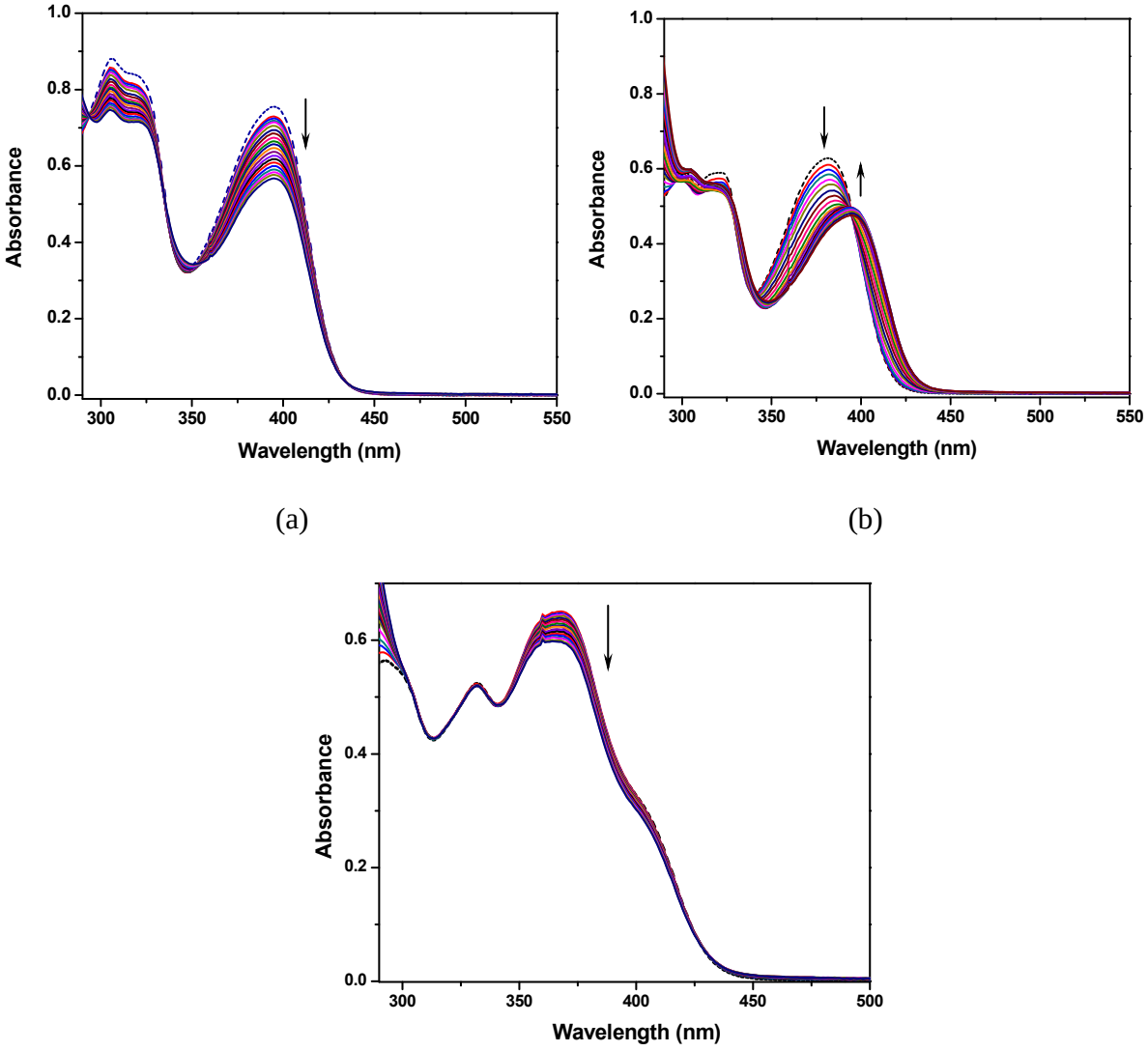

Fig. 5.24 Absorption spectral changes of complex (a) **9a**·$3H_2O$·CH_3OH, (b) **9b** and (c) **9c**·H_2O in 0.1 M phosphate buffer (pH 7.2) containing 10% DMF in presence of increasing amounts of CT–DNA (0 – 385 µM for (a) and (c); 0 – 176 µM for (b) respectively). Dotted line represents the spectrum in absence of CT–DNA

In order to get better insight into the DNA binding events, we performed competitive binding experiments using ethidium bromide as intercalator. A fixed concentration of CT–DNA pretreated with ethidium bromide was titrated with the solutions of nickel complexes and emission spectral changes were recorded. The enhanced fluorescence of

ethidium bromide arising from the intercalation of its phenanthridium ring between adjacent base pairs of DNA got quenched in presence of metal complexes. These data indicated the binding of metal complexes with CT–DNA. The fluorescence quenching curves and Stern–Volmer plots for the complexes **9**-**10** are represented in Figures 5.25–5.30. Their binding affinities for CT–DNA were determined and compared in terms of Stern–Volmer quenching constants which were calculated as described in previous chapters and listed in Table 5.9. All plots were close to linearity affording the K_{SV} values with the order of 10^4–10^5. These K_{SV} values are higher than the external binders but lower than those of putative intercalators. It can be seen that the complex **9a**·$3H_2O$·CH_3OH exhibited comparatively greater affinity for binding with DNA than **9b** which may be due to the bis–speciation of **9a**·$3H_2O$·CH_3OH.

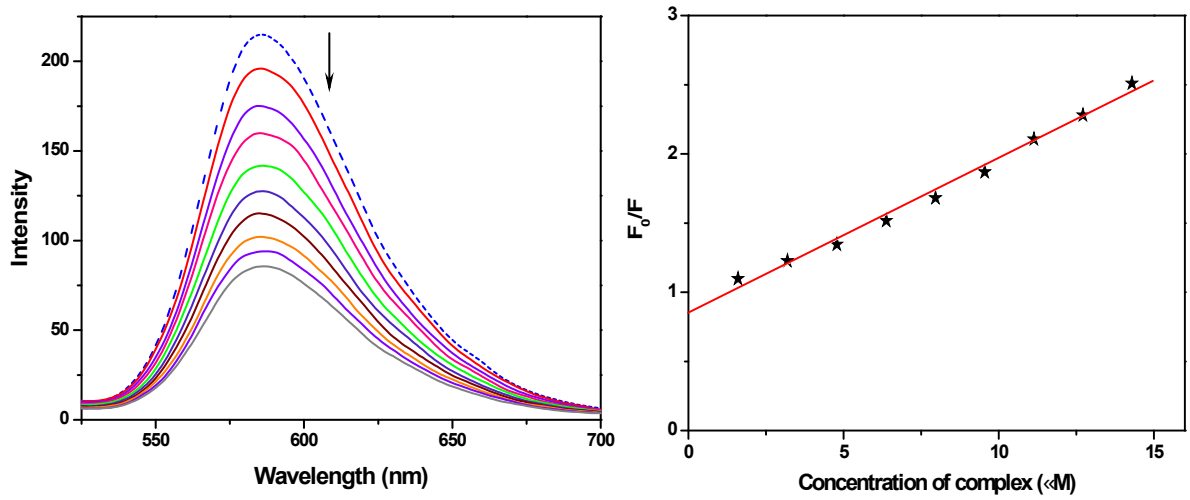

(a) (b)

Fig. 5.25 (a) Fluorescence emission spectra of the EB−DNA in presence of **9a**·$3H_2O$·CH_3OH in 0.1 M phosphate buffer (pH 7.2) containing 5% DMF. λ_{ex} = 250 nm and λ_{em} = 585 nm. [EB] = 5 μM, [DNA] = 25 μM, [**9a**] = 0–14.29 μM. Dotted line represents the spectrum in the absence of complex; (b) Stern–Volmer plot for interaction of **9a**·$3H_2O$·CH_3OH with CT–DNA

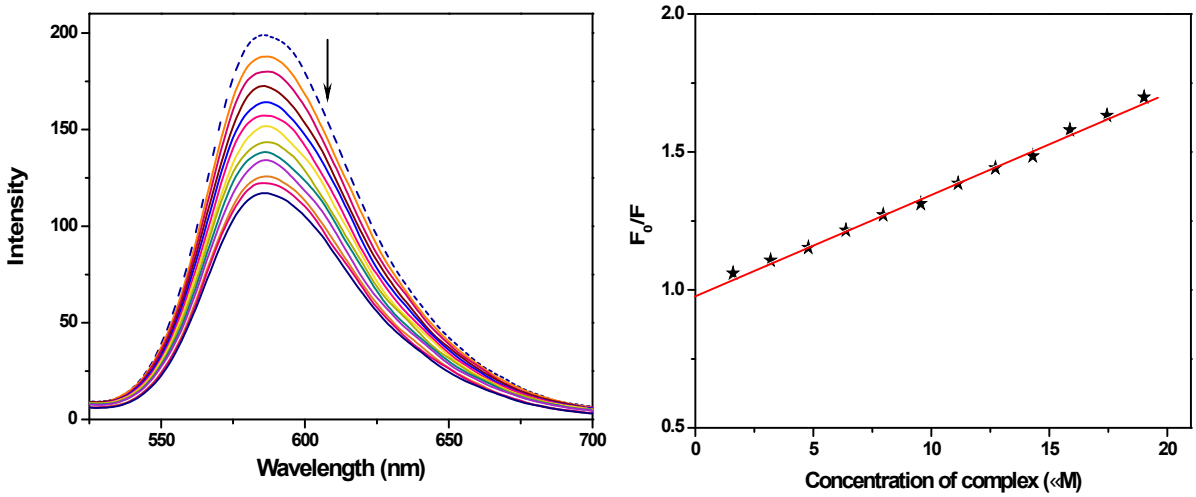

(a) (b)

Fig. 5.26 (a) Fluorescence emission spectra of the EB−DNA in presence of **9b** in 0.1 M phosphate buffer (pH 7.2) containing 5% DMF. λ_{ex} = 250 nm and λ_{em} = 585 nm. [EB] = 5 µM, [DNA] = 25 µM, [**9b**] = 0–19.01 µM. Dotted line represents the spectrum in the absence of complex; (b) Stern−Volmer plot for interaction of **9b** with CT−DNA

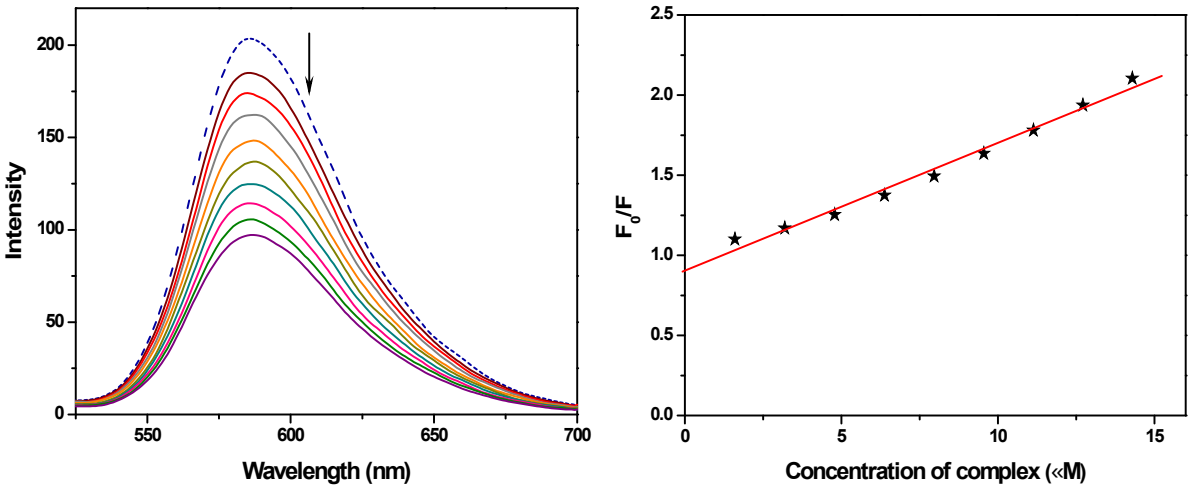

(a) (b)

Fig. 5.27 (a) Fluorescence emission spectra of the EB−DNA in presence of **9c**·H_2O in 0.1 M phosphate buffer (pH 7.2) containing 5% DMF. λ_{ex} = 250 nm and λ_{em} = 585 nm. [EB] = 5 µM, [DNA] = 25 µM, [**9c**] = 0–14.29 µM. Dotted line represents the spectrum in the absence of complex; (b) Stern−Volmer plot for interaction of **9c** with CT−DNA

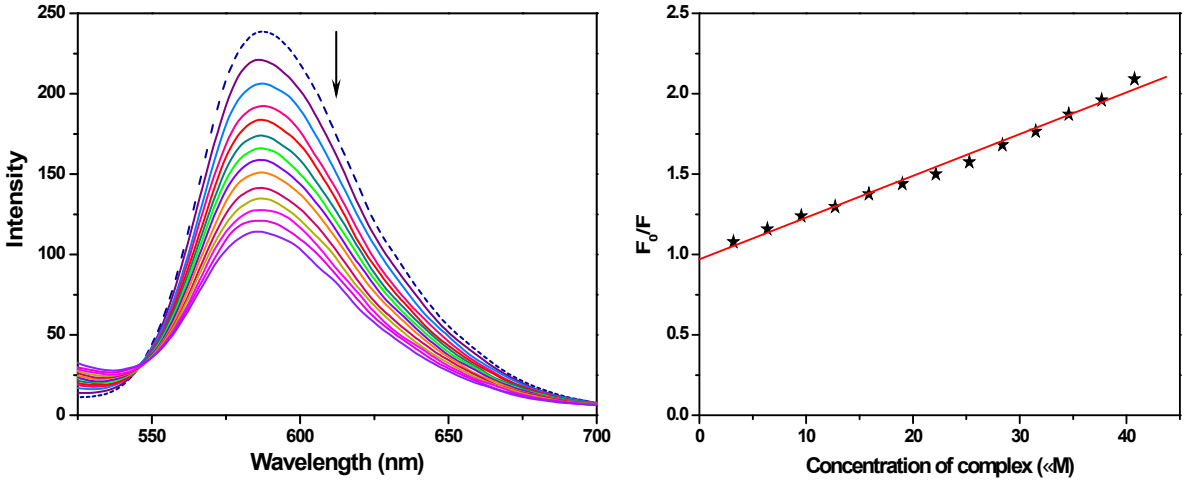

(a) (b)

Fig. 5.28 (a) Fluorescence emission spectra of the EB−DNA in presence of **10a** in 0.1 M phosphate buffer (pH 7.2) containing 5% DMF. λ_{ex} = 250 nm and λ_{em} = 585 nm. [EB] = 5 µM, [DNA] = 25 µM, [**10a**] = 0 – 40.75 µM. Dotted line represents the spectrum in the absence of complex; (b) Stern−Volmer plot for interaction of **10a** with CT−DNA

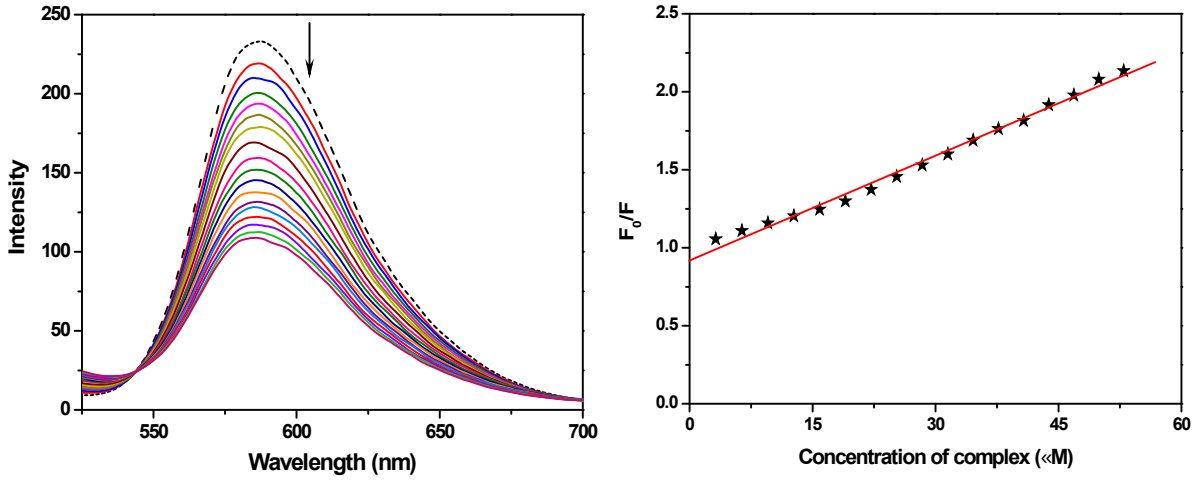

(a) (b)

Fig. 5.29 (a) Fluorescence emission spectra of the EB−DNA in presence of **10b** in 0.1 M phosphate buffer (pH 7.2) containing 5% DMF. λ_{ex} = 250 nm and λ_{em} = 585 nm. [EB] = 5 µM, [DNA] = 25 µM, [**10b**] = 0–52.95 µM. Dotted line represents the spectrum in the absence of complex; (b) Stern−Volmer plot for interaction of **10b** with CT−DNA

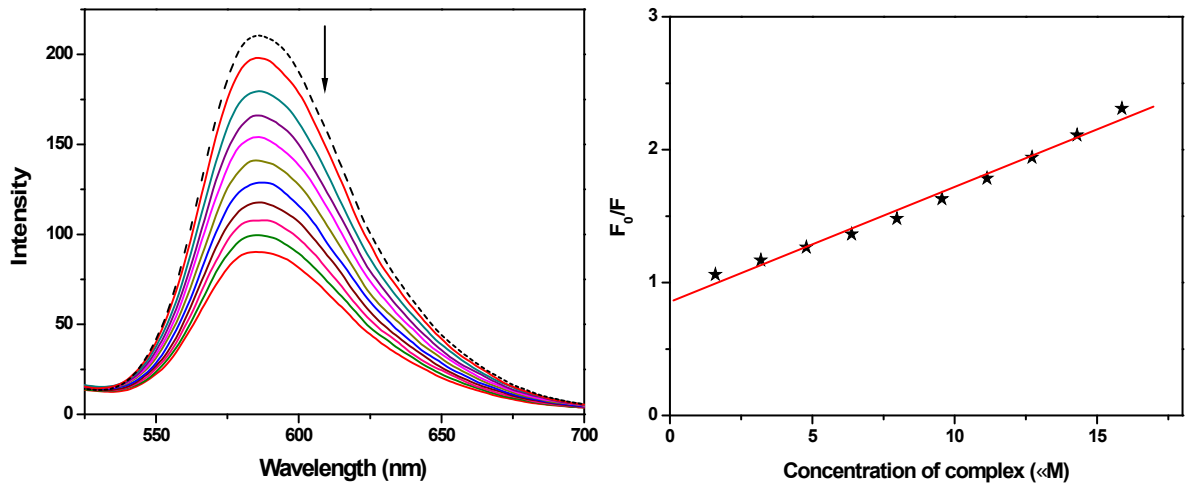

(a) (b)

Fig. 5.30 (a) Fluorescence emission spectra of the EB−DNA in presence of **10c** in 0.1 M phosphate buffer (pH 7.2) containing 5% DMF. λ_{ex} = 250 nm and λ_{em} = 585 nm. [EB] = 5 μM, [DNA] = 25 μM, [**10c**] = 0–15.87 μM. Dotted line represents the spectrum in the absence of complex; (b) Stern–Volmer plot for interaction of **10c** with CT–DNA

Table 5.9 Binding constants and Stern-Volmer quenching constants for DNA interaction of complexes **9-10**

Compound	K_b	K_{SV}
9a·3H_2O·CH_3OH	2.65×10^4	1.33×10^5
9b	1.05×10^4	3.75×10^4
9c·H_2O	6.81×10^4	8.90×10^4
10a	–	2.68×10^4
10b	–	2.42×10^4
10c	–	1.01×10^4

A comparative study of the data listed in Table 5.9 predicted higher binding affinity of the nickel complexes derived from PhimpH (**9a**, **b** and **c**) for CT DNA than those derived from ^{t}BuPhimpH (**10a**, **b** and **c**). Hence these complexes paralleled the behavior of cobalt analogues of these two ligands in this regard which have been described in *Chapter 4*.

In order to probe the conformational changes in DNA induced by the nickel complexes during DNA interaction event, CD spectral behavior of DNA was investigated in the absence and presence of nickel complexes **9**–**10** (Fig. 5.31). The CD spectrum of CT–DNA consisted of one positive band near 275 nm due to base stacking and one negative band near 248 nm due to helicity which are the characteristic of the right handed B–conformation of DNA. A significant decrease in the intensity of both positive and negative bands resulted from the incubation of DNA with metal complexes however no major shift in the wavelength could be observed. Notably, classical intercalators cause significant changes in intensities of both, positive and negative bands due to the enhancement of base stacking and stabilization of helicity whereas small molecules exhibiting groove binding or electrostatic interactions with DNA cause no perturbations.[355,455]

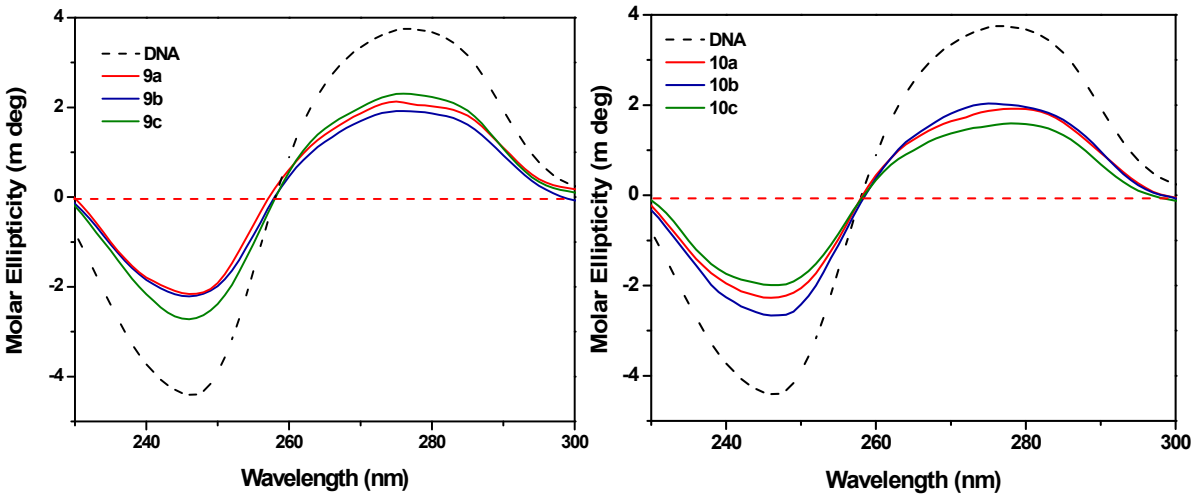

(a) (b)

Fig. 5.31 Circular dichroism spectra in 0.1 M phosphate buffer (pH 7.2) containing 10% methanol after 10 min incubation at 25 °C. (a) CT–DNA and its interaction with complexes **9a**·$3H_2O$·CH_3OH, **9b** and **9c**·H_2O; (b) CT–DNA and its interaction with complexes **10a**, **10b** and **10c**

Considering the lower values of binding constants and CD spectral behavior of DNA in presence of nickel complexes **9-10**, a partial intercalative mode of interaction with DNA was suggested for these complexes. It is worth mentioning that copper analogues of this family of complexes also exhibited partial intercalation with DNA.[404]

5.2.8. Nuclease activity

Nuclease activity of nickel complexes **9-10** was investigated under physiological conditions by agarose gel electrophoresis in the absence of any external activator like H_2O_2 or BME. Results of the DNA cleavage studies are illustrated in Fig. 5.32.

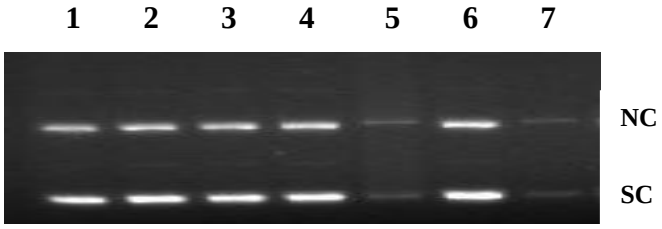

Fig. 5.32 Gel electrophoresis separations showing the cleavage of supercoiled pBR322 DNA (100 ng) by complexes **9-10** (50 μM each). Samples were incubated at 37 °C for 2 h in 0.1 M phosphate buffer containing 10% DMF. Lane 1, DNA control; lane 2, DNA + **9a**·$3H_2O$·CH_3OH; lane 3, DNA + **10a**; lane 4, DNA + **9b**; lane 5, DNA + **10b**; lane 6, DNA + **9c**·H_2O; lane 7, DNA + **10c**

It was noticed that no complex derived from PhimpH ligand (**9a**·$3H_2O$·CH_3OH, **9b** or **9c**·H_2O) could exhibit DNA cleavage activity (Fig. 5.32, lanes 2, 4 and 6 respectively). However, nickel complexes **10b** and **10c** derived from ^{t}BuPhimpH ligand catalyzed the DNA cleavage very efficiently leading to the vanishing of both NC and SC bands simultaneously (Fig. 5.32, lanes 5 and 7 respectively). This type of vanishing attests the extensive oxidative degradation of DNA resulting from the cleavage at multiple sites of DNA.[490] Recalling from the previous reports[477] and comparing the results with those of

Chapter 4, the self–activated DNA degradation as exhibited by complexes **10b** and **10c** is attributed to the presence of *tert*–butyl groups in the ligand frame. Interestingly, the complex **10a** which is also derived from the ligand ^{t}BuPhimpH bearing the *tert*–butyl substituents could not exhibit any nuclease activity. Hence, the presence of *tert*–butyl groups is not solely responsible for imparting the complexes with self–activated DNA cleavage activity and there may be several other contributing factors, a precise description of which demands further investigations.

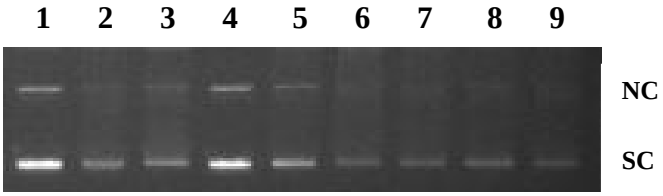

Fig. 5.33 Gel electrophoresis separations showing the cleavage of supercoiled pBR322 DNA (100 ng) by complexes **10b** (50 μM each). Samples were incubated at 37 °C for 2 h in 0.1 M phosphate buffer containing 10% DMF. Lane 1, DNA control; lane 2, DNA + **10b**; lane 3, DNA + **10b** + D_2O (10%); lane 4–8, DNA + **10b** + NaN_3, L-histidine, DMSO, ethanol, urea respectively (20 mM each); lane 9, DNA + **10b** + catalase (10 U)

In order to establish the roles of various reactive oxygen species (hydroxyl radical, singlet oxygen and hydrogen peroxide) in DNA strand scission mechanism, DNA cleavage experiments were carried out in presence of potential radical scavengers. Results of the inhibition experiments using **10b** as the representative complex are illustrated in Fig. 5.33. It is evident that significant inhibition of the DNA strand scission activity was observed in presence of sodium azide (Fig. 5.33, lane 4). A slight inhibition of DNA cleavage could also be observed in presence of L-histidine (Fig. 5.33, lane 5). These data suggested that singlet oxygen and/or singlet oxygen like species are responsible for the DNA damage mediated by complex **10b**. The extent of DNA cleavage was almost unaffected in the presence of

hydroxyl radical scavengers (DMSO, ethanol and urea; Fig. 5.33, lanes 6, 7 and 8 respectively) or catalase (Fig. 5.33, lane 9). Hence the roles of hydroxyl radical or hydrogen peroxide in DNA cleavage were ruled out.

5.2.9. Protein interaction studies

Non–covalent binding of complexes with serum albumins may be significant for the development of efficient therapeutics.[498] Binding behaviors of the metal complexes **9J10** with albumins were investigated by tryptophan fluorescence quenching experiment using bovine serum albumin (BSA) as the model substrate. For this purpose, a fixed concentration of albumin was titrated with increasing concentrations of metal complexes and the changes in the emission spectrum were monitored using the excitation wavelength of 295 nm. Binding of metal complexes with albumin gave rise to significant decrease in the emission intensity which was also accompanied with a remarkable red shift in case of complex **10a**. The fluorescence quenching curves of complexes **9J10** are represented in Figures 5.34–5.39. These data clearly indicated that the protein underwent considerable changes in its secondary structure as a consequence of binding with metal complexes. Stern–Volmer plots and Scatchard plots for complexes **9J10** are represented in Figures 5.34–5.39. The K_{SV} values were calculated from Stern–Volmer plots whereas the binding constants (K) and the number of binding sites (n) were calculated by applying Scatchard equation (*Chapter 1*). All complexes showed moderate binding affinities with serum albumins and highest binding affinity was observed for the complex **9a**·$3H_2O$·CH_3OH (Table 5.10).

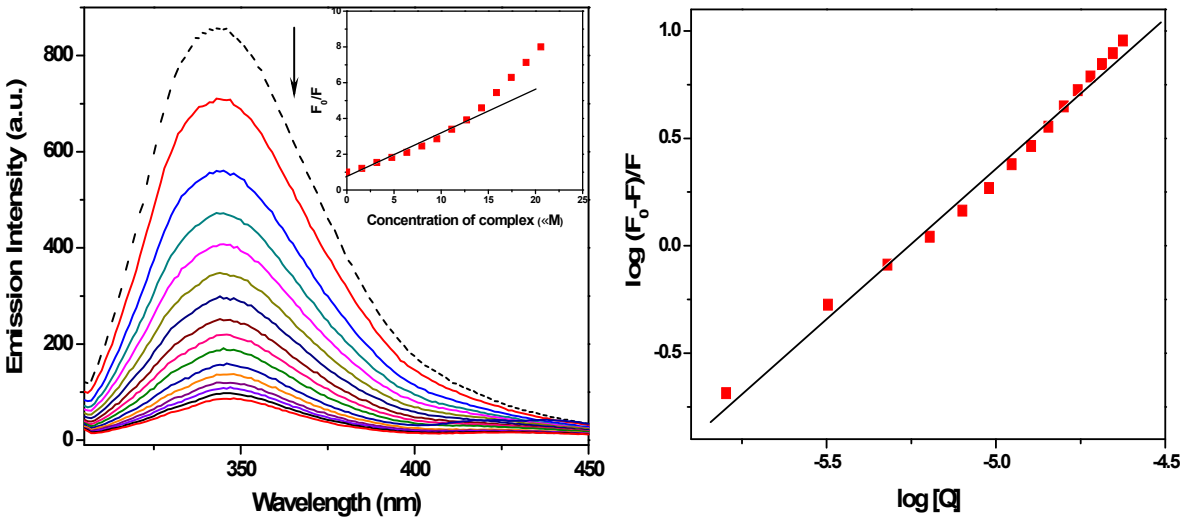

(a) (b)

Fig. 5.34 (a) Fluorescence emission spectra of BSA in presence of complex **9a**·3H_2O·CH_3OH in 0.1 M phosphate buffer (pH 7.2) containing 2% DMF. [BSA] = 2 μM, [**9a**] = 0–20.58 μM, λ_{ex} = 295 nm and λ_{em} = 344 nm. Dotted line represents the spectrum in the absence of complex; inset: Stern–Volmer plot of complex **9a**·3H_2O·CH_3OH; (b) Plot of log (F_0-F)/F vs. log [Q] for complex **9a**·3H_2O·CH_3OH

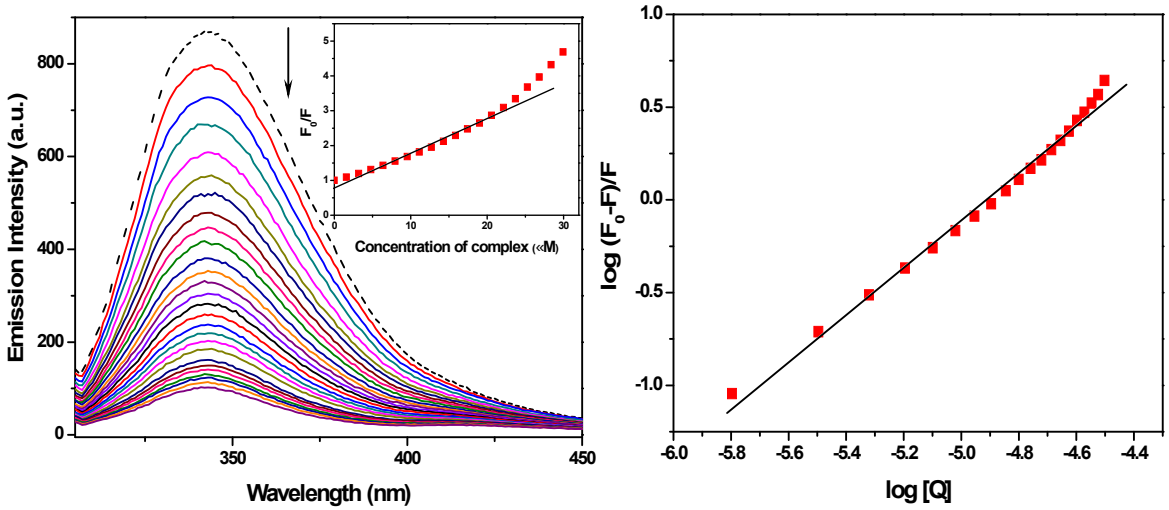

(a) (b)

Fig. 5.35 (a) Fluorescence emission spectra of BSA in presence of complex **9b** in 0.1 M phosphate buffer (pH 7.2) containing 2% DMF. [BSA] = 2 μM, [**9b**] = 0–29.94 μM, λ_{ex} = 295 nm and λ_{em} = 344 nm. Dotted line represents the spectrum in the absence of complex; inset: Stern–Volmer plot of complex **9b**; (b) Plot of log (F_0-F)/F vs. log [Q] for complex **9b**

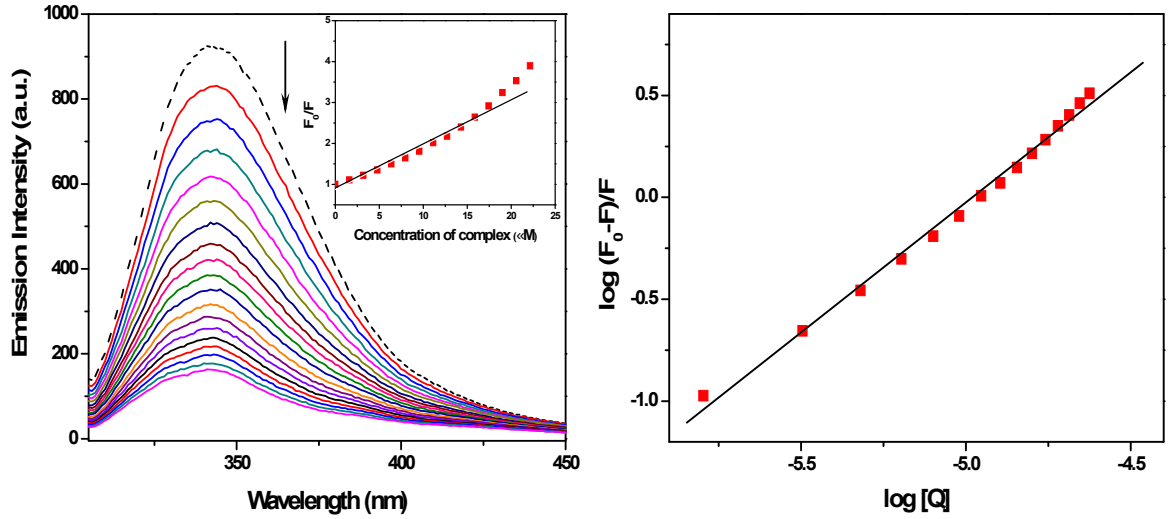

(a) (b)

Fig. 5.36 (a) Fluorescence emission spectra of BSA in presence of complex **9c**·H_2O in 0.1 M phosphate buffer (pH 7.2) containing 2% DMF. [BSA] = 2 μM, [**9c**] = 0–22.15 μM, λ_{ex} = 295 nm and λ_{em} = 344 nm. Dotted line represents the spectrum in the absence of complex; inset: Stern–Volmer plot of complex **9c**·H_2O; (b) Plot of log (F_0-F)/F vs. log [Q] for complex **9c**·H_2O

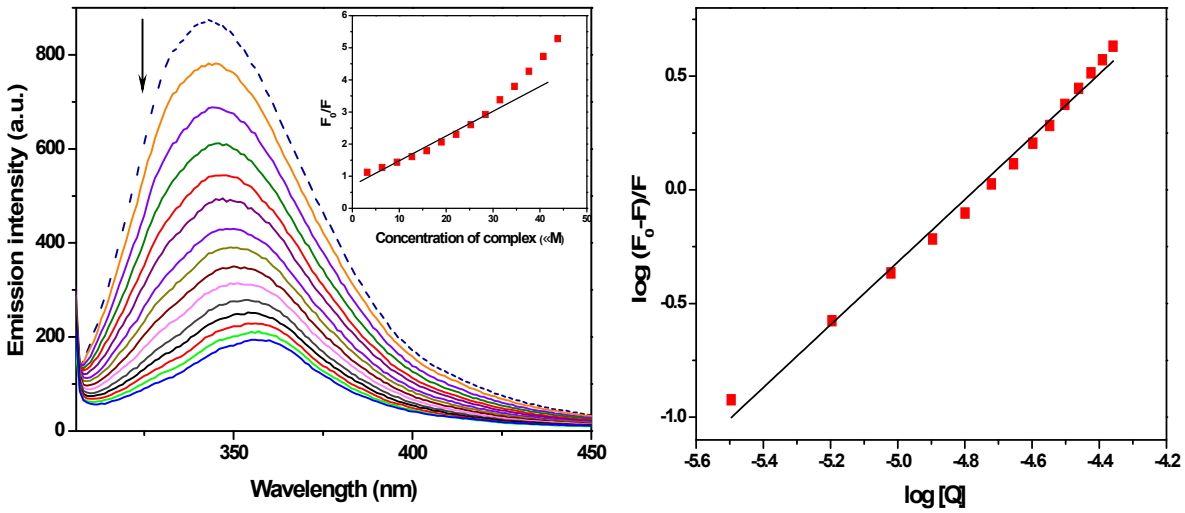

(a) (b)

Fig. 5.37 (a) Fluorescence emission spectra of BSA in presence of complex **10a** in 0.1 M phosphate buffer (pH 7.2) containing 2% DMF. [BSA] = 2 μM, [**10a**] = 0–43.81 μM, λ_{ex} = 295 nm and λ_{em} = 344 nm. Dotted line represents the spectrum in the absence of complex; inset: Stern–Volmer plot of complex **10a**; (b) Plot of log (F_0-F)/F vs. log [Q] for complex **10a**

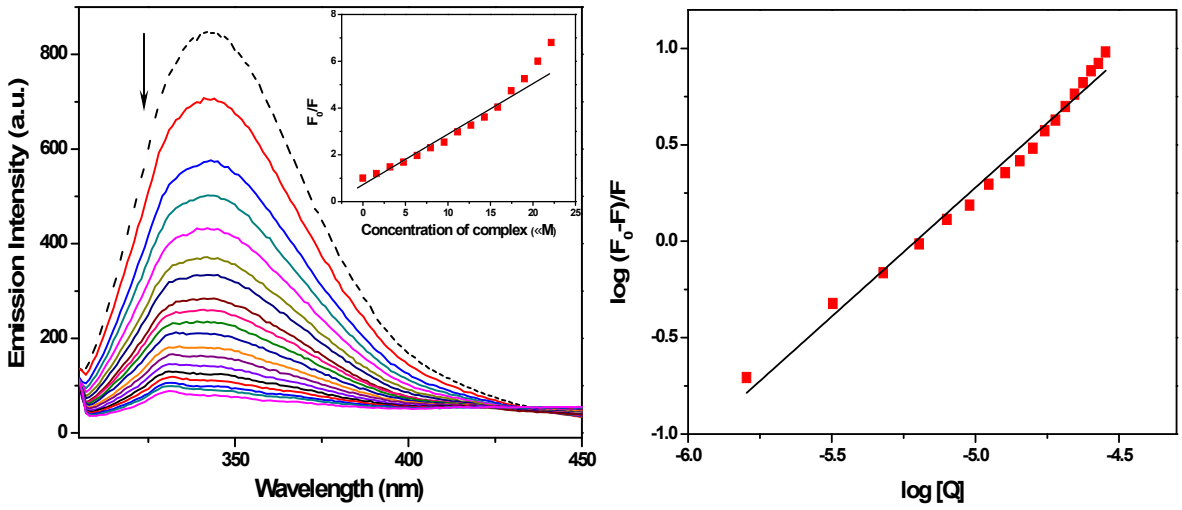

(a) (b)

Fig. 5.38 (a) Fluorescence emission spectra of BSA in presence of complex **10b** in 0.1 M phosphate buffer (pH 7.2) containing 2% DMF. [BSA] = 2 μM, [**10b**] = 0–22.15 μM, λ_{ex} = 295 nm and λ_{em} = 344 nm. Dotted line represents the spectrum in the absence of complex; inset: Stern–Volmer plot of complex **10b**; (b) Plot of log (F_0-F)/F vs. log [Q] for complex **10b**

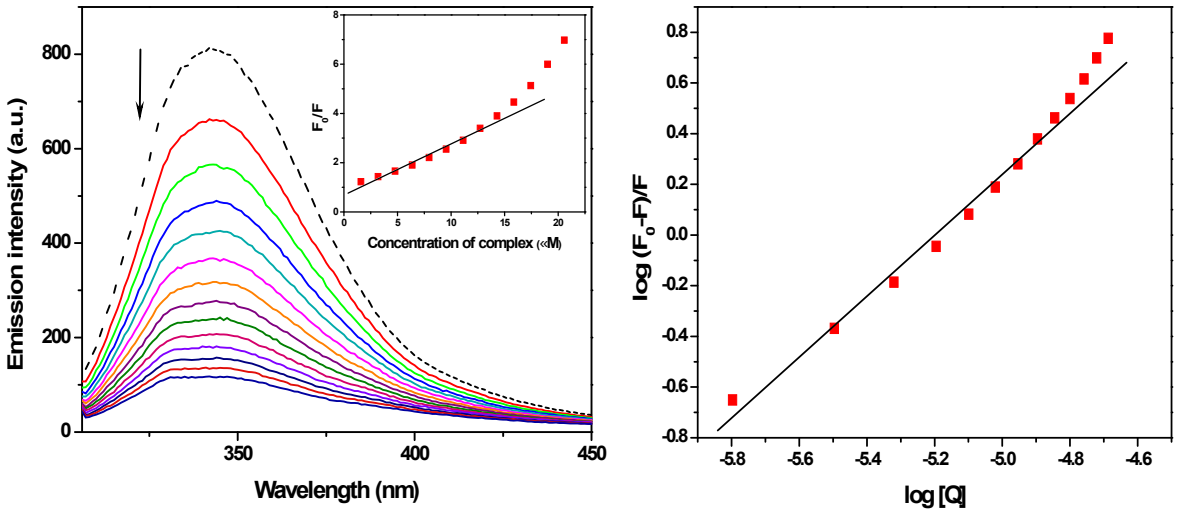

(a) (b)

Fig. 5.39 (a) Fluorescence emission spectra of BSA in presence of complex **10c** in 0.1 M phosphate buffer (pH 7.2) containing 2% DMF. [BSA] = 2 μM, [**10c**] = 0–20.58 μM, λ_{ex} = 295 nm and λ_{em} = 344 nm. Dotted line represents the spectrum in the absence of complex; inset: Stern–Volmer plot of complex **10c**; (b) Plot of log (F_0-F)/F vs. log [Q] for complex **10c**

Table 5.10 Stern–Volmer quenching constants, binding constants and number of binding sites for interactions of complexes **9J10** (**a**, **b** and **c**) with BSA

Complex	K_{SV} (M^{-1})	K_q (M^{-1})	K (M^{-1})	n
9a·$3H_2O$·CH_3OH	3.31×10^5	3.31×10^{13}	2.28×10^7	1.40
9b	1.26×10^5	1.26×10^{13}	1.93×10^6	1.28
9c·H_2O	1.24×10^5	1.24×10^{13}	2.29×10^6	1.28
10a	1.10×10^5	1.10×10^{13}	3.77×10^6	1.37
10b	3.06×10^5	3.06×10^{13}	9.24×10^6	1.34
10c	2.95×10^5	2.95×10^{13}	1.70×10^6	1.20

To investigate the preferential binding sites of these complexes in BSA, we carried out competitive binding experiments using warfarin and ibuprofen as markers for the site I and site II respectively and complexes **9a**·$3H_2O$·CH_3OH and **10a** as representatives of the series.[499,500] The details of the experiments are similar to those described in *Chapter 4*. The emission spectral behavior of serum albumin (SA) bound warfarin in presence of complexes **9a**·$3H_2O$·CH_3OH and **10a** are shown in Figures 5.40 (a) and 5.42 (a) respectively. Binding of both complexes with warfarin bound protein resulted the quenching of its fluorescence which may be attributed to the reduction in warfarin binding capacity at the primary binding site of serum albumin. These data indicated the binding of metal complexes within warfarin site I located in subdomain IIA.[499] The emission spectral properties of metal complex–BSA system were also investigated in the presence of ibuprofen (Figures 5.40 (b) and 5.42 (b)) and the results are summarized in the form of modified Stern–Volmer plots (Figures 5.41 and 5.43 respectively).[500]

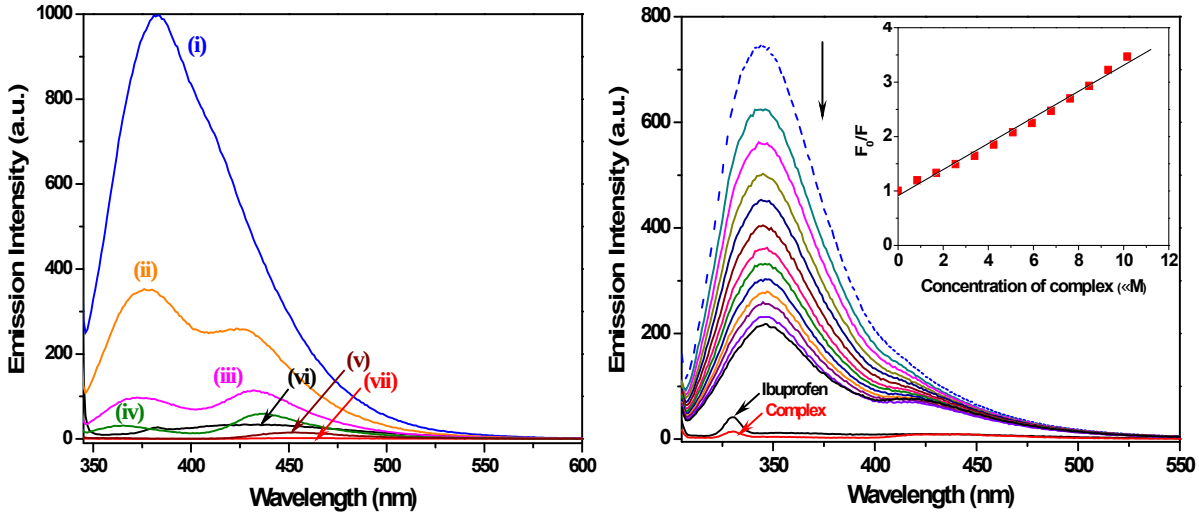

(a) (b)

Fig. 5.40 Fluorescence emission spectra of (a) warfarin (80 µM) and BSA (40 µM) equilibrated for 1 h in phosphate buffer (pH 7.2) containing 10% DMF in (i) absence or (ii-v) presence of complex **9a**·$3H_2O$·CH_3OH (ii) 20 µM, (iii) 40 µM, (iv) 80 µM and (v) 160 µM respectively; λ_{ex}=335 nm, λ_{ex}=378 nm. BSA (40 µM) and the complex **9a**·$3H_2O$·CH_3OH (160 µM) ((vi) and (vii) respectively) independently exhibited negligible emission under similar experimental conditions. (b) BSA (2 µM) treated with the site marker ibuprofen (2 µM) in 0.1 M phosphate buffer (pH 7.2) containing 2% DMF in absence (dotted line) and presence of complex **9a**·$3H_2O$·CH_3OH. [**9a**] = 0–10 µM; λ_{ex}=295 nm, λ_{ex}=344 nm. Incubation time = 2 min. Ibuprofen (2 µM) and **9a**·$3H_2O$·CH_3OH (100 µM) exhibited negligible emission intensity under similar experimental conditions, inset: Stern–Volmer plot for complex **9a**·$3H_2O$·CH_3OH

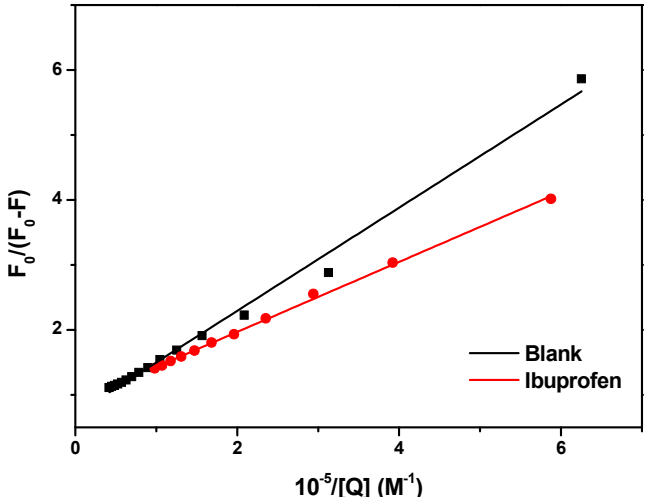

Fig. 5.41 Modified Stern–Volmer plot for complex **9a**·$3H_2O$·CH_3OH in the absence and presence of ibuprofen

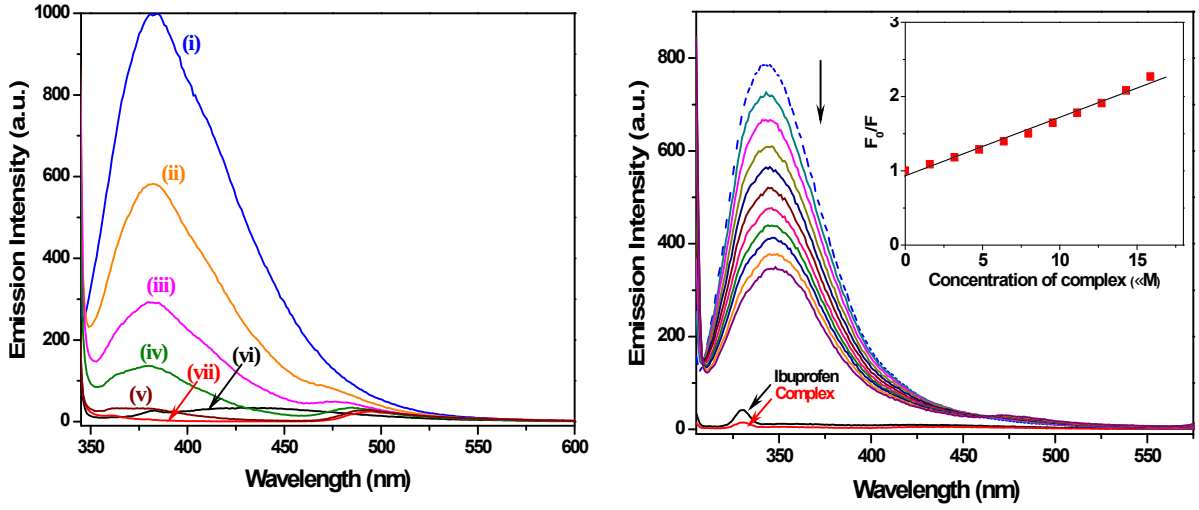

(a) (b)

Fig. 5.42 Fluorescence emission spectra of (a) warfarin (80 µM) and BSA (40 µM) equilibrated for 1 h in phosphate buffer (pH 7.2) containing 10% DMF in (i) absence or (ii-v) presence of complex **10a** (ii) 20 µM, (iii) 40 µM, (iv) 80 µM and (v) 160 µM respectively; λ_{ex}=335 nm, λ_{ex}=378 nm. BSA (40 µM) and the complex **10a** (160 µM) ((vi) and (vii) respectively) independently exhibited negligible emission under similar experimental conditions. (b) BSA (2 µM) treated with the site marker ibuprofen (2 µM) in 0.1 M phosphate buffer (pH 7.2) containing 2% DMF in absence (dotted line) and presence of complex **10a**. [**10a**] = 0–16 µM; λ_{ex}=295 nm, λ_{ex}=344 nm. Incubation time = 2 min. Ibuprofen (2 µM) and **10a** (100 µM) exhibited negligible emission intensity under similar experimental conditions, inset: Stern–Volmer plot for complex **10a**

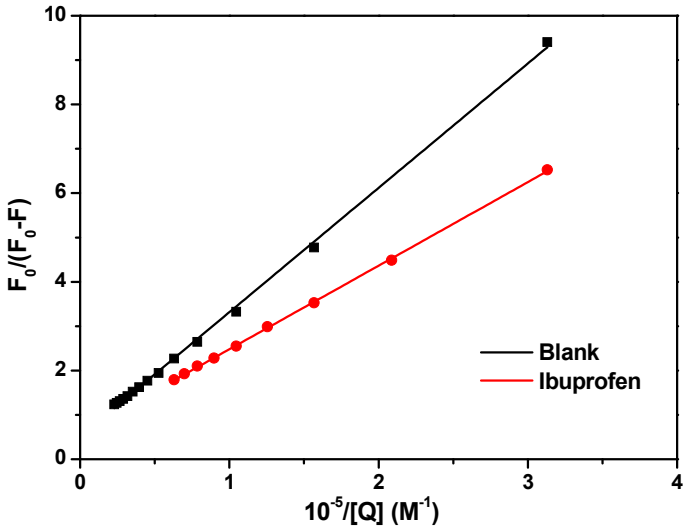

Fig. 5.43 Modified Stern–Volmer plot for complex **10a** in the absence and presence of ibuprofen

It is evident that the fluorescence properties of the metal complex–BSA system underwent considerable changes in the presence of ibuprofen. Hence it was concluded that the complexes could bind to the warfarin binding site (site I) as well as ibuprofen binding site (site II) during protein interaction event.

5.3. Conclusions

A family of mononuclear nickel complexes with phenolato oxygen donor ligands was synthesized and characterized. Their phenoxyl radical analogues were generated through chemical oxidation and characterized by UV-visible, EPR and electrochemical studies. The formation of phenoxyl radical species as a consequence of ligand-centered oxidation was also supported by theoretical calculations. DNA binding properties and nuclease activities of the parent complexes were investigated and extensive DNA degradation was observed resulting from the cleavage at multiple sites in DNA through a self–activating mechanism. The results inferred from the present piece of work highlighted the role of *tert*–butyl groups in nuclease activity in relevance with previous reports.[477] Besides, these results emphasized that the presence of *tert*–butyl groups is not solely responsible for the self–activated DNA cleavage activity and there may also be several other contributing factors. Protein interaction properties of these complexes were also investigated with BSA and their binding sites were accessed in presence of different site markers.

5.4. Experimental section

5.4.1. Reagents and materials

Analytical grade reagents Phenylhydrazine (S. D. Fine, Mumbai, India), salicylaldehyde (Sisco Research Laboratories Pvt. Ltd., Mumbai, India), sodium azide, warfarin, ibuprofen,

3,5–di–*tert*–butyl–2–hydroxybenzaldehyde (Sigma Aldrich, Steinheim, Germany), sodium perchlorate monohydrate (Himedia Laboratories Pvt. Ltd., Mumbai, India), ethylenediaminetetraacetic acid, nickel chloride hexahydrate (Merck Limited, Mumbai, India), pyridine–2–aldehyde, sodium hydride and 2–chloropyridine (Acros organics, USA) were used as obtained. The supercoiled pBR322 DNA and CT DNA were purchased from Bangalore Genei (India) and stored at 4 °C. Agarose (molecular biology grade), ethidium bromide and bovine serum albumin were obtained from Sigma Aldrich. Tris(hydroxymethyl)aminomethane–HCl (Tris–HCl) buffer and phosphate buffer were prepared in deionised water. The stock solutions of BSA were prepared as described in *Chapter 1*. Stock solutions of ibuprofen, warfarin and metal complexes were prepared in dimethylformamide. Solvents used for spectroscopic studies were HPLC grade and purified by standard procedures before use.

5.4.2. Synthesis of ligands

Synthesis of 2J((2JphenylJ2J(pyridinJ2Jyl)hydazono)methyl)phenol (PhimpH), 2,4Jdi-*tert*JbutylJ6J((phenyl(pyridinJ2Jyl)hydazono)methyl)phenol (^{t}BuPhimpH) and 1JphenylJ1J(pyridinJ2Jyl)J2J(pyridinJ2JylmethyleneJhydrazine (Pyimpy)

The ligands PhimpH, ^{t}BuPhimpH and Pyimpy were prepared according to the reported procedures.[332,381,477]

5.4.3. Synthesis of nickel complexes

Caution! Perchlorate salts of metal complexes with organic ligands are potentially explosive. Only a small amount of material should be prepared and handled with caution.

Synthesis of $[Ni(Phimp)_2]\cdot 3H_2O\cdot CH_3OH$ ($9a\cdot 3H_2O\cdot CH_3OH$)

A batch of ligand (0.145 g, 0.5 mmol) was dissolved in 15 mL of acetonitrile and NaH (0.021 g, 0.9 mmol) was added to it with continuous stirring and the reaction solution was stirred for 1 h. The solution of the ligand became turbid. To this stirring solution a batch of $NiCl_2\cdot 6H_2O$ (0.060 g, 0.25 mmol) taken in 15 mL of acetonitrile was added slowly and the reaction was continued overnight. A bright yellow solid appeared in the solution which was washed with little amount of acetonitrile and subsequently with diethyl ether. The yellow precipitate obtained was recrystallized in dichloromethane. Slow evaporation of the dichloromethane: methanol (9:1) solution of compound afforded X–ray diffraction quality crystals. Yield (0.145 g, 91%); Anal. Calc. for $C_{37}H_{38}N_6O_6Ni$ C, 61.60; H, 5.31; N, 11.65; Found C, 61.27; H, 5.24; N, 11.79; Selected IR data (KBr, ν_{max}/cm^{-1}): 1602 ($\nu_{C=N}$); μ_{eff} (297 K): 2.95 μ_B; $\Lambda_M/\Omega^{-1}cm^2mol^{-1}$ (DMF): 1; UV–visible [CH_3OH, λ_{max}/nm ($\varepsilon/M^{-1}cm^{-1}$)]: 255 (37740), 311 (28220), 324 *sh* (24720), 393 *sh* (21440), 407 (23740); ESI–MS (acetonitrile, pos.): m/z 635.16 (100%) $[M+H]^+$; 657.14 (6.6%) $[M+Na]^+$.

Synthesis of [Ni(Phimp)Cl] (9b)

A batch of ligand (0.145 g, 0.5 mmol) was dissolved in 5 mL of acetonitrile and NaH (0.021 g, 0.9 mmol) was added to it with continuous stirring and the reaction solution was stirred for 1 h. The solution of the ligand became turbid due to the deprotonation of the ligand. Now, in a separate flask, a batch of $NiCl_2\cdot 6H_2O$ (0.119 g, 0.5 mmol) was dissolved in 5 mL of dimethylformamide and stirred vigorously. The deprotonated ligand suspension was added dropwise to the above stirring metal salt solution over a period of 30 min. After the addition of whole amount of ligand, 15 mL of acetonitrile was added to the above reaction mixture and stirred overnight. A deep yellow precipitate appeared which was

filtered and washed with little amount of diethylether. The compound was recrystallized in acetone containing few drops of dimethylformamide. Yield: (0.180 g, 95%); Anal. Calc. for $C_{18}H_{14}N_3OClNi$ C, 56.53; H, 3.69; N, 10.99; Found C, 55.94; H, 3.80; N, 11.56; Selected IR data (KBr, ν_{max}/cm^{-1}): 1602 ($\nu_{C=N}$); $\Lambda_M/\Omega^{-1}cm^2mol^{-1}$ (DMF): 51; UV–visible [CH_3OH, λ_{max}/nm ($\varepsilon/M^{-1}cm^{-1}$)]: 249 (20080), 304 (13500), 320 (12860), 395 (11880); ESI–MS (acetonitrile, pos.): m/z 346.04 (100%) $[M\text{-}Cl]^+$; 404.00 (3.4%) $[M+Na]^+$.

Synthesis of [Ni(Phimp)(Pyimpy)](ClO_4)·H_2O (9c·H_2O)

A batch of complex [Ni(Phimp)Cl] (**9b**) (0.190 g, 0.5 mmol) was dissolved in 6 mL methanol: dimethylformamide (5:1) mixture and a batch of ligand Pyimpy (0.137 g, 0.5 mmol) dissolved in 15 mL methanol was added to it dropwise with continuous stirring over a period of 1 h. The color of the solution turned brownish red. After stirring for 3 h, a batch of $NaClO_4·H_2O$ (0.072 g, 0.5 mmol) was added to the reaction mixture. The reaction was stirred for further 2 h. A yellow precipitate appeared in the reaction mixture which was filtered and washed with little amount of methanol and subsequently with diethylether. Slow evaporation of methanolic solution of compound afforded nice block shaped crystals of X–ray diffraction quality. Yield (0.216 g, 60%); Anal. Calc. for $C_{35}H_{30}N_7O_6ClNi$ C, 56.90; H, 4.09; N, 13.27; Found C, 57.27; H, 4.32; N, 13.20; Selected IR data (KBr, ν_{max}/cm^{-1}): 1602 ($\nu_{C=N}$), 1098, 623 (ν_{ClO4^-}); μ_{eff} (297 K): 3.20 μ_B; $\Lambda_M/\Omega^{-1}cm^2mol^{-1}$ (DMF): 66; UV–visible [CH_3OH, λ_{max}/nm ($\varepsilon/M^{-1}cm^{-1}$)]: 251 (28900), 294 (18620), 334 (17480), 364 (19180), 408 (10260); ESI–MS (acetonitrile, pos.): m/z 620.16 (100%) $[M\text{-}ClO_4]^+$.

Synthesis of [Ni(^{t}BuPhimp)$_2$] (10a)

A batch of ^{t}BuPhimpH (0.400 g, 1 mmol) was dissolved in 20 mL of acetonitrile and NaH (0.034 g, 1.4 mmol) was added to it with continuous stirring. The reaction solution was allowed to stir for 1 h. The solution of the ligand became deep yellow in color. To this stirring solution, a batch of $NiCl_2 \cdot 6H_2O$ (0.119 g, 0.5 mmol) in 5 mL of acetonitrile was added as suspension and the reaction was stirred for 2 h. A bright yellow solid appeared in the solution which was washed with little amount of acetonitrile and subsequently with diethyl ether. Yield (0.394 g, 91%); Anal. Calc. for $C_{52}H_{60}N_6O_2Ni$ C, 72.64; H, 7.03; N, 9.77; Found C, 72.15; H, 6.90; N, 9.92; Selected IR data (KBr, ν_{max}/cm^{-1}): 1607 ($\nu_{C=N}$); μ_{eff} (297 K): 3.17 μ_B; $\Lambda_M/\Omega^{-1}cm^2mol^{-1}$ (DMF): 135; UV–visible [CH_3OH, λ_{max}/nm ($\varepsilon/M^{-1}cm^{-1}$)]: 235 (12800), 255 (10820), 316 (10940), 332 (9540), 425 (4920); ESI-MS (acetonitrile, pos.): m/z 858.40 (100%) $[M]^+$.

Synthesis of [Ni(^{t}BuPhimp)Cl] (10b)

A batch of ^{t}BuPhimpH (0.200 g, 0.5 mmol) was dissolved in 20 mL of distilled THF and NaH (0.024 g, 1 mmol) was added to it with continuous stirring. The reaction mixture was allowed to stir for 1 h. The solution of the ligand became deep yellow in color. The deprotonated ligand solution was added dropwise to the stirring solution of $NiCl_2 \cdot 6H_2O$ (0.119 g, 0.5 mmol) in 5 mL of dimethylformamide over a period of 30 min. The color of the solution changed to yellow–brown. No precipitation could be observed even after the addition of whole of the deprotonated ligand solution. The reaction was continued to stir for further 4 h and filtered. Filtrate of the reaction mixture afforded yellow–brown colored good quality crystals after slow evaporation. Yield (0.126 g, 51%); Anal. Calc. for $C_{26}H_{30}N_3OClNi$ C, 63.13; H, 6.11; N, 8.49; Found C, 64.02; H, 6.23; N, 8.39; Selected IR

data (KBr, ν_{max}/cm^{-1}): 1607 ($\nu_{C=N}$); $\Lambda_M/\Omega^{-1}cm^2mol^{-1}$ (DMF): 25; UV–visible [CH_3OH, λ_{max}/nm ($\varepsilon/M^{-1}cm^{-1}$)]: 228 (17940), 257 (16780), 282 *sh* (10780), 316 (13280), 407 (8940), 425 (10260); ESI–MS (acetonitrile, pos.): m/z 458.16 (100%) $[M\text{-}Cl]^+$.

Synthesis of [Ni(^{t}BuPhimp)(Pyimpy)](ClO_4) (10c)

A batch of complex [Ni(^{t}BuPhimp)Cl] (**10b**) (0.150 g, 0.303 mmol) was dissolved in 10 mL methanol and a batch of ligand Pyimpy (0.082 g, 0.303 mmol) dissolved in 3 mL methanol was added to it dropwise with continuous stirring over a period of 1 h. The color of the solution changed to yellow–orange. After stirring for 15 min, a batch of $NaClO_4 \cdot H_2O$ (0.050 g, 0.35 mmol) was added to the reaction mixture. The reaction was stirred for further 2 h and filtered to afford a yellow solid which was washed with little amount of methanol and subsequently with diethylether. Yield (0.142 g, 57%); Anal. Calc. for $C_{43}H_{44}N_7O_5ClNi$ C, 62.00; H, 5.32; N, 11.77; Found C, 62.57; H, 5.45; N, 11.34; Selected IR data (KBr, ν_{max}/cm^{-1}): 1607 ($\nu_{C=N}$), 1101, 623 (ν_{ClO4^-}); μ_{eff} (297 K): 3.42 μ_B; $\Lambda_M/\Omega^{-1}cm^2mol^{-1}$ (DMF): 65; UV–visible [CH_3OH, λ_{max}/nm ($\varepsilon/M^{-1}cm^{-1}$)]: 257 (31160), 286 *sh* (23160), 333 (22900), 353 (21580), 423 *sh* (10120), 442 (11680); ESI–MS (acetonitrile, pos.): m/z 732.28 (100%) $[M\text{-}ClO_4]^+$.

5.4.4. XJray crystallography

The X–ray data collection and processing for $[Ni(Phimp)_2]\cdot 3H_2O\cdot CH_3OH$ (**9a**$\cdot 3H_2O\cdot CH_3OH$) and $[Ni(Phimp)(Pyimpy)](ClO_4)\cdot H_2O$ (**9c**$\cdot H_2O$) were performed on Bruker Kappa Apex–II CCD diffractometer by using graphite monochromated Mo–Kα radiation (λ = 0.71073 Å) at 293-296 K to a maximum $^-$ range of 28°. In case of **9a**$\cdot 3H_2O\cdot CH_3OH$, the cation is situated about the center of inversion and full molecule was generated by "GROW" command. The details regarding the structure solution and

refinement are similar to those described in *Chapter 2*. The matrix parameters for **9a**·$3H_2O$·CH_3OH and **9c**·H_2O are listed in Table 5.11.

Table 5.11 Crystal data and structure refinement details for $[Ni(Phimp)_2]·3H_2O·CH_3OH$ (**9a**·$3H_2O$·CH_3OH) and $[Ni(Phimp)(Pyimpy)](ClO_4)·H_2O$ (**9c**·H_2O)

	9a·$3H_2O$·CH_3OH	**9c**·H_2O
Empirical formula	$C_{38}H_{36}N_6O_9Ni$	$C_{35}H_{28}N_7O_6ClNi$
Formula weight ($gmol^{-1}$)	779.42	736.78
Temperature /K	293(2)	296(2)
λ (Å) (Mo-Kα)	0.71073	0.71073
Crystal system	Hexagonal	Monoclinic
Space group	*R -3 c*	*P 21/c*
a (Å)	20.8652(16)	10.8865(5)
b (Å)	20.8652(16)	18.9550(8)
c (Å)	49.166(3)	16.9518(7)
~ (°)	90.00	90.00
β (°)	90.00	98.581(2)
γ (°)	120.00	90.00
V ($Å^3$)	18537(4)	3458.9(3)
Z	18	4
ρ_{calc} (gcm^{-3})	1.257	1.415
F(000)	7308	1520
Theta range for data collection	1.40 ─ 28.26	1.62 ─ 28.23
Index ranges	$-16 < h < 27$, $-27 < k < 9$, $-65 < l < 42$	$-13 < h < 14$, $-25 < k < 22$, $-22 < l < 18$
Refinement method	Full matrix least–squares on F^2	Full matrix least–squares on F^2
Data/restraints/parameters	14220/0/ 248	8457/0/452
GOF[a] on F^2	0.946	0.988
R_1[b] [$I > 2\sigma(I)$]	0.0784	0.0591
R_1[all data]	0.1435	0.1539
wR_2[c] [$I > 2\sigma(I)$]	0.1896	0.1424
wR_2 [all data]	0.2421	0.1881

5.4.5. Theoretical studies

Theoretical calculations were performed using Density Functional Theory (DFT) with Becke's three–parameter hybrid exchange functional and the Lee–Yang–Parr correlational

functional (B3LYP) supplemented with the standard LanL2DZ basis–set.[197] The atomic coordinates of **9c**·H_2O were taken from its crystal structure. The optimized geometries corresponding to the minimum on the potential energy surface have been obtained by solving self–consistent field equation iteratively. The calculations were performed with the *Gaussian 03* (G03) suite[511] of programs and orbital diagrams were constructed at isosurface of 0.02 using *Gaussview 3.0*[512].

5.4.6. DNA binding and cleavage experiments

DNA binding experiments were performed in 0.1 M phosphate buffer (pH 7.2) using a solution of calf thymus (CT) DNA which gave a ratio of absorbance at 260 and 280 nm (A_{260}/A_{280}) of *ca.* 1.8, indicating that the CT–DNA was sufficiently protein free.[332,404] Absorption titration experiments were carried out with complex concentration of 30─50 μM varying the CT–DNA concentration from 0─385 μM in 0.1 M phosphate buffer (pH 7.2). The binding constants K_b were calculated according to the reported method.[332,404] Fluorescence quenching experiments were carried out by successive addition of metal complexes (0–53 μM) to the DNA (25 μM) solutions containing 5 μM ethidium bromide (EB) in 0.1 M phosphate buffer (pH 7.2) and the reaction mixture was incubated for 2 min after each successive addition of quencher molecules. For better solubility of complexes 2% DMF was used. These samples were excited at 250 nm and emissions were observed between 500 and 700 nm. Stern–Volmer quenching constants K_{SV} were calculated according to the reported procedure.[332,404] Circular dichroism (CD) spectra of CT–DNA in absence and presence of metal complexes were recorded with a 0.1 cm pathJlength cuvette after 15 min incubation at 25 °C with three scans averaged for each CD spectrum. The concentration of the complexes and CT–DNA were 50 and 200 μM respectively.

Cleavage of plasmid DNA was monitored by using agarose gel electrophoresis. Supercoiled pBR322 DNA (100 ng) in Tris–boric acid–EDTA (TBE) buffer (pH 8.2) was treated with metal complexes (50 μM) in the absence of additives. The mechanism of DNA cleavage by complex **10b** was studied in presence of DMSO, ethanol, urea, NaN_3, L–histidine (20 mM each), D_2O (10%) and catalase (10 U) as scavenging agents. The samples were incubated for 2 h at 37 °C followed by the addition of loading buffer (25% bromophenol blue and 30% glycerol) prior to the gel electrophoresis. The details regarding the procedures of DNA binding and DNA cleavage experiments have been described in previous chapters.

5.4.7. Protein binding experiments

The stock solutions of BSA were prepared as described in previous chapters (*Chapters 1, 3 and 4*). Quenching of the intrinsic fluorescence of tryptophan residues in BSA was carried out using metal complexes (**9-10**) as quencher molecules. BSA solution (2×10^{-6} M) in 0.1 M phosphate buffer (pH 7.2) with 2% DMF was equilibrated for 30 min at room temperature and the emission spectrum was recorded between 300 and 600 nm using the excitation wavelength of 295 nm which is selective for tryptophan residues.[346] Incremental additions of the quenchers (0–44 μM) were made to the BSA solution followed by an incubation period of 2 min after each successive addition and the spectra were recorded. Binding behaviors of the quencher molecules with serum albumin were compared using Stern–Volmer and Scatchard graphs.[347] In order to investigate the binding site of metal complexes, site marking experiments were carried out in presence of warfarin and ibuprofen (for site I and site II respectively). For this purpose, BSA was equilibrated with warfarin ([BSA] = 40 μM; [warfarin] = 80 μM) or ibuprofen ([BSA] = [ibuprofen] = 2 μM) in 0.1 M

phosphate buffer (pH = 7.2) for 1 h at 25 °C and emission spectral changes were recorded in presence of varying concentrations of metal complexes.[499,500]

6.1. Introduction

Metal ion sensing is an important area of chemical research[513-524] and can be accomplished by various types of techniques including atomic absorption spectroscopy (AAS), colorimetry, spectrophotometry and voltammetry[525-528]. Investigation of literature[513-524] revealed that metal ion sensing by fluorescence quenching or, conversely, enhancement of fluorescence can also provide important information concerning metal ion detection. In fact, fluorometric methods are highly sensitive and appreciable for the detection of metal ions, particularly of paramagnetic nature which results generally with the quenching of fluorescence though, in some cases enhancement in the emission intensity has also been achieved.[528]

Nickel, a biologically important metal ion[77] is supposed to be involved in protein structure and function[78]. Nickel also activates certain enzymes and is an important constituent of the active site of several enzymes participating in various microbial pathways including carbon monoxide dehydrogenase CODH, acetylCoA synthase (ACS) and methyl-coenzyme M reductase (MCR)[529,530]. Deficiency of nickel in plants may lead to the disorder of urease enzyme causing the accumulation of urea up to toxic level. Moreover, this deficiency may cause scarcity of usable nitrogen sources giving rise to disorder in growth[75]. Higher concentrations may induce inhibition of root functions, plant growth[531] and photosynthesis[532-535].

Nickel complexes possess considerable significance in modern industry and are used for making Ni-Cd batteries, stainless steel, electronic equipments and for electroplating.[531] Finely divided nickel functions as a catalyst in the hydrogenation of vegetable oils.[80] The increased usage of nickel-containing products may cause their accumulation in the

ecosystem leading to detrimental effects on human health. Nickel is known to cause skin allergies, lung fibrosis, acute pneumonitis, poisoning of kidney as well as cardiovascular systems and neoplastic transformations.[531] It is known to bind with amino acids, peptides, proteins and nucleic acids and promotes lipid and protein oxidation.[536] It can cross the human placenta and may cause lipid peroxidative damage to the placental membrane leading to potential embryotoxicity.[537] Recently, Costa and co-workers reported that nickel ions may induce transgenic silencing by inhibiting the histone demethylation process and thereby increasing H3K9 dimethylation.[538,539] Nickel can also exhibit neurotoxic effects and exposure to nickel may cause apoptosis of olfactory sensory and cerebral cortex neurons alongwith the disruption of neurotransmitters.[540] Hence detection of Ni^{2+} possesses considerable environmental significance. In the recent years there has been an upsurge of interest in the synthesis and characterization of metal-selective fluorescence chemosensors because the concentration and the localization for a particular metal ion are extremely important. Herein, the sensing of Ni^{2+} by fluorescence enhancement is described. However, fluorescence probes for Ni^{2+} are scarce[519,520,524,541-544] because fluorescence is quenched by the paramagnetic Ni^{2+} ion.[544-545]

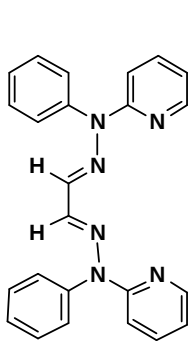

Gimpy

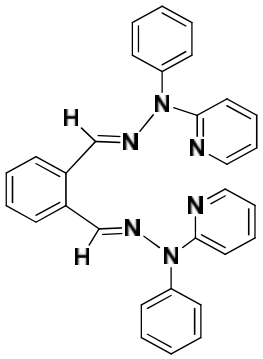

Timpy

Scheme 6.1 Schematic drawings of ligands Gimpy and Timpy

We have been working with Gimpy and Timpy (shown in Scheme 6.1) where copper complexes exhibited fluorescence when they were reacted with nitric oxide.[413] Herein we describe the fluorescence properties of Gimpy and Timpy and their responses in terms of fluorescence due to the presence of different metal ions in solution. A novel enhancement of emission intensity in presence of Ni^{2+} ions prompted us to synthesize nickel complexes derived from Gimpy and Timpy. We have synthesized $[(Ni(Gimpy)(\mu–Cl))_2](ClO_4)_2$ (**11**) and $[(Ni(Timpy)(\mu–Cl))_2](ClO_4)_2{\cdot}2(CH_3)_2CO$ (**12**$\cdot 2(CH_3)_2CO$) and characterised by different spectroscopic studies. Molecular structures of Gimpy and $[(Ni(Timpy)(\mu–Cl))_2](ClO_4)_2{\cdot}2(CH_3)_2CO$ (**12**$\cdot 2(CH_3)_2CO$) were determined by X-ray crystallography. Magnetic properties and redox properties of the complexes were investigated.

6.2. Results and discussion

6.2.1. Synthesis and characterization of the ligands

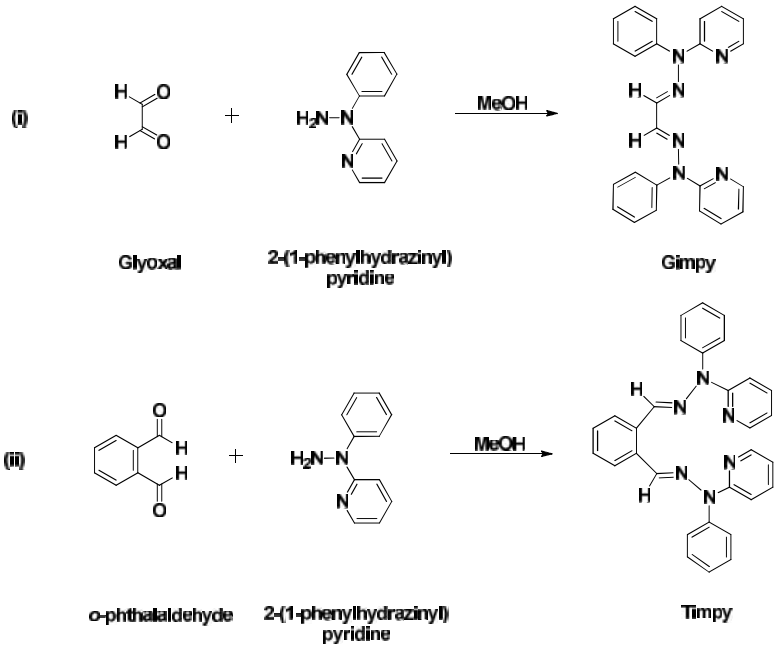

Scheme 6.2 Schematic representation of syntheses of ligands (i) Gimpy and (ii) Timpy respectively

The ligand Gimpy (or Timpy) was obtained by condensation reaction between a 1:2 mixture of glyoxal (or *o*-phthalaldehyde) and 2–(1–phenylhydrazinyl)pyridine in methanolic solution following reported procedures.[413] Synthetic routes for the preparation of ligands Gimpy and Timpy are shown in Scheme 6.2.

6.2.2. Synthesis and characterization of nickel complexes

The nickel complexes $[(Ni(Gimpy)(\mu–Cl))_2](ClO_4)_2$ (**11**) was synthesized by the reaction of $NiCl_2{\cdot}6H_2O$ with Gimpy in 1:1 molar ratio and isolated as a yellow colored compound. Similar reaction of $NiCl_2{\cdot}6H_2O$ with Timpy afforded $[(Ni(Gimpy)(\mu–Cl))_2](ClO_4)_2{\cdot}2(CH_3)_2CO$ (**12**$\cdot 2(CH_3)_2CO$) as a green colored microcrystalline compound. Both reactions were performed in open atmosphere and the compounds were obtained in good yields. Synthetic procedures of complexes **11** and **12**$\cdot 2(CH_3)_2CO$ are summarized in Scheme 6.3.

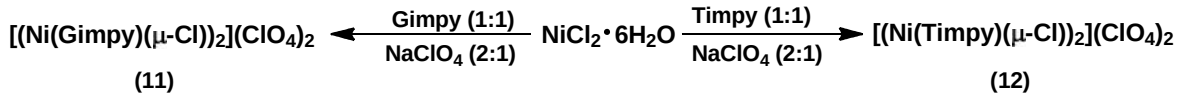

Scheme 6.3 Schematic drawing of synthesis of complexes **11** and **12**$\cdot 2(CH_3)_2CO$

Table 6.1 Data for yield, elemental analysis, IR and conductivity

Complex	Yield %	Elemental analysis			Selected IR data (cm^{-1})[a]	Conductivity i_M ($t^{-1}cm^2mol^{-1}$)
		C	H	N		
11	82	49.55	3.73	14.83	1604, 1077, 625	153[b]
12$\cdot 2(CH_3)_2CO$	70	55.19	4.38	11.41	1599, 1099, 623	190[b]

[a]KBr pallets, solvent: [b]dimethylformamide

(i) IR spectral studies

The coordination of azomethine nitrogen in complexes **11** and **12.**2$(CH_3)_2CO$ was evident in the IR spectra from a shift of about 15 cm^{-1} to higher wavenumbers in $\nu_{C=N}$ as compared to those of free ligands (1589 and 1584 cm^{-1}, respectively).[385] Complexes **11** and **12.**2$(CH_3)_2CO$ also showed peaks at 1077 and 1099 cm^{-1}, respectively, along with a peak near 623 cm^{-1} suggesting the presence of non–coordinated perchlorate ions outside their coordination sphere.[332]

(ii) Electronic properties

Electronic absorption spectra of complexes **11** and **12.**2$(CH_3)_2CO$ in methanol consisted of intense absorption bands within 200–400 nm region. These bands were assigned as π–π* intra–ligand transitions (Fig. 6.1, Table 6.2). The absorption band in the UV–visible spectra of complex **11** beyond 400 nm associated with high extinction coefficient value was assigned as ligand-to-metal charge transfer transitions (LMCT)[546] (Fig. 6.1, Table 6.2) however, no corresponding LMCT band could be observed for **12.**2$(CH_3)_2CO$.

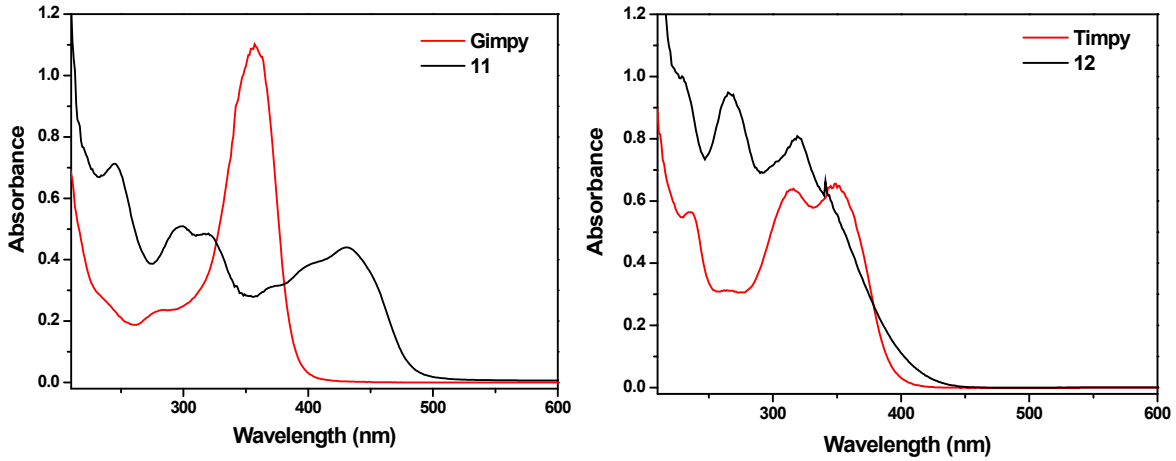

(a) (b)

Fig. 6.1 Electronic absorption spectra of (a) Gimpy and its nickel complex **11**, (b) Timpy and its nickel complex **12**·2$(CH_3)_2CO$ (20 μM each) in methanol at 298 K

Table 6.2 UV–visible spectral data of complexes **11** and **12.**$2(CH_3)_2CO$

Complex	$^{a}_{max}$/nm (£/$M^{-1}cm^{-1}$)[a]
11	245 (35930), 298 (25750), 319 (24390), 369 *sh* (15590), 401 *sh* (19300), 430 (22240)
12·$2(CH_3)_2CO$	229 *sh* (49905); 265 (47330), 320 (40310), 342 *sh* (30955)

[a]UV–visible data recorded in methanol

(iii) ESI-Mass spectroscopy

The complexes **11** and **12**·$2(CH_3)_2CO$ were subjected to ESI–mass spectrometric analysis in acetonitrile : water (1:1) mixture and analyzed under positive mode. The electro–spray ionization mass spectrum (ESI-MS) of **11** showed a peak with m/z value of 485.07 probably due to the formation of [**11**-$2(ClO_4)$]$^{2+}$ cation with loss of two perchlorate ions present outside the coordination sphere (Fig. 6.2).

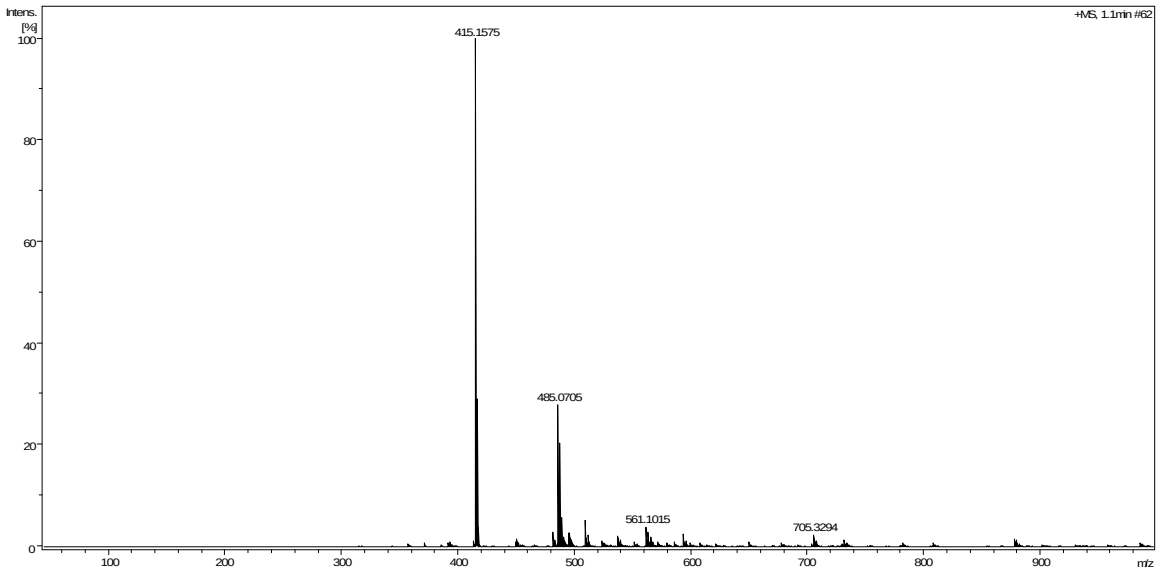

Fig. 6.2 The ESI–mass spectrum of [(Ni(Gimpy)(μ–Cl))$_2$]$(ClO_4)_2$ (**11**) in acetonitrile showing the peak at (m/z) 485.07 corresponding to the formation of [M-$2(ClO_4)$]$^{2+}$ cation

Similarly, the peak observed at (m/z) 561.10 in ESI–Mass spectrum of **12**·2$(CH_3)_2CO$ was assigned to the formation of [**12**-2$(ClO_4)_2]^{2+}$ cation due to the loss of two uncoordinated perchlorate anions (Fig. 6.3).

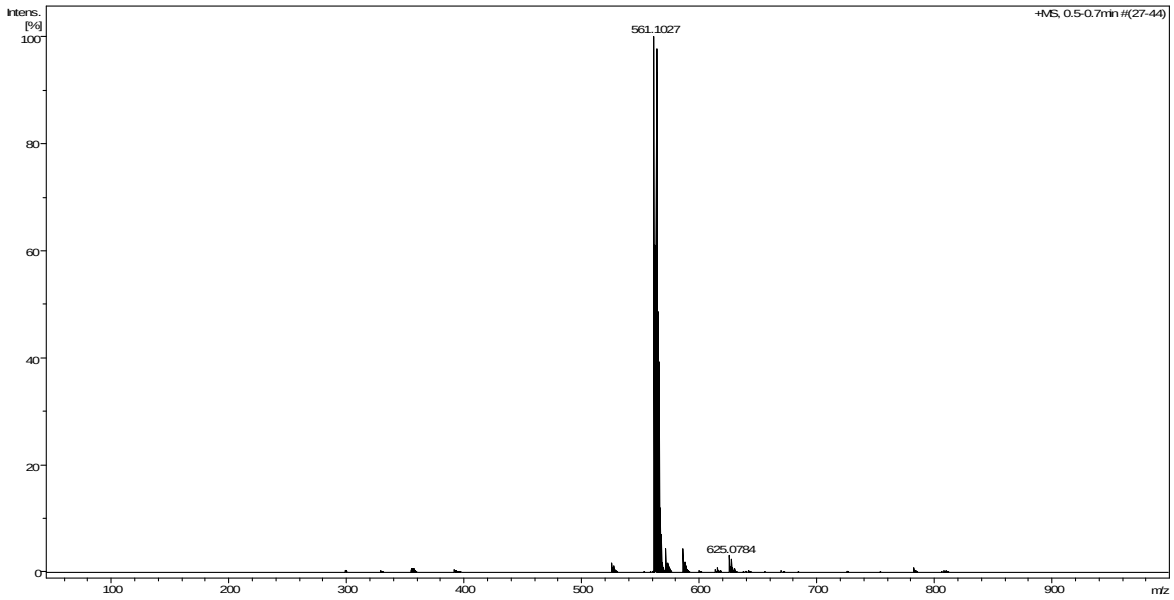

Fig. 6.3 The ESI–mass spectrum of $[(Ni(Timpy)(\mu–Cl))_2](ClO_4)_2 \cdot 2(CH_3)_2CO$ (**12**·2$(CH_3)_2CO$) in acetonitrile showing the peak at (m/z) 561.10 corresponding to the formation of $[M\text{-}2(ClO_4)]^{2+}$ cation

(iv) Conductivity measurements

The molar conductivity measurements for complexes **11** and **12**·2$(CH_3)_2CO$ in DMF solutions (ca. 10^{-3} M) gave conductivity values of 153 $\Omega^{-1}cm^2mol^{-1}$ and 190 $\Omega^{-1}cm^2mol^{-1}$ respectively. These data indicated their bi-univalent nature in solution.[387]

6.2.3. Description of molecular structures

Crystals of Gimpy suitable for X-ray diffraction were grown by slow evaporation of solution of compound in dichloromethane : DMF mixture (99:1). The molecular structure of Gimpy is illustrated in Fig. 6.4.

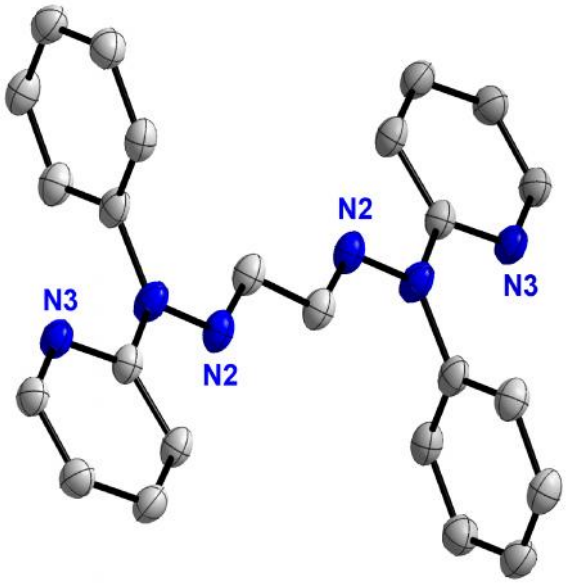

Fig. 6.4 ORTEP representation of the crystal structure of **Gimpy** showing atom numbering scheme and displacement ellipsoid (50% probability level). Hydrogen atoms are omitted for clarity

The molecule is situated about a crystallographic centre of inversion so that the imine bonds [N2=C12 = 1.2856(17) Å] are *anti*. The central C12–C12^{i} bond length is 1.441(2) Å, an observation consistent with some delocalisation of π–electron density over the central chromophore (symmetry operation i: ½-x, ½-y, 1-z). Indeed, the sum of the angles around the amine-N1 atom of 359.5° and the co-planarity of the pyridyl ring with the 2–hydrazinylideneethylidene)hydrazine backbone [the N2–N1–C1–N3 torsion angle is 174.18(11)°], suggest that the delocalisation extends throughout the molecule with the exception of the phenyl rings which are approximately perpendicular to the central plane [N2–N1–C6–C7 = 100.53(14)°]. In the crystal packing of Gimpy, supramolecular chains aligned along [1 0 1] are formed by pyridyl-C–H···π(phenyl) edge-to-face interactions (Fig. 6.5), and these assemble into layers in the ab-plane with no significant intermolecular interactions between them (Fig. 6.6).

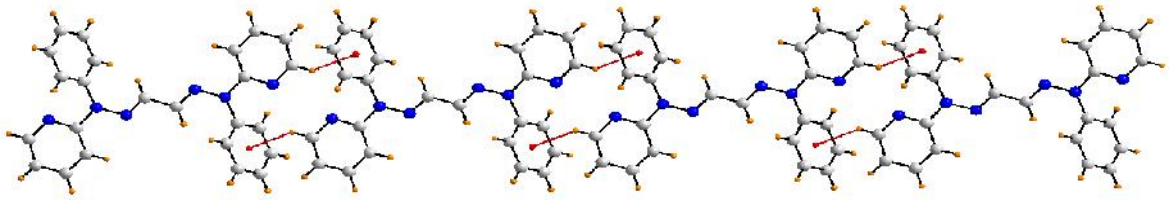

Fig. 6.5 Supramolecular chain in Gimpy aligned along [1 0 1] and sustained by C–H···π interactions [C2–H2···Cg(C6-C11)^{i} = 2.87 Å, C2···Cg(C6-C11)^{i} = 3.6488(15) Å with angle at H2 = 140^{o} for symmetry operation i: 1-x, 2-y, 1-z] shown as red dashed lines

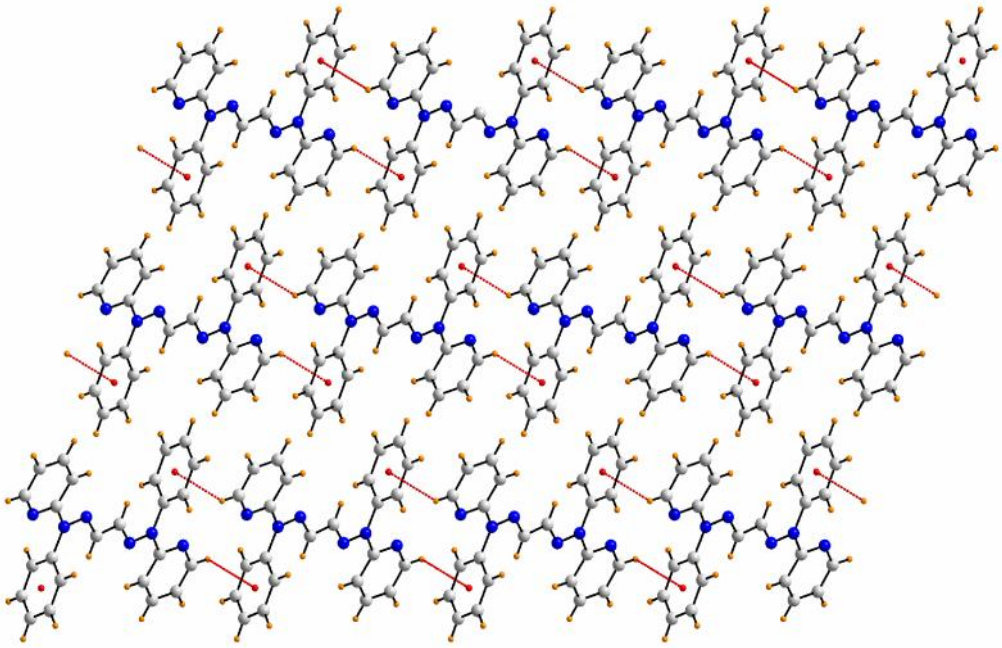

Fig. 6.6 A view in projection down the *b*-axis of the assembly of supramolecular chains in the *ab*-plane and the stacking of these along the *c*-axis; no significant intermolecular interactions connect the chains. The C–H···π interactions are shown as red dashed lines

To investigate the mode of binding of the ligands with metal center, X–ray quality crystals of **12**.2$(CH_3)_2CO$ were grown by diffusion of acetone in the solution of compound in dichloromethane and subjected to X–ray diffraction studies. Molecular structure of **12**.2$(CH_3)_2CO$ along with the coordination environment of the metal centers is represented in Fig. 6.7. The asymmetric unit of **12**.2$(CH_3)_2CO$ comprises half a binuclear dication being

located about a centre of inversion, one perchlorate anion, providing the charge balance, and a lattice acetone molecule of solvation.

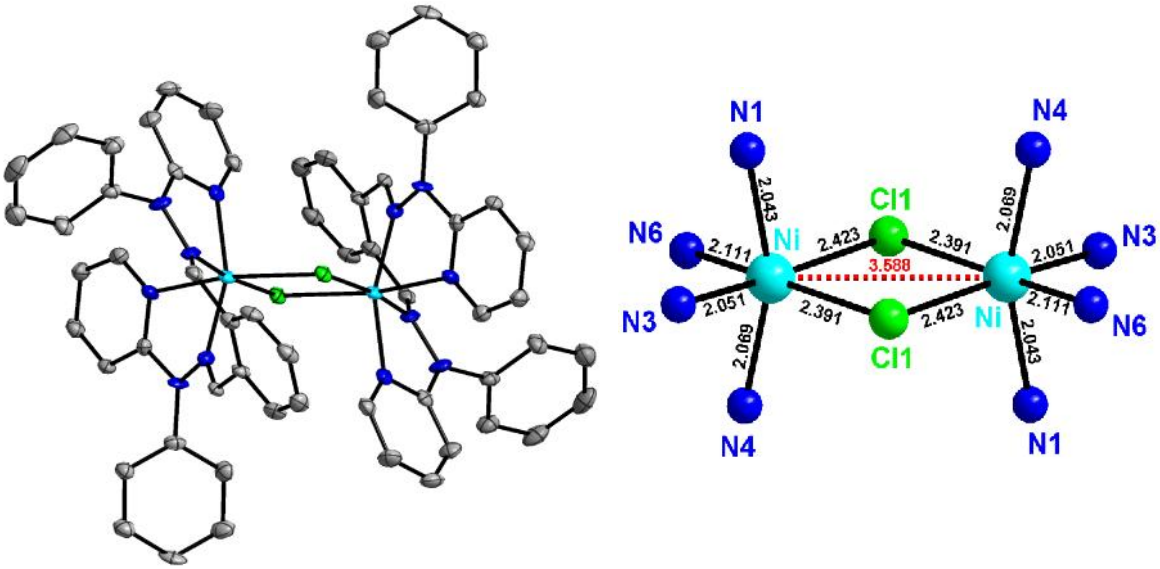

(a) (b)

Fig. 6.7 (a) ORTEP representation of the crystal structure of **12**·2$(CH_3)_2CO$ showing atom numbering scheme and displacement ellipsoid (50% probability level). Hydrogen atoms are omitted for clarity; (b) octahedral disposition of donors exhibiting the bond distances from metal centers

In the dication, the Ni atoms are bridged by Cl atoms that showed nearly equivalent Ni–Cl bond lengths. These bond distances are consistent with those reported by Hahn et al. [547] however, the distances reported by Salehzadeh and co−workers are more than our values[548]. The remaining four sites in the distorted octahedral geometry about the Ni atom are defined by two mutually *cis* pyridyl–N atoms and two *cis* imino–N atoms provided by the tetradentate Timpy ligand. The octahedral coordination geometry is based on a *cis*–Cl_2N_4 donor set. The Ni–N bond lengths span a relatively narrow range but Ni–N6 bond length, with the N6 being *trans* to a chloride [the N6–Ni–Cl1 bond angle is 166.91(10)º], is significantly longer than the other Ni–N bonds. The average bond distances of nickel to

imine and pyridine nitrogens are 2.060 Å and 2.077 Å respectively which are consistent with the reported values in structurally related complexes.[548-549] The greatest deviation from the ideal octahedral geometry is manifested in the N1–Ni–N4 bond angle of 159.06(13)º. Selected bond lengths along with the bond angles are collated in Table 6.3.

Table 6.3 Selected bond lengths (Å) and bond angles (˚) for **12**·2$(CH_3)_2CO$

Bond length (Å)		Bond angles (˚)	
Ni−N(1)	2.043(4)	N(1)−Ni−N(3)	77.76(14)
Ni−N(3)	2.051(3)	N(1)−Ni−N(4)	159.06(13)
Ni−N(4)	2.069(4)	N(3)−Ni−N(4)	88.62(14)
Ni−N(6)	2.111(3)	N(1)−Ni−N(6)	90.80(13)
Ni−Cl(1)	2.423(11)	N(3)−Ni−N(6)	99.93(14)
Ni−Cl(1)^{i}	2.391(11)	N(4)−Ni−N(6)	75.80(13)
		N(1)−Ni−Cl(1)^{i}	97.22(10)
		N(3)−Ni−Cl(1)^{i}	91.90(1)
		N(4)−Ni−Cl(1)^{i}	99.08(10)
		N(6)−Ni−Cl(1)^{i}	166.91(10)
		N(1)−Ni−Cl(1)	97.74(10)
		N(3)−Ni−Cl(1)	173.23(11)
		N(4)−Ni−Cl(1)	97.07(10)
		N(6)−Ni−Cl(1)	85.08(10)
		Cl(1)^{i}−Ni−Cl(1)	83.60(4)
		Ni^{i}−Cl(1)−Ni	96.40(4)

Symmetry equivalents: (i) 1-x, 1-y, 1-z

The crystal structure of **2**.2$(CH_3)_2CO$ features a large number of C–H···O interactions, involving each of the oxygen atoms (atom O3 is bifurcated) that consolidate a three−dimensional architecture. The crystal packing may be described as comprising columns of complex dications aligned along the a-axis interconnected by complex-C–H···O(perchlorate) interactions; the acetone molecules associated with the dications via C–H···O interactions (Fig. 6.8). The geometric parameters characterizing the intermolecular interactions are included in Table 6.4.

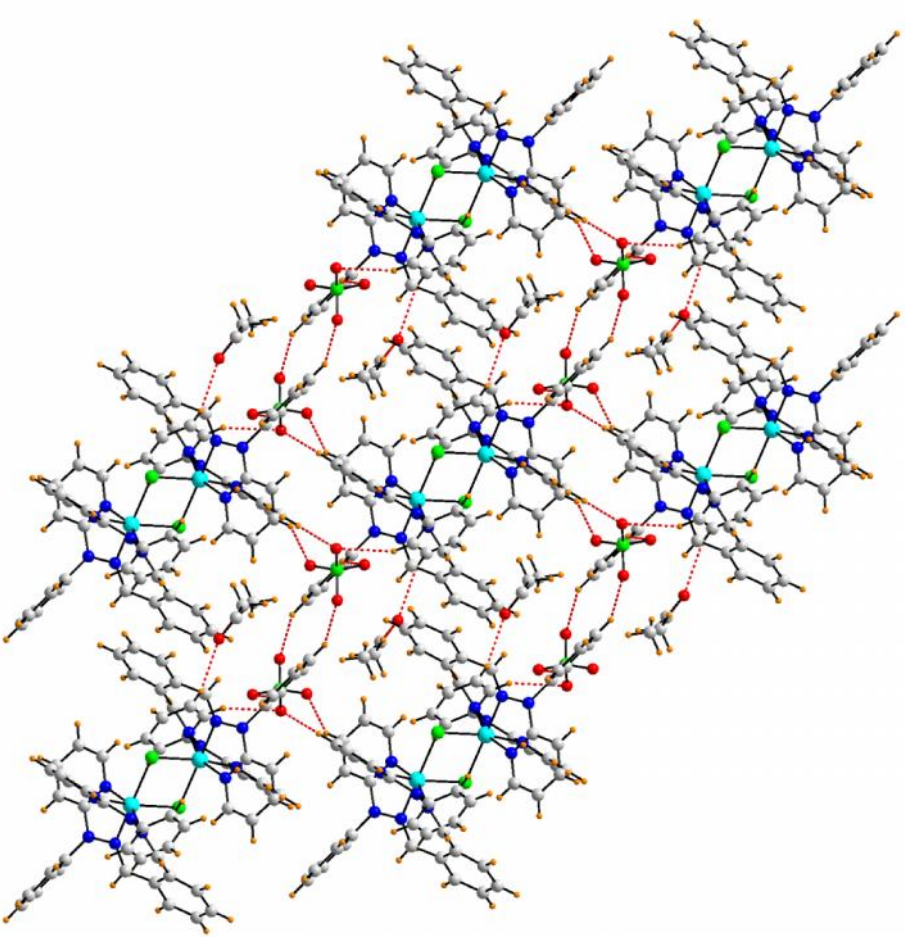

Fig. 6.8 A view in projection down the *a*-axis of the unit cells of **12**.2$(CH_3)_2CO$. The C–H···O interactions are shown as orange dashed lines

Table 6.4 Geometric parameters for intermolecular interactions in **12**.2$(CH_3)_2CO$

DJH···A	**D···A (Å)**	**H···A (Å)**	**DJH···A (°)**
C3–H3···O2^{i}	3.362(6)	2.519(7)	147.90(32)
C9–H9···O4^{ii}	3.274(7)	2.473(9)	141.96(32)
C11–H11···O1^{ii}	3.382(6)	2.482(6)	158.15(32)
C24–H24···O5^{iii}	3.273(6)	2.436(5)	146.88(31)
C25–H25···O3^{iii}	3.420(5)	2.536(3)	154.94(23)
C29–H29···O3^{iv}	3.147(5)	2.443(11)	130.81(25)

Symmetry equivalents: (i) 1-x, 1-y, 2-z; (ii) 1-x, -y, 2-z; (iii) 1+x, y, z; (iv) 2-x, 1-y, 2-z

6.2.4. Magnetic properties

Dinuclear structure of the nickel complex authenticated by X–ray crystallographic technique prompted us to examine the magnetic properties of complexes at variable temperatures. Magnetic measurements were performed on crystalline samples of complexes **11** and **12**.2$(CH_3)_2CO$ in the temperature range 3 K–300 K under an applied magnetic field of 5000 G. The temperature dependence of molar magnetic susceptibility (χ_m) for each dinuclear Ni(II) compound is illustrated in Figures 6.9 and 6.10 in the form of χ_m versus T and χ_mT versus T plots. The χ_mT values for the dinuclear complexes **11** and **12**.2$(CH_3)_2CO$ at 300 K are 2.32 cm^3 K mol^{-1} and 2.12 cm^3 K mol^{-1} respectively which are consistent with that expected for two magnetically isolated spin triplets.[550-552] With the decreasing temperature, the susceptibility values (χ_m) for both complexes increased monotonically exhibiting a sudden increase in the values below 10 K. However, χ_mT versus T plots exhibited different types of behaviour for complexes **11** and **12**.2$(CH_3)_2CO$. As the temperature was lowered from 300 K to 13 K, the χ_mT product for **11** underwent a decrease from 2.32 cm^3 K mol^{-1} to 1.88 cm^3 K mol^{-1}. Such type of behaviour is exhibited by some Ni(II) dinuclear complexes exhibiting antiferromagnetic interactions.[552-553] With further reduction in temperature, the χ_mT values increased sharply to 2.76 cm^3 K mol^{-1} at 9 K and then underwent a sudden decrease reaching upto 1.10 cm^3 K mol^{-1} at 3 K indicating ferromagnetic interactions between two Ni(II) ions of the dinuclear species.[551,554-555] For **12**.2$(CH_3)_2CO$, χ_mT value increased continuously with decreasing temperature reaching a maximum of 3.71 cm^3 K mol^{-1} at 8 K and then decreased sharply to 3.46 cm^3 K mol^{-1} at 3 K. The magnetic behaviour of **12**.2$(CH_3)_2CO$ indicated the presence of intramolecular ferromagnetic exchange interactions between the two Ni(II) ions.[555] The final decrease in

$\chi_m T$ products may be due to the saturation effect or interdimer antiferromagnetic interaction.[556]

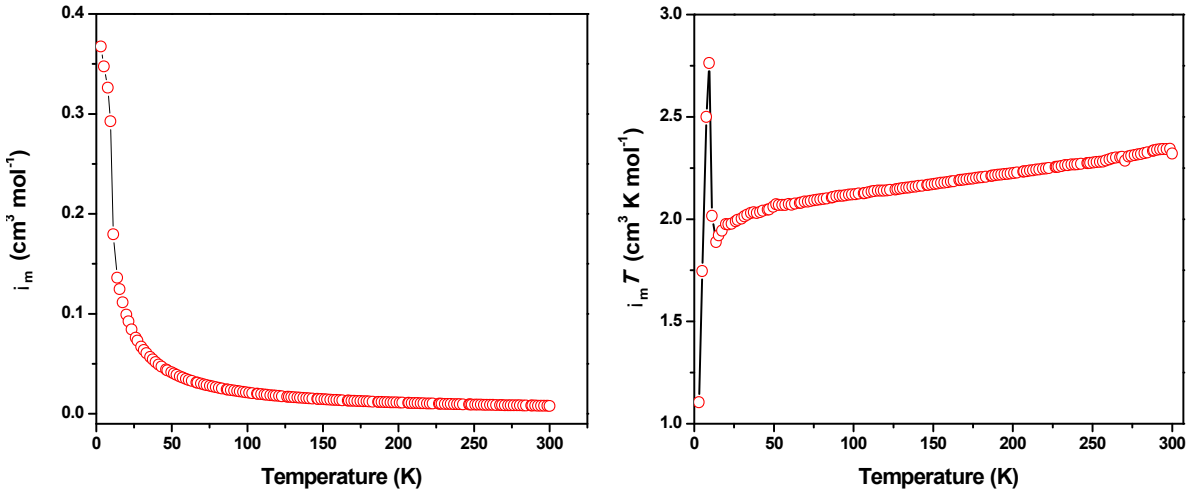

(a) (b)

Fig. 6.9 (a) Molar magnetic susceptibility (χ_m) vs. temperature (T) curve for **11** and (b) plot of $\chi_m T$ vs T

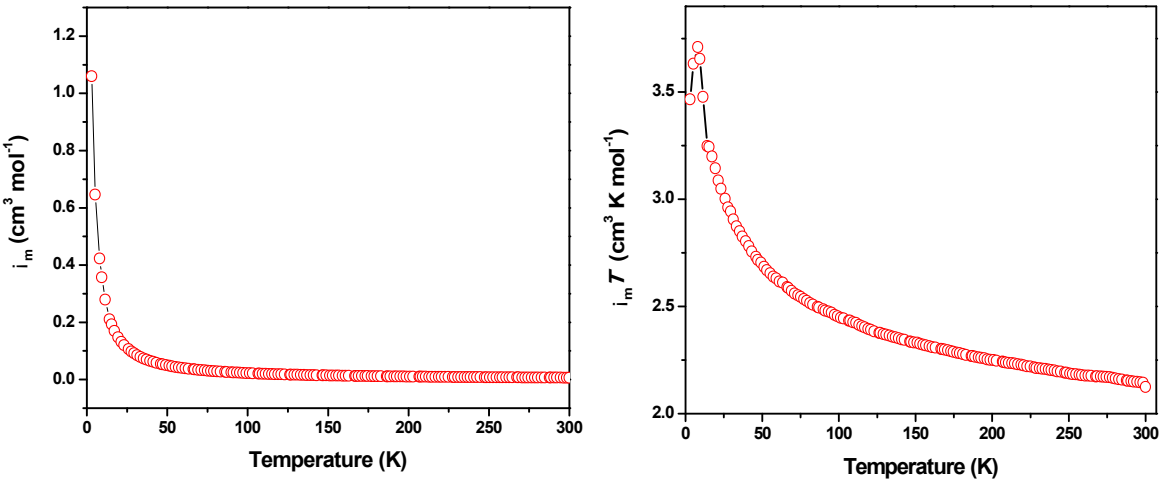

(a) (b)

Fig. 6.10 (a) Molar magnetic susceptibility (χ_m) vs. temperature (T) curve for **12**.2$(CH_3)_2CO$ and (b) plot of $\chi_m T$ vs T

6.2.5. Photophysical properties

In order to see the influence of the presence of metal ions on absorption spectra of Gimpy and Timpy, their UV–visible spectra were recorded at room temperature in methanol containing equimolar concentrations of various divalent metal salts namely $MnCl_2 \cdot 4H_2O$, $FeCl_2$, $CoCl_2 \cdot 6H_2O$, $NiCl_2 \cdot 6H_2O$, $CuCl_2 \cdot 2H_2O$, $ZnCl_2$, $CdCl_2 \cdot H_2O$ and $HgCl_2$. A considerable change in the electronic absorption spectrum profile of Gimpy was observed in presence of Cd^{2+} and Cu^{2+} ions, however, rest of the metal ions including Ni^{2+} could only bring about little or negligible change in the spectrum profile (Fig. 6.11, a). In case of Timpy, only Cu^{2+} ion could exhibit a remarkable change in the absorption spectrum (Fig. 6.11, b).

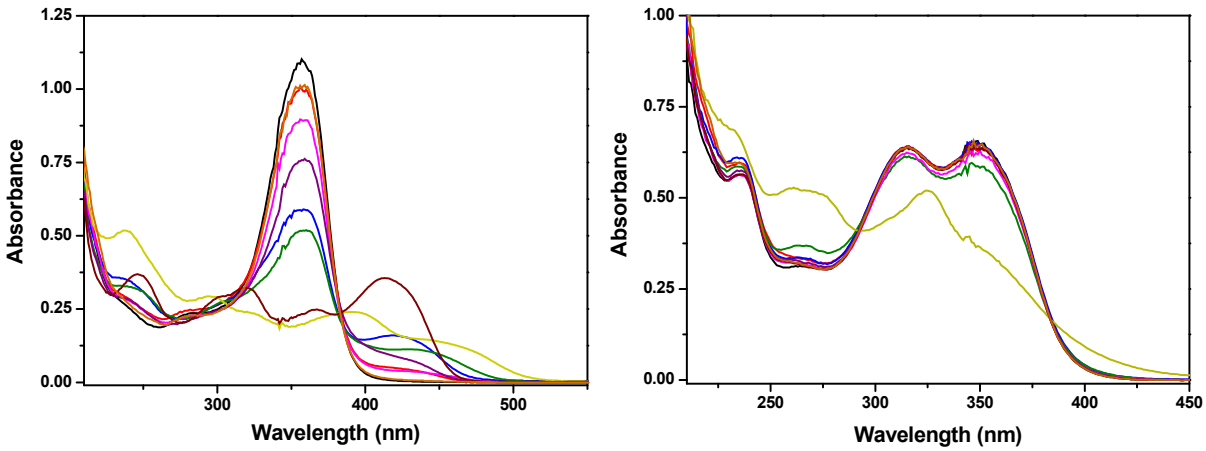

(a) (b)

Fig. 6.11 Absorption spectral changes of (a) Gimpy (20 μM) and (b) Timpy (20 μM) in presence of equimolar concentrations of different divalent metal ions in methanol at 298 K (Mn^{2+}(red), Fe^{2+}(blue), Co^{2+}(green), Ni^{2+}(pink), Cu^{2+}(yellow), Zn^{2+}(purple), Cd^{2+}(brown) and Hg^{2+}(orange) respectively)

Gimpy and Timpy display photoluminescence properties and show emission spectra with λ_{em} 415, 435 and 460 nm upon excitation at 370 nm in methanol.[413] The emission spectra of each of Gimpy and Timpy (50 μM) were also recorded in presence of 1 equivalent

of $MnCl_2·4H_2O$, $FeCl_2$, $CoCl_2·6H_2O$, $NiCl_2·6H_2O$, $CuCl_2·2H_2O$, $ZnCl_2$, $CdCl_2·H_2O$ and $HgCl_2$ in methanol at 298 K. Both Gimpy and Timpy showed a significant enhancement in intensity in the presence of Ni^{2+} ions with the maxima at 447 and 435 nm respectively whereas no significant change was observed when solutions were charged with any of other metal ions investigated (Figures 6.12–6.13).

These data indicated that Gimpy and Timpy could detect the Ni^{2+} ions in solution and might serve as turn–on fluorescent probes. This detection of Ni^{2+} ions by Gimpy and Timpy is of considerable importance since Ni^{2+}-responsive fluorescent probes are rare.[527] Job's plots by continuous variation method afforded a 1:1 stoichiometry between Gimpy (or Timpy) and Ni^{2+} (Figures 6.14 and 6.15 respectively).

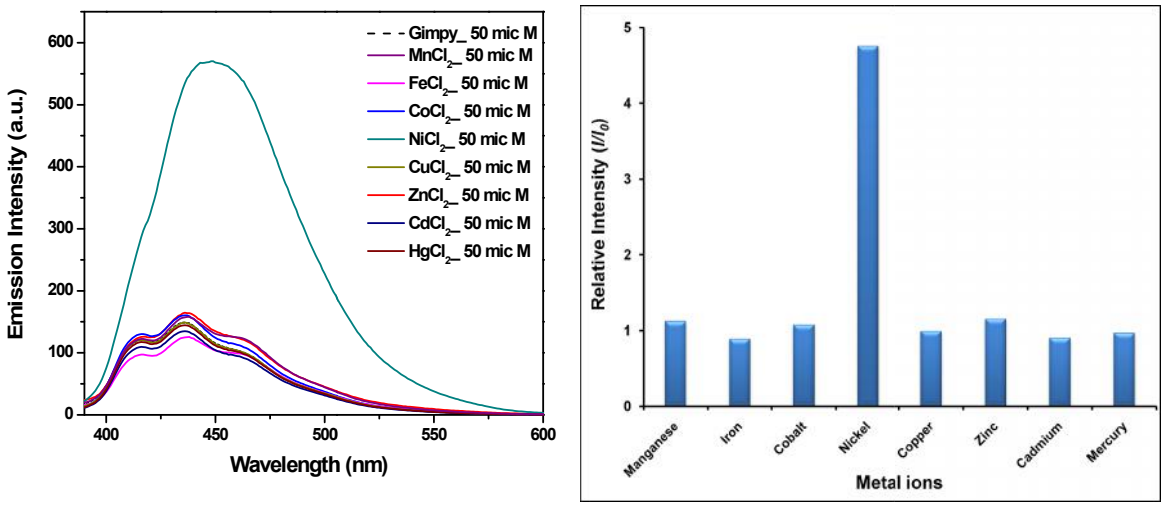

(a) (b)

Fig. 6.12 (a) Fluorescence emission spectra of Gimpy (50 μM) in presence of different metal ions (50 μM) in methanol at 298 K; (b) bar representation of sensitivity of Gimpy towards different metal ions in methanol at 298 K. Relative intensity is given as the ratio of emission intensity of Gimpy in presence (I) and absence (I_0) of equimolar concentrations of metal ions respectively

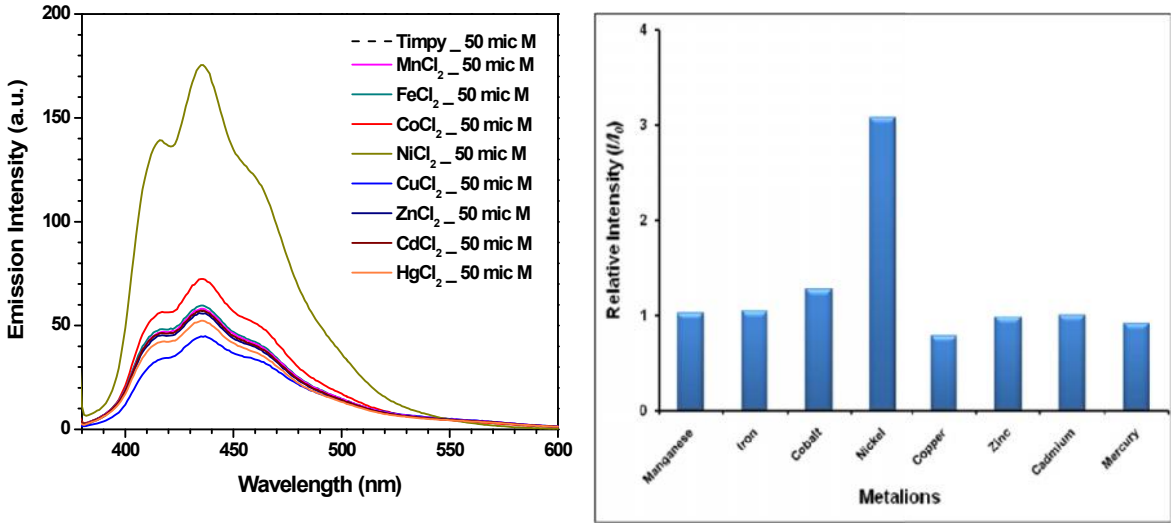

(a) (b)

Fig. 6.13 (a) Fluorescence emission spectra of Timpy (50 μM) in presence of different metal ions (50 μM) in methanol at 298 K; (b) bar representation of sensitivity of Timpy towards different metal ions in methanol at 298 K. Relative intensity is given as the ratio of emission intensity of Gimpy in presence (I) and absence (I_0) of equimolar concentrations of metal ions respectively

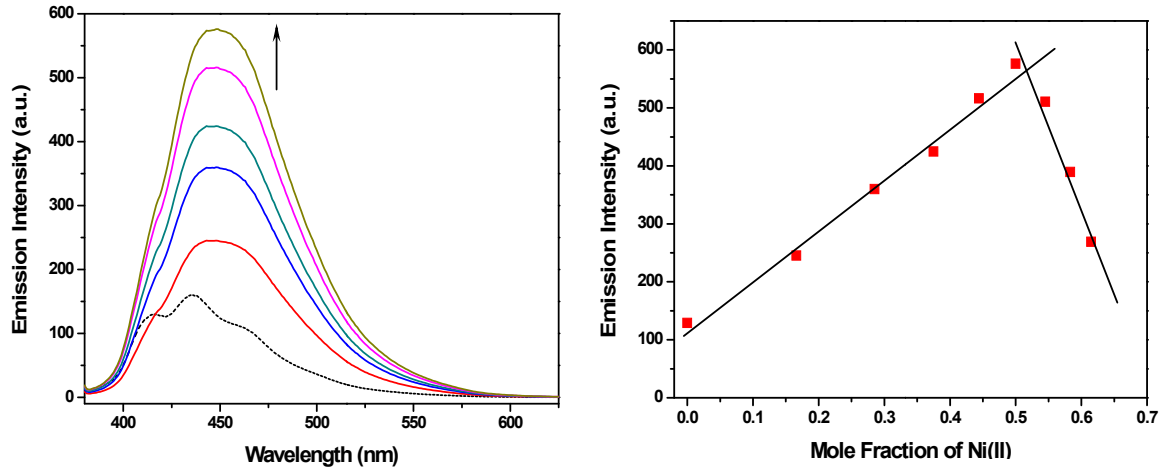

(a) (b)

Fig. 6.14 (a) Emission spectra of Gimpy (50 μM) in absence (dotted line) and presence of Ni^{2+} ions (10, 20, 30, 40 and 50 μM respectively) (solid lines) in methanol at 298 K; (b) Job's plot of Gimpy (50 μM) with varying concentrations of Ni^{2+} ion exhibiting (1:1) stoichiometry where the fluorescent intensity at 447 nm was plotted against the mole fraction of Ni^{2+}

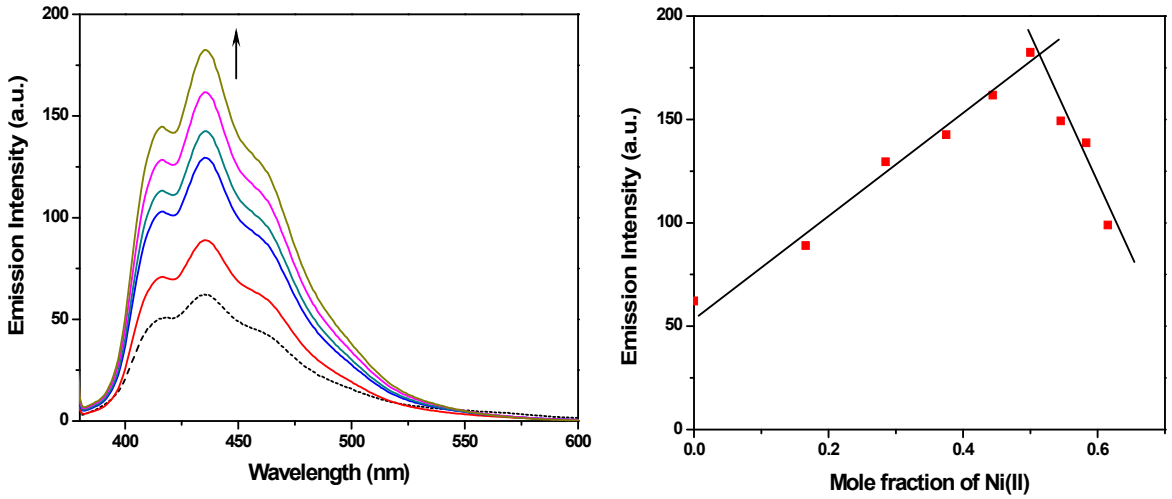

(a) (b)

Fig. 6.15 (a) Emission spectra of Timpy (50 μM) in absence (dotted line) and presence of Ni^{2+} ions (10, 20, 30, 40 and 50 μM respectively) (solid lines) in methanol at 298 K; (b) Job's plot of Timpy (50 μM) with varying concentrations of Ni^{2+} ion exhibiting (1:1) stoichiometry where the fluorescent intensity at 435 nm was plotted against the mole fraction of Ni^{2+}

In order to detect the binding mode of Gimpy and Timpy with Ni^{2+} as well as to establish the structure of the fluorescent species formed in the solution giving rise to emission intensity enhancement, we isolated the complexes (**11** and **12**·2$(CH_3)_2CO$) formed by the reaction between each of Gimpy and Timpy with $NiCl_2·6H_2O$ in 1:1 ratio from the same solvent, i.e. methanol. However, the isolated complexes could not exhibit any emission properties. It is important to note that, the absorption spectra of Gimpy and Timpy in presence of equimolar concentrations of Ni^{2+} ions did not match well with the spectra of methanolic solutions of **11** and **12**·2$(CH_3)_2CO$ respectively (Fig. 6.16). Electronic absorption spectral changes of Gimpy and Timpy in presence of varying concentrations of Ni^{2+} are illustrated in Fig. 6.17 (a) and (b) respectively. Hence, it was concluded that the isolated complexes do not afford the same chemical species in solution which are responsible for the enhancement in fluorescence intensity.

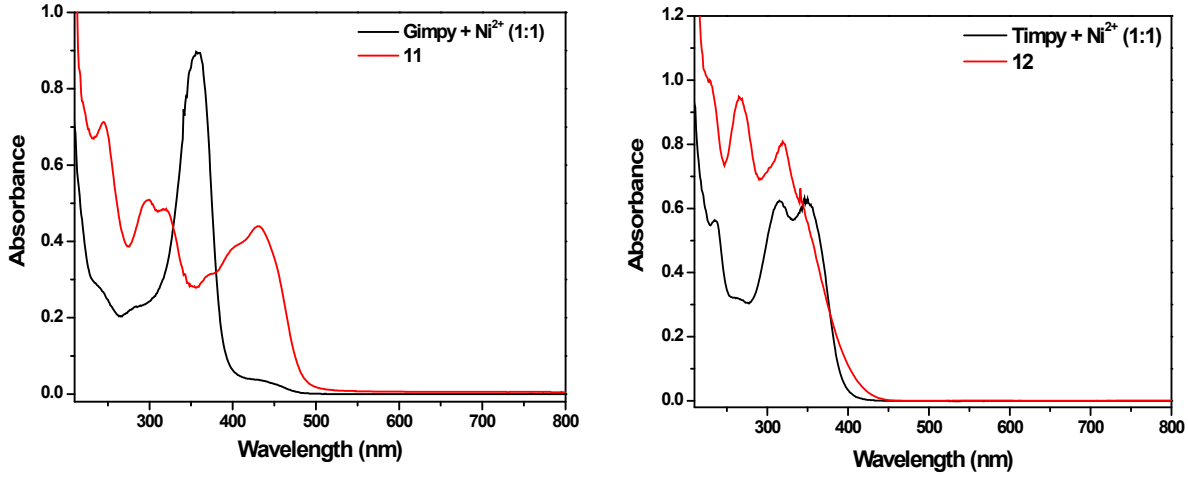

(a) (b)

Fig. 6.16 Electronic absorption spectra of (a) **11** (20 μM) and equimolar mixture of Gimpy and $NiCl_2$ (20 μM each); (b) **12**.2$(CH_3)_2CO$ (20 μM) and equimolar mixture of Timpy and $NiCl_2$ (20 μM each) in methanol at 298 K

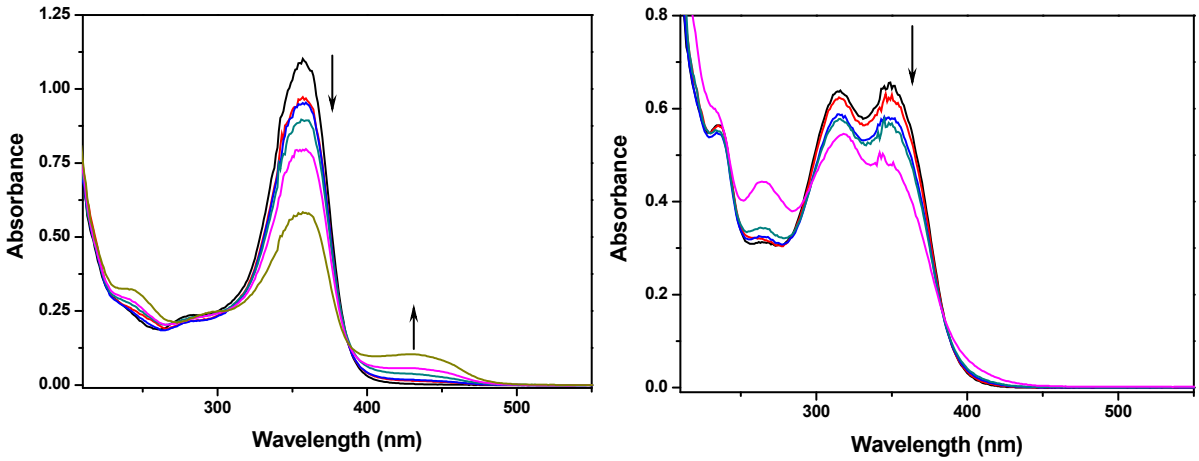

(a) (b)

Fig. 6.17 Absorption spectral changes of (a) Gimpy (20 μM) in presence of increasing concentrations of $NiCl_2$ (5, 10, 20, 100 and 200 μM respectively) and (b) Timpy (20 μM) in presence of increasing concentrations of $NiCl_2$ (20, 100, 200 and 500 μM respectively) in methanol at 298 K

6.2.6. Electrochemical properties

To investigate the redox behaviour of complexes **11** and **12**.2$(CH_3)_2CO$ at room temperature, cyclic voltammetric experiments were carried out under nitrogen atmosphere

within the potential range +1.000 V to -1.000 V at a scan rate of 0.1 V/s using Ag/AgCl as reference electrode, glassy carbon as working electrode and platinum wire as auxiliary electrode. Fig. 6.18 shows the cyclic voltammograms of ca. 10^{-3} M dichloromethane solutions of **11** and **12**.2$(CH_3)_2CO$ in the potential range 0.000 V to -1.000 V however no redox process was observed in the potential range 0.000 V to +1.000 V. Complex **11** exhibited two quasi−reversible redox processes with $E_{1/2}$ values of -0.402 V (ΔE = 177 mV) and -0.580 V (ΔE = 82 mV) vs Ag/AgCl, respectively. These redox couples were probably due to the formation of Ni^{II}/Ni^{I} and Ni^{I}/Ni^{I} species, respectively. Similar processes for **12**.2$(CH_3)_2CO$ gave rise to irreversible peaks with potential values of -0.044 V and -0.630 V vs. Ag/AgCl respectively. One additional redox couple was also observed in the cyclic voltammogram of **11** with the $E_{1/2}$ value of -0.966 V (ΔE = 176 mV) vs. Ag/AgCl which is probably due to the ligand−centered reduction process. The electrochemical data for both complexes are summarised in Table 6.5.

Table 6.5 Electrochemical data of complexes **11** and **12**.2$(CH_3)_2CO$ at 298 K[a] vs. Ag/AgCl

Complex	$Ni^{II}Ni^{II}/Ni^{II}Ni^{I}$		$Ni^{II}Ni^{II}/Ni^{I}Ni^{I}$			
	$E_{1/2}$[b] (V)	ΔE_p[c] (mV)	$E_{1/2}$[b] (V)	ΔE_p[c] (mV)	$E_{1/2}$[b] (V)	ΔE_p[c] (mV)
11	-0.402	177	-0.580	82	-0.966	176
12.2$(CH_3)_2CO$[d]	-0.044	–	0.630	–	–	–

[a] Measured in dichloromethane with 0.1 M tetrabutylammonium perchlorate (TBAP); scan rate = 0.1 V/s; [b] $E_{1/2}$ = 1/2 (E_{pa} + E_{pc}); [c] ΔE_p = (E_{pa} − E_{pc}); [d] Due to the irreversible redox processes only single potential values are given for **12**.2$(CH_3)_2CO$.

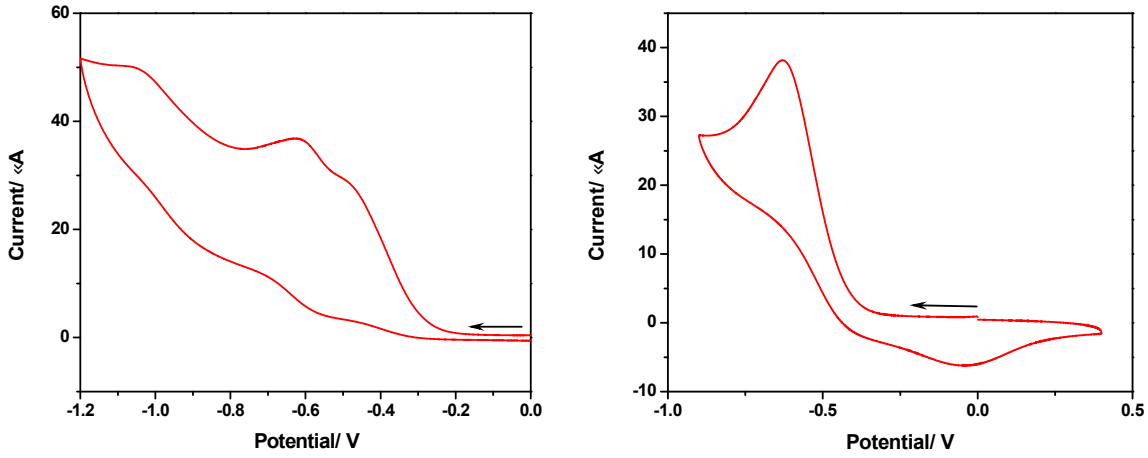

(a) (b)

Fig. 6.18 Cyclic voltammograms of 10^{-3} M solutions of (a) **11** and (b) **12**.2$(CH_3)_2CO$ in dichloromethane at 298 K under nitrogen atmosphere in presence of 0.1 M TBAP as supporting electrolyte, glassy-carbon is used as working electrode, Ag/AgCl as reference electrode and platinum wire as auxiliary electrode; scan rate 0.1 V/s

6.3. Conclusions

Two tetradentate ligands Gimpy and Timpy were found to be fluorescent and were exploited for metal ion sensing studies. Each of the molecules exhibited a significant enhancement of intensity in their emission spectrum in the presence of Ni^{2+} ions but not other metal ions. These data suggest that these molecules may be utilized as molecular probes to detect the presence of Ni^{2+} ions. The two ligands afforded dinuclear nickel complexes and molecular structures of Gimpy as well as the representative complex **12**.2$(CH_3)_2CO$ were determined by X-ray crystallography. Methanolic solutions of the isolated dinuclear nickel complexes did not exhibit fluorescence indicating that the species present in the solution and that responsible for the enhancement of fluorescence intensity of Gimpy and Timpy have different structures.

6.4. Experimental section

6.4.1. Reagents and materials

Analytical grade reagents phenylhydrazine (S. D. Fine, Mumbai, India), sodium perchlorate monohydrate (Himedia Laboratories Pvt. Ltd., Mumbai, India), nickel chloride hexahydrate (Ranbaxy Fine Chem. Ltd., New Delhi, India), glyoxal (S. D. Fine Chem. Ltd., Mumbai, India), phthalaldehyde, sodium hydride and 2-chloropyridine (Acros Organics, USA) were used as obtained. Solvents used for spectroscopic studies were HPLC grade and purified by standard procedures before use.

6.4.2. Synthesis of ligands

Synthesis of 1,2Jbis(2JphenylJ2J(pyridinJ2Jyl)hydrozono)ethane (Gimpy) and 1,2Jbis((2JphenylJ2J(pyridinJ2Jyl)hydrozono)methyl)benzene (Timpy)

Ligands Gimpy and Timpy were prepared according to the reported procedures.[413]

6.4.3. Synthesis of nickel complexes

Caution **!** Perchlorate salts of metal complexes with organic ligands are potentially explosive. Only small amounts of materials should be prepared and these should be handled with great care.

Synthesis of $[(Ni(Gimpy)(«JCl))_2](ClO_4)_2$ (11)

$NiCl_2{\cdot}6H_2O$ (0.238 g, 1 mmol) dissolved in methanol (5 mL) was stirred rapidly over a magnetic stirrer. A batch of Gimpy (0.390 g, 1 mmol) dissolved in 20 mL of a dichloromethane:methanol (1:1) mixture was added and the colour of the solution changed to yellow. The stirring was continued for further 3 h after which sodium perchlorate monohydrate (0.280 g, 2 mmol) was added to the reaction mixture. The reaction was

allowed to stir for 1 h and then filtered. The filtrate was reduced in volume *in vacuo* to afford a yellow solid which was washed with a small amount of dichloromethane, dried and then washed with excess water. Yield: 82%. *Anal*. (%) Calcd. for $C_{48}H_{40}Cl_4N_{12}O_8Ni_2$: C, 49.19; H, 3.44; N, 14.34. Found: C, 49.55; H, 3.73; N, 14.83. Selected IR data (KBr,ν_{max}/cm^{-1}): 1604, $\nu_{C=N}$; 1077, 625, ν_{ClO4}^-. UV-visible [CH_3CN, λ_{max}/nm ($\varepsilon/M^{-1}cm^{-1}$)]: 243 (40480), 301 (26920), 311 (26080), 366 *sh* (12520), 411 (24008); [CH_3OH, λ_{max}/nm ($\varepsilon/M^{-1}cm^{-1}$)]: 245 (35930), 298 (25750), 319 (24390), 369 *sh* (15590), 401 *sh* (19300), 430 (22240); ESI-MS: (acetonitrile, positive ion): m/z 485.07 $[M\text{-}2(ClO_4)]^{2+}$. $\Lambda_M/\Omega^{-1}cm^2mol^{-1}$ (DMF): 153 (1:2).

Synthesis of $[(Ni(Timpy)(\text{«}JCl))_2](ClO_4)_2\cdot 2(CH_3)_2CO$ ($12\cdot 2(CH_3)_2CO$)

$NiCl_2\cdot 6H_2O$ (0.238 g, 1 mmol) dissolved in methanol (5 mL) was stirred rapidly over a magnetic stirrer. A batch of Timpy (0.470 g, 1 mmol) dissolved in dichloromethane (15 mL) was added to the reaction mixture and the solution turned green. The stirring was continued for 4 h, followed by the addition of a batch of sodium perchlorate monohydrate (0.280 g, 2 mmol). The reaction mixture was stirred for further 4 h. The volume of the reaction mixture was reduced to 8 mL *in vacuo* and acetone (20 mL) was added to afford a green solid which was filtered, washed with small amount of acetone and dried. Yield: 70%. *Anal*. (%) Calcd. for $C_{66}H_{60}Cl_4N_{12}O_{10}Ni_2$: C, 55.03; H, 4.20; N, 11.67. Found: C, 55.19; H, 4.38; N, 11.41. Selected IR data (KBr, ν_{max}/cm^{-1}): 1599, $\nu_{C=N}$; 1099, 623, ν_{ClO4}^-. UV-visible [CH_3CN, λ_{max}/nm ($\varepsilon/M^{-1}cm^{-1}$)]: 224 (60360); 265 (50280); 319 (42000); 341 *sh* (31280); [CH_3OH, λ_{max}/nm ($\varepsilon/M^{-1}cm^{-1}$)]: 229 *sh* (49905); 265 (47330), 320 (40310), 342 *sh* (30955); ESI-MS (acetonitrile, positive ion): m/z 561.10 $[M\text{-}2(ClO_4)]^{2+}$. $\Lambda_M/\Omega^{-1}cm^2mol^{-1}$ (DMF): 190 (1:2).

6.4.4. X-ray crystallography

X-ray diffraction measurements for Gimpy were performed on an Agilent Supernova dual diffractometer with an Atlas (Cu) detector (ω scan technique) using graphite monochromatized Cu Kα radiation so that $^{-}_{max}$ was 74.4º.[557] Data for **12**.2$(CH_3)_2CO$ were similarly measured but with Mo Kα radiation and $^{-}_{max}$ of 27.1º.

Table 6.6 Crystallographic parameters and refinement details for Gimpy and complex **12**·2$(CH_3)_2CO$

	Gimpy	**12**·2$(CH_3)_2CO$
Formula	$C_{24}H_{20}N_6$	$C_{60}H_{48}Cl_2N_{12}Ni_2$, 2($ClO_4$), 2($C_3H_6O$)
Formula weight	392.46	1440.48
Crystal system	Monoclinic	Triclinic
Space group	*C*2/*c*	$P\bar{1}$
a/Å	19.4557(8)	10.6356(7)
b/Å	5.8884(2)	12.4950(8)
c/Å	18.7591(7)	12.7358(8)
α/°	90	92.260(5)
β/°	110.750(4)	101.934(6)
γ/°	90	102.225(6)
V/Å^3	2387.4(6)	1612.21(18)
Z	4	1
ρ/g cm^{-3}	1.297	1.484
F(000)	824	744
μ/mm^{-1}	0.639 (Cu *K*α)	0.819 (Mo *K*α)
Measured data	8312	25308
Theta range for data collection/°	4.9–74.4	2.2–27.1
Unique data	2028	7067
Observed data ($I \geq 2.0\sigma(I)$)	1829	4575
R, obs. data; all data	0.048; 0.137	0.066; 0.141
a; *b* in weighting scheme	0.090; 0.716	0.071; 0.483
R_w, obs. data; all data	0.052; 0.142	0.115; 0.166
Residual electron density peaks/e Å^{-3}	0.22, -0.26	0.83, -0.77

The structures were solved by direct methods (SHELXS 97[558] through the WinGX Interface[559]) and refined (anisotropic displacement parameters, H atoms in the riding model approximation and a weighting scheme of the form $w = 1/[\sigma^2(F_o^2) + aP^2 + bP]$ where $P =$

(F_o^2 + $2F_c^2$)/3) with SHELXL97 on F^2.[558] In **12**.2$(CH_3)_2CO$ the [-110] reflection was omitted as it was affected by the beam-stop. The crystal data and structure refinement details for Gimpy and the nickel complex **12**·2$(CH_3)_2CO$ are given in Table 6.6.

7.1. Introduction

In the past decade, substantial interest has aroused in the design and development of novel di- or multi-nuclear first row transition metal complexes due to their significant biological relevance[333] and potential to serve as synthetic models for the metalloenzymes purported to contain two or more catalytic metal ions at their active sites[28,560,561]. Metal complexes which could hydrolyze DNA with high sequential and structural selectivity can be utilized as therapeutic agents and as indispensible tool for gene manipulation also.[28] On the other hand, considering the very sensitive nature of DNA towards oxidative cleavage, most of the studies on artificial DNAs are focused to the agents exhibiting oxidative type of DNA cleavage.[562] Many redox–active complexes giving rise to non–specific oxidative cleavage of DNA have been proved to be an invaluable tool for the investigation of intermolecular interactions between biological macromolecules like protein and DNA.[563] Several reports including those by Karlin and co–workers[563-564] have shown that nuclearity of the complexes might play a pivoting role in the oxidative cleavage of nucleic acids[333,565]. It has also been noticed that several di- or multi-nuclear transition metal complexes exhibit excellent nuclease activities while their corresponding mono-nuclear analogues are inactive.[561] In such cases, the enhanced nucleolytic efficiency associated with the polynuclear complexes results from the synergism between the two metal centers.[333,355] Notably, almost all of the catalysts developed till date, require an excess over nucleic acid substrate to exhibit measurable activities. The quest for the catalysts exhibiting multi-turnover behavior makes enough room for further development of nucleolytic agents exhibiting better efficiencies in this regard.[28,561] Additionally, a slight modification in the ligand frame may also dramatically influence the chemical properties and reactivities of the

complexes.[477,565] In *Chapters 4 and 5*, it has been observed that the incorporation of *tert*–butyl groups in the ligand frame turned out in excellent nuclease activity while the corresponding complexes lacking these substituents were found inactive. Herein, we describe the synthesis and characterization of dinuclear copper(II) and cobalt(II) complexes derived from the bidentate ligands Simpy and Impy and an account of their biological activities. Molecular structures of the complexes derived from Simpy were authenticated by X-ray crystallographic studies. The chemical structures of Simpy and Impy are represented in Scheme 7.1. It is important to note that both ligands, namely, Simpy and Impy offer essentially similar donor environment however, they differ in their pendant groups.

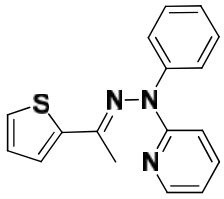

Simpy

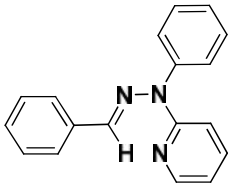

Impy

Scheme 7.1 Schematic drawings of ligands Simpy and Impy

7.2. Results and discussion

7.2.1. Synthesis and characterization of ligands

The ligand Simpy was synthesized by the condensation reaction between a 1:1 mixture of 2–acetylthiophene (or 1–(thiophen–2–yl)ethanone) and 2–(1–phenylhydrazinyl)pyridine in methanolic solution catalyzed by traces of concentration hydrochloric acid. The ligand Impy was prepared by the condensation reaction between a 1:1 mixture of benzaldehyde and 2–(1–phenylhydrazinyl)pyridine in methanol. The synthetic routes for the preparation of ligands Simpy and Impy are shown in Scheme 7.2.

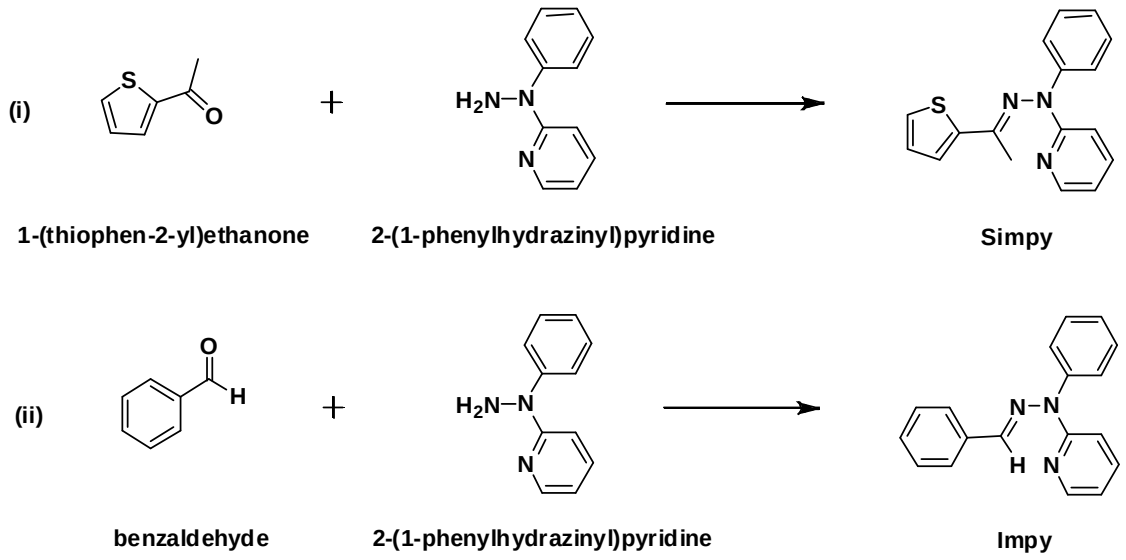

Scheme 7.2 Schematic representation of syntheses of ligands (i) Simpy and (ii) Impy respectively

The ligands were characterized by various physical and spectroscopic techniques including elemental analysis, IR, UV–visible and NMR spectroscopy as well as by mass–spectrometry and the data are represented in Tables 7.1 and 7.2. In the IR spectra of both ligands, the sharp peak near 1580 cm^{-1} was assigned to the stretching frequency of azomethine function (–CH=N–). The absorption spectra of the ligands exhibited intense bands in the region of 200–350 nm probably arising from π–π* and n–π* transitions (*vide infra*). The ^{1}H and ^{13}C NMR spectra of Simpy are illustrated in Figures 7.1 and 7.2 respectively. Presence of a sharp singlet near 2.085 ppm for three protons in ^{1}H NMR spectrum and a peak at 17.77 ppm in ^{13}C NMR spectrum indicated the presence of a methyl group in Simpy. Rest of the protons in Simpy were accountable from well resolved signals in the aromatic region (6.5–8.5 ppm) (Fig. 7.1). The ligand Simpy was also characterized by ESI–mass spectrometric technique and the spectrum is shown in Fig. 7.3. The spectrum consisted of

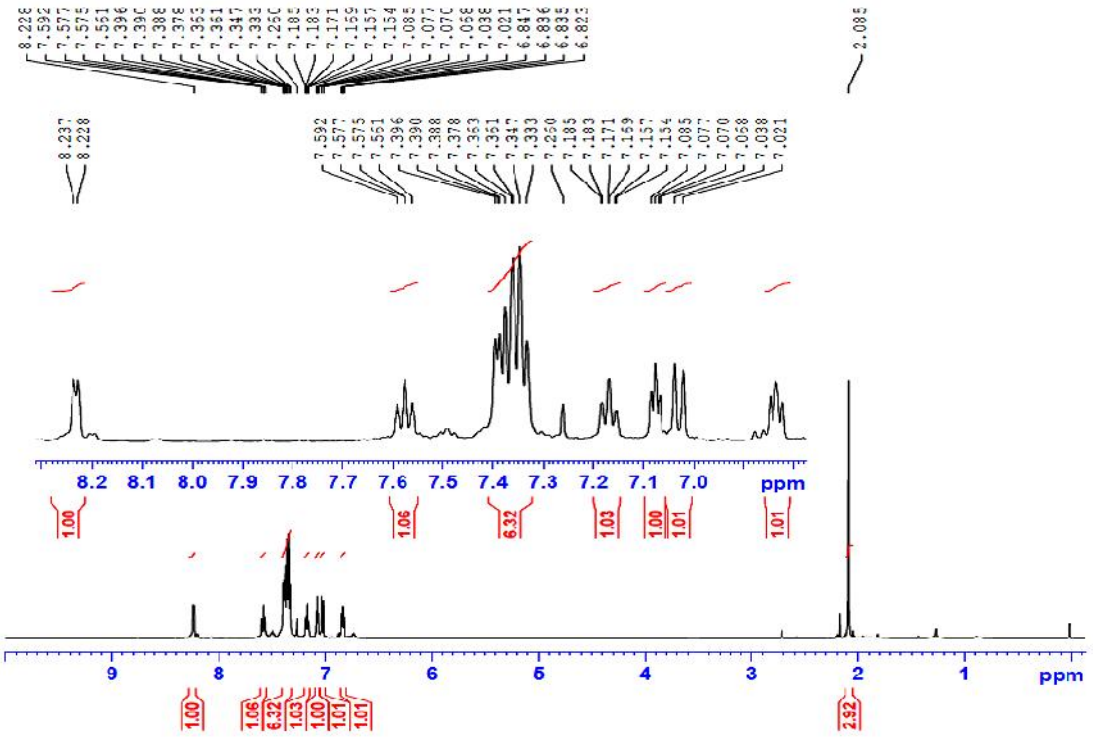

Fig. 7.1 ^{1}H NMR spectrum of ligand Simpy in $CDCl_3$

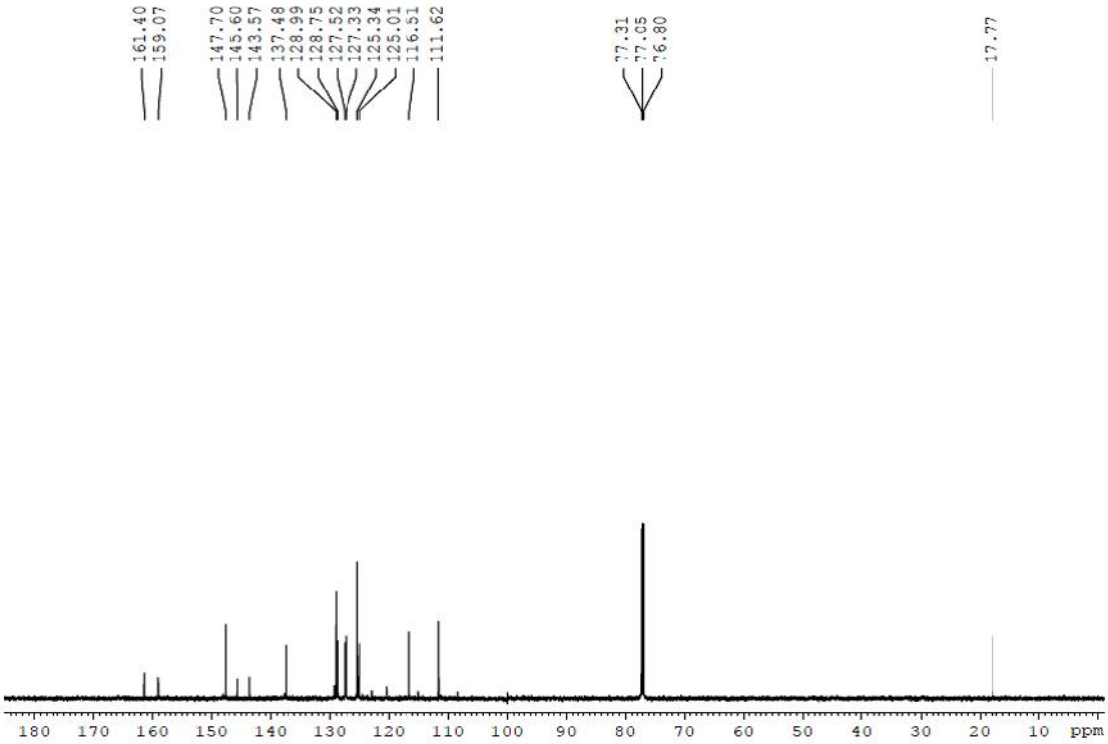

Fig. 7.2 ^{13}C NMR spectrum of ligand Simpy in $CDCl_3$

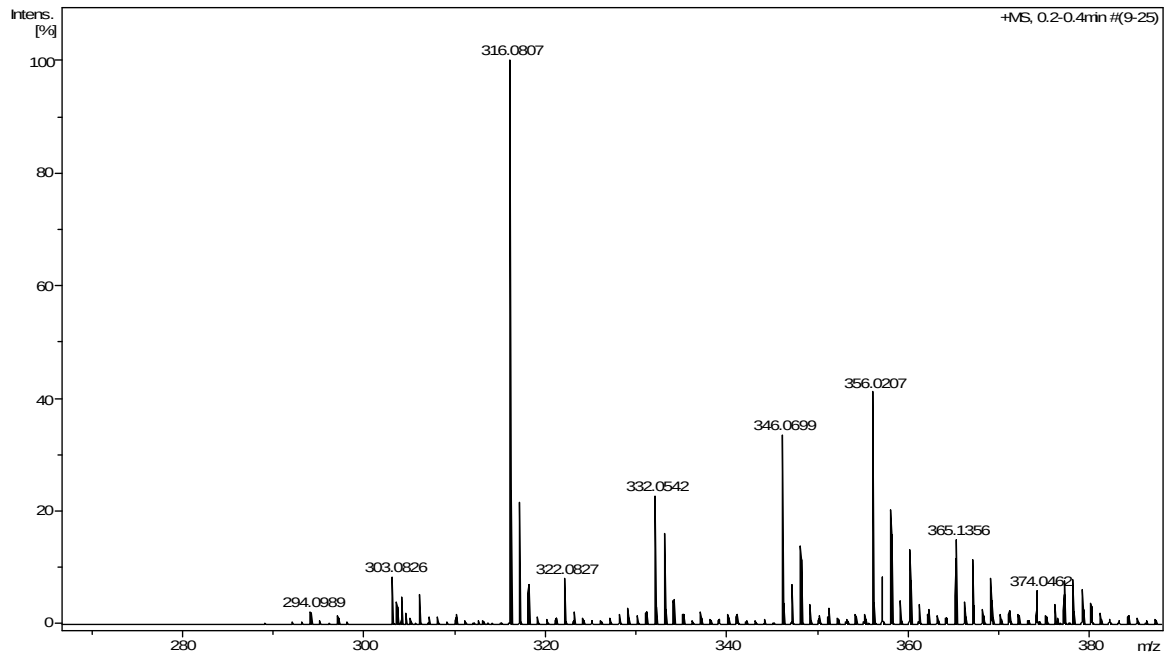

Fig. 7.3 The ESI–mass spectrum of Simpy in acetonitrile under positive mode exhibiting the peaks at (m/z) 294.09 (2.3%), 316.08 (100%) and 332.05 (22.8%) corresponding to $[M+H]^+$, $[M+Na]^+$ and $[M+K]^+$ cations (M = ligand) respectively

Fig. 7.4 Mass spectrum of Impy

the peaks with m/z values 294.09 (relative intensity 2.3%), 316.08 (relative intensity 100%) and 332.05 (relative intensity 22.8%) probably because of the formation of $[M+H]^+$, $[M+Na]^+$ and $[M+K]^+$ cations (M = Simpy) respectively. The ligand Impy was characterized by mass spectrometry and the spectrum exhibited a molecular ion peak with m/z value of 273 (relative intensity 5.79%) (Fig. 7.4). The peaks appearing at m/z 169 and 196 are probably due to the formation of cations by cleavage of N–N bond with imine nitrogen and N–C bond of the phenyl ring respectively.

7.2.2. Synthesis and characterization of metal complexes

All metal complexes $[\{M(Simpy)(\mu\text{-}Cl)Cl\}_2]$ (M = Cu and Co in **13a** and **13b** respectively) and $[\{M(Impy)(\mu\text{-}Cl)Cl\}_2]$ (M = Cu and Co in **14a** and **14b** respectively) were synthesized by the reactions of ligand and the corresponding metal chloride salts in 1:1 molar ratio through gradual addition of ligands to the metal salts solutions. All the reactions were performed in open atmosphere and ended up with binuclear complexes with good yields. The synthetic strategy adopted for preparing the metal complexes (**13-14**) is illustrated in Scheme 7.3.

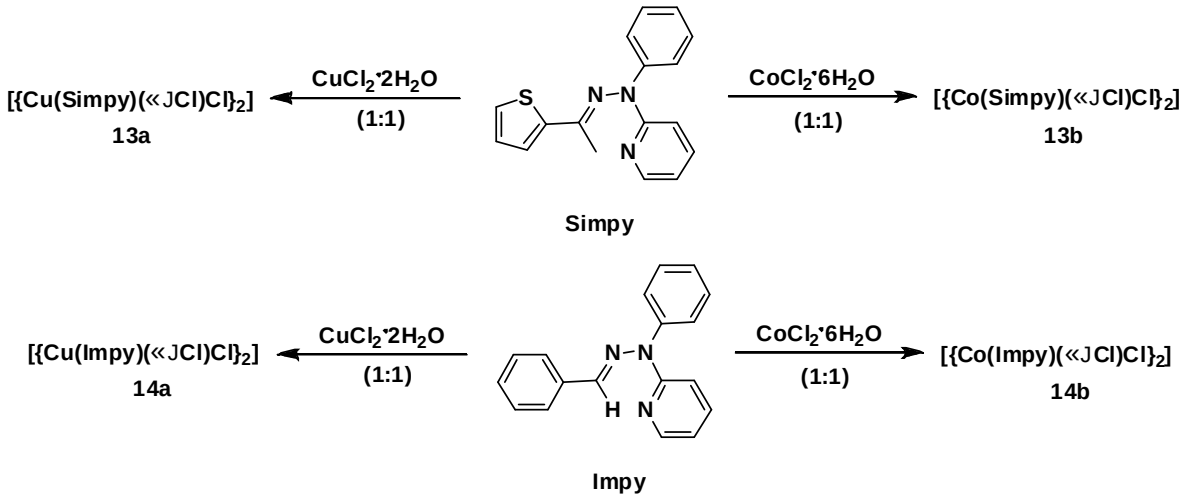

Scheme 7.3 Schematic representation of syntheses of complexes **13-14**

Table 7.1 Data for yield, elemental analysis, IR and conductivity measurements

Complex	Yield %	Elemental analysis				IR data (cm^{-1})[a]	Conductivity
		C	H	N	S	¬C=N	i_M (t^{-1} cm^2mol^{-1})[b]
Simpy	83	68.87	5.05	14.79	11.27	1583	J
Impy	72	78.87	5.64	15.45	J	1581	J
13a	75	47.33	3.61	9.92	7.31	1607	13 (neutral)
13b	64	47.99	3.52	10.01	7.61	1608	55 (neutral)
14a	54	52.85	3.74	10.02	J	1607	15 (neutral)
14b	50	53.18	3.81	10.26	J	1608	57 (neutral)

[a]KBr pellets, [b]Solvent: acetonitrile

(i) IR spectral studies

In all complexes (**13-14**), the $\nu_{(-CH=N-)}$ was found at ~25 cm^{-1} higher wavenumbers as compared to those in the free ligands (Table 7.1). These shifts in the stretching frequencies of $\nu_{(-CH=N-)}$ predicted the coordination of the azomethine nitrogen to the metal centers.[385]

(ii) Electronic properties

The intense absorption bands observed in the electronic spectra of ligands (Simpy and Impy) and their complexes between 200–350 nm were assignable to the intra–ligand π–π* transitions. Interestingly, no new bands could be observed in the absorption spectra of complexes in methanol. The absorption spectra of ligands and their metal complexes are given in Fig. 7.5 and the spectral data are collated in Table 7.2.

Table 7.2 UV–visible spectral data of Simpy, Impy and their complexes (**13-14**)

Compound	$^a\lambda_{max}$/nm (£/$M^{-1}cm^{-1}$)
Simpy	202 (17748), 246 *sh* (11898), 267 (14602), 280 (14434), 350 *sh* (6534)
Impy	204 (25222), 233 (20186), 324 (25476)
13a·$4H_2O$	204 (46160), 245 *sh* (29896), 268 (36970), 354 *sh* (15480)
13b	204 (36306), 245 *sh* (27244), 266 (32828), 279 (31998), 350 (15316)
14a	205 (44620), 233 (43330), 326 (46638)
14b	205 (42856), 233 (46196), 325 (54794)

[a]UV–visible data recorded in methanol

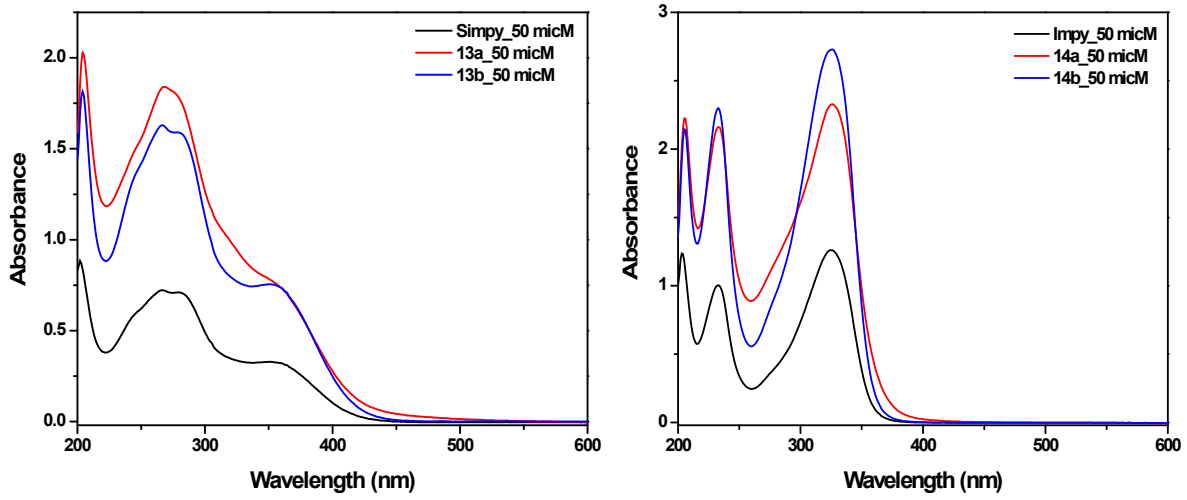

(a) (b)

Fig. 7.5 UV–visible spectra of (a) Simpy and its complexes (50 µM each) and (b) Impy and its complexes (50 µM each) in methanol

(iii) ESIJmass spectrometry

The complexes **13a**·4H_2O and **13b** were subjected to ESI–mass spectral analysis in 1:1 mixture of acetonitrile and water under positive ion mode and their spectra are represented in Figures 7.6 and 7.7 respectively. The mass spectrum of **13a** exhibited peaks with m/z values of 816.95 (relative intensity 4.4%) and 874.91 (relative intensity 0.9%) which were ascribed to the formation of the cations $[M\text{-}Cl]^+$ and $[M+Na]^+$ respectively (Fig. 7.6). Moreover, the peaks found in the mass spectrum of **13a** with m/z values of 390.98 (relative intensity 44.7%) and 448.94 (relative intensity 2.3%) are probably due to the formation of dications $[M\text{-}2Cl]^{2+}$ and $[M+2Na]^{2+}$ respectively (Fig. 7.6). In a similar way the peaks with m/z values of 386.99 (relative intensity 34%), 444.95 (relative intensity 3.7%), 808.96 (relative intensity 32.9%) and 866.92 (relative intensity 1.9%) found in the ESI–mass spectrum of **13b** were assigned to the formation of dications $[M\text{-}2Cl]^{2+}$and $[M+2Na]^{2+}$ and monocations $[M\text{-}Cl]^+$ and $[M+Na]^+$ respectively (Fig. 7.7).

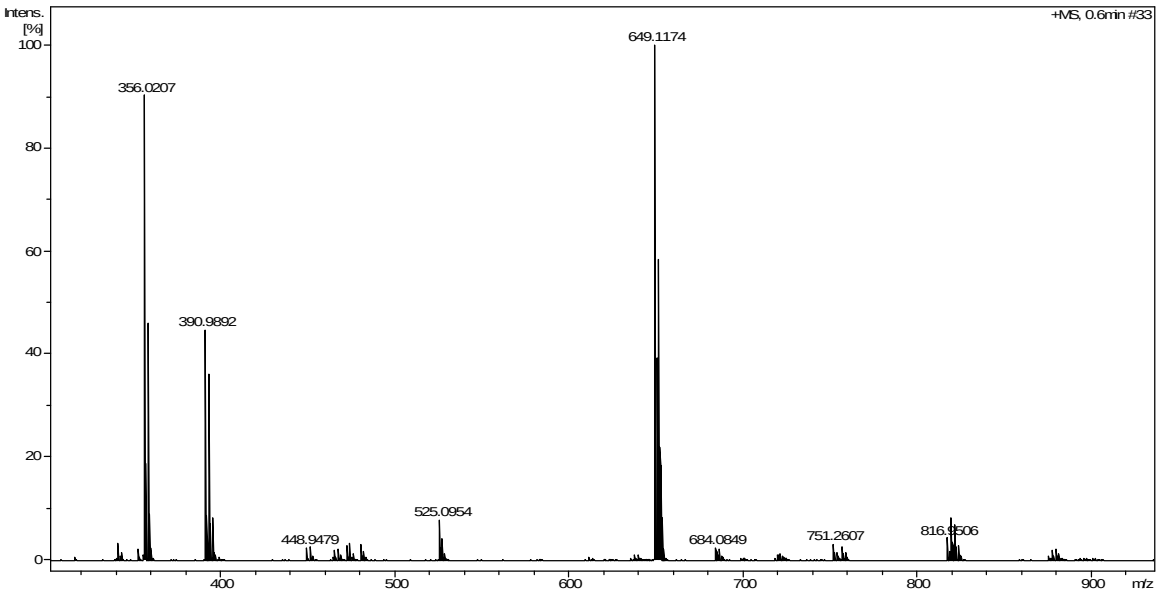

Fig. 7.6 The ESI–mass spectrum of **13a** in acetonitrile under positive mode exhibiting the peaks at (m/z) 390.98 (44.7%), 448.94 (2.3%), 816.95 (4.4%) and 874.91 (0.9%) corresponding to $[M\text{-}2Cl]^{2+}$, $[M+2Na]^{2+}$, $[M\text{-}Cl]^{+}$ and $[M+Na]^{+}$ cations respectively

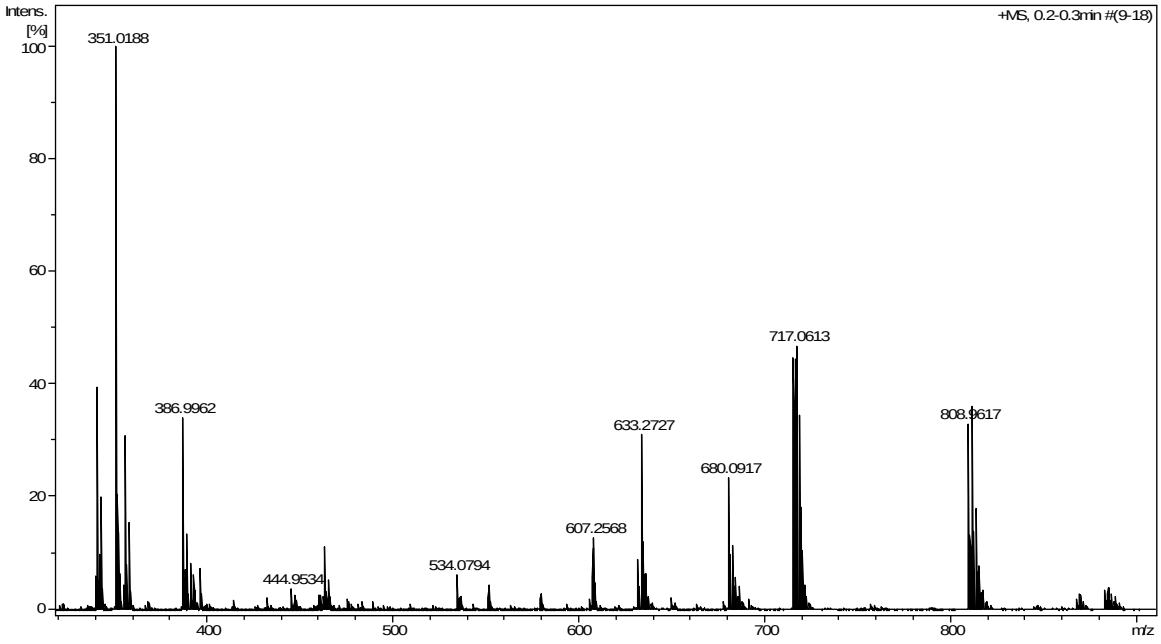

Fig. 7.7 The ESI–mass spectrum of **13b** in acetonitrile under positive mode exhibiting the peaks at (m/z) 386.99 (34%), 444.95 (3.7%), 808.96 (32.9%) and 866.92 (1.9%) corresponding to $[M\text{-}2Cl]^{2+}$, $[M+2Na]^{2+}$, $[M\text{-}Cl]^{+}$ and $[M+Na]^{+}$ cations respectively

(iv) Conductivity measurements

Molar conductivity values in acetonitrile solution (ca. 10^{-3} M) for all complexes (**13**-**14**) were found to be within the range 13–57 Ω^{-1} cm^2 M^{-1} at 25°C suggesting their neutral and non–electrolytic behavior in solution (Table 7.1).[387]

7.2.3. Description of molecular structures

In order to confirm the mode of coordination of ligand Simpy, the molecular structures of **13a**·$4H_2O$ and **13b** were authenticated by X–ray diffraction methods. X-ray diffraction quality crystals of **13a**·$4H_2O$ were obtained by diffusion of diethyl ether in the solution of compound in dichloromethane. The asymmetric unit of **13a**·$4H_2O$ contained half of the molecule along with two lattice water molecules of solvation. The ORTEP representation of complex **13a**·$4H_2O$ along with the donor environment around the metal centers is depicted in Fig. 7.8 and selected bond distances and bond angles are listed in Table 7.3.

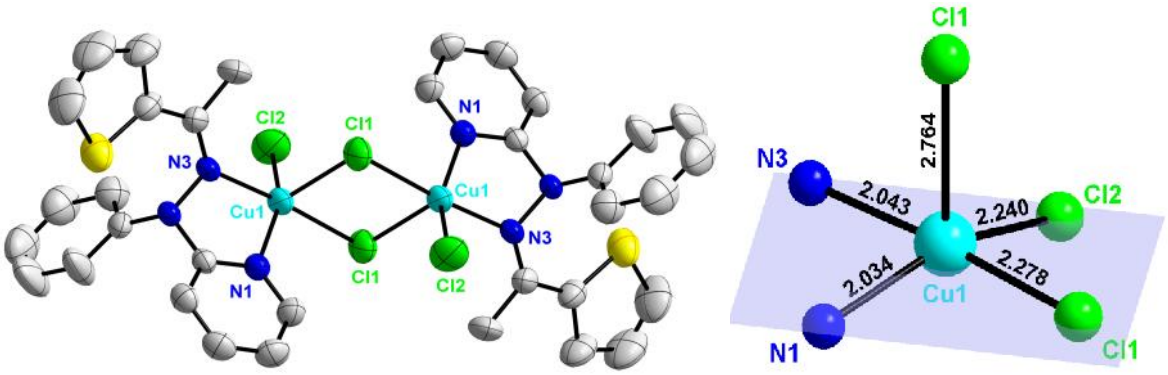

(a) (b)

Fig. 7.8 (a) ORTEP representation of the crystal structure of **13a**·$4H_2O$ showing atom numbering scheme and displacement ellipsoid (50% probability level). Hydrogen atoms are omitted for clarity; (b) distorted square-pyramidal disposition of donor atoms showing the bond distances from the metal centre

Table 7.3 Selected bond lengths (Å) and angles (˚) for [{Cu(Simpy)(μ-Cl)Cl}$_2$]·4H$_2$O (**13a**·4H$_2$O)

Bond Lengths [Å]		Bond Angles [deg]	
Cu(1) –N(1)	2.0341(36)	N(1)–Cu(1)–N(3)	78.159(132)
Cu(1) –N(3)	2.0430(31)	N(1)–Cu(1)–Cl(1)	93.719(98)
Cu(1) –Cl(1)	2.2785(13)	N(1)–Cu(1)–Cl(2)	153.932(107)
Cu(1) –Cl(2)	2.2400(18)	N(3)–Cu(1)–Cl(1)	171.109(98)
Cu(1) –Cl(1)^i	2.7641(14)	N(3)–Cu(1)–Cl(2)	95.893(104)
Cu(1)^i –Cl(1)	2.7642(14)	Cl(1)–Cu(1)–Cl(2)	92.996(56)
		N(1)–Cu(1)–Cl(1)^i	94.17(10)
		N(3)–Cu(1)–Cl(1)^i	91.05(10)
		Cl(1)–Cu(1)–Cl(1)^i	85.89(5)
		Cl(2)–Cu(1)–Cl(1)^i	111.42(6)
		Cu(1)–Cl(1)–Cu(1)^i	94.11(5)

Symmetry equivalents: (i) 1-x,-y,1-z

The complex exhibited a dinuclear structure with both metal atoms held in a penta–coordination donor environment. The ligand Simpy coordinated with the metal centers with pyridyl nitrogen (N1) and imine nitrogen (N3) exhibiting a bidentate binding mode. The structural index parameter (τ) for complexes **13a**·4H$_2$O was calculated and found to be 0.29.[135] The τ value for complex **13a**·4H$_2$O ascertained a distorted square–pyramidal geometry of donor atoms around the copper center. The distortion in the square–pyramidal geometry was manifested by the fact that the mean plane of the donor atoms (N1, N2, Cl1 and Cl2) forming the basal plane of the square-pyramid did not pass through the imine and pyridine nitrogens which were situated above and below it. The apical position of the square–pyramid was occupied by another chlorine atom (Cl1^i) which exhibited longer bond distance from the metal center than those present in the basal plane which might probably be due to Jahn–Teller distortion. The bridging chlorine atoms exhibited almost similar bond distances from the metal center holding the two copper atoms at a Cu(II)–Cu(II) distance of

3.706 Å. The non–bridging chlorine atoms were oriented *trans* to each other. The phenyl rings were roughly perpendicular to the ligand binding plane forming an angle of 73.93° whereas the angle between thiophene rings and the ligand binding plane was about 34.75°. The Cu(II)–N_{imine} distances, Cu(II)–$N_{pyridine}$ distances and mean Cu(II)–Cl distances were found to be 2.043 Å, 2.034 Å and 2.427 Å which were close to the reported values in analogous complexes.[566,567]

Several non–covalent interactions could also be observed in the crystal structure of **13a**·4H_2O. Intramolecular hydrogen bonding interactions existed between aryl hydrogen atoms of the pyridine rings and chlorine atoms. Methyl hydrogens also exhibited intramolecular interactions with terminal chlorine atoms (Fig. 7.9). The molecules were found associated with one another through intermolecular hydrogen bonding interactions between pyridyl hydrogen atoms and chlorine atoms which afforded an array of molecules linked together along "a" axis (Fig. 7.9).

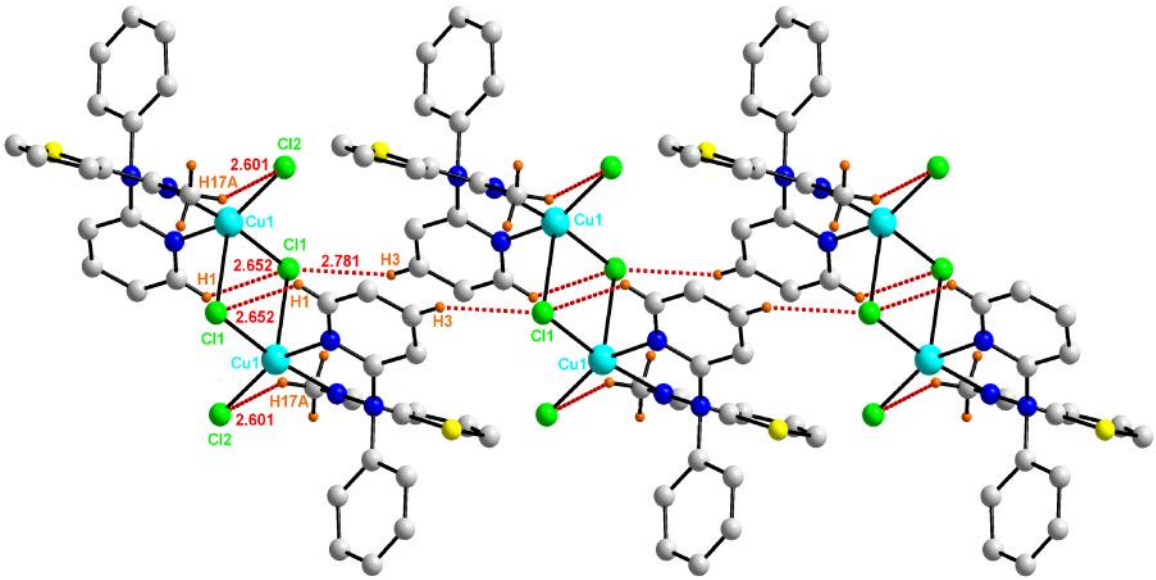

Fig. 7.9 Intermolecular hydrogen bonding network in [{Cu(Simpy)(μ-Cl)Cl}$_2$] (**13a**·4H_2O)

Table 7.4 Geometric parameters for non-covalent interactions of complex **13a**·$4H_2O$

DJH···A	DJH (Å)	D···A (Å)	H···A (Å)	DJH···A (°)
C1JH1···Cl1	0.930(5)	3.233(5)[a]	2.653(1)[a]	121.07(30)[a]
C11JH11···N3	0.930(6)	2.753(7)[a]	2.415(4)[a]	101.32(35)[a]
C17JH17A···Cl2	0.960(7)	3.437(7)[a]	2.606(2)[a]	144.98(38)[a]
C3JH3···Cl1	0.930(5)	3.512(5)[b]	2.781(1)[b]	136.16(30)[b]
C4JH4···Cl2	0.930(4)	3.917(5)[b]	2.988(2)[b]	176.87(27)[b]
C10JH10···O1	0.930(8)	3.639(17)[c]	2.808(15)[c]	149.31(56)[c]

Symmetry Equivalents: (a) x,y,z; (b) x-1/2,+y+1/2,+z; (c) x-1/2,+y-1/2,+z

A detailed list of intermolecular interactions in the crystal structure of **13a**·$4H_2O$ is given in Table 7.4. Additionally, aryl hydrogens of pyridine rings also showed C–H···π interactions with the thiophene rings at a distance of 2.896 Å from the centroid (Fig. 7.10). Three dimensional packing diagram of **13a**·$4H_2O$ is shown in Fig. 7.11.

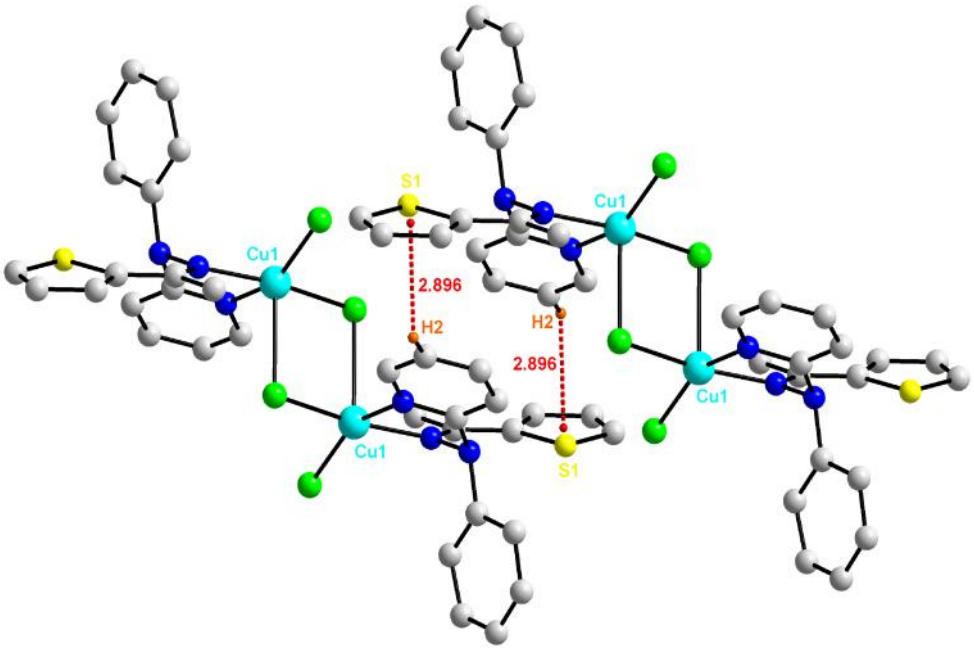

Fig. 7.10 C–H···π interactions in the crystal structure of [{Cu(Simpy)(μ-Cl)Cl}$_2$]·$4H_2O$ (**13a**·$4H_2O$)

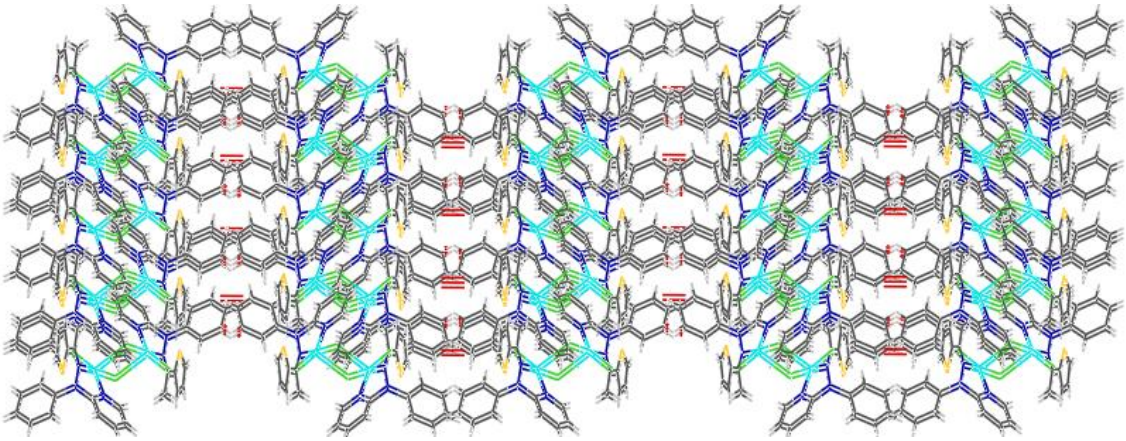

Fig. 7.11 Three-dimensional packing of [{Cu(Simpy)(μ-Cl)Cl}$_2$]·4H$_2$O (**13a**·4H$_2$O)

X-ray diffraction quality crystals of **13b** were obtained by diffusion of acetone in the solution of compound in dichloromethane. The asymmetric unit of **13b** contained two half molecules situated at two−fold crystallographic symmetry axis and full structure was developed by the "GROW" command. The ORTEP representation of complex **13b** along with the donor environment around the metal centers is depicted in Figures 7.12 and selected bond distances and bond angles are listed in Table 7.5.

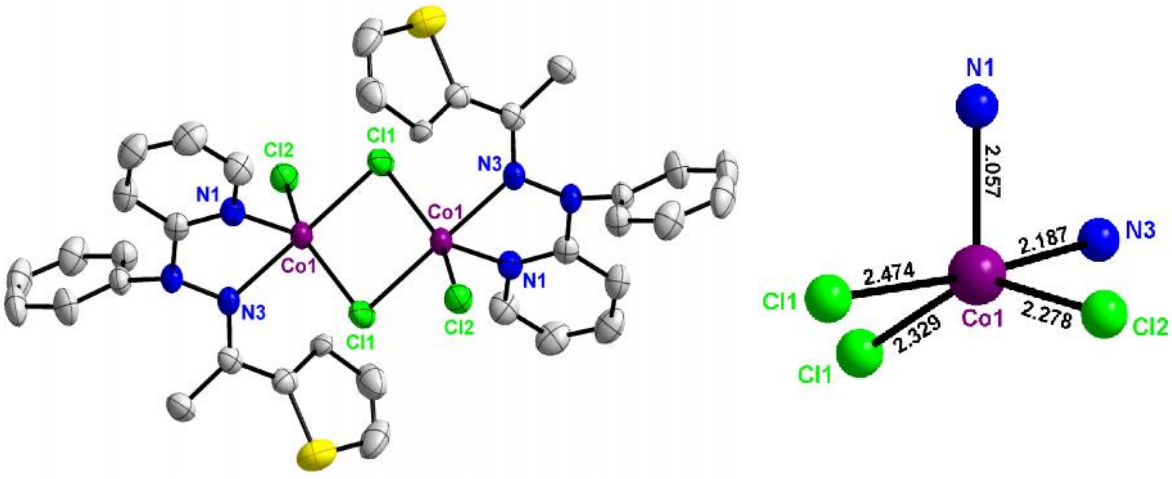

(a) (b)

Fig. 7.12 (a) ORTEP representation of the crystal structure of **13b** showing atom numbering scheme and displacement ellipsoid (50% probability level). Hydrogen atoms are omitted for clarity; (b) trigonal bipyramidal disposition of donor atoms showing the bond distances from the metal centre

Table 7.5 Selected bond lengths (Å) and angles (˚) for [{Co(Simpy)(μ-Cl)Cl}$_2$] (**13b**)

Bond Lengths [Å]		Bond Angles [deg]	
Co(1) –N(1)	2.0574(14)	N(1)–Co(1)–N(3)	75.207(52)
Co(1) –N(3)	2.1871(13)	N(1)–Co(1)–Cl(1)	99.944(41)
Co(1) –Cl(1)	2.4738(6)	N(1)–Co(1)–Cl(2)	105.594(41)
Co(1) –Cl(2)	2.2775(5)	N(3)–Co(1)–Cl(1)	173.878(37)
Co(1) –Cl(1)^{i}	2.3288(5)	N(3)–Co(1)–Cl(2)	90.401(36)
Co(2) –N(4)	2.0549(14)	Cl(1)–Co(1)–Cl(2)	94.554(17)
Co(2) –N(6)	2.1872(13)	N(1)–Co(1)–Cl(1)^{i}	110.382(43)
Co(2) –Cl(3)	2.4742(5)	N(3)–Co(1)–Cl(1)^{i}	94.539(36)
Co(2) –Cl(4)	2.2807(5)	Cl(1)–Co(1)–Cl(1)^{i}	83.581(17)
Co(2) –Cl(3)^{ii}	2.3297(5)	Cl(2)–Co(1)–Cl(1)^{i}	143.764(19)
		Co(1)–Cl(1)–Co(1)^{i}	96.419(18)
		N(4)–Co(2)–N(6)	75.076(52)
		N(4)–Co(2)–Cl(4)	105.626(42)
		N(4)–Co(2)–Cl(3)	100.085(41)
		N(6)–Co(2)–Cl(4)	90.301(36)
		N(6)–Co(2)–Cl(3)	173.916(37)
		Cl(4)–Co(1)–Cl(3)	94.609(17)
		N(4)–Co(2)–Cl(3)^{ii}	110.226(43)
		N(6)–Co(2)–Cl(3)^{ii}	94.650(35)
		Cl(4)–Co(2)–Cl(3)^{ii}	143.882(19)
		Cl(3)–Co(2)–Cl(3)^{ii}	83.493(16)
		Co(2)–Cl(3)–Co(2)^{ii}	96.507(17)

Symmetry equivalents: (i) 1-x,1-y,1-z; (ii) –x,-y,-z

The cobalt complex **13b** featured striking structural similarities with copper complex **13a**·4H_2O exhibiting a dinuclear structure with both Co(II) ions held in a penta−coordination donor environment. The structural index parameter (τ) for complexes **13b** was found to be 0.50 which indicated that the coordination geometry of each Co(II) ion was intermediate between the square-pyramidal and trigonal−bipyramidal.[135] Two of the coordination sites on each cobalt(II) ion were occupied by pyridine and imine nitrogen donors of ligand Simpy through bidentate coordination mode. The remaining three coordination sites were fulfilled

by the chloride ions. The two cobalt(II) centers were held 3.585 Å apart from each other through two bridging chloride ions whereas the third chloride ion was coordinated as terminal ligand. The non–bridging chlorine atoms were oriented *trans* to each other. The average angles formed by the phenyl rings and thiophene rings with the ligand binding plane were 63.61° and 62.38° respectively. The Co(II)–N_{imine} distances, Co(II)–$N_{pyridine}$ distances and mean Co(II)–Cl distances were found to be 2.187 Å, 2.057 Å and 2.360 Å which were close to the reported values in analogous complexes.[568-570]

The crystal packing in **13b** can be considered as groups of molecules held together by –C–H···π interactions and hydrogen bonding interactions giving rise to supramolecular polymer like species as depicted in Figures 7.13 and 7.14. These –C–H···π interactions were arising from the participation of methyl hydrogens, pyridine rings, phenyl rings and thiophene rings. A detailed account of non-covalent interactions observed in the crystal structure of **13b** is given in Table 7.6. The three-dimensional packing diagram of complex **13b** is represented in Fig. 7.15.

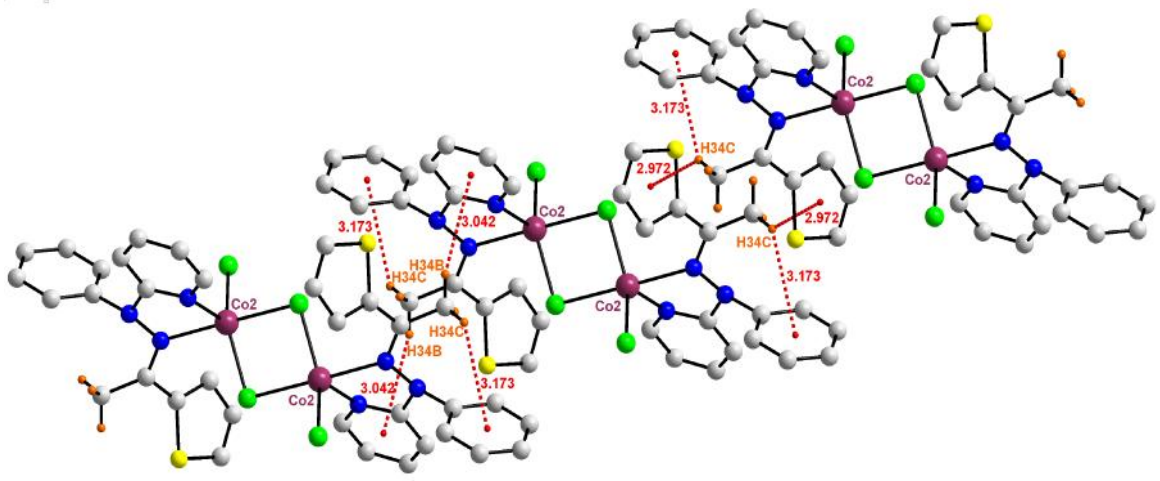

Fig. 7.13 C–H···π interactions in the crystal structure of [{Co(Simpy)(μ-Cl)Cl}$_2$] (**13b**)

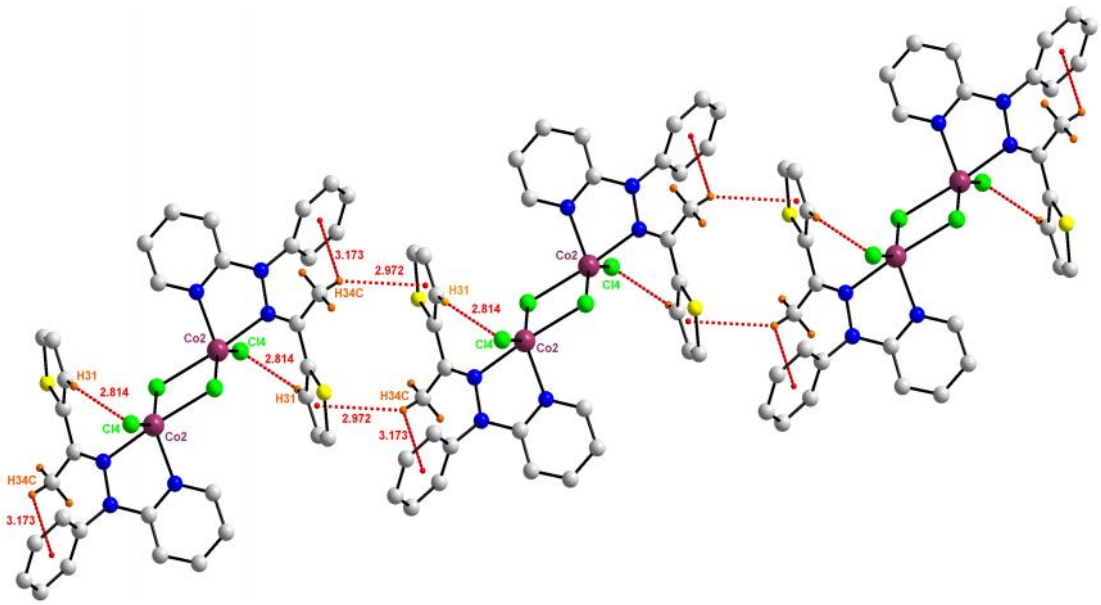

Fig. 7.14 C–H···π interactions and hydrogen bonding interactions in the crystal structure of [{Co(Simpy)(μ-Cl)Cl}$_2$] (**13b**)

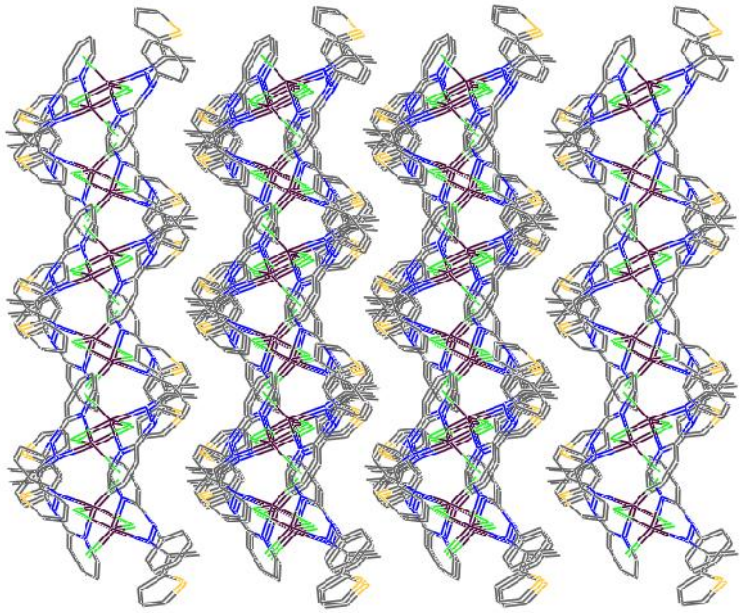

Fig. 7.15 Three-dimensional packing diagram of [{Co(Simpy)(μ-Cl)Cl}$_2$] (**13b**)

Table 7.6 Geometric parameters for non–covalent interactions of complex **13b**

DJH···A	DJH (Å)	D···A (Å)	H···A (Å)	DJH···A (˚)
C18JH18···Cl3	0.930(2)	3.477(2)[a]	2.899(1)[a]	121.59(12)[a]
C11JH11···N3	0.930(2)	3.010(2)[a]	2.801(1)[a]	93.84(12)[a]
C3JH3···Cl4	0.930(2)	3.588(2)[a]	2.979[a]	124.49(13)[a]
C1JH1···Cl1	0.930(2)	3.479(2)[a]	2.903(1)[a]	121.35(12)[a]
C17JH17A···N2	0.960(2)	2.765(2)[a]	2.520(1)[a]	94.48(12)[a]
C28JH28···N6	0.930(2)	3.012(2)[a]	2.801(1)[a]	93.97(12)[a]
C14JH14···Cl2	0.930(1)	3.632(2)[a]	2.818[a]	146.89(9)[a]
C14JH14···N3	0.930(1)	2.983(2)[a]	2.905(1)[a]	85.70(9)[a]
C34JH34A···N5	0.960(2)	2.757(2)[a]	2.506(1)[a]	94.77(12)[a]
C31JH31···Cl4	0.930(1)	3.632(2)[a]	2.814[a]	147.35(9)[a]
C31JH31···N6	0.930(1)	2.981(2)[a]	2.899(1)[a]	85.95(9)[a]
C17JH17B···S1	0.960(2)	3.259(2)[a]	2.758(1)[a]	113.24(11)[a]
C34JH34B···S2	0.960(2)	3.259(2)[a]	2.764(1)[a]	112.88(12)[a]
C20JH20···Cl2	0.930(2)	3.585(2)[b]	2.974[b]	124.65(13)[b]
C7JH7···Cl1	0.930(2)	3.686(2)[c]	2.960(1)[c]	136.02(12)[c]
C17JH17B···N1	0.960(2)	3.562(2)[d]	2.917(1)[d]	125.53(12)[d]
C24JH24···Cl3	0.930(2)	3.690(2)[e]	2.962[e]	136.17(12)[e]
C34JH34B···N4	0.960(2)	3.567(2)[f]	2.916(1)[f]	126.07(12)[f]

Symmetry equivalents: (a) x,y,z; (b) x-1,+y,+z; (c) x,+y-1,+z; (d) -x+1,-y,-z+1; (e) x,+y+1,+z; (f) -x,-y+1,-z

7.2.4. Catecholase activity

The complexes were investigated for their potential to exhibit catecholase like activity by catalyzing the oxidation of 3,5–di–*tert*–butylcatechol (3,5–DTBC) to 3,5–di–*tert*–butylbenzoquinone (3,5–DTBQ) in methanol medium. 3,5–DTBC was chosen as model substrate for catecholase activity studies due to its low redox potential facilitating its oxidation to quinone and bulky substituents which make further oxidation reactions such as ring opening much slower.[256] In the present family of complexes, only copper complex **13a**·4H_2O could exhibit significant catecholase–like activity. The time-dependent absorption spectral changes of complex **13a**·4H_2O (30 μM) in presence of 3,5–DTBC (100 equivalents)

are represented in Fig. 7.16. The gradual increment in the absorbance at 400 nm indicated the oxidation of 3,5–DTBC to 3,5–DTBQ.[252,256,571]

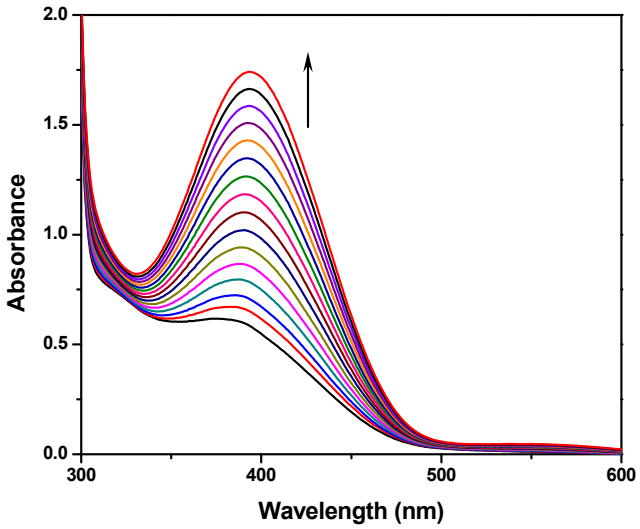

Fig. 7.16 Time–dependent absorption spectral changes exhibiting oxidation of 3,5–DTBC (3 mM) by complex **13a**·4H_2O (30 μM) in methanol over 2 h at 298 K under aerobic conditions

7.2.5. Nuclease activity

The nuclease activity of metal complexes was investigated by agarose gel electrophoresis by monitoring their ability to convert the supercoiled (SC) form of plasmid DNA to nicked (NC) form and/or linear (LC) form under physiological conditions. In the absence of external reagents like H_2O_2 or BME, only **13a**·4H_2O and **13b** could show appreciable nuclease activity. The results of the DNA cleavage activity exhibited by complexes **13a**·4H_2O and **13b** in the absence and presence of H_2O_2 (oxidizing agent) and BME (reducing agent) are shown in Fig. 7.17. It was observed that, in the absence of activators, complex **13a**·4H_2O could exhibit only single stranded DNA cleavage at a concentration of 50 μM which gave rise to the enhancement in the amount of NC form of DNA (Fig. 7.17, lane 5). However, at higher concentrations (100–200 μM), the band for the

SC form of DNA vanished with concomitant appearance of the LC form (Fig. 7.17, lane 6–7). Hence it was concluded that the complex **13a**·4H_2O could catalyze the double–stranded DNA cleavage also at higher concentrations. One important observation associated with the nuclease activity of complex **13a**·4H_2O was smearing of bands which occurred at higher complex concentrations. To investigate the effect of presence of activators on the extent of DNA strand scission, the experiments were also carried out in presence of H_2O_2 (200 μM) and varying concentrations of complex (50 μM–100 μM) (Fig. 7.17, lanes 8–9). Significant enhancement in the degree of cleavage was observed which ultimately gave rises to complete vanishing of the DNA band. Increase in the amount of NC form with concomitant appearing of LC form and complete vanishing of SC form could also be noticed with lower complex concentration in presence of BME (Fig. 7.17, lane 10). Smearing of bands could also be observed with BME when higher concentrations of **13a**·4H_2O (100 μM) were used (Fig. 7.17, lane 11). This type of smearing and vanishing of bands is indicative of extensive oxidative degradation of DNA.[490,572]

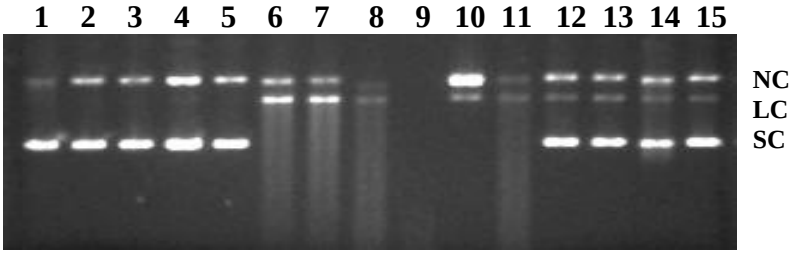

Fig. 7.17 Gel electrophoresis separation showing the cleavage of supercoiled pBR322 DNA (100 ng) by complexes **13a** and **13b** in presence of H_2O_2 (200 μM) and BME (200 μM). The samples were incubated at 37 ˚C for 2.5 h. Lane 1, DNA; lane 2, DNA + H_2O_2; lane 3, DNA + BME; lane 4, DNA + Simpy (200 μM); lanes 5–7, DNA + **13a** (50, 100 and 200 μM respectively); lanes 8–9, DNA + H_2O_2 + **13a** (50 and 100 μM respectively); lanes 10-11, DNA + BME + **13a** (50 and 100 μM respectively); lanes 12-13, DNA + **13b** (100 and 200 μM respectively); lane 14, DNA + H_2O_2 + **13b** (100 μM); lane 15, DNA + BME + **13b** (100 μM)

In case of complex **13b** simultaneous appearing of both NC and LC forms ascertained a double stranded scission of DNA (Fig. 7.17, lanes 12–13) however **13b** was found less effective in DNA cleavage than **13a**·$4H_2O$. The smearing of the bands enhanced in presence of H_2O_2 and BME predicting probably an oxidative nature of the DNA cleavage activity (Fig. 7.17, lanes 14–15).

7.3. Conclusions

A series of dinuclear copper(II) and cobalt(II) complexes derived from bidentate ligands has been synthesized and characterized by various physical and spectroscopic techniques. Molecular strctures of the representative complexes **13a**·$4H_2O$ and **13b** were authenticated by X-ray diffraction studies. Among these complexes, the copper complex **13a**·$4H_2O$ exhibited moderate catecholase like activity. Moreover, **13a**·$4H_2O$ and **13b** also exhibited extensive oxidative degradation of plasmid DNA through self–activating mechanism. Detailed kinetic investigations of catecholase activity and the mechanism of nuclease activity are in progress.

7.4. Experimental section

7.4.1. Reagents and materials

Analytical grade reagents Phenylhydrazine, 2–mercaptoethanol, hydrogen peroxide (S. D. Fine, Mumbai, India), sodium azide, 2–acetylthiophene, 3,5–di–*tert*–butylcatechol (Sigma Aldrich, Steinheim, Germany), ethylenediaminetetraacetic acid, copper chloride dihydrate, cobalt chloride hexahydrate (Merck Limited, Mumbai, India), sodium hydride and 2–chloropyridine (Acros organics, USA) were used as obtained. 2–(1–phenylhydrazinyl)pyridine was prepared according to the reported procedures.[332] The supercoiled pBR322 DNA was purchased from Bangalore Genei (India) and stored at 4 °C.

Agarose (molecular biology grade) and ethidium bromide were obtained from Sigma Aldrich. Catalase was obtained from Himedia Laboratories, India. Tris(hydroxymethyl)aminomethane–HCl (Tris–HCl) buffer and phosphate buffer were prepared in deionised water. Solvents used for spectroscopic studies were HPLC grade and purified by standard procedures before use.

7.4.2. Synthesis of ligands

Synthesis of 2J(1JphenylJ2J(1J(thiophenJ2Jyl)ethylidene)hydrazinyl)pyridine (Simpy)

A batch of 2–acetylthiophene (0.630 g, 5 mmol) was dissolved in 15 mL of methanol and 2 drops of concentrated hydrochloric acid were added to the solution. A batch of 2–(1–phenylhydrazinyl)pyridine (0.925 g, 5 mmol) dissolved in 10 mL of methanol was added to the reaction mixture and refluxed for 3 h. On slow evaporation of the reaction mixture, thick yellow colored needle shaped crystals of Simpy were obtained. Yield: (1.215 g, 83%); Anal. Calc. for $C_{17}H_{15}N_3S$ C, 69.59; H, 5.15; N, 14.32; S, 10.93; Found C, 68.87; H, 5.05; N, 14.79; S, 11.27. Selected IR data: 1583 ($\nu_{C=N}$), 1466, 1428, 1329, 1288, 1208, 1055, 733, 700. UV–visible [CH_3OH, λ_{max}/nm ($\varepsilon/M^{-1}cm^{-1}$)]: 202 (17748), 246 *sh* (11898), 267 (14602), 280 (14434), 350 *sh* (6534); ^{1}H NMR (500 MHz, δ/ppm, $CDCl_3$): 8.233 (d, J=4.5 Hz, 1H), 7.576 (t, J=8 Hz, 1H), 7.333-7.396 (m, 6H), 7.170 (t, J=7 Hz, 1H), 7.077 (t, J=4.5 Hz, 1H), 7.030 (d, J=8.5 Hz, 3H), 6.135 (t, J=6 Hz, 1H), 2.085 (s, 3H); ^{13}C NMR (500 MHz, δ/ppm, $CDCl_3$): 161.40, 159.07, 147.70, 145.60, 143.57, 137.48, 128.99, 128.75, 127.52, 127.33, 125.34, 125.01, 116.51, 111.62, 17.77. ESI–MS (acetonitrile, pos.): (m/z) 294.09 (2.3%) $[M+H]^+$, 316.08 (100%) $[M+Na]^+$, 332.05 (22.8%) $[M+K]^+$.

Synthesis of 2J(2Jbenzylidene J1J phenylhydrazinyl)pyridine (Impy)

A batch of 2–(1–phenylhydrazinyl)pyridine (0.925 g, 5 mmol) was dissolved in 10 mL of methanol and stirred over a magnetic stirrer. A batch of benzaldehyde (0.531 g, 5 mmol) dissolved in 10 mL of methanol was added to the reaction solution and stirred for 4 h. A yellow precipitate of Impy was obtained which was filtered and washed with little amount of methanol. Yield: (0.983 g, 72%); Anal. Calc. for $C_{36}H_{30}N_6Cl_4Co_2$ C, 79.10; H, 5.53; N, 15.37; Found C, 78.87; H, 5.64; N, 15.45. Selected IR data: 1581 ($\nu_{C=N}$), 1561, 1495, 1460, 1438, 1303, 1229, 1206, 1122. UV–visible [CH_3OH, λ_{max}/nm ($\varepsilon/M^{-1}cm^{-1}$)]: 204 (25222), 233 (20186), 324 (25476). MS: (m/z) 273 (5.79%).

7.4.3. Synthesis of metal complexes

Synthesis of [{Cu(Simpy)(«-Cl)Cl}$_2$]·4H$_2$O (13a·4H$_2$O)

A batch of copper(II) chloride dihydrate (0.171 g, 1 mmol) was dissolved in 5 mL of tetrahydrofuran and stirred over a magnetic stirrer. To this solution, a batch of ligand Simpy (0.293 g, 1 mmol) dissolved in 15 mL of tetrahydrofuran was added dropwise and the stirring was continued for further 6 h. A brownish–red precipitate was obtained which was filtered and washed with some amount of tetrahydrofuran and subsequently with diethylether. Yield (0.320 g, 75%); Anal. Calc. for $C_{34}H_{30}N_6Cl_4S_2Cu_2$ C, 47.72; H, 3.53; N, 9.82; S, 7.49; Found C, 47.33; H, 3.61; N, 9.92; S, 7.31. Selected IR data (KBr, ν_{max}/cm^{-1}): 1607 ($\nu_{C=N}$); $\Lambda_M/\Omega^{-1}cm^2mol^{-1}$ (ACN): 13; UV–visible [CH_3OH, λ_{max}/nm ($\varepsilon/M^{-1}cm^{-1}$)]: 204 (46160), 245 *sh* (29896), 268 (36970), 354 *sh* (15480); ESI–MS (acetonitrile, pos.): (m/z) 390.98 (44.7%) $[M\text{-}2Cl]^{2+}$, 448.94 (2.3%) $[M+2Na]^{2+}$, 816.95 (4.4%) $[M\text{-}Cl]^{+}$, 874.91 (0.9%) $[M+Na]^{+}$.

Synthesis of [{Co(Simpy)(«-Cl)Cl}$_2$] (13b)

The reaction was performed in similar manner as described for complex **13a**. Cobalt(II) chloride hexahydrate was taken in place of copper(II) chloride dihydrate and the product was obtained as bright green precipitate. Yield (0.270 g, 64%); Anal. Calc. for $C_{34}H_{30}N_6Cl_4S_2Co_2$ C, 48.24; H, 3.57; N, 9.93; S, 7.58; Found C, 47.99; H, 3.52; N, 10.01; S, 7.61. Selected IR data (KBr, ν_{max}/cm^{-1}): 1608 ($\nu_{C=N}$); $\Lambda_M/\Omega^{-1}cm^2mol^{-1}$ (ACN): 55; UV–visible [CH_3OH, λ_{max}/nm ($\varepsilon/M^{-1}cm^{-1}$)]: 204 (36306), 245 *sh* (27244), 266 (32828), 279 (31998), 350 (15316); ESI–MS (acetonitrile, pos.): (m/z) 386.99 (34%) $[M-2Cl]^{2+}$, 444.95 (3.7%) $[M+2Na]^{2+}$, 808.96 (32.9%) $[M-Cl]^{+}$, 866.92 (1.9%) $[M+Na]^{+}$.

Synthesis of [{Cu(Impy)(«-Cl)Cl}$_2$] (14a)

The reaction was performed in similar manner as described for complex **13a** except that Impy was used as ligand in place of Simpy. The complex was obtained as microcrystalline green colored compound. Yield (0.222 g, 54%); Anal. Calc. for $C_{36}H_{30}N_6Cl_4Cu_2$ C, 53.02; H, 3.71; N, 10.30; Found C, 52.85; H, 3.74; N, 10.02. Selected IR data (KBr, ν_{max}/cm^{-1}): 1607 ($\nu_{C=N}$); $\Lambda_M/\Omega^{-1}cm^2mol^{-1}$ (ACN): 15; UV–visible [CH_3OH, λ_{max}/nm ($\varepsilon/M^{-1}cm^{-1}$)]: 205 (44620), 233 (43330), 326 (46638).

Synthesis of [{Co(Impy)(«-Cl)Cl}$_2$] (14b)

The reaction was performed in similar manner as described for complex **13b** except that Impy was used as ligand in place of Simpy. The reaction mixture was reduced in volume to 8 mL *in vacuo* affording a green precipitate. Yield (0.201 g, 50%); Anal. Calc. for $C_{36}H_{30}N_6Cl_4Co_2$ C, 53.62; H, 3.75; N, 10.42; Found C, 53.18; H, 3.81; N, 10.26. Selected IR data (KBr, ν_{max}/cm^{-1}): 1608 ($\nu_{C=N}$); $\Lambda_M/\Omega^{-1}cm^2mol^{-1}$ (ACN): 57; UV–visible [CH_3OH, λ_{max}/nm ($\varepsilon/M^{-1}cm^{-1}$)]: 205 (42856), 233 (46196), 325 (54794).

7.4.4. X–ray crystallography

The X–ray data collection and processing for [{Cu(Simpy)(μ-Cl)Cl}$_2$]·4H_2O (**13a**·4H_2O) and [{Co(Simpy)(μ-Cl)Cl}$_2$] (**13b**) were performed at 296 K and 273 K respectively, on Bruker Kappa Apex–II CCD diffractometer by using graphite monochromated Mo–Kα radiation (λ = 0.71073 Å) with a maximum $^{-}$ range of 29°. The details regarding the structure solution and refinement are similar to those described in previous chapters. The matrix parameters for **13a**·4H_2O and **13b** are listed in Table 7.7.

Table 7.7 Crystallographic parameters and refinement details for **13a**·4H_2O and **13b**

	13a·4H_2O	**13b**
Empirical formula	$C_{34}H_{30}Cl_4N_6S_2O_4Cu_2$	$C_{34}H_{30}Cl_4N_6S_2Co_2$
Formula weight (gmol^{-1})	919.68	846.44
Temperature /K	296(2)	273(2)
λ (Å) (Mo-Kα)	0.71073	0.71073
Crystal system	Monoclinic	Triclinic
Space group	*C 2/c*	*P -1*
a (Å)	15.5620(14)	8.6665(9)
b (Å)	9.0065(8)	9.8935(10)
c (Å)	28.593(3)	20.639(2)
~ (°)	90.00	89.228(4)
γ (°)	90.00	89.998(5)
β (°)	95.301(5)	89.885(4)
V (Å^3)	3990.4(6)	1769.5(3)
Z	4	2
ρ_{calc} (gcm^{-3})	1.531	1.589
F(000)	1864	860.00
Theta range for data collection	2.85 − 29.36	2.06 −28.69
Index ranges	$-19 < h < 19$, $-9 < k < 11$, $-35 < l < 33$	$-11 < h < 11$, $-13 < k < 13$, $-22 < l < 27$
Refinement method	Full matrix least–squares on F^2	Full matrix least–squares on F^2
Data/restraints/parameters	4024/0/236	9133/0/436
GOF[a] on F^2	1.137	1.034
R_1[b] [$I > 2\sigma(I)$]	0.0627	0.0395
R_1[all data]	0.0769	0.0538
wR_2[c] [$I > 2\sigma(I)$]	0.1985	0.1021
wR_2 [all data]	0.2149	0.1126

7.4.5. Catecholase activity

Catechol oxidase activities of metal complexes were measured at 25 °C by time–dependent UV–visible spectroscopy. Solutions of complexes (30 μM) were treated with 100 equivalents of 3,5–di–*tert*–butylcatechol dissolved in dioxygen saturated methanol. No base was added to the solution in order to suppress oxidation of substrate by base. Catalytic oxidation of model substrate was evaluated spectrophotometrically over 2 h by monitoring the increase in absorbance at 400 nm with the intervals of 10 min under aerobic conditions.

7.4.6. DNA cleavage experiments

Cleavage of plasmid DNA (pBR322) was monitored by using agarose gel electrophoresis technique. Supercoiled pBR322 DNA (100 ng) in Tris–boric acid–EDTA (TBE) buffer (pH 8.2) was treated with metal complexes (50–200 μM) in the absence or presence of additives like H_2O_2 (200 μM) and BME (200 μM). The samples were incubated for 2.5 h at 37 °C followed by the addition of loading buffer (25% bromophenol blue and 30% glycerol) prior to the gel electrophoresis. The details regarding the procedure of DNA cleavage experiments have been described in previous chapters.